Department Chemie und Pharmazie

Friedrich-Alexander-Universität
Naturwissenschaftliche Fakultät

Tailoring the Surface Composition of Ionic Liquid-based Metal Complex Solutions for Supported Ionic Liquid Phase Catalysis

Maßgeschneiderte Oberflächenzusammensetzung von Metallkomplexlösungen auf Basis Ionischer Flüssigkeiten für die Supported Ionic Liquid Phase Katalyse

Der Naturwissenschaftlichen Fakultät
der Friedrich-Alexander-Universität Erlangen-Nürnberg

zur Erlangung des Doktorgrades Dr. rer. nat.

vorgelegt von

DANIEL HEMMETER

aus Weißenburg i. Bay.

Als Dissertation genehmigt von der Naturwissenschaftlichen Fakultät
der Friedrich-Alexander-Universität Erlangen-Nürnberg

Tag der mündlichen Prüfung:	01.10.2024
Gutachter:	Prof. Dr. Hans-Peter Steinrück Prof. Dr. Jörg Libuda Prof. Dr. Peter Licence (University of Nottingham, United Kingdom)

Contents

Published Papers

[P1] Formation and Surface Behavior of Pt and Pd Complexes with Ligand Systems Derived from Nitrile-functionalized Ionic Liquids Studied by XPS

D. Hemmeter, U. Paap, N. Taccardi, J. Mehler, P. S. Schulz, P. Wasserscheid, F. Maier, H.-P. Steinrück

ChemPhysChem **2023**, *24*, e202200391.

The author's contribution is the sample preparation including synthesis of the complexes, ARXPS and QMS investigation, data analysis, data interpretation and manuscript preparation.

[P2] The Buoy Effect: Surface Enrichment of a Pt Complex in IL Solution by Ligand Design

D. Hemmeter, D. Kremitzl, P. S. Schulz, P. Wasserscheid, F. Maier, H.-P. Steinrück

Chem. Eur. J. **2023**, *29*, e202203325.

The author's contribution is the sample preparation including synthesis of the complexes, ARXPS investigation, data analysis, data interpretation and manuscript preparation.

[P3] Structure and Surface Behavior of Rh Complexes in Ionic Liquids Studied Using Angle-Resolved X-ray Photoelectron Spectroscopy

D. Hemmeter, U. Paap, F. Maier, H.-P. Steinrück

Catalysts **2023**, *13*, 871.

The author's contribution is the sample preparation, ARXPS investigation, data analysis, data interpretation and manuscript preparation.

[P4] Understanding the Buoy Effect of Surface-Enriched Pt Complexes in Ionic Liquids: A Combined ARXPS and Pendant Drop Study

D. Hemmeter, U. Paap, N. Wellnhofer, A. Gezmis, D. Kremitzl, P. Wasserscheid, H.-P. Steinrück, F. Maier

ChemPhysChem **2023**, *24*, e202300612.

The author's contribution is the sample preparation including synthesis of the complexes, ARXPS investigation, data analysis, data interpretation and manuscript preparation.

[P5] Exploring the Interfacial Behavior of Ruthenium Complexes in Ionic Liquids: Implications for Supported Ionic Liquid Phase Catalysts

D. Hemmeter, L. Sanchez Merlinsky, L. M. Baraldo, F. Maier, F. J. Williams, H.-P. Steinrück

Phys. Chem. Chem. Phys. **2024**, *26*, 7602-7610.

The author's contribution is the sample preparation, ARXPS and QMS investigation, data analysis, data interpretation and manuscript preparation.

[P6] Tailoring the Surface Enrichment of a Pt Catalyst in Ionic Liquid Solutions by Choice of the Solvent

D. Hemmeter, A. Gezmis, D. Kremitzl, P. Wasserscheid, F. Maier, H.-P. Steinrück

Adv. Mater. Interfaces **2024**, *11*, 2301085.

The author's contribution is the sample preparation including synthesis of the complexes, ARXPS investigation, data analysis, data interpretation and manuscript preparation.

[P7] Unlocking the Fluorine-Free Buoy Effect: Surface-Enriched Ruthenium Polypyridine Complexes in Ionic Liquids

L. Sanchez Merlinsky, D. Hemmeter, L. M. Baraldo, F. Maier, H.-P. Steinrück, F. J. Williams

ChemistryOpen **2024**, *13*, e202400092.

Shared first authorship with L. Sanchez Merlinsky. The author's contribution is the sample preparation, ARXPS investigation, data analysis, data interpretation and manuscript preparation.

[P8] Hydrogenation with Dissolved Pt-complexes Homogenously Distributed in the Ionic Liquid or Enriched at the Gas/Ionic Liquid Interface

S. Khan Antara, D. Hemmeter, Z. Zhai, D. Kremitzl, F. Maier, T. M. Koller, H.-P. Steinrück, M. Haumann

ChemCatChem **2024**, *16*, e202400574.

The author's contribution is the sample preparation including synthesis of the complexes for all collaborative groups and the ARXPS-related contributions (including investigation, data analysis, data interpretation and manuscript preparation regarding the ARXPS results).

Acknowledgments/Danksagungen

Zunächst bedanke ich mich bei Herrn Prof. Dr. Hans-Peter Steinrück für die langjährige Unterstützung, die mir spürbar während unserer Zusammenarbeit und zuvor als Student zukam. Ich habe Ihre beeindruckenden Mentoreigenschaften, Ihre Erfahrung und wertvollen Ratschläge in allen Belangen sehr zu schätzen gewusst und bin stolz, mit einem solch erfolgreichen Wissenschaftler zusammengearbeitet haben zu dürfen. Weiterhin danke ich Ihnen für die Unterstützung bei den erfolgreichen Bewerbungen für Stipendien der Studienstiftung des Deutschen Volkes und des Verbandes der Chemischen Industrie.

Ebenso danke ich Dr. Florian Maier für die vertrauensvolle und angenehme Betreuung auf Augenhöhe. Vor allem bin ich dankbar für die produktiven Impulse, die inspirierenden Diskussionen und für deine Maier'schen Feinschliffe bei den finalen Forschungsergebnissen, die wesentlich zum Erfolg dieser Arbeit beigetragen haben. Danke auch für deinen Einsatz bei der Bewerbung für das Kekulé-Stipendium.

Besonderer Dank gilt auch meinen Laborkollegen Dr. Francesco Greco und Dr. Ulrike Paap, die mich ausführlich an die Oberflächenforschung herangeführt und eine freundschaftliche Arbeitsatmosphäre im Labor ermöglicht haben. Weiterhin danke ich Dr. Jade Barreto für die angenehme Zeit im Labor gegen Ende meiner Arbeit.

Danke auch an alle weiteren aktiven und ehemaligen Mitglieder der IL-Gruppe mit denen ich zusammenarbeiten durfte: Dr. Rajan Adhikari, Dr. Radha Gobinda Bhuin, Afra Gezmis, Dr. Bettina Heller, Dr. Simon Jaekel, Dr. Matthias Lexow, Dr. Stephen Massicot, Dr. Manuel Meusel, Dr. Sunghwan Shin, Timo Talwar und Dr. Leonhard Winter. Vielen Dank für die nette Arbeitsatmosphäre!

Ich bin ebenso sehr dankbar für die technische Unterstützung von Bernd Kreß, Hans-Peter Bäumler und Norman Anja Schmidt, die jederzeit mit ihrer Erfahrung und Expertise bei allen Problemen zur Verfügung standen. Danke auch für die schönen sportlichen Momente beim Fußball, Bernd und HP!

Großer Dank gilt auch allen Weiteren, die das angenehme Zusammenwirken am Lehrstuhl ermöglichen und immer zur Unterstützung zur Verfügung stehen: Dr. Andreas Bayer, Susana Kreß und Andrea Meixner-Wolf, das Werkstattteam, Andrea Buchner, Gertrud

Weiß und Martin Kolacyak. Gleichermaßen möchte ich allen weiteren Mitgliedern und Ehemaligen des Lehrstuhls für die besondere Zeit danken.

Dankeschön auch an die Kollaborationspartner vom Lehrstuhl für Chemische Reaktionstechnik (CRT) Prof. Dr. Peter Wasserscheid, Prof. Dr. Marco Haumann, Dr. Nicola Taccardi, Dr. Julian Mehler und Sharmin Khan Antara. Ich bin sehr dankbar für euere katalytische und synthetische Expertise und den produktiven Austausch mit euch. Ein spezieller Dank gilt Daniel Kremitzl, der mit erfolgreichen Synthesen einen sehr großen Beitrag zum Erfolg dieser Arbeit beigetragen hat. Ein weiterer Dank gilt Dr. Andreas Bösmann für die zuverlässigen Dichtemessungen von ILs und Katalysatorlösungen. Ebenso danke ich Alexander Bergen und Prof. Dr. Karsten Meyer vom Lehrstuhl für Anorganische und Allgemeine Chemie sowie Dr. Thomas Koller und Ziwen Zhai vom Institute of Advanced Optical Technologies für die anregenden Gespräche und effiziente Zusammenarbeit.

I'm very grateful for the collaboration with Prof. Dr. Federico Williams and Luciano Sanchez Merlinsky. Thank you so much for the enjoyable and productive times we spent together in the DASSA lab. Also, thanks to Prof. Dr. Luis M. Baraldo for his synthetic expertise and creative impulses.

I also want to thank James F. Wishart for hosting my stay at Brookhaven National Laboratory in New York and making this memorable time in the USA possible. Thanks to Matthew Bird, Andrew Cook, Rupali Ganesh Deokar, Katie Huber, Kazuhiro Iwamatsu, Bobby Layne, Lakshmy Kannadi Valloli and Nicole Zmich for welcoming me so kindly.

Ich bedanke mich besonders bei der Stiftung Stipendien-Fonds des Verbandes der Chemischen Industrie (VCI) für die Unterstützung meiner Arbeit im Rahmen des Kekulé-Stipendiums.

Ein wichtiger Dank geht an meine Freunde Nicolas Johner, Saskia Prusch, Lilli Reißenweber, Moritz Schwind und Raphael Tonn, die ich im Laufe meines Studiums kennenlernen und unvergessliche Stunden mit ihnen verbringen durfte.

Die letzten Danksagungen widme ich meiner Partnerin Anna-Lisa, meinen Eltern und Brüdern, die mich mit ihrer Liebe, ihrem Rückhalt und ihrer Unterstützung immer angetrieben und einen besinnlichen Rückzugsort geboten haben.

1 Introduction

Modern science and technology are substantially shaped by the need for sustainable manufacture and processing of materials across the value chain. One major objective to be addressed is the comprehensive transformation of the chemical industry towards processes with efficient avoidance or recycling of waste and secondary products.[1] With special focus on atom-economical and selective conversions, it is safe to say that the development, optimization and upscaling to commercial operation of novel catalytic systems play a decisive role for this paradigm change.[2]

The overall performance of catalysts is essentially influenced by the microscopic nature, i. e. composition, structure and electronic properties of the active sites.[3, 4] Technical heterogeneous catalysts feature a non-uniform and defect-rich surface structure and thus an intricate spectrum of catalytic centers differing in activity and selectivity.[5] Especially for the production of more value-added products, the very selectivity problem poses economic and ecological limitations, owing to the required separation of the product mixture.[6-8] Despite significant progress in increasing the selectivity of heterogeneous catalysts in recent decades[9-11], homogeneous organometallic catalysis has gained increasing appeal providing uniform reactivity with well-accessible information on structure-performance relationships.[12] Based on this knowledge, the structural variability of organometallic chemistry in solution affords deliberate design of the catalysts and thus sensitive control over activity and selectivity on the molecular level. However, in contrast to heterogeneous systems, costly procedures for catalyst separation and recovery can limit lucrative application[13].

With the aim of combining the facile engineering of heterogeneous systems and the powerful catalytic performance of metal complexes, techniques for immobilization of homogeneous catalysts in product-separable phases have received significant attention.[14, 15] One intensively investigated approach is the heterogenization of organometallics by physicochemical grafting onto the surface of solid support materials, e. g. by covalent bonding[16] or electrostatic interactions[17]. However, the static fixation can considerably compromise the tunability and characterizability, and can impose negative effects on activity and selectivity[18, 19] – the principal advantages of homogeneous organometallic catalysis. As a consequence, the productivity of these systems for commercial use has been questioned.[19] An alternative strategy addresses immobilization of the homogeneous catalyst

in a supported liquid phase (SLP).[20, 21] For this, a solid high-surface area support is impregnated with a thin film of catalyst solution. The macroscopic properties of the catalytic system are still governed by the powdery support material affording the favorable reaction engineering of heterogeneous catalysis with efficient separation of catalyst and products. Within the immobilized liquid film, however, the well-defined homogeneous surrounding principally grants the full spectrum of chemical preferences provided by organometallic catalysis. This concept is illustrated in *Figure 1a*.

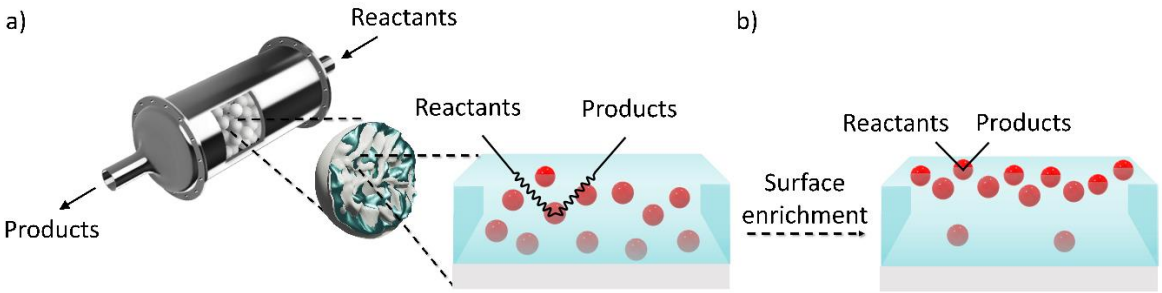

Figure 1: Schematic representation of the supported liquid phase (SLP) concept (for ionic liquids: supported ionic liquid phase, SILP) a) from the macroscopic (left) to the microscopic scale (right) and b) reduction of the diffusion pathways of reactants and products upon enrichment of the catalytically active species (red spheres) at the liquid/gas interface.

Ionic liquids (ILs) have afforded immense scope for scientific and technological innovation for this type of catalyst immobilization, termed as the supported ionic liquid phase (SILP) concept.[22] ILs are salts typically comprising bulky organic cations and/or anions with low charge density, yielding low melting points, oftentimes below room temperature. Given their ionic character, ILs show quasi negligible vapor pressures and therefore intrinsically provide coatings with excellent persistence toward leaching into the surrounding gas phase, even after extensive time-on-stream, e. g. more than 800 h in Rh-catalyzed hydroformylation[23]. The mostly organic backbone of the ions, on the other hand, affords task-specific molecular design for deliberate tuning of physicochemical properties for optimum performance regarding, for instance, solvation and coordination behavior, hydrophobicity, miscibility and wetting capability. SILP systems have been successfully trialed for various other industry-relevant conversions, such as hydrogenation[24, 25], hydroformylation[26, 27], carbonylation[28] and hydrosilylation[29, 30], to name but a few. Beyond that, a study by Werner *et al.* demonstrated the adaptable character of the SILP concept by systematically varying the IL, the support material and the catalyst complex achieving remarkably mild conditions in water-gas-shift catalysis.[31]

In this context, a fundamental understanding on the nature of the IL/gas interface offers interesting parameters for optimization in SILP catalysis.[32] In principle, a particularly high catalyst concentration directly at the IL/gas interface, where the feedstock concentration is at its maximum, would result in most efficient catalyst utilization, as is signified in *Figure 1b*. This benefit becomes particularly obvious considering the high viscosities of ILs and thus the much slower diffusion rates of dissolved solutes in solution compared to conventional solvents[33-35]; surface enrichment of the catalyst would minimize the diffusion pathways in the liquid phase. The interfacial behavior of organometallic complexes in ILs, however, has received little attention in literature. Early works on the composition of the IL/vacuum interface of dissolved metal compounds in ILs in our group has revealed strong enrichment of $[Pt(NH_3)_4]^{2+}$ in $[C_2C_1Im][C_2OSO_3]$, while Cl^- counterions were found depleted from the surface using angle-resolved X-ray photoelectron spectroscopy (ARXPS).[36] This surface activity was attributed to the higher polarizability of the larger metal-containing cation.[36] A subsequent study found the phosphine ligand TPPTS as a suitable surface-active ligand to trigger surface enrichment, while the precursor complex without TPPTS did not exhibit surface affinity.[37] A more recent investigation by the groups of *J. M. Slattery* and *T. K. Minton* identified a Ru complex carrying a trioctylphosphine and a *para*-cymene ligand as highly affine to the IL/vacuum interface using reactive-atom scattering (RAS), time-of-flight secondary ion mass spectrometry (TOF-SIMS) and XPS.[38]

This PhD work aims at providing the fundamental parameters for deliberate control over the local catalyst concentration at the IL/vacuum interface using ARXPS. This technique provides not only detailed insights into the surface composition of the samples but also chemical information on the metal complexes under investigation. After the introductory *Chapters 1, 2* and *3*, the results obtained in this thesis will be presented in *Chapter 4*. *Chapter 4.1* addresses the interfacial behavior and interesting chemical properties of a variety of catalysts with different ligand systems and how to deliberately modify the ligands to achieve enrichment at the IL/vacuum interface. In particular, specific groups attached to the ligands that "pull" the complex towards the interface in a buoy-like fashion will be presented. *Chapters 4.2 – 4.4* discuss the influence of the bulk concentration, temperature and the solvent on surface enrichment effects of catalysts established in *Chapter 4.1*.

2 Fundamentals

2.1 X-ray Photoelectron Spectroscopy (XPS)

X-ray photoelectron spectroscopy is among the most powerful and frequently used ultra-high vacuum (UHV)-based surface science methods and was applied as the primary experimental technique in this work. The kinetic energy profile of photoelectrons emitted from a material upon irradiation with X-rays yields quantitative insights into the composition of the near-surface region along with chemical information, e. g. on oxidation state, bonding conditions and other interactions of the atoms under investigation.

The photoelectric effect provides the basis for this technique and the fundamental considerations will be discussed along *Figure 2* in the following. Interaction of matter with photons of the energy $h\nu$, which exceeds the sum of the binding energy E_B and the work function of the material Φ_{mat}, yields emission of photoelectrons with a defined kinetic energy E_{kin}. Using an energy-dispersive spectrometer/analyzer with the work function Φ_{sp}, $E_{kin,sp}$ is accessible. Typically, XP spectra are presented as the counts of photoelectrons detected per second ("intensity") against E_B, which can be obtained from *Equation* (*Eq*) *1*, as is evident from *Figure 2*. The Fermi energies E_F of a conductive sample and the spectrometer are aligned by connecting them electrically.

$$E_B = h\nu - E_{kin,sp} - \Phi_{sp} \qquad (Eq\ 1)$$

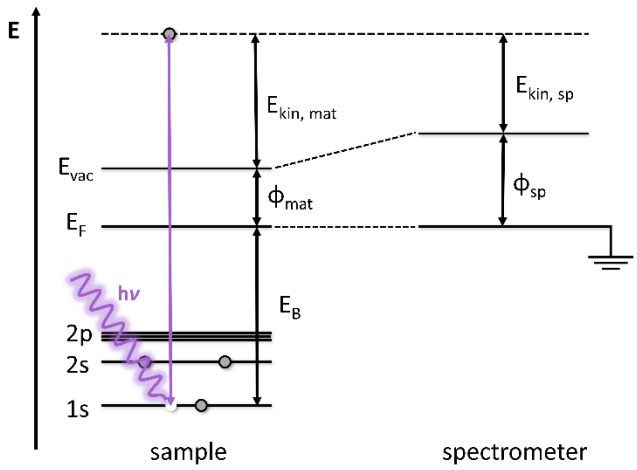

Figure 2: Schematic energy level diagram for photoemission of an 1s electron and detection using an energy-dispersive spectrometer.

The detected binding energy is sensitive to the element and its chemical environment, while the signal intensity quantitatively reflects the atomic composition of the material within the accessible information depth (ID). The ID corresponds to the depth, from where ~95% of the photoelectrons contributing to a certain XP signal originate, considering only inelastic scattering.[39] It can be described by

$$ID = 3\,\lambda_{(E_{kin})} \cos\vartheta \qquad (Eq\ 2)$$

where $\lambda_{(Ekin)}$ is the inelastic mean free path (IMFP), which depends on the kinetic energy of the photoelectrons, and ϑ is the emission angle with respect to the surface normal. Upon passing the sample towards the analyzer, the intensity, I, of the photoelectrons is attenuated, according to the exponential decay

$$\frac{I}{I_0} = e^{\frac{-d}{\lambda_{(E_{kin})} cos\vartheta}} \qquad (Eq\ 3)$$

where I_0 is the non-attenuated intensity and d is the distance travelled through the sample. With typical λ values in lab-based XPS being lower than 4 nm in solid/liquid matter,[40, 41] *Equations 2* and *3* reflect the intrinsic sensitivity of XPS to the sample/vacuum interface. As is also evident from these equations and from *Figure 3*, the surface sensitivity of XPS can be tuned upon variation of the electron emission angle ϑ – a technique referred to as angle-resolved XPS (ARXPS). At 0° (normal emission), the ID is 6 – 9 nm in organic materials,[42] which corresponds to several molecular layers in the surface near region of the sample, and the spectra typically reflect the nominal composition. However, even for these relatively bulk-sensitive measurements, strong surface enrichment effects can cause significant deviations from the nominal composition, as was observed multiple times during the herein presented work (see *Chapter 4*). At 80° (grazing emission), the ID decreases to 1.0 – 1.5 nm, which mainly reflects the topmost molecular layer of the sample.[42]

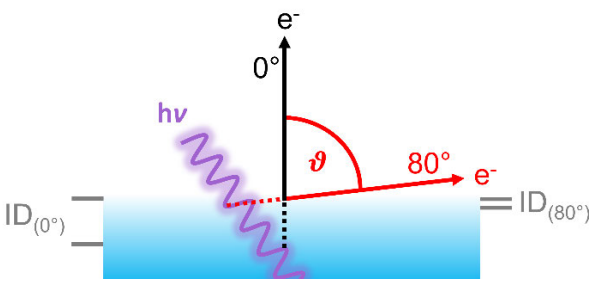

Figure 3: Angular dependency of the surface sensitivity in X-ray photoelectron spectroscopy (XPS).

2.2 Ionic Liquids and their Structure at the IL/gas Interface

Even though the first ever report on an IL dates back to more than a century ago[43] (see Ref. 44 for an historic review on ILs), it was only over the past few decades that they have received intense attention for applications in manifold fields of research. Among many more, these range from catalysis[32, 45, 46] to electrochemical devices[47, 48], organic synthesis[49, 50] and lubricants[51, 52]. In a rather small but growing number of cases, ILs have also been successfully utilized in piloted or commercialized processes.[53]

The low melting point of ILs is the result of preventing high lattice energies by using bulky ions with low symmetry and charge density. A selection of cations and anions frequently used in ILs is shown in *Figure 4*. The cationic backbones are commonly derived from heterocyclic structures, such as imidazolium, pyrrolidinium or piperidinium, or are ammonium- or phosphonium-based. Frequently used anions feature fluorinated moieties, such as in $[Tf_2N]^-$, $[TfO]^-$ and $[PF_6]^-$, which, however, can raise environmental and safety concerns due to toxicity and bioaccumulation,[54, 55] or release of toxic products upon hydrolysis[56]. Fluorine-free anions, such as acetate $[OAc]^-$, alkylsulfates $[C_nOSO_3]^-$, or amino acid-based anions have received increasing interest offering less concerning alternatives.[57, 58]

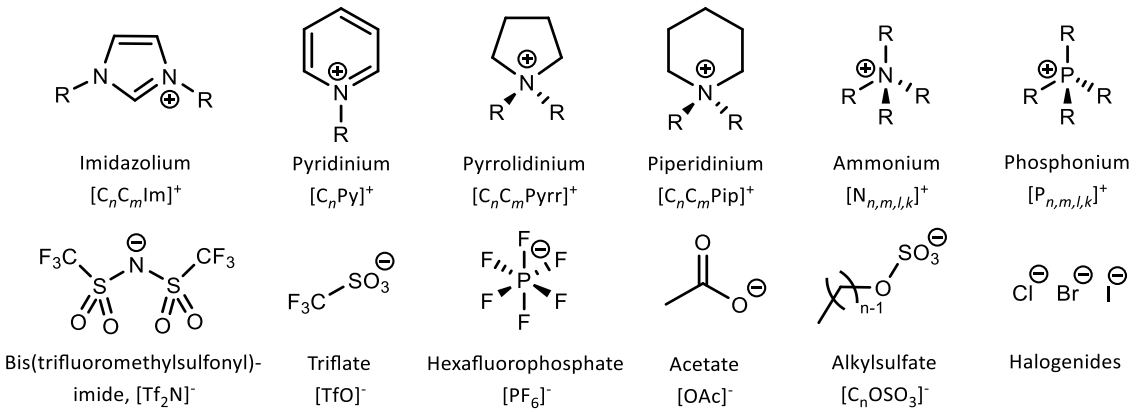

Figure 4: Common cations (top) and anions (bottom) in ILs.

A deep understanding on the versatile spectrum of interactions and the resulting structural organization in ILs is essential for their effective and task-specific utilization.[59] For various applications, this particularly holds true for the composition and structure of the IL/gas interfacial region.[32, 60] The IL/gas or vacuum interface has been thoroughly accessed with a wide array of surface-sensitive methods to extract the surface composition

of neat ILs and mixtures including preferred surface orientations and configurations of ions and functional groups, surface layering, and enrichment effects.[60-82]

In particular, ARXPS was intensively used by many groups, including ours, to study the IL/vacuum interface.[68, 71, 83-90] The following ARXPS characterization of the well-studied IL $[C_4C_1Im][PF_6]$ is intended to serve as an example for showcasing typical compositional or orientational peculiarities at the IL/vacuum interface. A detailed ARXPS study on this IL was already published before by our group.[88]

Figure 5 depicts a survey scan and high-resolution region scans of the C 1s, N 1s and F 1s region of $[C_4C_1Im][PF_6]$ at 0° (normal emission, more bulk-sensitive, black) and 80° emission angle (grazing emission, more surface-sensitive, red). For both angles, the survey

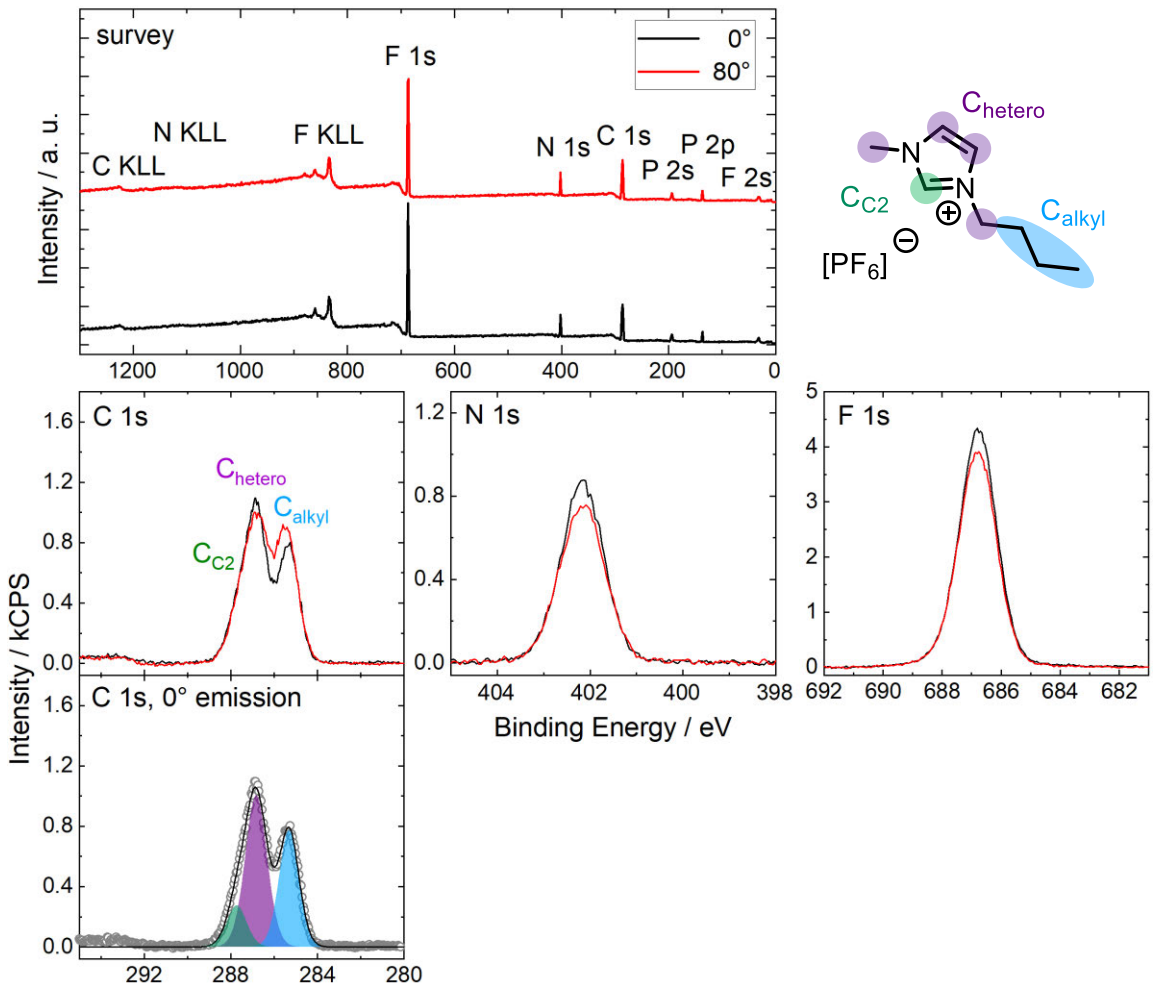

Figure 5: Survey, C 1s, N 1s and F 1s XP spectra of neat $[C_4C_1Im][PF_6]$ in 0° (black) and 80° emission (red). Additionally, the applied color-coded deconvolution for the C 1s region is shown for the 0° emission spectrum (see peak assignments and chemical structure).

scan shows signals for all core levels expected from the molecular structure of clean $[C_4C_1Im][PF_6]$. The broad signal envelope detected in the C 1s region from ~289 to 284 eV includes all the carbon species of $[C_4C_1Im]^+$. A typical deconvolution procedure involves distinction of three different types of C atoms contributing to the signal envelope: C atoms bound to two heteroatoms, C_{C2} (green), C atoms bound to one heteroatom, C_{hetero} (violet), and C atoms bound to only other carbon atoms and hydrogen, C_{alkyl} (blue).[42, 88] The applied deconvolution with color-coded peaks is shown for the 0° emission spectrum in *Figure 5*. The N 1s and F 1s regions show single peaks at 402.2 and 686.8 eV, corresponding to the N atoms bound within the imidazolium ring, N_{Im}, and the F atoms of the $[PF_6]^-$ anion, respectively.

Comparing 0° and 80° spectra affords insights into the orientation of ions in the outermost layer and on segregation effects in IL mixtures and solutions at the IL/vacuum interface. The C_{alkyl} signal shows a higher intensity at 80°, while all other signals slightly decrease. These observations are due to a preferential orientation of the $[C_4C_1Im]^+$ cation terminating the surface with its C_4 chains, while the imidazolium ring and the anions reside below this domain of alkyl chains. This effect is well-known for imidazolium-based ILs with extended alkyl chains (number of carbon atoms $n \geq 4$), which typically show a higher degree of surface activity than shorter chains.[60, 67, 68, 79, 80] The magnitude of the enrichment of the alkyl chains at the IL/vacuum interface was found to be highly dependent on the size of the anion, with smaller anions facilitating a more densely packed alkyl surface layer [68, 91, 92]. Also, different functionalities attached to the alkyl substituents can lead to an entirely different surface activity[71, 88].

Apart from these orientational or configurational effects, mixtures or solutions of ILs can also exhibit an enrichment of one or more components at the surface, that is, an enhanced surface concentration of these components relative to the bulk concentration.[36, 37, 68, 72, 77, 93-98] Recently, this effect has been demonstrated for binary mixtures of the fluorinated IL $[PFC_4C_1Im][PF_6]$ and the non-fluorinated analog $[C_4C_1Im][PF_6]$.[88] Using ARXPS, the fluorinated $[PFC_4C_1Im]^+$ cations were found significantly enriched at the IL/vacuum interface with the PFC_4 chains preferably terminating the surface.[88] The surface affinity of $[PFC_4C_1Im][PF_6]$ induced by the PFC_4 chains also inspired the ligand design for surface enrichment of a Pt complex presented in this work.[P2, P4, P6, P8]

3 Experimental Details

3.1 Materials and Sample Preparation

ILs and metal complexes employed within the framework of this thesis are presented in *Tables 1* and *2*, respectively, including the abbreviations used, full names, molecular weights and molecular structures. Note that the metal complexes will be referred to as "catalysts" in the following, even though some of the employed complexes might not have proven yet to be catalytically active for a specific reaction.

[C_2C_1Im][PF_6] (synthesis grade) was purchased from Sigma-Aldrich. Since surface-active contaminations were found using XPS, the IL was extracted using toluene according to the procedure detailed in [P6]. [C_2C_1Im][OAc] (purity 98%), [C_4C_1Im][Cl] (purity 99.5%), [C_2C_1Im][C_2OSO_3], [C_4C_1Im][PF_6] (purity 99% and 99.5%), [C_8C_1Im][PF_6], [C_4C_1Im][Tf_2N], [C_2C_1Im][TfO], [C_4C_1Im][TfO] and [C_8C_1Im][TfO] (all purity 99%) were purchased from Iolitec. [C_3CNC_1Im][Tf_2N] was synthesized by Dr. Julian Mehler (Chair of Chemical Engineering I, Friedrich-Alexander-Universität (FAU) Erlangen-Nürnberg), and [C_1CNC_1Pip][Tf_2N] was synthesized by Dr. Nicola Taccardi (Chair of Chemical Engineering I, FAU Erlangen-Nürnberg) according to the procedures presented in [P1]. [C_3CNC_1Im][PF_6] and [C_3CNPFC_4Im][PF_6] were synthesized by Daniel Kremitzl (Chair of Chemical Engineering I, FAU Erlangen-Nürnberg) according to procedures presented in [P2] and [P4]. *Cis*-[$PtCl_2(CH_3CN)_2$] (purity 98%), [$PdCl_2(CH_3CN)_2$] (purity 99.99%), **12** (purity 98%) and TPPTS (purity 95%) were purchased from Sigma-Aldrich. **6-11** were synthesized by Luciano Sanchez Merlinsky (Universidad de Buenos Aires, Argentina) according to procedures presented in [P5] and [P7]. Except where stated otherwise, all materials were used as delivered.

Detailed procedures for preparation of individual catalyst and ligand solutions can be found in [P1-P8]. Typically, the solutions, where a solid catalyst or ligand was available, were prepared by stirring the solute in the IL for several hours under ambient conditions. For preparation of solutions of **1-5**, the following general procedure applies (for additional details see [P1-P8] and *Chapter 4.1.1*): Mixtures of the precursor *cis*-[$PtCl_2(CH_3CN)_2$] or [$PdCl_2(CH_3CN)_2$] and the ligand were reacted in stoichiometric amounts in the respective

Table 1: Nomenclature, molecular weights and structures of ILs used. The color coding indicates the assignment of carbon species to XP signals discussed in *Chapter 4* (green: C_{C2}, violet: C_{hetero}, blue: C_{alkyl}).

Abbreviation	Name	Molecular weight / g /mol	Molecular Structure
$[C_2C_1Im][PF_6]$	1-ethyl-3-methylimidazolium hexafluorophosphate	256.13	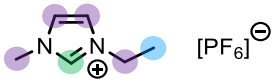
$[C_2C_1Im][OAc]$	1-ethyl-3-methylimidazolium acetate	170.21	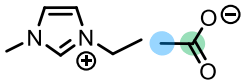
$[C_2C_1Im][TfO]$	1-ethyl-3-methylimidazolium trifluoromethanesulfonate	260.24	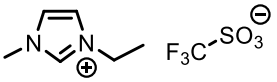
$[C_2C_1Im][C_2OSO_3]$	1-ethyl-3-methylimidazolium ethylsulfat	236.29	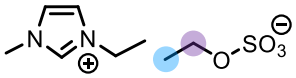
$[C_4C_1Im][PF_6]$	1-butyl-3-methylimidazolium hexafluorophosphate	284.18	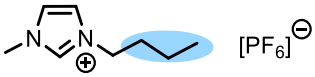
$[C_4C_1Im][Tf_2N]$	1-butyl-3-methylimidazolium bis(trifluoromethylsulfonyl)imide	419.37	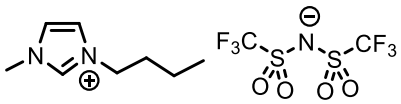
$[C_4C_1Im][TfO]$	1-butyl-3-methylimidazolium trifluoromethanesulfonate	288.29	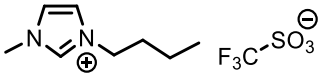
$[C_4C_1Im][Cl]$	1-butyl-3-methylimidazolium chloride	174.68	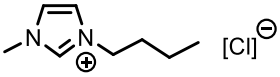
$[C_8C_1Im][PF_6]$	1-methyl-3-octylimidazolium hexafluorophosphate	340.29	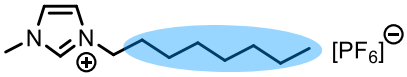
$[C_8C_1Im][TfO]$	1-methyl-3-octylimidazolium trifluoromethanesulfonate	344.40	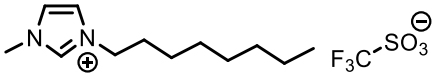
$[C_3CNC_1Im][Tf_2N]$	1-(3-cyanopropyl)-3-methylimidazolium bis(trifluoromethylsulfonyl)imide	430.34	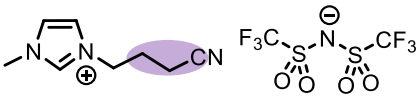
$[C_1CNC_1Pip][Tf_2N]$	1-(1-cyanomethyl)-1-methylpiperidinium bis(trifluoromethylsulfonyl)imide	419.36	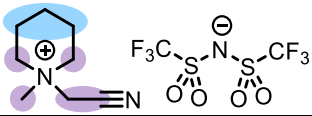
$[C_3CNC_1Im][PF_6]$	1-(3-cyanopropyl)-3-methylimidazolium hexafluorophosphate	295.16	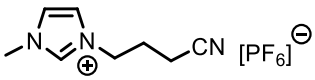
$[C_3CNPFC_4Im][PF_6]$	1-(3-cyanopropyl)-3-(3,3,4,4,4-pentafluorobutyl)imidazolium hexafluorophosphate	427.20	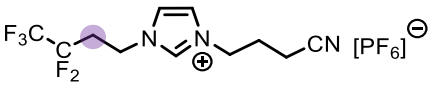

Table 2: Molecular structures and weights of complexes used. The color coding indicates the assignment of carbon species to XP signals discussed in *Chapter 4* (green: C_{C2}, violet: C_{hetero}, blue: C_{alkyl}). For assigment of IL-derived ligands (complexes **1**-**5**) and structure of the $[Tf_2N]^-$ anion, see *Table 1*.

Formula	Abbreviation used in this thesis	Molecular weight / g /mol	Molecular Structure
$[PtCl_2(C_3CNC_1Im)_2][Tf_2N]_2$	**1**	1126.66	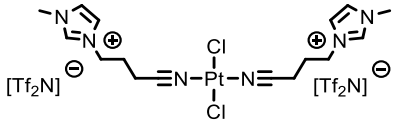
$[PdCl_2(C_3CNC_1Im)_2][Tf_2N]_2$	**2**	1038.00	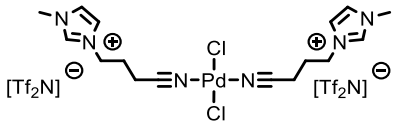
$[PtCl_2(C_1CNC_1Pip)_2][Tf_2N]_2$	**3**	1104.70	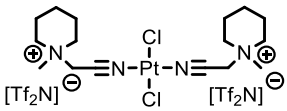
$[PtCl_2(C_3CNC_1Im)_2][PF_6]_2$	**4**	856.30	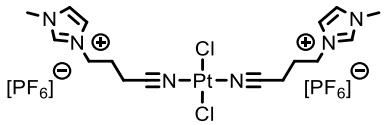
$[PtCl_2(C_3CNPFC_4Im)_2][PF_6]_2$	**5**	1120.38	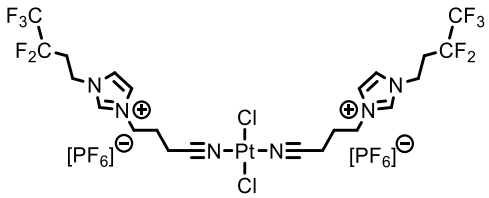
$[Ru(tpy)(bpy)Cl][PF_6]$	**6**	670.94	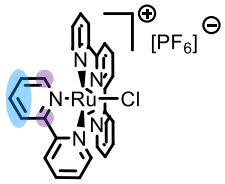
$[Ru(tpy)(dcb)Cl][PF_6]$	**7**	758.96	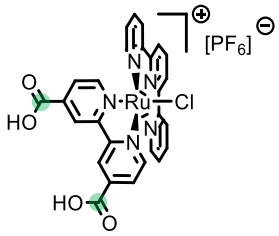

Table 2 continued.

Formula	Abbreviation used in this thesis	Molecular weight / g /mol	Molecular Structure
$[Ru(dcbNa)_2((C_9)_2bpy)][PF_6]_2$	**8**	1376.01	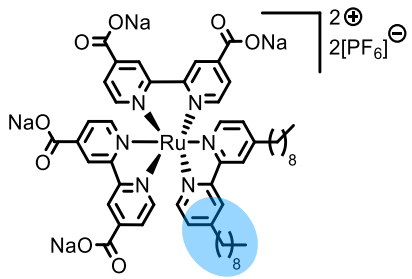
$[Ru(dcbNa)_2((C_1)_2bpy)][PF_6]_2$	**9**	1151.58	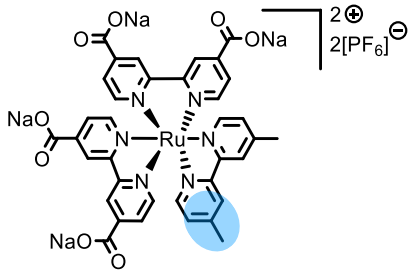
$[Ru(dcbNa)_2((OC_2)_2bpy)][PF_6]_2$	**10**	1211.63	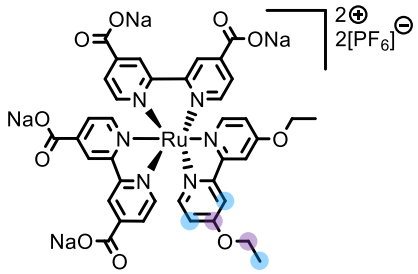
$[Ru(dcbNa)_2((t\text{-}C_4)_2bpy)][PF_6]_2$	**11**	1235.74	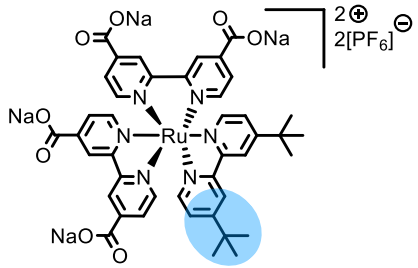
$[Rh(COD)_2][TfO]$	**12**	468.34	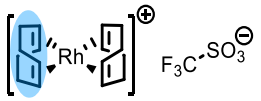
$[Rh(COD)(TPPTS)_2][TfO]$	**13**	1497.00	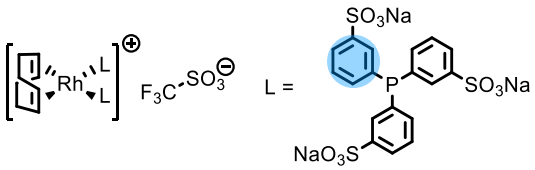

IL at 100 °C under medium vacuum (MV) conditions using Schlenk-techniques until the metal precursor was fully consumed and the released volatile CH_3CN ligands were fully removed yielding clear solutions (see also *Scheme 1*). Typically, the solutions were further stirred for 1 h under the applied conditions to ensure quantitative conversion. For solutions of **5**, *cis*-[$PtCl_2(CH_3CN)_2$] and the ligand IL [C_3CNPFC_4Im][PF_6] were first reacted without additional IL solvent for 1 h under the conditions applied above until solidification of the mixture before adding the IL solvent to continue the reaction as described above.[P2] 1‰$_{mol}$ solutions were prepared by simple dilution of freshly prepared, more concentrated solutions.[P4, P6] For a 1‰$_{mol}$ solution of **5** in [C_4C_1Im][PF_6] and solutions of **5** in [C_2C_1Im][PF_6], strong X-ray induced decomposition of the complex was observed due to the presence of traces of iodine species in the ILs.[P4], [P6] For preventing this effect, the ILs were cleaned by extraction with Millipore water (resistivity 18.2 MΩ·cm), as detailed in [P4], prior to preparation of the catalyst solutions. Preemptively, the cleaning procedure was also applied to all other ILs for preparation of the 1‰$_{mol}$ solutions of **5** and a 10‰$_{mol}$ of **5** in [C_4C_1Im][Tf_2N].[P6] For successful preparation of a 33.3‰$_{mol}$ solution of **3** in [C_1CNC_1Pip][Tf_2N], UHV conditions were required, while in MV, solidification of the entire mixture upon reaction progress was observed.[P1] In case of the ligand substitution reaction of **12** with TPPTS in [C_2C_1Im][C_2OSO_3], TPPTS was dissolved under inert gas conditions for 70 h before **12** was added and the reaction mixture was stirred under vacuum for 24 h to yield a clear solution.[P3]

3.2 ARXPS Instrument: Dual Analyzer System for Surface Analysis (DASSA)

ARXPS measurements were conducted using the Dual Analyzer System for Surface Analysis (DASSA) chamber dedicated to examination of the IL/vacuum interface. The DASSA setup is detailed in Ref. 42; a sketched representation is shown in *Figure 6*. Equipped with two identical analyzers, the DASSA instrument allows for simultaneous acquisition of XP spectra in 0° emission and 80° emission, which grants the following benefits: a) the sample can be kept horizontally at all times to ensure a planar liquid surface and to prevent the danger of dripping, b) time-efficient investigations with c) minimization of X-ray-induced chemical reactions during the measurements, and d) identical conditions for 0° and 80° measurements for best comparability.

The setup consists of an inert box (*violet* in *Figure 6*, filled with N_2 of purity grade: 5.0) enabling introduction of the samples into the fast entry load-lock (FEL, *green*) under exclusion of air and moisture. In the FEL, the samples were degassed (typically down to a base pressure below $5 \cdot 10^{-7}$ mbar) for several hours before transfer to the preparation chamber (*blue*, typical base pressure below $5 \cdot 10^{-10}$ mbar). The manipulator arm is equipped with two measurement stages: The low temperature (LT) stage can be temperature-controlled via cooling with pre-cooled N_2 gas and radiative heating within in a range from 150 to 1300 K, while the high temperature (HT) stage is dedicated for temperature ranges from room temperature to 1700 K via electron impact heating.[42] The preparation chamber further comprises a quadrupole mass spectrometer (QMS; Hiden HAL 3F 511) and low energy electron diffraction (LEED) optics. The analysis chamber (typical base pressure below $1 \cdot 10^{-10}$ mbar) is equipped with two identical ARGUS-type analyzers at 0° and 80° angle relative to the surface normal of the horizontally kept sample, a monochromated XM 1000 Al-Kα X-ray source with an energy resolution of 0.4 eV (at parameters applied for high-resolution region scans, see below)[42] and a non-monochromated DAR400 Al-Kα/Mg-Kα dual source both mounted at magic angle to the analyzers. The chamber additionally comprises an UV source, an electron and ion gun and a QMS.

Detailed procedures for treatment of the samples upon introduction into the chamber can be found in [P1-P8]. Unless stated otherwise, application of the samples onto the setup-compatible sample holders[42] and introduction into the chamber were conducted under ambient conditions. In case of solid residuals, the particles settled to the ground of the sample holder and were expected not to affect the measurements. Solid IL samples were typically applied as hot liquids (~80 °C) after melting and thoroughly degassing under MV conditions using standard Schlenk-techniques. The film thickness of the liquid samples was typically ~0.5 mm; with this, the IL/solid interface did not affect the composition at the IL/vacuum interface. Owing to this fact, except where stated otherwise, "surface" corresponds to the IL/vacuum interface throughout this thesis.

XP spectra were acquired in the LT stage exclusively using the monochromated Al-Kα X-ray source (hν=1486.6 eV) at 14.00 kV, 238 W. Aperture 3 was exclusively used. Survey spectra were recorded with a pass energy of 150 eV and the high-resolution region spectra

were recorded at 35 eV pass energy. QMS spectra were recorded using the Hiden HAL 3F 511 in the preparation chamber run with the secondary electron multiplier (SEM) detector.

Absence of common Si-based surface-active contaminations[99] was checked for every solution using ARXPS.[P1-P8]

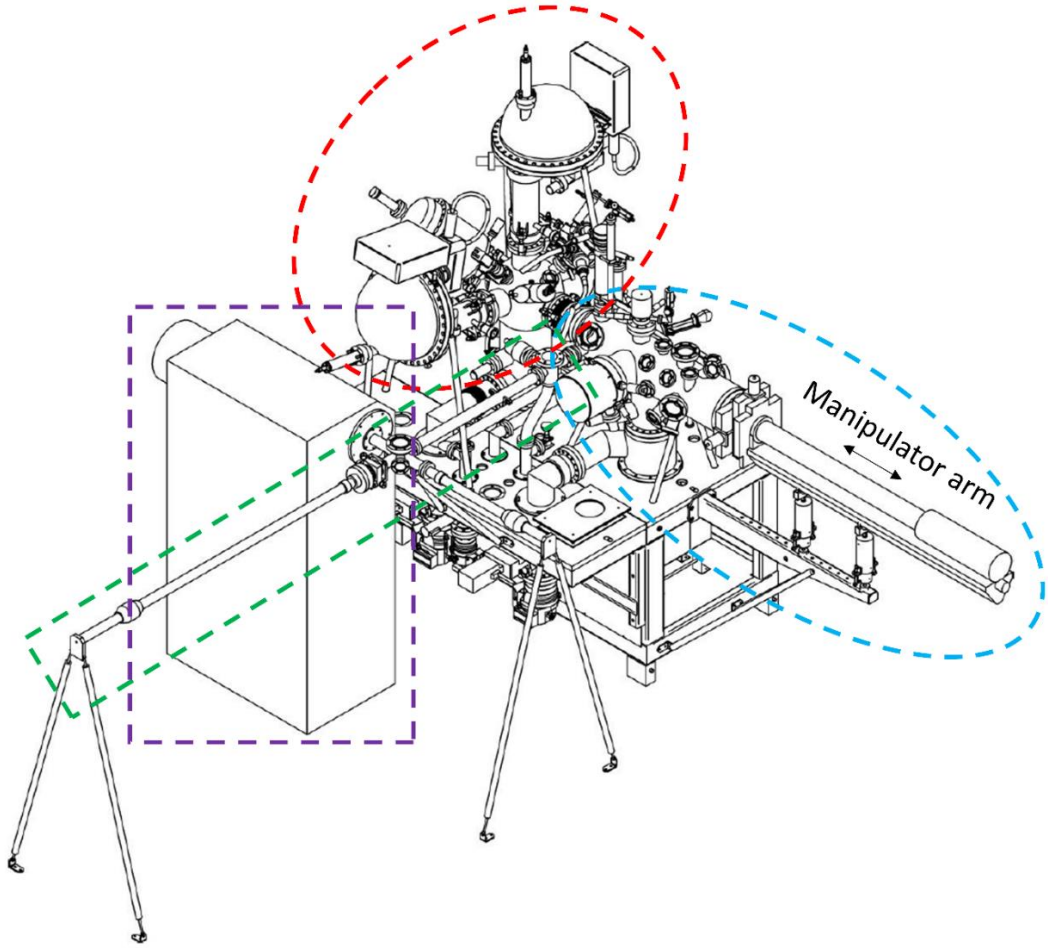

Figure 6: Sketch of the Dual Analyzer System for Surface Analysis (DASSA) setup consisting of an inert box entry system (violet), a fast entry load-lock (green), a preparation (blue) and an analysis chamber (red) with its 0° and 80° analyzers. The sketch was adapted from the original user manual.[100]

3.3 Data Evaluation

Detailed procedures for evaluation of the recorded data can be found in [P1-P8]. The CasaXPS software (version 2.3.16Dev6) was used for analyzing the XPS data. A two-point linear background was subtracted for all non-metallic signals. In case of C_{Tf2N}, C_{TfO}, C_{CF3}

or C_{CF2} peaks in the C 1s region, a three-point linear background was used. For metallic signals, a Shirley-type background was subtracted. Peaks were fitted using a Gauss-Lorentzian function with 30% Lorentzian contribution. Fitting of spin-orbit-resolved peaks was conducted constraining the peak intensities according to the expected degeneracy ratio of the orbitals, the binding energy difference[101] and the full width at half maximum (FWHM) to equal values. No constraints were used for fitting of the Pd 3d peaks owing to a clearly broader Pd $3d_{3/2}$ peak than the Pd $3d_{5/2}$ peak. For the same reason, no FWHM constraints were applied to Rh 3d peaks; peak area and binding energy separation, however, were constraint to yield the best fit with a minor contribution of an oxidized Rh species[P3]. The assignment of C atoms to XPS signals discussed in *Chapter 2.2* was expanded to neat ILs and solutions employed in this thesis and is shown color-coded in *Tables 1* and *2*. Individual fitting procedures can be found in [P1-P8]. The derived intensities are expected to reflect the actual surface composition within an uncertainty range of 5-10%. Raw peak intensities were corrected using atomic sensitivity factors (ASFs) derived from Ref. 102. *Table 3* provides an overview of used ASFs and differences in binding energy for spin-orbit-resolved peaks. To compensate for the inherently lower overall intensity detected at grazing emission, the 80° spectra were multiplied by the geometry factor[42]. This procedure facilitates the comparison of individual peaks for deducing orientational and enrichment effects.

Individual procedures for referencing the binding energy scales of the spectra can be found in [P1-P8]. For solutions of $[Tf_2N]^-$ or $[TfO]^-$ ILs, 0° spectra were referenced to the F 1s signal of the $C_{CF3/CFx}$ groups at 688.8 eV. For solutions of $[PF_6]^-$ ILs and the solutions of $[C_4C_1Im][Cl]$ with $[PF_6]^-$-based materials dissolved, 0° spectra were referenced to the F 1s signal of the $[PF_6]^-$ anion at 686.8 eV. 80° spectra were referenced to the binding energy of the N_{Im} signal at 0°. Application of this procedure to Pt 4f and Cl 2p signals resulted in a shift to lower binding energy for the 80°. Since these shifts were observed for all solutions, independently of surface enrichment effects, surface core level shifting was ruled out and 0° and 80° spectra were thus aligned for better comparability of the spectra. 0° spectra of solutions of complexes **6-11** and spectra of neat $[C_2C_1Im][OAc]$ were referenced to the C_{alkyl} signal at 285.0 eV. 80° spectra were referenced as described above. In all publications, except for [P6], the intensities of all recorded spectra were normalized to the sum over all atomic sensitivity factor-corrected intensities of an individual presented solution to account

for potential minor changes of the photon flux between the different measurement series. For individual normalization procedures see [P1-P8]. For sake of clarity, the normalized intensities presented in the publications were also used herein, which is not affecting the trends observed and the conclusions derived.

Table 3: Atomic sensitivity factors (ASFs) applied to the raw intensities recorded in XPS and binding energy differences ΔBE for spin-orbit-resolved signals employed(/*observed) in this thesis.

Core Level	**ASF**	**ΔBE / eV**
C 1s	0.30	
Cl 2p	0.85	1.60
F 1s	1.00	
I $3d_{5/2}$	6.17	
N 1s	0.46	
Na 1s	2.04	
O 1s	0.67	
P 2p	0.46	0.90
Pd 3d	5.13	5.30-5.36*
Pt 4f	5.72	3.35
Rh 3d	4.61	4.70
Ru 3d	4.08	4.20
S 2p	0.64	1.21

4 Results

The majority of the results presented in this dissertation were published in peer-reviewed journal articles [P1 – P8]. This chapter summarizes and links the individual findings of these publications. For detailed discussions and further information, the reader is referred to the articles annexed in *Chapter 8*. An additional set of data unpublished within the timeframe of this thesis is presented in *Chapter 9*. Molecular structures of ILs and complexes employed are presented in *Tables 1* and *2*, respectively.

4.1 Chemical Properties and Surface Composition of Catalysts with Different Ligand Systems in IL Solutions

4.1.1 Catalysts with IL-derived Ligand Systems[P1, P2, P4, P6, P8]

A fundamental requirement for the study of catalyst solutions using ARXPS is a sufficient solubility of the catalyst in the IL. While for catalytic conversions a relatively low solubility in the ppm range is typically acceptable, adequate intensities can only be detected in ARXPS with a (surface) concentration of, as a rule of thumb, ≥1%$_{mol}$. Introducing IL building blocks into the ligand system was an intuitive approach to obtain complexes that are highly soluble in various ILs. With respect to potential catalytic applications, such charge-tagged complexes have shown a particularly high resistance against catalyst leaching, including, among many examples[103, 104], catalysts with nitrile-functionalized IL cations as ligands[105-108]. The following paragraphs present the formation of such catalysts, their interfacial behavior and rational design of the ligand system for deliberate surface enrichment, as well as a short discussion of the impact of the surface enrichment in hydrogenation of ethene.

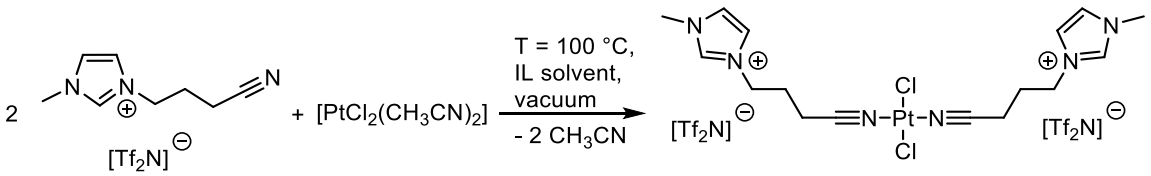

Scheme 1: Preparation of $[PtCl_2(C_3CNC_1Im)_2][Tf_2N]_2$ (**1**) in excess $[C_3CNC_1Im][Tf_2N]$, which acts as both solvent and ligand. Complexes **1-5** were prepared in a similar way also directly in other ILs.[P1, P2, P4, P6] Note that also unfunctionalized ILs were successfully applied as solvents, so that the CN-functionalized ligand IL was reacted in stoichiometric amounts with the metal precursor.[P2, P4, P6]

While in previously published preparation routes for Pd derivatives, $PdCl_2$ and stoichiometric amounts of the ligand were reacted at room temperature and ambient pressure in volatile solvents such as dichloromethane or acetonitrile[105-107], we targeted a pathway directly in the respective IL solvent.[P1] This approach will be exemplarily demonstrated along the formation of **1** in $[C_3CNC_1Im][Tf_2N]$, as is depicted in *Scheme 1*: At elevated temperature (100 °C) and under vacuum, the CH_3CN ligands of the metal precursor *cis*-$[PtCl_2(CH_3CN)_2]$ are quantitively substituted by the IL cation and immediately pumped off.[P1, P2, P4, P6]

The formation of the final product was monitored using XPS in 0° emission and QMS, as shown in *Figure 7* for a mixture of $[PtCl_2(CH_3CN)_2]$ and $[C_3CNC_1Im][Tf_2N]$ with 1:4 molar ratio (due to consumption of the solvent being the ligand source, quantitative formation of the final product yielded a 1:2 molar ratio, that is, 33.3%$_{mol}$ of the final product in the IL).[P1] XP spectra of the precursor solution at room temperature in *Figure 7* (green) revealed relatively low intensities of the precursor-specific Pt 4f and Cl 2p signals at 74.2 and 199.0 eV, which is due to the fact, that the precursor showed low solubility yielding only a suspension with remaining solid particles.[P1] The N 1s region showed two distinct peaks corresponding to the N atoms incorporated into the imidazolium ring, N_{Im}, at 402.1 eV and a joint signal from N atoms of uncoordinated CN groups of the IL cation and $[Tf_2N]^-$, $N_{CN/Tf2N}$, at 399.7 eV.[P1] Owing to the low solubility of the precursor, N atoms of coordinated CN groups of the CH_3CN ligands were expected to only show a minor contribution at ~401.3 eV, $N_{CNcoord}$ (see discussion below). The room temperature mass spectrum of the precursor solution in *Figure 7b* (green) revealed small signals at 12-15, 24-28 and 38-41 amu assigned to CH_3CN vapor,[109] indicating slow abstraction of the labile ligands under UHV.[P1] Heating the mixture to 100 °C (black in *Figure 7b*) resulted in a strong increase of these signals disclosing a boost of the reaction toward practical rates.[P1] Upon progress of the reaction, the CH_3CN-specific signals and the overall pressure in the chamber decreased to a minimum (not shown), while solid precursor particles were visibly consumed eventually yielding a clear solution.[P1]

Comparing the XP spectra of the precursor suspension (green) with a fully reacted solution (black) shown in *Figure 7a* clearly revealed a strong increase of the Pt 4f and Cl 2p signals at 74.4 and 199.1 eV, respectively. In fact, the intensity now excellently conformed with the nominal intensity expected from quantitative formation of the desired product

(33.3%$_{mol}$ concentration).[P1] Additionally, the N 1s region clearly showed a third peak at 401.3 eV after reaction labelled $N_{CNcoord}$, whose intensity nicely matched the 1:2 Pt:$N_{CNcoord}$ ratio expected from the structure of **1**.[P1] The applied deconvolution of the N 1s region with color-coded peaks is also shown in *Figure 7a*.[P1] Since the appearance of this peak was accompanied by an equivalent decline of the $N_{CN/Tf2N}$ signal at 399.6 eV, this effect was assigned to successful coordination of $[C_3CNC_1Im]^+$ to the metal via the CN groups: upon coordination, the CN group acts as an electron donor resulting in a shift to higher binding energy.[P1]

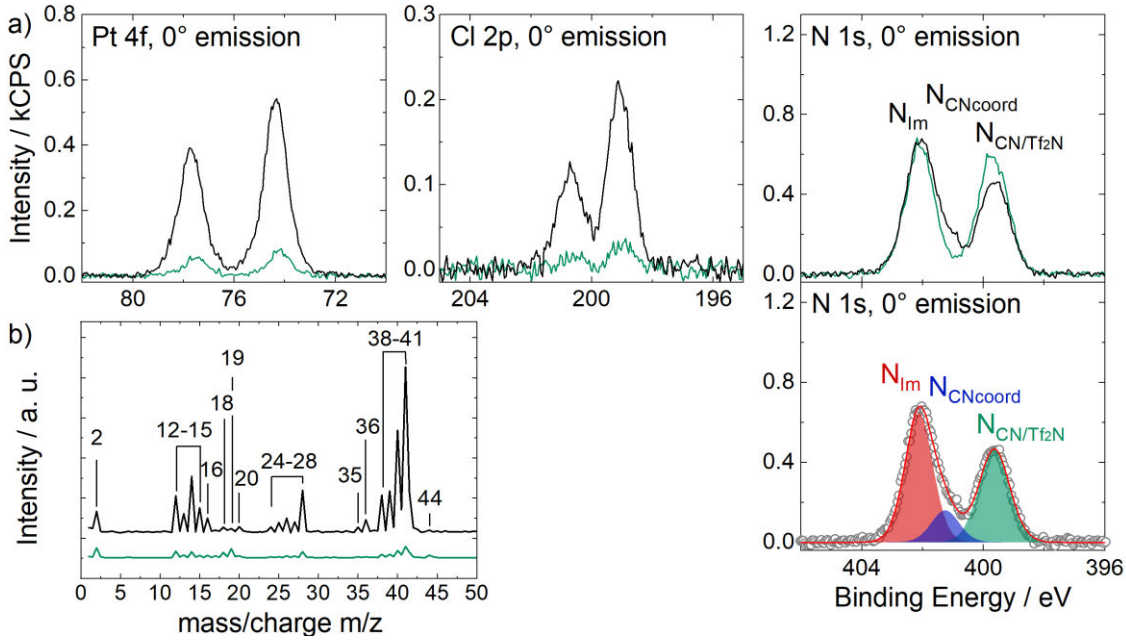

Figure 7: a) Pt 4f, Cl 2p and N 1s XP spectra of a suspension of $[PtCl_2(CH_3CN)_2]$ in $[C_3CNC_1Im][Tf_2N]$ with 1:4 molar ratio before (green) and after (black) ligand substitution to yield a clear solution of **1** recorded in 0° emission at room temperature and color-coded deconvolution applied to the N 1s spectrum after reaction, b) mass spectra of the initial reaction mixture at room temperature (green) and at 100 °C (black). Adapted from [P1] under CC-BY-NC-ND license.

The *in vacuo* preparation route has proven feasible for a variety of complexes in the respective CN-functionalized ILs (complexes **1**-**3**)[P1] or in unfunctionalized ILs, namely in $[C_4C_1Im][PF_6]$ (**4** and **5**)[P2, P4], $[C_2C_1Im][PF_6]$, $[C_8C_1Im][PF_6]$, $[C_4C_1Im][Tf_2N]$ (all **5**)[P6] in various concentrations.[P1, P2, P4, P6] In almost all cases, the reaction was also successful under medium vacuum (MV) conditions using Schlenk-techniques, which allowed for stirring of the mixture and thus a more practical and widely applicable preparation protocol (see *Chapter 3* for details).[P1] The preparation route was not successful in $[C_4C_1Im][Cl]$ owing to coordination of Cl^- from the solvent rather than the CN-functionalized ligands.[P6]

XPS has also proven to provide interesting information on the electronic properties of the coordinating moieties and the metal centers.[P1] *Figure 8a* contrasts the N 1s spectra recorded in 0° emission of 33.3%$_{mol}$ solutions of **1** (*middle*, see also above) and **2** (*bottom*) in [C_3CNC_1Im][Tf_2N], and **3** (*top*) in [C_1CNC_1Pip][Tf_2N]. While for solutions of **1** and **2** the N_{CN} atoms gave a joint signal with the N_{Tf2N} atoms $N_{CN/Tf2N}$ at 399.6 eV, the N_{CN} signal from the solution of **3** was detected separated at 400.5 eV and thus shifted about 0.9-1.0 eV (*b*) to higher binding energy.[P1] This finding indicated a significantly higher electron density at the CN group in the imidazolium derivative [C_3CNC_1Im][Tf_2N] due to the longer separation between the functionalization and the electron-withdrawing N atoms of the heterocycles, compared to [C_1CNC_1Pip][Tf_2N].[P1] With this, our results complemented a ^{15}N-NMR study on pyridinium ILs, unveiling that longer CN-functionalized chains, indeed, result in higher negative charges localized at the nitrile N atoms[110].

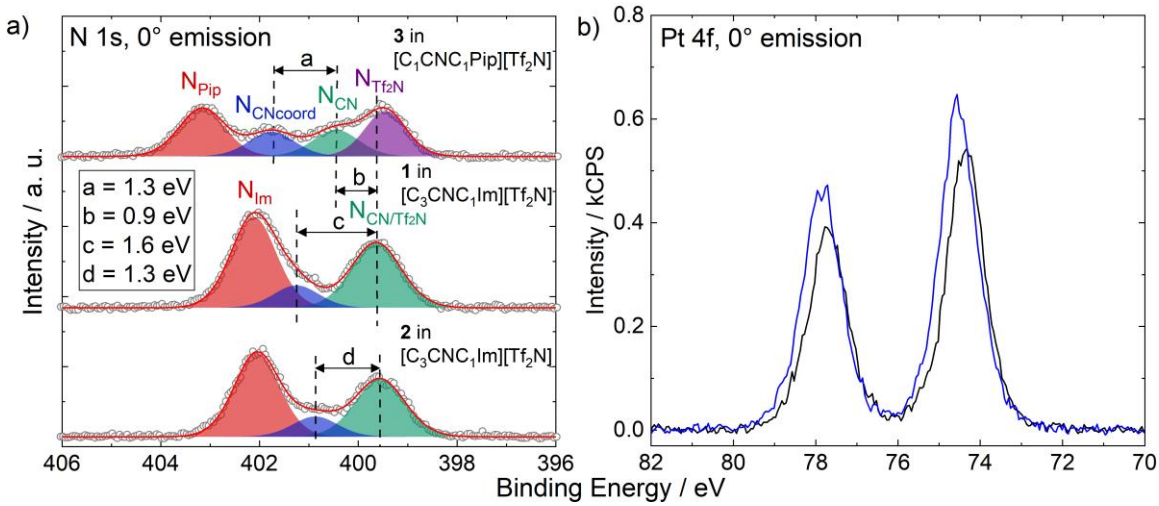

Figure 8: a) N 1s region spectra of 33.3%$_{mol}$ solutions of **1** (middle) and **2** in [C_3CNC_1Im][Tf_2N] (bottom), and **3** in [C_1CNC_1Pip][Tf_2N] (top), b) Pt 4f region spectra of solutions of **1** in [C_3CNC_1Im][Tf_2N] (black) and **3** in [C_1CNC_1Pip][Tf_2N] (blue). All spectra were recorded at 0° emission angle. Adapted from [P1] under CC-BY-NC-ND license.

This behavior, in turn, suggested a stronger coordination power of the [C_3CNC_1Im]$^+$ cation when compared to [C_1CNC_1Pip]$^+$: The binding energy difference between the N_{CN} and $N_{CNcoord}$ signals of solutions **1** in [C_3CNC_1Im][Tf_2N] (1.6 eV, see *Figure 8*, *middle*) and **3** in [C_1CNC_1Pip][Tf_2N] (1.3 eV, *top*), induced by coordination of the CN groups to the metal, is about +0.3 eV higher for the long-chained derivative, which is in line with a stronger donation of electron density to the metal upon coordination.[P1] In fact, as depicted in *Figure 8b*, an according shift of the Pt 4f signals by 0.2 eV to lower binding energy for

the solution of **1** was also detected, though the magnitude of this shift is on the border of experimental uncertainty.[P1] Interestingly, the solution of **2** in $[C_3CNC_1Im][Tf_2N]$ also showed an about 0.3 eV lower coordination-induced binding energy shift, which agreed with a weaker Pd-N bond than Pt-N found computationally for related systems[111].[P1]

In the following passages, the interfacial behavior of the complexes and a successful modification of the ligand system to deliberately maximize the local catalyst concentration at the surface will be discussed along **4** and **5** as model systems in the well-studied commercially available IL $[C_4C_1Im][PF_6]$. **4** is equivalent to **1,** only with $[PF_6]^-$ as counter anions instead of $[Tf_2N]^-$. The ligand system of **5** was complemented with fluorous butyl chains (PFC_4)[P2, P4], which have exhibited surface activity in binary mixtures of ILs before[77, 88, 97]. The complexes were prepared as $[PF_6]^-$ salts to ensure distinct peaks in the XP spectra for the PFC_4 chains, which would otherwise superimpose with signals of $[Tf_2N]^-$ also carrying CF_3 groups.[P1, P2, P4, P6, P8] Accordingly, the IL was chosen to be an $[PF_6]^-$ IL and the non-functionalized butyl chain of $[C_4C_1Im]^+$ affords a separated, IL-specific C_{alkyl} signal (see *Chapter 2* for assignment) to extract a detailed picture of the surface composition.[P2, P4]

Figure 9a depicts the Pt 4f, F 1s, N 1s, and C 1s XP spectra of a $5\%_{mol}$ solution of **4** in $[C_4C_1Im][PF_6]$ in 0° (black, more bulk-sensitive) and 80° emission (red, more surface-sensitive). Apart from the Pt $4f_{7/2}$ signal detected at 74.3 eV, the F 1s and N 1s regions showed single peaks at 686.8 and 402.2 eV corresponding to the F atoms of $[PF_6]^-$, $F_{PF6,}$ and N_{Im} atoms, respectively, both from complex and IL. Notably, owing to the relatively low catalyst concentration of $5\%_{mol}$ and partial overlay with the N_{Im} (cf. *Figures 7* and *8*), no sufficiently accurate deconvolution of a $N_{CNcoord}$ peak was achieved.[P2, P4] Also, no N_{CN} signal (~400 eV, cf. *Figures 7* and *8)* was detected since the solvent $[C_4C_1Im][PF_6]$ did not contain a CN group.[P2] The C 1s region showed an envelope which is equivalent to what has been discussed in *Chapter 2.2* involving C_{C2}, C_{hetero} and C_{alkyl} species. The intensities detected at 0° excellently agreed with the nominal composition of the solution.[P2, P4] At 80°, however, the Pt 4f signals declined to ~50% of the 0° signals, while the F 1s and N 1s signals showed a slight decrease and the C_{alkyl} signal significantly increased at 80° of ~30%.[P2, P4] These findings are in line with a surface preferably terminated with the C_4 chains of the $[C_4C_1Im]^+$ cation, as previously discussed in *Chapter 2.2*. while the imidazolium rings and $[PF_6]^-$ anions form a layer beneath. The fact that the Pt signal showed

the largest decline was attributed to a preferential orientation of the complex in the near-surface region where the charged imidazolium moieties of the ligands are incorporated into the imidazolium/$[PF_6]^-$ layer and the Pt center is located slightly below this layer. In this picture, **4** would be present in the first molecular layer and homogeneously distributed, even though the Pt center is depleted from the outer surface and does not exhibit surface enrichment.[P2, P4]

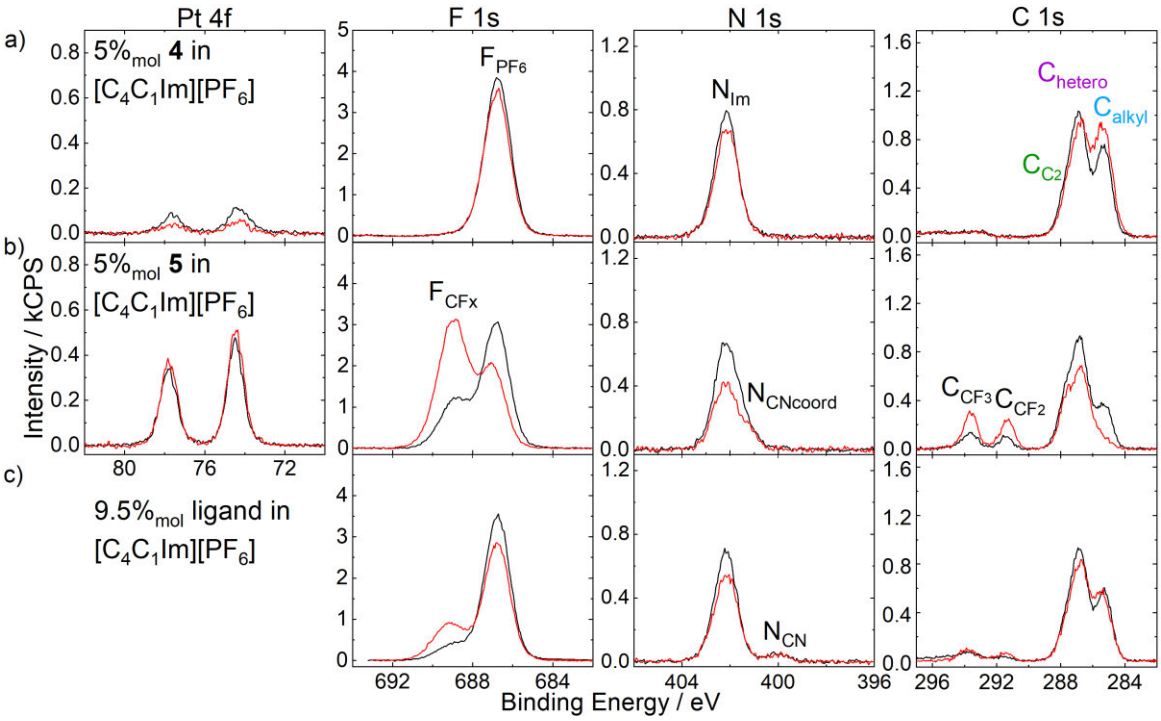

Figure 9: Pt 4f, F 1s, N 1s, and C 1s spectra of $5\%_{mol}$ solutions of a) **4**, b) **5** and c) $9.5\%_{mol}$ solution of $[C_3CNPFC_4Im][PF_6]$ in $[C_4C_1Im][PF_6]$ in 0° (black) and 80° (red) emission. Note that the solutions shown in b) and c) contain the same IL:PFC_4 ratio of 2:19. Adapted from [P2] and [P4] under CC-BY-NC-ND and CC-BY-NC licenses.

XP spectra of an equivalent solution of **5**, which only differs from **4** in the PFC_4 chains, are shown in *Figure 9b.* The spectra showed additional signals in the F 1s and C 1s regions, F_{CFx} at 688.8, C_{CF3} at 293.7 and C_{CF2} at 291.4 eV, which originate from the PFC_4 chains.[P2, P4] While the F_{CFx} atoms all contribute to a single signal, the fluorinated carbon atoms C_{CF3} and C_{CF2} can be clearly distinguished due to the number of F atoms bound to them.[88] Also, non-fluorinated C atoms from the PFC_4 chains contributed to the C_{hetero} signal (see *Table 2* for detailed assignment). In addition, the $N_{CNcoord}$ signal at 401.3 eV was now evidently discriminable from the N_{Im} signal showing a much higher intensity.[P2, P4] In fact, all complex-specific Pt 4f, F_{CFx}, $N_{CNcoord}$, C_{CF3} and C_{CF2} signals showed much higher intensities

as compared to the solution of **4**.[P2, P4] This effect was even observed in the more bulk-sensitive 0° measurements.[P2, P4] Aside from that, the intensity of the solvent-specific C_{alkyl} signal at 285.2 eV was detected eminently lower. These observations clearly revealed a strong enrichment of complex **5** at the IL/gas interface and the associated depletion of the $[C_4C_1Im]^+$ cations.[P2, P4] The enrichment is solely caused by the presence of the PFC_4 chains, which trigger localization of the complex at the interface in a buoy-like fashion – referred to as the "buoy effect".[P2, P4]

More detailed insights into the catalyst-enriched surface could be extracted from comparison of 0° and 80° spectra in *Figure 9b*. All complex-specific signals increase at 80° being most prominent for the F_{CFx}, C_{CF3} and C_{CF2} signals, while the Pt 4f peaks only showed a weak increase.[P2, P4] We assigned this behavior to a preferential surface orientation of **5** with the PFC_4 chains exposed to the vacuum and the Pt center located beneath.[P2, P4] The C_{alkyl} signal showed a drastic decline at 80° to an extent where it is only a small shoulder of the C 1s envelope stressing the extreme enrichment of **5** and the concomitant depletion of the solvent.[P2, P4]

Additional information on the buoy effect was elucidated by investigating the surface tension of the two solutions using the pendant drop (PD) method (experiments conducted by Dr. Ulrike Paap, Chair of Physical Chemistry II, FAU Erlangen-Nürnberg).[P4] The surface tension of the catalyst solutions was measured under ultra-clean vacuum conditions in a newly developed chamber.[112, P4] At 298 K, the solution of **4** showed a surface tension of 43.9 mN/m, which is even slightly higher than observed for neat $[C_4C_1Im][PF_6]$ with a surface tension of 43.4 mN/m.[P4] In contrast, for the solution of **5** a value of 40.0 mN/m was found at 298 K, which is significantly lower than for the solution of the non-surface-active derivative and the neat IL. These observations attested the lowering in surface free energy, signified by the measured surface tension, as the driving force of the strong accumulation of **5** at the IL/vacuum interface.[P4]

Given that the strong enrichment of **5** at the IL/vacuum interface was solely induced by the buoy-like character of the two PFC_4-functionalized ligands, the interfacial behavior of the ligand as an individual solute without being attached to the metal center was investigated.[P4] For this, a solution with $9.5\%_{mol}$ concentration of only the ligand $[C_3CNPFC_4Im][PF_6]$ in $[C_4C_1Im][PF_6]$ was prepared providing an identical IL:ligand ratio

of 2:19 as in the 5%$_{mol}$ solution of **5**; the only difference is the absence of the Cl_2Pt-moiety as the coordination partner.[P4] The XP spectra shown in *Figure 9c* clearly revealed much lower intensities for the ligand-specific signals and a much higher intensity for the IL-specific C_{alkyl} signal, when compared to the solution of **5** in *Figure 9b*. In fact, the intensities corresponded only to a moderate surface enrichment of the ligand itself in the IL, and, consequently, the surface enrichment of uncoordinated $[C_3CNPFC_4Im][PF_6]$ was found much less pronounced than for **5**, which carries two of these surface-active ligands.[P4] This is due to the fact that for removing **5** from the IL/vacuum interface and diffusion into the bulk, the cooperative removal of two surface-affine PFC_4 chains must be accomplished.[P4] In a broader sense, this result indicated that the catalyst design with two (or even more) surface-active ligands bound to the metal center rather than one yields a much higher degree of enrichment.[P4]

With the successfully achieved accumulation of **5** at the IL/vacuum interface and a non-enriched catalyst **4** suitable for comparison, the impact of the surface enrichment on the catalytic performance in hydrogenation of ethene was studied (catalytic experiments conducted by Sharmin Khan Antara, Chair of Chemical Engineering I, FAU Erlangen-Nürnberg, for details see [P8]). The reactor setup involved a pool with a stationary film of IL solution with well-defined planar gas-liquid contact area (71 x 22.5 mm) to study the impact of the enhanced catalyst concentration at the surface.[P8] 0.05%$_{mol}$ and 1%$_{mol}$ solutions of **5** and **4** in $[C_4C_1Im][PF_6]$ were investigated and, indeed, the solutions of **5** yielded a two times higher activity. However, visibly and confirmed upon investigation with *in situ* light scattering (experiments conducted by Ziwen Zhai, Institute of Advanced Optical Technologies - Thermophysical Properties, FAU Erlangen-Nürnberg), metallic Pt particles acting also as heterogeneous catalysts have formed under the reductive conditions of the hydrogenation reaction.[P8]

ARXPS analyses were conducted before and after the hydrogenation experiment for the 1%$_{mol}$ solutions.[P8] Pt 4f and F 1s XP spectra at 0° (left) and 80° (right) of solutions of **5** (*top*) and **4** (*bottom*) are shown in *Figure 10*. During transfer between the experimental setups used for catalysis and the ARXPS analyses, the relatively large Pt particles settled to the ground of the vessel and no metallic Pt could be observed in XPS (BE ~ 71.7 eV[P4]).[P8] Before catalytic conversion, the spectra resemble the characteristics discussed above for the 5%$_{mol}$ solutions and reflect surface enrichment of **5**, while **4** showed

no surface affinity.[P8] After the catalytic experiment, however, the solution of **5** showed a pronounced decrease in intensity of the complex-specific Pt 4f and F_{CFx} signals at both 0° and 80°, while the F_{PF6} signal remained constant at 0° and showed a minor increase at 80°.[P8] All other core levels (not shown) reflected similar characteristics.[P8] These observations were in line with a lower amount of **5** dissolved in solution due to formation of metallic Pt particles.[P8] For the solution of **4** (*bottom*), the signal intensities remain on a steady level before and after the catalytic experiment due to a lower degree of Pt particle formation as a result of the lower activity of **4**.[P8] The higher activity of **5** was assigned to the higher catalyst concentration at the IL/gas interface.[P8]

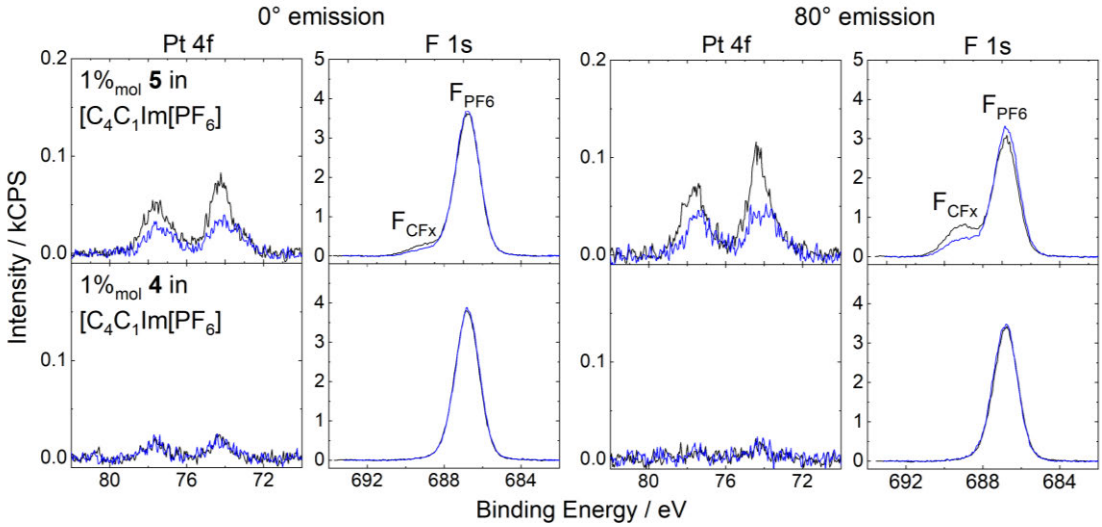

Figure 10: Pt 4f and F 1s XP spectra of $1\%_{mol}$ solutions of **5** (top) and **4** (bottom) in $[C_4C_1Im][PF_6]$ in 0° (left) and 80° emission (right) at room temperature before (black) and after (blue) catalytic hydrogenation of ethene (run at 313 K for 18 h, gas feed 17 mL/min Ar, 4 mL/min H_2 and 4 mL/min C_2H_4, partial pressure H_2 0.1 MPa, total pressure 0.62 MPa). Adapted from [P8] under CC-BY-NC license.

4.1.2 Polypyridyl-based Catalysts[P5, P7]

Polypyridyl ligands offer a large diversity of structures and are widespread in various of organometallic application areas – bipyridine was even denoted as the "most widely used ligand"[113], at the turn of the millennium. In view of catalysis, polypyridyl complexes raised significant interest in water oxidation[114, 115], the water gas shift reaction[116, 117] and CO_2 reduction[118], among more examples[119]. A Ru-based polypyridyl complex was also investigated in CO_2 reduction in $[C_2C_1Im][Tf_2N]$ for coordination of CO_2 to create a formate species.[120]

A first set of Ru(II)-based polypyridyl complexes, **6** and **7**, was investigated in the ILs $[C_4C_1Im][PF_6]$ and $[C_2C_1Im][OAc]$.[P5] The complexes both contain the tridentate ligand 2,2′:6′,2″-terpyridin (tpy), the bidendate ligands 2,2'-bipyridine (bpy) or 2,2'-bipyridine-4,4'-dicarboxylic acid (dcb), respectively, and a Cl ligand, while the counterion is $[PF_6]^-$. Solutions with a nominal catalyst concentration of 2.5‰$_{mol}$ were prepared. Complex **6** showed good solubility in $[C_4C_1Im][PF_6]$ with some remnants of undissolved complex, while in $[C_2C_1Im][OAc]$ no solid residuals could be visually identified indicating full dissolution. Complex **7** was found more or less undissolved in $[C_4C_1Im][PF_6]$ and XPS investigations of the dispersion did not show any complex-related signals. In $[C_2C_1Im][OAc]$, however, **7** exhibited a sufficiently high solubility but also showed remnants of undissolved particles. While for $[C_4C_1Im][PF_6]$ a widely inert character was expected, the basic character of $[C_2C_1Im][OAc]$ increases the potential for deprotonation of C_{C2} atoms of the $[C_2C_1Im]^+$ cation forming acetic acid and the respective N-heterocyclic carbene (NHC) capable of coordination. In fact, an NHC-acetic acid complex and acetic acid were detected in the gas-phase over $[C_2C_1Im][OAc]$ by UPS and MS[121], but the general presence of NHCs in $[OAc]^-$-based ILs is still under debate.[122]

Figure 11a depicts the C 1s/Ru 3d and N 1s XP spectra of the nominal 2.5‰$_{mol}$ solution of **6** in $[C_4C_1Im][PF_6]$. The Ru $3d_{5/2}$ signal was detected at 280.8 eV, which is in a comparable range as found for solid Ru(II) complexes[123]. With a spin-orbit separation of 4.2 eV, the Ru $3d_{3/2}$ signal coincided with the intense $C_{alkyl/aryl}$ signal at 285.0 eV, as is visible from *Figure 11b* providing the color-coded deconvolution. The C_{hetero} and $C_{alkyl/aryl}$ signals contain contributions from the complex and IL.[P5] The N 1s region displayed the N_{Im} signal at 401.9 eV and a low-intensity peak at 399.9 eV corresponding to the coordinated N atoms of the tpy and bpy ligands, $N_{tpy/bpy}$.[P5] The Ru:$N_{tpy/bpy}$ ratio of 1.0:5.0 in 0° emission excellently agreed with the stoichiometry of the complex indicating intactness of the coordination sphere; intactness of the Ru-Cl bond, however, could not be confirmed since no Cl 2p signal was detected owing to the low catalyst concentration.[P5] In accordance with the fact that not all of the complex is dissolved, the Ru 3d and $N_{tpy/bpy}$ signals showed lower intensity than expected from the nominal 2.5‰$_{mol}$ concentration. Since the 0° spectra contain ~85-90% contribution of the bulk and only ~10-15% of the topmost surface layer, the actual concentration could be determined quite accurately, even in case of depletion, which will be discussed below. The intensity corresponded to a concentration of ~1.3‰$_{mol}$.[P5]

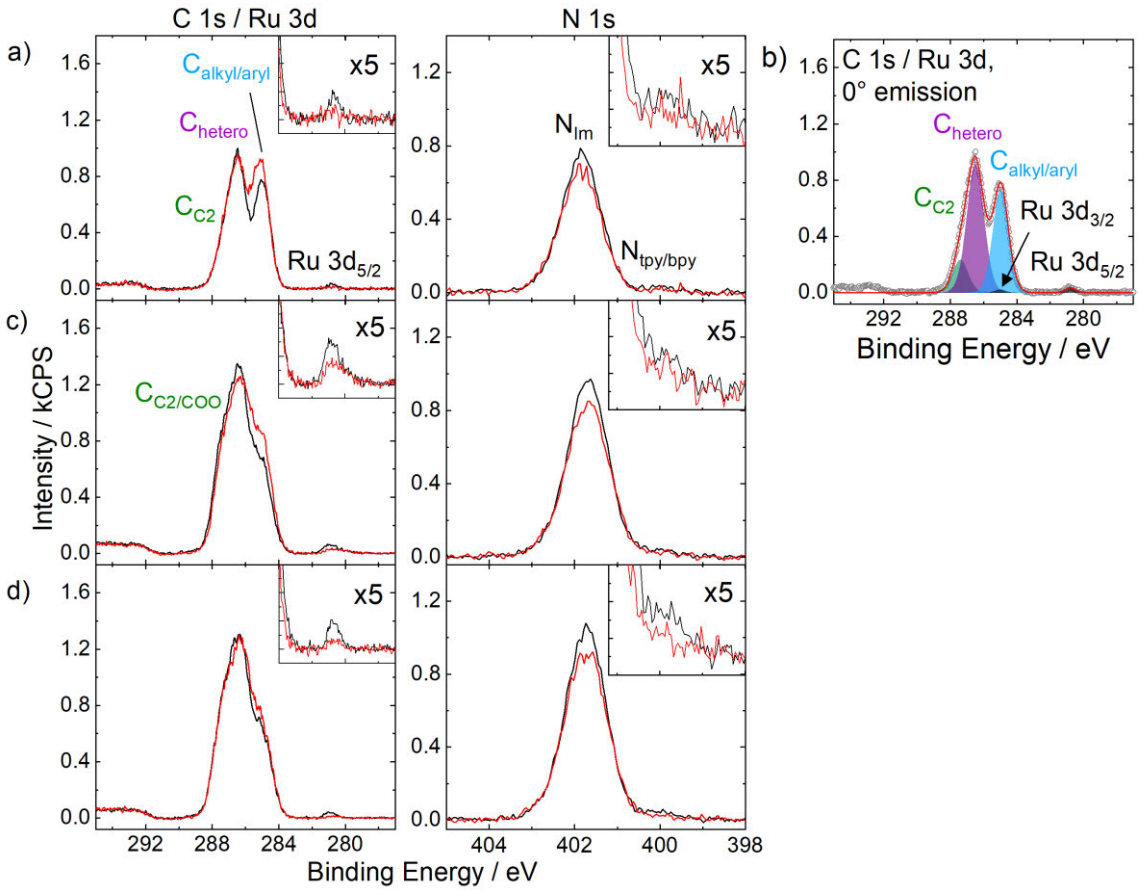

Figure 11: C 1s/Ru 3d and N 1s XP spectra of nominal 2.5%$_{mol}$ solutions of a) **6** in [C_4C_1Im][PF_6], c) **6** in [C_2C_1Im][OAc] and d) **7** in [C_2C_1Im][OAc] in 0° (black) and 80° emission (red) with upscaled Ru $3d_{5/2}$ and $N_{tpy/bpy}$ signals (x5) shown in the insets; b) applied deconvolution of the C 1s/Ru 3d region depicted in a) exemplarily shown in 0° emission. Reproduced from [P5] with permission from the PCCP Owner Societies.

Comparing 0° and 80° emission spectra in *Figure 11a* revealed a ~50% decrease of the Ru $3d_{5/2}$ at 80° (see inset in C 1s/Ru 3d spectrum for 5x amplified intensities) indicating depletion of **6** from the IL/vacuum interface.[P5] This indication was confirmed by a simple estimation of the exponential damping (IMPF: 2.8 nm for Ru 3d photoelectrons, topmost molecular layer consists only of IL ions (~0.4 nm[124])), which yielded a similar decrease of the Ru 3d signal, while a pure orientational effect with the tpy and/or bpy ligands exposed to the vacuum and an overall homogeneous distribution of the complex at the interface yielded only ~30% signal reduction at 80°.[P5] Conforming with the depletion of **6**, the $N_{tpy/bpy}$ signal also showed a strong decline with increasing surface sensitivity (see inset in N 1s spectrum for 5x amplified signal). The increase of the $C_{alkyl/aryl}$ signal reflected the preferential termination of the surface with the butyl chains of the solvent, as discussed in *Chapter 2.2*.

In contrast to the $[C_4C_1Im][PF_6]$ solution, **6** showed full dissolution in $[C_2C_1Im][OAc]$ and visibly yielded a higher intensity for the Ru $3d_{5/2}$ signal, as depicted in *Figure 11c*.[P5] Closer inspection of this signal revealed a major peak at 280.9 eV conforming with the species found in solution of $[C_4C_1Im][PF_6]$ and, additionally, an unexpected low-binding energy shoulder at 280.0 eV accounting for ~20% of the overall Ru 3d intensity. The overall intensity of the Ru 3d signal agreed well with the intensity expected from nominal composition of the solution; this was also true for the here actually detected Cl 2p signal.[P5] A possible explanation for the second metal species was extracted from the $N_{tpy/bpy}$ signal, which showed an intensity deficit at 0°, hence indicating a deficiency of ligands. This could be due to substitution of a fraction of polypyridyl ligands which then evaporated under UHV. The substitution could be triggered by coordination of $[OAc]^-$ or NHCs formed in solution, even though no evidence for coordinated anions nor for NHC species was observed in XPS.[P5] However, acetic acid vapor, which must form alongside NHC species, was detected by QMS supporting the presence of NHC in solution, similar to the UPS and MS results by *Hollóczki et al*[121]. Acetic acid vapor was also observed for neat $[C_2C_1Im][OAc]$.[P5] It should be further noted that both the Ru 3d signals and the $N_{tpy/bpy}$ showed very low intensities, and the latter was detected in close vicinity to the very intense N_{Im} signal, introducing a relatively large uncertainty into quantitative statements; the exact nature of the species present remained therefore inaccessible using XPS.[P5]

Interestingly, the different Ru species were found to exhibit a different interfacial behavior, as is evident comparing normal and grazing emission spectra in *Figure 11c*: While the major contribution at 280.9 eV energy showed a significant decline to ~50% at 80°, the low-binding energy species at 280.0 eV remained virtually constant. Similar to the $[C_4C_1Im][PF_6]$ solution, **6** showed depletion in $[C_2C_1Im][OAc]$, whereas the minority species was found homogeneously distributed at the surface, which, again, is an indication for a different coordination sphere around the metal center. Also, the $C_{alkyl/aryl}$ signal showed a significant increase, which is due to an orientational effect at the surface with the alkyl moieties of both cation and anion exposed to the vacuum, similar to the surface orientation discussed above for $[C_4C_1Im][PF_6]$.[P5] This behavior was first reported by *Zhang et al.* for a binary mixture[94] and was confirmed in [P5] for neat $[C_2C_1Im][OAc]$ and the catalyst solutions.[P5]

Investigation of the solution of **7** in [C_2C_1Im][OAc], also yielded a significantly lower intensity of the Ru $3d_{5/2}$ signal at 280.9 eV than expected, owing to the lower solubility than the nominal concentration, as shown in *Figure 11d*. At 0°, the Ru:Cl:$N_{tpy/bpy}$ ratio of 1:1.3:6.1 agreed quite well with the molecular structure of the complex indicating its intactness.[P5] Notably, the solution showed a significant amount of a surface-active contamination, which was removed by mild Ar^+ sputtering.[P5] The observation that the Ru 3d signal was detected at the same binding energy as observed for solutions discussed above and that an acceptable Ru:ligand ratio was found confirmed efficient employment of sputtering for these systems.[P5] Intriguingly, in contrast to **6**, no low-binding energy feature was observed for the solution of **7** in [C_2C_1Im][OAc], indicating a higher stability of the complex in the IL due to the carboxylic acid/carboxy groups.[P5]

The carboxylic acid/carboxy groups, however, do not seem to have a significant impact on the interfacial behavior of the complex, since comparing normal and grazing emission spectra reflected similar characteristics as discussed above revealing depletion of **7** from the IL/vacuum interface.

Since complexes **6** and **7** have shown significant depletion from the IL/vacuum interface, we deliberately modified the ligands with a variety of non-fluorinated side chains to achieve surface segregation in a systematic study of another set of Ru polypyridyl complexes (**8-11**, synthesized by Luciano Sanchez Merlinsky, Universidad de Buenos Aires, Argentina).[P7] The environmental and toxicologic concerns of per- and polyfluoroalkyl substance (PFAS)-based side chains[54, 55], as used in *Chapter 4.1.1* to facilitate surface enrichment of **5**, and the proposed ban of such substances on the European Union level (see Ref. 125 for a critical review) motivated us to only focus on non-fluorinated modifications.[P7]

In complexes **8-11**, all coordination sites are occupied by bpy ligands, in specific, two disodium 2,2'-bipyridine-4,4'-dicarboxylate (dcbNa) ligands introducing charges for satisfying solubilities and one bpy ligand modified with two C_9 (in complex **8**), C_1 (**9**), ethoxy (OC_2, **10**) and tert-butyl (t-C_4, **11**) groups as the potentially surface-active moieties.[P7] The complexes were synthesized as $[PF_6]^-$ salts.[P7] Recently published by another group, a Ru complex with a trioctylphosphine and a *para*-cymene ligand showed strong enrichment at the IL/vacuum interface.[38] However, the authors studied only one

complex and the solution showed a surface-active polysiloxane contamination, which might have influenced the enrichment effect.[38] Metallosurfactant-like complexes were also investigated in aqueous solution showing enrichment with special focus on structural properties at the water/air interface and shapes of micelles and vesicles.[126-130] In terms of catalysis, however, the focus was laid on studying the impact of the metallomicelles and vesicles on catalytic conversions[131, 132] rather than exploiting the high local catalyst concentration at the liquid/gas interface, for which this thesis aims at providing a basis.

$[C_2C_1Im][OAc]$ was chosen as the solvent providing satisfying solubilities of all the complexes. $1\%_{mol}$ solutions of **8-11** have visibly provided full dissolution of the complexes and are discussed in the following to systematically compare the interfacial behavior of the attached organic groups.

Figure 12a depicts C 1s/Ru 3d and N 1s XP spectra of the solution of **8**. Very intense Ru $3d_{5/2}$ and N_{bpy} signals were detected at 280.9 and 400.0 eV, which are at a similar binding energy as found for the catalyst solutions shown in *Figure 11*. The Ru $3d_{5/2}$ signal clearly corresponded to only one Ru species (see inset for 5x enhanced signal) ruling out a chemical alteration in solution as observed for the solution of **6** in $[C_2C_1Im][OAc]$.[P5, P7] Also, the Ru 3d:N_{bpy} ratio excellently matched the stoichiometry of the complex confirming stability in solution.[P7] Both the Ru $3d_{5/2}$ and the N_{bpy} signals showed a largely enhanced intensity at 0° and 80° compared to the nominal composition (cf. solutions in *Figure 11* with a comparable actual concentration or higher), which is again indicative for pronounced enrichment at the IL/vacuum interface.[P7] The C_{alkyl} signal, which contains contributions from the IL and the ligand system of **8**, showed an immense increase at 80°, while the Ru $3d_{5/2}$ and N_{bpy} signals only slightly increased revealing the C_9 chains as the surface-active moieties terminating the surface.[P7] The strong enrichment of **8** goes along with a strong decrease of the IL-specific N_{Im} signal indicative for the depletion of the solvent.[P7] Overall, these results are in analogy to the buoy-like enrichment encountered in *Chapter 4.1.1*, which was induced by PFA-based side chains and provide an interesting and environmentally less concerning alternative to these systems.[P7]

This fluorine-free buoy effect was not detected for equivalent solutions of the complexes **9-11** without long alkyl chains shown in *Figures 12b-d*.[P7] The complex-specific Ru $3d_{5/2}$ and N_{bpy} signals showed intensities barely discriminable from the

background and the spectra resemble findings discussed for solutions of complexes **6** and **7**. Overall, these findings suggested depletion from the IL/vacuum interface also for **9-11** in [C_2C_1Im][OAc], and thus revealed that the C_1-, OC_2 or t-C_4-modified bpy ligands are not suitable for inducing enrichment of the complexes.[P7]

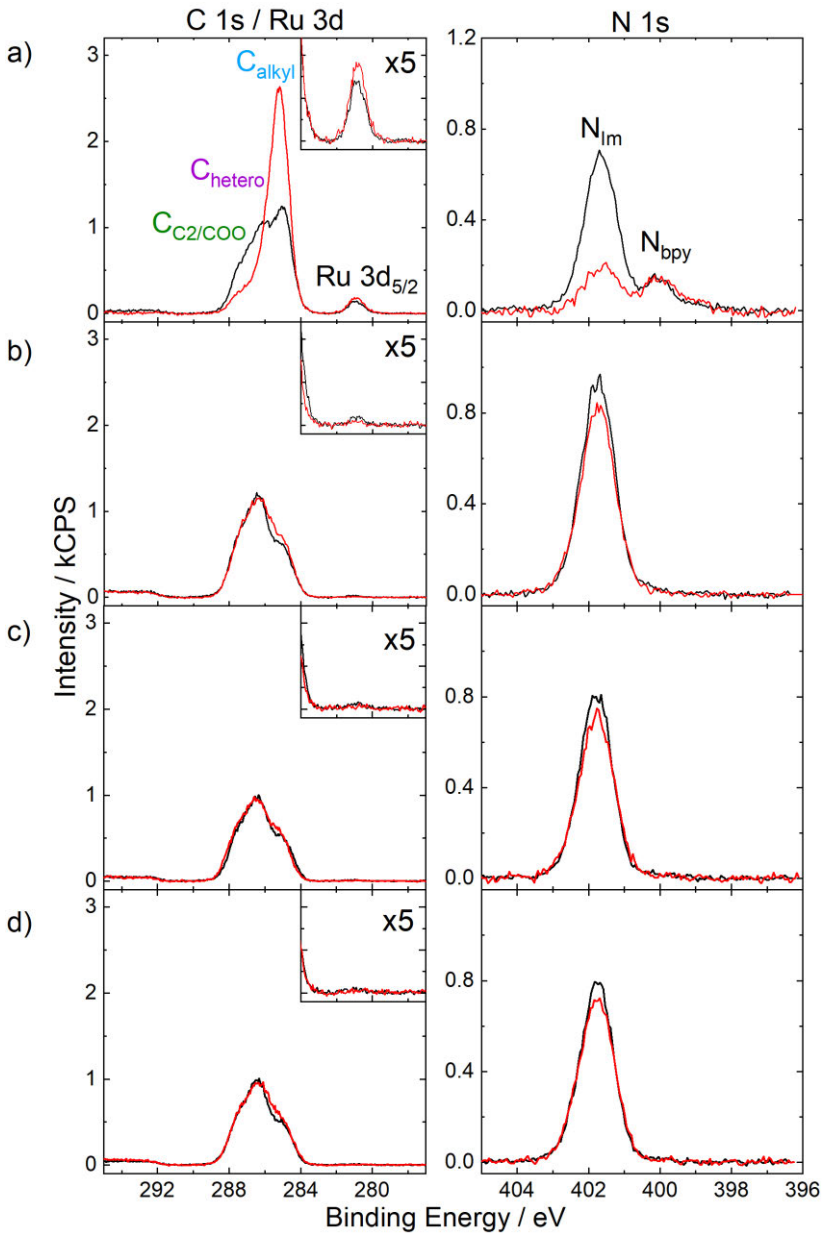

Figure 12: C 1s/Ru 3d and N 1s XP spectra of 1%$_{mol}$ solutions of a) **8**, b) **9**, c) **10** and d) **11** in [C_2C_1Im][OAc] in 0° (black) and 80° emission (red). Upscaled Ru $3d_{5/2}$ signals (x5) are depicted in the insets. Adapted from [P7] under CC BY license.

4.1.3 Cyclooctadiene- and TPPTS-based Schrock-Osborn-type Catalysts[P3]

Similar to the polypyridyl complexes discussed in *Chapter 4.1.2*, the uncharged nature of cyclooctadiene (COD) as sole ligands attached to metal cations (such as Rh(I) in the following) yield charged metal complexes promising sufficient solubilities in ILs. We employed commercially available $[Rh(COD)_2][TfO]$ (**12**), which, indeed, showed a particularly high solubility in the IL solvents employed, that is, $[C_nC_1Im][TfO]$ (n=2, 4, 8) and $[C_2C_1Im][C_2OSO_3]$. In terms of catalysis in ILs, an early work has revealed a higher overall conversion in hydrogenation of cyclohexene when using a $[Rh(COD)_2]^+$-based catalyst compared to Wilkinson's catalyst.[133] $[Rh(COD)_2]^+$ complexes were also used as catalyst precursors, e. g. for *in situ* formation of catalysts with Schrock-Osborn-type structure $[Rh(COD)(L)_2][X]$ (L=phosphine ligand) in asymmetric hydrogenation.[134, 135] A similar *in situ* formation of such a catalyst was also attempted in [P3] using L=TPPTS, which has been used before for similar intentions in our group[37], and will be presented after discussing XPS analyses of $[Rh(COD)_2][TfO]$ solutions in the ILs.

Rh 3d and C 1s XP spectra of a $20\%_{mol}$ solution of **12** in $[C_2C_1Im][TfO]$ are shown in *Figure 13a*. Besides the major spin-orbit-resolved Rh 3d signals of Rh(I) at 313.9 and 309.2 eV, additional smaller contributions shifted about 1 eV to higher binding energy (indicated by arrow and shown color-coded in *Figure 13b*) were detected indicating a more oxidized Rh species.[P3] These features were also detected in a solution prepared under full exclusion of air, as well as, in the solid compound and no indication of X-ray-induced oxidation of the catalyst was found (not shown), which suggested presence of the oxidized species already in the commercial $[Rh(COD)_2][TfO]$ powder[P3]; note that an additional oxidized Rh species was also reported for commercial samples of Wilkinson's catalyst using XPS.[136] In the C 1s region, the C_{TfO} signal at 292.9 eV is due to the IL anion and the C atoms of the COD ligands were assigned to give a joint signal with C_{alkyl} species of the IL cation, $C_{alkyl/COD}$. It is worth noting that the COD ligands contain chemically non-equivalent C atoms due to a) coordination to the metal center and b) different hybridization (sp^2 and sp^3)[137, 138] for which differences in binding energy could be expected. However, the considerations discussed below supported validity of assuming a joint $C_{alkyl/COD}$ signal with equal C_{COD} atoms.[P3]

The intensities detected from the Rh 3d and $C_{alkyl/COD}$ signals at 0° were found to only reflect 63% and 58% of the nominally expected values, while all other signals (not shown)

showed a slightly higher intensity of ~10%.[P3] Owing to the latter fact, a similarly higher intensity must be expected for the C_{alkyl} contribution to $C_{alkyl/COD}$, so that the lower intensity observed for the $C_{alkyl/COD}$ signal (58% of nominal) was attributed to the contribution of C_{COD} atoms, which consequently was only 45% of the expected intensity.[P3] The fact that the COD content is therefore lower than the Rh content suggested partial non-intactness of the complex in $[C_2C_1Im][TfO]$ and/or under UHV conditions[P3], which will be outlined in more detail below. Note that non-intactness of $[C_2C_1Im]^+$ was ruled out with the N_{Im}:C_{C2}:C_{hetero} ratio, which excellently agreed with the molecular structure of the cation, and with the ~10% higher N 1s intensity at 0°.[P3] At 80°, the Rh 3d and $C_{alkyl/COD}$ significantly declined revealing a strong depletion of the metal species present in solution from the topmost molecular layer.[P3] Since the topmost molecular layer only contributes with ~10-15% to the 0° spectra and since visual inspection indicated that all of **12** was dissolved in the IL, the strong intensity deficit of Rh 3d and $C_{alkyl/COD}$ at 0° must also be attributed to the non-intactness of **12** in solution.[P3] The lack of COD carbon becomes evident from *Figure 12c*, which contrasts the C 1s region expected from nominal composition (*top*: $C_{alkyl/COD}$ expected to be larger than C_{hetero}) and the actually detected XP spectrum.

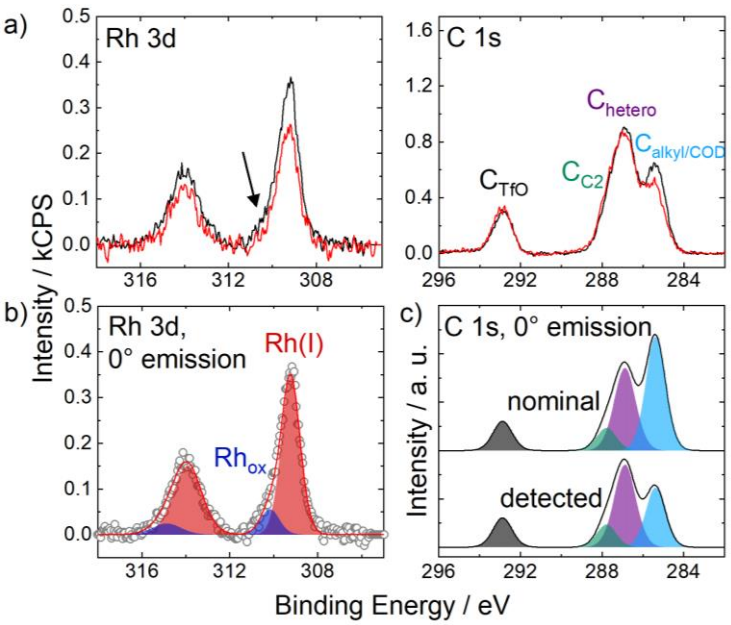

Figure 13: Rh 3d (left) and C 1s (right) XP spectra of a 20%$_{mol}$ solution of **12** in $[C_2C_1Im][TfO]$ in 0° (black) and 80° (red) emission, b) deconvolution applied for the Rh region at 0°, c) deconvolution applied for the C 1s region exemplarily shown at 0° involving spectra actually detected (bottom) and expected from nominal composition (top). Reproduced from [P3] under license CC BY 4.0.

We provided three different approaches to deduce the COD content per metal center present[P3]: approaches a) and b) assume full superposition of C_{alkyl} and C_{COD} and differ in estimation of the contribution of C_{COD} to $C_{alkyl/COD}$ from a) F 1s, O 1s, N_{Im}, C_{C2}, C_{hetero} and S 2p signals and b) from only the N_{Im} signal and c) allowing considerable binding energy shifts of chemically differing C atoms in COD ligands by estimating the C_{COD} contribution to the entire cationic signal envelope from the N_{Im} signal. All approaches yielded a 1.4:1 COD:Rh ratio in solution instead of 2:1; the fact that the different pathways showed similar results supported the assumption of a joint $C_{alkyl/COD}$ signal.[P3]

The overall intensity deficit of the Rh 3d signal measured in 0° (about ~40%) as compared to the nominal Rh content was also found in $[C_4C_1Im][TfO]$, $[C_8C_1Im][TfO]$ and $[C_2C_1Im][C_2OSO_3]$ confirming similar effects as described above.[P3] An even lower COD content than Rh was also observed for all ILs except for $[C_8C_1Im][TfO]$, where the Rh and COD matched the 1:2 ratio indicating that the longer alkyl chains in this IL might prevent (or decrease) ligand loss.[P3] The COD deficit relative to Rh found in the former ILs could be explained by substitution of COD with $[TfO]^-$ or $[C_2OSO_3]^-$ anions, which are able to coordinate via the SO_3^- groups, e. g. in η^1-$OS(O)_2R$, η^2-$O_2S(O)R$, or μ-$O_2S(O)R$ motifs[139]. In fact, this conjecture was supported by the O 1s XP spectrum of the 20%$_{mol}$ catalyst solution in $[C_2C_1Im][TfO]$ (not shown) showing a minor high-binding energy shoulder, which could correspond to coordination of the anion.[P3] Besides this effect, the strong Rh deficit at 0° observed for all solutions could be explained by formation of species preferably located in the bulk of the solution and thus not accessible with XPS, possibly nanoparticles or clusters formed from **12**.

Inspired by the application of $[Rh(COD)_2]^+$ complexes to form $[Rh(COD)(L)_2][X]$ (L=phosphine ligand) *in situ*[134, 135], we attempted to exploit the deficit of COD in solution for increasing the local Rh concentration at the IL/vacuum interface by offering a more surface-active phosphine ligand.[P3] TPPTS was previously found to exhibit surface activity in a similar Rh complex.[37] We chose $[C_2C_1Im][C_2OSO_3]$ where TPPTS has shown a high solubility, even though the reported solubility of 16.6%$_{mol}$[37] by far exceeded the maximum solubility found within the scope of this thesis of ~7%$_{mol}$, which was assessed using the P 2p XP signal of a saturated solution.[P3] To ensure full solubility of TPPTS in the precursor solution, we used a slightly lower TPPTS concentration of 5.9%$_{mol}$ for formation of

[Rh(COD)(TPPTS)$_2$][TfO] (**13**) with stoichiometric amount of [Rh(COD)$_2$][TfO] yielding a final concentration of **13** of 3.1%$_{mol}$ when quantitative formation is assumed.[P3]

Figure 14 contrasts the obtained solution of **13** in [C_2C_1Im][C_2OSO_3] (*top*) and a TPPTS-only solution with an identical TPPTS content (*bottom*). Comparison of the P 2p signals revealed a 0.7 eV shift of the signal to higher binding energy for the solution of **13** which confirmed coordination of the phosphine ligand to the metal center. According to the relatively strong donation capabilities of TPPTS, the Rh 3d$_{5/2}$ signal was detected at 309.0 eV, which is 0.2 eV lower in binding energy as observed for a 20%$_{mol}$ solution of **12** in the IL.[P3] Owing to the low intensity of the Rh 3d signal, however, a relatively large uncertainty must be expected for the binding energy. In contrast to the solution without adding TPPTS, the Rh 3d intensity at 0° found for the solution of **13**, indeed, matched the value expected from the nominal composition, which revealed a higher relative metal content in the near-surface region when compared to the precursor solution, where a deficit of Rh was found at 0°.[P3] The aryl C atoms of TPPTS gave a joint signal with C_{alkyl} and C_{COD} atoms, $C_{alkyl/COD/aryl}$, which showed a strong increase at 80° confirming the surface activity of the TPPTS ligand.[P3] The extent of the increase is slightly lower than found for the TPPTS-only solution, which was assigned to the contribution of COD to the signal exhibiting no surface activity.[P3] Owing to the low concentration and the damping of the relatively large TPPTS ligand, which is preferentially located at the surface, no Rh 3d or P 2p signals could be detected. With the absence of these signals, strong enrichment of **13** at the surface could be excluded.

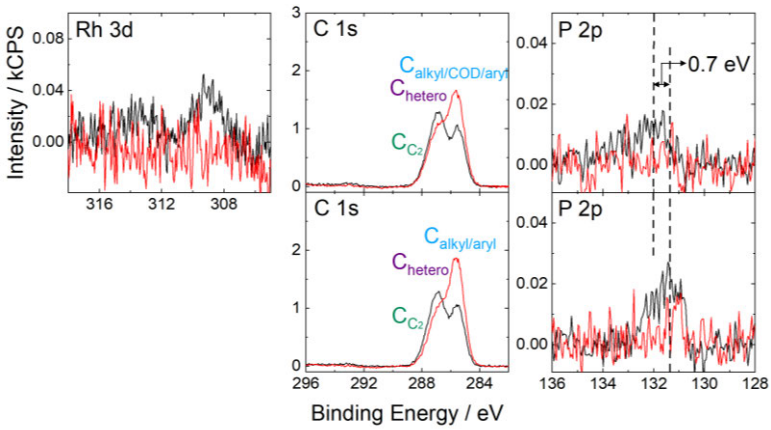

Figure 14: Rh 3d, C 1s and P 2p XP spectra of a 3.1%$_{mol}$ solution of **13** (top) and C 1s and P 2p XP spectra of a solution of TPPTS in [C_2C_1Im][C_2OSO_3] with similar overall TPPTS content in 0° (black) and 80° emission (red). Reproduced from [P3] under license CC BY 4.0.

Chapter 4.1 has provided chemical and surface-compositional information on the catalysts under investigation with rational modifications of the ligand system to facilitate enhancement of the catalyst concentration at the IL/vacuum interface. Apart from structural features of the ligands, surface enrichment effects are also highly affected by the surrounding of the catalyst and external conditions.[P2, P4, P6, P7] In the following chapters, the influence of the bulk concentration of the catalyst, the sample temperature and the IL solvent will be discussed mainly for solutions of **5** and **8**, which have shown strong surface enrichment (see *Chapters 4.1.1* and *4.1.2*).

4.2 Influence of the Bulk Concentration on the Surface Composition[P2, P4, P7]

Owing to the excellent solubility of **5** in ILs, we studied this complex over a wide concentration range of 1-30%$_{mol}$ in $[C_4C_1Im][PF_6]$, which is the solvent used above for demonstrating the buoy effect for **5**.[P2, P4] The normalized content of the Pt 4f signal, which is plotted in *Figure 15a* (*top*) against the molar concentration, is the detected signal intensity divided by the nominal one and thus a measure of the enrichment. A value of 1 (indicated by a grey dashed line) corresponds to a situation with homogeneous distribution of the catalyst at the surface and random surface orientations and configurations of the molecules.[P2, P4] In both 0° (black) and 80° emission (red), the normalized content clearly increased upon decreasing the bulk concentration of the catalyst revealing most pronounced surface enrichment of the catalyst at lowest concentration.[P2, P4] This result is greatly promising for catalytic applications, where low catalyst concentrations are practical, with most efficient metal utilization using a minimum of catalyst in the bulk with a maximized surface concentration. A similar trend was found previously for binary mixtures of the fluorinated IL $[PFC_4C_1Im][PF_6]$ in $[(C_1O)_2Im][PF_6]$[97] and in $[C_4C_1Im][PF_6]$[88].

Inspection of the absolute Pt 4f intensities shown in *Figure 15a* (*bottom*) provided more detailed insights into the surface composition upon varying the catalyst concentration.[P2, P4] While at 0° (black) the intensities increased with increasing concentration according to the higher bulk content of the catalyst up to 30%$_{mol}$, the 80° intensities (red) only showed a strong initial increase from 1 to 5%$_{mol}$ but remain more or less on a steady level at higher concentrations (note that the slight increase going from 5%$_{mol}$ to higher concentrations was

due to the contribution of the bulk with its higher Pt content to the 80° spectra).[P2, P4] These results suggested that the surface layer is already in the saturation regime at 5%$_{mol}$ while a concentration of 1%$_{mol}$ is not sufficient to achieve saturation.[P2, P4]

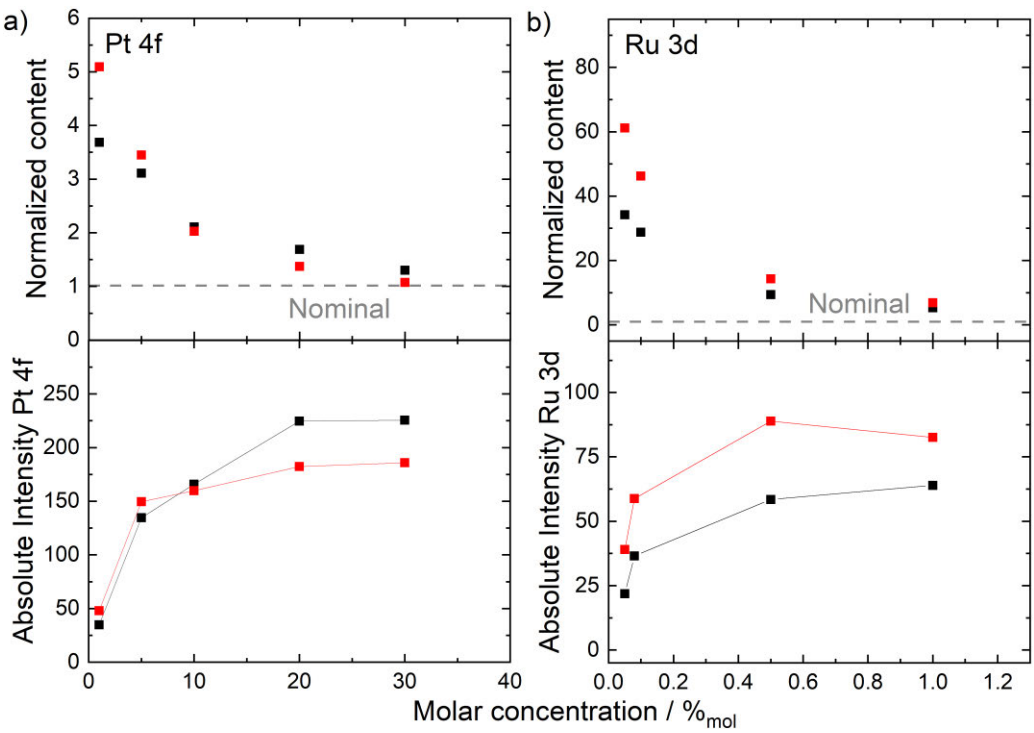

Figure 15: Normalized contents (top) and total peak intensities (bottom) derived from metal signals of a) **5** in [C_4C_1Im][PF_6], and b) **8** in [C_2C_1Im][OAc], in 0° (black) and 80° emission (red) upon varying the catalyst bulk concentration. Adapted from [P2], [P4] and [P7] under CC-BY-NC-ND, CC-BY-NC and CC BY licenses.

We further aimed to correlate the concentration-dependent peculiarities extracted from XPS to the surface tension of the solutions using the PD method (experiments conducted by Dr. Ulrike Paap and Afra Gezmis, Chair of Physical Chemistry II, FAU Erlangen-Nürnberg). *Figure 16* depicts the obtained surface tension for solutions of **5** in [C_4C_1Im][PF_6] with a catalyst concentration between 0-10%$_{mol}$ at 298 K (black) and the total peak area detected in XPS signals at 80° (blue open squares) against the molar catalyst concentration.[P4] Aside from the Pt 4f signal, the XPS data is now complemented with the F_{CFx} (blue open triangles) and C_{alkyl} (blue open circles) signals.[P4] In accordance with the Pt 4f signal, these signals show an increase and a decrease, respectively, upon increasing the concentration until a plateau is reached at 5%$_{mol}$ to again emphasize a situation where the surface is saturated with the complex at 5%$_{mol}$ or higher.[P2, P4] The surface tension values (black solid squares), however, showed a steady decrease with increasing concentration without displaying a

plateau at 5 and 10%$_{mol}$, even though XPS evidenced a similar composition of the topmost surface layer.[P2, P4] This behavior was attributed to a significant change in cohesive forces upon changing the catalyst concentration in the layers below the topmost surface layer, which corresponds to a change in surface tension. This behavior is known for aqueous surfactant solutions where the surface tension decreases beyond saturation until the critical micelle concentration was reached.[140] Even though the microscopic surface composition of IL mixtures derived from ARXPS was nicely correlated to surface tension data for IL mixtures in the recent past[77, 98, 141], a complete representation of the ARXPS data with the surface tension was not achieved for the system investigated herein.[P2, P4]

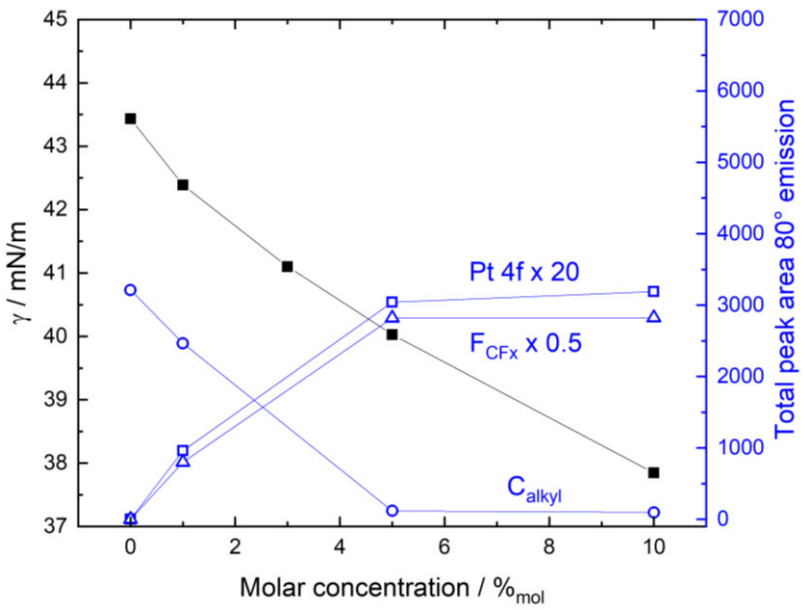

Figure 16: Surface tension γ at 298 K (black full squares, referring to left vertical axis) and total peak areas of the Pt 4f (blue open squares, x20), F_{CFx} (blue open triangles, x0.5) and C_{alkyl} signals (blue open circles) in 80° emission at room temperature (referring to right vertical axis) of solutions of **5** in [C_4C_1Im][PF_6] over a concentration range of 0–10%$_{mol}$. Adapted from [P4] under CC-BY-NC license.

As is also visible from *Figure 15b*, variation of the concentration of **8** in [C_2C_1Im][OAc] yielded similar outcomes as found for **5** in [C_4C_1Im][PF_6]; however, we were able to study the Ru-based system at particularly low concentrations ranging from 0.05%$_{mol}$ to 1%$_{mol}$ (mind the different concentration scales in *Figures 15a* and *b*)[P7]: The enrichment also increased upon lowering the concentration (*Figure 15b*, *top*) and the absolute Ru 3d intensities at 80° (*Figure 15b*, *bottom*, red) showed a plateau at 0.5%$_{mol}$ and higher. At lower concentrations, the absolute intensity strongly decreased indicating saturation of the surface with **8** already at 0.5%$_{mol}$, which is much lower than found for the Pt complex **5** (no

saturation at 1%$_{mol}$).[P7] This effect is certainly influenced by the surface tension of the different solvents ([C_4C_1Im][PF_6]: 43.4 mN/m under vacuum[P4] and [C_2C_1Im][OAc]: 47.1 mN/m at 298 K[142]), which has shown to substantially affect the surface affinity of solutes in solution, as will be discussed in detail in *Chapter 4.4*. However, also the structure of the complexes could contribute to the saturation concentration influencing the packing density of complexes at the IL/vacuum interface.

4.3 Temperature Dependency of the Catalyst Concentration at the Surface[P4]

The thermal stability of **5** and the wide liquid window of the [C_4C_1Im][PF_6] solutions allowed us to study the influence of the temperature on the catalyst enrichment in this IL.[P4] In this chapter, we will first discuss the results obtained from a 1%$_{mol}$ solution corresponding to a situation where the surface was unsaturated with the complex at room temperature (see previous chapter) and compare to a solution within the saturation range, that is, 5%$_{mol}$.

Figure 17a depicts the normalized Pt and C_{alkyl} contents recorded in 0° and 80° from a 1%$_{mol}$ solution within a temperature range from 233-353 K.[P4] Both analyzation geometries unambiguously reflected a decrease of the Pt content upon raising the temperature, while the IL-specific C_{alkyl} content increased.[P4] These findings clearly corresponded to a lower degree of catalyst enrichment at the surface at higher temperatures.[P4] Subsequently recording XP spectra at room temperature after measurements at the temperature extrema (open circles and triangles in *Figure 17*) revealed reversibility of the thermal effect.[P4] An according temperature dependence was reported before for a binary mixture of the fluorinated IL [PFC_4C_1Im][PF_6] in [C_4C_1Im][PF_6] and was assigned to the larger contribution of the entropic term -TΔS to the surface free energy favoring a less ordered, that is, a less catalyst-enriched surface for our solutions.[88]

In contrast, temperature-dependent measurements of a 5%$_{mol}$ solution of **5** in [C_4C_1Im][PF_6] over a temperature range from 213-313 K, shown in *Figure 17b*, revealed virtually constant normalized contents at all temperatures measured.[P4] With this, no temperature effect was observed and the saturation of the surface with the complex was kept over the entire temperature range.[P4]

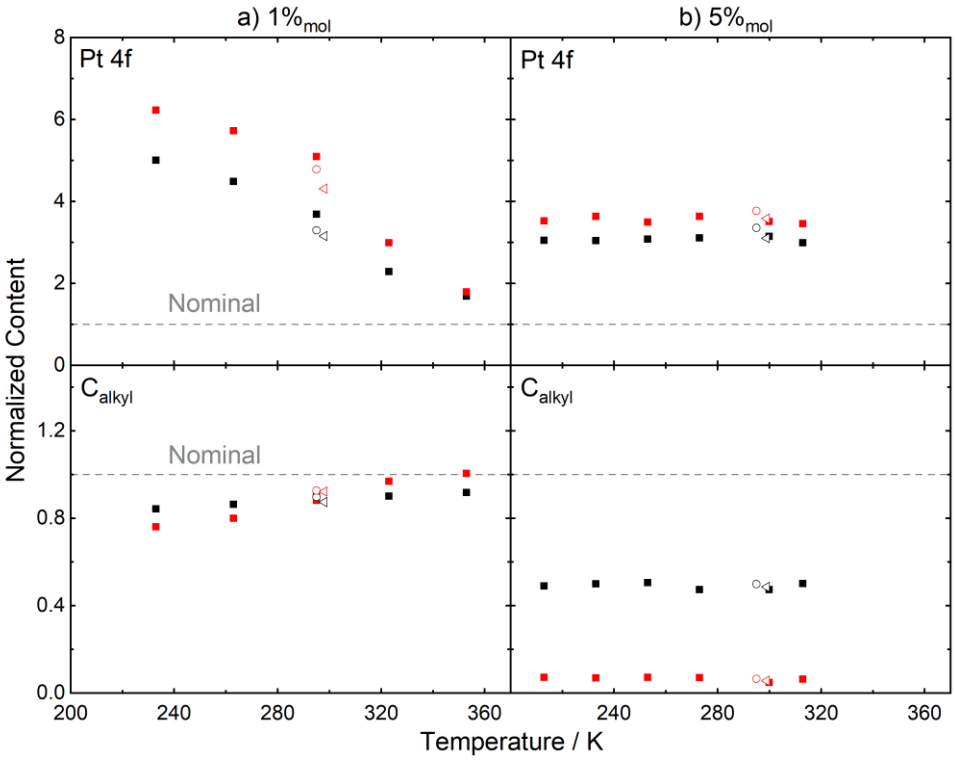

Figure 17: Normalized contents derived from Pt 4f (top) and C_{alkyl} (bottom) signals of a) a $1\%_{mol}$ and b) a $5\%_{mol}$ solution of **5** in $[C_4C_1Im][PF_6]$ in 0° (black squares) and 80° emission (red squares) at different temperatures. After measurements at the temperature extremes of the measurement series, the sample was brought back to room temperature and measured again (open circles after cooling series and open triangles after heating series). Adapted from [P4] under CC-BY-NC license.

4.4 Influence of the Solvent on the Surface Composition[P3, P6]

The final parameter affecting surface enrichment phenomena discussed herein is the IL solvent. While the influence of the IL on the electronic properties of organometallics was addressed several times using XPS[143-145], the different interfacial behavior of catalysts when varying the solvent IL was, to the best of my knowledge, not reported before. Solutions of the surface-active catalyst **5** have proven well-applicable for this intention[P6], which will be discussed first before providing complementary results from solutions of **12**.

As mentioned above, the preparation route for **5** in IL solution outlined in *Chapter 4.1.1* has proven suitable in $[C_2C_1Im][PF_6]$, $[C_4C_1Im][PF_6]$, $[C_8C_1Im][PF_6]$ and $[C_4C_1Im][Tf_2N]$, and **5** was found completely soluble in these ILs at all concentrations discussed in the following.[P6] The only difference in the $[PF_6]^-$ ILs is the length of the alkyl chains attached

to the $[C_nC_1Im]^+$ cation, which results in a higher surface affinity of the solvent cation with longer chains, as discussed in *Chapter 2.2*. $[C_4C_1Im][Tf_2N]$ was used to extract the influence of the anion on the surface enrichment compared to $[C_4C_1Im][PF_6]$ sharing the same cation.[P6] $[Tf_2N]^-$ ILs have shown a higher surface affinity than analogues based on $[PF_6]^-$ or other anions in mixtures of ILs.[72, 74, 94, 96, 146-148] To broaden the dataset with another anion, we also intended to use $[C_4C_1Im][Cl]$ as the solvent.[P6] However, since preparation of **5** was not successful in this IL, as outlined in *Chapter 4.1.1*, we additionally compared solutions of only the ligand $[C_3CNPFC_4Im][PF_6]$ in $[C_4C_1Im][Cl]$ and $[C_4C_1Im][PF_6]$.[P6]

Pt 4f and C_{alkyl} XP spectra of 1‰$_{mol}$ solutions of **5** in $[C_2C_1Im][PF_6]$ (black), $[C_4C_1Im][PF_6]$ (green), $[C_8C_1Im][PF_6]$ (blue) at 0° (left panel) and 80° (right panel) are depicted in *Figure 18a*. For comparison, the Pt 4f spectra of a 1‰$_{mol}$ solution of **5** in $[C_4C_1Im][Tf_2N]$ (orange) are shown. In the series of the $[PF_6]^-$-based IL solutions, the Pt 4f signal of **5** showed a strong gradual decrease at 0° and 80° upon increasing the C_n chain length. This effect was also observed for all other complex-specific signals (not shown)[P7], while the IL-specific C_{alkyl} signals reflected an inverse trend, which is most evident in the 80° spectra: the $[C_2C_1Im][PF_6]$ solution showed only a minor C_{alkyl} intensity, whereas in $[C_4C_1Im][PF_6]$ values close to nominal were found and the $[C_8C_1Im][PF_6]$ solution showed a much higher intensity than expected from the nominal composition.[P7] Overall, these findings clearly displayed a decreasing degree of surface enrichment of **5** in ILs with increasing C_n chain length owing to the higher surface affinity of longer C_n chains facilitating competition of the IL for presence at the surface.[P7] In fact, the Pt 4f intensity detected from the $[C_8C_1Im][PF_6]$ solution is in line with the nominal composition of the solution demonstrating that the surface affinity of **5** could even be suppressed to yield a homogeneous surface distribution by adequate choice of IL solvent.[P7]

The comparison of the Pt 4f intensities detected for the $[C_4C_1Im][PF_6]$ (green) and $[C_4C_1Im][Tf_2N]$ (orange) solutions in *Figure 18a* immediately revealed a much lower signal for the $[Tf_2N]^-$ solution and, consequently, a strong influence of the anion on the surface concentration of the solute[P7]. The intensities found for the $[C_4C_1Im][Tf_2N]$ solution quantitatively conformed with homogeneous distribution of **5** rather than surface enrichment, similar as in $[C_8C_1Im][PF_6]$. This finding was also accompanied by a slight increase of the C_{alkyl} signal at 80° for $[C_4C_1Im][Tf_2N]$ (not shown), which is indicative for

a larger presence of the alkyl chains at the outer surface when compared to the solution of $[C_4C_1Im][PF_6]$, where this signal showed a slight decrease at 80°.[P6]

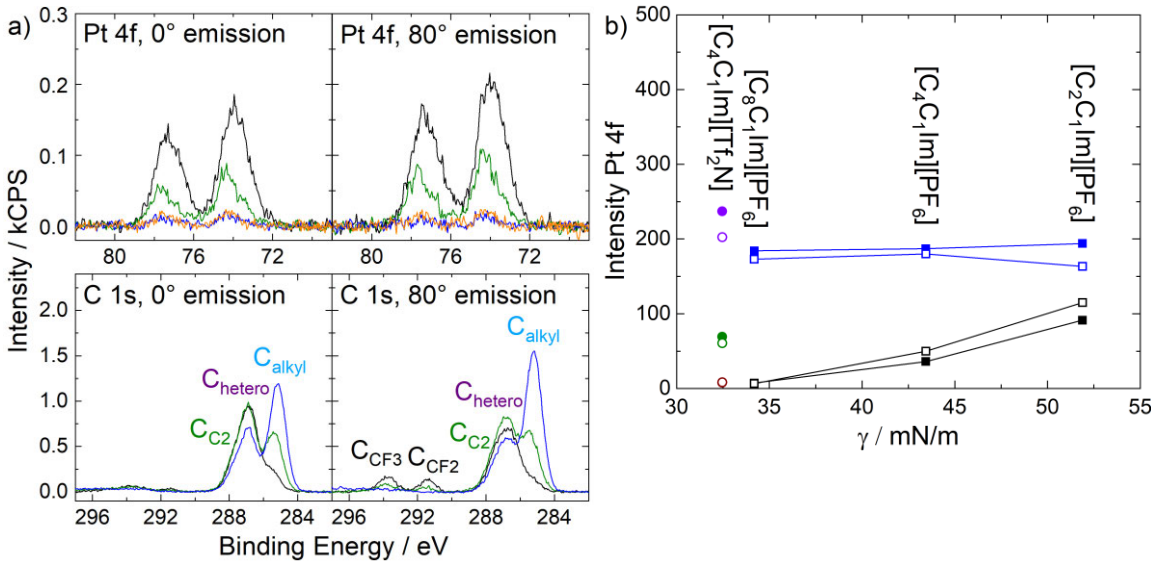

Figure 18: a) Pt 4f (top) and C 1s (bottom) XP spectra of $1\%_{mol}$ solutions of **5** in $[C_2C_1Im][PF_6]$ (black), $[C_4C_1Im][PF_6]$ (green) and $[C_8C_1Im][PF_6]$ (blue) in 0° (left) and 80° emission (right) at room temperature and Pt 4f spectrum of a $1\%_{mol}$ solution of **5** in $[C_4C_1Im][Tf_2N]$ (orange), b) absolute Pt 4f intensity from solutions of **5** with concentrations of $1\%_{mol}$ in the $[PF_6]^-$ ILs (black), $1\%_{mol}$ in $[C_4C_1Im][Tf_2N]$ (red brown), $10\%_{mol}$ in the $[PF_6]^-$ ILs (blue), $10\%_{mol}$ in $[C_4C_1Im][Tf_2N]$ (green) and $20\%_{mol}$ in $[C_4C_1Im][Tf_2N]$ (violet) in 0° (full symbols) and 80° emission (open symbols) against the surface tension γ of the neat ILs at 298 K. Note that for $1\%_{mol}$ in $[C_4C_1Im][Tf_2N]$ the signals for 0° (full) and 80° (open) fall on top of each other. Adapted from [P7] under CC BY license.

Overall, for the $1\%_{mol}$ solutions, the local concentration of the catalyst at the surface was found to be strongly influenced by the length of the C_n chain in the $[C_nC_1Im]^+$ cations and the nature of the anion.[P6] These structural features translate into a different interfacial behavior and thus, different surface tension values of the neat ILs.[69] The Pt 4f intensity detected for solutions with different ILs and concentrations plotted against the surface tension values γ of the neat ILs at 298 K obtained under ultra-clean vacuum conditions (experiments conducted by Dr. Ulrike Paap and Afra Gezmis, Chair of Physical Chemistry II, FAU Erlangen-Nürnberg) is depicted in *Figure 18b*. The previously discussed higher Pt 4f intensity at both 0° and 80° and thus stronger enrichment with decreasing alkyl chain length found for the $1\%_{mol}$ solutions of the $[PF_6]^-$ ILs (full and open black squares) excellently goes along with an increase in surface tension when decreasing the chain length.[P6] This is due to the most effective lowering in surface free energy upon accumulation of the surface-active complex **5** at the IL/vacuum interface when the surface

tension of the IL is high.[P6] The surface tension values of $[C_8C_1Im][PF_6]$ and $[C_4C_1Im][Tf_2N]$ (full and open dark red circles) are even low enough to facilitate homogeneous distribution, as discussed above.[P6]

In contrast to the $1\%_{mol}$ solutions, higher concentrations of $10\%_{mol}$ in the $[PF_6]^-$ ILs resulted in a constant Pt 4f intensity at 0° and 80° (full and open blue squares). The $10\%_{mol}$ solution of **5** in $[C_4C_1Im][PF_6]$ was already found to show saturation of the surface with the complex, as discussed in *Chapter 4.2.1*.[P2, P4] With a similar Pt 4f intensity and overall similar characteristics as the $[C_4C_1Im][PF_6]$ solution, surface saturation with the catalyst was also concluded for $[C_2C_1Im][PF_6]$ and $[C_8C_1Im][PF_6]$.[P6] Especially for the solution of $[C_8C_1Im][PF_6]$, where no surface enrichment of **5** was found at $1\%_{mol}$, this finding was quite surprising.[P6] Apparently, a higher bulk concentration of **5** renders accumulation of the complex at the interface more favorable, even to an extent where the surface is fully saturated.[P6] A different behavior was found for a $10\%_{mol}$ solution of $[C_4C_1Im][Tf_2N]$ (full and open green circles), where the Pt 4f intensity at 0° and 80° agreed well with the nominal composition indicating absence of enrichment or depletion phenomena.[P6] However, at $20\%_{mol}$, the Pt 4f intensity strongly exceeded the nominally expected value at 0° and 80° by a factor of 1.7 and 1.5, respectively, indicating surface enrichment of the catalyst.[P6] While at $10\%_{mol}$, the particularly low surface tension of $[C_4C_1Im][Tf_2N]$ prevented enrichment of **5**, increasing the concentration to $20\%_{mol}$ resulted in a situation where surface enrichment is more favorable than homogeneous distribution.[P6]

To confirm the effect of different anions on the surface composition, we studied $9.5\%_{mol}$ solutions of only the ligand $[C_3CNPFC_4Im][PF_6]$ in $[C_4C_1Im][Cl]$, wherein synthesis of **5** was not successful, and in $[C_4C_1Im][PF_6]$.[P6] The $[C_4C_1Im][PF_6]$ solution showed significant surface enrichment of the dissolved ligand but less pronounced when compared to a solution of **5** with the overall same amount of ligand (attached to the Pt center) in solution, as was already discussed in *Chapter 4.1.1*.[P4] Comparison of the XP spectra F 1s, N 1s and C 1s XP spectra of the two ligand solutions ($[C_4C_1Im][Cl]$ *top*, $[C_4C_1Im][PF_6]$ *bottom*) shown in *Figure 19* revealed a slightly more pronounced increase of the F_{CFx} signal and, in turn, a more pronounced decrease of the N_{Im}, C_{C2} and C_{hetero} signals at 80° for the $[C_4C_1Im][Cl]$ solution. Additionally, the C_{alkyl} signal showed a decrease at 80°, while for the solution of $[C_4C_1Im][PF_6]$ this signal showed no angular dependency. These findings conformed with a higher surface concentration of $[C_3CNPFC_4Im][PF_6]$ in $[C_4C_1Im][Cl]$,

which is in line with a much higher surface tension of neat $[C_4C_1Im][Cl]$, that is, 49.9 mN/m[P6], than compared to $[C_4C_1Im][PF_6]$ with a surface tension of 43.4 mN/m at 298 K and complement the findings discussed above.[P6]

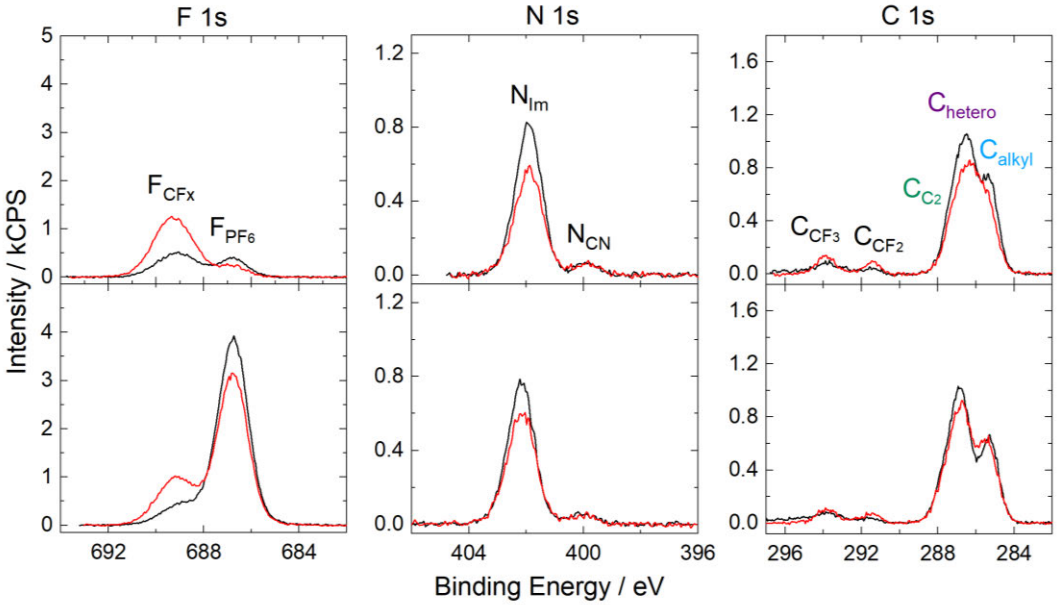

Figure 19: F 1s, N 1s, and C 1s XP spectra of 9.5%$_{mol}$ solutions of $[C_3CNPFC_4Im][PF_6]$ in $[C_4C_1Im][Cl]$ (top) and $[C_4C_1Im][PF_6]$ (bottom) in 0° (black) and 80° emission (red). Adapted from [P7] under CC BY license.

The concept of tailoring the surface concentration of solutes by variation of the solvent was also expanded to solutions of the Rh complex **12** in $[TfO]^-$-based ILs.[P3] In contrast to complex **5**, dissolving **12** in all ILs under investigation (see *Chapter 4.1.3*) resulted in strong depletion from the IL/vacuum interface of the metal species present in solution.[P3] Upon increasing the chain length on the $[C_nC_1Im]^+$ cation of the solvent from n = 2 to 4 and 8, the depletion of Rh even increased owing to the higher surface affinity of the longer chains, similar to what has been discussed for **5** in $[PF_6]^-$ ILs.[P3]

5 Summary

The nature of the IL/gas interface, in particular, the local catalyst concentration at this interface, is expected to significantly influence the catalytic performance in SILP catalysis and other concepts based on high interfacial areas between IL phase and the reactant/product environment. From this perspective, the aim of this thesis was to provide the fundamental parameters for the deliberate control over catalyst enrichment and depletion at the IL/vacuum interface. The ARXPS studies presented herein afforded valuable insights into the surface composition and how to deliberately modify the catalyst concentration at the surface by design of the ligand system, the bulk concentration of the catalyst, the temperature and the IL solvent. Apart from surface-compositional aspects, the experiments also furnished information on the chemical behavior of the catalysts in ILs.

Several organometallic catalysts with different ligand systems were investigated. Pt and Pd catalysts with ligand systems derived from CN-functionalized IL cations served as model systems for the majority of ARXPS experiments presented herein, providing high solubilities and stability under elevated temperatures, irradiation with X-rays and vacuum conditions. For these systems, a novel vacuum-driven preparation route directly in the IL was established, which was applicable to a variety of IL solvents. XPS has not only shown to be a powerful tool to monitor the formation of these catalysts in IL solution but also for extracting chemical information, which conformed with literature findings obtained from other experimental methods.

Since the initially studied catalysts showed no affinity to the IL/vacuum interface, these systems served as the starting point for demonstration of targeted surface enrichment by modification of the ligand systems with surface-active fluorinated alkyl groups. These groups acted like buoys localizing and accumulating the catalyst at the IL/vacuum interface. The results also indicated that the degree of enrichment is higher when employing two surface-active ligands instead of one. The impact of the buoy effect on the catalytic performance in ethene hydrogenation indicated a higher activity of the surface-enriched catalysts; this effect was, however, observed along formation of Pt particles limiting the significance for homogeneously catalyzed reactions to some extent. The herein described buoy effect is nonetheless promising to be transferred to other homogeneous catalysts, which do not exhibit particle formation under reaction conditions.

ARXPS investigations on a first set of Ru polypyridyl complexes containing a tpy and a bpy ligand revealed a change in the coordination sphere in [C_2C_1Im][OAc], while the complexes remained intact in more inert [C_4C_1Im][PF_6]. Functionalization of the ligand system with carboxylic acid groups, however, ensured chemical stability also in [C_2C_1Im][OAc]. These complexes were found depleted from the IL/vacuum interface in both ILs.

In a second set of Ru polypyridyl complexes carrying only bpy ligands, several functionalities attached to the ligand system were investigated to facilitate surface enrichment of these catalysts. In view of the environmental and safety concerns of PFA-based groups, which were used for demonstration of the buoy effect with the Pt catalysts, only PFA-free functionalities were considered including C_9, C_1, OC_2 and t-C_4 groups. The C_9 groups induced strong enrichment of the catalyst at the IL/vacuum interface, while all other complexes showed depletion demonstrating the fluorine-free or PFA-free buoy effect of the long hydrophobic alkyl chains.

Another measurement series on the cyclooctadiene-based catalyst [$Rh(COD)_2$][TfO] revealed non-intactness of the catalyst in [C_2C_1Im][TfO], [C_4C_1Im][TfO] and [C_2C_1Im][C_2OSO_3] under the applied vacuum conditions, evident from a Rh deficit and an even higher COD deficit found in XPS. Only in [C_8C_1Im][TfO], the Rh:COD ratio matched the stoichiometry of the complex, even though a strong concomitant deficit of these two species also suggested chemical alteration of a fraction of the catalyst in this IL. The present metal species showed depletion from the IL/vacuum interface in all ILs. Offering the phosphine ligand TPPTS for ligand substitution, however, resulted in XPS signals at 0° conforming with the nominal composition indicating presence of the complex in the near-surface region as expected from the weigh-in. Since no Rh signal was found at 80°, strong surface enrichment of the catalyst at the IL/vacuum interface could be excluded. However, the Rh concentration in the near-surface region could be enhanced relative to the depleted precursor complex by employing the TPPTS ligands.

Besides the surface activity of the ligand system, other parameters, that is, the bulk concentration, temperature and the IL solvent, were found to affect the local catalyst concentration at the surface. As exemplified for the surface-active Pt and Ru catalysts, the surface enrichment is more pronounced at lower bulk concentrations, which offers most

efficient atom utilization at the surface with a minimum employment of catalyst. The absolute amount of catalyst at the IL/vacuum interface has shown to increase with increasing bulk concentration until saturation of the surface with catalyst was reached.

Variation of the sample temperature has shown to afford sensitive control over the enrichment of the catalyst, as was studied for the surface-active Pt catalyst. In a concentration regime, where the surface was not saturated with the catalyst, the degree of enrichment showed an increase upon lowering the temperature. The fact that this effect was reversible constitutes the applied temperature to a delicate parameter for adjustment of the catalyst concentration at the surface. In the saturation regime, the surface composition was found constant at all temperatures investigated.

Finally, selection of the solvent strongly affected the catalyst concentration at the surface, as found for solutions of the surface-active Pt catalyst. As a general trend, a higher surface tension of the IL resulted in a higher degree of surface enrichment of the catalyst. ILs with a particularly low surface tension $[C_8C_1Im][PF_6]$ and $[C_4C_1Im][Tf_2N]$ even facilitated suppression of the catalyst's surface activity to afford homogeneous distribution at the surface. At sufficiently high concentrations, however, the surface was highly populated with the catalyst in all ILs under investigation. Nonetheless, for the solvent $[C_4C_1Im][Tf_2N]$ with lowest surface tension, a higher catalyst concentration was required to induce surface enrichment.

6 Zusammenfassung

Die Beschaffenheit der IL/Gas-Grenzfläche, insbesondere die lokale Katalysatorkonzentration an der Oberfläche, kann die Leistungsfähigkeit von SILP-Katalysatoren und anderen Systemen mit großen Grenzflächen zwischen der IL-Phase und der Reaktanten/Produktphase erheblich beeinflussen. Unter diesem Gesichtspunkt war das Ziel dieser Arbeit, die grundlegenden Parameter für die gezielte Steuerung der Konzentration von metallorganischen Katalysatoren an der IL/Vakuum-Grenzfläche durch Oberflächenanreicherung oder -abreicherung des Katalysators bereitzustellen. Die hier vorgestellten ARXPS-Studien lieferten wertvolle Erkenntnisse über die Oberflächenzusammensetzung der untersuchten Systeme und die gezielte Veränderung der Konzentration des Katalysators an der Oberfläche durch die Wahl und Struktur der Liganden, der Konzentration im Volumen der Lösung, der Temperatur und des IL-Lösungsmittels. Darüber hinaus lieferten die Experimente auch Informationen über chemische Eigenschaften der Metallkomplexe in ILs.

Es wurden mehrere metallorganische Katalysatoren mit unterschiedlichen Ligandensystemen untersucht. Pt- und Pd-Katalysatoren mit Liganden, die von CN-funktionalisierten IL-Kationen abgeleitet sind, dienten als Modellsysteme für einen erheblichen Anteil der hier vorgestellten ARXPS-Experimente, besonders durch ihre hohen Löslichkeiten und durch ihre Stabilität gegenüber höheren Temperaturen, Röntgenstrahlen und Vakuumbedingungen. Für die Synthese dieser Verbindungen wurde ein neuer Weg unter Vakuum direkt in der jeweiligen IL etabliert, der für eine Vielzahl von IL-Lösungsmitteln anwendbar war. XPS hat sich nicht nur als eine leistungsfähige Methode zur Nachverfolgung der Bildung dieser Katalysatoren in Lösung erwiesen, sondern diente auch zur Untersuchung chemischer Eigenschaften der Komplexe und der ILs, die mit den Literaturergebnissen anderer experimenteller Methoden übereinstimmten.

Da die ursprünglich untersuchten Katalysatoren keine besondere Affinität zur IL/Vakuum-Grenzfläche zeigten, sondern homogen verteilt waren, dienten diese Systeme als Ausgangspunkt für die Demonstration einer gezielten Oberflächenanreicherung durch Modifizierung der Liganden mit oberflächenaktiven fluorierten Alkylgruppen. Diese Gruppen wirkten wie Bojen, die den Katalysator an der IL/Vakuum-Grenzfläche lokalisieren und anreichern, wobei der Grad der Anreicherung höher einzuschätzen ist,

wenn zwei oberflächenaktive Liganden anstelle von einem verwendet werden. Die Auswirkungen des Bojeneffekts auf die katalytische Leistung bei der Hydrierung deuteten auf eine höhere Aktivität der oberflächenangereicherten Katalysatoren hin; dieser Effekt wurde jedoch zusammen mit einer Bildung von Pt-Partikeln beobachtet, was die Aussagekraft für die gewünschte Anwendung in der homogenen Katalyse einschränkte. Im Prinzip ist der Bojeneffekt jedoch auch auf andere Katalysatoren übertragbar, die keine Partikelbildung unter den Reaktionsbedingungen zeigen, sodass der Einfluss der Oberflächenanreicherung auf die katalytische Leistungsfähigkeit dieser homogenen Katalysatoren genauer untersucht werden kann.

Weitere ARXPS-Untersuchungen mit einer Reihe von Ru-Polypyridyl-Komplexen, die einen tpy- und einen bpy-Liganden enthalten, ergaben eine Veränderung der Koordinationssphäre in [C_2C_1Im][OAc], während die Komplexe in der recht inerten IL [C_4C_1Im][PF_6] intakt blieben. Die Funktionalisierung des bpy-Liganden mit Carbonsäure-gruppen sorgte jedoch auch in [C_2C_1Im][OAc] für chemische Stabilität. Die Komplexe zeigten eine Abreicherung an der IL/Vakuum-Grenzfläche in beiden ILs.

Bei einer zweiten Reihe von Ru-Polypyridylkomplexen, die nur bpy-Liganden beinhalten, wurden verschiedene an einen Liganden gebundene Funktionalitäten untersucht, um die Metallkomplexe an der Oberfläche anzureichern. Angesichts der negativen Wirkung auf Umwelt und Gesundheit von PFA-Materialien, die zur vorigen Demonstration des Bojeneffekts mit den Pt-Katalysatoren verwendet wurden, wurden nur PFA-freie Funktionalitäten in Betracht gezogen, darunter C_9-, C_1-, OC_2- und t-C_4-Gruppen. Die hydrophoben C_9-Gruppen bewirkten eine starke Anreicherung des Katalysators an der IL/Vakuum-Grenzfläche, während alle anderen Komplexe Abreicherung zeigten, was den fluorfreien- oder PFA-freien Bojeneffekt der langen Alkylketten belegte.

Eine weitere Messreihe behandelte den Komplex [$Rh(COD)_2$][TfO] und zeigte, dass der Katalysator in [C_2C_1Im][TfO], [C_4C_1Im][TfO] und [C_2C_1Im][C_2OSO_3] unter den angewandten Vakuumbedingungen nicht intakt war, was durch ein Rh-Defizit und ein noch höheres COD-Defizit mittels XPS nachgewiesen wurde. Nur bei [C_8C_1Im][TfO] stimmte das Rh:COD-Verhältnis mit der Stöchiometrie des Komplexes überein, obwohl ein starkes, miteinander einhergehendes Defizit dieser beiden Spezies auch auf eine chemische Veränderung eines Teils des Katalysators in dieser IL hindeutete. Die vorhandene

Metallverbindung zeigte eine Abreicherung von der IL/Vakuum-Grenzfläche in allen ILs. Bereitstellung des Phosphinliganden TPPTS für eine Ligandensubstitution führte jedoch zu XPS-Signalen in 0° entsprechend der nominellen Zusammensetzung, was auf das Vorhandensein des Komplexes in der erwarteten Menge im oberflächennahen Bereich hindeutete. Da bei 80° kein Rh-Signal gefunden wurde, konnte eine starke Oberflächenanreicherung des Katalysators an der IL/Vakuum-Grenzfläche ausgeschlossen werden. Letztlich konnte die Rh-Konzentration im oberflächennahen Bereich Liganden jedoch gegenüber dem abgereicherten Vorläuferkomplex durch Koordination von TPPTS erhöht werden.

Neben dem Einfluss der Liganden auf die Oberflächenzusammensetzung der Katalysatorlösungen wurden noch weitere Parameter für eine gezielte Einstellung der Oberflächenkonzentration des Katalysators untersucht, nämlich die Katalysatorkonzentration im Volumen, die Temperatur und das IL-Lösungsmittel. Die oberflächenaktiven Pt- und Ru-Katalysatoren zeigten eine stärkere Oberflächenanreicherung bei niedrigeren Volumenkonzentrationen. Anwendungsbezogen verspricht dieses Ergebnis eine möglichst effiziente Nutzung des Katalysators an der Oberfläche bei minimalem Materialaufwand. Die absolute Menge des Katalysators an der IL/Vakuum-Grenzfläche nahm mit zunehmender Konzentration im Volumen zu; bis hin zur Sättigung der Oberfläche mit dem Katalysator.

Weiterhin zeigte die Temperatur einen starken Einfluss auf die Anreicherung des Katalysators, welcher für den oberflächenaktiven Pt-Katalysator untersucht wurde. In einem Konzentrationsbereich unterhalb der Oberflächensättigung nahm der Grad der Anreicherung bei Temperaturerniedrigung zu. Dieser Effekt war reversibel und stellt daher die Probentemperatur als einen empfindlichen Parameter für die Einstellung der Katalysatorkonzentration an der Oberfläche heraus. Im Sättigungsbereich war die Oberflächenzusammensetzung bei allen untersuchten Temperaturen konstant.

Auch die Wahl des Lösungsmittels wirkte sich stark auf die Katalysatorkonzentration an der Oberfläche aus. Wie sich für Lösungen des oberflächenaktiven Pt-Katalysators gezeigt hat, gilt, dass eine höhere Oberflächenspannung der IL zu einer stärkeren Oberflächenanreicherung des Katalysators führt. ILs mit einer besonders niedrigen Oberflächenspannung wie $[C_8C_1Im][PF_6]$ und $[C_4C_1Im][Tf_2N]$ unterdrückten sogar die

Oberflächenaktivität des Katalysators, sodass eine homogene Verteilung an der Oberfläche resultierte. Bei ausreichend hohen Konzentrationen war die Oberfläche jedoch in allen untersuchten ILs stark mit dem Katalysator angereichert. Für das Lösungsmittel $[C_4C_1Im][Tf_2N]$ mit der geringsten Oberflächenspannung war jedoch eine höhere Katalysatorkonzentration erforderlich, um die Oberflächenanreicherung zu bewirken.

7 References

1. Zimmerman, J. B.; Anastas, P. T.; Erythropel, H. C.; Leitner, W., Designing for a green chemistry future. *Science* **2020**, *367* (6476), 397-400.
2. Lanzafame, P.; Perathoner, S.; Centi, G.; Gross, S.; Hensen, E. J. M., Grand challenges for catalysis in the Science and Technology Roadmap on Catalysis for Europe: moving ahead for a sustainable future. *Catal. Sci. Technol.* **2017**, *7* (22), 5182-5194.
3. Buurmans, I. L. C.; Weckhuysen, B. M., Heterogeneities of individual catalyst particles in space and time as monitored by spectroscopy. *Nat. Chem.* **2012**, *4* (11), 873-886.
4. Eremin, D. B.; Ananikov, V. P., Understanding active species in catalytic transformations: From molecular catalysis to nanoparticles, leaching, "Cocktails" of catalysts and dynamic systems. *Coord. Chem. Rev.* **2017**, *346* (C), 2-19.
5. Nørskov, J. K.; Bligaard, T.; Hvolbæk, B.; Abild-Pedersen, F.; Chorkendorff, I.; Christensen, C. H., The nature of the active site in heterogeneous metal catalysis. *Chem. Soc. Rev.* **2008**, *37* (10), 2163-2171.
6. Zaera, F., Outstanding Mechanistic Questions in Heterogeneous Catalysis. *J. Phys. Chem. B* **2002**, *106* (16), 4043-4052.
7. Somorjai, G. A.; Kliewer, C. J., Reaction selectivity in heterogeneous catalysis. *React. Kinet. Catal. Lett.* **2009**, *96* (2), 191-208.
8. Cavani, F.; Centi, G.; Perego, C.; Vaccari, A., Selectivity in catalytic oxidation: an issue or an opportunity for innovation? *Catal. Today* **2005**, *99* (1), 1-3.
9. Wang, A.; Li, J.; Zhang, T., Heterogeneous single-atom catalysis. *Nat. Rev. Chem.* **2018**, *2* (6), 65-81.
10. Deng, X.; Wang, J.; Guan, N.; Li, L., Catalysts and mechanisms for the selective heterogeneous hydrogenation of carbon-carbon triple bonds. *Cell Rep. Phys. Sci.* **2022**, *3* (9), 101017.
11. Zaera, F., Designing Sites in Heterogeneous Catalysis: Are We Reaching Selectivities Competitive With Those of Homogeneous Catalysts? *Chem. Rev.* **2022**, *122* (9), 8594-8757.
12. Herrmann, W. A.; Cornils, B., Organometallic Homogeneous Catalysis—Quo vadis? *Angew. Chem. Int. Ed. Engl.* **1997**, *36* (10), 1048-1067.
13. Cole-Hamilton, D. J.; Tooze, R. P., Homogeneous Catalysis — Advantages and Problems. In *Catalyst Separation, Recovery and Recycling: Chemistry and Process Design*, Cole-Hamilton, D. J.; Tooze, R. P., Eds. Springer Netherlands: Dordrecht, 2006; pp 1-8.
14. Marset, X.; Ramón, D. J.; Guillena, G., Alternative Solvent Systems in Catalysis. In *Catalyst Immobilization: Methods and Applications*, Benaglia, M.; Puglisi, A., Eds. Wiley-VCH Verlag GmbH & Co. KGaA: Weinheim, 2020; pp 187-216.
15. Piermatti, O.; Abu-Reziq, R.; Vaccaro, L., Strategies to Immobilized Catalysts. In *Catalyst Immobilization*, Benaglia, M.; Puglisi, A., Eds. Wiley-VCH: Weinheim, Germany, 2020; pp 1-22.
16. González-Arellano, C.; Corma, A.; Iglesias, M.; Sánchez, F., Improved Palladium and Nickel Catalysts Heterogenised on Oxidic Supports (Silica, MCM-41, ITQ-2, ITQ-6). *Adv. Synth. Catal.* **2004**, *346* (11), 1316-1328.
17. Mazzel, M.; Marconi, W.; Riocci, M., Asymmetric hydrogenation of substituted acrylic acids by Rh′-aminophosphine chiral complex supported on mineral clays. *J. Mol. Catal.* **1980**, *9* (4), 381-387.
18. Blaser, H.-U.; Pugin, B.; Studer, M., Enantioselective Heterogeneous Catalysis: Academic and Industrial Challenges. In *Chiral Catalyst Immobilization and Recycling*, De Vos, D. E.; Vankelecom, I. F. J.; Jacobs, P. A., Eds. 2000; pp 1-17.
19. Hübner, S.; de Vries, J. G.; Farina, V., Why Does Industry Not Use Immobilized Transition Metal Complexes as Catalysts? *Adv. Synth. Catal.* **2016**, *358* (1), 3-25.
20. Acres, G. J. K.; Bond, G. C.; Cooper, B. J.; Dawson, J. A., The use of supported solutions of rhodium trichloride for homogeneous catalysis. *J. Catal.* **1966**, *6* (1), 139-141.

21. Herman, J. M.; van den Berg, P. J.; Scholten, J. J. F., The industrial hydroformylation of olefins with a rhodium-based supported liquid phase catalyst: I: Description of the catalyst system, catalyst characterization and preparation, together with some orienting hydroformylation experiments with propyl. *Chem. Eng. J.* **1986**, *32* (2), 101-110.
22. Riisager, A.; Fehrmann, R.; Haumann, M.; Wasserscheid, P., Supported Ionic Liquid Phase (SILP) Catalysis: An Innovative Concept for Homogeneous Catalysis in Continuous Fixed-Bed Reactors. *Eur. J. Inorg. Chem.* **2006**, *2006* (4), 695-706.
23. Jakuttis, M.; Schönweiz, A.; Werner, S.; Franke, R.; Wiese, K.-D.; Haumann, M.; Wasserscheid, P., Rhodium–Phosphite SILP Catalysis for the Highly Selective Hydroformylation of Mixed C4 Feedstocks. *Angew. Chem. Int. Ed.* **2011**, *50* (19), 4492-4495.
24. Mehnert, C. P.; Mozeleski, E. J.; Cook, R. A., Supported ionic liquid catalysis investigated for hydrogenation reactions. *Chem. Commun.* **2002**, (24), 3010-3011.
25. Brünig, J.; Csendes, Z.; Weber, S.; Gorgas, N.; Bittner, R. W.; Limbeck, A.; Bica, K.; Hoffmann, H.; Kirchner, K., Chemoselective Supported Ionic-Liquid-Phase (SILP) Aldehyde Hydrogenation Catalyzed by an Fe(II) PNP Pincer Complex. *ACS Catal.* **2018**, *8* (2), 1048-1051.
26. Marinkovic, J. M.; Riisager, A.; Franke, R.; Wasserscheid, P.; Haumann, M., Fifteen Years of Supported Ionic Liquid Phase-Catalyzed Hydroformylation: Material and Process Developments. *Ind. Eng. Chem. Res.* **2019**, *58* (7), 2409-2420.
27. Hatanaka, M.; Yasuda, T.; Uchiage, E.; Nishida, M.; Tominaga, K.-i., Continuous Gas-Phase Hydroformylation of Propene with CO2 Using SILP Catalysts. *ACS Sustain. Chem. Eng.* **2021**, *9* (35), 11674-11680.
28. Riisager, A.; Jørgensen, B.; Wasserscheid, P.; Fehrmann, R., First application of supported ionic liquid phase (SILP) catalysis for continuous methanol carbonylation. *Chem. Commun.* **2006**, (9), 994-996.
29. Kukawka, R.; Pawlowska-Zygarowicz, A.; Dzialkowska, J.; Pietrowski, M.; Maciejewski, H.; Bica, K.; Smiglak, M., Highly Effective Supported Ionic Liquid-Phase (SILP) Catalysts: Characterization and Application to the Hydrosilylation Reaction. *ACS Sustain. Chem. Eng.* **2019**, *7* (5), 4699-4706.
30. Bartlewicz, O.; Pietrowski, M.; Kaczmarek, M.; Maciejewski, H., SILP materials based on TiO2–SiO2 and TiO2–SiO2/lignin supports as new catalytic materials for hydrosilylation reaction – synthesis, physicochemical characterization and catalysis. *RSC Adv.* **2021**, *11* (38), 23355-23364.
31. Werner, S.; Szesni, N.; Kaiser, M.; Fischer, R. W.; Haumann, M.; Wasserscheid, P., Ultra-Low-Temperature Water–Gas Shift Catalysis using Supported Ionic Liquid Phase (SILP) Materials*. *ChemCatChem* **2010**, *2* (11), 1399-1402.
32. Steinrück, H.-P.; Wasserscheid, P., Ionic Liquids in Catalysis. *Catal. Lett.* **2015**, *145* (1), 380-397.
33. Morgan, D.; Ferguson, L.; Scovazzo, P., Diffusivities of Gases in Room-Temperature Ionic Liquids: Data and Correlations Obtained Using a Lag-Time Technique. *Ind. Eng. Chem. Res.* **2005**, *44* (13), 4815-4823.
34. Camper, D.; Becker, C.; Koval, C.; Noble, R., Diffusion and Solubility Measurements in Room Temperature Ionic Liquids. *Ind. Eng. Chem. Res.* **2006**, *45* (1), 445-450.
35. He, M.; Peng, S.; Liu, X.; Pan, P.; He, Y., Diffusion coefficients and Henry's constants of hydrofluorocarbons in [HMIM][Tf2N], [HMIM][TfO], and [HMIM][BF4]. *J. Chem. Thermodyn.* **2017**, *112*, 43-51.
36. Maier, F.; Gottfried, J. M.; Rossa, J.; Gerhard, D.; Schulz, P. S.; Schwieger, W.; Wasserscheid, P.; Steinrück, H.-P., Surface Enrichment and Depletion Effects of Ions Dissolved in an Ionic Liquid: An X-ray Photoelectron Spectroscopy Study. *Angew. Chem. Int. Ed.* **2006**, *45* (46), 7778-7780.
37. Kolbeck, C.; Paape, N.; Cremer, T.; Schulz, P. S.; Maier, F.; Steinrück, H.-P.; Wasserscheid, P., Ligand Effects on the Surface Composition of Rh-Containing Ionic

Liquid Solutions Used in Hydroformylation Catalysis. *Chem. Eur. J.* **2010**, *16* (40), 12083-12087.
38. Smoll, E. J.; Chen, X.; Hall, L. M.; D'Andrea, L.; Slattery, J. M.; Minton, T. K., Probing a Ruthenium Coordination Complex at the Ionic Liquid–Vacuum Interface with Reactive-Atom Scattering, X-ray Photoelectron Spectroscopy, and Time-of-Flight Secondary Ion Mass Spectrometry. *J. Phys. Chem. C* **2020**, *124* (1), 382-397.
39. Jablonski, A.; Powell, C. J., Information depth and the mean escape depth in Auger electron spectroscopy and x-ray photoelectron spectroscopy. *J. Vac. Sci. Tech. A* **2002**, *21* (1), 274-283.
40. Seah, M. P.; Dench, W. A., Quantitative electron spectroscopy of surfaces: A standard data base for electron inelastic mean free paths in solids. *Surf. Interface Anal.* **1979**, *1* (1), 2-11.
41. Tanuma, S.; Powell, C. J.; Penn, D. R., Calculations of electron inelastic mean free paths. V. Data for 14 organic compounds over the 50–2000 eV range. *Surf. Interface Anal.* **1994**, *21* (3), 165-176.
42. Niedermaier, I.; Kolbeck, C.; Steinrück, H.-P.; Maier, F., Dual analyzer system for surface analysis dedicated for angle-resolved photoelectron spectroscopy at liquid surfaces and interfaces *Rev. Sci. Instrum.* **2016**, *87* (4), 045105.
43. Walden, P., Ueber die Molekulargrösse und elektrische Leitfähigkeit einiger geschmolzenen Salze. *Bull. Acad. Imp. Sci. Saint-Pétersbourg* **1914**, 405-422.
44. Welton, T., Ionic liquids: a brief history. *Biophys. Rev.* **2018**, *10* (3), 691-706.
45. Welton, T., Ionic liquids in catalysis. *Coord. Chem. Rev.* **2004**, *248* (21), 2459-2477.
46. van Rantwijk, F.; Sheldon, R. A., Biocatalysis in Ionic Liquids. *Chem. Rev.* **2007**, *107* (6), 2757-2785.
47. MacFarlane, D. R.; Forsyth, M.; Howlett, P. C.; Pringle, J. M.; Sun, J.; Annat, G.; Neil, W.; Izgorodina, E. I., Ionic Liquids in Electrochemical Devices and Processes: Managing Interfacial Electrochemistry. *Acc. Chem. Res.* **2007**, *40* (11), 1165-1173.
48. Tiago, G. A. O.; Matias, I. A. S.; Ribeiro, A. P. C.; Martins, L. M. D. R. S., Application of Ionic Liquids in Electrochemistry—Recent Advances. *Molecules* **2020**, *25* (24), 5812.
49. Chiappe, C.; Pieraccini, D., Ionic liquids: solvent properties and organic reactivity. *J. Phys. Org. Chem.* **2005**, *18* (4), 275-297.
50. Martins, M. A. P.; Frizzo, C. P.; Moreira, D. N.; Zanatta, N.; Bonacorso, H. G., Ionic Liquids in Heterocyclic Synthesis. *Chem. Rev.* **2008**, *108* (6), 2015-2050.
51. Bermúdez, M.-D.; Jiménez, A.-E.; Sanes, J.; Carrión, F.-J., Ionic Liquids as Advanced Lubricant Fluids. *Molecules* **2009**, *14* (8), 2888-2908.
52. Cai, M.; Yu, Q.; Liu, W.; Zhou, F., Ionic liquid lubricants: when chemistry meets tribology. *Chem. Soc. Rev.* **2020**, *49* (21), 7753-7818.
53. Greer, A. J.; Jacquemin, J.; Hardacre, C., Industrial Applications of Ionic Liquids. *Molecules* **2020**, *25* (21), 5207.
54. Brendel, S.; Fetter, É.; Staude, C.; Vierke, L.; Biegel-Engler, A., Short-chain perfluoroalkyl acids: environmental concerns and a regulatory strategy under REACH. *Env. Sci. Eur.* **2018**, *30* (1), 9.
55. Bonato, M.; Corrà, F.; Bellio, M.; Guidolin, L.; Tallandini, L.; Irato, P.; Santovito, G., PFAS Environmental Pollution and Antioxidant Responses: An Overview of the Impact on Human Field. *Int. J. Environ. Res. Public Health* **2020**, *17* (21), 8020.
56. Freire, M. G.; Neves, C. M. S. S.; Marrucho, I. M.; Coutinho, J. A. P.; Fernandes, A. M., Hydrolysis of Tetrafluoroborate and Hexafluorophosphate Counter Ions in Imidazolium-Based Ionic Liquids. *J. Phys. Chem. A* **2010**, *114* (11), 3744-3749.
57. Beil, S.; Markiewicz, M.; Pereira, C. S.; Stepnowski, P.; Thöming, J.; Stolte, S., Toward the Proactive Design of Sustainable Chemicals: Ionic Liquids as a Prime Example. *Chem. Rev.* **2021**, *121* (21), 13132-13173.
58. de Jesus, S. S.; Maciel Filho, R., Are ionic liquids eco-friendly? *Renew. Sustain. Energy Rev.* **2022**, *157*, 112039.

59. Hayes, R.; Warr, G. G.; Atkin, R., Structure and Nanostructure in Ionic Liquids. *Chem. Rev.* **2015**, *115* (13), 6357-6426.
60. Lovelock, K. R. J., Influence of the ionic liquid/gas surface on ionic liquid chemistry. *Phys. Chem. Chem. Phys.* **2012**, *14* (15), 5071-5089.
61. Gannon, T. J.; Law, G.; Watson, P. R.; Carmichael, A. J.; Seddon, K. R., First Observation of Molecular Composition and Orientation at the Surface of a Room-Temperature Ionic Liquid. *Langmuir* **1999**, *15* (24), 8429-8434.
62. Law, G.; Watson, P. R.; Carmichael, A. J.; Seddon, K. R., Molecular composition and orientation at the surface of room-temperature ionic liquids: Effect of molecular structure. *Phys. Chem. Chem. Phys.* **2001**, *3* (14), 2879-2885.
63. Sloutskin, E.; Ocko, B. M.; Tamam, L.; Kuzmenko, I.; Gog, T.; Deutsch, M., Surface Layering in Ionic Liquids: An X-ray Reflectivity Study. *J. Am. Chem. Soc.* **2005**, *127* (21), 7796-7804.
64. Krischok, S.; Eremtchenko, M.; Himmerlich, M.; Lorenz, P.; Uhlig, J.; Neumann, A.; Öttking, R.; Beenken, W. J. D.; Höfft, O.; Bahr, S.; Kempter, V.; Schaefer, J. A., Temperature-Dependent Electronic and Vibrational Structure of the 1-Ethyl-3-methylimidazolium Bis(trifluoromethylsulfonyl)amide Room-Temperature Ionic Liquid Surface: A Study with XPS, UPS, MIES, and HREELS. *J. Phys. Chem. B* **2007**, *111* (18), 4801-4806.
65. Nakajima, K.; Ohno, A.; Suzuki, M.; Kimura, K., Observation of Molecular Ordering at the Surface of Trimethylpropylammonium Bis(trifluoromethanesulfonyl)imide Using High-Resolution Rutherford Backscattering Spectroscopy. *Langmuir* **2008**, *24* (9), 4482-4484.
66. Nishi, N.; Yasui, Y.; Uruga, T.; Tanida, H.; Yamada, T.; Nakayama, S.-i.; Matsuoka, H.; Kakiuchi, T., Ionic multilayers at the free surface of an ionic liquid, trioctylmethylammonium bis(nonafluorobutanesulfonyl)amide, probed by x-ray reflectivity measurements. *J. Chem. Phys.* **2010**, *132* (16).
67. Santos, C. S.; Baldelli, S., Gas–liquid interface of room-temperature ionic liquids. *Chem. Soc. Rev.* **2010**, *39* (6), 2136-2145.
68. Steinrück, H.-P., Recent developments in the study of ionic liquid interfaces using X-ray photoelectron spectroscopy and potential future directions. *Phys. Chem. Chem. Phys.* **2012**, *14* (15), 5010-5029.
69. Tariq, M.; Freire, M. G.; Saramago, B.; Coutinho, J. A. P.; Lopes, J. N. C.; Rebelo, L. P. N., Surface tension of ionic liquids and ionic liquid solutions. *Chem. Soc. Rev.* **2012**, *41* (2), 829-868.
70. Villar-Garcia, I. J.; Fearn, S.; De Gregorio, G. F.; Ismail, N. L.; Gschwend, F. J. V.; McIntosh, A. J. S.; Lovelock, K. R. J., The ionic liquid–vacuum outer atomic surface: a low-energy ion scattering study. *Chem. Sci.* **2014**, *5* (11), 4404-4418.
71. Kolbeck, C.; Niedermaier, I.; Deyko, A.; Lovelock, K. R. J.; Taccardi, N.; Wei, W.; Wasserscheid, P.; Maier, F.; Steinrück, H.-P., Influence of Substituents and Functional Groups on the Surface Composition of Ionic Liquids. *Chem. Eur. J.* **2014**, *20* (14), 3954-3965.
72. Villar-Garcia, I. J.; Fearn, S.; Ismail, N. L.; McIntosh, A. J. S.; Lovelock, K. R. J., Fine tuning the ionic liquid–vacuum outer atomic surface using ion mixtures. *Chem. Commun.* **2015**, *51* (25), 5367-5370.
73. Tesa-Serrate, M. A.; Marshall, B. C.; Smoll, E. J., Jr.; Purcell, S. M.; Costen, M. L.; Slattery, J. M.; Minton, T. K.; McKendrick, K. G., Ionic Liquid–Vacuum Interfaces Probed by Reactive Atom Scattering: Influence of Alkyl Chain Length and Anion Volume. *J. Phys. Chem. C* **2015**, *119* (10), 5491-5505.
74. Nakajima, K.; Nakanishi, S.; Lísal, M.; Kimura, K., Surface structures of binary mixture of ionic liquids. *J. Mol. Liq.* **2017**, *230*, 542-549.
75. Smoll, E. J.; Tesa-Serrate, M. A.; Purcell, S. M.; D'Andrea, L.; Bruce, D. W.; Slattery, J. M.; Costen, M. L.; Minton, T. K.; McKendrick, K. G., Determining the composition of

the vacuum–liquid interface in ionic-liquid mixtures. *Faraday Discuss.* **2018**, *206* (0), 497-522.

76. Smoll, E. J., Jr.; Purcell, S. M.; D'Andrea, L.; Slattery, J. M.; Bruce, D. W.; Costen, M. L.; McKendrick, K. G.; Minton, T. K., Probing Conformational Heterogeneity at the Ionic Liquid–Vacuum Interface by Reactive-Atom Scattering. *J. Phys. Chem. Lett.* **2019**, *10* (2), 156-163.
77. Koller, T. M.; Lenahan, F. D.; Schmidt, P. S.; Klein, T.; Mehler, J.; Maier, F.; Rausch, M. H.; Wasserscheid, P.; Steinrück, H.-P.; Fröba, A. P., Surface Tension and Viscosity of Binary Mixtures of the Fluorinated and Non-fluorinated Ionic Liquids [PFBMIm][PF6] and [C4C1Im][PF6] by the Pendant Drop Method and Surface Light Scattering. *Int. J. Thermophys.* **2020**, *41* (10), 144.
78. Huang, Q.; Huang, Y.; Luo, Y.; Li, L.; Zhou, G.; Chen, X.; Yang, Z., Molecular-level insights into the structures, dynamics, and hydrogen bonds of ethylammonium nitrate protic ionic liquid at the liquid–vacuum interface. *Phys. Chem. Chem. Phys.* **2020**, *22* (24), 13780-13789.
79. Costa, R.; Pereira, C. M.; Silva, A. F.; Brevet, P.-F.; Benichou, E., Ordering and Nonideality of Air–Ionic Liquid Interfaces in Surface Second Harmonic Generation. *J. Phys. Chem. B* **2020**, *124* (19), 3954-3961.
80. Nakajima, K.; Lísal, M.; Kimura, K., Surfaces of Ionic Liquids. In *Surface and Interface Science*, Wandelt, K., Ed. Wiley-VCH Verlag GmbH & Co. KGaA: Weinheim, Germany, 2020; Vol. 7, pp 351-389.
81. Bomhardt, K.; Schneider, P.; Glaser, T.; Dürr, M., Surface Properties of Ionic Liquids: A Mass Spectrometric View Based on Soft Cluster-Induced Desorption. *J. Am. Soc. Mass. Spectrom.* **2022**, *33* (6), 974-980.
82. Zhai, Z.; Paap, U.; Gezmis, A.; Maier, F.; Steinrück, H.-P.; Koller, T. M., Surface tension and viscosity of binary ionic liquid mixtures from high vacuum up to pressures of 10 MPa. *J. Mol. Liq.* **2023**, *386*, 122388.
83. Lockett, V.; Sedev, R.; Bassell, C.; Ralston, J., Angle-resolved X-ray photoelectron spectroscopy of the surface of imidazolium ionic liquids. *Phys. Chem. Chem. Phys.* **2008**, *10* (9), 1330-1335.
84. Lockett, V.; Sedev, R.; Harmer, S.; Ralston, J.; Horne, M.; Rodopoulos, T., Orientation and mutual location of ions at the surface of ionic liquids. *Phys. Chem. Chem. Phys.* **2010**, *12* (41), 13816-13827.
85. Men, S.; Hurisso, B. B.; Lovelock, K. R. J.; Licence, P., Does the influence of substituents impact upon the surface composition of pyrrolidinium-based ionic liquids? An angle resolved XPS study. *Phys. Chem. Chem. Phys.* **2012**, *14* (15), 5229-5238.
86. Blundell, R. K.; Delorme, A. E.; Smith, E. F.; Licence, P., An ARXPS and ERXPS study of quaternary ammonium and phosphonium ionic liquids: utilising a high energy Ag Lα′ X-ray source. *Phys. Chem. Chem. Phys.* **2016**, *18* (8), 6122-6131.
87. Caporali, S.; Pedio, M.; Chiappe, C.; Pomelli, C. S.; Acres, R. G.; Bardi, U., Surface study of metal-containing ionic liquids by means of photoemission and absorption spectroscopies. *Surf. Sci.* **2016**, *648*, 360-365.
88. Heller, B. S. J.; Lexow, M.; Greco, F.; Shin, S.; Partl, G.; Maier, F.; Steinrück, H.-P., Temperature-Dependent Surface Enrichment Effects in Binary Mixtures of Fluorinated and Non-Fluorinated Ionic Liquids. *Chem. Eur. J.* **2020**, *26* (5), 1117-1126.
89. Calisi, N.; Martinuzzi, S.; Giaccherini, A.; Pomelli, C. S.; Guazzelli, L.; Caporali, S., Temperature and angle resolved XPS study of BMIm Cl and BMIm FeCl4. *J. Electron. Spectrosc. Relat. Phenom.* **2021**, *247*, 147034.
90. Seidl, V.; Bosch, M.; Paap, U.; Livraghi, M.; Zhai, Z.; Wick, C. R.; Koller, T. M.; Wasserscheid, P.; Maier, F.; Smith, A.-S.; Bachmann, J.; Steinrück, H.-P.; Meyer, K., Bis-polyethylene glycol-functionalized imidazolium ionic liquids: A multi-method approach towards bulk and surface properties. *Journal of Ionic Liquids* **2022**, *2* (2), 100041.

91. Kolbeck, C.; Cremer, T.; Lovelock, K. R. J.; Paape, N.; Schulz, P. S.; Wasserscheid, P.; Maier, F.; Steinrück, H. P., Influence of Different Anions on the Surface Composition of Ionic Liquids Studied Using ARXPS. *J. Phys. Chem. B* **2009**, *113* (25), 8682-8688.
92. Maier, F.; Cremer, T.; Kolbeck, C.; Lovelock, K. R. J.; Paape, N.; Schulz, P. S.; Wasserscheid, P.; Steinrück, H. P., Insights into the surface composition and enrichment effects of ionic liquids and ionic liquid mixtures. *Phys. Chem. Chem. Phys.* **2010**, *12* (8), 1905-1915.
93. Nakajima, K.; Miyashita, M.; Suzuki, M.; Kimura, K., Surface structures of binary mixtures of imidazolium-based ionic liquids using high-resolution Rutherford backscattering spectroscopy and time of flight secondary ion mass spectroscopy. *J. Chem. Phys.* **2013**, *139* (22), 224701.
94. Zhang, Y.; Khalifa, Y.; Maginn, E. J.; Newberg, J. T., Anion Enhancement at the Liquid–Vacuum Interface of an Ionic Liquid Mixture. *J. Phys. Chem. C* **2018**, *122* (48), 27392-27401.
95. Khalifa, Y.; Broderick, A.; Newberg, J. T., Surface enhancement of water at the ionic liquid-gas interface of [HMIM][Cl] under ambient water vapor. *J. Phys. Condens. Matter* **2018**, *30* (32), 325001.
96. Heller, B. S. J.; Kolbeck, C.; Niedermaier, I.; Dommer, S.; Schatz, J.; Hunt, P.; Maier, F.; Steinrück, H.-P., Surface Enrichment in Equimolar Mixtures of Non-Functionalized and Functionalized Imidazolium-Based Ionic Liquids. *ChemPhysChem* **2018**, *19* (14), 1733-1745.
97. Heller, B. S. J.; Paap, U.; Maier, F.; Steinrück, H.-P., Pronounced surface enrichment of fluorinated ionic liquids in binary mixtures with methoxy-functionalized ionic liquids. *J. Mol. Liq.* **2020**, *305*, 112783.
98. Paap, U.; Seidl, V.; Meyer, K.; Maier, F.; Steinrück, H.-P., Direct Correlation of Surface Tension and Surface Composition of Ionic Liquid Mixtures—A Combined Vacuum Pendant Drop and Angle-Resolved X-ray Photoelectron Spectroscopy Study. *Molecules* **2022**, *27* (23), 8561.
99. Gottfried, J. M.; Maier, F.; Rossa, J.; Gerhard, D.; Schulz, P. S.; Wasserscheid, P.; Steinrück, H.-P., Surface Studies on the Ionic Liquid 1-Ethyl-3-Methylimidazolium Ethylsulfate Using X-Ray Photoelectron Spectroscopy (XPS). *Z. Phys. Chem.* **2006**, *220* (10), 1439-1453.
100. Multiprobe User's Guide, Project 121502, Omicron NanoTechnology GmbH, Taunusstein, 2014.
101. Moulder, J. F.; Stickle, W. F.; Sobol, P. E.; Bomben, K. D., *Handbook of X-ray Photoelectron Spectroscopy. A Reference Book of Standard Spectra for Identification and Interpretation of XPS Data*. Perkin-Elmer Corporation, Physical Electronics Division: Eden Prairie, MN, USA, 1992.
102. Wagner, C. D.; Davis, L. E.; Zeller, M. V.; Taylor, J. A.; Raymond, R. H.; Gale, L. H., Empirical Atomic Sensitivity Factors for Quantitative Analysis by Electron Spectroscopy for Chemical Analysis. *Surf. Interface Anal.* **1981**, *3* (5), 211-225.
103. Limberger, J.; Leal, B. C.; Monteiro, A. L.; Dupont, J., Charge-tagged ligands: useful tools for immobilising complexes and detecting reaction species during catalysis. *Chem. Sci.* **2015**, *6* (1), 77-94.
104. Šebesta, R.; Kmentová, I.; Toma, Š., Catalysts with ionic tag and their use in ionic liquids. *Green Chem.* **2008**, *10* (5), 484-496.
105. Zhao, D.; Fei, Z.; Geldbach, T. J.; Scopelliti, R.; Dyson, P. J., Nitrile-Functionalized Pyridinium Ionic Liquids: Synthesis, Characterization, and Their Application in Carbon−Carbon Coupling Reactions. *J. Am. Chem. Soc.* **2004**, *126* (48), 15876-15882.
106. Zhao, D.; Fei, Z.; Scopelliti, R.; Dyson, P. J., Synthesis and Characterization of Ionic Liquids Incorporating the Nitrile Functionality. *Inorg. Chem.* **2004**, *43* (6), 2197-2205.
107. Fei, Z.; Zhao, D.; Pieraccini, D.; Ang, W. H.; Geldbach, T. J.; Scopelliti, R.; Chiappe, C.; Dyson, P. J., Development of Nitrile-Functionalized Ionic Liquids for C−C Coupling

Reactions: Implication of Carbene and Nanoparticle Catalysts. *Organometallics* **2007**, *26* (7), 1588-1598.

108. Cui, Y.; Biondi, I.; Chaubey, M.; Yang, X.; Fei, Z.; Scopelliti, R.; Hartinger, C. G.; Li, Y.; Chiappe, C.; Dyson, P. J., Nitrile-functionalized pyrrolidinium ionic liquids as solvents for cross-coupling reactions involving in situ generated nanoparticle catalyst reservoirs. *Phys. Chem. Chem. Phys.* **2010**, *12* (8), 1834-1841.
109. NIST Mass Spectrometry Data Center; Wallace, W. E.; director, "Mass Spectra". In *NIST Chemistry WebBook, NIST Standard Reference Database Number 69*, Linstrom, P. J.; Mallard, W. G., Eds. National Institute of Standards and Technology, Gaithersburg MD, 20899, (retrieved April 13, 2022).
110. Lethesh, K. C.; Van Hecke, K.; Van Meervelt, L.; Nockemann, P.; Kirchner, B.; Zahn, S.; Parac-Vogt, T. N.; Dehaen, W.; Binnemans, K., Nitrile-Functionalized Pyridinium, Pyrrolidinium, and Piperidinium Ionic Liquids. *J. Phys. Chem. B* **2011**, *115* (26), 8424-8438.
111. Kuznetsov, M. L.; Kukushkin, V. Y.; Pombeiro, A. J. L., Reactivity of Pt- and Pd-bound nitriles towards nitrile oxides and nitrones: substitution vs.cycloaddition. *Dalton Trans.* **2008**, (10), 1312-1322.
112. Paap, U.; Kreß, B.; Steinrück, H.-P.; Maier, F., Probing Surface and Interfacial Tension of Ionic Liquids in Vacuum with the Pendant Drop and Sessile Drop Method. *Int. J. Mol. Sci.* **2022**, *23* (21), 13158.
113. Kaes, C.; Katz, A.; Hosseini, M. W., Bipyridine: The Most Widely Used Ligand. A Review of Molecules Comprising at Least Two 2,2‘-Bipyridine Units. *Chem. Rev.* **2000**, *100* (10), 3553-3590.
114. Wasylenko, D. J.; Ganesamoorthy, C.; Koivisto, B. D.; Henderson, M. A.; Berlinguette, C. P., Insight into Water Oxidation by Mononuclear Polypyridyl Ru Catalysts. *Inorg. Chem.* **2010**, *49* (5), 2202-2209.
115. Domínguez, S. E.; Juarez, M. V.; Pieslinger, G. E.; Baraldo, L. M., A Strongly Coupled Biruthenium Complex as Catalyst for the Water Oxidation Reaction. *Eur. J. Inorg. Chem.* **2022**, *2022* (1), e202100843.
116. Mahajan, D.; Creutz, C.; Sutin, N., Homogeneous catalysis of the water gas shift reaction by (polypyridine)rhodium(I) complexes. *Inorg. Chem.* **1985**, *24* (13), 2063-2067.
117. Ishida, H.; Tanaka, K.; Morimoto, M.; Tanaka, T., Isolation of intermediates in the water gas shift reactions catalyzed by [Ru(bpy)2(CO)Cl]+ and [Ru(bpy)2(CO)2]2+. *Organometallics* **1986**, *5* (4), 724-730.
118. Elgrishi, N.; Chambers, M. B.; Wang, X.; Fontecave, M., Molecular polypyridine-based metal complexes as catalysts for the reduction of CO2. *Chem. Soc. Rev.* **2017**, *46* (3), 761-796.
119. Winter, A.; Newkome, G. R.; Schubert, U. S., Catalytic Applications of Terpyridines and their Transition Metal Complexes. *ChemCatChem* **2011**, *3* (9), 1384-1406.
120. Kern, S.; van Eldik, R., Mechanistic Insight from Activation Parameters for the Reaction of a Ruthenium Hydride Complex with CO2 in Conventional Solvents and an Ionic Liquid. *Inorg. Chem.* **2012**, *51* (13), 7340-7345.
121. Hollóczki, O.; Gerhard, D.; Massone, K.; Szarvas, L.; Németh, B.; Veszprémi, T.; Nyulászi, L., Carbenes in ionic liquids. *New J. Chem.* **2010**, *34* (12), 3004-3009.
122. Chiarotto, I.; Mattiello, L.; Pandolfi, F.; Rocco, D.; Feroci, M., NHC in Imidazolium Acetate Ionic Liquids: Actual or Potential Presence? *Frontiers in Chemistry* **2018**, *6*, 355.
123. Shepherd, R. E.; Proctor, A.; Henderson, W. W.; Myser, T. K., Assessment of the .pi.-acceptor capability of selected ligands based on the photoelectron spectra of ruthenium ammine complexes. *Inorg. Chem.* **1987**, *26* (15), 2440-2444.
124. Lexow, M.; Maier, F.; Steinrück, H.-P., Ultrathin ionic liquid films on metal surfaces: adsorption, growth, stability and exchange phenomena. *Adv. Phys.: X* **2020**, *5* (1), 1761266.
125. Spyrakis, F.; Dragani, T. A., The EU’s Per- and Polyfluoroalkyl Substances (PFAS) Ban: A Case of Policy over Science. *Toxics* **2023**, *11* (9), 721.

126. Bowers, J.; Danks, M. J.; Bruce, D. W.; Heenan, R. K., Surface and Aggregation Behavior of Aqueous Solutions of Ru(II) Metallosurfactants: 1. Micellization of [Ru(bipy)2(bipy‘)][Cl]2 Complexes. *Langmuir* **2003**, *19* (2), 292-298.
127. Bowers, J.; Danks, M. J.; Bruce, D. W.; Webster, J. R. P., Surface and Aggregation Behavior of Aqueous Solutions of Ru(II) Metallosurfactants: 2. Adsorbed Films of [Ru(bipy)2(bipy‘)][Cl]2 Complexes. *Langmuir* **2003**, *19* (2), 299-305.
128. Bowers, J.; Amos, K. E.; Bruce, D. W.; Heenan, R. K., Surface and Aggregation Behavior of Aqueous Solutions of Ru(II) Metallosurfactants: 4. Effect of Chain Number and Orientation on the Aggregation of [Ru(bipy)2(bipy‘)]Cl2 Complexes. *Langmuir* **2005**, *21* (13), 5696-5706.
129. Bowers, J.; Amos, K. E.; Bruce, D. W.; Webster, J. R. P., Surface and Aggregation Behavior of Aqueous Solutions of Ru(II) Metallosurfactants. 3. Effect of Chain Number and Orientation on the Structure of Adsorbed Films of [Ru(bipy)2(bipy‘)]Cl2 Complexes. *Langmuir* **2005**, *21* (4), 1346-1353.
130. Griffiths, P. C.; Fallis, I. A.; Chuenpratoom, T.; Watanesk, R., Metallosurfactants: Interfaces and micelles. *Adv. Colloid Interface Sci.* **2006**, *122* (1), 107-117.
131. Hay, R. W.; Govan, N.; Parchment, K. E., A metallomicelle catalysed hydrolysis of a phosphate triester, a phosphonate diester and O-isopropyl methylfluorophosphonate (Sarin). *Inorg. Chem. Commun.* **1998**, *1* (6), 228-231.
132. Goedheijt, M. S.; Hanson, B. E.; Reek, J. N. H.; Kamer, P. C. J.; van Leeuwen, P. W. N. M., Accelerated Biphasic Hydroformylation by Vesicle Formation of Amphiphilic Diphosphines. *J. Am. Chem. Soc.* **2000**, *122* (8), 1650-1657.
133. Suarez, P. A. Z.; Dullius, J. E. L.; Einloft, S.; De Souza, R. F.; Dupont, J., The use of new ionic liquids in two-phase catalytic hydrogenation reaction by rhodium complexes. *Polyhedron* **1996**, *15* (7), 1217-1219.
134. Nindakova, L. O.; Shainyan, B. A.; Albanov, A. I.; Shmidt, F. K., Double Stereoselection in the Hydrogenation over Cationic Rh(I) Complexes with Two Different Chiral Ligands. *Russ. J. Org. Chem.* **2003**, *39* (7), 926-932.
135. Wu, H.; Yang, J.; Peters, B. B. C.; Massaro, L.; Zheng, J.; Andersson, P. G., Asymmetric Full Saturation of Vinylarenes with Cooperative Homogeneous and Heterogeneous Rhodium Catalysis. *J. Am. Chem. Soc.* **2021**, *143* (48), 20377-20383.
136. Carvalho, M.; Wieserman, L. F.; Hercules, D. M., Spectroscopic Characterization of Wilkinson's Catalyst Using X-ray Photoelectron Spectroscopy (ESCA). *Appl. Spectrosc.* **1982**, *36* (3), 290-296.
137. Díaz, J.; Paolicelli, G.; Ferrer, S.; Comin, F., Separation of the sp3 and sp2 components in the C1s photoemission spectra of amorphous carbon films. *Phys. Rev. B.* **1996**, *54* (11), 8064-8069.
138. Fujimoto, A.; Yamada, Y.; Koinuma, M.; Sato, S., Origins of sp3C peaks in C1s X-ray Photoelectron Spectra of Carbon Materials. *Anal. Chem.* **2016**, *88* (12), 6110-6114.
139. Werner, H.; Bosch, M.; E. Schneider, M.; Hahn, C.; Kukla, F.; Manger, M.; Windmüller, B.; Weberndörfer, B.; Laubender, M., Preparation, molecular structure and reactivity of mono- and di-nuclear sulfonato rhodium(I) complexes. *J. Chem. Soc., Dalton Trans.* **1998**, (21), 3549-3558.
140. Schott, H., Saturation adsorption at interfaces of surfactant solutions. *J. Pharm. Sci.* **1980**, *69* (7), 852-854.
141. Shimizu, K.; Heller, B. S. J.; Maier, F.; Steinrück, H.-P.; Lopes, J. N. C., Probing the Surface Tension of Ionic Liquids Using the Langmuir Principle. *Langmuir* **2018**, *34* (14), 4408-4416.
142. Almeida, H. F. D.; Teles, A. R. R.; Lopes-da-Silva, J. A.; Freire, M. G.; Coutinho, J. A. P., Influence of the anion on the surface tension of 1-ethyl-3-methylimidazolium-based ionic liquids. *J. Chem. Thermodyn.* **2012**, *54*, 49-54.

143. Men, S.; Lovelock, K. R. J.; Licence, P., Directly probing the effect of the solvent on a catalyst electronic environment using X-ray photoelectron spectroscopy. *RSC Adv.* **2015**, *5* (45), 35958-35965.
144. Men, S.; Jiang, J., X-ray photoelectron spectroscopy as a probe of the interaction between rhodium acetate and ionic liquids. *Chem. Phys. Lett.* **2016**, *646*, 125-129.
145. Men, S.; Jin, Y., Rhodium Catalyst-Ionic Liquids Interaction by X-ray Photoelectron Spectroscopy Data. *Russ. J. Phys. Chem. A* **2018**, *92*, 2472.
146. Souda, R., Surface segregation in binary mixtures of imidazolium-based ionic liquids. *Surf. Sci.* **2010**, *604* (19), 1694-1697.
147. Nakajima, K.; Oshima, S.; Suzuki, M.; Kimura, K., Surface structures of equimolar mixtures of imidazolium-based ionic liquids using high-resolution Rutherford backscattering spectroscopy. *Surf. Sci.* **2012**, *606* (21), 1693-1699.
148. Oz, E.; Sahin, O.; Okur, H. I.; Suzer, S., Surface Propensity of Anions in a Binary Ionic-Liquid Mixture Assessed by Full-Range Angle-Resolved X-ray Photoelectron Spectroscopy and Surface-Tension Measurements. *ChemPhysChem* **2020**, *21* (21), 2397-2401.
149. Ganapatibhotla, L. V. N. R.; Zheng, J.; Roy, D.; Krishnan, S., PEGylated Imidazolium Ionic Liquid Electrolytes: Thermophysical and Electrochemical Properties. *Chem. Mater.* **2010**, *22* (23), 6347-6360.
150. Döbbelin, M.; Azcune, I.; Bedu, M.; Ruiz de Luzuriaga, A.; Genua, A.; Jovanovski, V.; Cabañero, G.; Odriozola, I., Synthesis of Pyrrolidinium-Based Poly(ionic liquid) Electrolytes with Poly(ethylene glycol) Side Chains. *Chem. Mater.* **2012**, *24* (9), 1583-1590.
151. Cecchini, M. M.; Charnay, C.; De Angelis, F.; Lamaty, F.; Martinez, J.; Colacino, E., Poly(ethylene glycol)-Based Ionic Liquids: Properties and Uses as Alternative Solvents in Organic Synthesis and Catalysis. *ChemSusChem* **2014**, *7* (1), 45-65.
152. Deng, Y.; Besse-Hoggan, P.; Sancelme, M.; Delort, A.-M.; Husson, P.; Costa Gomes, M. F., Influence of oxygen functionalities on the environmental impact of imidazolium based ionic liquids. *J. Hazard. Mater.* **2011**, *198*, 165-174.
153. Tang, S.; Baker, G. A.; Zhao, H., Ether- and alcohol-functionalized task-specific ionic liquids: attractive properties and applications. *Chem. Soc. Rev.* **2012**, *41* (10), 4030-4066.
154. Kuhlmann, E.; Himmler, S.; Giebelhaus, H.; Wasserscheid, P., Imidazolium dialkylphosphates—a class of versatile, halogen-free and hydrolytically stable ionic liquids. *Green Chem.* **2007**, *9* (3), 233-242.
155. Dick, E. J.; Fouda, A. E. A.; Besley, N. A.; Licence, P., Probing the electronic structure of ether functionalised ionic liquids using X-ray photoelectron spectroscopy. *Phys. Chem. Chem. Phys.* **2020**, *22* (3), 1624-1631.

8 Appendix

In the following, publications [P1 – P8] are reproduced under licenses CC-BY-NC-ND ([P1], [P2]), CC BY 4.0 ([P3]), CC-BY-NC ([P4] and [P8]), with permission from the PCCP Owner Societies ([P5]) and CC BY ([P6] and [P7]).

[P1] Formation and Surface Behavior of Pt and Pd Complexes with Ligand Systems Derived from Nitrile-functionalized Ionic Liquids Studied by XPS

D. Hemmeter, U. Paap, N. Taccardi, J. Mehler, P. S. Schulz, P. Wasserscheid, F. Maier, H.-P. Steinrück, *ChemPhysChem* **2023**, *24*, e202200391.

The author's contribution is the sample preparation including synthesis of the complexes, ARXPS and QMS investigation, data analysis, data interpretation and manuscript preparation.

Front Cover: D. Hemmeter, U. Paap, N. Taccardi, J. Mehler, P. S. Schulz, P. Wasserscheid, F. Maier, H.-P. Steinrück, *ChemPhysChem* **2023**, *24*, e202200915.

Cover Profile: D. Hemmeter, U. Paap, N. Taccardi, J. Mehler, P. S. Schulz, P. Wasserscheid, F. Maier, H.-P. Steinrück, *ChemPhysChem* **2023**, *24*, e202200914.

[P2] The Buoy Effect: Surface Enrichment of a Pt Complex in IL Solution by Ligand Design

D. Hemmeter, D. Kremitzl, P. S. Schulz, P. Wasserscheid, F. Maier, H.-P. Steinrück, *Chem. Eur. J.* **2023**, *29*, e202203325.

The author's contribution is the sample preparation including synthesis of the complexes, ARXPS investigation, data analysis, data interpretation and manuscript preparation.

Front Cover: D. Hemmeter, D. Kremitzl, P. S. Schulz, P. Wasserscheid, F. Maier, H.-P. Steinrück, *Chem. Eur. J.* **2023**, *29*, e202204022.

Cover Profile: D. Hemmeter, D. Kremitzl, P. S. Schulz, P. Wasserscheid, F. Maier, H.-P. Steinrück, *Chem. Eur. J.* **2023**, *29*, e202204023.

[P3] Structure and Surface Behavior of Rh Complexes in Ionic Liquids Studied Using Angle-Resolved X-ray Photoelectron Spectroscopy

D. Hemmeter, U. Paap, F. Maier, H.-P. Steinrück, *Catalysts* **2023**, *13*, 871.

The author's contribution is the sample preparation, ARXPS investigation, data analysis, data interpretation and manuscript preparation.

[P4] Understanding the Buoy Effect of Surface-Enriched Pt Complexes in Ionic Liquids: A Combined ARXPS and Pendant Drop Study

D. Hemmeter, U. Paap, N. Wellnhofer, A. Gezmis, D. Kremitzl, P. Wasserscheid, H.-P. Steinrück, F. Maier, *ChemPhysChem* **2023**, *24*, e202300612.

The author's contribution is the sample preparation including synthesis of the complexes, ARXPS investigation, data analysis, data interpretation and manuscript preparation.

[P5] Exploring the Interfacial Behavior of Ruthenium Complexes in Ionic Liquids: Implications for Supported Ionic Liquid Phase Catalysts

D. Hemmeter, L. Sanchez Merlinsky, L. M. Baraldo, F. Maier, F. J. Williams, H.-P. Steinrück, *Phys. Chem. Chem. Phys.* **2024**, *26*, 7602-7610.

The author's contribution is the sample preparation, ARXPS and QMS investigation, data analysis, data interpretation and manuscript preparation.

[P6] Tailoring the Surface Enrichment of a Pt Catalyst in Ionic Liquid Solutions by Choice of the Solvent

D. Hemmeter, A. Gezmis, D. Kremitzl, P. Wasserscheid, F. Maier, H.-P. Steinrück, *Adv. Mater. Interfaces* **2024**, *11*, 2301085.

The author's contribution is the sample preparation including synthesis of the complexes, ARXPS investigation, data analysis, data interpretation and manuscript preparation.

[P7] Unlocking the Fluorine-Free Buoy Effect: Surface-Enriched Ruthenium Polypyridine Complexes in Ionic Liquids

L. Sanchez Merlinsky, D. Hemmeter, L. M. Baraldo, F. Maier, H.-P. Steinrück, F. J. Williams, *ChemistryOpen* **2024**, *13*, e202400092.

Shared first authorship with L. Sanchez Merlinsky. The author's contribution is the sample preparation, ARXPS investigation, data analysis, data interpretation and manuscript preparation.

[P8] Hydrogenation with Dissolved Pt-complexes Homogenously Distributed in the Ionic Liquid or Enriched at the Gas/Ionic Liquid Interface

S. Khan Antara, D. Hemmeter, Z. Zhai, D. Kremitzl, F. Maier, T. M. Koller, H.-P. Steinrück, M. Haumann

ChemCatChem **2024**, *16*, e202400574.

The author's contribution is the sample preparation including synthesis of the complexes for all collaborative groups and the ARXPS-related contributions (including investigation, data analysis, data interpretation and manuscript preparation regarding the ARXPS results).

8.1 Publication 1, [P1]

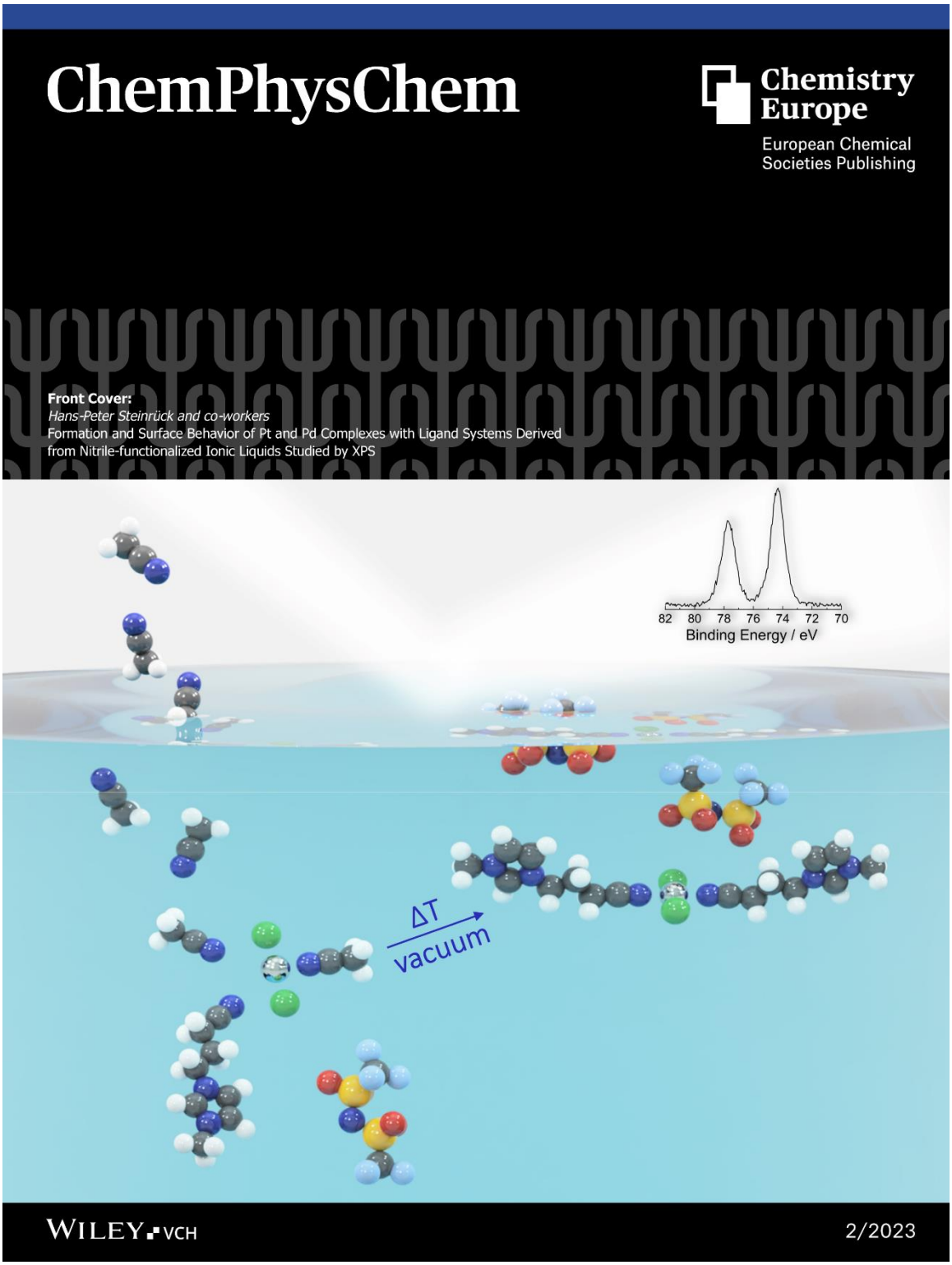

Check for updates

ChemPhysChem

Cover Profile
doi.org/10.1002/cphc.202200914

Chemistry Europe
European Chemical Societies Publishing

www.chemphyschem.org

Formation and Surface Behavior of Pt and Pd Complexes with Ligand Systems Derived from Nitrile-functionalized Ionic Liquids Studied by XPS

Daniel Hemmeter | Ulrike Paap | Dr. Peter Schulz | Prof. Dr. Peter Wasserscheid | Dr. Florian Maier | Prof. Dr. Hans-Peter Steinrück

PC-II
www.chemistry.nat.fau.eu

crt
www.crt.tf.fau.de

The front cover artwork is provided by the groups of Prof. Hans-Peter Steinrück and Prof. Peter Wasserscheid at the Friedrich-Alexander-Universität (FAU) Erlangen-Nürnberg. The image shows substitution of volatile acetonitrile ligands by a nitrile-functionalized imidazolium cation. The formed cationic complex and the counter ions exhibit a specific preferential orientation at the ionic liquid/gas interface, which can be studied by angle-resolved XPS. Read the full text of the Research Article at 10.1002/cphc.202200391.

What aspects of this work do you find most exciting?

It was particularly exciting being able to demonstrate the power of angle-resolved XPS as a variable tool for investigating chemical transformations, electronic properties and surface physics of these highly interesting catalysts at the same time. Another encouraging aspect is that the complexes have proven very suitable for upcoming research interests in our group.

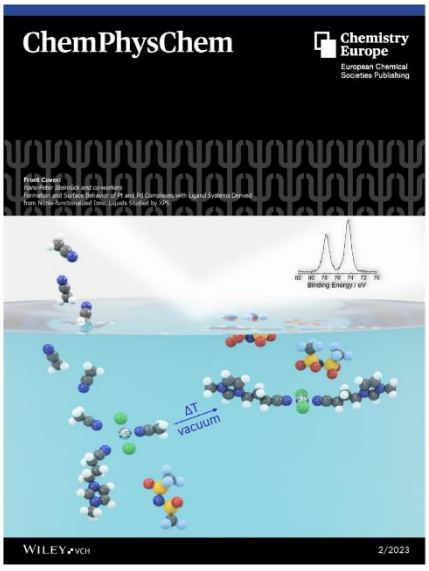

Is your current research mainly fundamental or rather applied?

We always target a fundamental understanding on the nature of interface and bulk properties of ionic liquids. However, our long-term ambition is to demonstrate the potential of rational surface design in ionic liquid solutions as an optimization parameter in catalytic processes. Current topics will therefore certainly lay an excellent basis for more application-driven investigations. The highly collaborative research culture at the FAU and in the ionic liquid community in general provides a perfect environment for this.

ChemPhysChem

Cover Profile
doi.org/10.1002/cphc.202200914

Chemistry Europe
European Chemical Societies Publishing

What new scientific questions does this work raise?

The complexes under investigation are homogeneously distributed at the IL/gas interface. This prompts the question how the surface concentration of this type of complex – or other organometallic catalysts – can be deliberately modified, e. g. for surface enrichment or depletion. In many ionic liquid-based catalytic applications, this is expected to have a strong impact on the efficiency of the process.

Who designed the cover?

Daniel Hemmeter, Florian Maier und Hans-Peter Steinrück conceptualized the design. Daniel Hemmeter did the 3D modelling and rendering.

Acknowledgements

The authors thank the Deutsche Forschungsgemeinschaft (DFG, German Research Foundation) for support in the course of the Collaborative Research Council (CRC)/ Sonderforschungsbereich (SFB) 1452 – Project-ID 431791331.

Check for updates

ChemPhysChem

Research Article
doi.org/10.1002/cphc.202200391

Chemistry Europe
European Chemical Societies Publishing

www.chemphyschem.org

Formation and Surface Behavior of Pt and Pd Complexes with Ligand Systems Derived from Nitrile-functionalized Ionic Liquids Studied by XPS

Daniel Hemmeter,[a] Ulrike Paap,[a] Nicola Taccardi,[b] Julian Mehler,[b] Peter S. Schulz,[b] Peter Wasserscheid,[b] Florian Maier,[a] and Hans-Peter Steinrück*[a]

We studied the formation and surface behavior of Pt(II) and Pd(II) complexes with ligand systems derived from two nitrile-functionalized ionic liquids (ILs) in solution using angle-resolved X-ray photoelectron spectroscopy (ARXPS). These ligand systems enabled a high solubility of the metal complexes in IL solution. The complexes were prepared by simple ligand substitution under vacuum conditions in defined excess of the coordinating ILs, $[C_3CNC_1Im][Tf_2N]$ and $[C_1CNC_1Pip][Tf_2N]$, to immediately yield solutions of the final products. The ILs differ in the cationic head group and the chain length of the functionalized substituent. Our XPS measurements on the neat ILs gave insights in the electronic properties of the coordinating substituents revealing differences in donation capability and stability of the complexes. Investigations on the composition of the outermost surface layers using ARXPS revealed no surface affinity of the nitrile-functionalized chains in the neat ILs. Solutions of the formed complexes in the nitrile ILs showed homogeneous distribution of the solute at the surface with the heterocyclic moieties preferentially orientated towards the vacuum, while the metal centers are rather located further away from the IL/vacuum interface.

Introduction

Ionic liquids (ILs) have emerged as innovative reaction media for catalytic applications.[1] These liquid salts are typically characterized by charge-delocalized and low-symmetry cations and/or anions to yield low melting points, often below room temperature. Unlike conventional volatile solvents, ILs exhibit extremely low vapor pressures and high thermal stability providing a wide temperature range for catalytic transformations with very low solvent-caused gaseous emissions to the environment (even though classifying ILs as "green" solvents remains disputable[2]). Beyond that, the mostly organic nature of the IL ions spans a vast structural and functional diversity. Rational design of ILs allows for deliberate adaption of their physicochemical properties for specific solvation, miscibility, or coordination behavior. Thus, these liquids are attractive solvents for the immobilization of organometallic catalysts.[3] For instance, ILs have been successfully employed for various transformations in liquid-liquid biphasic catalysis, where the formed product segregates from the catalyst solution in an easily separable phase.[4] However, the use of a relatively expensive IL in large quantities may pose economic limitations to the commercialization of an otherwise attractive IL-based reaction concept.[1c]

An inspiring alternative with low IL loading and very efficient IL utilization is supported ionic liquid phase (SILP) catalysis.[5] SILP systems comprise a thin film of an IL-metal complex solution, which is dispersed over a porous support material with large surface area. These materials are solid on the macroscopic scale and enable efficient separation of catalyst and product - the key advantage of heterogeneous catalysis. Within the adsorbed liquid phase, however, the homogeneous character of the catalyst is retained granting the powerful catalytic performance of molecular organometallic catalysis. In SILP systems, reactants passing the gas/IL interface react with the dissolved catalyst in the IL film while products evaporate from the IL phase back into the gas phase. It has been shown that the diffusion of gases in ILs is significantly slower than in conventional solvents, owing to the high viscosity of ILs.[6] Thus, phase-transfer and transport phenomena at the gas/IL interface and within the IL phase can play an essential role for the overall performance of SILP catalysts and are governed by the composition of the gas/IL interface.

X-ray photoelectron spectroscopy (XPS) has demonstrated great potential for analysis of the surface structure in IL-based materials.[1c,7] This technique provides quantitative information on the elemental composition at the near-surface region and is also sensitive to the electronic environment of the chemical species studied. Men *et al.* successfully employed XPS for probing the influence of the ligands[8] and the nature of the solvent[9] on the electronic architecture of transition metal

[a] D. Hemmeter, U. Paap, Dr. F. Maier, Prof. Dr. H.-P. Steinrück
Lehrstuhl für Physikalische Chemie 2, Friedrich-Alexander-Universität Erlangen-Nürnberg, Egerlandstr. 3, 91058 Erlangen, Germany
E-mail: hans-peter.steinrueck@fau.de

[b] Dr. N. Taccardi, Dr. J. Mehler, Dr. P. S. Schulz, Prof. Dr. P. Wasserscheid
Lehrstuhl für Chemische Reaktionstechnik, Friedrich-Alexander-Universität Erlangen-Nürnberg, Egerlandstr. 3, 91058 Erlangen, Germany

Supporting information for this article is available on the WWW under https://doi.org/10.1002/cphc.202200391

ChemPhysChem
Research Article
doi.org/10.1002/cphc.202200391
Chemistry Europe
European Chemical Societies Publishing

complexes in IL solution. The surface sensitivity of XPS can be varied by changing the emission angle, which is referred to as angle-resolved XPS (ARXPS): In normal emission, that is, 0° emission angle with respect to the surface normal, the information depth (ID) is 6–9 nm in organic matter, when using Al–Kα or Mg–Kα radiation.[10] This emission geometry typically reflects the bulk composition, while in grazing emission – in our case, 80° with an ID of 1.0–1.5 nm – mainly the topmost molecular layer of the sample under investigation is probed (note that the ID also depends on the kinetic energy of the photoelectrons). This makes ARXPS a powerful tool for investigating enrichment effects and preferential orientation of molecules at the surface.

ARXPS studies on organometallic catalysts dissolved in ILs have been scarcely reported in literature. An early work of our group on the interfacial structure of transition metal compounds in IL solution revealed enrichment of the $[Pt(NH_3)_4]^{2+}$ cation in $[EMIm][EtOSO_3]$ at the IL/vacuum interface, while the Cl^- counterions were found surface-depleted.[11] This behavior was attributed to the high polarizability of the large metal-containing ions, lowering the surface free-energy. In addition, the impact of the ligand system on the surface-affinity of metal complexes was demonstrated using a Rh(I) catalyst.[12] The employed precursor complex $[Rh(acac)(CO)_2]$ was not detected in the outermost surface layer. However, after substitution of the carbonyl ligands with the SO_3-functionalized triphenylphosphine ligand, TPPTS, the resulting organometallic species was found enriched at the IL/vacuum interface.[12]

In this report, we present the preparation of Pt and Pd complexes containing ligand systems derived from nitrile-functionalized IL cations and their interfacial behavior in IL solution probed by ARXPS. Related systems have been intensively studied by the group of P. J. Dyson stressing the potential of nitrile-functionalized ILs and IL-derived complexes for applications in catalysis.[13] Introducing IL building blocks into the molecular structure of the complexes promises particularly high solubility in ILs, which is beneficial when a high content of dissolved metal is essential, for instance in electrodeposition applications.[14] In our case, the highly concentrated solutions allow for detailed XPS investigations due to the strong metal and ligand signals. In view of catalysis, strong interactions of the organometallic solute with the solvent facilitate catalyst retention in the IL phase under operating conditions.[15] The complexes discussed herein involve the nitrile-functionalized IL cations 1-(3-cyanopropyl)-3-methylimidazolium, $[C_3CNC_1Im]^+$, and 1-(1-cyanomethyl)-1-methylpiperidinium, $[C_1CNC_1Pip]^+$, as ligand systems, as depicted in scheme 1. For preparation of these species, the coordinating ILs serve as the solvent and are used in defined excess to give the final complexes dissolved in this IL. The imidazolium derivative features a long functionalized side chain for spatial separation of the cationic head group and the metal center in the final complex. Imidazolium cations have already been successfully utilized as ligands with a variety of coordinating functionalities,[15–16] or by forming N-heterocyclic carbene (NHC) complexes.[17] In contrast, $[C_1CNC_1Pip][Tf_2N]$ comprises a short

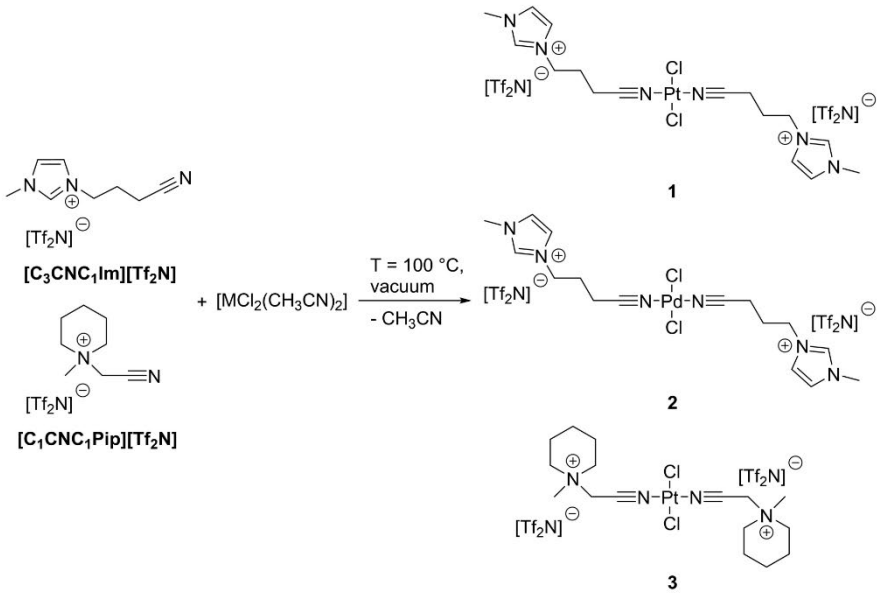

Scheme 1. Preparation of Pt and Pd complexes with ionic ligand systems derived from $[C_3CNC_1Im][Tf_2N]$ and $[C_1CNC_1Pip][Tf_2N]$.

ChemPhysChem
Research Article
doi.org/10.1002/cphc.202200391
Chemistry Europe
European Chemical Societies Publishing

functionalized substituent maximizing charge repulsion between the cationic heterocycle and the metal center. Compared with the imidazolium system, no additional coordination sites are available. Since XP spectra of these nitrile-functionalized ILs have not been reported yet, we start with a detailed characterization of the neat ILs by ARXPS.

Results and Discussion

Neat ILs

We first address the characterization of the nitrile-functionalized ILs employed for coordination, $[C_3CNC_1Im][Tf_2N]$ and $[C_1CNC_1Pip][Tf_2N]$, by ARXPS. As shown by the survey spectra in *figures S1* and *S2* of the supporting information (SI), no other but the expected signals were detected for both ILs in 0° and 80° confirming their high purity. We will first discuss and compare normal emission spectra (0°), representing the bulk composition of the ILs, before approaching the surface structure of the neat samples in grazing emission (80°).

Figure 1a depicts F 1s, N 1s and C 1s region spectra of neat $[C_3CNC_1Im][Tf_2N]$ (note that the full set of spectra is shown in *figure S1*). The F 1s spectrum showed a single peak corresponding to the fluorine atoms in the $[Tf_2N]^-$ anion. In the N 1s region, two distinct signals with similar intensities were detected at 402.1 and 399.7 eV. The N_{Im} signal at higher binding energy was assigned to the quasi-equivalent nitrogen atoms of the imidazolium ring. At lower binding energy, signals of the nitrile functionality and the anionic nitrogen were found superimposed to give a joint $N_{CN/Tf2N}$ peak, despite differing formal charge and chemical environment of the two nitrogen species. For this signal, best agreement was found fitting a single peak rather than deconvolution of the two nitrogen moieties. C 1s signals of anionic and cationic species, C_{Tf2N} and $C_{C3CNC1Im}$, were detected at 293.0 and 286.8 eV, respectively. Even though several species with different chemical environment contribute to the $C_{C3CNC1Im}$ signal, the peak shape was found highly symmetric, and the best fit was obtained employing only one component without further deconvolution. It is worth emphasizing that the $C_{C3CNC1Im}$ envelope at 286.8 eV is at a typical C_{hetero} position for imidazolium carbon bound to nitrogen and does not show a distinct C_{alkyl} feature at ≈285 eV as expected for the side chain carbon atoms solely bound to carbon and hydrogen.[1c] We propose that this is due to the electron-withdrawing effect of the cyano group extending over several atoms within the functionalized substituent. Within the assessed uncertainty range, the quantitative analysis of the normal emission spectra shows very good accordance with the nominal composition as specified in table 1a.

F 1s, N 1s and C 1s region scans of neat $[C_1CNC_1Pip][Tf_2N]$ are depicted in Figure 1b. The N 1s region showed three well-separable signals at 403.1, 400.6 and 399.5 eV, corresponding to nitrogen atoms of the cationic heterocycle, the nitrile functionality and the anion, respectively. The peaks were deconvolved without constraints. The C 1s envelope of the carbon atoms involved in the cation was fitted with a modification of an empiric fitting procedure for unfunctionalized piperidinium ILs reported by Men *et al.*[18] This approach keeps up with the established nomenclature for well-studied 1,3-alkylimidazolium-based cations,[1c] that is, C_{hetero} and $C_{alkyl/aliphatic}$ at 287.0 and 285.5 eV, respectively. The shoulder at the higher binding energy of 287.9 eV indicates a 2:3 intensity ratio with the C_{hetero} signal; the resulting assignment of the carbon species is depicted as inset in Figure 1c. Owing to the strong electron-withdrawing character of the nitrile functionality, the carbon atom in α-position to the CN group contributed to the signal $C_{\alpha C-CN}$. The 2:3 atomic ratio between $C_{\alpha C-CN}$ and C_{hetero} was constrained in the fitting of the C 1s spectra. As can be seen from table 1b, the quantitative analysis of the bulk-sensitive

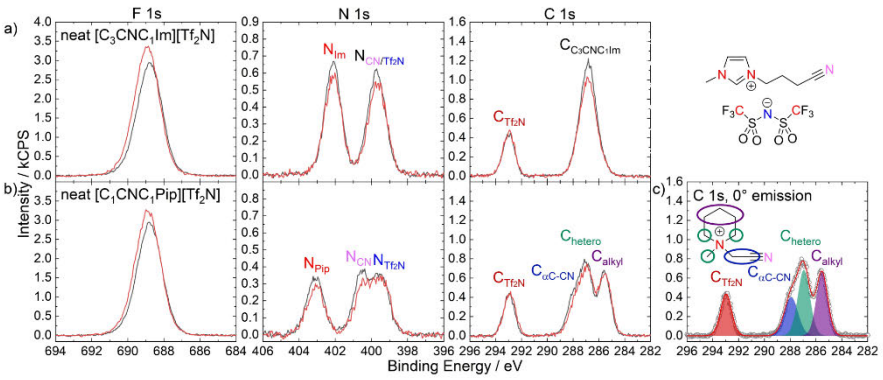

Figure 1. F 1s (left), N 1s (middle) and C 1s (right) spectra of a) neat $[C_3CNC_1Im][Tf_2N]$ (with assignment of signals to molecular structure) and b) $[C_1CNC_1Pip][Tf_2N]$ in 0° (black) and 80° (red) emission; c) C 1s spectrum of neat $[C_1CNC_1Pip][Tf_2N]$ in 0° emission with applied deconvolution and assignment of signals to molecular structure. All spectra were recorded at room temperature.

ChemPhysChem
Research Article
doi.org/10.1002/cphc.202200391
Chemistry Europe
European Chemical Societies Publishing

Table 1. Quantitative analysis of ARXPS core level spectra of $[C_3CNC_1Im][Tf_2N]$ and $[C_1CNC_1Pip][Tf_2N]$ at room temperature.

a) Neat $[C_3CNC_1Im][Tf_2N]$	F 1 s	O 1 s	S 2p	N 1 s Im	N 1 s CN/Tf_2N	C 1 s Tf_2N	C 1 s C_3CNC_1Im
Binding Energy/eV	688.8	532.7	169.7	402.1	399.7	293.0	286.8
Nominal	6	4	2	2	2	2	8
Experimental, 0°	6.2	4.1	2.1	2.0	2.0	2.0	7.7
Experimental, 80°	7.2	3.9	2.1	1.8	1.8	2.1	7.0

b) Neat $[C_1CNC_1Pip][Tf_2N]$	F 1 s	O 1 s	S 2p	N 1 s Pip	N 1 s CN	N 1 s Tf_2N	C 1 s Tf_2N	C 1 s αC–CN	C 1 s hetero	C 1 s alkyl
Binding Energy/eV	688.8	532.7	169.7	403.1	400.6	399.5	293.0	287.9	287.0	285.5
Nominal	6	4	2	1	1	1	2	2	3	3
Experimental, 0°	5.9	4.0	2.1	1.0	1.0	1.0	1.9	2.1	3.2	2.8
Experimental, 80°	6.7	3.8	2.1	0.9	0.9	1.0	2.0	1.9	2.9	2.9

spectra recorded in 0° reveals again very good agreement with the nominal stoichiometry.

Comparing normal emission spectra of $[C_3CNC_1Im][Tf_2N]$ and $[C_1CNC_1Pip][Tf_2N]$ in Figures 1a and 1b provides valuable insights into the electronic structure of their nitrile-functionalized chains, which are the potential coordination sites for complex formation. As discussed above, for $[C_3CNC_1Im][Tf_2N]$ the nitrogen atoms of the nitrile functionality were detected at the same binding energy as the anionic nitrogen atoms at 399.7 eV, and thus are shifted by about 0.9 eV toward lower binding energy as compared to the N_{CN} of the piperidinium derivative at 400.6 eV. In an initial state picture, we assign this shift to a substantially higher electron density on the nitrile functionality originating from the spatial separation to the positively charged imidazolium ring and the electron-donating effect of the extended alkyl chain. By contrast, in the short-chained piperidinium analogue, the nitrile group is in close proximity to the positively charged nitrogen atom of the heterocycle withdrawing electron density from the potential coordination site. Our findings thus clearly indicate a higher donation power for the long-chained derivative $[C_3CNC_1Im][Tf_2N]$. This is in line with ^{15}N-NMR results reported by Lethesh *et al.*,[14a] which reveal a considerably high electron density at nitrile nitrogen atoms in nitrile-functionalized ILs with chain lengths of 4 carbon atoms (including the nitrile carbon atom) or more.

Enrichment effects and preferential orientation of the ions at the surface are particularly interesting for the surface affinity of the target complexes. In the following, XP spectra recorded at 0° and 80° emission angle will be compared for both ILs to obtain an overall picture of the surface structure. As can be seen in Figure 1a, for $[C_3CNC_1Im][Tf_2N]$ the F 1s and to some extent also the C_{Tf2N} signals showed higher intensity at 80°. The O 1s signal exhibited a minor decrease, while the S 2p signal showed no angular dependency (see SI *figure S1* and table 1a). These findings reflect the preferential *cis*-conformation of the $[Tf_2N]^-$ anion at the surface with the CF_3 groups pointing toward the vacuum, while the sulfonyl moieties are directed toward the bulk, as has been concluded from previous studies for ILs containing the $[Tf_2N]^-$ anion.[1c] The N 1s signals and the cation-related $C_{C3CNC1Im}$ signal showed a consistent decrease in intensity at 80°. For the $N_{CN/TF2N}$ signal it is worth noting that the preferential arrangement of the anion in the outermost surface layer should lead to a situation with the contribution of the anionic nitrogen (N_{Tf2N}) showing virtually no angular dependency (as can be clearly seen in case of $[C_1CNC_1Pip][Tf_2N]$, see below). The intensity decrease found for the $N_{CN/TF2N}$ signal in 80° must therefore be entirely accounted to the location of the nitrile group being further away from the surface, that is, preferentially pointing more towards the bulk. This contrasts the surface enrichment of unfunctionalized, and several functionalized substituents found in 1,3-alkylimidazolium-based ILs with chain lengths of 4 carbon atoms or more.[1c,19] It has been shown that distinctive interactions between side chain functionalities and the aromatic head-group can inhibit enrichment of the substituents at the IL/vacuum interface.[20] In fact, interactions between cyano functionalities and the head group were also found in nitrile-functionalized ILs, along with a rich spectrum of interionic hydrogen-bonding.[13a,c] These multifaceted interactions within the molecular network of nitrile-functionalized ILs apparently lead to preferential conformations of the $[C_3CNC_1Im]^+$ cation without surface enrichment of the functionalized alkyl chain.

The ARXPS spectra of $[C_1CNC_1Pip][Tf_2N]$ are depicted in Figure 1b. They revealed similar phenomena as observed for the longer-chained imidazolium derivative. Upon increasing the surface sensitivity of the measurement, the anion-specific F 1s and C_{Tf2N} signals showed an enhancement on the same order of magnitude as observed for $[C_3CNC_1Im][Tf_2N]$ (see also *figure S2* in the SI and table 1b). Notably, the expected constant intensity of the N_{Tf2N} signal in 0° and 80° was now clearly observable for $[C_1CNC_1Pip][Tf_2N]$ due to the separation of the N_{CN} and the N_{Tf2N} peaks. Again, these findings confirm the same preferential orientation of the $[Tf_2N]^-$ anion at the surface as discussed above also for $[C_1CNC_1Pip][Tf_2N]$. The N 1s signals originating from the cation, and $C_{\alpha C-CN}$ and C_{hetero} consistently showed a small decrease in intensity when going from 0° to 80° emission angle, while for the three aliphatic carbon atoms of the piperidinium head group no significant change of the C_{alkyl} signal was found. This indicates that the piperidinium ring in the outermost surface layer is preferentially orientated in a way that the C_{alkyl} carbon atoms are rather directed toward the surface, while the positively charged nitrogen and, most notably, the nitrile-functionalized substituent attached thereto are pointing toward the bulk of the liquid.

ChemPhysChem
Research Article
doi.org/10.1002/cphc.202200391
Chemistry Europe
European Chemical Societies Publishing

Preparation and Bulk Characterization of the Pt and Pd Complexes in IL Solution

$[MCl_2(CH_3CN)_2]$ (M: Pt(II) or Pd(II)) complexes were chosen as the precursors for the preparation of the target compounds. The labile CH_3CN ligands are expected to be immediately pumped off under vacuum conditions when offering $[C_3CNC_1Im]^+$ and $[C_1CNC_1Pip]^-$ for ligand substitution (see scheme 1). The starting material *cis*-$[PtCl_2(CH_3CN)_2]$ employed for formation of $[PtCl_2(C_3CNC_1Im)_2][Tf_2N]_2$ (**1**) and $[PtCl_2(C_1CNC_1Pip)_2][Tf_2N]_2$ (**3**) is known to nearly quantitatively transform into the *trans*-stereoisomer upon heating to temperatures above 75 °C.[21] As 100 °C was chosen as the reaction temperature (see below), the *trans*-configuration is also expected for the final products. This is also in compliance with the thermodynamically favored structure owing to the bulkiness and charge of the IL-derived ligands. The precursor $[PdCl_2(CH_3CN)_2]$ used for preparation of $[PdCl_2(C_3CNC_1Im)_2][Tf_2N]_2$ (**2**) was found to preferentially show *trans*-configuration,[22] which also suggests a similar geometry in the final complex.

The preparation of the target materials in IL solution was monitored by XPS. In the following, our approach will be exemplarily discussed in detail for the reaction mixture of *cis*-$[PtCl_2(CH_3CN)_2]$ in $[C_3CNC_1Im][Tf_2N]$ with 1:4 molar ratio (that is, 20 $\%_{mol}$ metal content per uncoordinated nitrile IL; note that complete abstraction of the CH_3CN ligands and coordination of two equivalents of the $[C_3CNC_1Im]^+$ cation results in a solution of **1** in the remaining $[C_3CNC_1Im][Tf_2N]$ with 1:2 molar ratio). This concentration has provided adequate signal intensities for detailed XPS studies.

We first discuss normal emission XP spectra (0°) of the unreacted reaction mixture, that is, a suspension of the precursor in the IL (for preparative details see experimental section), shown in green in Figure 2a. The precursor-specific Pt 4f and Cl 2p signals showed only small intensities, corresponding to only 2–3 $\%_{mol}$, which is much lower than expected from the stoichiometric metal content of 20 $\%_{mol}$. This strong deviation could be either attributed to the low solubility of the precursor in the IL and/or implies a very slow rate of ligand substitution under applied conditions. Furthermore, the N 1s and C 1s signals, and the corresponding anion-related signals (not shown) were virtually identical to the ones of neat $[C_3CNC_1Im][Tf_2N]$ (cf. Figure 1a, and *figure S1* in the SI). It is worth noting that the experimentally obtained atomic ratios of all IL-related elements agree well with the expected stoichiometric composition confirming the intactness of the solvent in presence of *cis*-$[PtCl_2(CH_3CN)_2]$.

Figure 2b depicts mass spectra of the reaction mixture in the UHV apparatus at room temperature (green) and while heating the mixture in UHV up to T = 100 °C (black). Apart from the contribution of residual gas in the chamber, signals for CH_3CN at 12–15, 24–28 and 38–41 amu[23] were already detected at room temperature, disclosing moderate abstraction of the labile ligands under UHV conditions. Upon heating the mixture to 100 °C, the ligand-related signals showed a very strong increase in intensity and thus, T = 100 °C was chosen as reaction temperature in the following to provide practical reaction rates. In addition to the CH_3CN-specific mass regions, a significant increase was also detected for the signals at 35 and 36 amu. These are assigned to a side reaction, namely, the formation of HCl by abstraction of an acidic proton of the imidazolium ring (most likely, the most acidic proton in C_2-position) and a chloride ligand. This side reaction would also give rise to the possibility of formation of N-heterocyclic carbene (NHC) complexes, as has been observed for other systems.[17] However, as will be pointed out below, no such species or significant deviation from expected stoichiometry of the desired complexes were identified within the accuracy of

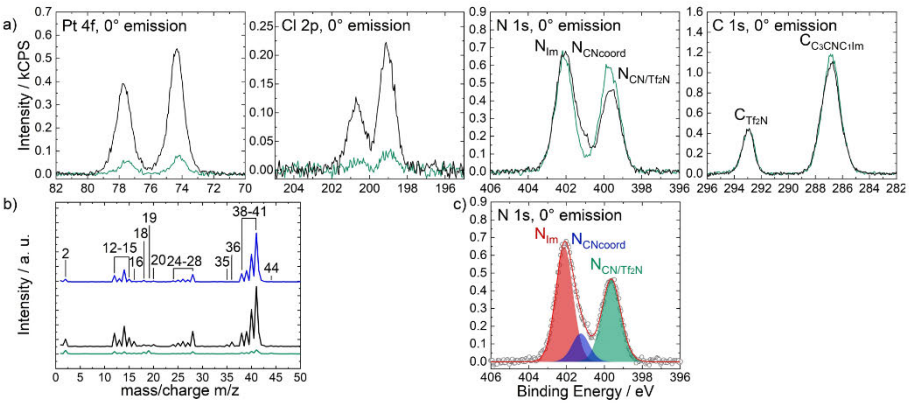

Figure 2. a) Pt 4 f, Cl 2p, C 1s and N 1s spectra of a reaction mixture of cis-$[PtCl_2(CH_3CN)_2]$ in $[C_3CNC_1Im][Tf_2N]$ with 1:4 molar ratio before (green) and after (black) ligand substitution at T = 100 °C. Spectra were recorded in 0° emission at room temperature, b) mass spectra of this reaction mixture at room temperature (green), at T = 100 °C (black) and an equivalent mixture of cis-$[PtCl_2(CH_3CN)_2]$ in $[C_1CNC_1Pip][Tf_2N]$ at T = 100 °C (blue), c) deconvolution applied to the N 1s region shown in a).

ChemPhysChem
Research Article
doi.org/10.1002/cphc.202200391
Chemistry Europe
European Chemical Societies Publishing

our investigations. Notably, the $[C_1CNC_1Pip][Tf_2N]$ reaction mixture without comparably acidic protons in the piperidinium cation did not show any indication for elimination of HCl into the gas phase when heating to 100 °C in UHV (blue spectrum in Figure 2b). Continuous recording of mass spectra over time at 100 °C was used to monitor the progress of the formation of the final complexes *via* the intensity of the CH_3CN-specific signals. The peaks were found slowly decreasing upon reaction progress. This was also reflected in a decrease of the overall pressure in the UHV chamber with reaction time (for details see experimental section).

Next, we address the normal emission XP spectra (0°) of the completely reacted solution of *cis*-$[PtCl_2(CH_3CN)_2]$ in $[C_3CNC_1Im][Tf_2N]$ with 1:4 molar ratio at room temperature (black) in Figure 2a. Note that this sample was prepared by stirring the precursor suspension for 8 h at 100 °C under medium vacuum (MV) conditions using standard Schlenk-techniques to yield a clear brown solution (for preparative details see experimental section). Comparing XP spectra before (green) and after (black) the reaction showed a significant increase in intensity of the Pt 4f and Cl 2p signals, confirming the transformation of the precursor material to a soluble species. In particular, the Pt and Cl content derived from the more bulk-sensitive 0° spectra matched very well with the nominal values of a 1:2 solution of **1** in $[C_3CNC_1Im][Tf_2N]$, as shown in table 2, indicating complete ligand substitution. While the C 1s region showed no significant changes in the C_{Tf2N} and $C_{C3CNC1Im}$ signals, the N 1s region considerably changed: we observed an additional signal at 401.3 eV (low-binding energy shoulder of the N_{Im} peak), denoted as $N_{CNcoord}$. This change was accompanied by an equivalent decrease in the $N_{CN/Tf2N}$ signal at 399.6 eV. These concomitant effects are assigned to the successful coordination of the nitrile-functionalized cation to the metal: upon bonding, electron density is donated from the nitrile group towards the Pt center, which results in a shift of the nitrile nitrogen to higher binding energy. Figure 2c finally depicts the full deconvolution of the N 1s spectrum after reaction. The quantitative analysis of the 0° XP spectra in table 2 *(top)* revealed very good accordance of the experimentally derived values with the nominal composition expected from a quantitative ligand substitution. Notably, the observed ligand substitution under vacuum conditions in defined excess of the coordinating ILs shows no concentration-dependence: XPS measurements for reaction mixture of *cis*-$[PtCl_2(CH_3CN)_2]$ in $[C_3CNC_1Im][Tf_2N]$ with 1:9 molar ratio (that is, 10 $\%_{mol}$ metal content per uncoordinated nitrile IL, yielding an 1:7 solution) and a mixture with 1:19 molar ratio (that is, 5 $\%_{mol}$, yielding an 1:17 solution) show identical qualitative results, as shown in *table S1* in the SI.

In addition to the formation of $[PtCl_2(C_3CNC_1Im)_2][Tf_2N]_2$ (**1**), we also investigated the formation of $[PdCl_2(C_3CNC_1Im)_2][Tf_2N]_2$ (**2**), and $[PtCl_2(C_1CNC_1Pip)_2][Tf_2N]_2$ (**3**) by XPS. The corresponding quantitative analysis is provided in table 2 *(middle and bottom, respectively)*. Again, we find excellent agreement between the experimentally obtained and the nominal compositions, verifying quantitative ligand substitution. Thus, our XPS data showed that the concept of replacing labile and volatile CH_3CN ligands of the precursor by nitrile-functionalized cations at 100 °C under vacuum indeed leads to the desired complexes dissolved in a high amount within the ILs. Interestingly, while the synthesis of **1** in $[C_3CNC_1Im][Tf_2N]$ was only possible at elevated temperatures, the equivalent solution of **2** was already obtained at room temperature by stirring *in vacuo* for several days. Regardless of this fact, a reaction temperature of 100 °C was also chosen to reduce the reaction time to 8 h. One should also note that solutions of **1** and **2** were both successfully prepared under UHV (=thin film of precursor/IL suspension heated on sample holder in UHV) and MV conditions using standard Schlenk-techniques including stirring the mixture. In contrast, the formation of **3** in $[C_1CNC_1Pip][Tf_2N]$ was only observed under UHV conditions keeping the sample for 20 h at 100 °C. Attempts for preparation under MV conditions resulted in solidification of the entire mixture upon reaction progress, which indicates lower stability of the final complex in IL

Table 2. Quantitative analysis of XPS core level spectra of 2:1 mixtures of **1** and **2** in $[C_3CNC_1Im][Tf_2N]$ and **3** in $[C_1CNC_1Pip]$ $[Tf_2N]$ at room temperature.

1:2 of 1 in $[C_3CNC_1Im][Tf_2N]$	Pt 4f		Cl 2p	F 1 s	O 1 s	S 2p	N 1 s Im	N 1 s CN coord		N 1 s CN/Tf_2N		C 1 s Tf_2N	C 1 s C_3CNC_1Im
Binding Energy/eV	76.0		199.9	688.8	532.7	169.7	402.1	401.3		399.6		293.0	286.9
Nominal	0.25		0.5	6	4	2	2	0.5		1.5		2	8
Experimental, 0°	0.25		0.49	6.0	4.0	2.0	2.0	0.50		1.6		2.0	7.8
Experimental, 80°	0.19		0.36	7.2	3.9	2.1	1.9	0.33		1.6		2.2	7.1
1:2 of 2 in $[C_3CNC_1Im][Tf_2N]$	Pd 3d		Cl 2p	F 1 s	O 1 s	S 2p	N 1 s Im	N 1 s CN coord		N 1 s CN/Tf_2N		C 1 s Tf_2N	C 1 s C_3CNC_1Im
Binding Energy/eV	342.0		199.7	688.8	532.6	169.6	402.1	400.9		399.6		292.9	286.8
Nominal	0.25		0.5	6	4	2	2	0.5		1.5		2	8
Experimental, 0°	0.24		0.47	5.8	3.9	2.0	1.9	0.46		1.4		1.9	8.7
Experimental, 80°	0.16		0.33	7.1	3.8	2.0	1.7	0.34		1.3		2.1	7.9
1:2 of 3 in $[C_1CNC_1Pip][Tf_2N]$	Pt 4f	Cl 2p	F 1 s	O 1 s	S 2p	N 1 s Pip	N 1 s CN coord	N 1 s CN	N 1 s Tf_2N	C 1 s Tf_2N	C 1 s αC–CN	C 1 s het	C 1 s alkyl
Binding Energy/eV	76.2	200.0	688.8	532.7	169.7	403.2	401.8	400.5	399.5	293.0	288.0	286.9	285.6
Nominal	0.25	0.5	6	4	2	1	0.5	0.5	1	2	2	3	3
Experimental, 0°	0.28	0.55	6.0	3.9	2.0	1.0	0.53	0.53	0.98	1.9	2.0	3.1	2.9
Experimental, 80°	0.24	0.46	7.0	3.8	2.0	0.90	0.45	0.38	0.94	2.0	1.9	2.8	2.8

ChemPhysChem
Research Article
doi.org/10.1002/cphc.202200391
Chemistry Europe
European Chemical Societies Publishing

solution. Apparently, obtaining a stable solution of **3** in $[C_1CNC_1Pip][Tf_2N]$ requires the complete exclusion of air and moisture, as found under UHV. The lower stability could be due to the strong charge repulsion between the cationic heteroatom of the ligand and the metal center. Preparation of an equivalent solution of the Pd derivative with the short chained piperidinium ligand $[PdCl_2(C_1CNC_1Pip)_2][Tf_2N]_2$ was not successful as indicated by a) sub-stoichiometric intensities of Pd 3d and Cl 2p, b) the absence of a $N_{CNcoord}$ signal, and c) the visible formation of Pd black upon heating.

Figure 3a compares N 1s spectra of the successfully prepared solutions of **1**, **2** and **3** in the respective ILs. We first compare the mixtures of the Pt complexes with different ligand systems **1** and **3**. The solution of **1** (*middle spectrum*) showed a coordination-induced binding energy difference of 1.6 eV between $N_{CNcoord}$ and N_{CN}, whereas for the solution of **3** (*top*) a shift of 1.3 eV was detected. This finding confirmed the significantly higher electron donation power of the nitrile functionality in $[C_3CNC_1Im]^+$ compared to the short-chained piperidinium ligand $[C_1CNC_1Pip]^+$ as concluded from the spectra of the neat ILs (see above). Comparing the positions of the Pt 4f signals showed a higher binding energy of 0.2 eV in the solution of **3**, as depicted in Figure 3b. Even though the magnitude of this shift is close to the experimental uncertainty, a more electron-rich Pt center in compound **1** would be in accordance with expectations from the stronger donation power of the $[C_3CNC_1Im]^+$ ligand. It is essential to note that the binding energy shifts could also be influenced by backdonation of excess electron density from the metal to the CN ligand via π-binding modes. π-backbonding in organonitrile-Pt(II) complexes has been excluded in early works on the nature of the Pt–N bond, but was recently reconsidered by Casella *et al.*[24] In fact, the authors found a significant contribution of backdonation from the metal center into anti-bonding orbitals of the ligands to the overall bonding situation. Comparing the N 1s spectra of **1** and **2** (*bottom*) revealed an about 0.3 eV smaller coordination-induced binding energy shift of 1.3 eV for the Pd derivative. This in line with a lower Pd–N bond energy in comparison with Pt–N bonds in nitrile complexes previously found in a computational study by Kuznetsov *et al.*[25]

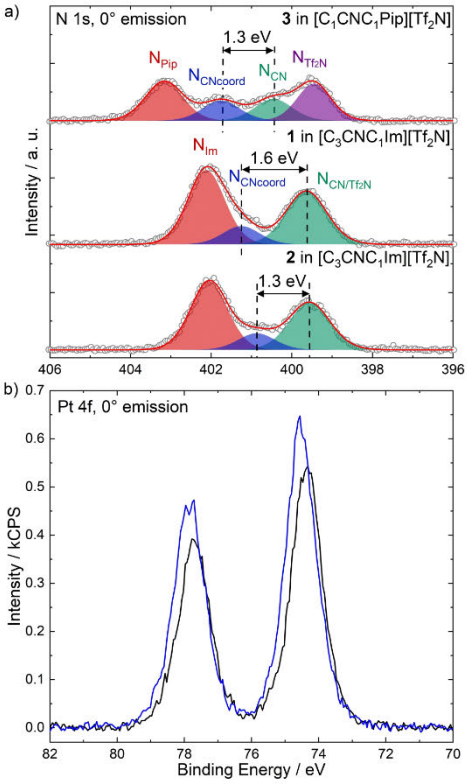

Figure 3. a) N 1s region spectra of solutions of **1** and **2** in $[C_3CNC_1Im][Tf_2N]$, and **3** in $[C_1CNC_1Pip][Tf_2N]$, b) Pt 4f region spectra of solutions of **1** in $[C_3CNC_1Im][Tf_2N]$ (black) and **3** in $[C_1CNC_1Pip][Tf_2N]$ (blue). All spectra were recorded at 0° emission angle. The solutions have a molar complex:IL ratio of 1:2.

Surface Characterization

Comparison of spectra recorded in 0° and 80° emission in Figure 4 provided valuable insights into the microscopic constitution of the IL/vacuum interface. Table 2 gives an overview on the atomic ratios derived from quantitative analysis of the peak intensities for both emission angles, and *figures S3*, *S4* and *S5* in the SI demonstrate the surface cleanliness of the samples under investigation.

We first address the surface composition of **1** in $[C_3CNC_1Im][Tf_2N]$ in detail before comparing solutions of **2** and **3** in the respective parent ILs. As can be extracted from table 2, the F 1s signal and to a lesser extent also the C_{Tf2N} signal showed larger values at an emission angle of 80°, while for the remaining anion-related signals no significant angular dependency was found. This is in line with the preferential orientation of the $[Tf_2N]^-$ anion at the surface discussed for the neat ILs (see above). As shown in Figure 4a, the Pt 4f signal was smaller at 80° than at 0°, as were the complex-specific Cl 2p and $N_{CNcoord}$ signals. For the latter signal, we expect a larger uncertainty compared to the Pt 4f and Cl 2p peaks, owing to the deconvolution of partly superimposed N_{Im} and $N_{CNcoord}$ signals. N_{Im} and $C_{C3CNC1Im}$ signals originate from both ligand and solvent and showed a slight decrease on the border of experimental uncertainty – similar to the measurement of neat $[C_3CNC_1Im][Tf_2N]$. These considerations suggest that the imidazolium moieties of the $[PtCl_2(C_3CNC_1Im)_2]^+$ cation are located closer to the IL/vacuum interface than the metal center and the chloride ligands. Overall, we thus assign the observed behavior to a preferential orientation of the complex in the topmost layer, and not to a depletion of the complex. For a depletion

ChemPhysChem
Research Article
doi.org/10.1002/cphc.202200391
Chemistry Europe
European Chemical Societies Publishing

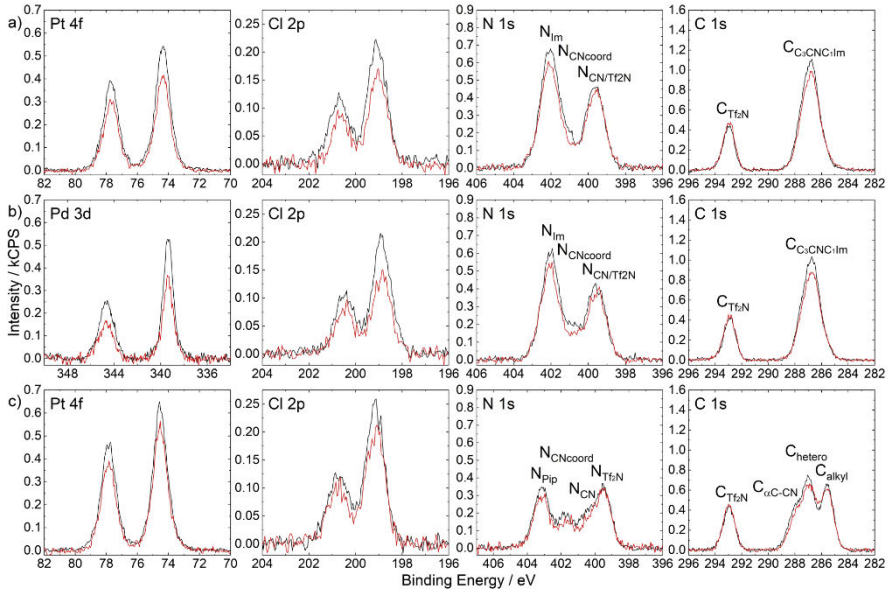

Figure 4. Pt 4f, Cl 2p, N 1s and C 1s spectra of solutions of a) **1** in $[C_3CNC_1Im][Tf_2N]$, b) **2** in $[C_3CNC_1Im][Tf_2N]$ and c) **3** in $[C_1CNC_1Pip][Tf_2N]$ with 1:2 molar ratio in 0° (black) and 80° (red) emission. The spectra were recorded at room temperature.

from the topmost layer, one would expect lower than nominal Pt and Cl signals also at 0°, which was not observed.

The ARXPS spectra of the Pd-containing derivative **2** in $[C_3CNC_1Im][Tf_2N]$, shown in Figure 4b, exhibited similar peculiarities. While for the Cl 2p signal at 80° a similar decrease, as compared to 0°, was seen as for the Pt derivative **1**, the magnitude of the decline of the Pd 3d signal was slightly more pronounced than that of the Pt 4f signal. This observation is attributed to the significantly lower kinetic energy and consequently lower IMFP of the Pd 3d photoelectrons as compared to Pt the 4f photoelectrons (~1145 vs ~1410 eV). The intensity decrease of the complex-specific $N_{CNcoord}$ signal was in line with the decline of the Cl 2p signal. These observations confirmed a similar orientation of the $[PdCl_2(C_3CNC_1Im)_2]^+$ cation in **2** as proposed for the $[PtCl_2(C_3CNC_1Im)_2]^+$ cation in **1**. It should be noted that while the size of the metal atom could have a significant influence on the surface structure, this issue cannot be studied with systems described herein owing to the similar ionic radii of Pt(II) and Pd(II).

Finally, we discuss the differences in the surface structure when employing the short-chained nitrile-functionalized ligand system. Figure 4c depicts ARXPS spectra of **3** in $[C_1CNC_1Pip][Tf_2N]$. Similar to our findings for solutions of **1** and **2** in $[C_3CNC_1Im][Tf_2N]$, the complex-related Pt 4f, Cl 2p and $N_{coordCN}$ signals showed a consistently lower intensity at 80°. The extent of this decrease was significantly less pronounced than for the longer-chained imidazolium derivative. We attribute this observation to the shorter functionalized chain of the ligand system resulting in a location of the metal center closer to the IL/vacuum interface when compared to solutions of **1** and **2** in $[C_3CNC_1Im][Tf_2N]$. At the same time, N_{Pip} and the cation-related C 1s species $C_{\alpha C-CN}$, C_{hetero} and C_{alkyl} decreased to a similar magnitude as found for the neat IL emphasizing that the observed changes with emission angle are due to the orientation of the complex at the interface with an otherwise homogeneous distribution in the IL solution.

As a last point, we note that ARXPS spectra of the complexes dissolved in the respective nitrile-functionalized ILs in lower concentrations (1:7 and 1:17 solutions, cf. above) showed qualitatively identical results concerning formation and surface structure compared with the 1:2 solution, as is evident from *tables S1, S2* and *S3* in the SI. Consequently, no concentration-dependent enrichment or depletion effects were observed, in contrast to observations found for IL mixtures.[26]

Conclusions

We have studied the preparation and surface configuration of Pt and Pd complexes with two different ligand systems derived from nitrile-functionalized IL cations in IL solution by XPS. For the synthesis of the complexes, we performed vacuum-driven

ChemPhysChem
Research Article
doi.org/10.1002/cphc.202200391
Chemistry Europe
European Chemical Societies Publishing

ligand substitution reactions, where the coordinating ILs act as the substituting ligand and the solvent. The ILs were used in a defined excess to immediately give solutions in the desired concentration after quantitative formation of the final complexes. The coordinating ILs, $[C_3CNC_1Im][Tf_2N]$ and $[C_1CNC_1Pip][Tf_2N]$, differ in chain length of the functionalized substituent and possess different cationic head groups. Preparation of the complexes involving the long-chained imidazolium ligand was successful using standard Schlenk-techniques in MV and UHV, while syntheses of the derivatives with the short-chained piperidinium ligand were only successful for the Pt complex **3** applying UHV conditions. XPS on the neat ILs indicated a significantly higher electron density at the uncoordinated cyano group of the long-chained imidazolium derivative, which is in line with previous studies on the electronic properties of nitrile-functionalized ILs.[14a] This results in a stronger donation power of the coordinating nitrile functionality in the $[C_3CNC_1Im]^+$ cation. Our findings also reflected a stronger M–N bond for the Pt complex **1** than for the Pd derivative **2**, as reported previously.[25] The ARXPS measurements on the neat ILs revealed no surface enrichment of the nitrile-functionalized chains, in contrast to long unfunctionalized and a variety of functionalized substituents.[1c,19–20] The catalyst solutions showed homogeneous distribution of the solute in IL solution at the surface. Notably, no concentration-dependent enrichment or depletion effects have been observed for solutions of all three complexes, with complex:IL molar ratio from 1:2 to 1:17. The metal-containing cations showed preferential orientations with the cationic moieties directed towards the vacuum, while the metal centers and the chloride ligands are pointing towards the bulk. We are convinced that this report contributes to the understanding of the interfacial behavior of organometallic catalysts in IL solution. Chemical modifications of the ligand systems for targeted enrichment of the catalyst in IL solution are currently under investigation.

Experimental

Materials

Cis-$[PtCl_2(CH_3CN)_2]$ (purity 98%) and $[PdCl_2(CH_3CN)_2]$ (purity 99.99%) were purchased from Sigma-Aldrich and used as delivered.

Synthesis $[C_3CNC_1Im][Tf_2N]$

A 100 mL 3-neck flask equipped with a reflux condenser, argon inlet and a dropping funnel, was charged with 19.9 ml 1-methylimidazole (20.5 g, 250 mmol) under light argon flow. To this, 23.9 mL 4-Chlorobutyronitrile (25.9 g, 250 mol) were slowly added, and the dropping funnel rinsed with 10 ml of acetonitrile. The mixture was allowed to react for 72 h at 60 °C. After this time, the raw product was dissolved in 50 ml of water and washed with DCM (2 X 25 mL). With respect to the starting 1-methylimidazole, 0.8 eq. of $Li[Tf_2N]$ (57.4 g, 200 mmol) dissolved in 50 ml of water were added. To the formed biphasic mixture 50 ml of DCM were added and the mixture was further stirred overnight. Using a separatory funnel, the lower organic phase was collected and washed with distilled water until the aqueous phase tested negative for chloride using $AgNO_3$. The solvent was removed using a rotary evaporator and the final product was dried at 60 °C and <1 mbar overnight. The product was obtained as clear and slightly yellowish liquid. ^1H- and ^{13}C-spectra were consistent with those in the literature (for detailed information, see SI).[27]

Synthesis $[C_1CNC_1Pip][Tf_2N]$

A 250 mL 2-neck flask equipped with a reflux condenser, argon inlet and a dropping funnel, was charged with a solution of 15 mL of N-methylpiperidine (12.2 g, 0.12 mol) in 100 mL of dry acetone under light argon flow. To this solution, it was slowly added a solution of 10 mL Chloroacetonitrile (11.9 g, 0.16 mol) in 50 mL dry acetone. The mixture was allowed to react 18 h at room temperature. After this time, a suspension of the product in acetone was obtained. This suspension was transferred in a 500 mL flask charged with 300 mL diethylether, and the solid was decanted and washed with small portion of diethylether (5 X 50 mL). The resulting white crystalline solid was dried in vacuum and redissolved in 150 mL distilled water. To this solution, 1.05 eq. with respect to the starting N-Methylpiperidine, of $Li[Tf_2N]$ were added. The mixture was vigorously stirred for 30 min and then 100 mL of methylene chloride were added and the stirring continued for 1 h. The final mixture was transferred to a separatory funnel and let to settle. It resulted in a triphasic mixture, the lower organic phases were collected and washed with small portions of distilled water until the aqueous phase tested negative to the $AgNO_3$ for chloride. The resulting organic phases were evaporated by mean of a rotavapor and the final product was finally dried at 80 °C <1 mbar overnight. The product was obtained as colorless viscous liquid. ^1H- and ^{13}C-NMR Spectra were consistent with those in the literature.[14a]

Sample Preparation

The solutions of **1** and **2** in $[C_3CNC_1Im][Tf_2N]$ were prepared under MV conditions using standard Schlenk-techniques. The solution of **3** in $[C_1CNC_1Pip][Tf_2N]$ was prepared under UHV conditions. Detailed procedures are outlined in the following.

1:4 Suspension of Cis-$[PtCl_2(CH_3CN)_2]$ in $[C_3CNC_1Im][Tf_2N]$

A mixture of *cis*-$[PtCl_2(CH_3CN)_2]$ (48.7 mg, 0.137 mmol) and $[C_3CNC_1Im][Tf_2N]$ (239 mg, 0.555 mmol) was vigorously stirred for 3 h under ambient conditions to yield a yellow suspension.

1:2 Solution of 1 in $[C_3CNC_1Im][Tf_2N]$

Cis-$[PtCl_2(CH_3CN)_2]$ (69.9 mg, 0.197 mmol) was suspended in $[C_3CNC_1Im][Tf_2N]$ (343 mg, 0.796 mmol) (molar ratio IL:precursor of 4.05:1) under ambient conditions. The reaction mixture was stirred *in vacuo* at 100 °C for 8 h to yield a clear, brown solution (molar ratio IL:**1** of 2.05:1).

1:2 Solution of 2 in $[C_3CNC_1Im][Tf_2N]$

$[PdCl_2(CH_3CN)_2]$ (44.7 mg, 0.172 mmol) was suspended in $[C_3CNC_1Im][Tf_2N]$ (297 mg, 0.691 mmol) (molar ratio IL:precursor of 4.01:1) under ambient conditions. The reaction mixture was stirred *in vacuo* at 100 °C for 8 h to yield a clear, deep red solution (molar ratio IL:**2** of 2.01:1).

ChemPhysChem
Research Article
doi.org/10.1002/cphc.202200391
Chemistry Europe
European Chemical Societies Publishing

1:2 Solution of 3 in $[C_1CNC_1Pip][Tf_2N]$

Cis-$[PtCl_2(CH_3CN)_2]$ (90.4 mg, 0.255 mmol) was suspended in $[C_1CNC_1Pip][Tf_2N]$ (428 mg, 1.02 mmol) (molar ratio IL:precursor of 4.01:1) under ambient conditions. The precursor suspension was applied onto the setup-compatible molybdenum sample holder under ambient conditions and immediately introduced into the UHV system. Under UHV conditions, the mixture was then slowly heated to 100 °C. The heating rate was individually adjusted to not exceed a pressure in the chamber of $2\cdot10^{-7}$ mbar. At reaction temperature, the suspension gradually turned to a brown liquid and the mixture was kept at this temperature until no residuals of the starting material were visible to give a deep brown solution. This corresponded to a final pressure of $1.0\cdot10^{-8}$ mbar at 100 °C after a reaction time of 20 h.

The liquid samples were applied onto molybdenum sample holders under ambient conditions and immediately introduced into the load-lock of the vacuum chamber. Here, the samples were left for degassing for at least 12 h before performing further preparation steps or XPS measurements. Temperatures of the samples were measured with a type K thermocouple attached to the molybdenum sample holder.

ARXPS Measurements and Data Evaluation

ARXPS measurements were performed in the DASSA (dual analyzer system for surface analysis) apparatus, which is detailed in Ref [10]. By means of two identical ARGUS type analyzers, the setup allows for simultaneous acquisition of XP spectra at 0° and 80° emission angle with respect to the surface normal. This ensures a) minimization of X-ray induced chemical processes in the sample, b) identical conditions for normal and grazing emission measurements and c) a planar liquid surface for investigating macroscopic films without danger of dripping. Monochromated Al–Kα radiation was used (Source: XM 1000, 14 kV, 238 W, $h\nu = 1486.6$ eV).

Survey spectra were recorded with a pass energy of 150 eV. High-resolution region scans were recorded with a pass energy of 35 eV to provide an overall energy resolution of 0.4 eV. Unless specified otherwise, all normal emission spectra were referenced to the F 1s signal of the $[Tf_2N]$ anion at 688.8 eV. Grazing emission spectra were referenced to the binding energy of the N 1s signals of the heterocyclic cations, that is, N_{Im} or N_{Pip}, in normal emission; in addition, the 80° emission Pt 4f and Cl 2p spectra were shifted about +0.1–0.2 eV to align them with the 0° spectra.

Peak intensities were quantitatively analyzed by using atomic sensitivity factors (ASFs).[28] The XP spectra were normalized to the overall intensity obtained from the measurement of the solution of **1** in $[C_3CNC_1Im][Tf_2N]$ with 1:2 molar ratio. For non-metallic signals, a two-point linear background was subtracted from the XP spectra, except for the C 1s region, where a three-point linear background was applied. For metallic species, the background was subtracted using a Shirley-type function. All peaks were fitted with a Gauss-Lorentzian function with 30% Lorentzian contribution. Procedures for deconvolution of C 1s and N 1s peaks recorded for neat ILs are detailed in the results and discussion section. For fitting of N 1s signals of solutions of **1** and **2** in $[C_3CNC_1Im][Tf_2N]$, FWHM constraints were applied according to the signals observed in the neat IL, which showed an 1.0:1.1 ratio for N_{Im}:$N_{CN/Tf2N}$. This resulted in the same FWHM values for N_{Im} and $N_{CNcoord}$ which was constrained accordingly. For the solution of **3** in $[C_1CNC_1Pip][Tf_2N]$, the best fit was achieved by constraining all N 1s peaks to similar FWHM values. For the more diluted mixtures (yielding 1:7 and 1:17 solutions) the coordination-induced binding energy shifts (difference in binding energy between $N_{CNcoord}$ and N_{CN} signals) found for the 1:2 solutions was additionally constraint to 1.6 eV for solutions of **1** in $[C_3CNC_1Im][Tf_2N]$, and 1.3 eV for **2** in $[C_3CNC_1Im][Tf_2N]$ and **3** in $[C_1CNC_1Pip][Tf_2N]$, respectively, due to the small complex-related signals. Spin-orbit resolved signals were deconvolved and constraint according to the expected degeneracy ratio of the respective orbitals and identical FWHM values. The difference in binding energy was constrained as follows: 1.21 eV for S 2p, 1.60 eV for Cl 2p, 3.35 eV for Pt 4f. Owing to a particularly pronounced broadening of the Pd $3d_{3/2}$ peaks, no constraints were applied for the spin-orbit resolved Pd 3d signals. For a visual comparison of ARXPS spectra, the lower intensity in grazing emission was compensated with a scaling factor derived from the sum of intensities of all core-level spectra obtained at 0° and 80° emission angle (geometry factor).[10] Atomic ratios derived from quantitative analysis of the peak intensities agree with the nominal composition within an uncertainty range of ±10%.

QMS Measurements

Mass spectra were recorded using a quadrupole mass spectrometer (QMS, Hiden Analytical) with a secondary electron multiplier detector. The intensities in the mass spectra of different solutions in Figure 2b were normalized to the overall total chamber pressures.

Acknowledgements

Funded by the Deutsche Forschungsgemeinschaft (DFG, German Research Foundation) – Project-ID 431791331 – SFB 1452. Open Access funding enabled and organized by Projekt DEAL.

Conflict of Interest

The authors declare no conflict of interest.

Data Availability Statement

The data that support the findings of this study are available from the corresponding author upon reasonable request.

Keywords: catalysis · ionic liquids · organometallic chemistry · surface science · X-ray photoelectron spectroscopy

[1] a) T. Welton, *Coord. Chem. Rev.* **2004**, *248*, 2459–2477; b) J. D. Scholten, B. C. Leal, J. Dupont, *ACS Catal.* **2012**, *2*, 184–200; c) H.-P. Steinrück, P. Wasserscheid, *Catal. Lett.* **2015**, *145*, 380–397; d) R. L. Vekariya, *J. Mol. Liq.* **2017**, *227*, 44–60; e) B. Karimi, M. Tavakolian, M. Akbari, F. Mansouri, *ChemCatChem* **2018**, *10*, 3173–3205; f) O. Bartlewicz, I. Dąbek, A. Szymańska, H. Maciejewski, *Catalysts* **2020**, *10*, 1227; g) P. Xu, S. Liang, M.-H. Zong, W.-Y. Lou, *Biotechnol. Adv.* **2021**, *51*, 107702; h) A. Wolny, A. Chrobok, *Nanomaterials* **2021**, *11*, 2030; i) G.-R. Zhang, B. J. M. Etzold, *Adv. Funct. Mater.* **2021**, *31*, 2010977.
[2] N. Winterton, *Clean Technol. Environ. Policy* **2021**, *23*, 2499–2522.
[3] X. Marset, D. J. Ramón, G. Guillena, in: *Catalyst Immobilization: Methods and Applications* (Eds.: M. Benaglia, A. Puglisi), Wiley-VCH Verlag GmbH & Co. KGaA, Weinheim, **2020**, pp. 187–216.
[4] a) J. Dupont, R. F. de Souza, P. A. Z. Suarez, *Chem. Rev.* **2002**, *102*, 3667–3692; b) M. Haumann, A. Riisager, *Chem. Rev.* **2008**, *108*, 1474–1497; c) T. J. Geldbach, D. Zhao, N. C. Castillo, G. Laurenczy, B. Weyershausen,

ChemPhysChem
Research Article
doi.org/10.1002/cphc.202200391
Chemistry Europe
European Chemical Societies Publishing

P. J. Dyson, *J. Am. Chem. Soc.* **2006**, *128*, 9773–9780; d) R. Villa, E. Alvarez, R. Porcar, E. Garcia-Verdugo, S. V. Luis, P. Lozano, *Green Chem.* **2019**, *21*, 6527–6544; e) Y. Qiao, W. Ma, N. Theyssen, C. Chen, Z. Hou, *Chem. Rev.* **2017**, *117*, 6881–6928; f) S. Doherty, in: *Catalysis in Ionic Liquids: From Catalyst Synthesis to Application* (Eds.: C. Hardacre, V. Parvulescu), The Royal Society of Chemistry, Cambridge, **2014**, pp. 44–308.

[5] a) A. Riisager, R. Fehrmann, M. Haumann, P. Wasserscheid, *Eur. J. Inorg. Chem.* **2006**, *2006*, 695–706; b) J. M. Marinkovic, A. Riisager, R. Franke, P. Wasserscheid, M. Haumann, *Ind. Eng. Chem. Res.* **2019**, *58*, 2409–2420.

[6] a) D. Morgan, L. Ferguson, P. Scovazzo, *Ind. Eng. Chem. Res.* **2005**, *44*, 4815–4823; b) D. Camper, C. Becker, C. Koval, R. Noble, *Ind. Eng. Chem. Res.* **2006**, *45*, 445–450; c) M. He, S. Peng, X. Liu, P. Pan, Y. He, *J. Chem. Thermodyn.* **2017**, *112*, 43–51.

[7] a) H.-P. Steinrück, J. Libuda, P. Wasserscheid, T. Cremer, C. Kolbeck, M. Laurin, F. Maier, M. Sobota, P. S. Schulz, M. Stark, *Adv. Mater.* **2011**, *23*, 2571–2587; b) H.-P. Steinrück, *Phys. Chem. Chem. Phys.* **2012**, *14*, 5010–5029.

[8] S. Men, K. R. J. Lovelock, P. Licence, *Chem. Phys. Lett.* **2016**, *645*, 53–58.

[9] S. Men, K. R. J. Lovelock, P. Licence, *RSC Adv.* **2015**, *5*, 35958–35965.

[10] I. Niedermaier, C. Kolbeck, H.-P. Steinrück, F. Maier, *Rev. Sci. Instrum.* **2016**, *87*, 045105.

[11] F. Maier, J. M. Gottfried, J. Rossa, D. Gerhard, P. S. Schulz, W. Schwieger, P. Wasserscheid, H.-P. Steinrück, *Angew. Chem. Int. Ed.* **2006**, *45*, 7778–7780; *Angew. Chem.* **2006**, *118*, 7942–7944.

[12] C. Kolbeck, N. Paape, T. Cremer, P. S. Schulz, F. Maier, H.-P. Steinrück, P. Wasserscheid, *Chem. Eur. J.* **2010**, *16*, 12083–12087.

[13] a) D. Zhao, Z. Fei, R. Scopelliti, P. J. Dyson, *Inorg. Chem.* **2004**, *43*, 2197–2205; b) D. Zhao, Z. Fei, T. J. Geldbach, R. Scopelliti, P. J. Dyson, *J. Am. Chem. Soc.* **2004**, *126*, 15876–15882; c) Z. Fei, D. Zhao, D. Pieraccini, W. H. Ang, T. J. Geldbach, R. Scopelliti, C. Chiappe, P. J. Dyson, *Organometallics* **2007**, *26*, 1588–1598; d) Y. Cui, I. Biondi, M. Chaubey, X. Yang, Z. Fei, R. Scopelliti, C. G. Hartinger, Y. Li, C. Chiappe, P. J. Dyson, *Phys. Chem. Chem. Phys.* **2010**, *12*, 1834–1841.

[14] a) K. C. Lethesh, K. Van Hecke, L. Van Meervelt, P. Nockemann, B. Kirchner, S. Zahn, T. N. Parac-Vogt, W. Dehaen, K. Binnemans, *J. Phys. Chem. B* **2011**, *115*, 8424–8438; b) A. P. Abbott, F. Endres, D. R. Macfarlane, in: *Electrodeposition from Ionic Liquids*, 2 ed. (Eds.: F. Endres, D. MacFarlane, A. Abbott), Wiley-VCH Verlag GmbH & Co. KGaA, Weinheim, **2017**, pp. 1–15.

[15] J. Limberger, B. C. Leal, A. L. Monteiro, J. Dupont, *Chem. Sci.* **2015**, *6*, 77–94.

[16] a) C. S. Consorti, G. L. P. Aydos, G. Ebeling, J. Dupont, *Org. Lett.* **2008**, *10*, 237–240; b) M. Jankowska-Wajda, O. Bartlewicz, A. Szpecht, A. Zajac, M. Smiglak, H. Maciejewski, *RSC Adv.* **2019**, *9*, 29396–29404; c) K. L. Luska, K. Z. Demmans, S. A. Stratton, A. Moores, *Dalton Trans.* **2012**, *41*, 13533–13540; d) P. Wang, X. Chen, D.-L. Wang, Y.-Q. Li, Y. Liu, *Green Energy & Environ.* **2017**, *2*, 419–427; Environ. **2017**, 2, 419–427.

[17] a) M. Hasan, I. V. Kozhevnikov, M. R. H. Siddiqui, A. Steiner, N. Winterton, *J. Chem. Res.* **2000**, *2000*, 392–393; b) B. Karimi, D. Enders, *Org. Lett.* **2006**, *8*, 1237–1240; c) B. Mell, J. Rust, C. W. Lehmann, R. J. F. Berger, D. Otte, M. Ertl, U. Monkowius, F. Mohr, *Organometallics* **2021**, *40*, 890–898.

[18] S. Men, P. Licence, C.-L. Do-Thanh, H. Luo, S. Dai, *Phys. Chem. Chem. Phys.* **2020**, *22*, 11976–11983.

[19] F. Maier, T. Cremer, C. Kolbeck, K. R. J. Lovelock, N. Paape, P. S. Schulz, P. Wasserscheid, H. P. Steinrück, *Phys. Chem. Chem. Phys.* **2010**, *12*, 1905–1915.

[20] a) C. Kolbeck, I. Niedermaier, A. Deyko, K. R. J. Lovelock, N. Taccardi, W. Wei, P. Wasserscheid, F. Maier, H.-P. Steinrück, *Chem. Eur. J.* **2014**, *20*, 3954–3965; b) K. R. J. Lovelock, C. Kolbeck, T. Cremer, N. Paape, P. S. Schulz, P. Wasserscheid, F. Maier, H.-P. Steinrück, *J. Phys. Chem. B* **2009**, *113*, 2854–2864.

[21] a) F. P. Fanizzi, F. P. Intini, L. Maresca, G. Natile, *J. Chem. Soc. Dalton Trans.* **1990**, 199–202; b) V. Y. Kukushkin, *Platinum Met. Rev.* **1998**, *42*, 106–107.

[22] R. A. Walton, *Spectrochim. Acta* **1965**, *21*, 1795–1801.

[23] NIST Mass Spectrometry Data Center, W. E. Wallace, director, in *NIST Chemistry WebBook, NIST Standard Reference Database Number 69* (Eds.: P. J. Linstrom, W. G. Mallard), National Institute of Standards and Technology, Gaithersburg MD, 20899, (retrieved April 13, 2022).

[24] G. Casella, C. Fonseca Guerra, S. Carlotto, P. Sgarbossa, R. Bertani, M. Casarin, *Dalton Trans.* **2019**, *48*, 12974–12985.

[25] M. L. Kuznetsov, V. Y. Kukushkin, A. J. L. Pombeiro, *Dalton Trans.* **2008**, 1312–1322.

[26] B. S. J. Heller, M. Lexow, F. Greco, S. Shin, G. Partl, F. Maier, H.-P. Steinrück, *Chem. Eur. J.* **2020**, *26*, 1117–1126.

[27] a) Q.-S. Liu, H. Liu, L. Mou, *Acta Phys. -Chim. Sin.* **2016**, *32*, 617–623; b) Q. Zhang, Z. Li, J. Zhang, S. Zhang, L. Zhu, J. Yang, X. Zhang, Y. Deng, *J. Phys. Chem. B* **2007**, *111*, 2864–2872.

[28] C. D. Wagner, L. E. Davis, M. V. Zeller, J. A. Taylor, R. H. Raymond, L. H. Gale, *Surf. Interface Anal.* **1981**, *3*, 211–225.

Manuscript received: June 8, 2022
Revised manuscript received: September 23, 2022
Accepted manuscript online: September 26, 2022
Version of record online: October 20, 2022

ChemPhysChem

Supporting Information

Formation and Surface Behavior of Pt and Pd Complexes with Ligand Systems Derived from Nitrile-functionalized Ionic Liquids Studied by XPS

Daniel Hemmeter, Ulrike Paap, Nicola Taccardi, Julian Mehler, Peter S. Schulz, Peter Wasserscheid, Florian Maier, and Hans-Peter Steinrück*

The supporting information comprises wide scans and region spectra of all relevant core levels for the neat [C_3CNC_1Im][Tf_2N] (figure S1) and [C_1CNC_1Pip][Tf_2N] (figure S2), and for the solutions of the three complexes (**1**), (**2**) and (**3**), with 1:2 complex:IL molar ratio (figures S3-S5). The XP spectra contain all relevant regions of the ILs and complexes. In addition, Si 2p spectra are shown to confirm surface cleanliness concerning common contaminations observed in previous studies[1]. To demonstrate the absence of concentration dependences of the observed behavior, the quantitative analysis of the XP spectra of solution (**1**), (**2**) and (**3**) are provided in table S1, S2 and S3, respectively, for solutions with 1:2 (data from table 2), 1:7 and 1:17 molar ratio. The SI also includes ^{1}H (figure S6), ^{13}C (figure S7) and ^{19}F NMR data of [C_3CNC_1Im][Tf_2N].

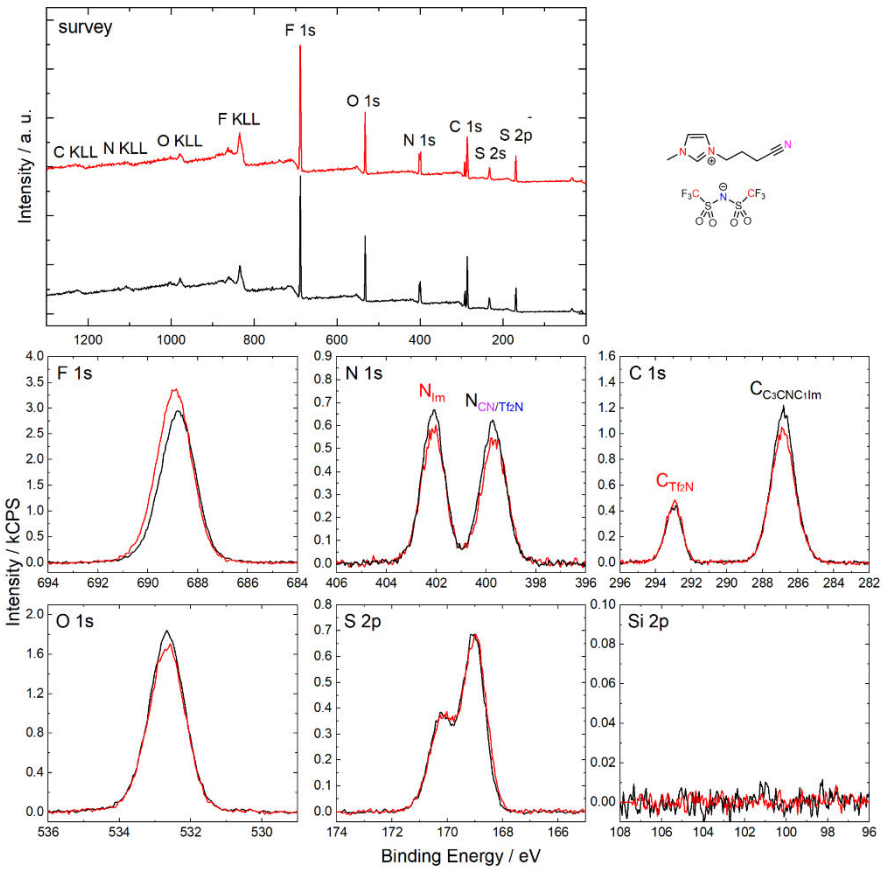

***Figure S1**: Survey, F 1s, N 1s, C 1s, O 1s, S 2p and Si 2p XP spectra of neat [C_3CNC_1Im][Tf_2N] in 0° (black) and 80° (red) emission recorded at room temperature with assignment of peaks to the molecular structure.*

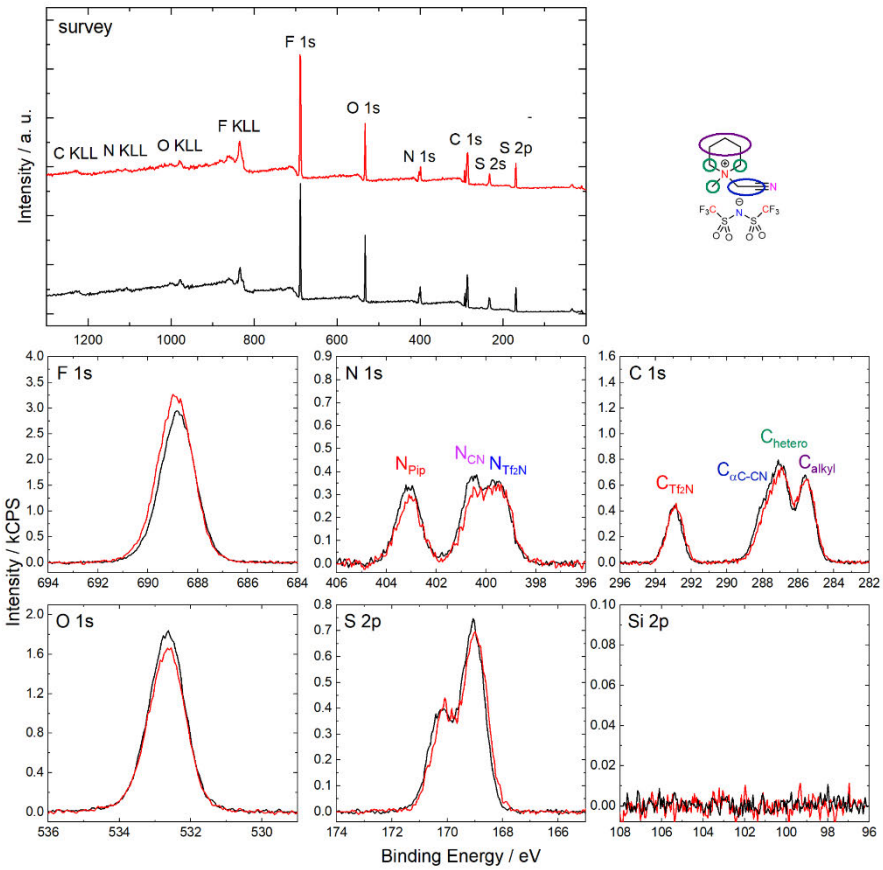

***Figure S2**: Survey, F 1s, N 1s, C 1s, O 1s, S 2p and Si 2p XP spectra of neat [C_1CNC_1Pip][Tf_2N] in 0° (black) and 80° (red) emission recorded at room temperature with assignment of peaks to the molecular structure.*

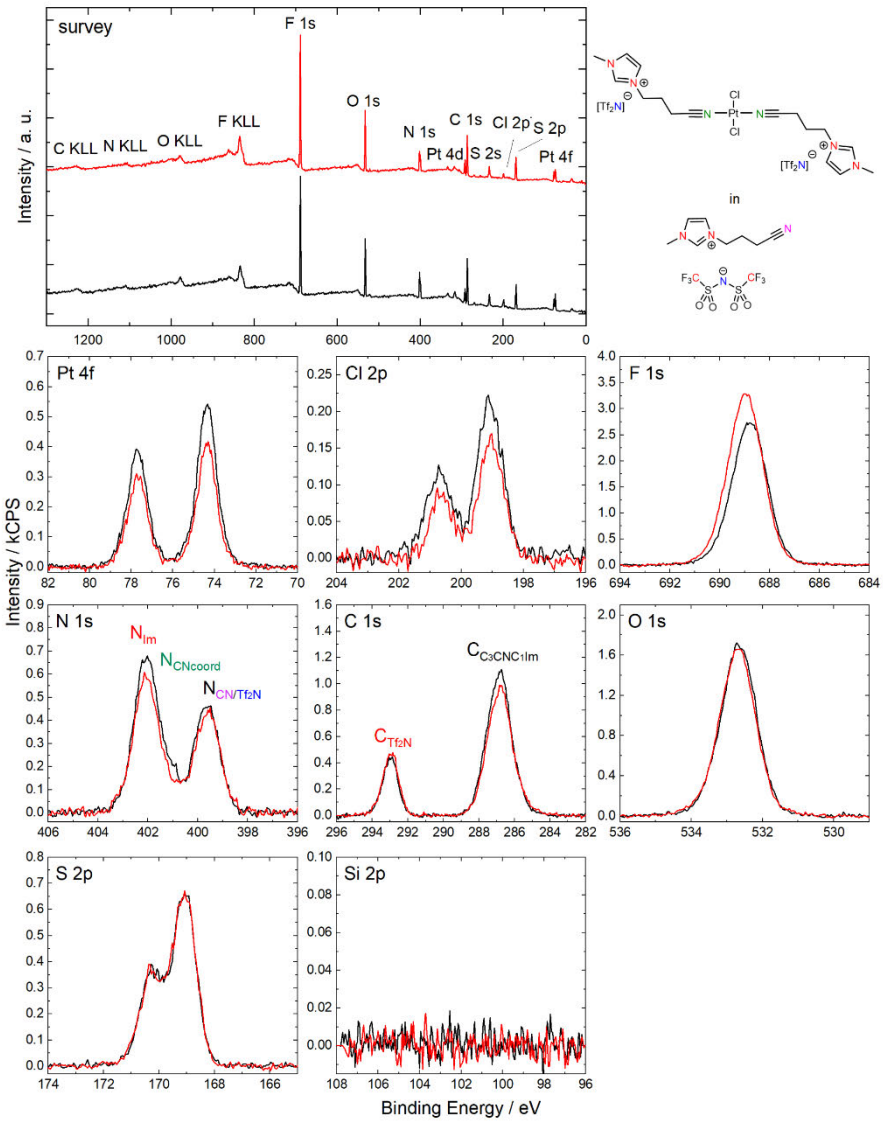

***Figure S3**: Survey, Pt 4f, Cl 2p, F 1s, N 1s, C 1s, O 1s, S 2p and Si 2p XP spectra of solutions of **1** in [C_3CNC_1Im][Tf_2N] with 1:2 molar ratio in 0° (black) and 80° (red) emission recorded at room temperature with assignment of peaks to the molecular structure.*

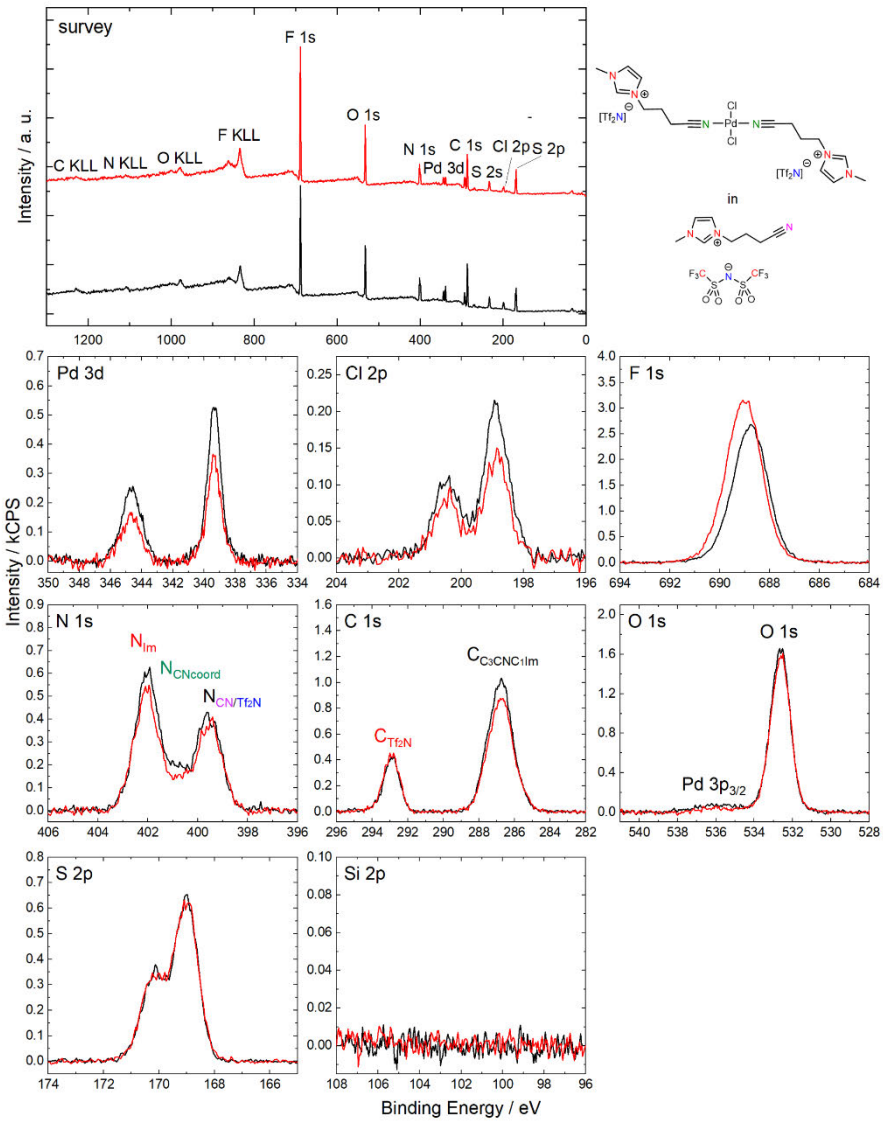

*Figure S4: Survey, Pd 3d, Cl 2p, F 1s, N 1s, C 1s, O 1s, S 2p and Si 2p XP spectra of solutions of **2** in [C_3CNC_1Im][Tf_2N] with 1:2 molar ratio in 0° (black) and 80° (red) emission recorded at room temperature with assignment of peaks to the molecular structure.*

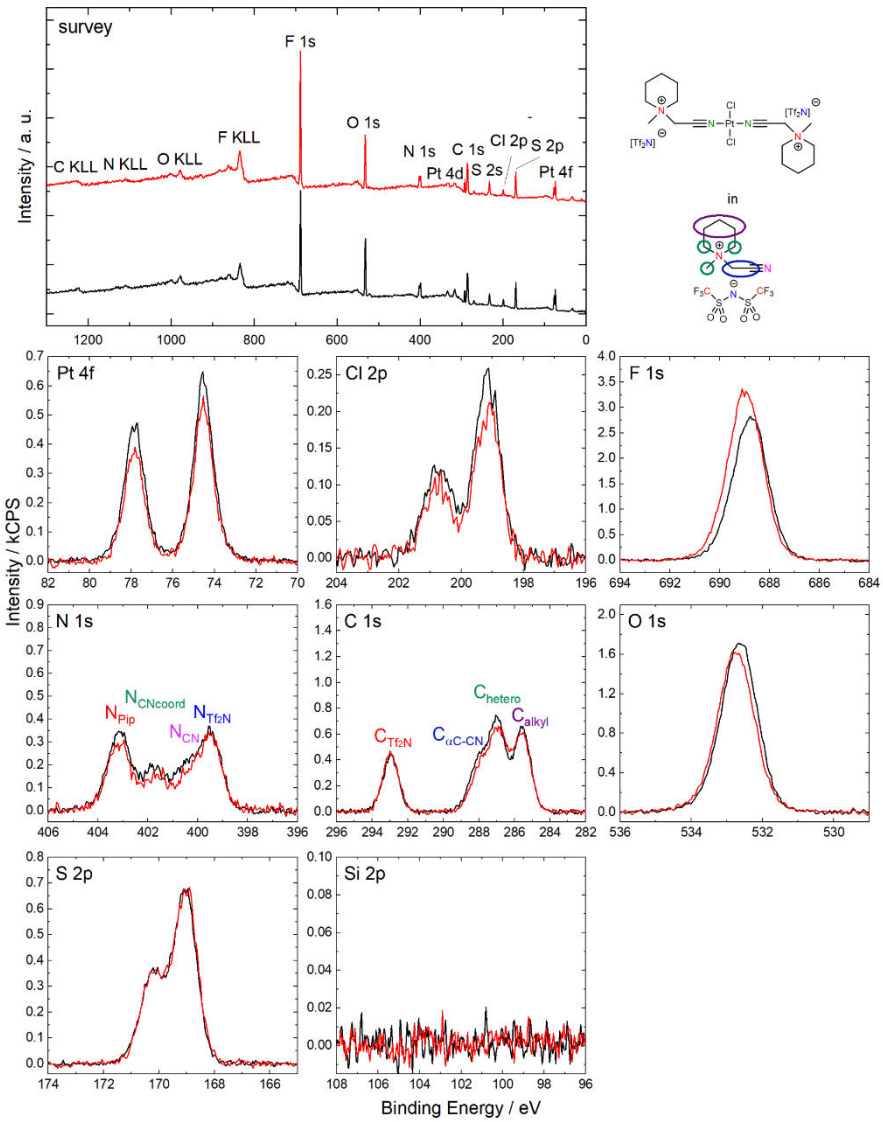

***Figure S5**: Survey, Pt 4f, Cl 2p, F 1s, N 1s, C 1s, O 1s, S 2p and Si 2p XP spectra of solutions of **3** in [C_1CNC_1Pip][Tf_2N] with 1:2 molar ratio in 0° (black) and 80° (red) emission recorded at room temperature with assignment of peaks to the molecular structure.*

Table S1: *Quantitative analysis of XPS core level spectra of 1:2, 1:7 and 1:17 solutions of* ***1*** *in [C_3CNC_1Im][Tf_2N] at room temperature.*

1:2 of 1 in [C_3CNC_1Im][Tf_2N]	Pt 4f	Cl 2p	F 1s	O 1s	S 2p	N 1s Im	N 1s CN coord	N 1s CN/Tf_2N	C 1s Tf_2N	C 1s C_3CNC_1Im
Nominal	0.25	0.5	6	4	2	2	0.5	1.5	2	8
Experimental, 0°	0.25	0.49	6.0	4.0	2.0	2.0	0.50	1.6	2.0	7.8
Experimental, 80°	0.19	0.36	7.2	3.9	2.1	1.9	0.33	1.6	2.2	7.1
1:7 of 1 in [C_3CNC_1Im][Tf_2N]										
Nominal	0.11	0.22	6	4	2	2	0.22	1.8	2	8
Experimental, 0°	0.10	0.22	6.2	4.1	2.0	2.0	0.23	1.8	2.0	7.7
Experimental, 80°	0.077	0.15	7.3	3.9	2.0	1.8	0.22	1.7	2.2	6.9
1:17 of 1 in [C_3CNC_1Im][Tf_2N]										
Nominal	0.053	0.11	6	4	2	2	0.11	1.9	2	8
Experimental, 0°	0.052	0.11	6.1	4.1	2.1	2.0	0.082	1.9	2.0	7.7
Experimental, 80°	0.041	0.076	7.0	3.9	2.2	1.9	0.027	1.8	2.2	7.2

Please note that in the more diluted 1:7 and 1:17 mixtures a larger uncertainty must be expected for the derived values from the $N_{CNcoord}$ signal in 80° emission owing to its low intensity. Nonetheless, information on the distribution of the complex in solution can be extracted from the Pt 4f and Cl 2p signals.

Table S2: *Quantitative analysis of XPS core level spectra of 1:2, 1.7 and 1:17 solutions of* ***2*** *in [C_3CNC_1Im][Tf_2N] at room temperature.*

1:2 of 2 in [C_3CNC_1Im][Tf_2N]	Pd 3d	Cl 2p	F 1s	O 1s	S 2p	N 1s Im	N 1s CN coord	N 1s CN/Tf_2N	C 1s Tf_2N	C 1s C_3CNC_1Im
Nominal	0.25	0.5	6	4	2	2	0.5	1.5	2	8
Experimental, 0°	0.24	0.47	5.8	3.9	2.0	1.9	0.46	1.4	1.9	8.7
Experimental, 80°	0.16	0.33	7.1	3.8	2.0	1.7	0.34	1.3	2.1	7.9
1:7 of 2 in [C_3CNC_1Im][Tf_2N]										
Nominal	0.11	0.22	6	4	2	2	0.22	1.8	2	8
Experimental, 0°	0.10	0.19	5.9	3.9	1.9	1.9	0.18	1.7	1.9	8.7
Experimental, 80°	0.068	0.15	6.9	3.7	2.0	1.7	0.080	1.6	2.0	8.1
1:17 of 2 in [C_3CNC_1Im][Tf_2N]										
Nominal	0.053	0.11	6	4	2	2	0.11	1.9	2	8
Experimental, 0°	0.048	0.093	5.8	3.8	1.9	1.9	0.076	1.8	1.9	8.8
Experimental, 80°	0.036	0.067	6.7	3.7	2.0	1.7	0.037	1.7	2.0	8.1

Please note that in the more diluted 1:7 and 1:17 mixtures a larger uncertainty must be expected for the derived values from the $N_{CNcoord}$ signal in 80° emission owing to its low intensity. Nonetheless, information on the distribution of the complex in solution can be extracted from the Pd 3d and Cl 2p signals.

Table S3: *Quantitative analysis of XPS core level spectra of 1:2, 1:7 and 1:17 mixtures of* ***3*** *in [C_1CNC_1Pip][Tf_2N] at room temperature.*

1:2 of 3 in [C_1CNC_1Pip][Tf_2N]	Pt 4f	Cl 2p	F 1s	O 1s	S 2p	N 1s Pip	N 1s CN coord	N 1s CN	N 1s Tf_2N	C 1s Tf_2N	C 1s αC-CN	C 1s het	C 1s alkyl
Nominal	0.25	0.5	6	4	2	1	0.5	0.5	1	2	2	3	3
Experimental, 0°	0.28	0.55	6.0	3.9	2.0	1.0	0.53	0.53	0.98	1.9	2.0	3.1	2.9
Experimental, 80°	0.24	0.46	7.0	3.8	2.0	0.90	0.45	0.38	0.94	2.0	1.9	2.8	2.8
1:7 of 3 in [C_1CNC_1Pip][Tf_2N]													
Nominal	0.11	0.22	6	4	2	1	0.22	0.78	1	2	2	3	3
Experimental, 0°	0.092	0.19	6.1	4.1	2.1	1.0	0.20	0.81	0.95	1.9	2.1	3.1	2.9
Experimental, 80°	0.090	0.16	6.9	3.8	2.1	0.89	0.19	0.69	0.93	2.1	1.8	2.7	3.0
1:17 of 3 in [C_1CNC_1Pip][Tf_2N]													
Nominal	0.053	0.11	6	4	2	1	0.11	0.89	1	2	2	3	3
Experimental, 0°	0.054	0.11	6.1	4.1	2.0	1.0	0.11	0.91	0.93	1.9	2.0	3.1	2.9
Experimental, 80°	0.052	0.11	7.0	3.8	2.0	0.87	0.12	0.71	0.98	2.0	1.9	2.8	2.8

^{1}H- and ^{13}C-spectra were consistent with those found in the literature.[2]

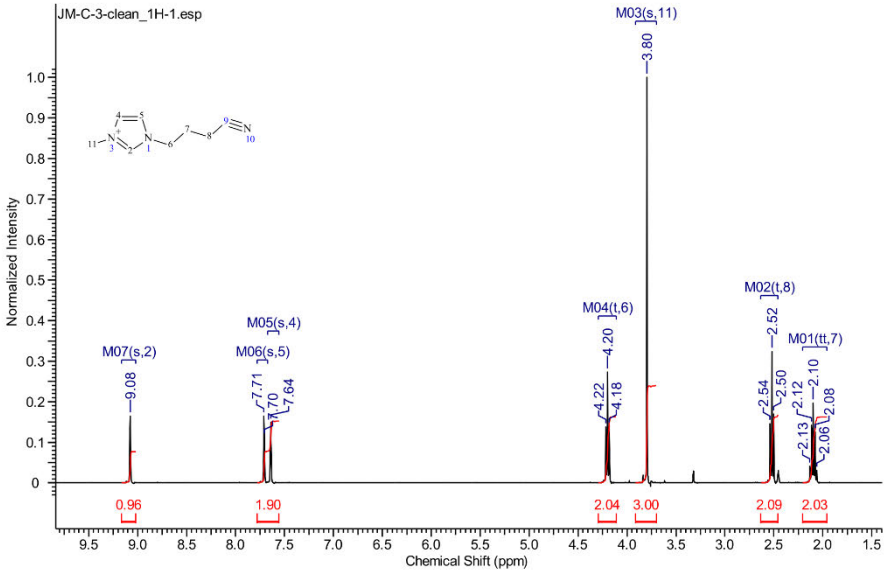

Figure S6: ^{1}H NMR spectrum of [C_3CNC_1Im][Tf_2N] (for measurement parameters and quantitative analysis see below).

^{1}H NMR (400 MHz, DMSO-d_6), δ ppm, 2.10 (tt, J=7.20, 7.00 Hz, 2 H) 2.52 (t, J=7.21 Hz, 2 H) 3.80 (s, 3 H) 4.20 (t, J=7.00 Hz, 2 H) 7.64 (s, 1 H) 7.71 (s, 1 H) 9.08 (s, 1 H).

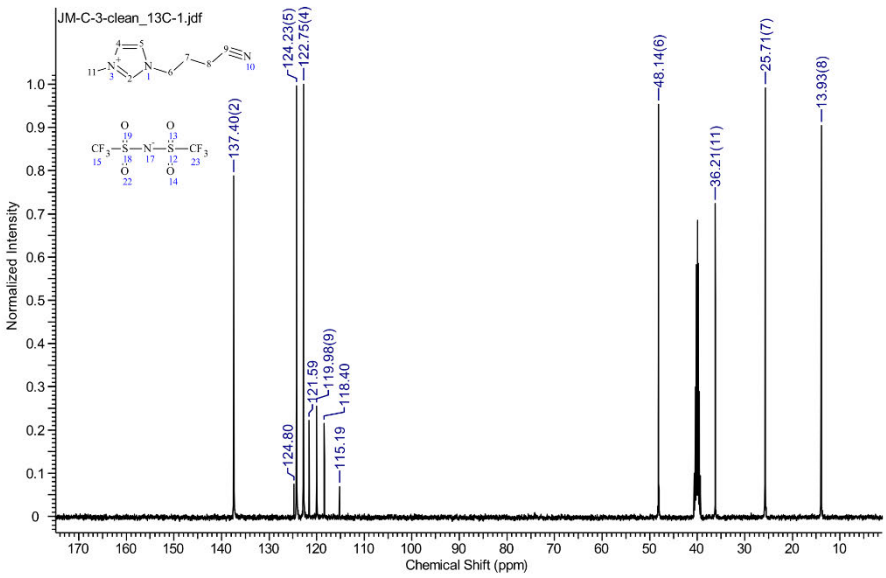

Figure S7: ^{13}C NMR spectrum of [C_3CNC_1Im][Tf_2N] (for measurement parameters and quantitative analysis see below).

^{13}C NMR (100 MHz, DMSO-d_6), δ ppm, 13.93 CH_2, 25.71 CH_2, 36.21 CH_3, 48.14 CH_2, 119.98 CN, 120.00 (q) CF_3, 122.75 CH, 124.23 CH, 137.40 CH.

^{19}F NMR (376 MHz, DMSO-d_6), δ ppm, 78.77

References

[1] J. M. Gottfried, F. Maier, J. Rossa, D. Gerhard, P. S. Schulz, P. Wasserscheid, H.-P. Steinrück, *Z. Phys. Chem.* **2006**, *220*, 1439-1453.

[2] a) Q.-S. Liu, H. Liu, L. Mou, *Acta Phys. -Chim. Sin.* **2016**, *32*, 617-623; b) Q. Zhang, Z. Li, J. Zhang, S. Zhang, L. Zhu, J. Yang, X. Zhang, Y. Deng, *J. Phys. Chem. B* **2007**, *111*, 2864-2872.

8.2 Publication 2, [P2]

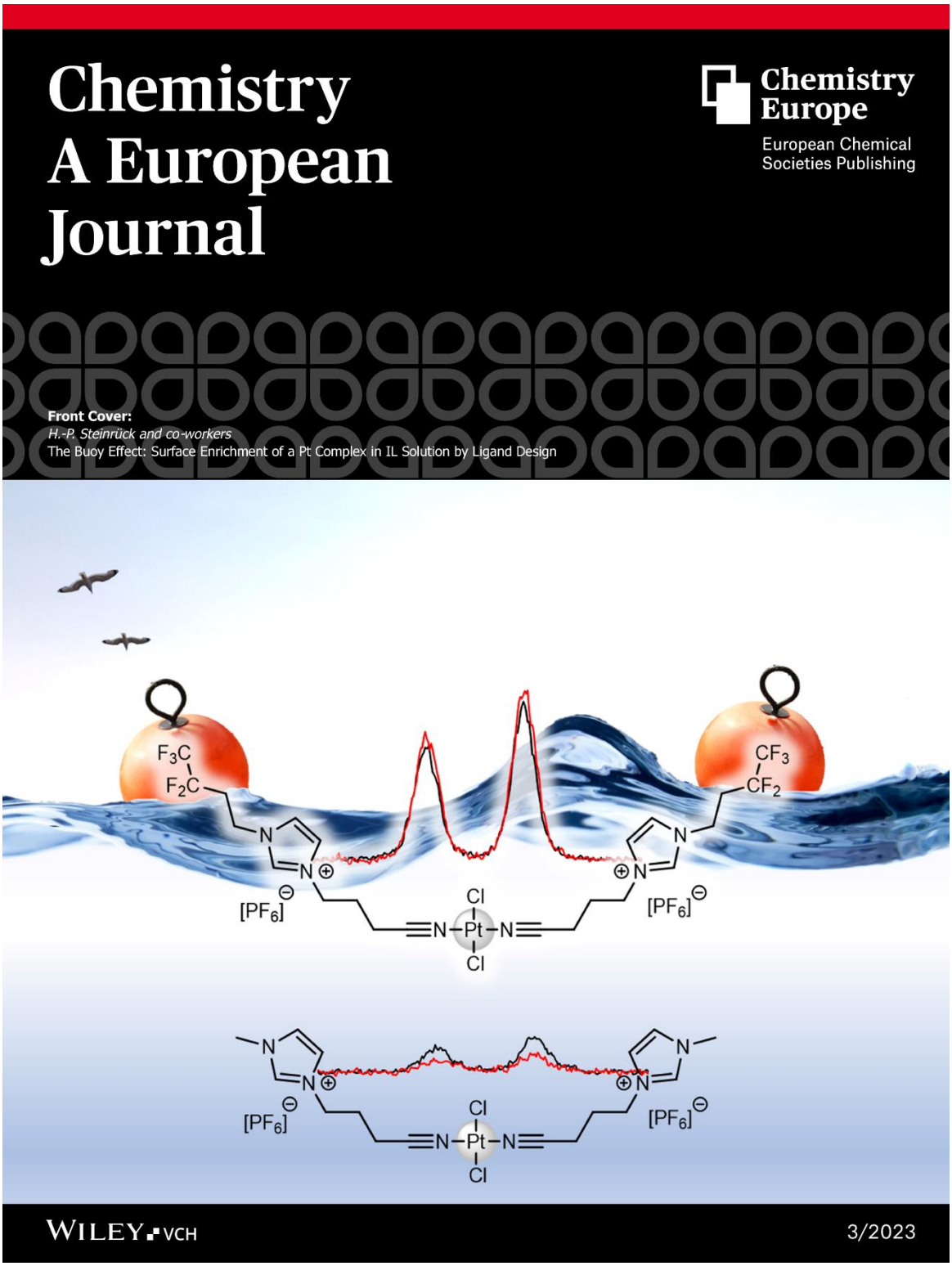

Check for updates

Chemistry–A European Journal

Cover Profile
doi.org/10.1002/chem.202204023

Chemistry Europe
European Chemical Societies Publishing

www.chemeurj.org

The Buoy Effect: Surface Enrichment of a Pt Complex in IL Solution by Ligand Design

Daniel Hemmeter Daniel Kremitzl Peter Schulz Peter Wasserscheid Florian Maier Hans-Peter Steinrück

CLINT Catalysis at Liquid Interfaces SFB 1452

Invited for the cover of this issue are the groups of Hans-Peter Steinrück and Peter Wasserscheid at the Friedrich-Alexander-Universität Erlangen-Nürnberg. The image depicts two Pt catalysts dissolved in an ionic liquid. For one of them, fluorinated side chains in the ligand system act as buoys leading to pronounced enrichment of the complex at the gas/IL interface, as is evidenced by strongly enhanced Pt signals in angle-resolved photoelectron spectroscopy. For the complex without fluorinated side chains, no such effect is observed. Read the full text of the article at 10.1002/chem.202203325.

What aspects of this project do you find most exciting?

An exciting aspect in research on ionic liquids in general is their enormous structural variability, which allows for deliberately tailoring their physicochemical properties for desired applications. Of course, this concept of task-specificity can also be applied to catalysts dissolved in ionic liquids, which opens a powerful route for manipulating the surface structure of these solutions.

What was the biggest surprise (on the way to the results presented in this paper)?

The extreme enrichment effect came as a delighting surprise to us. The accumulation of the catalyst at the gas/IL interface is even more pronounced than expected from the surface activity of the free ligand. This interesting behavior will be addressed in future works.

What future opportunities do you see (in the light of the results presented in this paper)?

A very high concentration of the catalyst at the gas/IL interface is expected to strongly influence the catalytic performance in processes involving high interface areas between reactant and catalyst phase, e.g., in SILP or liquid-liquid biphasic catalysis. As a next step on our research agenda, we will therefore address the impact of the surface enrichment on the outcome in model catalytic reactions. In this regard, one particularly interesting consideration is that the performance of the catalyst might not only be affected by the high surface concentration, but also due to the anisotropic environment at the gas/IL interface.

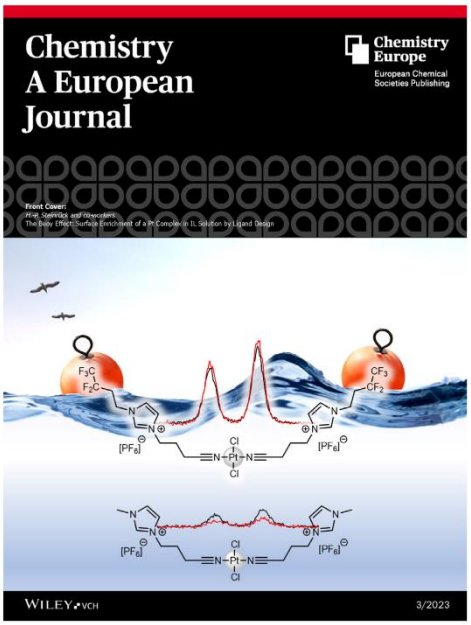

Check for updates

Chemistry–A European Journal

Research Article
doi.org/10.1002/chem.202203325

Chemistry Europe
European Chemical Societies Publishing

www.chemeurj.org

The Buoy Effect: Surface Enrichment of a Pt Complex in IL Solution by Ligand Design

Daniel Hemmeter,[a] Daniel Kremitzl,[b] Peter S. Schulz,[b] Peter Wasserscheid,[b, c] Florian Maier,[a] and Hans-Peter Steinrück*[a]

Abstract: The targeted enrichment of a Pt complex with an ionic liquid (IL)-derived ligand system in IL solution is demonstrated by using angle-resolved X-ray photoelectron spectroscopy. When the ligand system is complemented with fluorinated side chains, the complex accumulates strongly at the IL/gas interface, while in an equivalent solution of a complex without these substituents no such effect could be observed. This buoy-like behavior induces strong population of the complex at the outermost molecular layer close to surface saturation, which was studied over a range from 5 to 30 $\%_{mol}$. The surface enrichment was found to be most efficient at the lowest concentration, which is particularly favorable for catalytic applications such as supported ionic-liquid-phase (SILP) catalysis.

Introduction

From the early stages of modern ionic-liquid (IL) research, their use as novel solvents in catalysis has been envisaged as a major field of application.[1] ILs show many advantageous properties such as extremely low volatility, non-flammability, high thermal stability and wide-ranging tunability, which led to their successful use for catalytic transformations, for example, in electrocatalysis,[2] as well as organo[3] and metal-catalyzed[4] reactions. One particularly powerful application is immobilization of organometallic catalysts in supported ionic liquid phase (SILP) by impregnating a high-surface area substrate with a thin IL film containing a dissolved catalyst.[5] The resulting hybrid materials combine the advantages of heterogenous and homogeneous catalysis: Macroscopically, SILP systems are powdery solids just like classical heterogeneous catalysts enabling efficient separation of product and catalyst. At the same time, the metal complex is kept in well-defined, uniform surrounding within the microscopic IL film granting high selectivities as in homogeneous catalysis. Based on the structural variety of support, IL, and metal complex, SILP systems offer various parameters for systematic optimization towards specific transformations. This was impressively shown by Werner et al. who adjusted the interplay of these components for an optimum performance in water–gas shift catalysis at extraordinarily mild conditions.[6]

The SILP concept makes effective use of the rather expensive IL solvent by employing only nanometer thick coatings with very high surface areas.[7] Consequently, the interfacial behavior of the catalyst solution is essential for the efficient use in catalytic processes. This is particularly true for the gas/IL interface, where reactants first enter the IL film from the gas phase and then have to diffuse towards the catalytically active species. After reaction, the formed products have to diffuse back out of the IL phase, where they get carried away by the surrounding gas stream. The dissolution process and the transport paths within the liquid phase can pose significant limitations to the performance of SILP catalysts, owing to the much slower diffusion rates of solutes in ILs than in conventional molecular solvents.[8] However, in contrast to a simplistic picture with homogeneous distribution of the solute in the IL film, the concentration at the gas/IL interface can greatly differ from the bulk.[9] Control over the driving forces for these interface phenomena would open up the possibility of tailoring the gas/IL interface towards surface enrichment of the dissolved organometallic complex. This would minimize transport barriers and therefore enhance the overall efficiency of the SILP process.

The gas/IL or vacuum/IL interface was studied with a variety of methods, for example, by sum-frequency generation (SFG),[10] X-ray reflectivity,[10a,11] Rutherford backscattering spectroscopy,[12] metastable ion spectroscopy (MIES),[13] reactive atom scattering detected by laser-induced fluorescence (RAS-LIF),[14] and mass spectrometry (MS) techniques,[12b,15] to only name but a few. One particularly powerful method to obtain detailed insights into the nature of the near-surface region of

[a] D. Hemmeter, Dr. F. Maier, Prof. Dr. H.-P. Steinrück
Lehrstuhl für Physikalische Chemie 2
Friedrich-Alexander-Universität Erlangen–Nürnberg
Egerlandstr. 3, 91058 Erlangen (Germany)
E-mail: hans-peter.steinrueck@fau.de

[b] D. Kremitzl, Dr. P. S. Schulz, Prof. Dr. P. Wasserscheid
Lehrstuhl für Chemische Reaktionstechnik
Friedrich-Alexander-Universität Erlangen–Nürnberg
Egerlandstr. 3, 91058 Erlangen (Germany)

[c] Prof. Dr. P. Wasserscheid
Forschungszentrum Jülich GmbH, Helmholtz-Institute Erlangen-Nürnberg for Renewable Energy (IEK-11),
Egerlandstr. 3, 91058 Erlangen, (Germany)

Supporting information for this article is available on the WWW under https://doi.org/10.1002/chem.202203325

Chemistry–A European Journal | Research Article doi.org/10.1002/chem.202203325 | Chemistry Europe European Chemical Societies Publishing

ILs is X-ray photoelectron spectroscopy (XPS).[1f,16] The binding energies of the investigated elements are very sensitive to the oxidation state, bonding conditions, and inter/intramolecular interactions. The information depth (ID) of XPS depends on the emission angle: When using Al K_α radiation, electron emission along the surface normal, that is, at 0°, yields an ID of 6–9 nm in organic materials, which typically gives information about the bulk composition of the sample.[17] At 80°, the ID decreases to 1.0–1.5 nm, and consequently the signals originate mainly from the topmost molecular layer of the sample. Thus, angle-resolved XPS (ARXPS) has been successfully applied to identify the preferential surface orientation of neat ILs,[18] and enrichment and depletion phenomena in IL mixtures and solutions.[9,16d,19]

Recently, we reported an ARXPS study on the formation and surface behavior of Pt^{2+} and Pd^{2+} complexes of the type $[MCl_2(\text{cation-CN})_2]^{2+}$ with ligand systems derived from nitrile-functionalized IL cations in IL solution.[20] These dissolved complexes were well suited for detailed XPS studies due to their a) very high solubilities ensuring strong signal intensities, b) well-separated signals for extracting detailed chemical information, and c) high stability towards X-radiation and ultra-high vacuum (UHV) conditions. For these solutions, our measurements revealed homogeneous distribution of the complexes in the IL, that is, no enrichment in the outermost surface layers.

Herein, we present a novel route for the targeted enrichment of metal complexes by chemical modification of the ligand system. For this, the nitrile-functionalized ionic ligands were functionalized with a fluorinated substituent at the imidazolium ring (Scheme 1). Fluorous side chains have shown to be highly surface-active in binary mixtures of imidazolium-based ILs.[19a,b,21] We now exploit the surface-affine character of fluorinated side chains by their incorporation into the ligand system in order to "pull" the catalytically active metal center towards the surface in a buoy-like fashion. Using ARXPS, we first confirm the strong surface-activity of the fluorinated substituents for the neat ligand system 1-(3-cyanopropyl)-3-(3,3,4,4,4-pentafluorobutyl)imidazolium hexafluorophosphate, $[C_3CNPFC_4Im][PF_6]$. Thereafter, we demonstrate that the prepared solutions of $[PtCl_2(C_3CNPFC_4Im)_2][PF_6]_2$ (**1**) in $[C_4C_1Im][PF_6]$ indeed show the targeted strong enrichment of the metal complexes at the IL/vacuum interface.

Results and Discussion

As first step, we characterized the interfacial behavior of the ligand system, the neat IL $[C_3CNPFC_4Im][PF_6]$, using ARXPS. Directly after synthesis, $[C_3CNPFC_4Im][PF_6]$ was obtained as a liquid and thus could be measured in the liquid state at room temperature (for details see experimental section). Selected spectra of the F 1s, N 1s and C 1s regions, at 0° (black, bulk-sensitive) and 80° (red, surface-sensitive) emission, are presented in Figure 1a (for the full set of spectra see Figure S1 in the Supporting Information). The two F 1s peaks at 688.8 and 686.8 eV are assigned to the fluorine atoms of the alkyl chain and the $[PF_6]^-$ anion, respectively. The two N 1s signals at 402.3 and 400.0 eV with 2:1 intensity ratio stem from the nitrogen atoms of the imidazolium ring and the nitrile functionality of the C_3CN substituent, respectively. The C 1s peaks at 293.7 and 291.4 eV are assigned to the CF_3 and CF_2 groups of the fluorinated side chain, respectively, and the broad peak at ~287 eV includes all other carbon atoms within the $[C_3CNPFC_4Im]^+$ cation. Based on previous studies,[19a,b] we assign this broad peak to two contributions, the C_{C2} peak due to the carbon atom bound to two nitrogen atoms within the aromatic ring, and the $C_{hetero'}$ peak due to the remaining carbon atoms. The corresponding deconvolution is depicted in Figure 1b, with the peak assignment shown in Scheme 1, and the fitting procedure detailed in the Supporting Information. The quantitative analysis of the bulk-sensitive 0° emission spectra (Table S1a) reveals overall excellent agreement with the expected stoichiometry of the IL apart from the larger than expected intensity of the F_{CFx}. The latter is due to the pronounced enrichment of the fluorinated substituent at the outermost

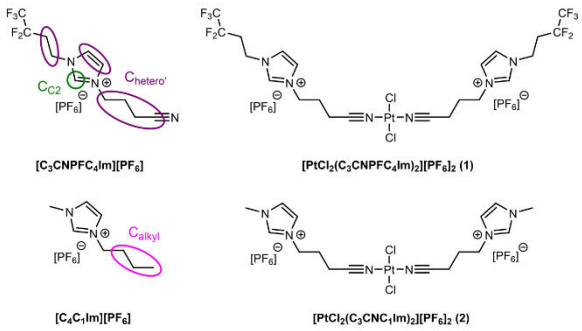

Scheme 1. Molecular structures of $[C_3CNPFC_4Im][PF_6]$, $[PtCl_2(C_3CNPFC_4Im)_2][PF_6]_2$ (**1**), $[C_4C_1Im][PF_6]$, and $[PtCl_2(C_3CNPFC_4Im)_2][PF_6]_2$ (**2**) with assignment of carbon species detected by XPS.

Chemistry–A European Journal
Research Article
doi.org/10.1002/chem.202203325
Chemistry Europe
European Chemical Societies Publishing

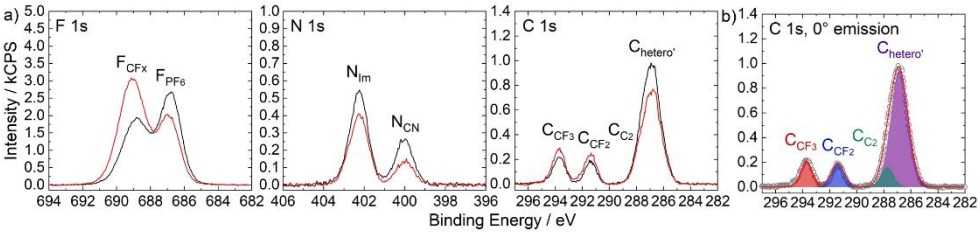

Figure 1. a) F 1s, N 1s, and C 1s spectra of neat $[C_3CNPFC_4Im][PF_6]$ in 0° (black) and 80° (red) emission and b) C 1s spectrum in 0° emission with applied deconvolution. The assignment of peaks to the molecular structure can be seen in Scheme 1. All spectra were recorded at room temperature.

surface layer (see below) that affects the 0° emission spectra as has been observed previously.[19b]

Comparing the 0° and 80° spectra depicted in Figure 1a provides information on the preferential orientation of the $[C_3CNPFC_4Im]^+$ cation at the surface. All signals specific for the fluorinated substituent, that is, F_{CFx}, C_{CF3} and C_{CF2}, exhibit a very strong enhancement at 80°, indicating the strong enrichment of the fluorinated substituents at the IL/vacuum interface also for this IL.[19b] Along with the very pronounced decrease of the N_{CN} signal at 80°, this suggests a perpendicular orientation of the $[C_3CNPFC_4Im]^+$ cation at the surface with the fluorinated substituents pointing towards the vacuum, while the CN functionalized side chain is directed towards the bulk. The similar decrease of the N_{Im} and F_{PF6} signals confirms that the positively charged imidazolium ring and the $[PF_6]^-$ anion are located at similar distances from the outer surface, as expected due to the strong electrostatic interactions.

To achieve the targeted surface enrichment, $[C_3CNPFC_4Im]^+$ was used as ligand system to yield $[PtCl_2(C_3CNPFC_4Im)_2][PF_6]_2$ (**1**). Compound **1** was prepared directly in $[C_4C_1Im][PF_6]$ (for details see experimental section) similar to a procedure reported previously.[20] To exemplify the buoy-effect, we also prepared an equivalent solution of $[PtCl_2(C_3CNC_1Im)_2][PF_6]_2$ (**2**), which does not contain fluorinated side chains.

In the following, we present the ARXPS data for a 5 $\%_{mol}$ solution of **1** in $[C_4C_1Im][PF_6]$. Figure 2a depicts the corresponding Pt 4f, F 1s, N 1s and C 1s spectra (for peak assignment, see Scheme 1; the full set of spectra is shown in Figure S2). The Pt 4f region shows the very intense spin-orbit-resolved signals of the Pt^{II} center. Similar to the neat ligand system in Figure 1a, the F 1s spectrum shows the two well-separated F_{CFx} and F_{PF6} signals; the latter now contains $[PF_6]^-$ anions from complex and solvent. This is also true for the N_{Im} signal. The small $N_{CNcoord}$ peak at 401.3 eV corresponds to the CN group coordinated to the metal center.[20] The absence of the signal from uncoordinated CN groups at ~400 eV (Figure 1) confirms the quantitative formation of **1** in $[C_4C_1Im][PF_6]$. The C 1s region shows the complex-specific C_{CF3} and C_{CF2} signals, and the broad peak at

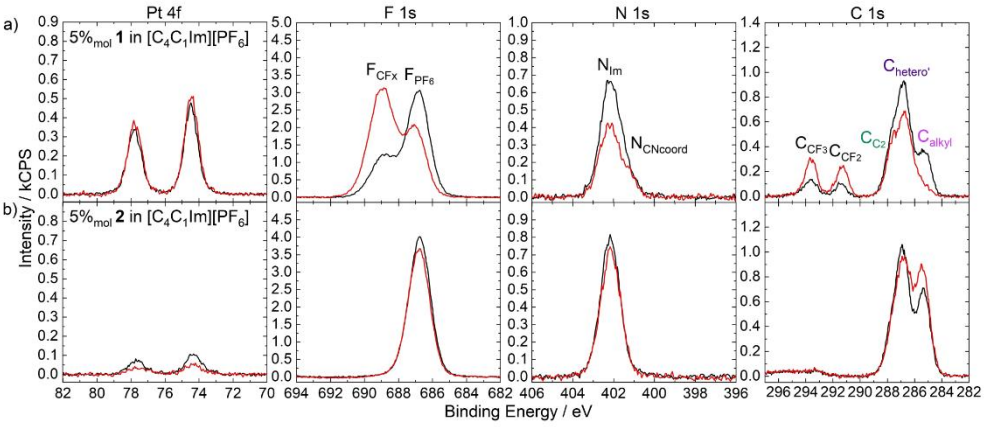

Figure 2. Pt 4f, F 1s, N 1s, and C 1s spectra of 5 $\%_{mol}$ solutions of a) **1** and b) **2** in $[C_4C_1Im][PF_6]$ in 0° (black) and 80° (red) emission. All spectra were recorded at room temperature.

Chemistry–A European Journal | Research Article doi.org/10.1002/chem.202203325 | Chemistry Europe European Chemical Societies Publishing

~287 eV. The latter includes contributions from ligand and solvent cations. Compared to the spectrum for the ligand system in Figure 1, this peak now additionally involves the C_{hetero} carbon atoms in the $[C_4C_1Im]^+$ cation. The additional peak at 285.2 eV, C_{alkyl}, corresponds to carbon atoms from the aliphatic substituent of $[C_4C_1Im][PF_6]$ solely bound to other carbon atoms.[19b]

The quantitative analysis of the 0° spectra in Table S1b, Figure 3a (Pt 4f and F 1s, •), and Figure S8 (all relevant core levels) shows for all complex-specific signals a much higher intensity than expected from the nominal composition of the solution. While the Pt 4f, Cl 2p and $N_{CNcoord}$ signals show a more than three times higher intensity, the F_{CFx} signal exhibits an almost fivefold intensity excess. At the same time, the solvent-specific C_{alkyl} signal shows less than half of the nominally expected intensity. We attribute this behavior to particularly pronounced enrichment of the solute at the IL/vacuum interface, which strikingly affects the more bulk-sensitive 0° emission spectra. This strong deviation from homogeneous distribution of the solute within the IL also accounts for the intensity deficit of the N_{Im} and F_{PF6} signals: With a strong surface enrichment of the large Pt-containing cation, the number density of solvent imidazolium rings and $[PF_6]^-$ ions in the near surface region is lower than expected from a homogeneous solution. This effect

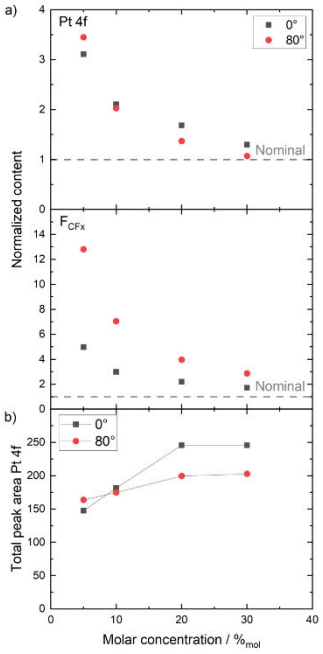

Figure 3. a) Normalized contents derived from Pt 4f and F_{CFx} signals and b) total peak areas of the Pt 4f signals in 0° (•) and 80° emission (•) over a concentration range from 5 to 30 $\%_{mol}$ of **1** in $[C_4C_1Im][PF_6]$.

is not observed for the $C_{hetero'}$ signal because several atoms from the surface-enriched complex contribute to this peak.

The comparison of the 0° and 80° spectra provides more detailed information on the surface composition of the solution. All complex-specific signals increase at 80°, with the increase being most pronounced for the F_{CFX}, C_{CF3} and C_{CF2} signals of the fluorous moieties of the ligand system. Both the Pt and Cl (Table S1b) signals only show a very weak increase. These observations are assigned to a preferential orientation of the complex at the surface with the fluorinated substituents pointing towards the vacuum – in a buoy-like fashion – whereas the metal center is located further away from the surface. The signals of all other species are found declined at 80°. The F_{PF6} and N_{Im} signals decrease concomitantly, as has been observed for the neat ligand system. The small complex-derived $N_{CNcoord}$ signal remains mostly unchanged, due to the superposition with the strongly decreasing N_{Im} signal. The $C_{hetero'}$ signal also decreases, due to a strong surface depletion of the solvent $[C_4C_1Im]^+$ cation. This decrease is even stronger for the solely solvent-specific C_{alkyl} signal, which underlines the extraordinary surface enrichment of the solute – and the associated depletion of the solvent from the IL/vacuum interface.

To verify that the buoy effect is indeed due to the fluorinated ligand system, we next present ARXP spectra of an equivalent solution of **2**, that is, the complex without the fluorinated groups in $[C_4C_1Im][PF_6]$ in Figure 2b (full set of spectra in Figure S3). By comparing these spectra to those of **1** in Figure 2a, it immediately becomes evident that for the non-fluorous solute no enrichment is observed. The Pt 4f signals recorded for the solution of **2** show a drastically lower intensity. The observed intensities at 0° are in good accordance with the nominal composition of the solution (Table S1c); the only exception is the small $N_{CNcoord}$ signal, which could not be resolved due to the low nominal concentration and the absence of surface enrichment. The comparison of the spectra at 0° and 80° in Figure 2b reveals a strong decline of the Pt 4f signal, enhancement of the solvent-specific C_{alkyl} signal, and a slight decrease of the F 1s and N 1s signals at 80°. These observations are typical for a preferential surface orientation of 1,3-alkylimidazolium cations with the aliphatic substituents pointing towards the vacuum.[1f,16a,b] We thus conclude that the surface is terminated by the alkyl chains from the solvent cation, while the metal complex is homogeneously distributed below and thus shows no surface-affinity. All in all, these findings are in stark contrast to results observed from solution of **1** and highlight the strong effect of the fluorinated substituents triggering enrichment of the metal complex at the IL/vacuum interface in a buoy-like behavior.

As the final step, we varied the concentration of **1** dissolved in $[C_4C_1Im][PF_6]$ from 5 to 30 $\%_{mol}$ (for the full sets of spectra, see Figures S2 and S4–S6). Figure 3a depicts the normalized contents, that is, the experimental divided by the nominal value (cf. Table S1b and S1d-f) for the Pt 4f and F_{CFX} signals in 0° (black squares) and 80° (red dots). The dashed lines at a value of 1 represent the nominal stoichiometry implying that all ions exhibit random distribution, orientation and configuration within the near-surface region. Inspection of Figure 3a clearly

Chemistry–A European Journal | Research Article doi.org/10.1002/chem.202203325 | Chemistry Europe European Chemical Societies Publishing

reveals that at both emission angles the normalized Pt and F_{CFx} contents drastically decrease upon increasing the molar concentration of the metal complex. This behavior indicates that the surface enrichment of the complex (relative to the bulk content) is most pronounced at low concentrations. Additional information can be derived from the absolute intensities of the Pt 4f signals at 0° (black squares) and 80° (red dots) in Figure 3b. Upon raising the molar concentration, the total intensity of the Pt 4f signal at 80° shows a weak increase, reaching a plateau at 20 $\%_{mol.}$ This observation suggests that already at low concentration, the topmost molecular layer is nearly saturated with the complex; thereby, the surface-active fluorinated chains of the ligand system terminate the surface while the Pt center is located beneath, as pointed out above. The Pt 4f signal at 0° shows a more pronounced increase by nearly a factor of 2, which is due to the fact that at this angle the signals also contain higher contributions from the bulk, where the Pt content increases according to the nominal complex concentrations. Hence, in a simplistic picture, our ARXPS data shows that the buoy-effect induces strong population of the surface with the complex, whereas the lower layers presumably have the nominal concentration. Notably, upon varying the concentration also conformational changes of the complex could contribute to the observed behavior.

Conclusions

We have demonstrated a drastic enrichment of complex **1** at the IL/vacuum interface by functionalizing an IL-derived ligand system with fluorinated substituents. The neat ligand system $[C_3CNPFC_4Im][PF_6]$ shows a pronounced preferential orientation of the $[C_3CNPFC_4Im]^+$ cations at the surface, with the fluorinated side chains pointing towards the vacuum whereas the nitrile-functionalized substituents are directed towards the bulk of the sample. This surface affinity of the fluorous groups is then used to induce strong accumulation of **1** at the IL/vacuum interface in $[C_4C_1Im][PF_6]$. In contrast, complex **2**, without fluorinated side chains, did not exhibit any surface enrichment in $[C_4C_1Im][PF_6]$; this emphasizes the buoy-like behavior of the surface-active substituents. In addition, the enrichment of **1** was studied over a concentration range of 5–30 $\%_{mol}$. The strongest enrichment relative to the bulk concentration was observed at lowest concentration of the complex; this is particularly beneficial for catalytic applications. In principle, the buoy-effect could be employed for surface enrichment of any given organometallic catalyst by simply introducing suitable fluorinated substituents into the ligand system. We are convinced that the accumulation of the catalyst at the IL/gas interface could be extremely beneficial for the optimization of catalytic systems with large interface areas between catalyst/IL solution and surrounding reactant/product phase, such as in SILP or in liquid–liquid biphasic catalysis. The effect of this type of surface enrichment in such catalytic systems is the subject of current investigations in our groups.

Experimental Section

Materials and synthesis: *Cis*-bis(acetonitrile)dichloroplatinum(II) (*cis*-$[PtCl_2(CH_3CN)_2]$, 98% purity) was purchased from Sigma–Aldrich. 1-Butyl-3-methylimidazolium hexafluorophosphate ($[C_4C_1Im][PF_6]$, purity 99.5%) was purchased from Iolitec. The chemicals were used as delivered.

3-Cyanopropyl-imidazole (C_3CNIm) was synthesized in the style of Cai et al.,[22] albeit with minor changes. 1-(3-Cyanopropyl)-3-methylimidazolium hexafluorophosphate ($[C_3CNC_1Im][PF_6]$) has already been synthesized in literature,[23] again using a slightly different procedure. The synthesis of the ligand IL 1-(3-cyanopropyl)-3-(3,3,4,4,4-pentafluorobutyl-imidazolium hexafluorophosphate ($[C_3CNPFC_4Im][PF_6]$) was developed in this work. Generally, metathesis reactions and recrystallizations were tuned towards purity in our work tolerating product losses. Furthermore, completely grease-free labware was used for the synthesis of the surface-pure ILs in order to avoid surface-active contaminations found in previous studies.[24]

Synthesis C_3CNIm: Sodium hydroxide (1.99 g, 49.8 mmol) and imidazole (3.39 g, 49.8 mmol) were combined and stirred while heating to 100 °C until a homogeneous solution was obtained. The formed water was removed under vacuum at 100 °C over night. The resulting chunk was ground to a fine powder under constant argon flow and further dried for another 3 d. Using Schlenk techniques, the powder was dispersed in THF (25 mL) and 4-chlorobutyronitrile (5.16 g, 49.8 mmol) dissolved in THF (5 mL) was dropwise added while stirring. After 24 h, the mixture was slowly heated to reflux and stirred for another 2 d under inert atmosphere. The solvent was removed, the residue picked up in DCM (40 mL), and filtered. The filter residue was washed with DCM (20 mL) and the collected solution evaporated and dried under vacuum to give a brown oil (6.24 g, 46.2 mmol, 92.8%). MW: 135.17; ^{1}H NMR (399.60 MHz, [D$_6$]DMSO, 25 °C): $\delta = 7.63$ (s, 1H, N-*CH*-N), 7.19 (s, 1H, N-*CH*-CH), 6.90 (s, 1H, CH-*CH*-N), 4.03 (t, $^3J_{H\text{-}H} = 7.1$ Hz, 2H, N-CH_2-CH_2), 2.44 (t, $^3J_{H\text{-}H} = 7.3$ Hz, 2H, CH_2-CH_2-CN), 2.03 ppm (tt, $^3J_{H\text{-}H} = 7.1$ Hz, 2H, CH_2-CH_2-CH_2); $^{13}C\{^1H\}$ NMR (100.48 MHz, [D$_6$]DMSO, 25 °C): $\delta = 137.3$ (s, N-*CH*–N), 128.7 (s, N-CH-CH), 119.7 (s, CH_2-CN), 119.2 (s, CH-*CH*–N), 44.7 (s, N-CH_2-CH_2), 26.3 (s, CH_2-CH_2-CH_2), 13.7 ppm (s, CH_2-CH_2-CN)

Synthesis $[C_3CNPFC_4Im][PF_6]$: C_3CNIm (6.24 g, 46.2 mmol) was dissolved in acetonitrile (30 mL) and 1,1,1,2,2-pentafluoro-4-iodobutane (13.10 g, 47.8 mmol, 1.03 equiv.) dissolved in acetonitrile (30 mL), added dropwise to the stirred solution. The mixture was heated to reflux for 2 d, and the solvent subsequently removed. The resulting highly viscous oil was dissolved in water (150 mL) and under vigorous stirring, potassium hexafluorophosphate (6.84 g, 37.2 mmol, 0.80 equiv.) dissolved in water (70 mL) was slowly added. The mixture was further stirred at room temperature for 30 min and then cooled to 0 °C. The supernatant was decanted and the solid rinsed with ethanol and dissolved in warm ethanol (100 mL). The hot solution was filtered through a syringe filter, concentrated to 50 mL and cooled to 0 °C. After decanting and rinsing, the precipitate was further purified two times by dissolution in boiling ethanol (50 mL each), cooling to 0 °C, decanting the supernatant, and rinsing the precipitate with ethanol. The pure product was dried under vacuum to give a light brown, highly viscous oil. Yield: 9.83 g, 23.0 mmol, 49.8% (based on 4-imidazol-1-ylbutyronitrile); the product solidified after roughly 6 months, without any detectable changes in NMR or XPS (molten and cooled to room temperature under UHV, the sample remained liquid under measuring conditions), melting point: 62 ± 1 °C, MW: 427.20; ^{1}H NMR (399.60 MHz, [D4]MeOH, 25 °C): $\delta = 9.03$ (s, 1H, N-*CH*-N), 7.73 (s, 1H, N-*CH*-CH), 7.67 (s, 1H, CH-*CH*-N), 4.59 (t, $^3J_{H\text{-}H} = 7.3$ Hz, 2H, (N-CH_2-CH_2)$_{PF\text{-}side\text{-}chain}$), 4.34 (t, $^3J_{H\text{-}H} = 7.1$ Hz, 2H, (N-CH_2-CH_2)$_{CN\text{-}side\text{-}chain}$), 2.89 (tt, $^3J_{H\text{-}F} = 18.1$ Hz, $^3J_{H\text{-}H} = 7.3$ Hz, 2H, CH_2-CH_2-CF_2), 2.56 (t, $^3J_{H\text{-}H} = 7.3$ Hz, 2H, CH_2-CH_2-CN), 2.26 ppm (tt, $^3J_{H\text{-}H} = 7.2$ Hz, 2H, CH_2-CH_2-CH_2); $^{13}C\{^1H\}$ NMR (100.48 MHz, [D$_6$]DMSO, 25 °C): $\delta = 137.3$

Chemistry–A European Journal | Research Article doi.org/10.1002/chem.202203325 | Chemistry Europe European Chemical Societies Publishing

(s, N-CH–N), 123.1 (s, N-CH-CH), 122.7 (s, CH-CH–N), 119.7 (s, CH_2-CN), 118.7 (qt, $^1J_{C\text{-}F}$ = 285.0 Hz, $^2J_{C\text{-}F}$ = 35.7 Hz, CH_2-CF_2-CF_3), 115.2 (tq, $^1J_{C\text{-}F}$ = 253.2 Hz, $^2J_{C\text{-}F}$ = 38.1 Hz, CH_2-CF_2-CF_3), 48.1 (s, $(N\text{-}CH_2\text{-}CH_2)_{PF\text{-}side\text{-}chain}$), 41.6 (s, $(N\text{-}CH_2\text{-}CH_2)_{CN\text{-}side\text{-}chain}$), 30.0 (t, $^2J_{C\text{-}F}$ = 20.7 Hz, CH_2-CH_2-CF_2), 25.4 (s, CH_2-CH_2-CH_2), 13.6 ppm (s, CH_2-CH_2-CN); ^{19}F NMR (376.00 MHz, CD_3OD, 25 °C): δ = −73.9 (d, $^1J_{F\text{-}P}$ = 707.8 Hz, *PF6*-), −87.2 (s, CF_2-CF_3), −119.3 ppm (t, $^3J_{F\text{-}H}$ = 18.4 Hz, CH_2-CF_2-CF_3); ^{31}P NMR (161.76 MHz, CD_3OD, 25 °C): δ = −144.0 ppm (sept, $^1J_{P\text{-}F}$ = 708.4 Hz, *PF6*).

Synthesis [C_3CNC_1Im][PF_6]: At room temperature, 4-chlorobutyronitrile (7.07 g, 68.3 mmol, 1.02 equiv.) dissolved in acetonitrile (25 mL) were added to a solution of 1-methylimidazole (5.50 g, 67.0 mmol) in acetonitrile (25 mL) over several minutes. After heating the mixture to reflux for 2 d the solvent was removed and the residue dried under vacuum. The solid was dissolved in water (100 mL). Under vigorous stirring, a solution of potassium hexafluorophosphate (11.9 g, 64.9 mmol, 0.95 equiv.) in water (180 mL) was slowly added and the formed suspension further stirred for 30 min. The solution was evaporated to 40 mL under vacuum, and the precipitate was finely ground in the water. The mixture was filtered and subsequently washed with water (3 x 20 mL) and ice cold ethanol (40 mL). The powder was recrystallized from water at 60 °C, filtered, subsequently washed with water (60 mL) and ice cold ethanol (30 mL), and dried under vacuum to give white crystals. Yield: 14.3 g, 48.4 mmol, 72.2 % (based on 1-methylimidazole); MW: 295.16; ^{1}H NMR (399.60 MHz, [D_6]DMSO, 25 °C): δ = 9.11 (s, 1H, N-*CH*-N), 7.78 (s, 1H, N-*CH*-CH), 7.71 (s, 1H, CH-*CH*-N), 4.23 (t, $^3J_{H\text{-}H}$ = 6.9 Hz, 2H, N-CH_2-CH_2), 3.84 (s, 3H, CH_3-N), 2.57 (t, $^3J_{H\text{-}H}$ = 7.1 Hz, 2H, CH_2-CH_2-CN), 2.13 ppm (tt, $^3J_{H\text{-}H}$ = 7.1 Hz, 2H, CH_2-CH_2-CH_2); $^{13}C\{^1H\}$ NMR (100.48 MHz, [D_6]DMSO, 25 °C): δ = 136.9 (s, N-CH–N), 123.8 (s, N-CH-CH), 122.3 (s, CH-CH–N), 119.7 (s, CH_2-CN), 47.6 (s, N-CH_2-CH_2), 35.8 (s, CH_3-N), 25.2 (s, CH_2-CH_2-CH_2), 13.5 (s, CH_2-CH_2-CN) ppm; ^{19}F NMR (376.00 MHz, [D_6]DMSO, 25 °C): δ = −70.0 (d, $^1J_{F\text{-}P}$ = 711.5 Hz, *PF6*$^-$) ppm; ^{31}P NMR (161.76 MHz, [D_6]DMSO, 25 °C): δ = −143.6 ppm (sept, $^1J_{P\text{-}F}$ = 711.2 Hz, *PF6*$^-$).

Sample preparation:

Samples were prepared with modified procedures from ref. [20].

Solutions of 1 in [C_4C_1Im][PF_6]: Solutions of **1** with different concentrations were prepared following the same general procedure: *Cis*-[$PtCl_2(CH_3CN)_2$] was suspended in [C_3CNPFC_4Im][PF_6] under ambient conditions followed by stirring in vacuo at 100 °C for 1 h. Upon reaction, the mixtures gradually turned more viscous and eventually solidified. [C_4C_1Im][PF_6] was added under ambient conditions. The mixtures were further stirred in vacuo at 100 °C until no residuals of the precursor were visible (for individual reaction times see Table S2) to yield clear, yellow to brownish solutions.

The weighed proportions for solutions of **1** in [C_4C_1Im][PF_6] are shown in Table S2.

5 %$_{mol}$ solution of 2 in [C_4C_1Im][PF_6]: [C_3CNC_1Im][PF_6] (37.6 mg, 0.127 mmol) was dissolved in [C_4C_1Im][PF_6] (345 mg, 1.21 mmol). *Cis*-[$PtCl_2(CH_3CN)_2$] (22.5 mg, 0.063 mmol) was added to this solution. The resulting suspension was stirred in vacuo for 1 h at 105 °C to yield a clear, yellow solution.

The prepared solutions were applied onto the setup-compatible molybdenum sample holders (for details, see ref. [17]) under ambient conditions. The loaded sample holders were immediately introduced into the load-lock of the UHV system, where the samples were allowed to degas for several hours. Before conducting XPS measurements, the samples were heated to at least 40 °C for 30 min. under UHV conditions. Sample temperatures were measured with a type K thermocouple spot-welded to the molybdenum sample holder.

ARXPS measurements and data evaluation: The setup for our ARXPS measurements is detailed in ref. [17]. Measurement parameters were reported previously.[20] All XP spectra were normalized to the overall intensity detected from the 0° emission region scans of the 5 %$_{mol}$ solution of **1** in [C_4C_1Im][PF_6]. Procedures for peak fitting of the recorded spectra are outlined in the Supporting Information.

Acknowledgements

Funded by the Deutsche Forschungsgemeinschaft (DFG, German Research Foundation) Project-ID 431791331–SFB 1452. D.H. thanks the Stiftung Stipendien-Fonds of the German Chemical Industry Association (Verband der Chemischen Industrie, VCI) for a Kekulé fellowship. Open Access funding enabled and organized by Projekt DEAL.

Conflict of Interest

The authors declare no conflict of interest.

Data Availability Statement

The data that support the findings of this study are available from the corresponding author upon reasonable request.

Keywords: catalysis · ionic liquids · surface analysis · surface enrichment · X-ray photoelectron spectroscopy (XPS)

[1] a) T. Welton, *Chem. Rev.* **1999**, *99*, 2071–2084; b) P. Wasserscheid, W. Keim, *Angew. Chem. Int. Ed.* **2000**, *39*, 3772–3789; *Angew. Chem.* **2000**, *112*, 3926–3945; c) C. M. Gordon, *Appl. Catal. A* **2001**, *222*, 101–117; d) H. Olivier-Bourbigou, L. Magna, *J. Mol. Catal. A* **2002**, *182–183*, 419–437; e) T. Welton, *Biophys. Rev. Lett.* **2018**, *10*, 691–706; f) H.-P. Steinrück, P. Wasserscheid, *Catal. Lett.* **2015**, *145*, 380–397.

[2] a) A. Ejigu, D. A. Walsh in *Electrochemistry in Ionic Liquids: Volume 2: Applications* (Ed.: A. A. J. Torriero), Springer International, Heidelberg, **2015**, pp. 483–506; b) G.-R. Zhang, B. J. M. Etzold, *J. Energy Chem.* **2016**, *25*, 199–207.

[3] a) J. P. Hallett, T. Welton, *Chem. Rev.* **2011**, *111*, 3508–3576; b) Š. Toma, M. Mečiarová, R. Šebesta, *Eur. J. Org. Chem.* **2009**, *2009*, 321–327; c) D. Krištofíková, V. Modrocká, M. Mečiarová, R. Šebesta, *ChemSusChem* **2020**, *13*, 2828–2858.

[4] a) T. Welton, *Coord. Chem. Rev.* **2004**, *248*, 2459–2477; b) J. D. Scholten, B. C. Leal, J. Dupont, *ACS Catal.* **2012**, *2*, 184–200; c) S. Doherty in *Catalysis in Ionic Liquids: From Catalyst Synthesis to Application* (Eds.: C. Hardacre, V. Parvulescu), The Royal Society of Chemistry, Cambridge, **2014**, pp. 44–308.

[5] A. Riisager, R. Fehrmann, M. Haumann, P. Wasserscheid, *Eur. J. Inorg. Chem.* **2006**, *2006*, 695–706.

[6] S. Werner, N. Szesni, M. Kaiser, R. W. Fischer, M. Haumann, P. Wasserscheid, *ChemCatChem* **2010**, *2*, 1399–1402.

[7] M. Haumann, A. Schönweiz, H. Breitzke, G. Buntkowsky, S. Werner, N. Szesni, *Chem. Eng. Technol.* **2012**, *35*, 1421–1426.

[8] a) D. Morgan, L. Ferguson, P. Scovazzo, *Ind. Eng. Chem. Res.* **2005**, *44*, 4815–4823; b) D. Camper, C. Becker, C. Koval, R. Noble, *Ind. Eng. Chem. Res.* **2006**, *45*, 445–450; c) M. He, S. Peng, X. Liu, P. Pan, Y. He, *J. Chem. Thermodyn.* **2017**, *112*, 43–51.

Chemistry–A European Journal | Research Article doi.org/10.1002/chem.202203325 | Chemistry Europe European Chemical Societies Publishing

[9] a) F. Maier, J. M. Gottfried, J. Rossa, D. Gerhard, P. S. Schulz, W. Schwieger, P. Wasserscheid, H.-P. Steinrück, *Angew. Chem. Int. Ed.* **2006**, *45*, 7778–7780; *Angew. Chem.* **2006**, *118*, 7942–7944; b) C. Kolbeck, N. Paape, T. Cremer, P. S. Schulz, F. Maier, H.-P. Steinrück, P. Wasserscheid, *Chem. Eur. J.* **2010**, *16*, 12083–12087; c) C. Kolbeck, N. Taccardi, N. Paape, P. S. Schulz, P. Wasserscheid, H.-P. Steinrück, F. Maier, *J. Mol. Liq.* **2014**, *192*, 103–113; d) E. J. Smoll, X. Chen, L. M. Hall, L. D'Andrea, J. M. Slattery, T. K. Minton, *J. Phys. Chem. C* **2020**, *124*, 382–397.

[10] a) Y. Jeon, J. Sung, W. Bu, D. Vaknin, Y. Ouchi, D. Kim, *J. Phys. Chem. C* **2008**, *112*, 19649–19654; b) C. Peñalber-Johnstone, G. Adamová, N. V. Plechkova, M. Bahrami, T. Ghaed-Sharaf, M. H. Ghatee, K. R. Seddon, S. Baldelli, *J. Chem. Phys.* **2018**, *148*, 193841; c) F. Huo, J. Ding, J. Tong, H. He, *Mol. Simul.* **2022**, *48*, 844–854.

[11] a) E. Sloutskin, B. M. Ocko, L. Tamam, I. Kuzmenko, T. Gog, M. Deutsch, *J. Am. Chem. Soc.* **2005**, *127*, 7796–7804; b) F. Nemoto, S.-y. Nakamura, H. Abe, *J. Mol. Liq.* **2021**, *337*, 116381.

[12] a) K. Nakajima, A. Ohno, M. Suzuki, K. Kimura, *Langmuir* **2008**, *24*, 4482–4484; b) K. Nakajima, M. Miyashita, M. Suzuki, K. Kimura, *J. Chem. Phys.* **2013**, *139*, 224701; c) H. Hashimoto, A. Ohno, K. Nakajima, M. Suzuki, H. Tsuji, K. Kimura, *Surf. Sci.* **2010**, *604*, 464–469; d) K. Nakajima, M. Lísal, K. Kimura in *Surface and Interface Science* (Ed.: K. Wandelt), Wiley-VCH, Weinheim, **2020**, pp. 351–389.

[13] a) O. Höfft, S. Bahr, M. Himmerlich, S. Krischok, J. A. Schaefer, V. Kempter, *Langmuir* **2006**, *22*, 7120–7123; b) S. Krischok, M. Eremtchenko, M. Himmerlich, P. Lorenz, J. Uhlig, A. Neumann, R. Öttking, W. J. D. Beenken, O. Höfft, S. Bahr, V. Kempter, J. A. Schaefer, *J. Phys. Chem. B* **2007**, *111*, 4801–4806; c) S. Krischok, R. Öttking, W. J. D. Beenken, M. Himmerlich, P. Lorenz, O. Höfft, S. Bahr, V. Kempter, J. A. Schaefer, *Z. Phys. Chem.* **2006**, *220*, 1407–1416; d) A. Ulbrich, M. Reinmöller, W. J. D. Beenken, S. Krischok, *ChemPhysChem* **2012**, *13*, 1718–1724.

[14] S. M. Purcell, P. D. Lane, L. D'Andrea, N. S. Elstone, D. W. Bruce, J. M. Slattery, E. J. Smoll, Jr., S. J. Greaves, M. L. Costen, T. K. Minton, K. G. McKendrick, *J. Phys. Chem. B* **2022**, *126*, 1962–1979.

[15] a) K. Bomhardt, P. Schneider, T. Glaser, M. Dürr, *J. Am. Soc. Mass Spectrom.* **2022**, *33*, 974–980; b) J. Günster, O. Höfft, S. Krischok, R. Souda, *Surf. Sci.* **2008**, *602*, 3403–3407.

[16] a) H.-P. Steinrück, J. Libuda, P. Wasserscheid, T. Cremer, C. Kolbeck, M. Laurin, F. Maier, M. Sobota, P. S. Schulz, M. Stark, *Adv. Mater.* **2011**, *23*, 2571–2587; b) H.-P. Steinrück, *Phys. Chem. Chem. Phys.* **2012**, *14*, 5010–5029; c) Y. Khalifa, A. Broderick, J. T. Newberg, *J. Phys. Condens. Matter* **2018**, *30*, 325001; d) Y. Song, F. Huo, Y. Jiang, S. Zhang, S. Chen, *ChemPhysChem* **2018**, *19*, 2741–2750; e) A. Ulbrich, M. Reinmöller, W. J. D. Beenken, S. Krischok, *J. Mol. Liq.* **2014**, *192*, 77–86; f) K. R. J. Lovelock, I. J. Villar-Garcia, F. Maier, H.-P. Steinrück, P. Licence, *Chem. Rev.* **2010**, *110*, 5158–5190; g) A. Dimitrova, M. Walle, M. Himmerlich, S. Krischok, *J. Mol. Liq.* **2017**, *226*, 78–84; h) T. Kurisaki, D. Tanaka, Y. Inoue, H. Wakita, B. Minofar, S. Fukuda, S.-i. Ishiguro, Y. Umebayashi, *J. Phys. Chem. B* **2012**, *116*, 10870–10875.

[17] I. Niedermaier, C. Kolbeck, H.-P. Steinrück, F. Maier, *Rev. Sci. Instrum.* **2016**, *87*, 045105.

[18] a) C. Kolbeck, I. Niedermaier, A. Deyko, K. R. J. Lovelock, N. Taccardi, W. Wei, P. Wasserscheid, F. Maier, H.-P. Steinrück, *Chem. Eur. J.* **2014**, *20*, 3954–3965; b) K. R. J. Lovelock, C. Kolbeck, T. Cremer, N. Paape, P. S. Schulz, P. Wasserscheid, F. Maier, H. P. Steinrück, *J. Phys. Chem. B* **2009**, *113*, 2854–2864; c) N. Calisi, S. Martinuzzi, A. Giaccherini, C. S. Pomelli, L. Guazzelli, S. Caporali, *J. Electron Spectrosc. Relat. Phenom.* **2021**, *247*, 147034; d) V. Lockett, R. Sedev, C. Bassell, J. Ralston, *Phys. Chem. Chem. Phys.* **2008**, *10*, 1330–1335; e) V. Lockett, R. Sedev, S. Harmer, J. Ralston, M. Horne, T. Rodopoulos, *Phys. Chem. Chem. Phys.* **2010**, *12*, 13816–13827; f) R. K. Blundell, A. E. Delorme, E. F. Smith, P. Licence, *Phys. Chem. Chem. Phys.* **2016**, *18*, 6122–6131; g) S. Men, B. B. Hurisso, K. R. J. Lovelock, P. Licence, *Phys. Chem. Chem. Phys.* **2012**, *14*, 5229–5238.

[19] a) B. S. J. Heller, U. Paap, F. Maier, H.-P. Steinrück, *J. Mol. Liq.* **2020**, *305*, 112783; b) B. S. J. Heller, M. Lexow, F. Greco, S. Shin, G. Partl, F. Maier, H.-P. Steinrück, *Chem. Eur. J.* **2020**, *26*, 1117–1126; c) B. S. J. Heller, C. Kolbeck, I. Niedermaier, S. Dommer, J. Schatz, P. Hunt, F. Maier, H.-P. Steinrück, *ChemPhysChem* **2018**, *19*, 1733–1745; d) S. Caporali, M. Pedio, C. Chiappe, C. S. Pomelli, R. G. Acres, U. Bardi, *Surf. Sci.* **2016**, *648*, 360–365.

[20] D. Hemmeter, U. Paap, N. Taccardi, J. Mehler, P. Schulz, P. Wasserscheid, F. Maier, H.-P. Steinrück, *ChemPhysChem* **2022**, *23*, e202200391.

[21] T. M. Koller, F. D. Lenahan, P. S. Schmidt, T. Klein, J. Mehler, F. Maier, M. H. Rausch, P. Wasserscheid, H.-P. Steinrück, A. P. Fröba, *Int. J. Thermophys.* **2020**, *41*, 144.

[22] X. Cai, Q. Wang, Y. Liu, J. Xie, Z. Long, Y. Zhou, J. Wang, *ACS Sustainable Chem. Eng.* **2016**, *4*, 4986–4996.

[23] Q. Zhang, Z. Li, J. Zhang, S. Zhang, L. Zhu, J. Yang, X. Zhang, Y. Deng, *J. Phys. Chem. B* **2007**, *111*, 2864–2872.

[24] J. M. Gottfried, F. Maier, J. Rossa, D. Gerhard, P. S. Schulz, P. Wasserscheid, H.-P. Steinrück, *Z. Phys. Chem.* **2006**, *220*, 1439–1453.

Manuscript received: October 26, 2022
Accepted manuscript online: November 29, 2022
Version of record online: December 21, 2022

Chemistry–A European Journal

Supporting Information

The Buoy Effect: Surface Enrichment of a Pt Complex in IL Solution by Ligand Design

Daniel Hemmeter, Daniel Kremitzl, Peter S. Schulz, Peter Wasserscheid, Florian Maier, and Hans-Peter Steinrück*

The supporting information presents wide scans and region spectra recorded for neat $[C_3CNPFC_4Im][PF_6]$ (*figure S1*), mixtures of $[PtCl_2(C_3CNPFC_4Im)_2][PF_6]_2$ (**1**) in $[C_4C_1Im][PF_6]$ with $5\%_{mol}$, $10\%_{mol}$, $20\%_{mol}$ and $30\%_{mol}$ concentration of the complex (*figures S2* and *S4-S6*) and the mixture of $[PtCl_2(C_3CNC_1Im)_2][PF_6]_2$ (**2**) in $[C_4C_1Im][PF_6]$ with a concentration of $5\%_{mol}$ (*figure S3*). Apart from all relevant regions of ILs and complexes, Si 2p spectra are depicted to confirm absence of common surface-active contaminations observed in previous studies[1]. In addition, for all mixtures of **1** in $[C_4C_1Im][PF_6]$ studied, an overview of the most important spectra on top of each other (*figure S7*) and the derived normalized contents as a function of the concentration (*figure S8*) is given. Furthermore, the quantitative analysis of all sets of XP spectra (*table S1*) is shown. Finally, the NMR spectra of $[C_3CNPFC_4Im][PF_6]$ (*figures S9-S26*) and the weighed proportions for preparation of the solutions (*table S2*) are presented.

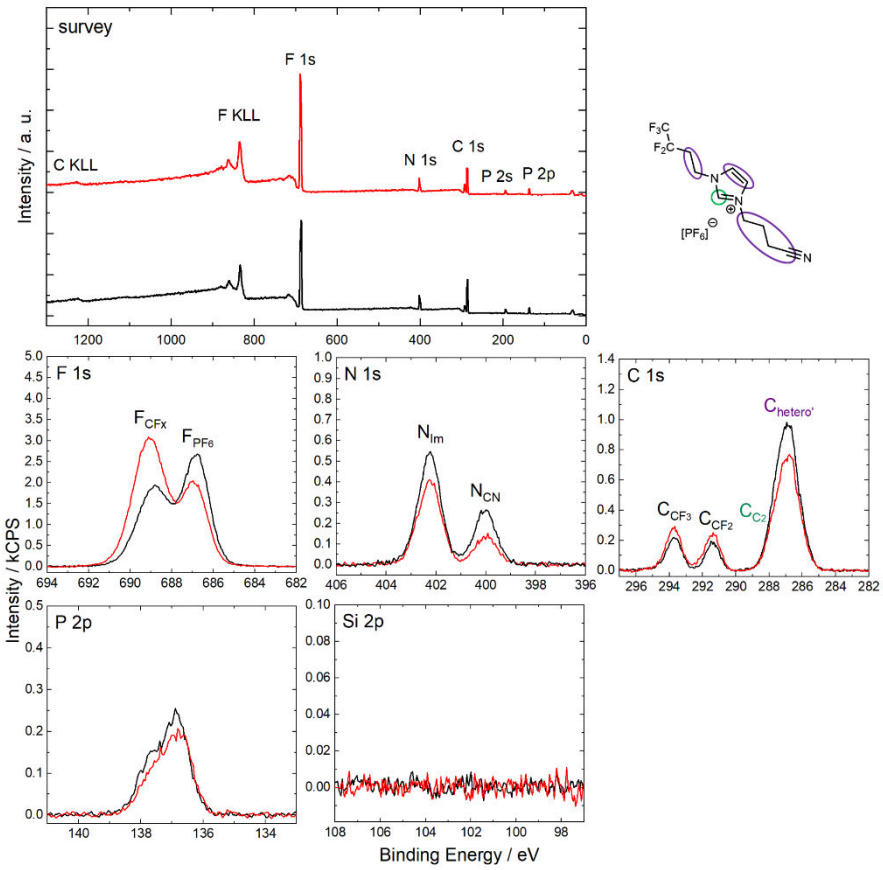

Figure S1: Survey, F 1s, N 1s, C 1s, P 2p and Si 2p XP spectra of neat [C_3CNPFC_4Im][PF_6] in 0° (black) and 80° (red) emission recorded at room temperature with assignment of peaks to the molecular structure.

Peak fitting: Area of C_{CF3} was set equal to C_{CF2} owing to superposition of C_{CF3} with shake up satellite of imidazolium ring.[2] Atomic sensitivity factor (ASF)-corrected area of C_{C2} was constraint to half of the ASF-corrected area of the N_{Im} signal. Binding energy difference between $C_{hetero'}$ and C_{C2} was set to 0.9 eV.[2]

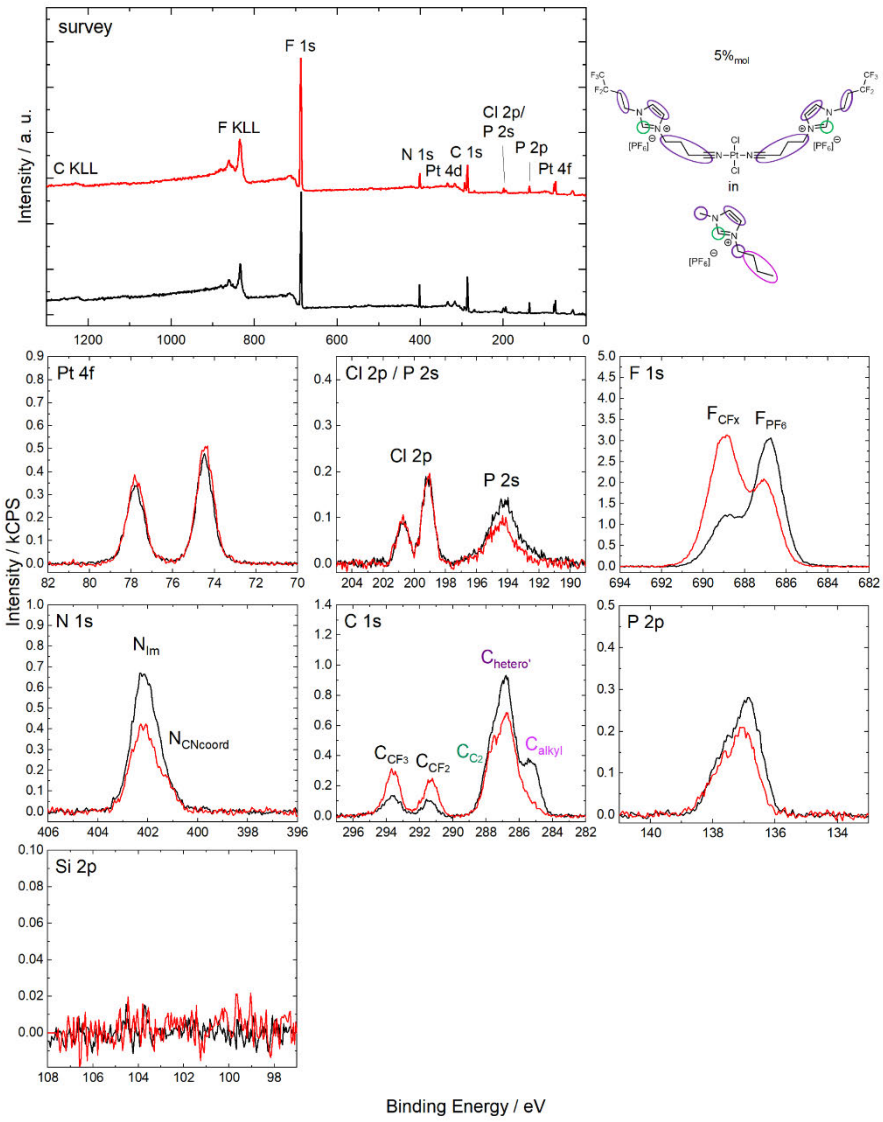

***Figure S2**: Survey, Pt 4f, Cl 2p/P 2s, F 1s, N 1s, C 1s, P 2p and Si 2p XP spectra of a 5%$_{mol}$ solution of **1** in [C_4C_1Im][PF_6] in 0° (black) and 80° (red) emission recorded at room temperature with assignment of peaks to the molecular structure.*

Peak fitting: Similar to procedure of neat [C_3CNPFC_4Im][PF_6] (see above) with following additional constraints: Full width at half maximum (FWHM) of N_{Im} and $N_{CNcoord}$ was constraint to identical values. FWHM of C_{C2} and C_{alkyl} was constraint to identical values.

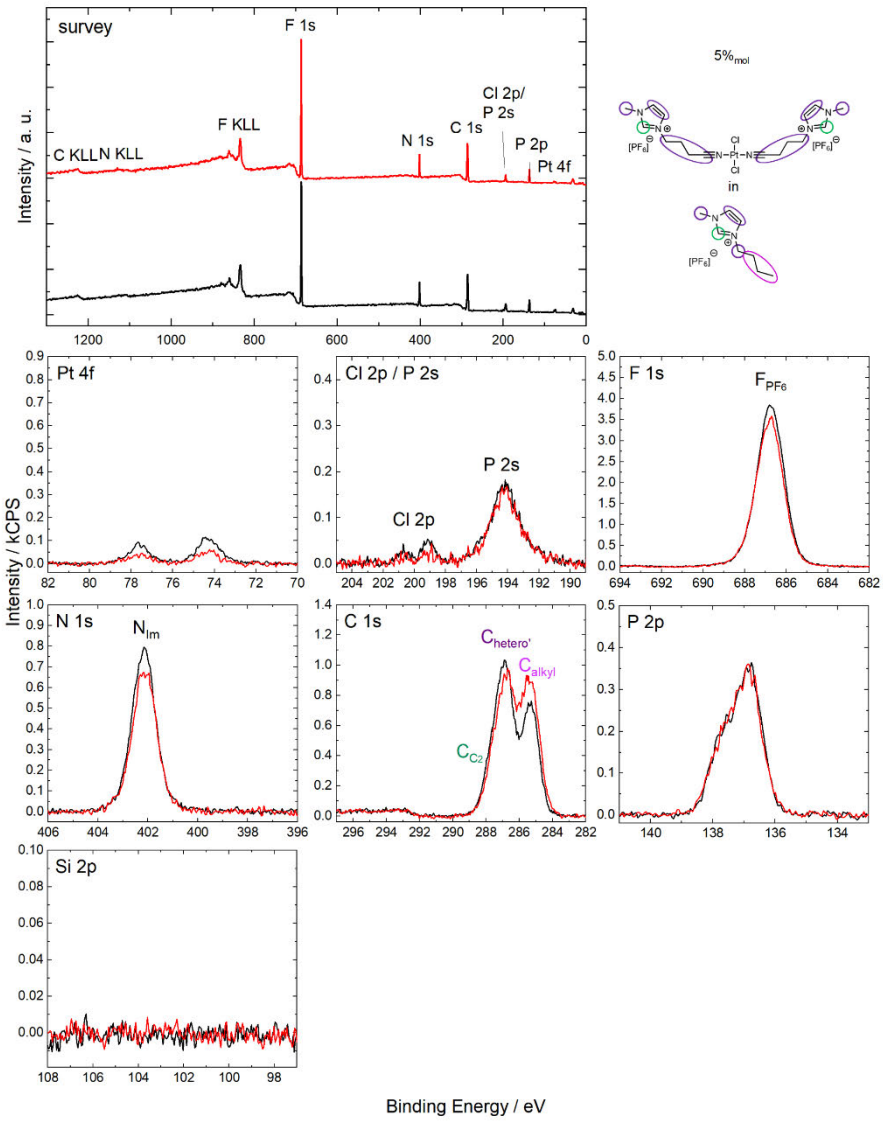

*Figure S3: Survey, Pt 4f, Cl 2p/P 2s, F 1s, N 1s, C 1s, P 2p and Si 2p XP spectra of a 5%$_{mol}$ solution of **2** in [C_4C_1Im][PF_6] in 0° (black) and 80° (red) emission recorded at room temperature with assignment of peaks to the molecular structure.*

Peak fitting: Similar to procedure of 5%$_{mol}$ solution of **1** (see above).

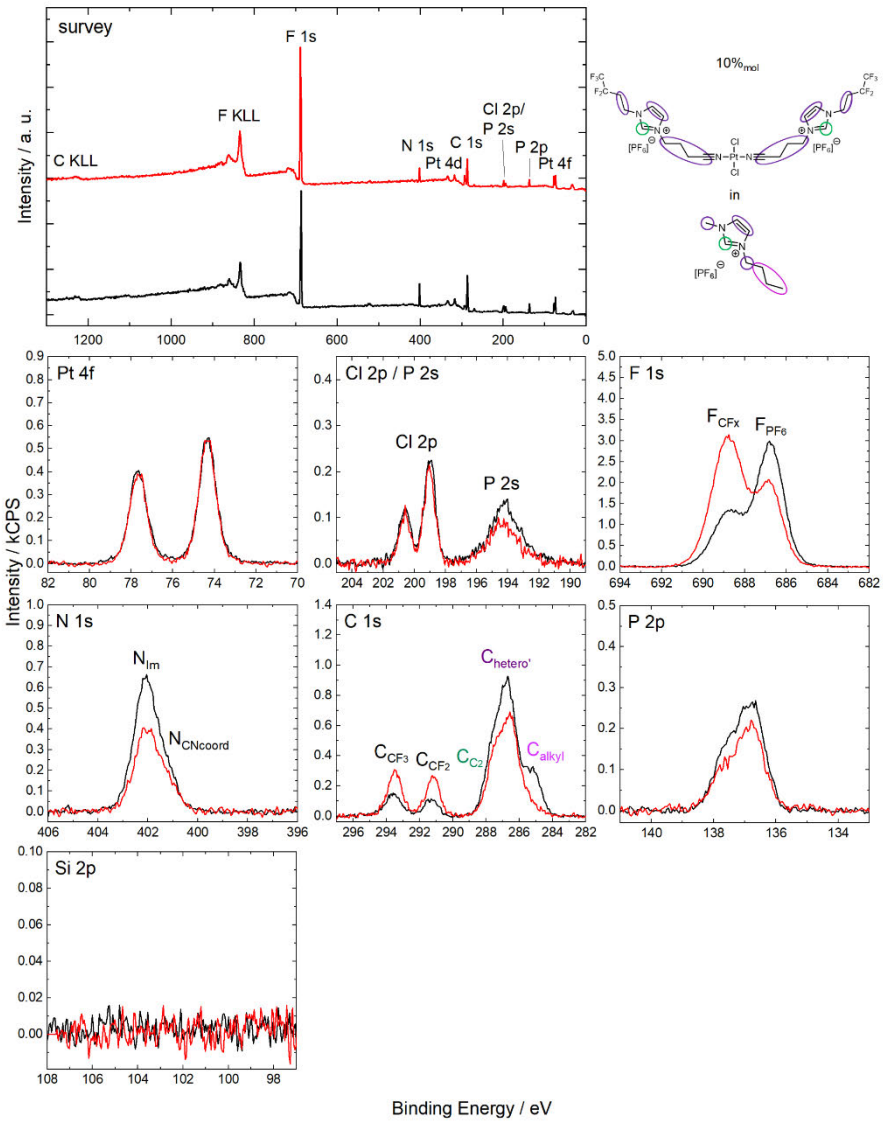

***Figure S4**: Survey, Pt 4f, Cl 2p/P 2s, F 1s, N 1s, C 1s, P 2p and Si 2p XP spectra of a 10%$_{mol}$ solution of **1** in [C_4C_1Im][PF_6] in 0° (black) and 80° (red) emission recorded at room temperature with assignment of peaks to the molecular structure.*

Peak fitting: Similar to procedure of 5%$_{mol}$ solution of **1** (see above).

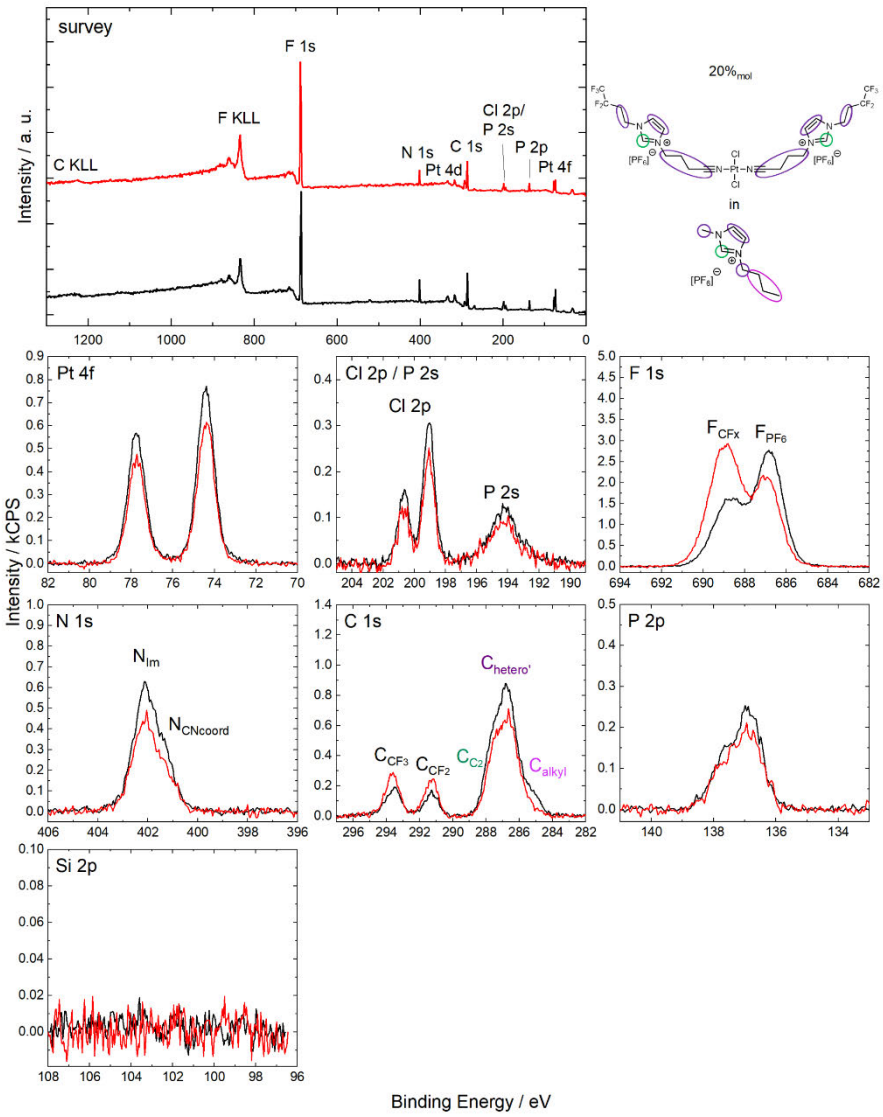

*Figure S5: Survey, Pt 4f, Cl 2p/P 2s, F 1s, N 1s, C 1s, P 2p and Si 2p XP spectra of a 20%$_{mol}$ solution of **1** in [C_4C_1Im][PF_6] in 0° (black) and 80° (red) emission recorded at room temperature with assignment of peaks to the molecular structure.*

Peak fitting: Similar to procedure of 5%$_{mol}$ solution of **1** (see above).

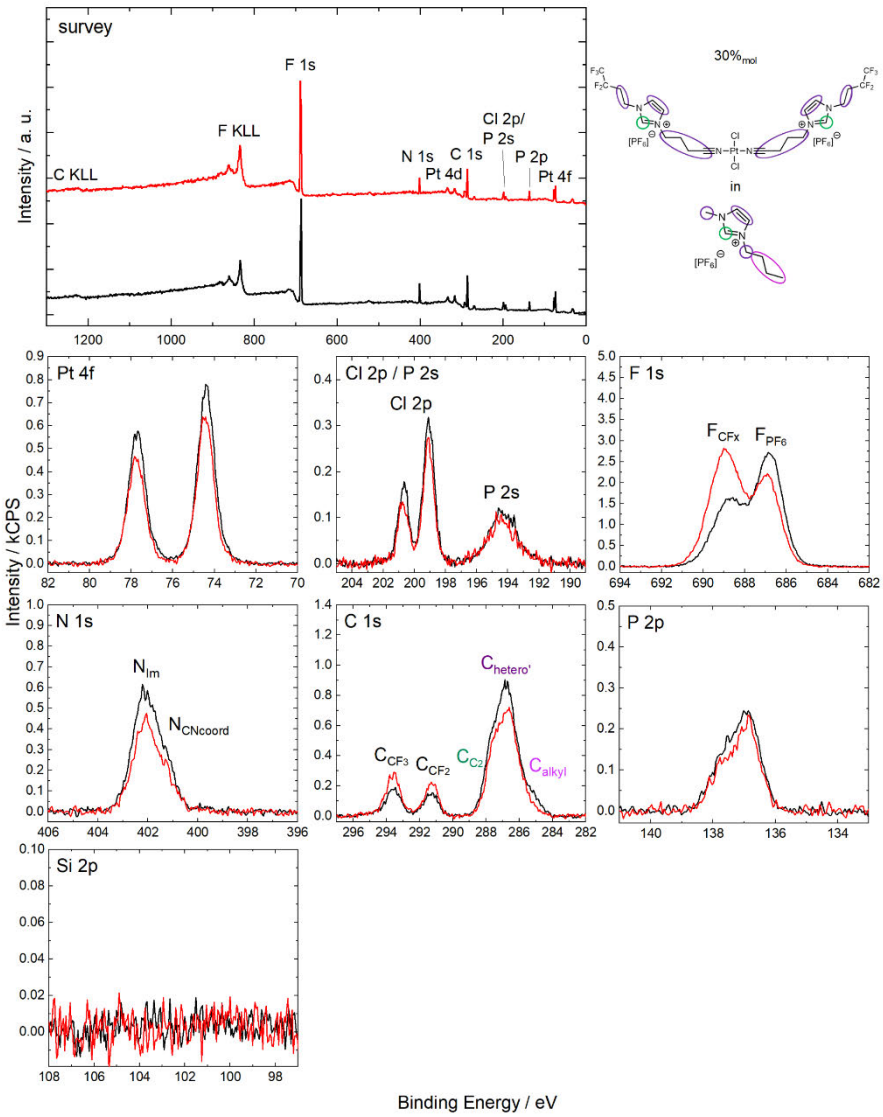

***Figure S6**: Survey, Pt 4f, Cl 2p/P 2s, F 1s, N 1s, C 1s, P 2p and Si 2p XP spectra of a 30%$_{mol}$ solution of **1** in [C_4C_1Im][PF_6] in 0° (black) and 80° (red) emission recorded at room temperature with assignment of peaks to the molecular structure.*

Peak fitting: Similar to procedure of 5%$_{mol}$ solution of **1** (see above).

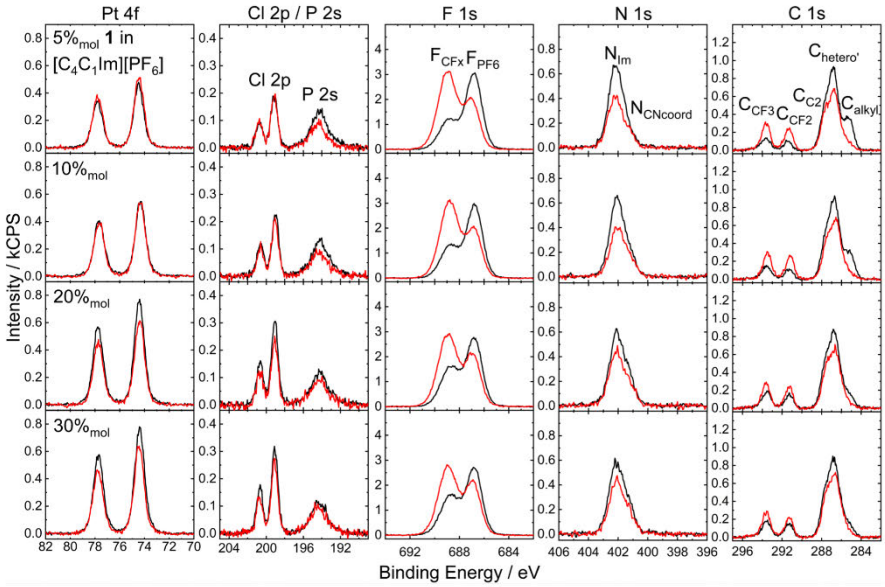

***Figure S7**: Overview on Pt 4f, Cl 2p/P 2s, F 1s, N 1s and C 1s XP spectra of solutions of **1** in $[C_4C_1Im][PF_6]$ with concentrations of 5, 10, 20 and 30%$_{mol}$ in 0° (black) and 80° (red) emission recorded at room temperature.*

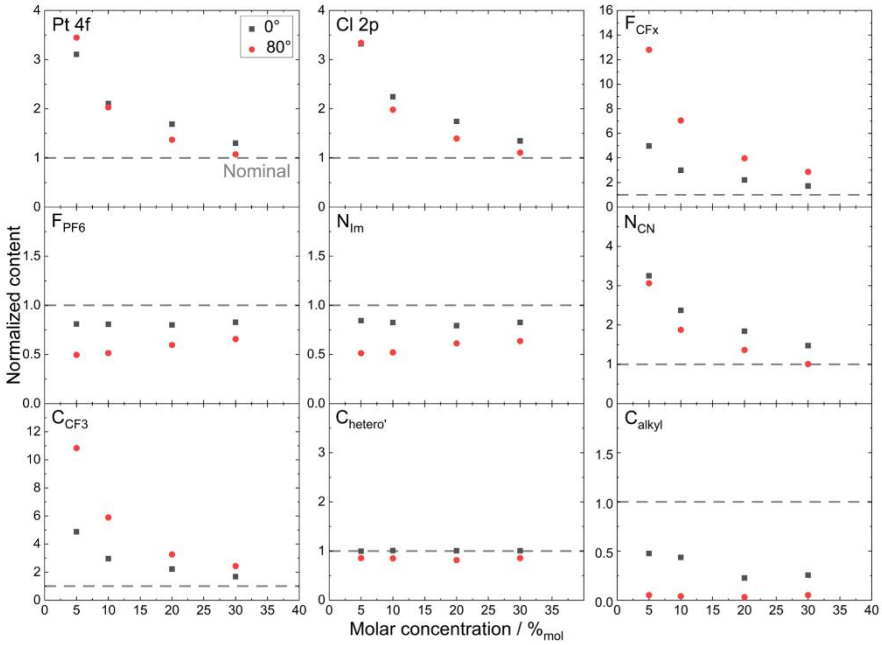

***Figure S8**: Normalized contents derived from Pt 4f, Cl 2p, F_{CFx}, F_{PF6}, N_{Im}, N_{CN}, C_{CF3}, $C_{hetero'}$ and C_{alkyl} signals in 0° (black squares) and 80° emission (red dots) over a concentration range from 5%$_{mol}$ to 30%$_{mol}$ of **1** in [C_4C_1Im][PF_6]. The dashed lines at a value of 1 represent nominal stoichiometry implying that all ions exhibit random distribution, orientation and configuration within the near-surface region.*

Table S1: *Quantitative analysis of XPS core level spectra of a) neat [C_3CNPFC_4Im][PF_6], b) 5%$_{mol}$ solution of **1**, c) 5%$_{mol}$ solution of **2**, d) 10%$_{mol}$ solution of **1**, e) 20%$_{mol}$ solution of **1** and f) 30%$_{mol}$ solution of **1** in [C_4C_1Im][PF_6]. Note that for sake of clarity the nominal value corresponds to the nominal composition of the solution and not to the exact concentration from weigh-in. The weighed proportions only marginally differ from nominal composition (see table S2).*

a) Neat [C_3CNPFC_4Im][PF_6]	Pt 4f	Cl 2p	F 1s CFx	F 1s PF_6	N 1s Im	N 1s CN/ CNcoord	C 1s CF_3	C 1s CF_2	C 1s C_2	C 1s hetero/ hetero′	C 1s alkyl	P 2p
Binding Energy / eV			688.8	686.8	402.3	400.0	293.7	291.4	287.8	286.9		137.3
Nominal			5	6	2	1	1	1	1	8		1
Experimental, 0°			5.7	5.8	1.9	0.9	1.1	1.1	1.0	7.4		1.1
Experimental, 80°			8.9	4.4	1.5	0.5	1.5	1.5	0.7	6.0		1.0
b) 5%$_{mol}$ 1 in [C_4C_1Im][PF_6]	**Pt 4f**	**Cl 2p**	**F 1s CFx**	**F 1s PF_6**	**N 1s Im**	**N 1s CN/ CNcoord**	**C 1s CF_3**	**C 1s CF_2**	**C 1s C_2**	**C 1s hetero/ hetero′**	**C 1s alkyl**	**P 2p**
Binding Energy / eV	76.1	199.9	688.8	686.8	402.2	401.3	293.7	291.4	287.8	286.9	285.2	137.3
Nominal	0.053	0.11	0.53	6.6	2.2	0.11	0.11	0.11	1.1	4.8	3.0	1.1
Experimental, 0°	0.16	0.35	2.6	5.4	1.9	0.34	0.51	0.51	0.9	4.8	1.4	0.97
Experimental, 80°	0.18	0.35	6.7	3.3	1.1	0.32	1.1	1.1	0.57	4.2	0.16	0.72
c) 5%$_{mol}$ 2 in [C_4C_1Im][PF_6]	**Pt 4f**	**Cl 2p**	**F 1s CFx**	**F 1s PF_6**	**N 1s Im**	**N 1s CN/ CNcoord**	**C 1s CF_3**	**C 1s CF_2**	**C 1s C_2**	**C 1s hetero/ hetero′**	**C 1s alkyl**	**P 2p**
Binding Energy / eV	76.0	199.9		686.8	402.2	-			287.7	286.8	285.3	137.3
Nominal	0.053	0.11		6.6	2.2	0.11			1.1	4.7	3.0	1.1
Experimental, 0°	0.049	0.10		6.6	2.2	-			1.1	4.6	3.2	1.2
Experimental, 80°	0.025	0.052		6.1	2.0	-			1.0	4.5	4.2	1.2
d) 10%$_{mol}$ 1 in [C_4C_1Im][PF_6]	**Pt 4f**	**Cl 2p**	**F 1s CFx**	**F 1s PF_6**	**N 1s Im**	**N 1s CN/ CNcoord**	**C 1s CF_3**	**C 1s CF_2**	**C 1s C_2**	**C 1s hetero/ hetero′**	**C 1s alkyl**	**P 2p**
Binding Energy / eV	76.0	199.8	688.7	686.8	402.1	401.2	293.6	291.3	287.7	286.8	285.1	137.2
Nominal	0.11	0.22	1.1	7.3	2.4	0.22	0.22	0.22	1.2	5.8	3.0	1.2
Experimental, 0°	0.23	0.50	3.3	5.9	2.0	0.53	0.66	0.66	1.0	5.8	1.3	1.1
Experimental, 80°	0.23	0.44	7.8	3.8	1.3	0.42	1.3	1.3	0.6	4.9	0.1	0.9
e) 20%$_{mol}$ 1 in [C_4C_1Im][PF_6]	**Pt 4f**	**Cl 2p**	**F 1s CFx**	**F 1s PF_6**	**N 1s Im**	**N 1s CN/ CNcoord**	**C 1s CF_3**	**C 1s CF_2**	**C 1s C_2**	**C 1s hetero/ hetero′**	**C 1s alkyl**	**P 2p**
Binding Energy / eV	76.1	199.9	688.7	686.8	402.2	401.3	293.6	291.3	287.7	286.8	285.1	137.3
Nominal	0.25	0.50	2.5	9.0	3.0	0.50	0.50	0.5	1.5	8.0	3.0	1.5
Experimental, 0°	0.42	0.87	5.5	7.2	2.4	0.92	1.1	1.1	1.2	8.1	0.68	1.3
Experimental, 80°	0.34	0.70	9.9	5.4	1.8	0.68	1.6	1.6	0.9	6.5	0.09	1.1
f) 30%$_{mol}$ 1 in [C_4C_1Im][PF_6]	**Pt 4f**	**Cl 2p**	**F 1s CFx**	**F 1s PF_6**	**N 1s Im**	**N 1s CN/ CNcoord**	**C 1s CF_3**	**C 1s CF_2**	**C 1s C_2**	**C 1s hetero/ hetero′**	**C 1s alkyl**	**P 2p**
Binding Energy / eV	76.1	199.9	688.7	686.8	402.2	401.3	293.6	291.3	287.7	286.8	285.1	137.3
Nominal	0.43	0.86	4.3	11.1	3.7	0.86	0.86	0.86	1.8	10.8	3.0	1.8
Experimental, 0°	0.56	1.2	7.4	9.2	3.1	1.3	1.4	1.4	1.5	10.9	0.76	1.8
Experimental, 80°	0.46	0.95	12.3	7.3	2.4	0.86	2.1	2.1	1.2	9.3	0.16	1.5

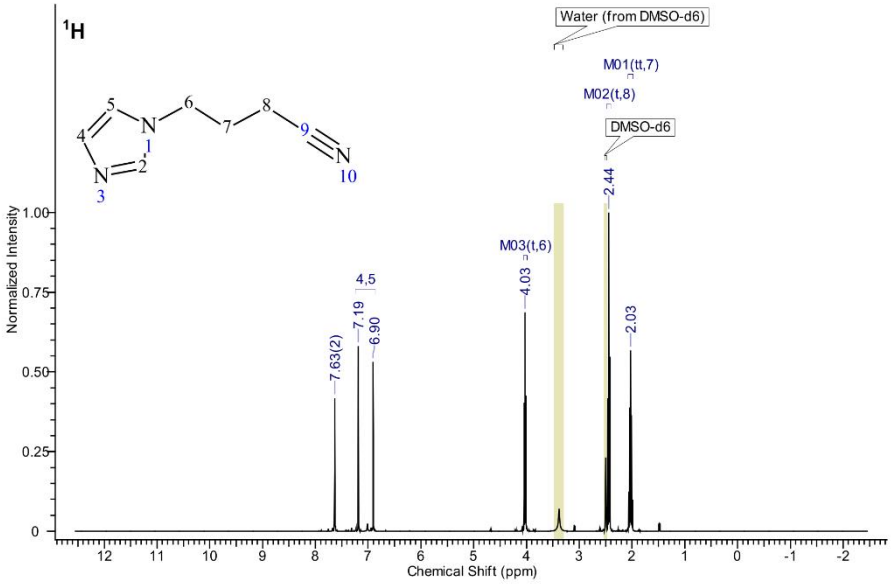

***Figure S9**: Full ¹H NMR spectrum of C_3CNIm (for measurement parameters and quantitative analysis see above).*

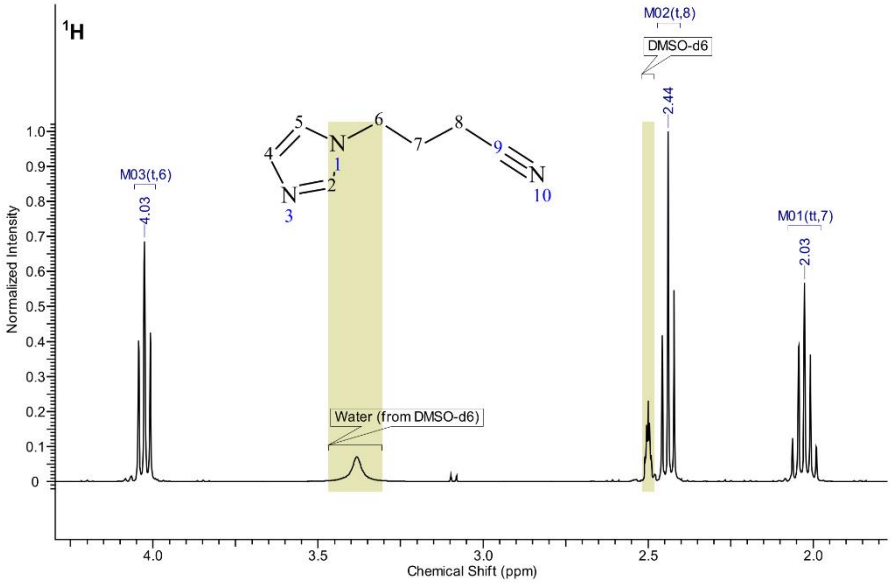

***Figure S10**: Detailed view of ¹H NMR spectrum shown in figure S9.*

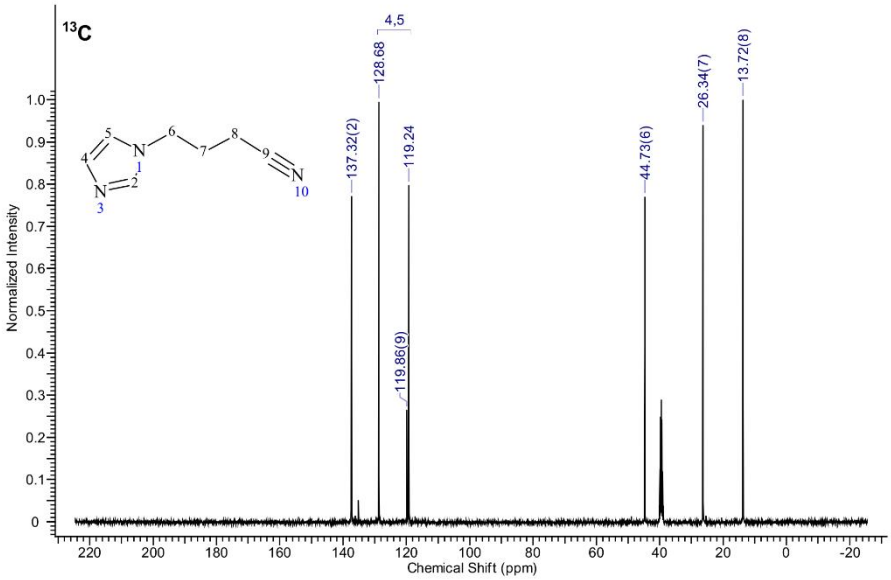

***Figure S11**: Full ^{13}C NMR spectrum of C_3CNIm (for measurement parameters and quantitative analysis see above).*

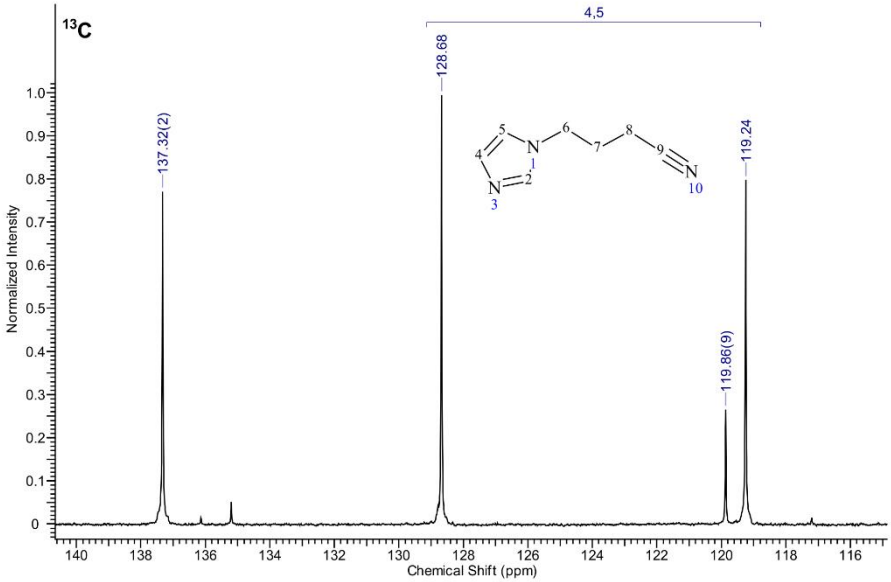

***Figure S12**: Detailed view of ^{13}C NMR spectrum shown in figure S11.*

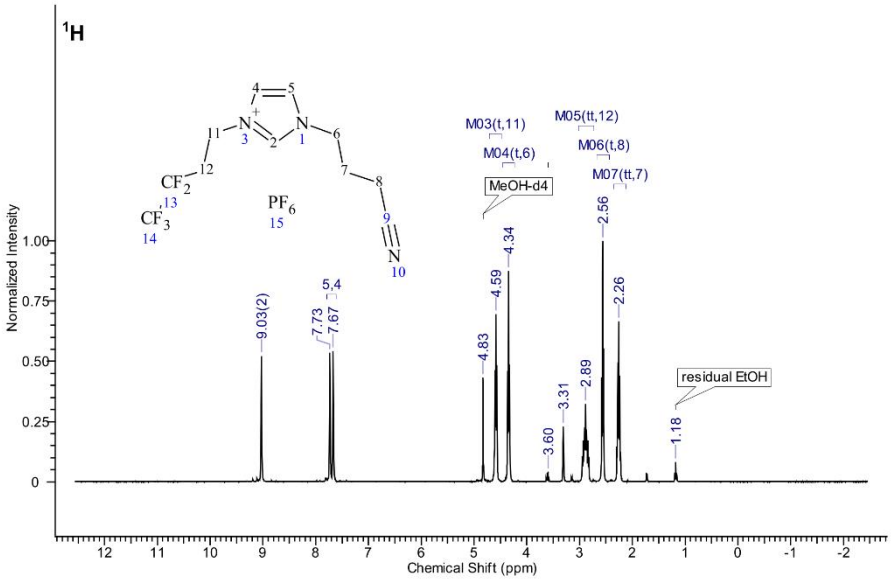

***Figure S13**: Full ^{1}H NMR spectrum of [C_3CNPFC_4Im][PF_6] (for measurement parameters and quantitative analysis see above).*

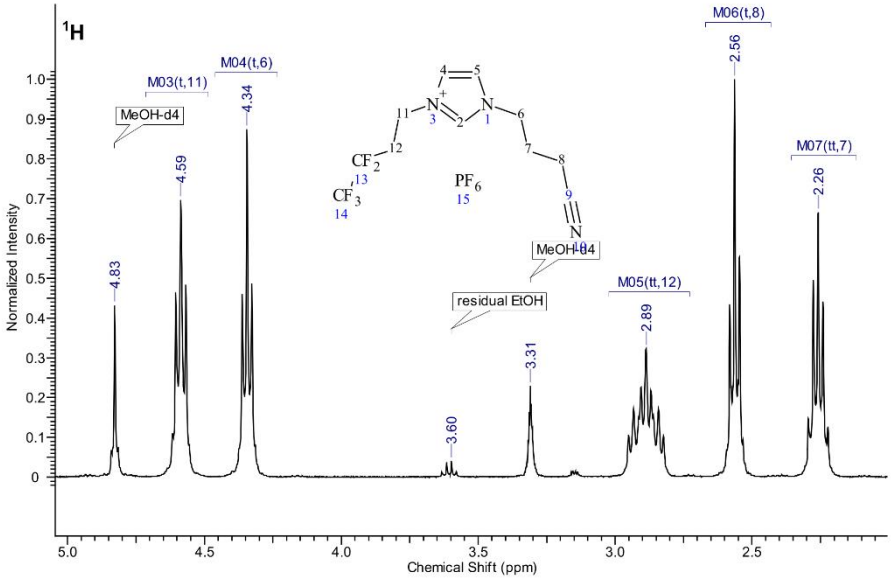

***Figure S14**: Detailed view of ^{1}H NMR spectrum shown in figure S13.*

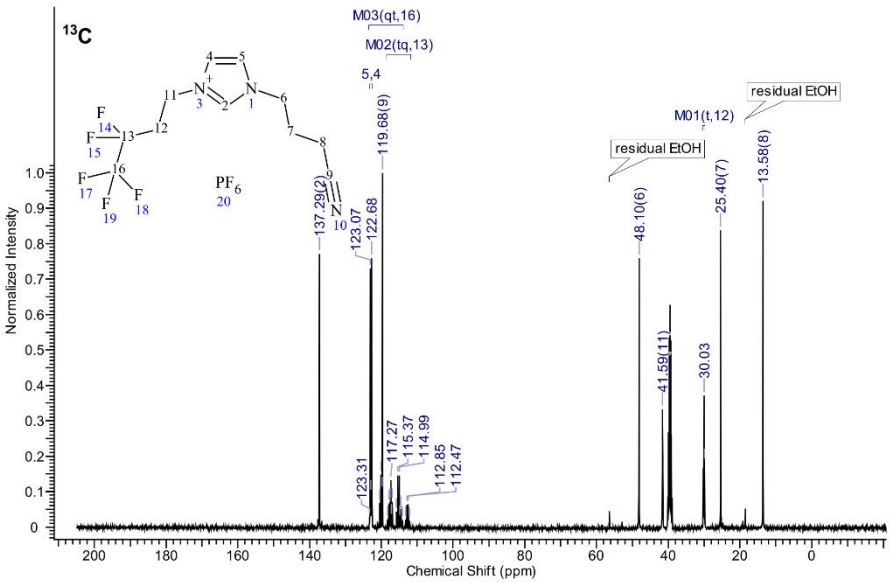

***Figure S15**: Full ^{13}C NMR spectrum of $[C_3CNPFC_4Im][PF_6]$ (for measurement parameters and quantitative analysis see above).*

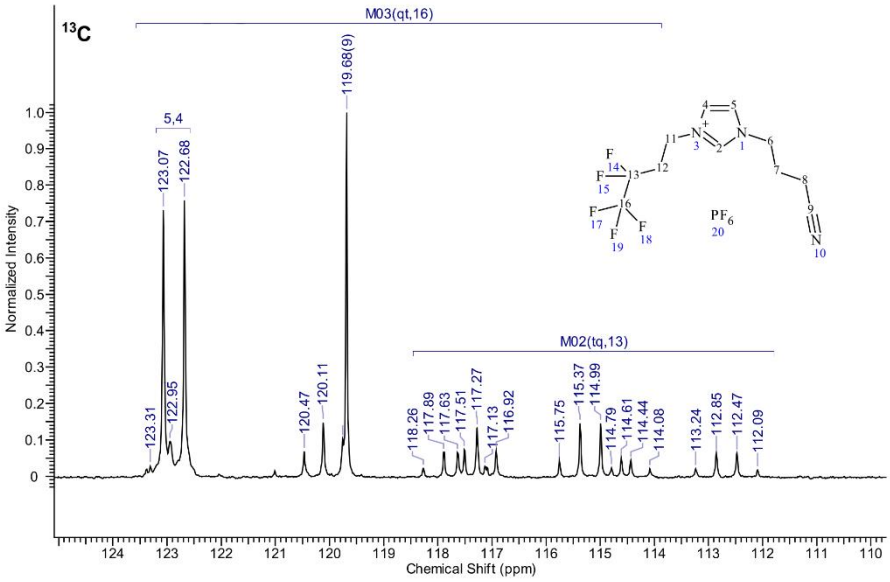

***Figure S16**: Detailed view of ^{13}C NMR spectrum shown in figure S15.*

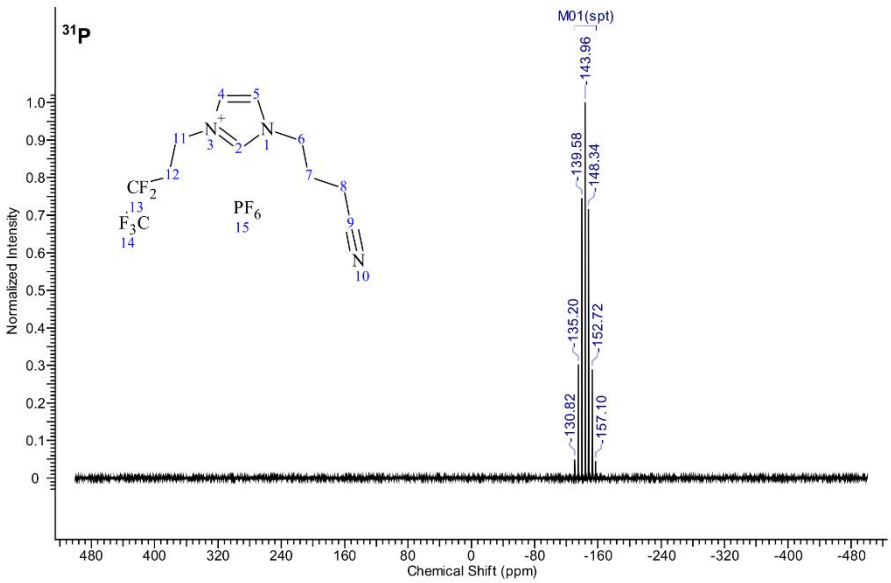

***Figure S17**: Full ^{31}P NMR spectrum of $[C_3CNPFC_4Im][PF_6]$ (for measurement parameters and quantitative analysis see above).*

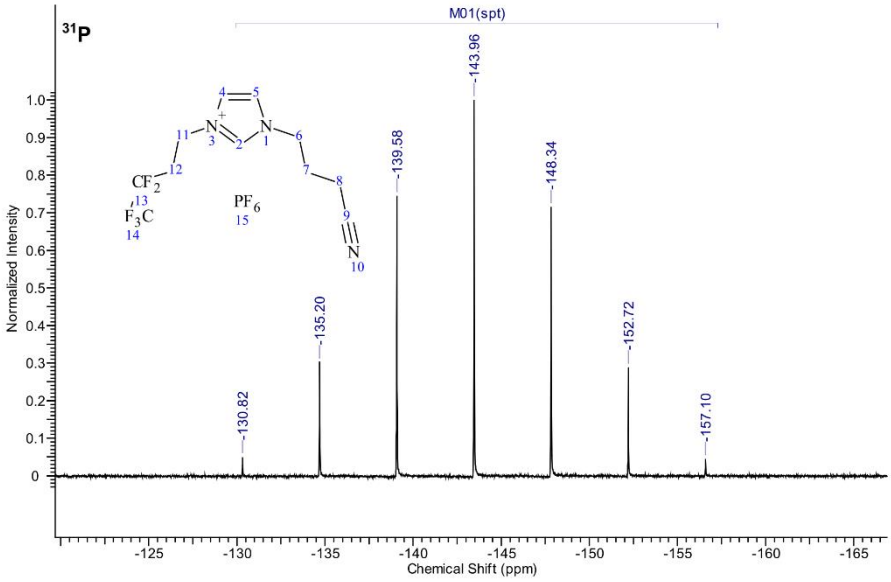

***Figure S18**: Detailed view of ^{31}P NMR spectrum shown in figure S17.*

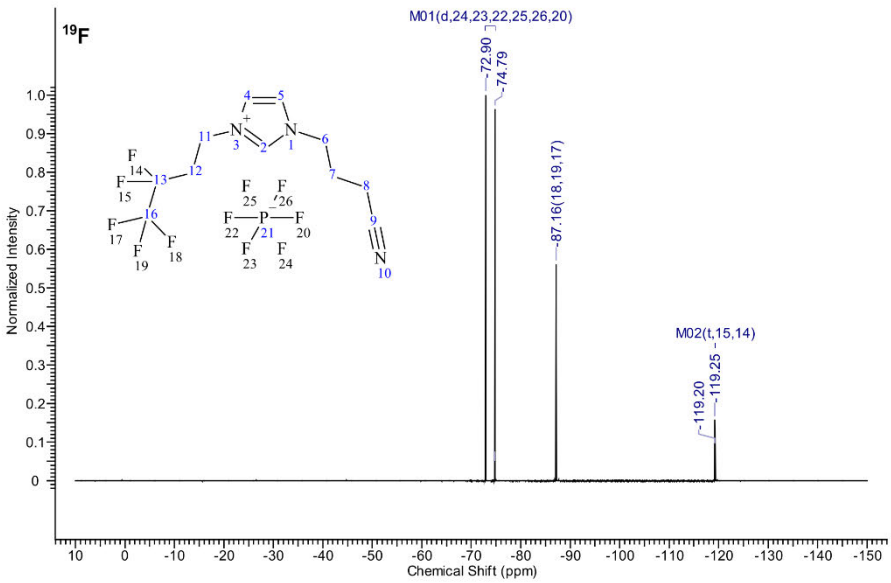

***Figure S19**: Full ^{19}F NMR spectrum of $[C_3CNPFC_4Im][PF_6]$ (for measurement parameters and quantitative analysis see above).*

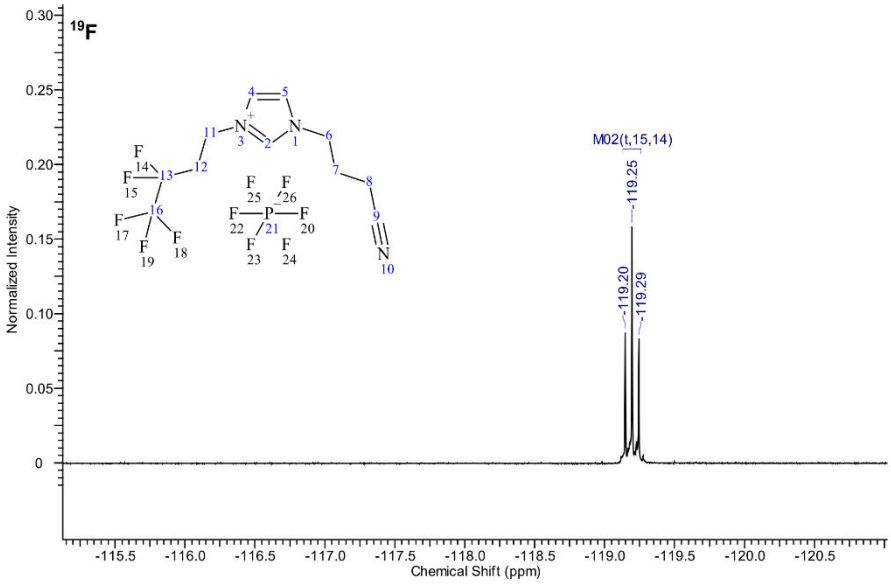

***Figure S20**: Detailed view of ^{19}F NMR spectrum shown in figure S19.*

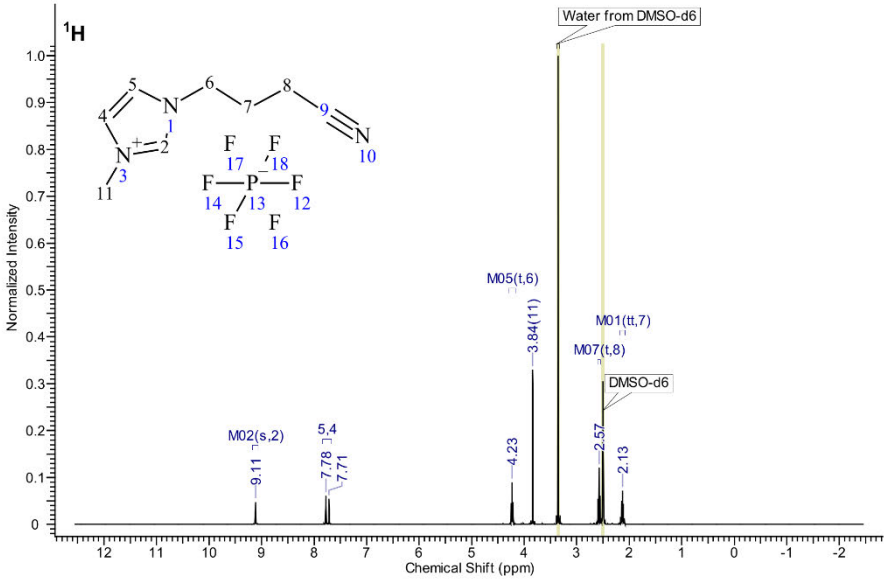

***Figure S21**: Full ^{1}H NMR spectrum of $[C_3CNC_1Im][PF_6]$ (for measurement parameters and quantitative analysis see above).*

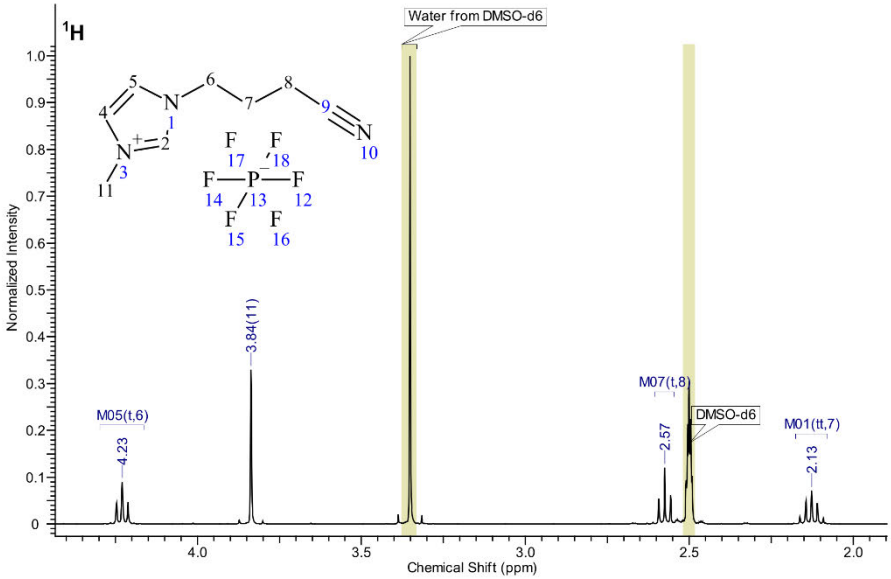

***Figure S22**: Detailed view of ^{1}H NMR spectrum shown in figure S21.*

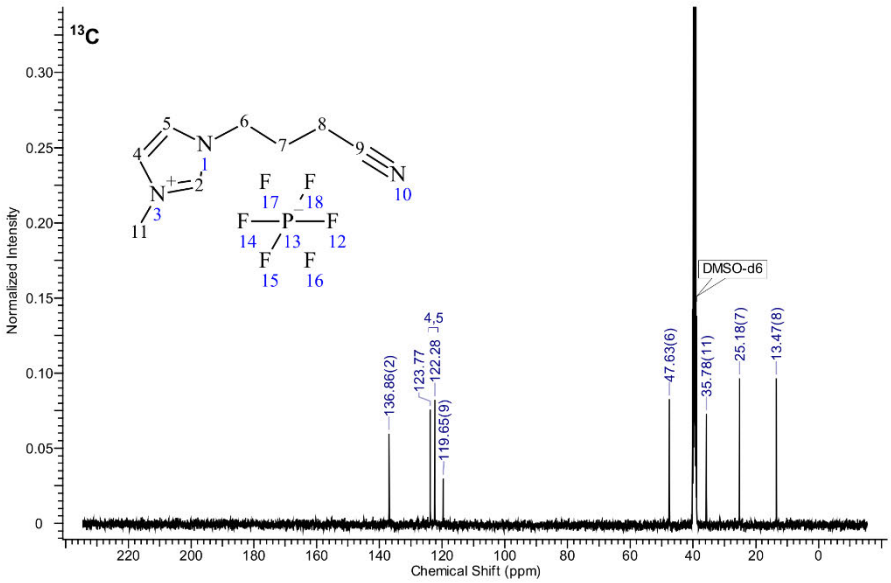

Figure S23: Full ^{13}C NMR spectrum of $[C_3CNC_1Im][PF_6]$ (for measurement parameters and quantitative analysis see above).

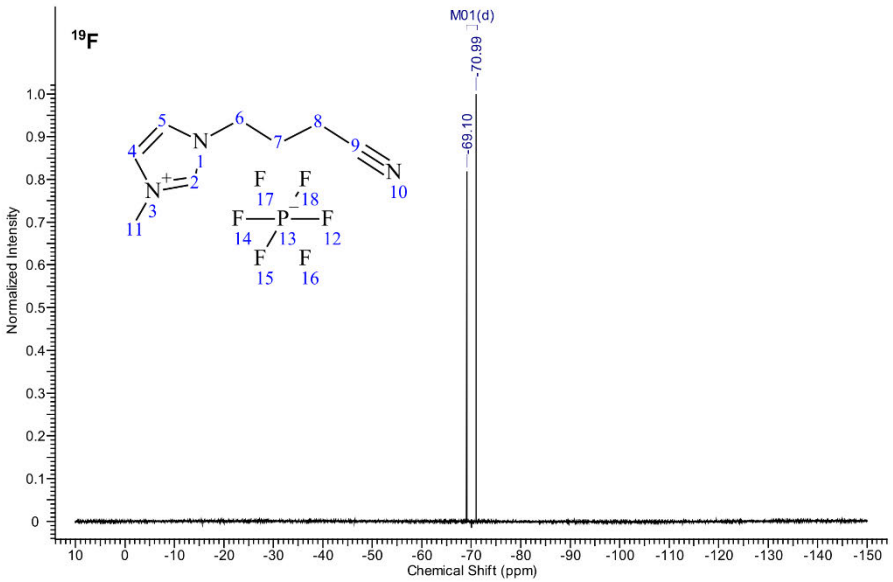

Figure S24: Full ^{19}F NMR spectrum of $[C_3CNC_1Im][PF_6]$ (for measurement parameters and quantitative analysis see above).

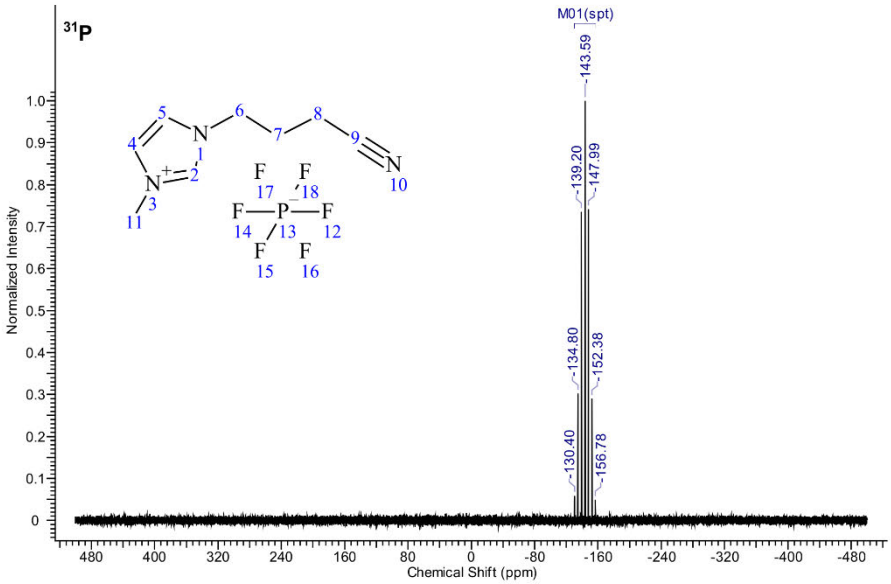

***Figure S25**: Full ^{31}P NMR spectrum of $[C_3CNC_1Im][PF_6]$ (for measurement parameters and quantitative analysis see above).*

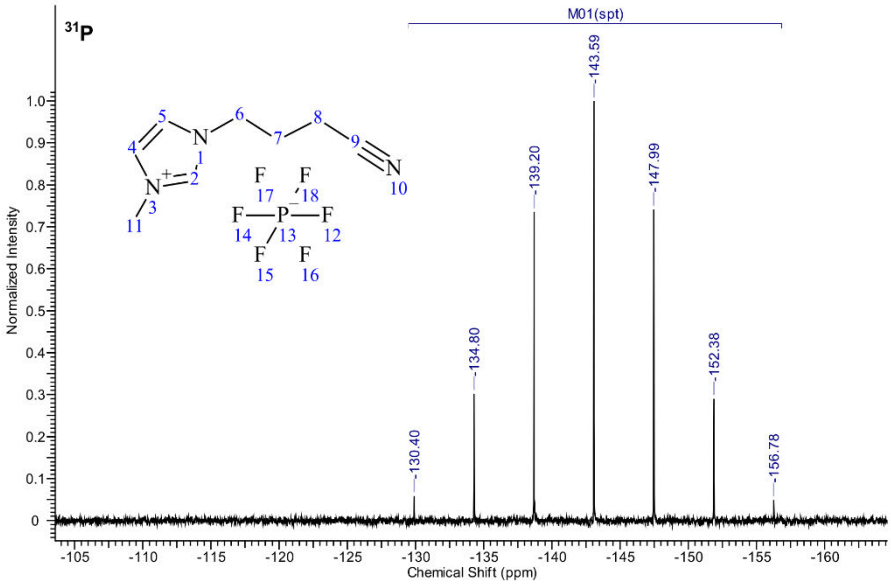

***Figure S26**: Detailed view of ^{31}P NMR spectrum shown in figure S25.*

Table S2: *Weighed proportions and reaction times (after addition of [C_4C_1Im][PF_6]) for preparation of solutions of* ***1*** *in [C_4C_1Im][PF_6].*

	5%$_{mol}$ **1** in [C_4C_1Im][PF_6]	10%$_{mol}$	20%$_{mol}$	30%$_{mol}$
Mass *Cis*-[$PtCl_2(CH_3CN)_2$] / mg	40.0	74.1	92.5	158
Amount of substance *Cis*-[$PtCl_2(CH_3CN)_2$] / mmol	0.113	0.209	0.260	0.445
Mass [C_3CNPFC_4Im][PF_6] / mg	98.8	180	224	384
Amount of substance [C_3CNPFC_4Im][PF_6] / mmol	0.231	0.417	0.525	0.899
Mass [C_4C_1Im][PF_6] / mg	612	538	298	297
Amount of substance [C_4C_1Im][PF_6] / mmol	2.14	1.88	1.04	1.04
Reaction time (after addition of [C_4C_1Im][PF_6])	90 min	3 h	3.5 h	5 h

References

[1] J. M. Gottfried, F. Maier, J. Rossa, D. Gerhard, P. S. Schulz, P. Wasserscheid, H.-P. Steinrück, *Z. Phys. Chem.* **2006**, *220*, 1439-1453.

[2] B. S. J. Heller, M. Lexow, F. Greco, S. Shin, G. Partl, F. Maier, H.-P. Steinrück, *Chem. Eur. J.* **2020**, *26*, 1117-1126.

[3] X. Cai, Q. Wang, Y. Liu, J. Xie, Z. Long, Y. Zhou, J. Wang, *ACS Sustain. Chem. Eng.* **2016**, *4*, 4986-4996.

[4] Q. Zhang, Z. Li, J. Zhang, S. Zhang, L. Zhu, J. Yang, X. Zhang, Y. Deng, *J. Phys. Chem. B* **2007**, *111*, 2864-2872.

[5] D. Hemmeter, U. Paap, N. Taccardi, J. Mehler, P. Schulz, P. Wasserscheid, F. Maier, H.-P. Steinrück, *ChemPhysChem* **2022**, e202200391.

[6] I. Niedermaier, C. Kolbeck, H.-P. Steinrück, F. Maier, *Rev. Sci. Instrum.* **2016**, *87*, 045105.

8.3 Publication 3, [P3]

catalysts

IMPACT FACTOR 3.9

CITESCORE 6.3

Article

Structure and Surface Behavior of Rh Complexes in Ionic Liquids Studied Using Angle-Resolved X-ray Photoelectron Spectroscopy

Daniel Hemmeter, Ulrike Paap, Florian Maier and Hans-Peter Steinrück

Special Issue
Recent Developments in Rh Catalysts II
Edited by
Dr. Imre Kovács

MDPI

https://doi.org/10.3390/catal13050871

catalysts

MDPI

Article

Structure and Surface Behavior of Rh Complexes in Ionic Liquids Studied Using Angle-Resolved X-ray Photoelectron Spectroscopy

Daniel Hemmeter, Ulrike Paap, Florian Maier and Hans-Peter Steinrück *

Lehrstuhl für Physikalische Chemie 2, Friedrich-Alexander-Universität Erlangen-Nürnberg, Egerlandstr. 3, 91058 Erlangen, Germany; daniel.hemmeter@fau.de (D.H.); ulrike.paap@fau.de (U.P.); florian.maier@fau.de (F.M.)
* Correspondence: hans-peter.steinrueck@fau.de

Abstract: We present an ARXPS study on the surface composition and interfacial behavior of commercial $[Rh(COD)_2][TfO]$ in $[C_2C_1Im][TfO]$, $[C_4C_1Im][TfO]$, $[C_8C_1Im][TfO]$, and $[C_2C_1Im][EtOSO_3]$. The complex was found to be non-intact in a solution of these ILs through the loss of COD ligands, accompanied by the depletion of the metal center from the IL/vacuum interface. Increasing the chain length of the aliphatic substituent on the imidazolium cation of the $[TfO]^-$-based ILs led to a more pronounced depletion from the interface, due to the higher surface affinity of the solvent cations with the longer alkyl chains. The loss of COD ligands offered facile in situ ligand substitution with surface-active TPPTS to afford a moderate increase in the surface concentration of Rh. We propose the formation of a Schrock−Osborn-type catalyst $[Rh(COD)(TPPTS)_2][TfO]$. Information on the surface composition and targeted design of the gas/IL interface is highly relevant for applications in IL-based catalytic systems, such as in supported ionic liquid phase (SILP) catalysis.

Keywords: catalysis; ionic liquids; rhodium catalysts; surface analysis; X-ray photoelectron spectroscopy (XPS)

check for updates

Citation: Hemmeter, D.; Paap, U.; Maier, F.; Steinrück, H.-P. Structure and Surface Behavior of Rh Complexes in Ionic Liquids Studied Using Angle-Resolved X-ray Photoelectron Spectroscopy. *Catalysts* **2023**, *13*, 871. https://doi.org/10.3390/catal13050871

Academic Editor: Maurizio Muniz-Miranda

Received: 12 April 2023
Revised: 3 May 2023
Accepted: 4 May 2023
Published: 11 May 2023

1. Introduction

Ionic liquids (ILs) are low-melting salts representing an innovative class of solvents and electrolytes [1–8]. These compounds typically feature extremely low vapor pressures, high thermal stability, and wide electrochemical windows. One particularly fascinating aspect is the tuneability of their chemical structure, which allows for adjusting their physicochemical properties, such as miscibility, solvation, and coordination behavior, over a wide range. This adaptability gives rise to a rich spectrum of potential applications, e.g., in organic [5,6,9–12], organometallic [13–15], and nanoparticle synthesis [16–18], as well as in electrocatalysis [19–21], biocatalysis [22,23], and other fields of catalytic approaches. In terms of catalysis, the unique properties of ILs create novel concepts for heterogeneous and heterogenized systems [24,25]: The solid catalyst with an ionic liquid layer (SCILL) approach is based on coating a classical heterogeneous catalyst with a thin film of IL to mainly improve the selectivity of the process [26,27]. In supported ionic liquid phase (SILP) catalysis, a homogeneous catalyst is dissolved in a thin IL film, which is immobilized on an inert solid support material [28–30]. For both concepts, the interfacial behavior, that is, the structural and chemical properties at the solid/liquid, liquid/liquid, and/or liquid/gas interface of the IL film strongly influences the overall performance of the process [24].

Interfacial properties of IL-based materials have been intensively studied under ambient conditions by means of various spectroscopic, microscopic, and scattering techniques, such as sum frequency generation (SFG) [31–34], second harmonic generation (SHG) [35–37], atomic force microscopy (AFM) [38–40] and spectroscopy (AFS) [41], scanning tunnelling microscopy (STM) [39,40,42], and X-ray reflectivity (XRR) [43,44] tech-

niques, to name a few. In addition, owing to the negligible volatility of ILs, ultra-high vacuum (UHV)-based surface science methods have also been successfully applied to access interfacial phenomena, for instance through low-energy ion scattering (LEIS) [45,46], mass spectrometry (MS) [47,48], high resolution electron energy loss spectroscopy (HREELS) [49], ultraviolet photoelectron spectroscopy (UPS) [49–51], metastable induced electron spectroscopy (MIES) [49,50], reactive atom scattering (RAS) [52–54], and UHV-based STM and AFM techniques [51,55–59].

X-ray photoelectron spectroscopy (XPS) has shown to be a particularly powerful tool for the analysis of the interface-near region of neat ILs [49–51,60–66], IL mixtures [67–72], and IL solutions [14,73–79]. With special interest in catalysis, significant effort has been dedicated to elucidate the nature and the interfacial behavior of organometallic complexes in IL solutions over recent years. Based on XPS core level shifts, it has been shown that the basicity of the IL anion has a significant influence on the electronic environment of the metal center [80,81], even affecting the reaction rate in catalyzed transformations [82]. In addition, the non-innocent character of IL cations has been reported, e.g., by coordination to the metal center forming N-heterocyclic carbene (NHC) complexes, [83] or via functional groups [14]. By performing angle-resolved XPS (ARXPS), a detailed structural picture of the IL/vacuum interface can be obtained, because in organic matter, the information depth (ID) decreases from 6–9 nm at 0° (normal electron emission), to 1.0–1.5 nm at an 80° (grazing electron emission) angle [84]. With ARXPS, preferential surface orientations and configurations, as well as the enrichment and depletion effects, are accessible [24,60,67–72,85–89], which has successfully been shown for IL-based catalyst solutions [14,73–76].

In this study, we address the composition and behavior at the IL/vacuum interface of the commercially available $[Rh(COD)_2][TfO]$ (COD = cyclooctadiene) metal complex in IL solution under well-defined UHV conditions using ARXPS. This metal complex is interesting for several reasons. (a) In an early study by Dupont et al. [90] on homogeneous catalysis in ILs, a $[Rh(COD)_2]^+$ catalyst showed a higher overall conversion in hydrogenation of cyclohexene than the more common Wilkinson catalyst. (b) Furthermore, $[Rh(COD)_2][TfO]$ was successfully employed for in situ preparation of Schrock−Osborn-type catalysts $[Rh(COD)(L)_2][TfO]$ (L = phosphine ligand) for asymmetric catalysis, through substitution of one of the COD ligands [91]. (c) As an ionic compound, $[Rh(COD)_2][TfO]$ promises high solubility in ILs, which should yield adequate signal intensities in XPS.

Our studies under vacuum conditions indicate that the dissolved catalyst loses COD ligands, which is accompanied by its depletion from the IL/vacuum interface. This behavior is observed for dissolving the catalyst in $[C_2C_1Im][TfO]$, $[C_4C_1Im][TfO]$, $[C_8C_1Im][TfO]$, and $[C_2C_1Im][EtOSO_3]$. Upon increasing the length of the aliphatic side chain on the imidazolium cation in the $[TfO]^-$-based solvent ILs, the depletion of the metal center from the interface is even more pronounced. This facile loss of COD from the initial complex opens an interesting route for modifying the complex, namely offering a surface-active ligand, such as trisodium 3,3′,3′′-phosphanetriyltri(benzene-1-sulfonate) (TPPTS), which already has been shown to strongly increase the surface concentration of Rh complexes in a previous study [73]. We propose the formation of a Schrock−Osborn-type catalyst, as depicted in Scheme 1. Our ARXPS measurements indicate a particular enhancement in the Rh concentration at the IL/vacuum interface upon ligand substitution, and with that they also expand the surface-active character of the substituting ligand to this system. The structures of complexes and ILs employed in this work are shown in Figure 1, with color-coding referring to the assignment of XP signals to the molecular structures.

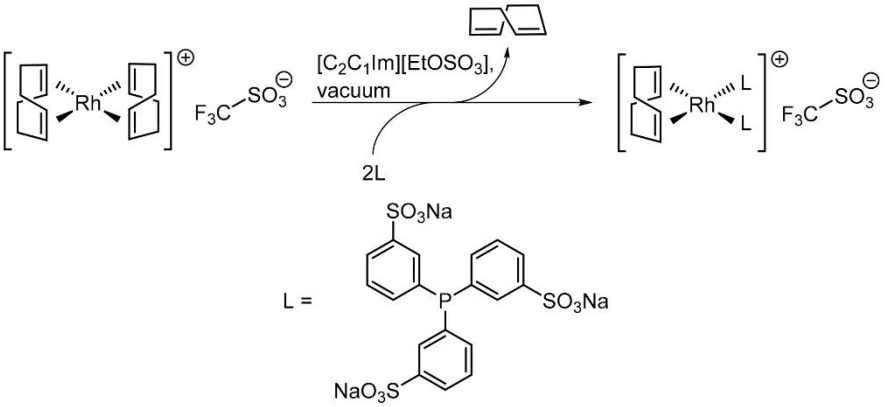

Scheme 1. Expected ligand substitution sequence generating a Schrock–Osborn-type catalyst [Rh(COD)(TPPTS)$_2$][TfO] in [C_2C_1Im][EtOSO$_3$] under vacuum conditions starting from [Rh(COD)$_2$][TfO].

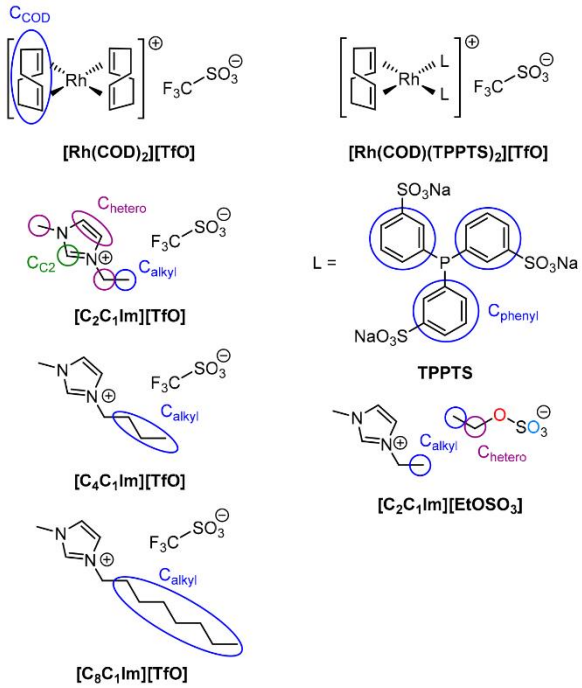

Figure 1. Molecular structures of [Rh(COD)$_2$][TfO] (top left), [Rh(COD)(TPPTS)$_2$][TfO] (top right), [C_2C_1Im][TfO] (middle top left) TPPTS (middle top right), [C_4C_1Im][TfO] (middle bottom left), [C_2C_1Im][EtOSO$_3$] (middle bottom right), and [C_8C_1Im][TfO] (bottom left) with the assignment of carbon and oxygen species detected in XPS.

2. Results and Discussion

2.1. [Rh(COD)$_2$][TfO] in [C$_n$C$_1$Im][TfO] (n = 2, 4, 8)

We found [Rh(COD)$_2$][TfO] to be highly soluble in [TfO]$^-$-based ILs. As a starting point, we prepared a mixture with 20%$_{mol}$ catalyst concentration in [C$_2$C$_1$Im][TfO] and characterized it using ARXPS. Figure 2a depicts the Rh 3d and C 1s spectra of this solution in 0° (black, more bulk-sensitive) and 80° (red, more surface-sensitive) emission geometry. The full set of spectra is shown in Figure S1 in the Supporting Information (SI), where in addition, the F 1s, O 1s, and S 2p signals of the anion and the N 1s signals of quasi-equivalent nitrogen atoms of the [C$_2$C$_1$Im]$^+$ cation are shown, along with a wide scan.

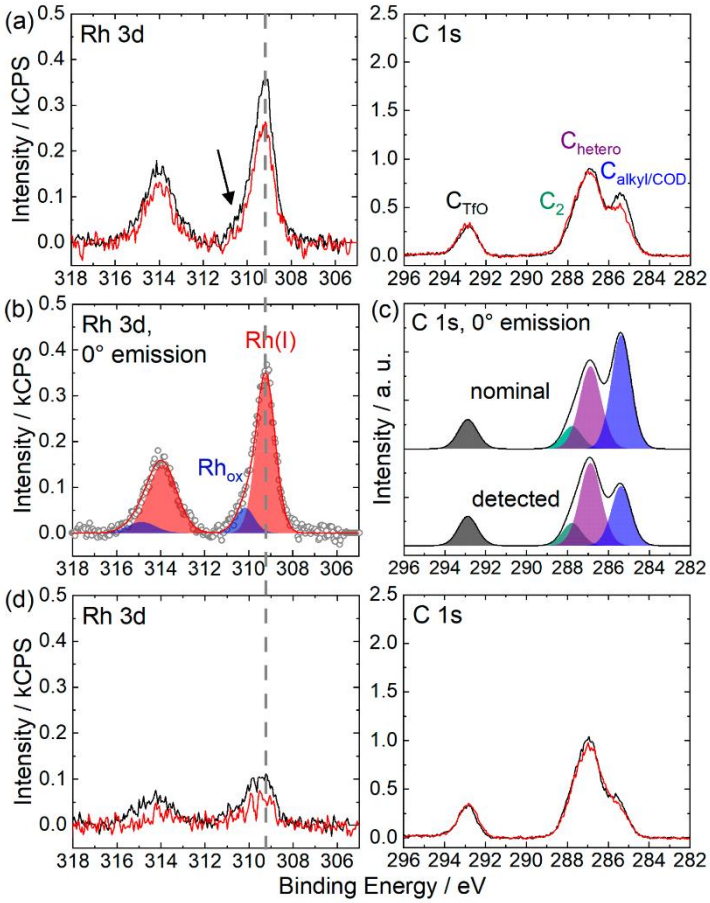

Figure 2. Rh 3d (left) and C 1s (right) XP spectra of solutions of [Rh(COD)$_2$][TfO] in [C$_2$C$_1$Im][TfO] with (**a**) 20%$_{mol}$ concentration and (**d**) 9%$_{mol}$ concentration in 0° (black) and 80° (red) emission recorded at room temperature. For the assignment of peaks to the molecular structure, see color-coding in Figure 1. (**b**) Applied deconvolution of the Rh region for the solution depicted in (**a**). (**c**) Deconvolution applied for the C 1s region recorded for the solution depicted in (**a**) and contrasted with the spectrum expected from nominal composition with the one actually detected (see Table 1).

Table 1. Quantitative analysis of ARXPS core level spectra of solutions of $[Rh(COD)_2][TfO]$ in $[C_2C_1Im][TfO]$, $[C_4C_1Im][TfO]$, and $[C_8C_1Im][TfO]$ (note that the exact weighed proportions and concentrations are given in Table S8 in the SI). The experimental uncertainty of the denoted composition values is 5–10%; to avoid rounding errors, three decimal digits are sometimes provided in the tables).

(a) $9\%_{mol}$ $[Rh(COD)_2][TfO]$ in $[C_2C_1Im][TfO]$	Rh $3d_{5/2}$	Rh $3d_{5/2}$ ox	C 1s TfO	C 1s C_2	C 1s hetero	C 1s *alkyl/COD*	N 1s	F 1s	O 1s	S 2p
Binding Energy/eV	309.4	310.7	292.9	287.8	286.9	285.5	402.2	688.8	532.3	169.4
Nominal	0.099	0.00	1.10	1.00	4.00	2.58 *1.00/1.58*	2.00	3.30	3.30	1.10
Experimental, 0°	0.053	0.012	1.22	1.04	4.15	1.43	2.09	3.57	3.70	1.20
Experimental, 80°	0.033		1.33	1.02	4.09	1.23	1.99	4.17	3.40	1.21
(b) $20\%_{mol}$ $[Rh(COD)_2][TfO]$ in $[C_2C_1Im][TfO]$	Rh $3d_{5/2}$	Rh $3d_{5/2}$ ox	C 1s TfO	C 1s C_2	C 1s hetero	C 1s *alkyl/COD*	N 1s	F 1s	O 1s	S 2p
Binding Energy/eV	309.2	310.2	292.9	287.8	286.9	285.4	402.2	688.8	532.4	169.4
Nominal	0.250	0.00	1.25	1.00	4.00	5.00 *1.00/4.00*	2.00	3.75	3.75	1.25
Experimental, 0°	0.158	0.026	1.40	1.11	4.44	2.91	2.22	4.20	4.37	1.40
Experimental, 80°	0.125		1.54	1.13	4.50	2.35	1.97	5.03	4.05	1.40
(c) $20\%_{mol}$ $[Rh(COD)_2][TfO]$ in $[C_4C_1Im][TfO]$	Rh $3d_{5/2}$	Rh $3d_{5/2}$ ox	C 1s TfO	C 1s C_2	C 1s hetero	C 1s *alkyl/COD*	N 1s	F 1s	O 1s	S 2p
Binding Energy / eV	309.3	310.2	292.9	287.8	286.9	285.4	402.3	688.8	532.4	169.4
Nominal	0.256	0.00	1.26	1.00	4.00	7.10 *3.00/4.10*	2.00	3.77	3.77	1.26
Experimental, 0°	0.140	0.017	1.46	1.18	4.72	4.83	2.28	4.06	4.34	1.39
Experimental, 80°	0.083		1.48	1.16	4.62	4.83	2.22	4.68	3.93	1.41
(d) $20\%_{mol}$ $[Rh(COD)_2][TfO]$ in $[C_8C_1Im][TfO]$	Rh $3d_{5/2}$	Rh $3d_{5/2}$ ox	C 1s TfO	C 1s C_2	C 1s hetero	C 1s *alkyl/COD*	N 1s	F 1s	O 1s	S 2p
Binding Energy/eV	309.3	310.4	292.9	287.8	286.9	285.3	402.3	688.8	532.4	169.4
Nominal	0.250	0.00	1.25	1.00	4.00	11.0 *7.00/4.00*	2.00	3.75	3.75	1.25
Experimental, 0°	0.144	0.017	1.38	1.16	4.65	9.33	2.14	3.87	4.16	1.39
Experimental, 80°	0.066		1.19	1.06	4.23	11.7	1.97	3.56	3.18	1.29

The spin−orbit-resolved Rh $3d_{3/2}$ and $3d_{5/2}$ signals are detected at 313.9 and 309.2 eV, respectively. From the fitted 0° spectrum in Figure 2b, an additional small feature at about 1 eV higher binding energy with respect to the major signal can be identified (indicated by an arrow), which indicates an oxidized species. Notably, the corresponding signal in the 80° emission is not detected to a significant extent, and thus is not quantified. The quantitative analysis shown in Table 1b reveals that the 0° signal of the oxidized species amounts to ~14% of the total Rh 3d signal.

As shown in the SI, comparable features are also detected in a similar mixture prepared under the full exclusion of air (Figure S2, spectrum b), and in the solid catalyst powder (spectrum d), indicating an inherent presence of oxidized Rh species. Similar findings were reported by Carvalho et al. for the XP spectra of a solid commercial sample of Wilkinson's catalyst [92]. Notably, we did not observe any X-ray-induced changes over the time period required for the acquisition of all core levels (Figure S2, spectrum c), which rules out that the high-binding energy species is due to beam damage.

The C 1s region in Figure 2a shows a signal at 292.9 eV, which is assigned to the carbon atom C_{TfO} of the $[TfO]^-$ anion, and the C 1s signals at 287.8 and 286.9 eV are assigned to the C_2 and C_{hetero} carbon atoms of the IL cation, respectively. The $C_{alkyl/COD}$ peak at 285.4 eV is attributed to the superposition of the signals of the aliphatic alkyl chain of the IL cation and the COD ligand of the metal-containing cation (for comparison, the ARXPS spectra of the neat IL $[C_2C_1Im][TfO]$ is depicted in Figure S3 in the SI). It is essential to note that the COD ligand involves sp^2 and sp^3 hybridized carbon species in equal amounts, which show significant differences in C 1s binding energy, as found by XPS for carbon materials [93,94]. Nonetheless, in accordance with the binding model for olefinic ligands after Dewar, Chatt, and Duncanson, the σ-donor and π-acceptor binding modes between the COD ligands and

the metal center impose sp^3-like character (rehybridization) for the coordinating carbon atoms [95,96]. Peak-fitting for quantitative analysis was done following an established deconvolution procedure for 1,3-alkylimidazolium cations [84], differentiating three different moieties from the $[C_2C_1Im]^+$ cation C_2, C_{hetero}, and $C_{alkyl/COD}$, as indicated in Figure 1.

The quantitative analysis of the peak intensities detected at 0° emission (as shown in Table 1b) provides information on the stoichiometric composition of the $20\%_{mol}$ mixture (note that the atomic ratio values given in the following are normalized to one imidazolium cation). Note that the nominal contributions of C_{alkyl} (1.0) and C_{COD} (16/4 = 4.0) to the joint $C_{alkyl/COD}$ signal are denoted below the nominal value for this peak. Interestingly, for the major Rh $3d_{5/2}$ signal at 309.2 eV we observe a significantly lower intensity than expected from the nominal composition (0.16 vs. 0.25; which is 63% of the nominal value; the experimental uncertainty of the denoted composition values is 5–10%; to avoid rounding errors, three decimal digits are sometimes provided in the tables). If we assume complete solubility of the metal complex, this observation indicates a strong depletion of the dissolved complex from the IL/vacuum interface, that is, the topmost surface layer. It was recently shown that pronounced enrichment/depletion phenomena in the IL/vacuum interface in catalyst solutions can also significantly affect the more bulk-sensitive 0° XP spectra [76]. A lower than nominal signal is also observed for the $C_{alkyl/COD}$ signal at 285.4 eV. The intensity ratio of $[C_2C_1Im]^+$-specific N 1s, C_2, and C_{hetero} signals is in perfect agreement with that of the nominal atomic composition of the IL cation, confirming its intactness. In addition, these signals concomitantly show a somewhat higher intensity (2.2, 1.1, and 4.4, respectively, that is, by 10%) than expected from the nominal composition of the solution (this is in line with the complex being depleted from the topmost layer); the same increase must also be expected for the C_{alkyl} contribution to the joint $C_{alkyl/COD}$ signal. Consequently, the observed deficiency of the $C_{alkyl/COD}$ signal (2.9 vs. 5.0; or for C_{COD} 1.8 vs. 4.0, that is, 45% of the nominal value) must be entirely assigned to the contribution of C_{COD}. The decrease in C_{COD} to 45% of the nominal value far exceeds that observed for Rh (63%). This indicates a partial non-intactness of the catalyst cation due to the loss of COD ligands, in addition to the depletion of the present complex from the IL/vacuum interface. An illustration of the detected and expected C 1s spectra from nominal proportions is depicted in Figure 2c. As the deconvolution of the C 1s spectra is challenging, we used different procedures for estimation of the actual COD content, which are outlined in the SI. All of the approaches yielded a ratio of about 1.4 COD ligands per metal center, as shown in Table S3b in the SI. The resulting free coordination sites at the Rh center could be occupied by the $[TfO]^-$ anion coordinating via the sulfonate group in manifold binding motifs, e.g., in η^1-$OS(O)_2CF_3$, η^2-$O_2S(O)CF_3$, or μ-$O_2S(O)CF_3$ fashion [97]. This assumption is supported by comparing the O 1s region scans of the catalyst solution (black) and neat $[C_2C_1Im][TfO]$ (blue) in Figure S4. In the catalyst solution, a minor signal (broadening) at higher binding energy with respect to the major peak at 532.4 eV is detected (indicated by an arrow), which is likely due to coordination of the sulfonate groups of the corresponding $[TfO]^-$ anions. However, an alternative explanation for this additional signal could be the above-mentioned oxidized Rh species of an unknown nature.

Interestingly, the extent of ligand loss is even higher in a more diluted solution with a catalyst concentration of $9\%_{mol}$ in the IL. The Rh 3d and C 1s spectra of this diluted solution are shown in Figure 2d (full set of spectra is depicted in Figure S5 in the SI) and the quantitative analysis of the peak intensities is shown in Table 1a. Quantification of the ligand loss yielded 0.8 COD molecules per metal center present in the solution (see Table S3a in the SI). This more pronounced loss of COD ligands is accompanied by a slight shift in Rh 3d signal by 0.2 eV to a higher binding energy with respect to the $20\%_{mol}$ solution, which confirms a (partially) different chemical environment for the metal centers in the solution, depending on the concentration.

The comparison of the XP spectra recorded for the $20\%_{mol}$ solution of $[Rh(COD)_2][TfO]$ in $[C_2C_1Im][TfO]$ at 0° (normal emission) and 80° (grazing emission), depicted in Figure 2a and Figure S1, provides further information on the composition of the IL/vacuum interface.

The quantitative analysis is provided in Table 1b. The Rh 3d signal showed a decline at 80°, which is to be expected for a depletion of the metal complex from the topmost molecular layer. Concomitantly, a lower 80° signal is also detected for $C_{alkyl/COD}$. As the ARXP spectra of neat $[C_2C_1Im][TfO]$ show no significant change in the C_{alkyl} signal at 80° (see Figure S3 and Table S1 in the SI), we attribute the decrease in intensity of the $C_{alkyl/COD}$ signal solely to the contribution of C_{COD}. Hence, as already pointed out above, the organometallic complexes studied here are preferably located in the bulk rather than at the IL/vacuum interface. However, it must be emphasized that the exact structure of the metal-containing cations is unknown due to the ligand loss of the initial catalyst. Notably, for the more diluted solution with a $9\%_{mol}$ catalyst concentration, the decline in Rh 3d signal upon going from 0° to 80° emission is more pronounced, indicating a lower surface concentration of the metal center.

The F 1s signals (see Figure S1) and, to a lower extent, the C_{TfO} signals, show a significantly higher intensity in grazing emission compared with the more bulk-sensitive 0° spectra. Furthermore, the S 2p signal shows a similar intensity at 0° and 80°, and the O 1s peak exhibits a minor decline. These findings are in line with a preferential surface orientation of the $[TfO]^-$ anion with the CF_3 group directed towards the vacuum, whereas the sulfonate group is directed towards the bulk. This orientation is well-known for anions carrying groups with perfluorinated carbon [24,89,98–103], and is also observed for the pure $[C_2C_1Im][TfO]$ (see Figure S3 and Table S1).

Next, we increased the chain length of the aliphatic substituent on the IL cation from C_2 to C_4 and C_8. Figure 3 shows the Rh 3d and C 1s spectra obtained from $20\%_{mol}$ solutions of $[Rh(COD)_2][TfO]$ in $[C_2C_1Im][TfO]$ (black, cf. Figure 2a), $[C_4C_1Im][TfO]$ (green), and $[C_8C_1Im][TfO]$ (orange); the full sets of spectra are shown in Figure S1, Figure S6 and Figure S8, respectively. Their quantitative analysis is provided in Table 1b–d. Overall, we obtain similar findings for the solutions in the longer-chained IL derivatives $[C_4C_1Im][TfO]$ and $[C_8C_1Im][TfO]$ as for $[C_2C_1Im][TfO]$: (a) The Rh species are detected at similar binding energies, indicating a similar overall chemical environment for the metal in solution when increasing the chain length on the imidazolium cation; (b) similar contents of the oxidized minority Rh species (14 ± 3%) with respect to the total Rh signal are detected in 0° emission; (c) for all solutions, the intensity of the major Rh signal is found much lower than expected from nominal composition (59% ± 4% of the nominal value), with a weak trend toward lower values for the longer alkyl chains ($[C_2C_1Im][TfO]$: 63%, $[C_4C_1Im][TfO]$: 55%, $[C_8C_1Im][TfO]$: 58%; as derived from Table 1). These lower values are attributed to the depletion of the metal from the IL/vacuum interface, as discussed above.

For the $[C_4C_1Im][TfO]$ solution, the contribution of the C_{COD} signal to $C_{alkyl/COD}$ shows a larger deficit than expected from the Rh signal, similar to the $[C_2C_1Im][TfO]$ solution as described above; for both, a COD:Rh ratio of ~1.4:1 is found; see Table S3 in the SI. However, such a deficit is not observed for the $[C_8C_1Im][TfO]$ solution, where Rh and C_{COD} both decrease to the same extent, yielding a nominal COD:Rh ratio of ~2.0:1 for the intact $[Rh(COD)_2]^+$ complex. A possible explanation for the absence of ligand loss in the $[C_8C_1Im][TfO]$ solution is that the longer alkyl chains in $[C_8C_1Im][TfO]$ stabilized the complex and prevented (or lower) the ligand loss. One should note here, that the alkyl and COD contributions to the $C_{alkyl/COD}$ peak in the C 1s spectrum cannot be easily separated. Therefore, three different approaches for calculating the COD:Rh ratios are discussed in the Supporting Information, and the most reliable numbers shown in Table S3 of SI are used here.

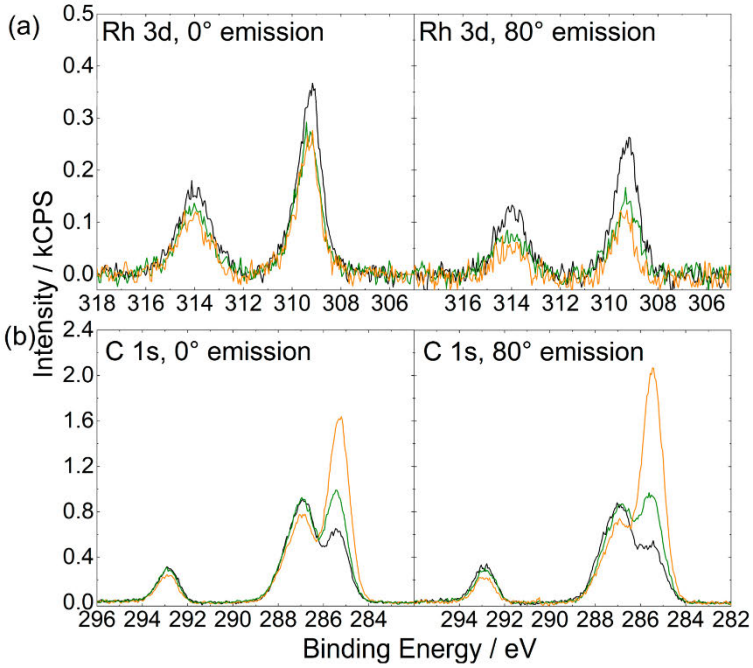

Figure 3. (**a**) Rh 3d and (**b**) C 1s XP spectra of 20%$_{mol}$ solutions of $[Rh(COD)_2][TfO]$ in $[C_2C_1Im][TfO]$ (black), $[C_4C_1Im][TfO]$ (green), and $[C_8C_1Im][TfO]$ (orange) in 0° (left) and 80° (right) emission. All of the spectra were recorded at room temperature.

As shown in Figure 3a, the Rh 3d intensity detected in the 0° emission is found to be lower for the $[C_4C_1Im][TfO]$ and $[C_8C_1Im][TfO]$ solutions compared with the solution of $[C_2C_1Im][TfO]$. This effect is much more pronounced in the more surface-sensitive 80° spectra, where the intensity gradually decreases upon increasing the chain length on the imidazolium cation. At the same time, the $C_{alkyl/COD}$ peak showed a strong increase when comparing 0° and 80° spectra for the $[C_8C_1Im][TfO]$ solution, while for the $[C_4C_1Im][TfO]$ solution, the intensity remains virtually constant and decreases for the solution of $[C_2C_1Im][TfO]$, as discussed above. This behavior indicates a more pronounced depletion of the present complex from the interface, due to the higher surface affinity of the solvent with longer substituents. It is well known that the IL/vacuum interface is preferentially populated with long alkyl chains, resulting in a lower surface tension [24,98,104].

2.2. $[Rh(COD)_2][TfO]$ in $[C_2C_1Im][EtOSO_3]$: Ligand Substitution Using TPPTS

In the previous section, pronounced depletion of the metal center from the IL/vacuum interface, along with ligand loss of $[Rh(COD)_2][TfO]$ dissolved in $[C_2C_1Im][TfO]$ and $[C_4C_1Im][TfO]$, was observed. The latter finding suggests a simple route towards the Schrock−Osborn-type $[Rh(COD)L_2][TfO]$ (L = TPPTS) complex. The expected reaction sequence is shown in Scheme 1. In a previous study, TPPTS has shown a particularly high solubility in $[C_2C_1Im][EtOSO_3]$ and exhibited surface activity [73]. In parallel with the solutions discussed above, we first consider a 20%$_{mol}$ solution of $[Rh(COD)_2][TfO]$ in $[C_2C_1Im][EtOSO_3]$, without adding TPPTS. Figure 4 depicts the ARXPS spectra and Table 2a shows the quantitative analysis of the peak intensities (note that the full set of spectra is shown in Figure S10 in the SI). The spectra show similar characteristics as have

been observed and discussed for $[TfO]^-$ ILs (see above), concerning Rh 3d binding energy, proportion of the oxidized Rh species, deficit of COD ligand, and depletion of the metal from the gas/IL interface. The ARXPS measurements on neat $[C_2C_1Im][EtOSO_3]$ (see Figure S11 for full set of spectra) reveal only a slight increase in the C_{alkyl} signal when comparing the 0° and 80° emission spectra, which corresponds to a preferential surface orientation with the ethyl substituents of the cation and anion towards the vacuum. With this, the decrease in the $C_{alkyl/COD}$ signal seen in Figure 4 has to be fully assigned to the depletion of the metal complex from the gas/IL interface. The O 1s region displays two distinguishable species. $O_{C\text{-}O\text{-}S}$ corresponds to oxygen atoms bound to carbon and to sulfur in the $[EtOSO_3]^-$ anion, while the O_{SO3} signal includes the remaining oxygen atoms from the IL anion and the oxygen atoms from the $[TfO]^-$ anion.

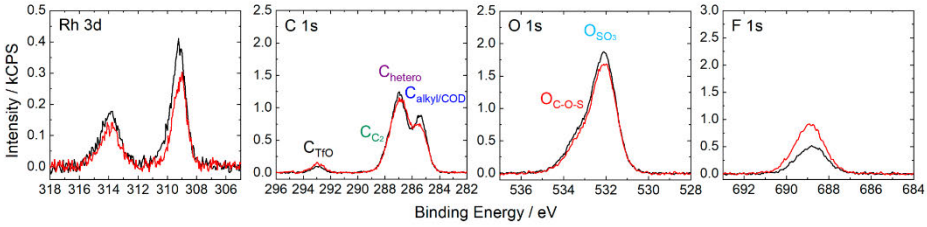

Figure 4. Rh 3d (left), C 1s (middle left), F 1s (middle right), and O 1s (right) XP spectra of a solution of $[Rh(COD)_2][TfO]$ in $[C_2C_1Im][EtOSO_3]$ in 0° (black) and 80° (red) emission recorded at room temperature. For the assignment of peaks to the molecular structure, see Figure 1.

Table 2. Quantitative analysis of ARXPS core level spectra of the solutions relevant for ligand substitution in $[C_2C_1Im][EtOSO_3]$ (note that the exact weighed proportions and concentrations are given in Table S8 in the SI; the experimental uncertainty of the denoted composition values is 5–10%; to avoid rounding errors, three decimal digits are sometimes provided in the tables).

(a) 20%$_{mol}$ $[Rh(COD)_2][TfO]$ in $[C_2C_1Im][EtOSO_3]$	Rh $3d_{5/2}$	Rh $3d_{5/2}$ ox	C 1s TfO	C 1s C_2	C 1s hetero	C 1s *alkyl/ COD*	N 1s	F 1s	O 1s C-O-S	O 1s SO_3	S 2p	P 2p	Na 1s
Binding Energy/eV	309.2	310.2	292.9	287.8	286.9	285.4	402.2	688.8	533.4	532.1	169.5		
Nominal	0.250	0.00	0.250	1.00	5.00	6.00 *2.00/4.00*	2.00	0.750	1.00	3.75	1.25		
Experimental, 0°	0.171	0.025	0.400	1.14	5.70	3.80	2.22	0.983	1.19	4.24	1.39		
Experimental, 80°	0.133		0.634	1.15	5.76	3.29	2.13	1.75	1.02	3.92	1.47		
(b) 5.9%$_{mol}$ solution of TPPTS in $[C_2C_1Im][EtOSO_3]$ (2:31.6 TPPTS:IL ratio)	Rh $3d_{5/2}$	Rh $3d_{5/2}$ ox	C 1s TfO	C 1s C_2	C 1s hetero	C 1s *alkyl/ phenyl*	N 1s	F 1s	O 1s C-O-S	O 1s SO_3	S 2p	P 2p	Na 1s
Binding Energy/eV				287.8	286.9	285.5	402.2		533.4	531.9	169.5	131.7	1071.9
Nominal				1.00	5.00	3.14	2.00		1.00	3.57	1.19	0.063	0.190
Experimental, 0°				0.959	4.80	3.58	1.74		1.12	3.58	1.20	0.060	0.122
Experimental, 80°				0.774	3.87	6.80	1.12		1.01	2.56	0.96		0.063
(c) $[Rh(COD)_2][TfO]$ and TPPTS in $[C_2C_1Im][EtOSO_3]$ (1:2:31.6 Rh:TPPTS:IL ratio)	Rh $3d_{5/2}$	Rh $3d_{5/2}$ ox	C 1s TfO	C 1s C_2	C 1s hetero	C 1s *alkyl/ COD/ phenyl*	N 1s	F 1s	O 1s C-O-S	O 1s SO_3	S 2p	P 2p	Na 1s
Binding Energy/eV	309.0			287.7	286.8	285.5	402.2	688.8	533.3	531.9	169.5	132.5	1071.9
Nominal	0.032	0.00	0.032	1.00	5.00	3.39	2.00	0.095	1.00	3.66	1.22	0.063	0.190
Experimental, 0°	0.031			1.00	4.99	3.55	1.85	0.122	1.10	3.61	1.25	0.054	0.122
Experimental, 80°				0.84	4.19	6.29	1.36	0.200	0.962	2.69	1.09		0.062

The peak intensity detected for the F 1s signal is significantly higher for 0° than expected from the nominal composition. In addition, the peak increase at 80° by far exceeded the magnitude typically observed for a pure orientational effect, as pointed out for the $[TfO]^-$ ILs discussed above. Besides the expected preferential orientation of the $[TfO]^-$ anion with the CF_3 group pointing towards the vacuum, these effects are

attributed to a selective enrichment of $[TfO]^-$ at the IL/vacuum interface. The much larger than nominal C_{TfO} signal, and its enhancement at 80°, supported this interpretation. Interestingly, the enrichment of the $[TfO]^-$ at the IL/vacuum interface is not accompanied by an enrichment of the original counter ion $[Rh(COD)_2]^+$, but rather indicates an ion metathesis at the surface with a higher surface concentration of $[C_2C_1Im]^+$ and $[TfO]^-$ and a lower surface concentration of $[Rh(COD)_2]^+$ and $[EtOSO_3]^-$. Apart from this effect, the behavior of the Rh-containing cation is similar to that in $[C_2C_1Im][TfO]$ and $[C_4C_1Im][TfO]$, in particular concerning the partial loss of the labile COD ligand.

As a next step, we address the desired ligand substitution using TPPTS according to Scheme 1. The maximum solubility of TPPTS in $[C_2C_1Im][EtOSO_3]$ was reported as 16.1%$_{mol}$ in the literature [73]. However, the XPS analysis of a saturated solution of TPPTS in $[C_2C_1Im][EtOSO_3]$ (concentration ~16.6%$_{mol}$ TPPTS, see experimental section and Table S8 for details), as shown in Figure S12 and Table S7, reveals a much lower intensity of TPPTS-specific P and Na signals than expected from the reported solubility. The intensity of the P 2p signal in the 0° emission corresponds to a solubility of ~7%$_{mol}$ of TPPTS in $[C_2C_1Im][EtOSO_3]$ (note that this finding is independent of using acetonitrile as a co-solvent, as has been used in literature [73], or not). Due to the very low intensity of the P 2p signal, a relatively high uncertainty must be expected for the derived solubility. For the ligand substitution reaction, we chose a slightly lower TPPTS content (5.9%$_{mol}$ TPPTS) to ensure full dissolution of the ligand before $[Rh(COD)_2][TfO]$ was added (see below). The full set of ARXPS spectra of the 5.9%$_{mol}$ solution of TPPTS in $[C_2C_1Im][EtOSO_3]$ is shown in Figure S13 (note that a detailed description of the relevant spectra is given below). The quantitative analysis of all signals shown in Table 2b reveals good agreement with the nominal composition, confirming the complete dissolution of TPPTS.

Finally, we discuss the spectra of the solution obtained by adding TPPTS to the ligand substitution, as shown in Figure 5a (full set of spectra shown in Figure S14). The nominal Rh:TPPTS ratio was chosen to be 1:2, as expected for the molecular structure of $[Rh(COD)(TPPTS)_2][TfO]$, and the nominal composition of the solution was chosen according to the 5.9%$_{mol}$ solution of TPPTS in $[C_2C_1Im][EtOSO_3]$, as discussed above. Thus, assuming the quantitative formation of the final complex, a Rh:TPPTS:IL ratio of 1:2:31.6 must be expected (yielding a concentration of 3.1%$_{mol}$ of $[Rh(COD)(TPPTS)_2][TfO]$) in the solution. The quantitative analysis is shown in Table 2c. The Rh $3d_{5/2}$ signal is found at 309.0 eV and thus slightly shifted by 0.2 eV to a lower binding energy compared with the 20%$_{mol}$ solution of $[Rh(COD)_2][TfO]$ in $[C_2C_1Im][EtOSO_3]$ without adding the ligand (cf. Table 2a). Even though the extent of this shift is on the limit of experimental uncertainty, it is in line with coordination of the strong electron donating phosphine ligands. Further proof for successful coordination of TPPTS to the metal center can be extracted from comparison with the spectra obtained from the equimolar solution of TPPTS in $[C_2C_1Im][EtOSO_3]$, as shown in Figures 5b and S13. Comparing the P 2p spectra (middle-right of Figure 5a,b) reveals a shift of 0.7 eV to a higher binding energy for the Rh-containing mixture, which is in accordance with the electron donation of the phosphorus atom to the metal center.

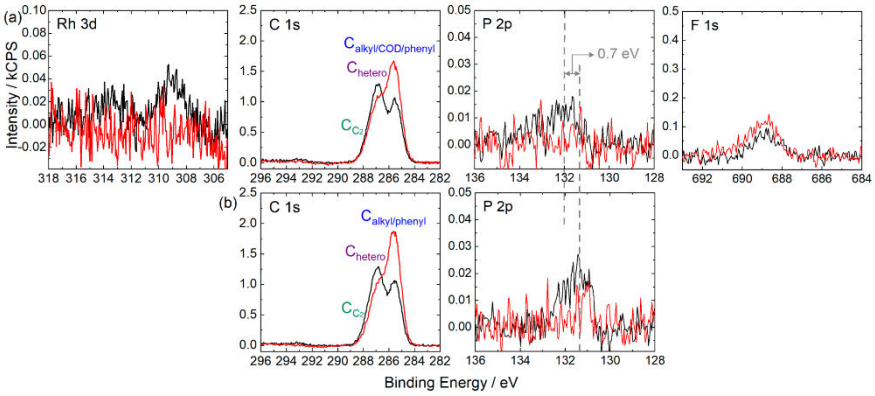

Figure 5. (**a**) Rh 3d (left), C 1s (middle left), F 1s (middle right), and P 2p (right) XP spectra of a solution of $[Rh(COD)_2][TfO]$ and TPPTS in $[C_2C_1Im][EtOSO_3]$ (ratio Rh:TPPTS:IL 1:2:31.6) and (**b**) C 1s and P 2p XP spectra of a solution of TPPTS in $[C_2C_1Im][EtOSO_3]$ (ratio TPPTS:IL 2:31.6) in 0° (black) and 80° (red) emission recorded at room temperature. For the assignment of peaks to the molecular structures, see Figure 1.

As shown in Table 2c, the experimental Rh content in the solution derived from the signal intensities in the 0° emission agrees well with the nominal composition, which is in contrast with the mixtures discussed above, without adding TPPTS, where only 55–68% of the nominal concentration was found (see Tables 1 and 2a). This confirms the presence of the metal complex in the topmost layer, that is, a significantly higher concentration in the surface-near region upon ligand substitution with TPPTS compared with the $[Rh(COD)_2][TfO]$ solutions. All other atomic species are in line with the nominal stoichiometry, except for F 1s and Na 1s. For the F 1s signal, this must be assigned to the enrichment of the $[TfO]^-$ anion at the IL/vacuum interface, as discussed for the $20\%_{mol}$ solution of $[Rh(COD)_2][TfO]$ in $[C_2C_1Im][EtOSO_3]$. For the Na 1s signal, this finding is in agreement with the TPPTS-only solution and indicated preferential depletion of Na^+ from the surface, whereby the SO_3^- groups could be charge-compensated by $[C_2C_1Im]^+$ cations [73]. In the C 1s region, the signals from the TPPTS ligand superimpose with the C_{alkyl} and C_{COD} signals to give a joint $C_{alkyl/COD/phenyl}$ signal. The intensity of this signal strongly increases at 80°, while all other signals show a decrease, except for the F 1s signal, which is due to the enrichment and preferred orientation of the $[TfO]^-$ anion at the surface. The increase in the $C_{alkyl/COD/phenyl}$ signal emphasizes the surface affinity of the TPPTS ligand. In comparison with the TPPTS-only solution (Figure 5b middle-left), the increase is less pronounced for the metal-containing solution, which could be attributed to the contribution of the non-surface-active COD ligand to the signal. This indicates a preferential surface orientation of the complex, with the TPPTS ligands terminating the surface, while the metal center and the COD ligand are directed towards the bulk. Note that due to the low concentration and specific orientation of the final complex, no Rh 3d signal and P 2p signal signals could be resolved at 80°. As can be extracted from Table 2c, the S 2p and O_{SO3} signals show a decrease at 80°, indicating that the non-polar phenyl moieties occupy the outer surface, while the charged SO_3^- groups point towards the bulk, similar to observations made previously [73].

3. Experimental Section

3.1. Materials and Synthesis

[Rh(COD)$_2$][TfO] (purity 98%) and TPPTS (purity 95%) were purchased from Sigma-Aldrich. [C$_2$C$_1$Im][TfO], [C$_4$C$_1$Im][TfO], [C$_8$C$_1$Im][TfO], and [C$_2$C$_1$Im][EtOSO$_3$] (purity of all ILs used was 99%) were purchased from Iolitec. The chemicals were used as delivered.

3.2. Sample Preparation

Exact weighed proportions and concentrations of the solutions employed are given in Table S8 in the SI.

3.3. Solutions of [Rh(COD)$_2$][TfO] in ILs

[Rh(COD)$_2$][TfO] was dissolved in the respective IL under ambient conditions for at least 3 h to produce clear, deep red solutions.

3.4. Saturated Solution of TPPTS in [C$_2$C$_1$Im][EtOSO$_3$]

TPPTS was stirred in [C$_2$C$_1$Im][EtOSO$_3$] under ambient conditions for 3 h. Bigger excess particles of TPPTS were allowed to settle to the ground of the vessel. A white suspension was obtained.

3.5. 5.9.%$_{mol}$ Solution of TPPTS in [C$_2$C$_1$Im][EtOSO$_3$]

TPPTS was stirred in [C$_2$C$_1$Im][EtOSO$_3$] under ambient conditions for 24 h. A small amount of fine particles remained undissolved and were allowed to settle to the ground of the vessel to yield a clear colorless solution. The remaining particles were assigned to insoluble contaminations due the relatively low purity grade of TPPTS (95%).

3.6. Solution for Ligand Substitution

TPPTS was dissolved by stirring for 70 h in [C$_2$C$_1$Im][EtOSO$_3$] in an inert gas atmosphere to yield a solution with similar characteristics as the 5.9%$_{mol}$ solution described above. [Rh(COD)$_2$][TfO] was added and the mixture was stirred for 24 h under vacuum conditions using standard Schlenk techniques to yield a clear, deep red solution. Note that no co-solvent was employed for the preparation of the solution, as it had been used for a similar ligand substitution reaction reported previously [73].

The samples were applied onto the setup-compatible [84] molybdenum sample holders under ambient conditions. Prior to performing the XPS analyses, the samples were left for degassing for at least 12 h in the load-lock of the UHV apparatus.

3.7. ARXPS Measurements and Data Evaluation

XPS analyses were conducted using the DASSA (dual analyzer system for surface analysis) setup comprising two identical analyzers in 0° and in 80° emission geometry. For details, see [84]. We used monochromatized Al-Kα radiation (Source: XM 1000, 14 kV, 238 W, hν = 1486.6 eV).

Survey scans were recorded with a pass energy of 150 eV, while high-resolution region scans were taken with a pass energy of 35 eV. Moreover, 0° spectra were referenced to the F 1s signal of the [TfO]$^-$ anion at 688.8 eV, and 80° spectra were referenced to the binding energy of the N 1s signals of the imidazolium ring at 80°. For the sake of comparability, XP spectra of neat [C$_2$C$_1$Im][EtOSO$_3$] and the solutions of TPPTS in [C$_2$C$_1$Im][EtOSO$_3$] were referenced to the N 1s imidazolium peak of the 20%$_{mol}$ solution of [Rh(COD)$_2$][TfO] in [C$_2$C$_1$Im][EtOSO$_3$].

For quantitative analysis of the intensities, atomic sensitivity factors were used [105]. XP spectra were normalized to the total intensity detected from the region scans of the 20%$_{mol}$ solution of [Rh(COD)$_2$][TfO] in [C$_2$C$_1$Im][TfO]. For the Rh 3d spectra, a Shirley background was subtracted, while for non-metallic species, a two-point linear background subtraction was performed. For the C 1s spectra, a three-point linear background was subtracted, if a C$_{TfO}$ signal at ~293 eV was detected. Peak fitting was achieved using a

Gauss−Lorentzian function with 30% Lorentzian contribution. Individual fitting procedures are outlined in the SI. Deconvolution of spin−orbit resolved signals was achieved using constraints according to the degeneracy ratio of the orbitals with identical full with at half maximum (FWHM) values. Spin−orbit-induced binding energy shifts were constraint as follows: 4.70 eV for Rh 3d, 0.90 eV for P 2p, and 1.21 eV for S 2p. For the sake of visual comparability, the inherently lower intensity of the 80° spectra was compensated for by scaling with a factor derived from the total intensity of all region spectra obtained in the two analyzation geometries [84].

During XPS measurements of solid $[Rh(COD)_2][TfO]$, an electron gun was used for charge compensation.

4. Conclusions

We studied the composition and surface behavior of $[Rh(COD)_2][TfO]$ in $[C_2C_1Im][TfO]$, $[C_4C_1Im][TfO]$, $[C_8C_1Im][TfO]$, and $[C_2C_1Im][EtOSO_3]$ under well-defined UHV conditions by ARXPS. In the ILs with ethyl and butyl chains, we found a deficit of COD ligands indicating non-intactness of the catalyst under measuring conditions. In all cases, the metal species present in the solution are depleted from the IL/vacuum interface. Increasing the chain length of the aliphatic substituent on the imidazolium cation of the $[TfO]^-$-based ILs leads to a more pronounced depletion from this interface, which is most likely due to a higher surface affinity of the solvent cations with longer chains. The stoichiometric deficiency of COD suggests a simple route towards increasing the metal concentration at the IL/vacuum interface by offering a surface-active ligand, such as TPPTS [73]. We propose the formation of a Schrock−Osborn catalyst $[Rh(COD)(TPPTS)_2][TfO]$ by ligand substitution. Indeed, ARXPS investigations show a higher concentration of the metal center at the interface after ligand substitution, as has been observed previously when employing TPPTS [73]. These results are highly relevant for the design of IL-based catalytic systems with high surface areas between catalyst solutions and fluid reactant/product surroundings, such as in SILP or biphasic catalysis.

Supplementary Materials: The following supporting information can be downloaded at: https://www.mdpi.com/article/10.3390/catal13050871/s1, Figure S1: Survey, Rh 3d, C 1s, F 1s, N 1s, O 1s, S 2p and Si 2p XP spectra of a 20%mol solution of [Rh(COD)2][TfO] in [C2C1Im][TfO] in 0° (black) and 80° (red) emission recorded at room temperature with assignment of peaks to the molecular structure; Figure S2: Rh 3d XP spectra of 20%mol solutions of [Rh(COD)2][TfO] in [C2C1Im][TfO] (a) prepared in air, (b) prepared under exclusion of air, (c) solution shown in (b) after more than 100 min of X-radiation. (d) shows the Rh 3d XP spectrum of the solid catalyst. For sake of comparability, the spectrum shown in (d) was referenced to the binding energy of the signal shown in (a). Note that the spectrum shown in (d) shows broadening due to charging of the solid sample. All spectra were recorded in 0° emission at room temperature; Figure S3: Survey, C 1s, F 1s, N 1s, O 1s, S 2p and Si 2p XP spectra of neat [C2C1Im][TfO] in 0° (black) and 80° (red) emission recorded at room temperature with assignment of peaks to the molecular structure; Figure S4: O 1s XP spectra of the 20%mol solution of [Rh(COD)2][TfO] in [C2C1Im][TfO] shown in Figure S1 (black) and neat [C2C1Im][TfO] shown in Figure S3 (blue) in 0° emission recorded at room temperature. The Arrow indicates the additional shoulder in the black spectrum most likely due to [TfO]− anions coordinating to the metal center (for details, see main text); Figure S5: Survey, Rh 3d, C 1s, F 1s, N 1s, O 1s, S 2p and Si 2p XP spectra of a 9%mol solution of [Rh(COD)2][TfO] in [C2C1Im][TfO] in 0° (black) and 80° (red) emission recorded at room temperature with assignment of peaks to the molecular structure; Figure S6: Survey, Rh 3d, C 1s, F 1s, N 1s, O 1s, S 2p and Si 2p XP spectra of a 20%mol solution of [Rh(COD)2][TfO] in [C4C1Im][TfO] in 0° (black) and 80° (red) emission recorded at room temperature with assignment of peaks to the molecular structure; Figure S7: Survey, C 1s, F 1s, N 1s, O 1s, S 2p and Si 2p XP spectra of neat [C4C1Im][TfO] in 0° (black) and 80° (red) emission recorded at room temperature with assignment of peaks to the molecular structure; Figure S8: Survey, Rh 3d, C 1s, F 1s, N 1s, O 1s, S 2p and Si 2p XP spectra of a 20%mol solution of [Rh(COD)2][TfO] in [C8C1Im][TfO] in 0° (black) and 80° (red) emission recorded at room temperature with assignment of peaks to the molecular structure; Figure S9: Survey, C 1s, F 1s, N 1s, O 1s, S 2p and Si 2p XP

spectra of neat [C8C1Im][TfO] in 0° (black) and 80° (red) emission recorded at room temperature with assignment of peaks to the molecular structure; Figure S10: Survey, Rh 3d, C 1s, F 1s, N 1s, O 1s, S 2p and Si 2p XP spectra of a 20%mol solution of [Rh(COD)2][TfO] in [C2C1Im][EtOSO3] in 0° (black) and 80° (red) emission recorded at room temperature with assignment of peaks to the molecular structure; Figure S11: Survey, C 1s, N 1s, O 1s, S 2p and Si 2p XP spectra of neat [C2C1Im][EtOSO3] in 0° (black) and 80° (red) emission recorded at room temperature with assignment of peaks to the molecular structure.; Figure S12: Survey, C 1s, F 1s, N 1s, O 1s, S 2p, P 2p, Na 1s and Si 2p XP spectra of a saturated solution of TPPTS in [C2C1Im][EtOSO3] in 0° (black) and 80° (red) emission recorded at room temperature with assignment of peaks to the molecular structure; Figure S13: Survey, C 1s, F 1s, N 1s, O 1s, S 2p, P 2p, Na 1s and Si 2p XP spectra of a 5.9%mol solution of TPPTS in [C2C1Im][EtOSO3] in 0° (black) and 80° (red) emission recorded at room temperature with assignment of peaks to the molecular structure; Figure S14: Survey, Rh 3d, C 1s, F 1s, N 1s, O 1s, S 2p, P 2p, Na 1s and Si 2p XP spectra of a solution of [Rh(COD)2][TfO] and TPPTS in [C2C1Im][EtOSO3] with 1:2:31.6 ratio in 0° (black) and 80° (red) emission recorded at room temperature with assignment of peaks to the molecular structure; Table S1: Quantitative analysis of ARXPS core level spectra of neat [C2C1Im][TfO]; Table S2: Atomic sensitivity factor (ASF)-corrected intensities obtained from XPS of a 20%mol solution of [Rh(COD)2][TfO] in [C2C1Im][TfO] in 0° emission relevant for the calculation of the actual COD content; Table S3: Estimation of COD content per metal center in 20%mol solutions of [Rh(COD)2][TfO] in [C2C1Im][TfO], [C4C1Im][TfO], [C8C1Im][TfO], [C2C1Im][EtOSO3] (a, c–e) and 9%mol solution in [C2C1Im][TfO] (b) using approaches I, I.2 and II outlined above. As the numbers derived from approach II (bold) are the most reliable one, they are used for the further discussion; Table S4: Quantitative analysis of ARXPS core level spectra of neat [C4C1Im][TfO]; Table S5: Quantitative analysis of ARXPS core level spectra of neat [C8C1Im][TfO]; Table S6: Quantitative analysis of ARXPS core level spectra of neat [C2C1Im][EtOSO3]; Table S7: Quantitative analysis of XPS core level spectra recorded in 0° emission of a solution of TPPTS in [C2C1Im][EtOSO3] assuming a solubility of 16.1%mol; Table S8: Weighed proportions for mixtures investigated in this work; Reference [106] is cited in the supplementary materials.

Author Contributions: Conceptualization, D.H., F.M. and H.-P.S.; methodology, D.H.; software, D.H.; validation, D.H., F.M. and H.-P.S.; formal analysis, D.H.; investigation, D.H. and U.P.; resources, D.H., F.M. and H.-P.S.; data curation, D.H.; writing—original draft preparation, D.H.; writing—review and editing, D.H., F.M. and H.-P.S.; visualization, D.H.; supervision, F.M. and H.-P.S.; project administration, F.M. and H.-P.S.; funding acquisition, H.-P.S. All authors have read and agreed to the published version of the manuscript.

Funding: Funded by the Deutsche Forschungsgemeinschaft (DFG, German Research Foundation)—Project-ID 431791331—SFB 1452. D. H. thanks the Stiftung Stipendien-Fonds of the German chemical industry association (Verband der Chemischen Industrie, VCI) for a Kekulé fellowship.

Data Availability Statement: The data that support the findings of this study are available from the corresponding author upon reasonable request.

Conflicts of Interest: The authors declare no conflict of interest.

References

1. Welton, T. Room-Temperature Ionic Liquids. Solvents for Synthesis and Catalysis. *Chem. Rev.* **1999**, *99*, 2071–2084. [CrossRef] [PubMed]
2. Welton, T. Ionic liquids in catalysis. *Coord. Chem. Rev.* **2004**, *248*, 2459–2477. [CrossRef]
3. Hallett, J.P.; Welton, T. Room-Temperature Ionic Liquids: Solvents for Synthesis and Catalysis. 2. *Chem. Rev.* **2011**, *111*, 3508–3576. [CrossRef] [PubMed]
4. Hayes, R.; Warr, G.G.; Atkin, R. Structure and Nanostructure in Ionic Liquids. *Chem. Rev.* **2015**, *115*, 6357–6426. [CrossRef]
5. Chiappe, C.; Pieraccini, D. Ionic liquids: Solvent properties and organic reactivity. *J. Phys. Org. Chem.* **2005**, *18*, 275–297. [CrossRef]
6. Marullo, S.; D'Anna, F.; Rizzo, C.; Billeci, F. Ionic liquids: "Normal" solvents or nanostructured fluids? *Org. Biomol. Chem.* **2021**, *19*, 2076–2095. [CrossRef]
7. Pešić, J.; Watson, M.; Papović, S.; Vraneš, M. Ionic Liquids: Review of their Current and Future Industrial Applications and their Potential Environmental Impact. *Recent Pat. Nanotechnol.* **2021**, *15*, 225–244. [CrossRef]
8. Greer, A.J.; Jacquemin, J.; Hardacre, C. Industrial Applications of Ionic Liquids. *Molecules* **2020**, *25*, 5207. [CrossRef]
9. Vekariya, R.L. A review of ionic liquids: Applications towards catalytic organic transformations. *J. Mol. Liq.* **2017**, *227*, 44–60. [CrossRef]

10. Martins, M.A.P.; Frizzo, C.P.; Moreira, D.N.; Zanatta, N.; Bonacorso, H.G. Ionic Liquids in Heterocyclic Synthesis. *Chem. Rev.* **2008**, *108*, 2015–2050. [CrossRef]
11. Dhameliya, T.M.; Nagar, P.R.; Bhakhar, K.A.; Jivani, H.R.; Shah, B.J.; Patel, K.M.; Patel, V.S.; Soni, A.H.; Joshi, L.P.; Gajjar, N.D. Recent advancements in applications of ionic liquids in synthetic construction of heterocyclic scaffolds: A spotlight. *J. Mol. Liq.* **2022**, *348*, 118329. [CrossRef]
12. Dai, C.; Zhang, J.; Huang, C.; Lei, Z. Ionic Liquids in Selective Oxidation: Catalysts and Solvents. *Chem. Rev.* **2017**, *117*, 6929–6983. [CrossRef]
13. Dyson, P. Review: Synthesis of organometallics and catalytic hydrogenations in ionic liquids. *Appl. Organomet. Chem. Appl. Organometal. Chem.* **2002**, *16*, 495–500. [CrossRef]
14. Hemmeter, D.; Paap, U.; Taccardi, N.; Mehler, J.; Schulz, P.; Wasserscheid, P.; Maier, F.; Steinrück, H.-P. Formation and surface behavior of Pt and Pd complexes with ligand systems derived from nitrile-functionalized ionic liquids studied by XPS. *ChemPhysChem* **2022**, *24*, e202200391.
15. Zhao, D.; Fei, Z.; Geldbach, T.J.; Scopelliti, R.; Dyson, P.J. Nitrile-Functionalized Pyridinium Ionic Liquids: Synthesis, Characterization, and Their Application in Carbon−Carbon Coupling Reactions. *J. Am. Chem. Soc.* **2004**, *126*, 15876–15882. [CrossRef]
16. He, Z.; Alexandridis, P. Nanoparticles in ionic liquids: Interactions and organization. *Phys. Chem. Chem. Phys.* **2015**, *17*, 18238–18261. [CrossRef]
17. Denicourt-Nowicki, A.; Léger, B.; Roucoux, A. N-Donor ligands based on bipyridine and ionic liquids: An efficient partnership to stabilize rhodium colloids. Focus on oxygen-containing compounds hydrogenation. *Phys. Chem. Chem. Phys.* **2011**, *13*, 13510–13517. [CrossRef]
18. Antonietti, M.; Kuang, D.; Smarsly, B.; Zhou, Y. Ionic Liquids for the Convenient Synthesis of Functional Nanoparticles and Other Inorganic Nanostructures. *Angew. Chem. Int. Ed.* **2004**, *43*, 4988–4992. [CrossRef]
19. Ejigu, A.; Walsh, D.A. Electrocatalysis in Room Temperature Ionic Liquids. In *Electrochemistry in Ionic Liquids: Volume 2: Applications*; Torriero, A.A.J., Ed.; Springer International Publishing: Heidelberg, Germany, 2015; pp. 483–506.
20. Zhang, G.-R.; Etzold, B.J.M. Ionic liquids in electrocatalysis. *J. Energy Chem.* **2016**, *25*, 199–207. [CrossRef]
21. Tan, X.; Sun, X.; Han, B. Ionic liquid-based electrolytes for CO_2 electroreduction and CO_2 electroorganic transformation. *Natl. Sci. Rev.* **2021**, *9*, nwab022. [CrossRef]
22. Itoh, T. Ionic Liquids as Tool to Improve Enzymatic Organic Synthesis. *Chem. Rev.* **2017**, *117*, 10567–10607. [CrossRef] [PubMed]
23. van Rantwijk, F.; Sheldon, R.A. Biocatalysis in Ionic Liquids. *Chem. Rev.* **2007**, *107*, 2757–2785. [CrossRef] [PubMed]
24. Steinrück, H.-P.; Wasserscheid, P. Ionic Liquids in Catalysis. *Catal. Lett.* **2015**, *145*, 380–397. [CrossRef]
25. Bartlewicz, O.; Dąbek, I.; Szymańska, A.; Maciejewski, H. Heterogeneous Catalysis with the Participation of Ionic Liquids. *Catalysts* **2020**, *10*, 1227. [CrossRef]
26. Meyer, C.; Hager, V.; Schwieger, W.; Wasserscheid, P. Enhanced activity and selectivity in n-octane isomerization using a bifunctional SCILL catalyst. *J. Catal.* **2012**, *292*, 157–165. [CrossRef]
27. Kernchen, U.; Etzold, B.; Korth, W.; Jess, A. Solid Catalyst with Ionic Liquid Layer (SCILL)—A New Concept to Improve Selectivity Illustrated by Hydrogenation of Cyclooctadiene. *Chem. Eng. Technol.* **2007**, *30*, 985–994. [CrossRef]
28. Riisager, A.; Fehrmann, R.; Haumann, M.; Wasserscheid, P. Supported Ionic Liquid Phase (SILP) Catalysis: An Innovative Concept for Homogeneous Catalysis in Continuous Fixed-Bed Reactors. *Eur. J. Inorg. Chem.* **2006**, *2006*, 695–706. [CrossRef]
29. Riisager, A.; Jørgensen, B.; Wasserscheid, P.; Fehrmann, R. First application of supported ionic liquid phase (SILP) catalysis for continuous methanol carbonylation. *Chem. Commun.* **2006**, *9*, 994–996. [CrossRef]
30. Marinkovic, J.M.; Riisager, A.; Franke, R.; Wasserscheid, P.; Haumann, M. Fifteen Years of Supported Ionic Liquid Phase-Catalyzed Hydroformylation: Material and Process Developments. *Ind. Eng. Chem. Res.* **2019**, *58*, 2409–2420. [CrossRef]
31. Baldelli, S. Interfacial Structure of Room-Temperature Ionic Liquids at the Solid–Liquid Interface as Probed by Sum Frequency Generation Spectroscopy. *J. Phys. Chem. Lett.* **2013**, *4*, 244–252. [CrossRef]
32. Peñalber-Johnstone, C.; Adamová, G.; Plechkova, N.V.; Bahrami, M.; Ghaed-Sharaf, T.; Ghatee, M.H.; Seddon, K.R.; Baldelli, S. Sum frequency generation spectroscopy of tetraalkylphosphonium ionic liquids at the air–liquid interface. *J. Chem. Phys.* **2018**, *148*, 193841. [CrossRef]
33. Huo, F.; Ding, J.; Tong, J.; He, H. Ionic liquid-air interface probed by sum frequency generation spectroscopy and molecular dynamics simulation: Influence of alkyl chain length and anion volume. *Mol. Simul.* **2022**, *48*, 844–854. [CrossRef]
34. Iwahashi, T.; Ishiyama, T.; Sakai, Y.; Morita, A.; Kim, D.; Ouchi, Y. Bi-layering at ionic liquid surfaces: A sum-frequency generation vibrational spectroscopy- and molecular dynamics simulation-based study. *Phys. Chem. Chem. Phys.* **2020**, *22*, 12565–12576. [CrossRef]
35. Sissaoui, J.; Budkina, D.S.; Vauthey, E. Probing Liquid Interfaces with Room-Temperature Ionic Liquids Using the Excited-State Dynamics of a Cationic Dye. *J. Phys. Chem. B* **2020**, *124*, 10546–10555. [CrossRef]
36. Nishi, N.; Ishimatsu, R.; Yamamoto, M.; Kakiuchi, T. Orientation of 1-Dodecyl-4-phenylpyridinium Ions Constituting an Ionic Liquid at the Ionic Liquid | Water Interface Studied by Second Harmonic Generation. *J. Phys. Chem. C* **2007**, *111*, 12461–12466. [CrossRef]
37. Costa, R.; Pereira, C.M.; Silva, A.F.; Brevet, P.-F.; Benichou, E. Ordering and Nonideality of Air–Ionic Liquid Interfaces in Surface Second Harmonic Generation. *J. Phys. Chem. B* **2020**, *124*, 3954–3961. [CrossRef]

38. An, R.; Wei, Y.; Qiu, X.; Dai, Z.; Wu, M.; Gnecco, E.; Shah, F.U.; Zhang, W. Ionic liquids on uncharged and charged surfaces: In situ microstructures and nanofriction. *Friction* **2022**, *10*, 1893–1912. [CrossRef]
39. Liu, S.; Peng, J.; Chen, L.; Sebastián, P.; Feliu, J.M.; Yan, J.; Mao, B. In-situ STM and AFM Studies on Electrochemical Interfaces in imidazolium-based ionic liquids. *Electrochim. Acta* **2019**, *309*, 11–17. [CrossRef]
40. Endres, F.; Borisenko, N.; El Abedin, S.Z.; Hayes, R.; Atkin, R. The interface ionic liquid(s)/electrode(s): In situ STM and AFM measurements. *Faraday Discuss.* **2012**, *154*, 221–233; discussion 313–333, 465–471. [CrossRef]
41. Rodenbücher, C.; Wippermann, K.; Korte, C. Atomic Force Spectroscopy on Ionic Liquids. *Appl. Sci.* **2019**, *9*, 2207. [CrossRef]
42. Pajkossy, T.; Müller, C.; Jacob, T. The metal–ionic liquid interface as characterized by impedance spectroscopy and in situ scanning tunneling microscopy. *Phys. Chem. Chem. Phys.* **2018**, *20*, 21241–21250. [CrossRef] [PubMed]
43. Sloutskin, E.; Ocko, B.M.; Tamam, L.; Kuzmenko, I.; Gog, T.; Deutsch, M. Surface Layering in Ionic Liquids: An X-ray Reflectivity Study. *J. Am. Chem. Soc.* **2005**, *127*, 7796–7804. [CrossRef] [PubMed]
44. Mars, J.; Hou, B.; Weiss, H.; Li, H.; Konovalov, O.; Festersen, S.; Murphy, B.M.; Rütt, U.; Bier, M.; Mezger, M. Surface induced smectic order in ionic liquids—An X-ray reflectivity study of $[C_{22}C_1im]^+[NTf_2]^-$. *Phys. Chem. Chem. Phys.* **2017**, *19*, 26651–26661, Erratum in *Phys. Chem. Chem. Phys.* **2018**, *20*, 24494–24495. [CrossRef] [PubMed]
45. Villar-Garcia, I.J.; Fearn, S.; De Gregorio, G.F.; Ismail, N.L.; Gschwend, F.J.V.; McIntosh, A.J.S.; Lovelock, K.R.J. The ionic liquid–vacuum outer atomic surface: A low-energy ion scattering study. *Chem. Sci.* **2014**, *5*, 4404–4418. [CrossRef]
46. Kauling, A.; Ebeling, G.; Morais, J.; Pádua, A.; Grehl, T.; Brongersma, H.H.; Dupont, J. Surface Composition/Organization of Ionic Liquids with Au Nanoparticles Revealed by High-Sensitivity Low-Energy Ion Scattering. *Langmuir* **2013**, *29*, 14301–14306. [CrossRef]
47. Nakajima, K.; Miyashita, M.; Suzuki, M.; Kimura, K. Surface structures of binary mixtures of imidazolium-based ionic liquids using high-resolution Rutherford backscattering spectroscopy and time of flight secondary ion mass spectroscopy. *J. Chem. Phys.* **2013**, *139*, 224701. [CrossRef]
48. Bomhardt, K.; Schneider, P.; Glaser, T.; Dürr, M. Surface Properties of Ionic Liquids: A Mass Spectrometric View Based on Soft Cluster-Induced Desorption. *J. Am. Soc. Mass. Spectrom.* **2022**, *33*, 974–980. [CrossRef]
49. Krischok, S.; Eremtchenko, M.; Himmerlich, M.; Lorenz, P.; Uhlig, J.; Neumann, A.; Öttking, R.; Beenken, W.J.D.; Höfft, O.; Bahr, S.; et al. Temperature-Dependent Electronic and Vibrational Structure of the 1-Ethyl-3-methylimidazolium Bis(trifluoromethylsulfonyl)amide Room-Temperature Ionic Liquid Surface: A Study with XPS, UPS, MIES, and HREELS. *J. Phys. Chem. B* **2007**, *111*, 4801–4806. [CrossRef]
50. Krischok, S.; Ulbrich, A.; Ikari, T.; Kempter, V.; Marschewski, M.; Höfft, O. Surface structure of [XMIm]Tf2N ultrathin ionic liquid films probed by metastable He atoms and photoelectron spectroscopies (UPS and XPS). *Nucl. Instrum. Methods Phys. Res. Sect. B Beam Interact. Mater. At.* **2014**, *340*, 51–57. [CrossRef]
51. Biedron, A.B.; Garfunkel, E.L.; Castner, E.W., Jr.; Rangan, S. Ionic liquid ultrathin films at the surface of Cu(100) and Au(111). *J. Chem. Phys.* **2017**, *146*, 054704. [CrossRef]
52. Smoll, E.J.; Tesa-Serrate, M.A.; Purcell, S.M.; D'Andrea, L.; Bruce, D.W.; Slattery, J.M.; Costen, M.L.; Minton, T.K.; McKendrick, K.G. Determining the composition of the vacuum–liquid interface in ionic-liquid mixtures. *Faraday Discuss.* **2018**, *206*, 497–522. [CrossRef]
53. Tesa-Serrate, M.A.; Marshall, B.C.; Smoll, E.J., Jr.; Purcell, S.M.; Costen, M.L.; Slattery, J.M.; Minton, T.K.; McKendrick, K.G. Ionic Liquid–Vacuum Interfaces Probed by Reactive Atom Scattering: Influence of Alkyl Chain Length and Anion Volume. *J. Phys. Chem. C* **2015**, *119*, 5491–5505. [CrossRef]
54. Purcell, S.M.; Lane, P.D.; D'Andrea, L.; Elstone, N.S.; Bruce, D.W.; Slattery, J.M.; Smoll, E.J., Jr.; Greaves, S.J.; Costen, M.L.; Minton, T.K.; et al. Surface Structure of Alkyl/Fluoroalkylimidazolium Ionic–Liquid Mixtures. *J. Phys. Chem. B* **2022**, *126*, 1962–1979. [CrossRef]
55. Meusel, M.; Gezmis, A.; Jaekel, S.; Lexow, M.; Bayer, A.; Maier, F.; Steinrück, H.-P. Time- and Temperature-Dependent Growth Behavior of Ionic Liquids on Au(111) Studied by Atomic Force Microscopy in Ultrahigh Vacuum. *J. Phys. Chem. C* **2021**, *125*, 20439–20449. [CrossRef]
56. Meusel, M.; Lexow, M.; Gezmis, A.; Bayer, A.; Maier, F.; Steinrück, H.-P. Growth of Multilayers of Ionic Liquids on Au(111) Investigated by Atomic Force Microscopy in Ultrahigh Vacuum. *Langmuir* **2020**, *36*, 13670–13681. [CrossRef]
57. Meusel, M.; Lexow, M.; Gezmis, A.; Schötz, S.; Wagner, M.; Bayer, A.; Maier, F.; Steinrück, H.-P. Atomic Force and Scanning Tunneling Microscopy of Ordered Ionic Liquid Wetting Layers from 110 K up to Room Temperature. *ACS Nano* **2020**, *14*, 9000–9010. [CrossRef]
58. Uhl, B.; Buchner, F.; Alwast, D.; Wgner, N.; Behm, R.J. Adsorption of the ionic liquid [BMP][TFSA] on Au(111) and Ag(111): Substrate effects on the structure formation investigated by STM. *Beilstein J. Nanotechnol.* **2013**, *4*, 903–918. [CrossRef]
59. Waldmann, T.; Huang, H.-H.; Hoster, H.E.; Höfft, O.; Endres, F.; Behm, R.J. Imaging an Ionic Liquid Adlayer by Scanning Tunneling Microscopy at the Solid | Vacuum Interface. *ChemPhysChem* **2011**, *12*, 2565–2567. [CrossRef]
60. Seidl, V.; Bosch, M.; Paap, U.; Livraghi, M.; Zhai, Z.; Wick, C.R.; Koller, T.M.; Wasserscheid, P.; Maier, F.; Smith, A.-S.; et al. Bis-polyethylene glycol-functionalized imidazolium ionic liquids: A multi-method approach towards bulk and surface properties. *J. Ion. Liq.* **2022**, *2*, 100041. [CrossRef]

61. Kolbeck, C.; Niedermaier, I.; Deyko, A.; Lovelock, K.R.J.; Taccardi, N.; Wei, W.; Wasserscheid, P.; Maier, F.; Steinrück, H.-P. Influence of Substituents and Functional Groups on the Surface Composition of Ionic Liquids. *Chem. Eur. J.* **2014**, *20*, 3954–3965. [CrossRef] [PubMed]
62. Kolbeck, C.; Killian, M.; Maier, F.; Paape, N.; Wasserscheid, P.; Steinrück, H.-P. Surface Characterization of Functionalized Imidazolium-Based Ionic Liquids. *Langmuir* **2008**, *24*, 9500–9507. [CrossRef] [PubMed]
63. Dick, E.J.; Fouda, A.E.A.; Besley, N.A.; Licence, P. Probing the electronic structure of ether functionalised ionic liquids using X-ray photoelectron spectroscopy. *Phys. Chem. Chem. Phys.* **2020**, *22*, 1624–1631. [CrossRef] [PubMed]
64. Kolbeck, C.; Cremer, T.; Lovelock, K.R.J.; Paape, N.; Schulz, P.S.; Wasserscheid, P.; Maier, F.; Steinrück, H.P. Influence of Different Anions on the Surface Composition of Ionic Liquids Studied Using ARXPS. *J. Phys. Chem. B* **2009**, *113*, 8682–8688. [CrossRef]
65. Men, S.; Sun, Y.; Licence, P.; Qu, J. X-ray photoelectron spectroscopy of morpholinium ionic liquids: Impact of a long alkyl side substituent on the cation–anion interactions. *Phys. Chem. Chem. Phys.* **2022**, *24*, 24845–24851. [CrossRef]
66. Lexow, M.; Maier, F.; Steinrück, H.-P. Ultrathin ionic liquid films on metal surfaces: Adsorption, growth, stability and exchange phenomena. *Adv. Phys. X* **2020**, *5*, 1761266. [CrossRef]
67. Heller, B.S.J.; Paap, U.; Maier, F.; Steinrück, H.-P. Pronounced surface enrichment of fluorinated ionic liquids in binary mixtures with methoxy-functionalized ionic liquids. *J. Mol. Liq.* **2020**, *305*, 112783. [CrossRef]
68. Heller, B.S.J.; Kolbeck, C.; Niedermaier, I.; Dommer, S.; Schatz, J.; Hunt, P.; Maier, F.; Steinrück, H.-P. Surface Enrichment in Equimolar Mixtures of Non-Functionalized and Functionalized Imidazolium-Based Ionic Liquids. *ChemPhysChem* **2018**, *19*, 1733–1745. [CrossRef]
69. Heller, B.S.J.; Lexow, M.; Greco, F.; Shin, S.; Partl, G.; Maier, F.; Steinrück, H.-P. Temperature-Dependent Surface Enrichment Effects in Binary Mixtures of Fluorinated and Non-Fluorinated Ionic Liquids. *Chem. Eur. J.* **2020**, *26*, 1117–1126. [CrossRef]
70. Paap, U.; Seidl, V.; Meyer, K.; Maier, F.; Steinrück, H.-P. Direct Correlation of Surface Tension and Surface Composition of Ionic Liquid Mixtures—A Combined Vacuum Pendant Drop and Angle-Resolved X-ray Photoelectron Spectroscopy Study. *Molecules* **2022**, *27*, 8561. [CrossRef]
71. Oz, E.; Sahin, O.; Okur, H.I.; Suzer, S. Surface Propensity of Anions in a Binary Ionic-Liquid Mixture Assessed by Full-Range Angle-Resolved X-ray Photoelectron Spectroscopy and Surface-Tension Measurements. *ChemPhysChem* **2020**, *21*, 2397–2401. [CrossRef]
72. Zhang, Y.; Khalifa, Y.; Maginn, E.J.; Newberg, J.T. Anion Enhancement at the Liquid–Vacuum Interface of an Ionic Liquid Mixture. *J. Phys. Chem. C* **2018**, *122*, 27392–27401. [CrossRef]
73. Kolbeck, C.; Paape, N.; Cremer, T.; Schulz, P.S.; Maier, F.; Steinrück, H.-P.; Wasserscheid, P. Ligand Effects on the Surface Composition of Rh-Containing Ionic Liquid Solutions Used in Hydroformylation Catalysis. *Chem. Eur. J.* **2010**, *16*, 12083–12087. [CrossRef]
74. Kolbeck, C.; Taccardi, N.; Paape, N.; Schulz, P.S.; Wasserscheid, P.; Steinrück, H.-P.; Maier, F. Redox chemistry, solubility, and surface distribution of Pt(II) and Pt(IV) complexes dissolved in ionic liquids. *J. Mol. Liq.* **2014**, *192*, 103–113. [CrossRef]
75. Maier, F.; Gottfried, J.M.; Rossa, J.; Gerhard, D.; Schulz, P.S.; Schwieger, W.; Wasserscheid, P.; Steinrück, H.-P. Surface Enrichment and Depletion Effects of Ions Dissolved in an Ionic Liquid: An X-ray Photoelectron Spectroscopy Study. *Angew. Chem. Int. Ed.* **2006**, *45*, 7778–7780. [CrossRef]
76. Hemmeter, D.; Kremitzl, D.; Schulz, P.S.; Wasserscheid, P.; Maier, F.; Steinrück, H.-P. The Buoy Effect: Surface Enrichment of a Pt Complex in IL Solution by Ligand Design. *Chem. Eur. J.* **2023**, *29*, e202203325. [CrossRef]
77. Dimitrova, A.; Walle, M.; Himmerlich, M.; Krischok, S. Surface composition of [BMP][Tf_2N] and [PMIm][Tf_2N] in the presence of NbF_5 and TaF_5. A photoelectron spectroscopy study. *J. Mol. Liq.* **2017**, *226*, 78–84. [CrossRef]
78. Kurisaki, T.; Tanaka, D.; Inoue, Y.; Wakita, H.; Minofar, B.; Fukuda, S.; Ishiguro, S.-i.; Umebayashi, Y. Surface Analysis of Ionic Liquids with and without Lithium Salt Using X-ray Photoelectron Spectroscopy. *J. Phys. Chem. B* **2012**, *116*, 10870–10875. [CrossRef] [PubMed]
79. Smoll, E.J.; Chen, X.; Hall, L.M.; D'Andrea, L.; Slattery, J.M.; Minton, T.K. Probing a Ruthenium Coordination Complex at the Ionic Liquid–Vacuum Interface with Reactive-Atom Scattering, X-ray Photoelectron Spectroscopy, and Time-of-Flight Secondary Ion Mass Spectrometry. *J. Phys. Chem. C* **2020**, *124*, 382–397. [CrossRef]
80. Men, S.; Jiang, J. X-ray photoelectron spectroscopy as a probe of the interaction between rhodium acetate and ionic liquids. *Chem. Phys. Lett.* **2016**, *646*, 125–129. [CrossRef]
81. Men, S.; Jin, Y. Rhodium Catalyst-Ionic Liquids Interaction by X-ray Photoelectron Spectroscopy Data. *Russ. J. Phys. Chem. A* **2018**, *92*, 2472.
82. Men, S.; Lovelock, K.R.J.; Licence, P. Directly probing the effect of the solvent on a catalyst electronic environment using X-ray photoelectron spectroscopy. *RSC Adv.* **2015**, *5*, 35958–35965. [CrossRef]
83. Men, S.; Jiang, J. Probing the Formation of the NHC-Palladium Species in Ionic Liquids by X-ray Photoelectron Spectroscopy. *Russ. J. Phys. Chem. A* **2018**, *92*, 1627–1630.
84. Niedermaier, I.; Kolbeck, C.; Steinrück, H.-P.; Maier, F. Dual analyzer system for surface analysis dedicated for angle-resolved photoelectron spectroscopy at liquid surfaces and interfaces. *Rev. Sci. Instrum.* **2016**, *87*, 045105. [CrossRef]
85. Steinrück, H.-P. Recent developments in the study of ionic liquid interfaces using X-ray photoelectron spectroscopy and potential future directions. *Phys. Chem. Chem. Phys.* **2012**, *14*, 5010–5029. [CrossRef]

86. Steinrück, H.-P.; Libuda, J.; Wasserscheid, P.; Cremer, T.; Kolbeck, C.; Laurin, M.; Maier, F.; Sobota, M.; Schulz, P.S.; Stark, M. Surface Science and Model Catalysis with Ionic Liquid-Modified Materials. *Adv. Mater.* **2011**, *23*, 2571–2587. [CrossRef]
87. Blundell, R.K.; Delorme, A.E.; Smith, E.F.; Licence, P. An ARXPS and ERXPS study of quaternary ammonium and phosphonium ionic liquids: Utilising a high energy Ag Lα' X-ray source. *Phys. Chem. Chem. Phys.* **2016**, *18*, 6122–6131. [CrossRef]
88. Men, S.; Hurisso, B.B.; Lovelock, K.R.J.; Licence, P. Does the influence of substituents impact upon the surface composition of pyrrolidinium-based ionic liquids? An angle resolved XPS study. *Phys. Chem. Chem. Phys.* **2012**, *14*, 5229–5238. [CrossRef]
89. Lockett, V.; Sedev, R.; Harmer, S.; Ralston, J.; Horne, M.; Rodopoulos, T. Orientation and mutual location of ions at the surface of ionic liquids. *Phys. Chem. Chem. Phys.* **2010**, *12*, 13816–13827. [CrossRef]
90. Suarez, P.A.Z.; Dullius, J.E.L.; Einloft, S.; De Souza, R.F.; Dupont, J. The use of new ionic liquids in two-phase catalytic hydrogenation reaction by rhodium complexes. *Polyhedron* **1996**, *15*, 1217–1219. [CrossRef]
91. Nindakova, L.O.; Shainyan, B.A.; Albanov, A.I.; Shmidt, F.K. Double Stereoselection in the Hydrogenation over Cationic Rh(I) Complexes with Two Different Chiral Ligands. *Russ. J. Org. Chem.* **2003**, *39*, 926–932. [CrossRef]
92. Carvalho, M.; Wieserman, L.F.; Hercules, D.M. Spectroscopic Characterization of Wilkinson's Catalyst Using X-ray Photoelectron Spectroscopy (ESCA). *Appl. Spectrosc.* **1982**, *36*, 290–296. [CrossRef]
93. Díaz, J.; Paolicelli, G.; Ferrer, S.; Comin, F. Separation of the sp3 and sp2 components in the C1s photoemission spectra of amorphous carbon films. *Phys. Rev. B Condens. Matter* **1996**, *54*, 8064–8069. [CrossRef]
94. Fujimoto, A.; Yamada, Y.; Koinuma, M.; Sato, S. Origins of sp3C peaks in C1s X-ray Photoelectron Spectra of Carbon Materials. *Anal. Chem.* **2016**, *88*, 6110–6114. [CrossRef]
95. Dewar, M.J.S. A Review of the-Complex Theory. *Bull. Soc. Chim. Fr.* **1951**, *18*, C79.
96. Chatt, J.; Duncanson, L.A. 586. Olefin co-ordination compounds. Part III. Infra-red spectra and structure: Attempted preparation of acetylene complexes. *J. Chem. Soc. (Resumed)* **1953**, 2939–2947. [CrossRef]
97. Werner, H.; Bosch, M.; Schneider, M.E.; Hahn, C.; Kukla, F.; Manger, M.; Windmüller, B.; Weberndörfer, B.; Laubender, M. Preparation, molecular structure and reactivity of mono- and di-nuclear sulfonato rhodium(I) complexes. *J. Chem. Soc. Dalton Trans.* **1998**, *21*, 3549–3558. [CrossRef]
98. Lovelock, K.R.J.; Kolbeck, C.; Cremer, T.; Paape, N.; Schulz, P.S.; Wasserscheid, P.; Maier, F.; Steinrück, H.P. Influence of Different Substituents on the Surface Composition of Ionic Liquids Studied Using ARXPS. *J. Phys. Chem. B* **2009**, *113*, 2854–2864. [CrossRef]
99. Nakajima, K.; Ohno, A.; Suzuki, M.; Kimura, K. Observation of Molecular Ordering at the Surface of Trimethylpropylammonium Bis(trifluoromethanesulfonyl)imide Using High-Resolution Rutherford Backscattering Spectroscopy. *Langmuir* **2008**, *24*, 4482–4484. [CrossRef]
100. Nakajima, K.; Lísal, M.; Kimura, K. Surfaces of Ionic Liquids. In *Surface and Interface Science*; Wandelt, K., Ed.; Wiley-VCH Verlag GmbH & Co. KGaA: Weinheim, Germany, 2020; pp. 351–389.
101. Maier, F.; Cremer, T.; Kolbeck, C.; Lovelock, K.R.J.; Paape, N.; Schulz, P.S.; Wasserscheid, P.; Steinrück, H.P. Insights into the surface composition and enrichment effects of ionic liquids and ionic liquid mixtures. *Phys. Chem. Chem. Phys.* **2010**, *12*, 1905–1915. [CrossRef]
102. Sanmartín Pensado, A.; Malfreyt, P.; Pádua, A.A.H. Molecular Dynamics Simulations of the Liquid Surface of the Ionic Liquid 1-Hexyl-3-methylimidazolium Bis(trifluoromethanesulfonyl)amide: Structure and Surface Tension. *J. Phys. Chem. B* **2009**, *113*, 14708–14718. [CrossRef] [PubMed]
103. Iwahashi, T.; Miyamae, T.; Kanai, K.; Seki, K.; Kim, D.; Ouchi, Y. Anion Configuration at the Air/Liquid Interface of Ionic Liquid [bmim]OTf Studied by Sum-Frequency Generation Spectroscopy. *J. Phys. Chem. B* **2008**, *112*, 11936–11941. [CrossRef] [PubMed]
104. Kolbeck, C.; Lehmann, J.; Lovelock, K.R.J.; Cremer, T.; Paape, N.; Wasserscheid, P.; Fröba, A.P.; Maier, F.; Steinrück, H.P. Density and Surface Tension of Ionic Liquids. *J. Phys. Chem. B* **2010**, *114*, 17025–17036. [CrossRef]
105. Wagner, C.D.; Davis, L.E.; Zeller, M.V.; Taylor, J.A.; Raymond, R.H.; Gale, L.H. Empirical Atomic Sensitivity Factors for Quantitative Analysis by Electron Spectroscopy for Chemical Analysis. *Surf. Interface Anal.* **1981**, *3*, 211–225. [CrossRef]
106. Gottfried, J.M.; Maier, F.; Rossa, J.; Gerhard, D.; Schulz, P.S.; Wasserscheid, P.; Steinrück, H.-P. Surface Studies on the Ionic Liquid 1-Ethyl-3-Methylimidazolium Ethylsulfate Using X-Ray Photoelectron Spectroscopy (XPS). *Z. Phys. Chem.* **2006**, *220*, 1439–1453. [CrossRef]

Supporting Information

Structure and Surface Behavior of Rh Complexes in Ionic Liquids Studied by Angle-Resolved X-ray Photoelectron Spectroscopy

by Daniel Hemmeter, Ulrike Paap, Florian Maier, Hans-Peter Steinrück

The supporting information (SI) presents fitting procedures and full sets of all relevant core levels recorded from 20‰$_{mol}$ solutions of $[Rh(COD)_2][TfO]$ in $[C_2C_1Im][TfO]$ (*figure S1*), $[C_4C_1Im][TfO]$ (*figure S6*), $[C_8C_1Im][TfO]$ (*figure S8*) and $[C_2C_1Im][EtOSO_3]$ (*figure S10*), as well as a 9‰$_{mol}$ solution of $[Rh(COD)_2][TfO]$ in $[C_2C_1Im][TfO]$ (*figure S5*) and neat $[C_2C_1Im][TfO]$ (*figure S3*), $[C_4C_1Im][TfO]$ (*figure S7*), $[C_8C_1Im][TfO]$ (*figure S9*) and $[C_2C_1Im][EtOSO_3]$ (*figure S11*). For the neat ILs, the quantitative analysis of the high-resolution region spectra is given (*tables 1, 4-6*). Moreover, ARXPS spectra are shown for a solution of $[Rh(COD)_2][TfO]$ and TPPTS in $[C_2C_1Im][EtOSO_3]$ with 1:2:31.6 ratio (*figure S14*), for a saturated solution of TPPTS in $[C_2C_1Im][EtOSO_3]$ (*figure S12,* quantitative analysis of 0° spectra in *table S7*)) and for a 5.9‰$_{mol}$ solution of TPPTS in $[C_2C_1Im][EtOSO_3]$ (*figure S13*), that is, a similar TPPTS:IL ratio as in the respective Rh-containing solution (*figure S14*). In all cases, Si 2p spectra are depicted to confirm absence of common surface-active contaminations observed in previous studies[107]. Furthermore, a waterfall plot of Rh 3d spectra (*figure S2*) is shown for a 20‰$_{mol}$ solution of $[Rh(COD)_2][TfO]$ in $[C_2C_1Im][TfO]$ prepared in air, under full exclusion of air and after more than 100 min of exposure to X-radiation, as well as for solid $[Rh(COD)_2][TfO]$. A comparison of O 1s spectra of the 20‰$_{mol}$ solution of $[Rh(COD)_2][TfO]$ in $[C_2C_1Im][TfO]$ and neat $[C_2C_1Im][TfO]$ is further presented (*figure S4*). In addition, details on the different approaches for estimating the loss of COD in the $[Rh(COD)_2][TfO]$ solutions are presented, together with an overview of the final results (*table S3*). Since the 20‰$_{mol}$ solution of $[Rh(COD)_2][TfO]$ in $[C_2C_1Im][TfO]$ serves for the exemplary calculation, the atomic sensitivity factor (ASF)-corrected intensities of relevant peaks are given (*table S2*). Finally, the weighed proportions for preparation of the solutions (*table S8*) and other material-related details are shown.

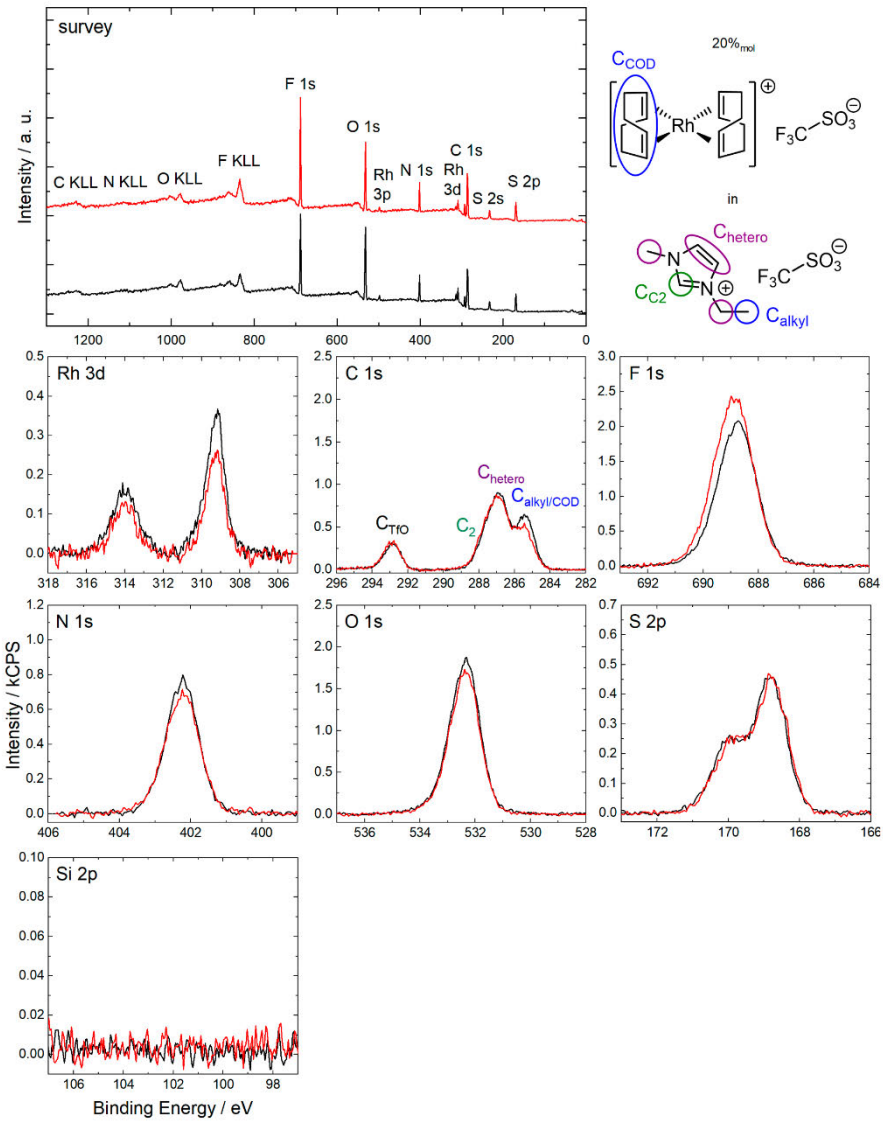

***Figure S1**: Survey, Rh 3d, C 1s, F 1s, N 1s, O 1s, S 2p and Si 2p XP spectra of a 20%$_{mol}$ solution of [Rh(COD)$_2$][TfO] in [C$_2$C$_1$Im][TfO] in 0° (black) and 80° (red) emission recorded at room temperature with assignment of peaks to the molecular structure.*

Fitting of the C 1s region was achieved using an established procedure for 1,3-alkylimidazolium based ILs[85]. The contribution of the C_{COD} signals is discussed in the main manuscript.

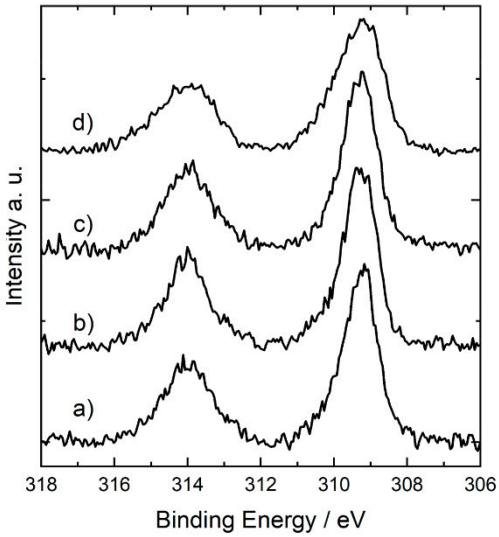

***Figure S2**: Rh 3d XP spectra of 20%$_{mol}$ solutions of [Rh(COD)$_2$][TfO] in [C$_2$C$_1$Im][TfO] a) prepared in air, b) prepared under exclusion of air, c) solution shown in b) after more than 100 min of X-radiation. d) shows the Rh 3d XP spectrum of the solid catalyst. For sake of comparability, the spectrum shown in d) was referenced to the binding energy of the signal shown in a). Note that the spectrum shown in d) shows broadening due to charging of the solid sample. All spectra were recorded in 0° emission at room temperature.*

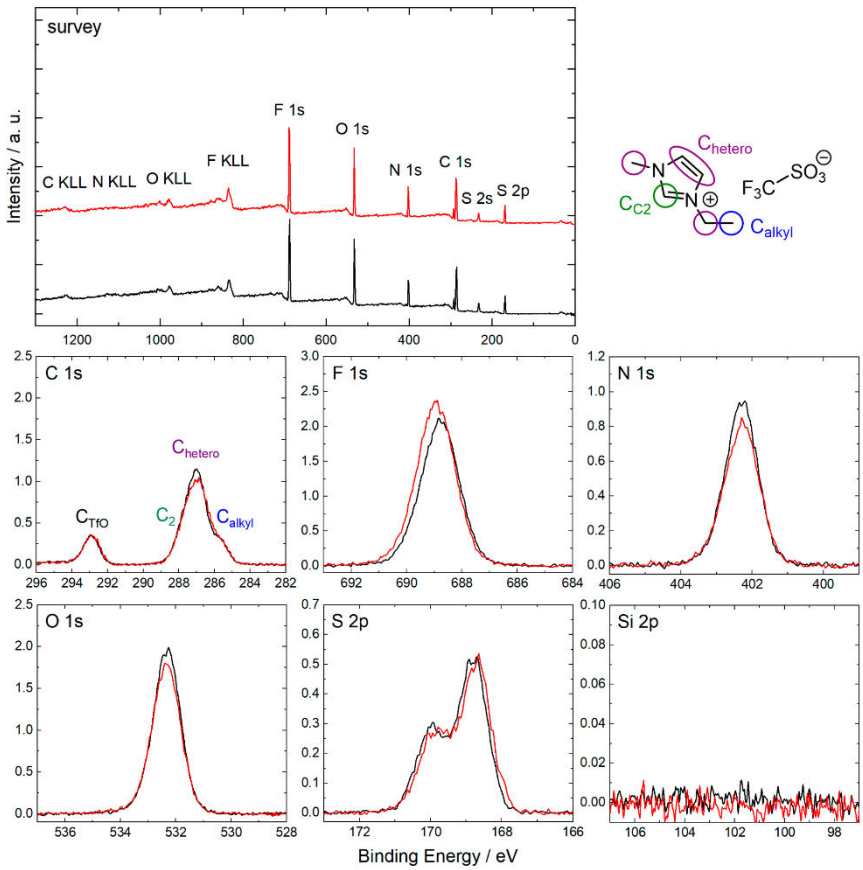

***Figure S3**: Survey, C 1s, F 1s, N 1s, O 1s, S 2p and Si 2p XP spectra of neat [C_2C_1Im][TfO] in 0° (black) and 80° (red) emission recorded at room temperature with assignment of peaks to the molecular structure.*

Fitting of the C 1s region was achieved using an established procedure for 1,3-alkylimidazolium based ILs[85].

***Table S1:** Quantitative analysis of ARXPS core level spectra of neat [C_2C_1Im][TfO].*

neat [C_2C_1Im][TfO]	C 1s TfO	C 1s C_2	C 1s hetero	C 1s alkyl	N 1s	F 1s	O 1s	S 2p
Binding Energy / eV	292.9	287.9	287.0	285.7	402.3	688.8	532.3	169.4
Nominal	1	1	4	1	2	3	3	1
Experimental, 0°	1.1	1.0	3.9	0.9	2.0	3.0	3.1	1.1
Experimental, 80°	1.2	1.0	3.8	0.8	1.8	3.4	2.9	1.1

Estimation of COD content in solution:

The estimation of the COD contents per metal center in the different solutions is challenging and we thus evaluated three different approaches, the results of which are provided in table S3. In the following, the 20%$_{mol}$ solution of $[Rh(COD)_2][TfO]$ serves as a sample calculation for assessment of the COD content. The ASF-corrected intensities are given in table S2 (see below):

Approach I: Assuming full superposition of signals originating from C_{alkyl} and C_{COD} carbon atoms to give joint $C_{alkyl/COD}$ signal.

The expected intensity per atom in the solution was calculated from the sum of ASF-corrected intensities of F 1s, O 1s, N 1s, C_2, C_{hetero} and S 2p signals I_j divided by the sum of atoms expected from stoichiometric composition N_j (note that the C_{TfO} signal was not involved due to overlaying with the shake-up signal from the aromatic imidazolium ring).

$$I_{per\ atom} = \frac{\sum_{F,O,N,C2,Chetero} I_j}{\sum_{F,O,N,C2,Chetero} N_j}$$

With this value, the expected intensity of C_{alkyl} carbon atoms I_{Calkyl} is known (note that the atomic ratios are normalized to one imidazolium cation).

$$I_{C_{alkyl}} = I_{per\ atom}$$

Subtraction from the total intensity of the $C_{alkyl/COD}$ signal $I_{Calkyl/COD}$ yields the intensity of C_{COD} carbon atoms I_{CCOD}.

$$I_{C_{COD}} = I_{C_{alkyl/COD}} - I_{C_{alkyl}}$$

The ratio between the ASF-corrected intensity of Rh I_{Rh} and the calculated intensity of C_{COD} I_{CCOD} carbon atoms yields the number of ligand atoms per metal center. This value divided by the number of carbon atoms in one COD ligand (8) yields the number of ligands per metal center n_{ligand}.

$$n_{ligand} = \frac{I_{C_{COD}}}{I_{Rh}} \Big/ 8$$

Approach I.2: Alternatively, the contribution of C_{alkyl} carbon atoms $I_{C_{alkyl}}$ to the $C_{alkyl/COD}$ signal can be estimated via the ASF-corrected intensity of the IL-specific N 1s signal $I_{N_{Im}}$. The $[C_2C_1Im]^+$ cation contains half as much C_{alkyl} atoms than imidazolium nitrogen atoms.

$$I_{C_{alkyl}} = \frac{I_{N_{Im}}}{2}$$

Approach II: Assumption of superposition of C_{COD} with all carbon atoms of the imidazolium cation, that is, chemically differing carbon atoms of the ligand (sp_3 and sp_2 carbon atoms) could appear at different binding energies (between 289 – 284 eV).

The expected intensity of carbon species of the $[C_2C_1Im]^+$ cation $I_{C_{C2C1Im+}}$ was estimated from the ASF-corrected area of the IL-specific N 1s signal I_{NIm}. The $[C_2C_1Im]^+$ cation contains three times more carbon atoms than nitrogen atoms.

$$I_{C_{C2C1Im+}} = 3I_{N_{Im}}$$

This intensity was subtracted from the total intensity of the joint envelope (~289 – 284 eV) in the C 1s region to yield the intensity of C_{COD} $I_{C_{COD}}$.

$$I_{C_{COD}} = I_{C_{C2C1Im+/COD}} - I_{C_{C2C1Im+}}$$

The number of COD ligands per metal atom n_{ligand} was calculated according to the procedure outlined above.

For the $[C_2C_1Im][TfO]$ solution, all procedures yield 1.4 COD ligands per metal center in solution, as is evident from table S3b. Since the different procedures for estimating the COD content in solution yield similar results, treatment of all ligand atoms and C_{alkyl} carbon atoms as one peak is valid for $[C_2C_1Im][TfO]$, and also for $[C_4C_1Im][TfO]$. However, for the $[C_8C_1Im][TfO]$ solution (table S3d), the different approaches yield variant results: Approaches I and I.2, which are based on the deconvolution of the C_{hetero} and the $C_{alkyl/COD}$ peaks, yield a lower COD:Rh ratio than approach II (1.4 and 1.6 vs 2.0). This discrepancy is attributed due to the significant shifting of the C_{alkyl} signal to lower binding energies upon increasing the chain length (cf. tables S1, S4 and S6). Hence, the peak fitting to deconvolute the C_{hetero} and $C_{alkyl/COD}$ peaks under the approach I & I.2 assumption that the C_{alkyl} and C_{COD} signals have the same binding energy is less reliable. Consequently, approach II, which is tolerant against different binding energies of C_{alkyl} and C_{COD} and does not rely on peak fitting, is considered as the most reliable approach.

Table S2: *Atomic sensitivity factor (ASF)-corrected intensities obtained from XPS of a 20%$_{mol}$ solution of [Rh(COD)$_2$][TfO] in [C$_2$C$_1$Im][TfO] in 0° emission relevant for the calculation of the actual COD content.*

20%$_{mol}$ [Rh(COD)$_2$][TfO] in [C$_2$C$_1$Im][TfO]	Rh 3d	C 1s C$_2$	C 1s hetero	C 1s alkyl/COD	N 1s	F 1s	O 1s	S 2p
ASF-corrected intensity	136.86	962.64	3850.57	2523.16	1927.52	3638.18	3788.87	1216.36

Table S3: *Estimation of COD content per metal center in 20%$_{mol}$ solutions of [Rh(COD)$_2$][TfO] in [C$_2$C$_1$Im][TfO], [C$_4$C$_1$Im][TfO], [C$_8$C$_1$Im][TfO], [C$_2$C$_1$Im][EtOSO$_3$] (a, c-e) and 9%$_{mol}$ solution in [C$_2$C$_1$Im][TfO] (b) using approaches I, I.2 and II outlined above. As the numbers derived from approach II (bold) are the most reliable one, they are used for the further discussion.*

		$n_{ligand,I}$	$n_{ligand,I.2}$	$n_{ligand,II}$
a)	9%$_{mol}$ [Rh(COD)$_2$][TfO] in [C$_2$C$_1$Im][TfO]	0.8	0.9	**0.8**
b)	20%$_{mol}$ [Rh(COD)$_2$][TfO] in [C$_2$C$_1$Im][TfO]	1.4	1.4	**1.4**
c)	20%$_{mol}$ [Rh(COD)$_2$][TfO] in [C$_4$C$_1$Im][TfO]	1.3	1.3	**1.4**
d)	20%$_{mol}$ [Rh(COD)$_2$][TfO] in [C$_8$C$_1$Im][TfO]	1.4	1.6	**2.0**
e)	20%$_{mol}$ [Rh(COD)$_2$][TfO] in [C$_2$C$_1$Im][EtOSO$_3$]	1.1	1.2	**1.3**

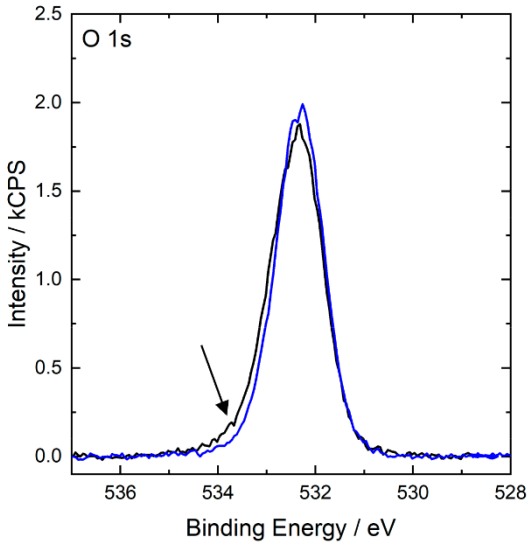

***Figure S4**: O 1s XP spectra of the 20%$_{mol}$ solution of [Rh(COD)$_2$][TfO] in [C$_2$C$_1$Im][TfO] shown in figure S1 (black) and neat [C$_2$C$_1$Im][TfO] shown in figure S3 (blue) in 0° emission recorded at room temperature. The Arrow indicates the additional shoulder in the black spectrum most likely due to [TfO]$^-$ anions coordinating to the metal center (for details, see main text).*

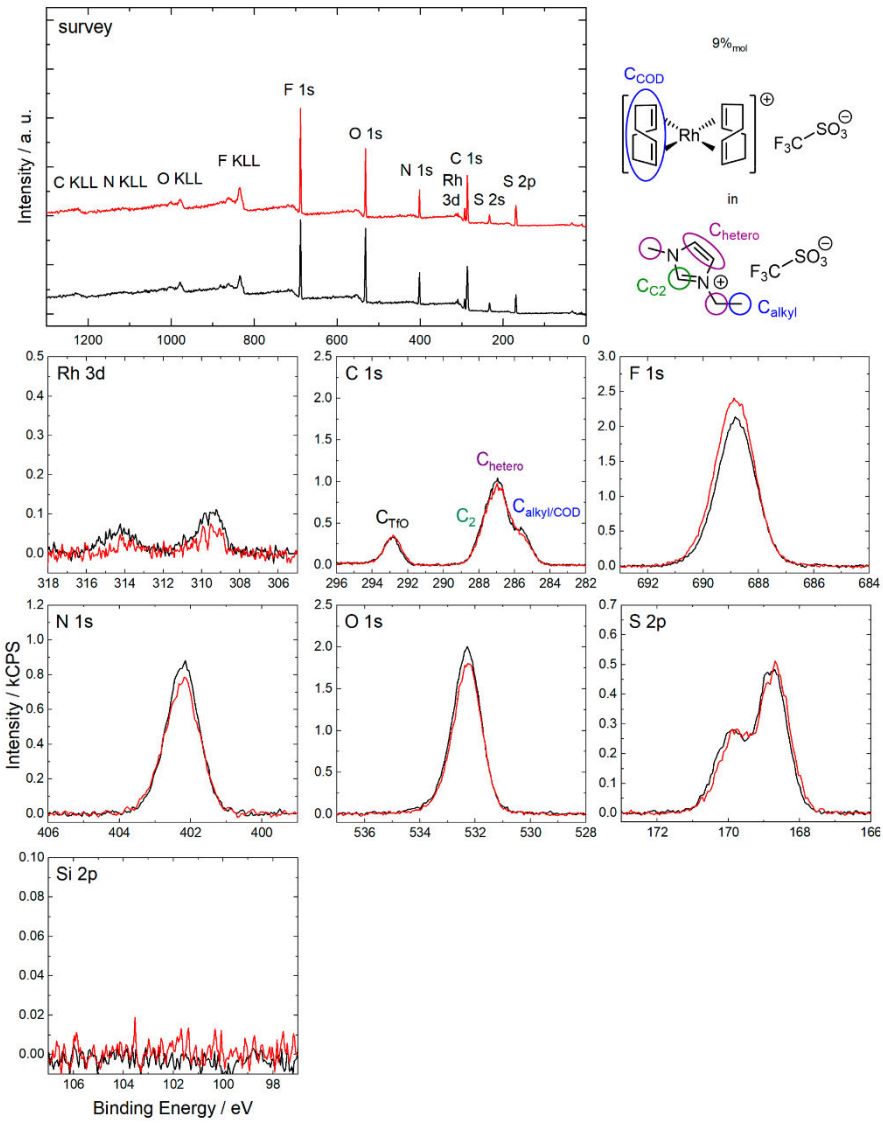

***Figure S5**: Survey, Rh 3d, C 1s, F 1s, N 1s, O 1s, S 2p and Si 2p XP spectra of a 9%$_{mol}$ solution of [Rh(COD)$_2$][TfO] in [C$_2$C$_1$Im][TfO] in 0° (black) and 80° (red) emission recorded at room temperature with assignment of peaks to the molecular structure.*

For fitting, the same procedure was applied as for the 20%$_{mol}$ solution of [Rh(COD)$_2$][TfO] in [C$_2$C$_1$Im][TfO] (see above).

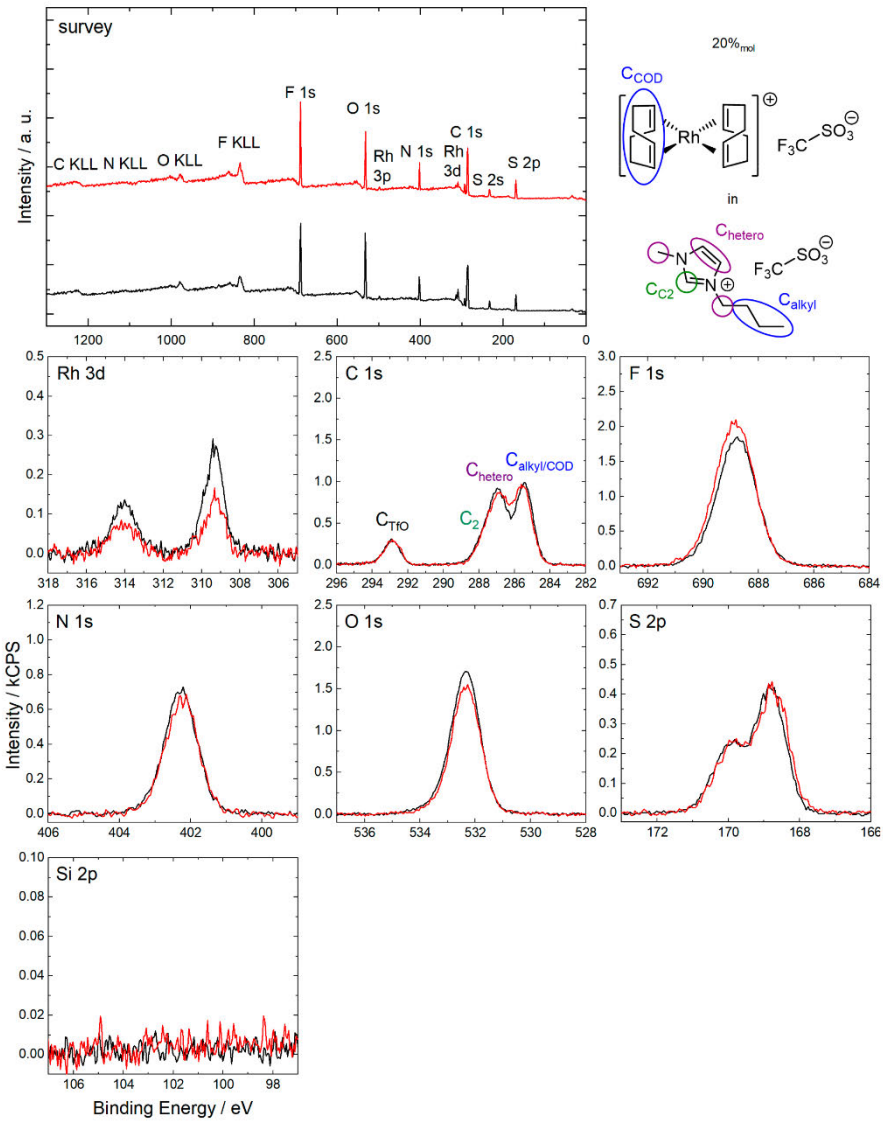

***Figure S6**: Survey, Rh 3d, C 1s, F 1s, N 1s, O 1s, S 2p and Si 2p XP spectra of a 20%$_{mol}$ solution of [Rh(COD)$_2$][TfO] in [C$_4$C$_1$Im][TfO] in 0° (black) and 80° (red) emission recorded at room temperature with assignment of peaks to the molecular structure.*

For fitting, the same procedure was applied as for the solution of [C$_2$C$_1$Im][TfO] (see above).

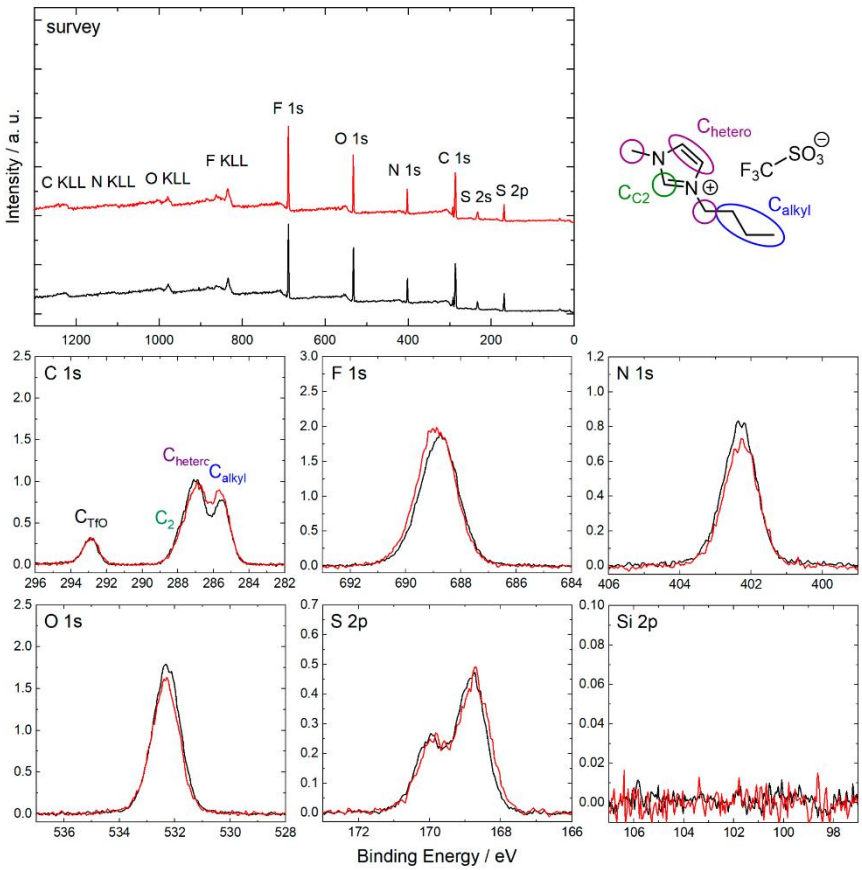

Figure S7: Survey, C 1s, F 1s, N 1s, O 1s, S 2p and Si 2p XP spectra of neat [C_4C_1Im][TfO] in 0° (black) and 80° (red) emission recorded at room temperature with assignment of peaks to the molecular structure.

For fitting, the same procedure was applied as for neat [C_2C_1Im][TfO] (see above).

Table S4: Quantitative analysis of ARXPS core level spectra of neat [C_4C_1Im][TfO].

neat [C_4C_1Im][TfO]	C 1s TfO	C 1s C_2	C 1s hetero	C 1s alkyl	N 1s	F 1s	O 1s	S 2p
Binding Energy / eV	292.9	287.9	287.0	285.5	402.3	688.8	532.3	169.4
Nominal	1	1	4	3	2	3	3	1
Experimental, 0°	1.1	1.0	3.9	2.8	2.0	3.1	3.1	1.1
Experimental, 80°	1.1	0.9	3.8	3.2	1.8	3.3	2.8	1.1

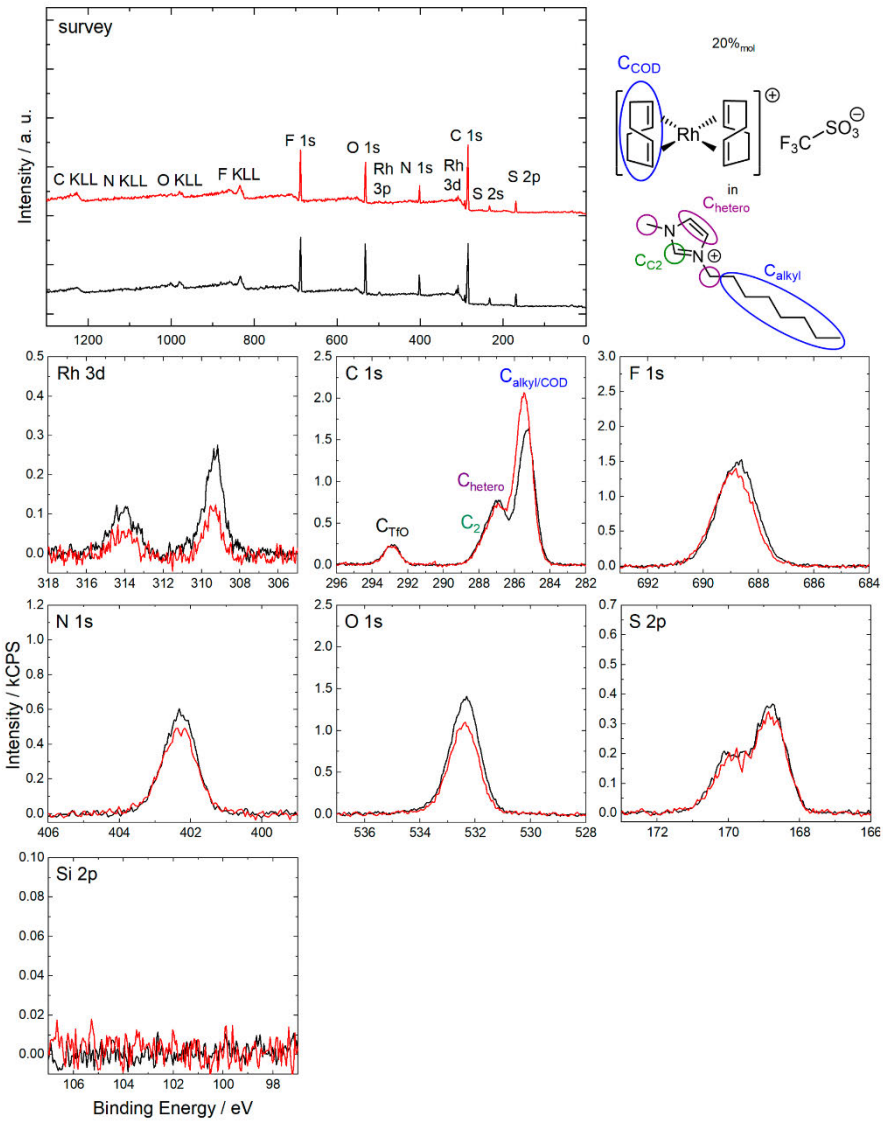

***Figure S8**: Survey, Rh 3d, C 1s, F 1s, N 1s, O 1s, S 2p and Si 2p XP spectra of a 20%$_{mol}$ solution of [Rh(COD)$_2$][TfO] in [C$_8$C$_1$Im][TfO] in 0° (black) and 80° (red) emission recorded at room temperature with assignment of peaks to the molecular structure.*

For fitting, the same procedure was applied as for the solution of [C$_2$C$_1$Im][TfO] (see above).

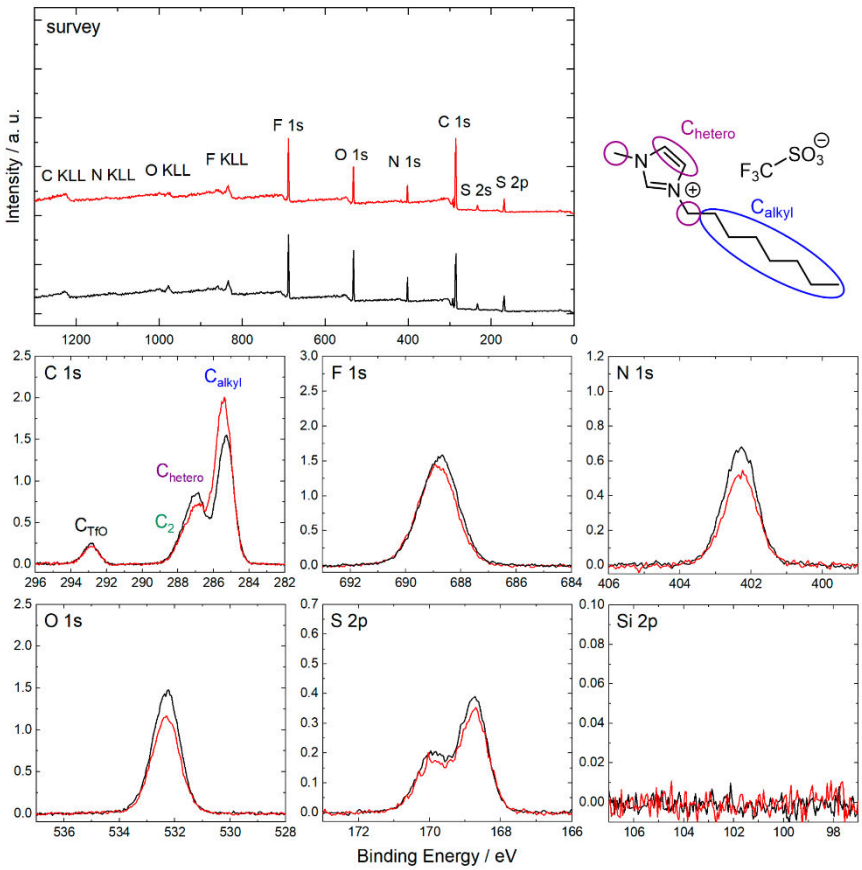

***Figure S9**: Survey, C 1s, F 1s, N 1s, O 1s, S 2p and Si 2p XP spectra of neat [C_8C_1Im][TfO] in 0° (black) and 80° (red) emission recorded at room temperature with assignment of peaks to the molecular structure.*

For fitting, the same procedure was applied as for neat [C_2C_1Im][TfO] (see above).

***Table S5:** Quantitative analysis of ARXPS core level spectra of neat [C_8C_1Im][TfO].*

neat [C_8C_1Im][TfO]	C 1s TfO	C 1s C_2	C 1s hetero	C 1s alkyl	N 1s	F 1s	O 1s	S 2p
Binding Energy / eV	292.9	287.8	286.9	285.3	402.3	688.8	532.3	169.4
Nominal	1	1	4	7	2	3	3	1
Experimental, 0°	1.0	1.0	4.0	6.8	2.0	3.1	3.1	1.1
Experimental, 80°	0.9	0.8	3.4	8.9	1.6	2.9	2.5	1.0

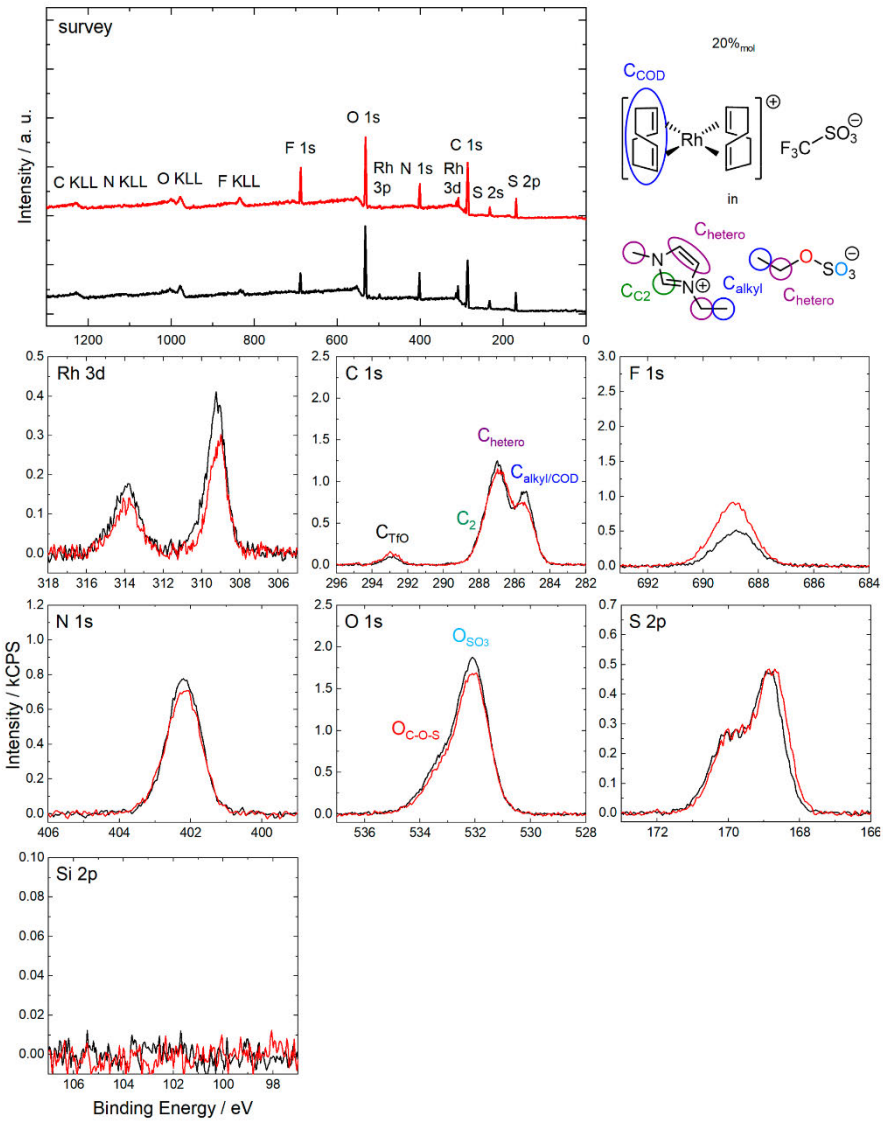

***Figure S10**: Survey, Rh 3d, C 1s, F 1s, N 1s, O 1s, S 2p and Si 2p XP spectra of a 20%$_{mol}$ solution of [Rh(COD)$_2$][TfO] in [C_2C_1Im][EtOSO$_3$] in 0° (black) and 80° (red) emission recorded at room temperature with assignment of peaks to the molecular structure.*

Fitting of the C 1s region was achieved using an established procedure for 1,3-alkylimidazolium based ILs[85]. In addition, the full width at half maximum (FWHM) of $O_{C\text{-}O\text{-}S}$ and O_{SO3} signals was set to equal values.

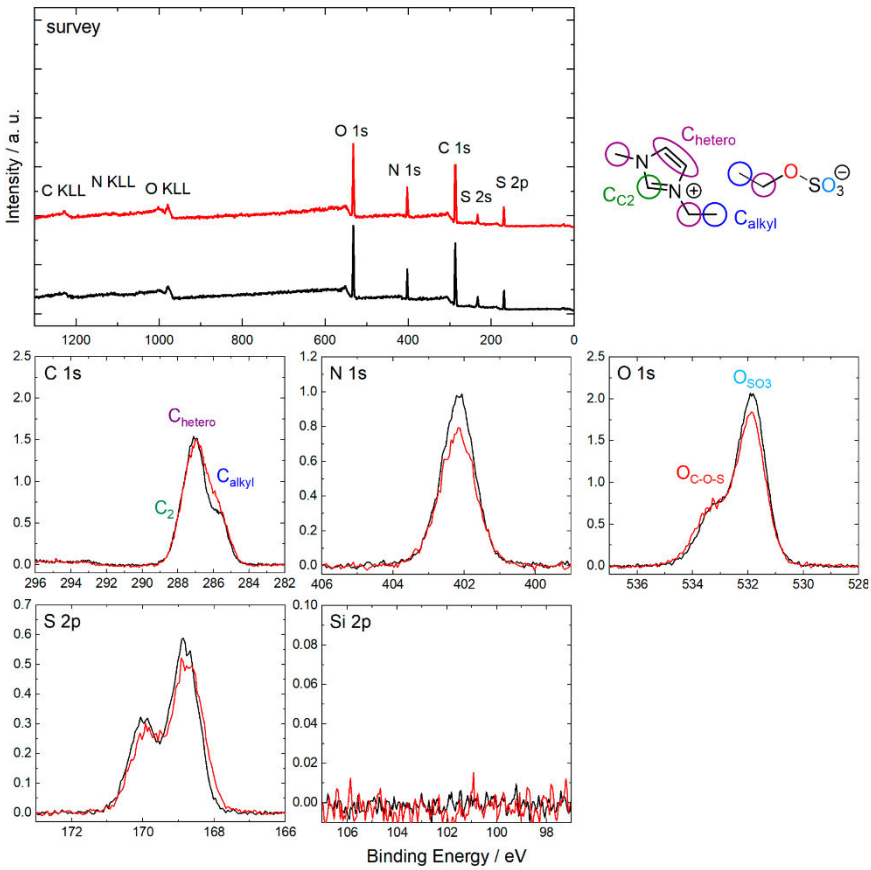

Figure S11: Survey, C 1s, N 1s, O 1s, S 2p and Si 2p XP spectra of neat [C_2C_1Im][$EtOSO_3$] in 0° (black) and 80° (red) emission recorded at room temperature with assignment of peaks to the molecular structure.

Fitting of the C 1s region was achieved using an established procedure for 1,3-alkylimidazolium based ILs[85]. In addition, the full width at half maximum (FWHM) of $O_{C\text{-}O\text{-}S}$ and O_{SO3} signals was set to equal values.

***Table S6:** Quantitative analysis of ARXPS core level spectra of neat [C_2C_1Im][$EtOSO_3$].*

neat [C_2C_1Im][$EtOSO_3$]	C 1s C_2	C 1s hetero	C 1s alkyl	N 1s	O 1s C-O-S	O 1s SO_3	S 2p
Binding Energy / eV	287.9	287.0	285.6	402.2	533.3	531.9	169.4
Nominal	1	5	2	2	1	3	1
Experimental, 0°	1.0	5.1	1.8	1.9	1.0	3.0	1.1
Experimental, 80°	1.1	5.3	2.1	1.7	1.1	2.8	1.0

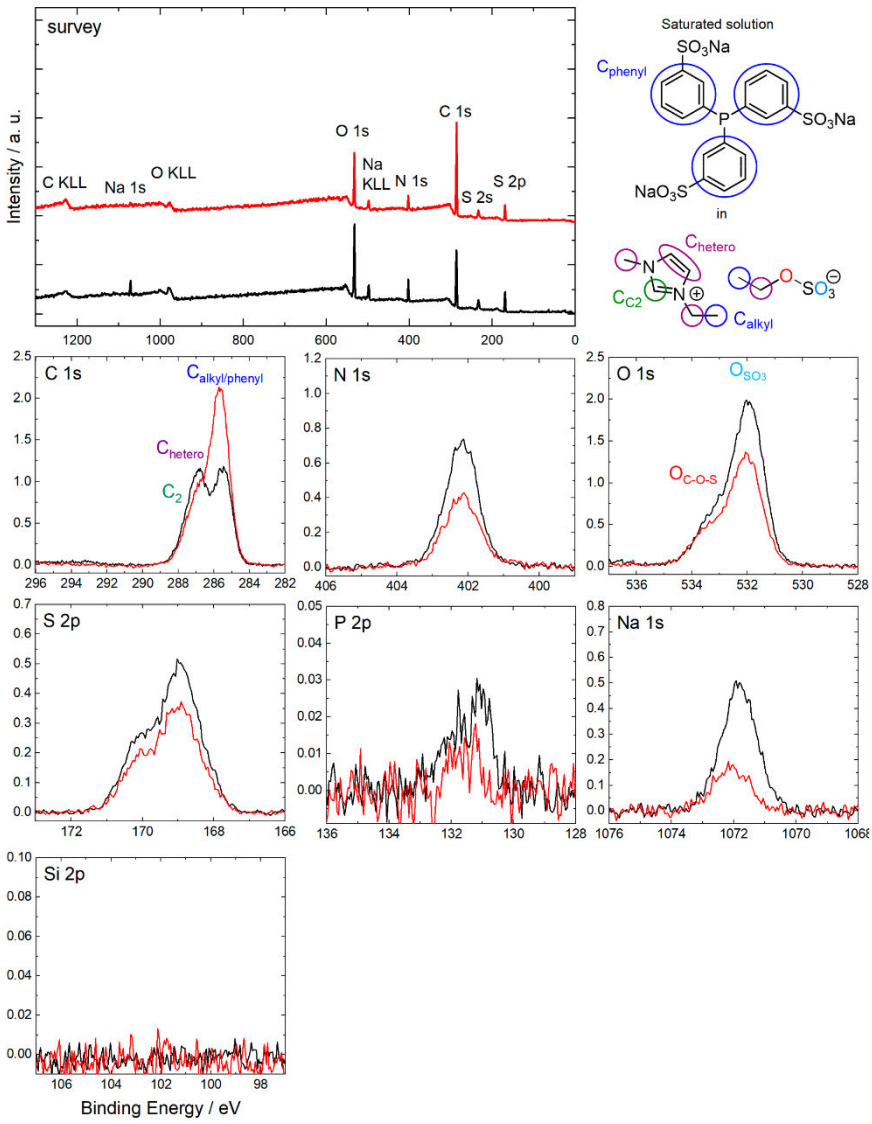

***Figure S12**: Survey, C 1s, F 1s, N 1s, O 1s, S 2p, P 2p, Na 1s and Si 2p XP spectra of a saturated solution of TPPTS in [C_2C_1Im][$EtOSO_3$] in 0° (black) and 80° (red) emission recorded at room temperature with assignment of peaks to the molecular structure.*

Fitting of the C 1s region was achieved using an established procedure for 1,3-alkylimidazolium based ILs[85]. In addition, the full width at half maximum (FWHM) of $O_{C\text{-}O\text{-}S}$ and O_{SO3} signals was set to equal values.

Table S7: *Quantitative analysis of XPS core level spectra recorded in 0° emission of a solution of TPPTS in $[C_2C_1Im][EtOSO_3]$ assuming a solubility of 16.1%$_{mol}$.*

Solution of TPPTS in $[C_2C_1Im][EtOSO_3]$ assuming a solubility of 16.1%$_{mol}$	C 1s C_2	C 1s hetero	C 1s *alkyl/COD*	N 1s	O 1s C-O-S	O 1s SO_3	S 2p	P 2p	Na 1s
Binding Energy / eV	287.8	286.9	285.5	402.2	533.3	532.0	169.5	131.5	1071.8
Nominal	1.00	5.00	5.46	2.00	1.00	4.73	1.58	0.192	0.577
Experimental, 0°	1.07	5.36	5.14	2.06	1.32	4.50	1.61	0.089	0.389

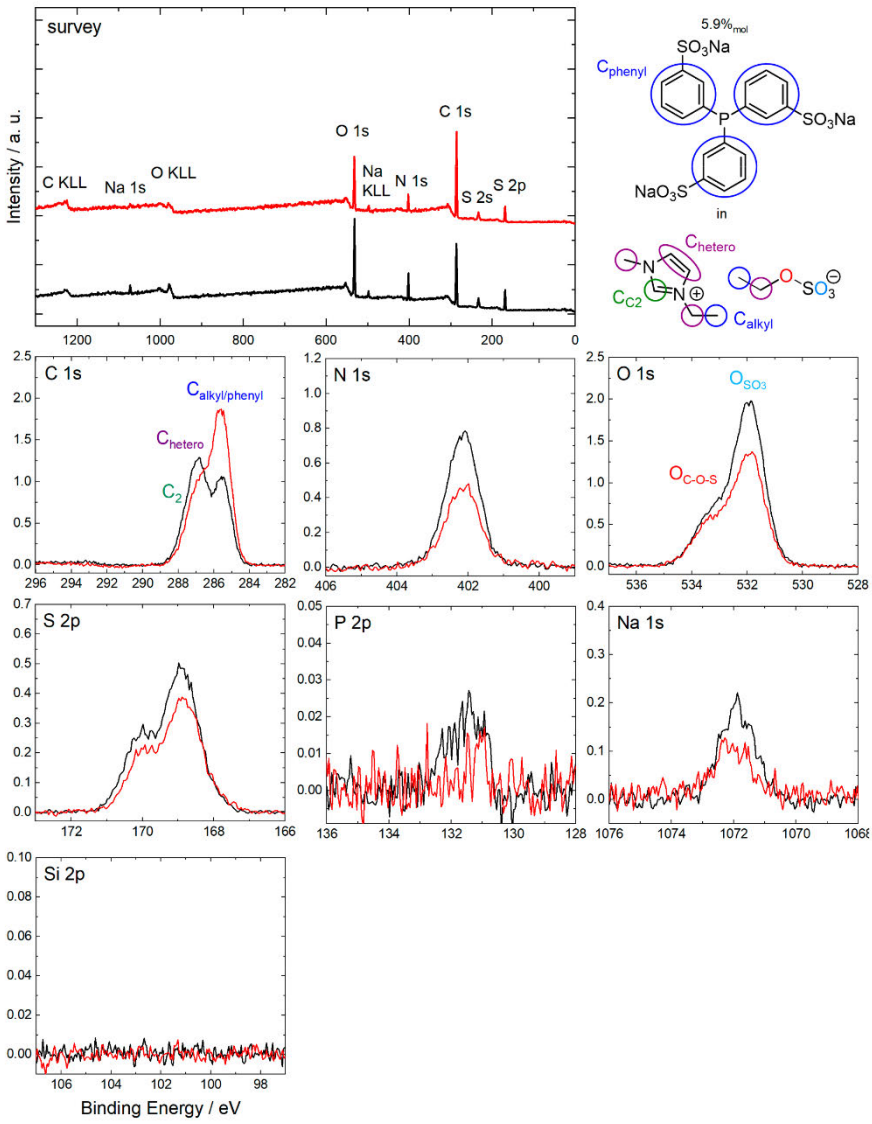

***Figure S13**: Survey, C 1s, F 1s, N 1s, O 1s, S 2p, P 2p, Na 1s and Si 2p XP spectra of a 5.9%$_{mol}$ solution of TPPTS in [C_2C_1Im][$EtOSO_3$] in 0° (black) and 80° (red) emission recorded at room temperature with assignment of peaks to the molecular structure.*

Fitting of the C 1s region was achieved using an established procedure for 1,3-alkylimidazolium based ILs[85]. In addition, the full width at half maximum (FWHM) of $O_{C\text{-}O\text{-}S}$ and O_{SO3} signals was set to equal values.

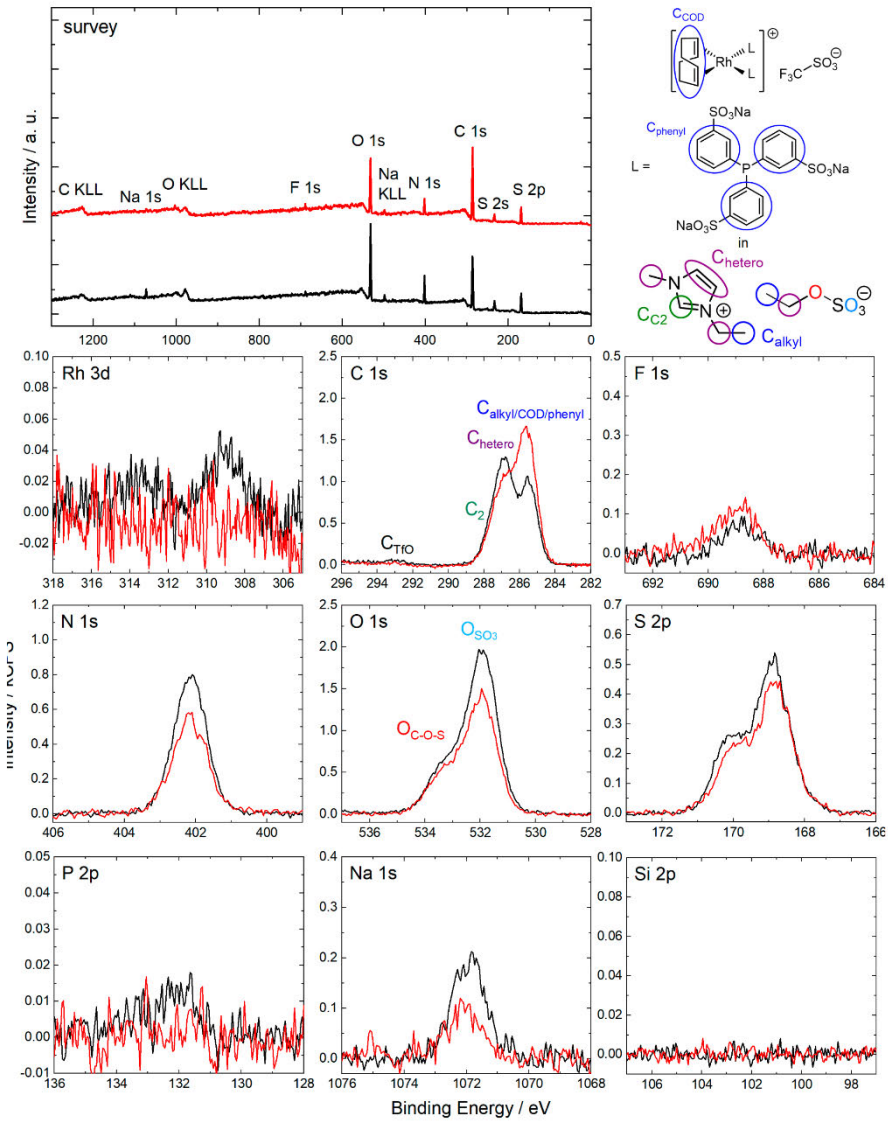

Figure S14: Survey, Rh 3d, C 1s, F 1s, N 1s, O 1s, S 2p, P 2p, Na 1s and Si 2p XP spectra of a solution of [Rh(COD)$_2$][TfO] and TPPTS in [C$_2$C$_1$Im][EtOSO$_3$] with 1:2:31.6 ratio in 0° (black) and 80° (red) emission recorded at room temperature with assignment of peaks to the molecular structure.

Fitting of the C 1s region was achieved using an established procedure for 1,3-alkylimidazolium based ILs[85]. In addition, the full width at half maximum (FWHM) of O_{C-O-S} and O_{SO3} signals was set to equal values.

Table S8: *Weighed proportions for mixtures investigated in this work.*

	20%$_{mol}$ [Rh(COD)$_2$][TfO] in [C_2C_1Im][TfO]	9%$_{mol}$ [Rh(COD)$_2$][TfO] in [C_2C_1Im][TfO]	20%$_{mol}$ [Rh(COD)$_2$][TfO] in [C_4C_1Im][TfO]	20%$_{mol}$ [Rh(COD)$_2$][TfO] in [C_8C_1Im][TfO]	20%$_{mol}$ [Rh(COD)$_2$][TfO] in [C_2C_1Im][EtOSO$_3$]	Saturated solution of TPPTS in [C_2C_1Im][EtOSO$_3$] (16.6%$_{mol}$ weigh-in of TPPTS)	Solution of TPPTS in [C_2C_1Im][EtOSO$_3$] (5.9%$_{mol}$ weigh-in of TPPTS)	[Rh(COD)$_2$][TfO] and TPPTS in [C_2C_1Im][EtOSO$_3$]
Mass [Rh(COD)$_2$][TfO] / mg	126	43.3	119	126	47.8			75.0
Amount of substance [Rh(COD)$_2$][TfO] / mmol	0.264	0.091	0.248	0.263	0.100			0.157
Mass IL / mg	279	241	278	366	95.1	644	1173	1185
Amount of substance IL / mmol	1.06	0.918	0.955	1.05	0.398	2.70	4.92	4.97
Mass [TPPTS] / mg						321	186	188
Amount of substance [TPPTS] / mmol						0.536	0.310	0.314
Exact molar concentration of complex in IL / %$_{mol}$	20.0	9.0	20.6	20.0	20.1	*	5.9	*Assuming full conversion:* 3.1
Exact ratio IL:solute	4.0:1	10.1:1	3.9:1	4.0:1	4.0:1	5.2:1	15.8:1	31.6:2:1 (IL:TPPTS:Rh)

* Solubility of TPPTS in [C_2C_1Im][EtOSO$_3$] given in literature: 16.1%$_{mol}$[74]

$M_{(Rh(COD)_2][TfO]}$ = 468.34 g/mol, $M_{[C_2C_1Im][TfO]}$ = 260.24 g/mol, $M_{[C_4C_1Im][TfO]}$ = 288.29 g/mol, $M_{[C_8C_1Im][TfO]}$ = 344.40 g/mol, $M_{[C_2C_1Im][EtOSO_3]}$ = 236.29 g/mol, M_{TPPTS} = 568.42 g/mol

Purity: [Rh(COD)$_2$][TfO]: 98%, [C_2C_1Im][TfO]/[C_4C_1Im][TfO]/[C_8C_1Im][TfO] [C_2C_1Im][EtOSO$_3$]: 99%, TPPTS: 95%

References (numbers according to main manuscript)

[106] Gottfried, J. M.; Maier, F.; Rossa, J.; Gerhard, D.; Schulz, P. S.; Wasserscheid, P.; Steinrück, H.-P., Surface Studies on the Ionic Liquid 1-Ethyl-3-Methylimidazolium Ethylsulfate Using X-Ray Photoelectron Spectroscopy (XPS). *Z. Phys. Chem.* **2006,** *220* (10), 1439-1453.

[85] Niedermaier, I.; Kolbeck, C.; Steinrück, H.-P.; Maier, F. Dual analyzer system for surface analysis dedicated for angle-resolved photoelectron spectroscopy at liquid surfaces and interfaces. *Rev. Sci. Instrum.* **2016**, *87*, 045105.

[74] Kolbeck, C.; Paape, N.; Cremer, T.; Schulz, P.S.; Maier, F.; Steinrück, H.-P.; Wasserscheid, P. Ligand Effects on the Surface Composition of Rh-Containing Ionic Liquid Solutions Used in Hydroformylation Catalysis. *Chem. Eur. J.* **2010**, *16*, 12083–12087.

8.4 Publication 4, [P4]

Check for updates

ChemPhysChem

Research Article
doi.org/10.1002/cphc.202300612

Chemistry Europe
European Chemical Societies Publishing

www.chemphyschem.org

Understanding the Buoy Effect of Surface-Enriched Pt Complexes in Ionic Liquids: A Combined ARXPS and Pendant Drop Study**

Daniel Hemmeter,[a] Ulrike Paap,[a] Nicolas Wellnhofer,[a] Afra Gezmis,[a] Daniel Kremitzl,[b] Peter Wasserscheid,[b, c] Hans-Peter Steinrück,[a] and Florian Maier*[a]

Recently, we demonstrated that Pt catalyst complexes dissolved in the ionic liquid (IL) $[C_4C_1Im][PF_6]$ can be deliberately enriched at the IL surface by introducing perfluorinated substituents, which act like buoys dragging the metal complex towards the surface. Herein, we extend our previous angle-resolved X-ray photoelectron spectroscopy (ARXPS) studies at complex concentrations between 30 and 5 $\%_{mol}$ down to 1 $\%_{mol}$ and present complementary surface tension pendant drop (PD) measurements under ultraclean vacuum conditions. This combination allows for connecting the microscopic information on the IL/gas interface derived from ARXPS with the macroscopic property surface tension. The surface enrichment of the Pt complexes is found to be most pronounced at 1 $\%_{mol}$. It also displays a strong temperature dependence, which was not observed for 5 $\%_{mol}$ and above, where the surface is already saturated with the complex. The surface enrichment deduced from ARXPS is also reflected by the pronounced decrease in surface tension with increasing concentration of the catalyst. We furthermore observe by ARXPS and PD a much stronger surface affinity of the buoy-complex as compared to the free ligands in solution. Our results are highly interesting for an optimum design of IL-based catalyst systems with large contact areas to the surrounding reactant/product phase, such as in supported IL phase (SILP) catalysis.

Introduction

With a broad spectrum of fascinating properties, ionic liquids (ILs) are promising solvents for application in key sectors of modern chemical industry and technology, for instance in catalysis,[1] electrochemical devices,[2] biomass processing[3] and separation technologies.[4] ILs are salts with low melting points – often below room temperature – typically characterized by bulky organic groups attached to their cations. Thus, these compounds combine typical salt characteristics, such as extremely low volatility and non-flammability, with the enormous molecular tunability of organic chemistry. The properties of ILs are governed by the versatile array of interactions between the ions (e.g. Coulombic, van der Waals and π–π interactions, hydrogen and halogen bonding), resulting in inherently different solvation, complexation and stabilization of solutes, compared to conventional molecular solvents.[5] These properties are particularly interesting in the field of catalysis, where ILs can play various roles ranging from "innocent" solvents to co-catalysts, catalyst modifiers and actual catalysts.[1b,6]

Besides their chemical effects on catalytic reactions, ILs have been efficiently employed as immobilization media in multiphase catalysis using dissolved transition metal complexes.[7] One particularly powerful approach is Supported Ionic Liquid Phase (SILP) catalysis, where a highly porous, solid support is coated with a thin IL film containing the dissolved metal complex.[8] The key advantage of this concept is that the resulting macroscopically solid SILP materials can be employed just like traditional heterogeneous catalysts, but enable homogeneous catalytic transformations within the microscopic liquid film.[8] SILP catalysis has been successfully tested for many industrially relevant reactions, such as hydrogenation,[9] carbonylation,[8b] hydrosilylation[10] and hydroformylation,[11] to name a few. Since SILP catalysts feature very thin IL films and high contact areas with the reactant/product phase, a fundamental understanding of the molecular composition and dynamics at the IL/gas interface is crucial for optimum performance.[1a] Particularly, a very high concentration of the catalytically active complex at the IL/gas interface could enhance the overall performance of the catalytic system. In this way, the highest catalyst concentration is located where the

[a] D. Hemmeter, Dr. U. Paap, N. Wellnhofer, A. Gezmis, Prof. Dr. H.-P. Steinrück, Dr. F. Maier
Lehrstuhl für Physikalische Chemie 2, Friedrich-Alexander-Universität Erlangen-Nürnberg, Egerlandstr. 3, 91058 Erlangen, Germany
E-mail: florian.maier@fau.de

[b] D. Kremitzl, Prof. Dr. P. Wasserscheid
Lehrstuhl für Chemische Reaktionstechnik, Friedrich-Alexander-Universität Erlangen-Nürnberg, Egerlandstr. 3, 91058 Erlangen, Germany

[c] Prof. Dr. P. Wasserscheid
Forschungszentrum Jülich, Helmholtz-Institute Erlangen-Nürnberg for Renewable Energies (IEK 11), Cauerstraße 1, 91058 Erlangen, Germany

[**] ARXPS: Angle-Resolved X-ray Photoelectron Spectroscopy

Supporting information for this article is available on the WWW under https://doi.org/10.1002/cphc.202300612

ChemPhysChem
Research Article
doi.org/10.1002/cphc.202300612
Chemistry Europe
European Chemical Societies Publishing

highest feedstock concentration is present. Moreover, rate limitation by feedstock dissolution processes can be avoided so that the intrinsic kinetics of the dissolved metal complex can be fully exploited.

While the interfacial properties of neat ILs and mixtures of ILs have been addressed quite thoroughly in the past decades and continue to attract intense interest,[1a,12] literature on IL-based catalyst solutions is rather scarce. A detailed study by the groups of *J. M. Slattery* and *T. K. Minton* revealed enrichment of a Ru catalyst at the IL/vacuum interface in $[C_2C_1Im][Tf_2N]$ by reactive-atom scattering (RAS), time-of-flight secondary ion mass spectrometry (TOF-SIMS) and X-ray photoelectron spectroscopy (XPS).[13] The ligand system featured the non-polar phosphine ligand $P(C_8H_{17})_3$, which is proposed to induce preferential population of the complex at the outer surface due to the aliphatic octyl chain.[13] The importance of the ligands' nature on the surface behavior of organometallic complexes was also investigated by our group over the past years.[14] Recently, we demonstrated that the concentration profile of Pt complexes can be deliberately altered by manipulating the ligand system.[14a] Using angle-resolved XPS (ARXPS), we found that perfluorinated substituents behave like buoys dragging the metal complex towards the IL/gas interface while the equivalent complex without these surface-affine substituents is homogeneously distributed within the topmost molecular layer and in the bulk of the solution. Studying solutions in a concentration range between 5–30 $\%_{mol}$, this buoy effect was found to be most effective at lowest catalyst loading indicating a high potential for SILP catalysis. The very high surface enrichment of the Pt complex (even close to saturation in the outermost layer at 5 $\%_{mol}$ bulk concentration) was accompanied by its preferential orientation with the fluorous groups pointing towards the vacuum side, which stresses their buoy-like character.[14a]

The present study aims to extend the knowledge on the buoy-like surface enrichment effect of the Pt complexes in IL solution using ARXPS and the pendant drop (PD) method; our recently developed PD setup allows for the determination of the surface tension under ultraclean vacuum conditions. We have recently demonstrated the potential of combining these two experimental methods by correlating the microscopic picture of the IL/gas interface obtained from ARXPS with the macroscopic surface tension using the PD method.[15] By means of the simple Langmuir principle, the composition of the topmost molecular layer was used to predict the surface tension of a binary IL mixture at various temperatures with particularly high accuracy.[15a] In this contribution, we will expand the complementary scope of ARXPS and the PD method to solutions of the Pt complexes in $[C_4C_1Im][PF_6]$. The metal complexes and ILs employed in this work are shown in Figure 1.

With respect to our previous study, we aim at new insights into these systems to answer the following relevant questions: a) Do we observe new phenomena, when extending our previous studies to much lower metal complex concentrations, that are closer to practical applications? b) How does the surface enrichment depend on temperature? c) Are the preferential enrichment and orientation effects derived from ARXPS also reflected in the surface tension values obtained from the PD analysis and thus, is the reduction in surface free energy the decisive driving force for the observed effects? d) Is there a difference in surface activity whether the ligands are attached to the metal or not?

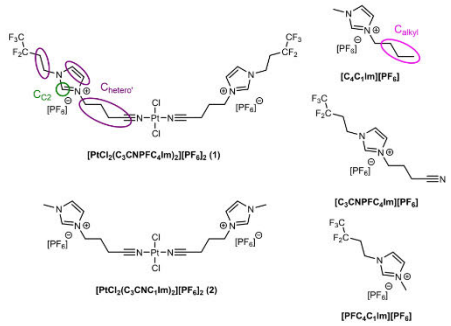

Figure 1. Molecular structures of materials employed in this work: $[PtCl_2(C_3CNPFC_4Im)_2][PF_6]_2$ (**1**) (top left), $[PtCl_2(C_3CNC_1Im)_2][PF_6]_2$ (**2**) (bottom left), 1-butyl-3-methylimidazolium hexafluorophosphate $[C_4C_1Im][PF_6]$ (top right), 1-(3-cyanopropyl)-3-(3,3,4,4,4-pentafluorobutyl)imidazolium hexafluorophosphate $[C_3CNPFC_4Im][PF_6]$ (middle right) and 3-methyl-1-(3,3,4,4,4-pentafluorobutyl)imidazolium hexafluorophosphate $[PFC_4C_1Im][PF_6]$ (bottom right) with assignment of carbon species detected in XPS.

Results and Discussion

Extending the Buoy Effect to More Diluted Systems

In our previous study, the variation of the concentration of **1** (see Figure 1) revealed that between 5 and 30 $\%_{mol}$ the IL/vacuum interface is close to saturation with the complex or, more specifically, with the surface-active fluorinated side chains.[14a] In the following, we extend the measurement series to a more diluted solution of 1 $\%_{mol}$ and compare the corresponding results with the concentration dependence found previously.[14a] Note that for the ARXPS measurements of this solution, water-cleaned $[C_3CNPFC_4Im][PF_6]$ and $[C_4C_1Im][PF_6]$ (see Figure 1) were used to avoid previously observed beam damage effects; a more detailed discussion is provided in the supporting information (SI) and the experimental section. Moreover, solutions with 5 and 10 $\%_{mol}$ that were already investigated by ARXPS,[14a] had to be prepared again in upscaled amounts (see experimental section) for the PD measurements presented here.

An overview of Pt 4f, Cl 2p, F 1s, N 1s and C 1s XP spectra at 0° (black, more bulk-sensitive) and 80° emission angle (red, more surface-sensitive) of solutions of **1** in $[C_4C_1Im][PF_6]$ with catalyst concentrations of 1, 5 and 10 $\%_{mol}$ is shown in Figure 2. The corresponding quantitative analysis is provided in Table 1a–c. The spectra shown in Figure 2b and 2c for the freshly prepared 5 and 10 $\%_{mol}$ solutions are in excellent agreement with the previous ARXPS data (also see Figure 3 below),[14a]

ChemPhysChem
Research Article
doi.org/10.1002/cphc.202300612
Chemistry Europe
European Chemical Societies Publishing

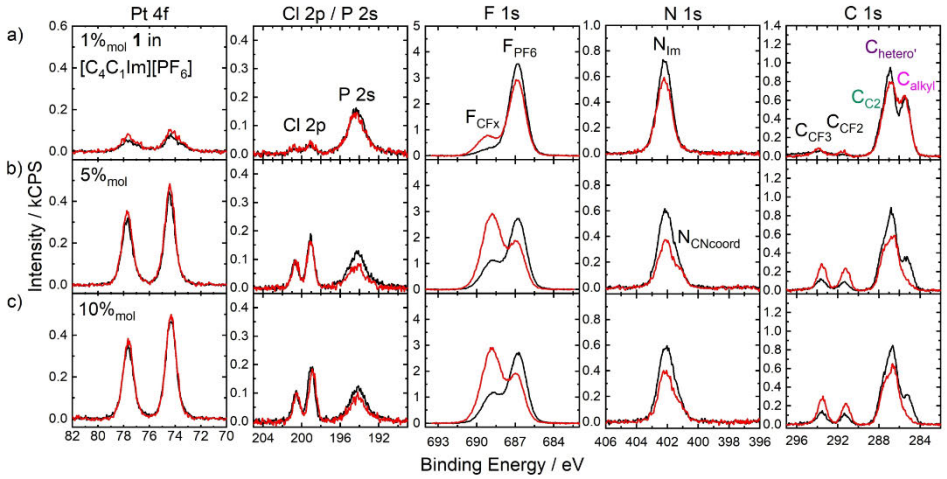

Figure 2. Pt 4f, Cl 2p/P 2s, F 1s, N 1s and C 1s XP spectra of solutions of **1** in $[C_4C_1Im][PF_6]$ with a) 1 $\%_{mol}$, b) 5 $\%_{mol}$ and c) 10 $\%_{mol}$ catalyst concentration in 0° (black) and 80° emission (red). For assignment of signals to the molecular structures see Figure 1. All spectra were recorded at room temperature.

emphasizing the reproducibility of these experiments and the successful up-scaling of the preparation procedure.[14a]

The spectra of the 1 $\%_{mol}$ solution are shown in Figure 2a (for the full set of spectra and a wide scan, see Figure S2). The spectra and their quantitative analysis reveal that the complex-specific Pt 4f, Cl 2p and F_{CFx} signals show a much higher intensity than expected from the nominal bulk composition in both emission angles (0.037/0.051 at 0°/80° vs nominally 0.010 for Pt, and 0.77/1.7 at 0°/80° vs nominally 0.10 for F_{CFx}; see Table 1a). This finding indicates a very pronounced enrichment of the complex at the IL/gas interface also for the highly diluted 1 $\%_{mol}$ solution. The magnitude of this enrichment with respect to the more concentrated solutions will be discussed below. The excellent agreement of the experimentally derived Pt and Cl content with the 1:2 atomic ratio in the complex indicates that the complex indeed is intact. Due to the low concentration and overlap with the N_{Im} signal of the imidazolium cations, no accurate deconvolution of the $N_{CNcoord}$ signal originating from the coordinated CN groups at 401.3 eV[14a,b] (cf. 5 and 10 $\%_{mol}$ solutions in Figures 2b and 2c) could be achieved. Interestingly, the spin-orbit resolved Pt 4f signals of the 1 $\%_{mol}$ solution are slightly broadened with respect to the 5 and 10 $\%_{mol}$ solutions, with the center of gravity of the peaks at 77.6 and 74.2 eV, that is, slightly shifted by about 0.1–0.2 eV to lower binding energy. This effect likely is due to the different surface structure of the topmost surface layer of the 1 $\%_{mol}$ solution, as will be discussed below. The F_{CFx} signal shows a more than two times higher intensity at 80° than at 0°, which is similar to the more concentrated solutions. The increase of the Pt 4f signal at 80° is less pronounced, which was also observed for the more concentrated solutions. This smaller increase with increasing surface sensitivity is assigned to the preferential orientation of **1** in the surface layer, namely the fluorinated groups pointing towards the vacuum, while the metal center resides beneath, as already proposed previously.[14a] This orientational effect leads to the damping of the Pt 4f signal by the surface-terminating CF_3 and CF_2 groups at 80°, and thus, to a lower increase of the Pt 4f signal at 80°, despite the overall surface enrichment of the whole complex.

In the C 1s region of the 1 $\%_{mol}$ solution in Figure 2a, the solvent-specific C_{alkyl} signal at 0° and 80° shows a slightly lower intensity than expected, with no angular dependence. This contrasts the situation for the more concentrated solutions shown in Figures 2b and 2c, where a much lower intensity was detected at 0° and the signal was barely visible at 80°. This behavior indicates that for the 1 $\%_{mol}$ solution, the surface depletion of the solvent (caused by the enrichment of the complex up to surface layer saturation) is much less pronounced.

Figure 3 depicts the quantitative analysis of the concentration-dependent behavior of **1** in $[C_4C_1Im][PF_6]$ solution. It contains the data for 1, 5 and 10 $\%_{mol}$ from this study (black and red squares for 0° and 80°, respectively) and the data for 5, 10, 20 and 30 $\%_{mol}$ from Ref. [14a] (green and violet dots for 0° and 80°, respectively); where overlapping, the two data sets agree perfectly within the margin of error, which demonstrates the reproducibility of the up-scaling and of the ARXPS measurements. Figure 3a shows the normalized contents of Pt and F_{CFx} atoms in 0° and 80° emission versus the molar concentration of **1**. The normalized content corresponds to the detected intensity divided by the intensity expected from nominal composition (a value of 1 reflects homogeneous distribution and random orientation at the IL/vacuum interface)

ChemPhysChem

Research Article
doi.org/10.1002/cphc.202300612

Chemistry Europe
European Chemical Societies Publishing

Table 1. Quantitative analysis of XPS core level spectra of a) 1 $\%_{mol}$, b) 5 $\%_{mol}$ and c) 10 $\%_{mol}$ solutions of **1** and solutions of d) $[C_3CNPFC_4Im][PF_6]$ with 9.5 $\%_{mol}$ and e) $[PFC_4C_1Im][PF_6]$ with 9.6 $\%_{mol}$ in $[C_4C_1Im][PF_6]$.*For the spin-orbit-split signals, the indicated binding energy values correspond to the larger peak, that is, Pt $4f_{7/2}$, Cl $2p_{3/2}$ and P $2p_{3/2}$.

a) 1 $\%_{mol}$ 1 in $[C_4C_1Im][PF_6]$	Pt 4f*	Cl 2p*	F 1s CFx	F 1s PF_6	N 1s Im	N 1s CNcoord	C 1s CF_3	C 1s CF_2	C 1s C_2	C 1s hetero'	C 1s alkyl	P 2p*
Binding Energy [eV]	74.2	199.1	688.8	686.8	402.2		293.9 (80°)	291.6 (80°)	287.8	286.9	285.4	136.9
Nominal	0.010	0.020	0.10	6.1	2.0	0.020	0.020	0.020	1.0	4.2	3.0	1.0
Experimental, 0°	0.037	0.074	0.77	5.9	2.0				1.0	4.0	2.7	1.1
Experimental, 80°	0.051	0.090	1.7	5.0	1.7		0.29	0.29	0.85	4.0	2.6	0.98
b) 5 $\%_{mol}$ 1 in $[C_4C_1Im][PF_6]$												
Binding Energy [eV]	74.4	199.1	688.8	686.8	402.2	401.3	293.7	291.4	287.7	286.8	285.2	136.8
Nominal	0.053	0.11	0.53	6.6	2.2	0.11	0.11	0.11	1.1	4.8	3.0	1.1
Experimental, 0°	0.17	0.36	2.6	5.3	1.8	0.40	0.51	0.51	0.90	4.9	1.4	0.98
Experimental, 80°	0.18	0.34	6.8	3.2	1.1	0.32	1.2	1.2	0.54	4.2	0.14	0.72
c) 10 $\%_{mol}$ 1 in $[C_4C_1Im][PF_6]$												
Binding Energy [eV]	74.3	199.0	688.8	686.8	402.1	401.3	293.6	291.3	287.7	286.8	285.1	136.8
Nominal	0.11	0.22	1.1	7.3	2.4	0.22	0.22	0.22	1.2	5.8	3.0	1.2
Experimental, 0°	0.22	0.46	3.2	6.0	2.1	0.45	0.65	0.65	1.0	5.8	1.4	1.1
Experimental, 80°	0.22	0.42	8.0	3.7	1.3	0.39	1.3	1.3	0.66	4.9	0.14	0.82
d) 9.5 $\%_{mol}$ $[C_3CNPFC_4Im][PF_6]$ in $[C_4C_1Im][PF_6]$						N 1s CN						
Binding Energy [eV]			688.8	686.8	402.2	400.0	293.9 (80°)	291.6 (80°)	287.7	286.8	285.3	136.8
Nominal			0.53	6.6	2.2	0.11	0.11	0.11	1.1	4.8	3.0	1.1
Experimental, 0°			1.1	6.6	2.1	0.16			1.1	4.7	2.7	1.2
Experimental, 80°			2.3	5.5	1.8	0.13	0.46	0.46	0.91	4.4	2.7	1.1
e) 9.6 $\%_{mol}$ $[PFC_4C_1Im][PF_6]$ in $[C_4C_1Im][PF_6]$												
Binding Energy [eV]			688.9	686.8	402.2		294.0 (80°)	291.7 (80°)	287.8	286.9	285.3	136.8
Nominal			0.53	6.6	2.2		0.11	0.11	1.1	4.5	3.0	1.1
Experimental, 0°			1.1	6.7	2.2				1.1	4.4	2.6	1.2
Experimental, 80°			2.1	5.7	1.9		0.40	0.40	0.94	4.4	2.5	1.1

The data for the 1 $\%_{mol}$ solution excellently complement the trend found previously, namely, the enrichment is most pronounced at lowest concentration of the catalyst.[14a] This is concluded from the fact that the normalized Pt 4f and F_{CFx} contents are largest for the lowest concentration of 1 $\%_{mol}$ at 0° and at 80°. Additional insight into the surface composition can be deduced from the total intensities of the Pt 4f signal in 80° emission shown in Figure 3b. For these surface-sensitive spectra, the Pt 4f intensity strongly increases from 1 to 5 $\%_{mol}$, but does not further increase significantly at higher concentrations. This behavior confirms the conclusion drawn in our previous work,[14a] namely that the surface is already close to saturation with the complex at 5 $\%_{mol}$ bulk content (the small increase at higher concentrations is assigned to the increasing bulk concentration, which contributes only moderately to the 80° signal). Clearly, the much smaller signal for the 1 $\%_{mol}$ solution indicates that at this low concentration the surface is still far from saturation, despite the fact that the degree of enrichment is highest among all studied solutions.

ChemPhysChem
Research Article
doi.org/10.1002/cphc.202300612
Chemistry Europe
European Chemical Societies Publishing

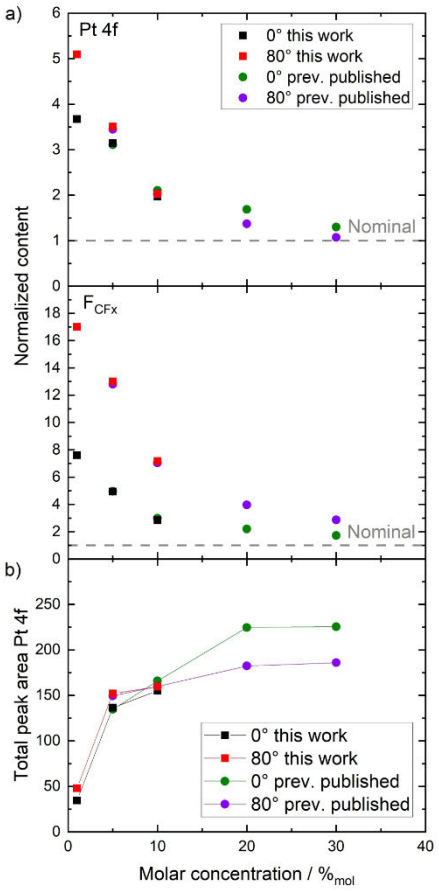

Figure 3. a) Normalized contents derived from Pt 4f (top) and F_{CFx} (bottom) signals, and b) total peak areas of the Pt 4f signals in 0° (black squares, green dots) and 80° emission (red squares, violet dots) over a concentration range from 1 $\%_{mol}$ to 30 $\%_{mol}$ of **1** in $[C_4C_1Im][PF_6]$. Data partly adapted from Ref. [14a]: Green (0° emission) and violet data points (80° emission) correspond to previously published results, while black (0° emission) and red (80° emission) squares is new data.

Temperature Dependence of the Surface Enrichment

Next, we discuss the influence of temperature on the surface composition of the catalyst solutions. Figure 4a shows the normalized contents of Pt, F_{CFx} and C_{alkyl} atoms derived from ARXPS in 0° (black) and 80° emission (red) for the 1 $\%_{mol}$ solution of **1** in $[C_4C_1Im][PF_6]$ from 233 to 353 K. Clearly, for both emission angles, the content of complex-specific Pt and F_{CFx} atoms decreases upon increasing the temperature. Since the 80° values are representative of the enrichment in the topmost layer (remember: a normalized content of 1 indicates no enrichment), we concentrate on discussing the 80° data in the following. At 80°, the normalized Pt content in the topmost layer decreases from 6.2 at 233 K to 1.8 at 353 K, that is, the enrichment decreases by a factor of more than 3 when going from lowest to highest temperature. A similar effect is seen for the normalized F_{CFx} content, which decreases from more than 26 at 233 K to less than 8 at 353 K. The apparent stronger enrichment of the F_{CFx} atoms is due to the preferred orientation of the complex at the IL/vacuum interface (see above), such that the Pt 4f photoelectrons are damped by fluorinated alkyl chains terminating the outer surface. In accordance with a lower surface enrichment of Pt and F_{CFx} atoms at higher temperatures, the normalized content of the solvent-specific C_{alkyl} atoms rises with increasing temperature, which confirms that the surface enrichment is strongest at lowest temperature and becomes less pronounced upon increasing the temperature. It is worth noting that the temperature dependence is also reflected in the Cl 2p, F_{PF6} and N_{Im} signals, as shown in Figure S3 in the SI. The latter two signals show a weaker slope since the contributing atoms originate from both, complex and solvent.

To check for reversibility, ARXP spectra were also acquired at room temperature after the measurements at the temperature extremes of 233 and 353 K (open circles and triangles in Figure 4, respectively). For all atoms, the resulting normalized contents lie within the experimental uncertainty and therefore, confirm that the surface enrichment and depletion effects are indeed reversible. The loss in preferential surface enrichment and depletion with increasing temperature has already been observed previously for a binary mixture of $[PFC_4C_1Im][PF_6]$ and $[C_4C_1Im][PF_6]$ (see Figure 1 for molecular structures) and has been assigned to the increase in magnitude of the entropic term $-T\Delta S^0$ of the surface free energy with increasing temperature, which favors a more random distribution of the constituents at elevated temperatures.[12d]

We also measured the temperature dependence for the 5 $\%_{mol}$ solution of the same complex in $[C_4C_1Im][PF_6]$. Interestingly, the normalized contents of all atoms are virtually constant over a wide temperature range from 213 to 313 K (Figure 4b, and Cl 2p, F_{PF6} and N_{Im} data in Figure S4). This is in accordance with the conclusion of a surface nearly saturated with the complex in the 5 $\%_{mol}$ solution over the entire investigated temperature range. For the more diluted 1 $\%_{mol}$ system without surface saturation, however, the temperature remains a significant parameter for manipulating the surface composition.

Pendant Drop Measurements of the Catalyst Solutions

In the following, we will relate the buoy effect-induced surface enrichment identified by ARXPS to the macroscopic property surface tension obtained from the PD method under well-defined and ultraclean vacuum conditions. Figure 5 depicts the surface tension values γ measured at 298 K of solutions of **1** in $[C_4C_1Im][PF_6]$ with 0, 1, 3, 5 and 10 $\%_{mol}$ concentration at 298 K (scale on the left side); see also Table 2. Also shown is the γ value of a solution of the equivalent complex without

ChemPhysChem
Research Article
doi.org/10.1002/cphc.202300612
Chemistry Europe
European Chemical Societies Publishing

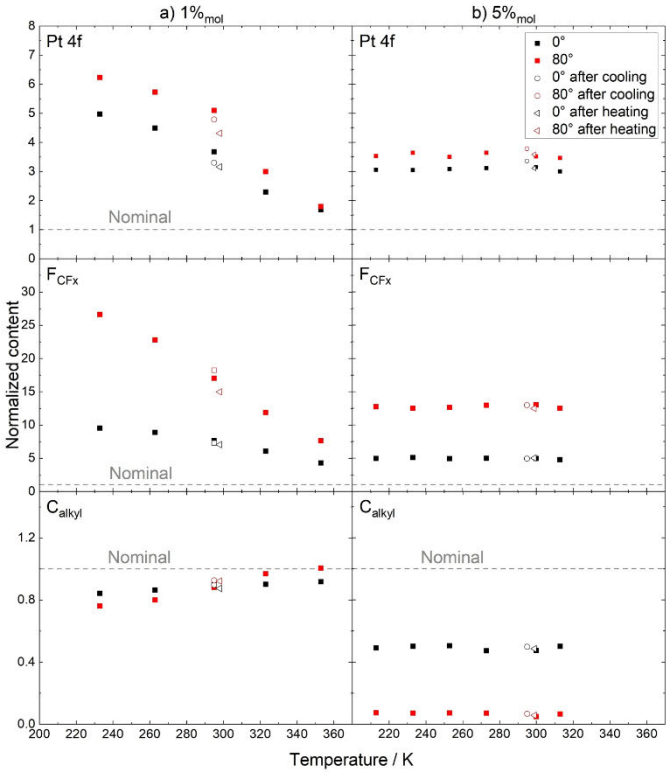

Figure 4. Normalized contents derived from Pt 4f (top), F_{CFx} (middle) and C_{alkyl} (bottom) signals of a) 1 $\%_{mol}$ and b) 5 $\%_{mol}$ solutions of **1** in $[C_4C_1Im][PF_6]$ in 0° (black squares) and 80° emission (red squares) upon variation of the sample temperature. After measurements at the temperature extremes at 233 K and 353 K (a) or 213 K and 313 K (b), the sample was allowed to cool/heat to room temperature and was measured again (open circles and triangles, respectively).

Table 2. Surface tension values at 298 K of neat $[C_4C_1Im][PF_6]$, solutions of **1** with molar concentrations of 1, 3, 5 and 10 $\%_{mol}$, a solution of **2** with a molar concentration of 5 $\%_{mol}$, as well as solutions of $[C_3CNPFC_4Im][PF_6]$ with 9.5 $\%_{mol}$ and $[PFC_4C_1Im][PF_6]$ with 9.6 $\%_{mol}$ in $[C_4C_1Im][PF_6]$ (relative uncertainty in γ values $\pm$0.04 mN/m).

	Surface tension γ [mN/m]
neat $[C_4C_1Im][PF_6]$	43.44
1 $\%_{mol}$ **1** in $[C_4C_1Im][PF_6]$	42.39
3 $\%_{mol}$ **1** in $[C_4C_1Im][PF_6]$	41.10
5 $\%_{mol}$ **1** in $[C_4C_1Im][PF_6]$ *(1:19 complex:IL, 2:19 PFC_4:IL)*	40.03
10 $\%_{mol}$ **1** in $[C_4C_1Im][PF_6]$	37.85
5 $\%_{mol}$ **2** in $[C_4C_1Im][PF_6]$	43.93
9.5 $\%_{mol}$ $[C_3CNPFC_4Im][PF_6]$ in $[C_4C_1Im][PF_6]$ *(2:19 PFC_4:IL)*	41.18
9.6 $\%_{mol}$ $[PFC_4C_1Im][PF_6]$ in $[C_4C_1Im][PF_6]$ *(2:19 PFC_4:IL)*	41.24

fluorinated side chains **2** with 5 $\%_{mol}$ concentration (green data point) at 298 K. The corresponding full set of temperature-dependent surface tension measurements is shown in Figure S5. Note that due to careful characterization and calibration procedures of our PD setup, the uncertainty in γ values relative to each other for different IL solutions and at different temperatures is $\pm$0.1 % ($\pm$0.04 mN/m),[15b] and thus, lies within the height of the solid squares shown in Figures 5 and S5. For the surface tension of the neat solvent $[C_4C_1Im][PF_6]$, we observe a value 43.4 mN/m, which is slightly higher than values reported in literature also using the PD method under ambient conditions (42.9 mN/m at 298 K,[16] 41.6 mN/m at 295 K[17]). Notably, we carefully checked the surface purity of the IL sample prior to the PD experiment using ARXPS to exclude surface-active contaminations, which are a common challenge when working with ILs.[18] Our slightly higher value compared to literature possibly is due to the complete absence of surface contaminations and/or absence of dissolved gases under the

ChemPhysChem
Research Article
doi.org/10.1002/cphc.202300612
Chemistry Europe
European Chemical Societies Publishing

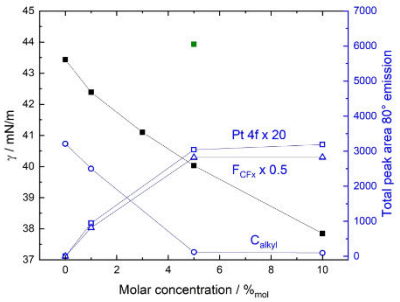

Figure 5. Surface tension γ (black full squares, referring to left vertical axis) of solutions of **1** in $[C_4C_1Im][PF_6]$ over a concentration range of 0–10 $\%_{mol}$; also shown is the value of a 5 $\%_{mol}$ solution of **2** in $[C_4C_1Im][PF_6]$ (green full square) at 298 K (relative uncertainty in γ values ± 0.04 mN/m). In addition, the total XPS peak area detected at 80° at room temperature (between 295 and 300 K) of Pt 4f (blue open squares, x20), F_{CFx} (blue open triangles, x0.5) and C_{alkyl} (blue open circles) signals are shown (referring to the right vertical axis).

applied ultraclean vacuum conditions in our measurements, which have been shown to significantly affect the surface tension.[15b]

When comparing the surface tension of the 5 $\%_{mol}$ solution of **1** (40.0 mN/m) with that of the equivalent solution of the non-fluorinated derivative **2** (43.9 mN/m) in Figure 5 and Table 2, we find a significantly larger value for the latter, which is even slightly higher than of the neat solvent (43.4 mN/m). This finding exemplifies the driving force for the buoy-like enrichment effect: Accumulation of the complex at the IL/vacuum interface and surface termination with the fluorinated side chains results in a lower surface free energy, that is, surface tension for solution of **1** with the fluorinated complex, as compared to solution of **2** without the fluorinated side chains.

Accordingly, the solutions of **1** show a decrease in surface tension upon increasing the catalyst concentration. To correlate the macroscopic quantity "surface tension" obtained by PD with the microscopic "surface composition" obtained from our 80° ARXP spectra, we included the total peak areas for the Pt 4f (multiplied by a factor of 20 for sake of clarity), F_{CFx} (multiplied by a factor of 0.5) and C_{alkyl} signals measured at room temperature (between 295 and 300 K) against the molar concentration in Figure 5 (blue scale at the right side). As discussed above, the number of Pt and F_{CFx} atoms at the surface strongly increases going from 0 to 1 and to 5 $\%_{mol}$, where they reach a plateau, which is assigned to saturation of the surface with complex. This behavior is also reflected in the intensity of the C_{alkyl} signal, which decreases to close to zero at 5 $\%_{mol}$. This observation is in line with the strong decrease of the surface tension going from 0 to 1 $\%_{mol}$ and above. Interestingly, the surface tension does not level off at 5 $\%_{mol}$, but continues to decrease from 5 to 10 $\%_{mol}$ of catalyst in solution, even though the XPS intensities detected in 80° remain constant, indicating a similar content of the catalyst in the topmost molecular layer. This finding indicates that the surface tension is not only governed by the structure of the outer surface, but is also significantly affected by the composition of the adjacent layers in the underlying near-surface region. A change in complex concentration in this region from 5 to 10 $\%_{mol}$ results in a different magnitude of cohesive forces between the topmost layer and the bulk and thus, a change in surface tension, even though the structure and composition of the saturated first molecular layer is similar. An analogue behavior is also known for aqueous solutions of surfactants, where the surface tension was found to further decrease upon increasing the bulk concentration of the surfactant even beyond surface saturation until eventually the critical micelle concentration is reached.[19] In this study, it was concluded that the small contributions of the bulk to the total surfactant surface concentration, which is given by the surface excess concentration and the bulk concentration, are responsible for the significant decrease in surface tension within this saturation adsorption region.[19]

Comparison of Complex and Free Ligands

Since the strong surface enrichment of **1** in solution of $[C_4C_1Im][PF_6]$ is induced by the fluorinated side chains (PFC_4) of the ligand system,[14a] we investigated the impact of the metal center on the accumulation of the PFC_4 substituents at the IL/vacuum interface and the resulting surface tension. Figure 6a shows the Pt 4f, F 1s, N 1s and C 1s spectra of the 5 $\%_{mol}$ solution of **1** (same spectra as in Figure 2b; complex:IL ratio = 1:19, that is, PFC_4:IL ratio = 2:19), and Figure 6b the spectra of a solution where only the ligand $[C_3CNPFC_4Im][PF_6]$ was dissolved with a similar nominal content of PFC_4 chains (PFC_4:IL ratio = 2:19) in $[C_4C_1Im][PF_6]$. The corresponding quantitative analyses are shown in Table 1b and 1d, respectively. Except for the N 1s region, the signals of the ligand-only solution (for the full set of spectra, see Figure S6) show binding energy values similar to the ones discussed for the solution of **1**. The only difference is that the N_{CN} signal at 400.0 eV of the non-coordinated ligand is shifted by about 1.3 eV to lower binding energy relative to the $N_{CN(coord)}$ signal of the coordinated N atoms in the solution of **1**, in line with previous results.[14a,b] With respect to intensities, the ligand-specific F_{CFx} signal and, to a lower extent, the N_{CN} signal both show a higher intensity than expected from nominal composition in both emission angles (1.1/2.3 at 0°/80° vs nominally 0.53 for F_{CFx}, and 0.16/0.13 at 0°/80° vs nominally 0.11 for N_{CN}; see Table 1d), which is in line with the behavior of the other ligand specific signals. In contrast, the C_{alkyl} signal, which is the only XP signal originating solely from the solvent, exhibits a slightly lower intensity (2.7/2.7 at 0°/80° vs nominally 3.0). Overall, these results confirm surface enrichment of the solute also for the ligand-only solution. Again, the F_{CFx} signal shows a pronounced increase by a factor of more than 2 when changing emission angle from 0 to 80°, while the N_{CN} signal shows a very weak decrease. This finding is in line with the preferred surface orientation of the dissolved ligand, with the fluorinated side chains preferentially oriented towards the vacuum and the CN group towards the bulk, as was also found for the neat ligand IL $[C_3CNPFC_4Im][PF_6]$.[14a]

ChemPhysChem
Research Article
doi.org/10.1002/cphc.202300612
Chemistry Europe
European Chemical Societies Publishing

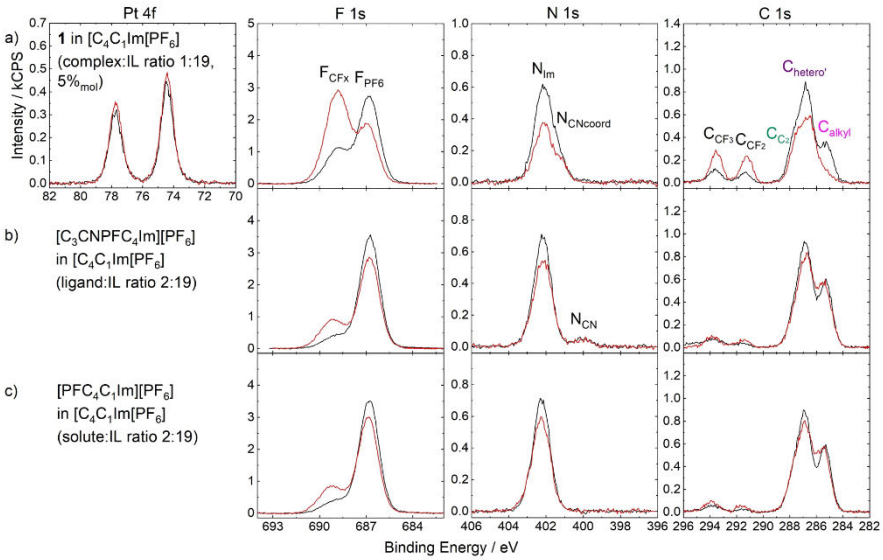

Figure 6. Pt 4f, F 1s, N 1s and C 1s spectra of solutions in $[C_4C_1Im][PF_6]$ of a) **1** with 5 $\%_{mol}$ catalyst concentration (same data as in Figure 2b), b) $[C_3CNPFC_4Im][PF_6]$ with 9.5 $\%_{mol}$, and c) $[PFC_4C_1Im][PF_6]$ with 9.6 $\%_{mol}$; measured at 0° (black) and 80° (red) emission. Note that the solutions have the same IL: PFC_4 ratio of 2:19. For assignment of signals to the molecular structures see Figure 1. All spectra were recorded at room temperature.

Comparing the peak intensities of the solution of **1** and the ligand-only solution in Figures 6a and 6b (and Tables S1b and S1d), respectively, reveals a strikingly higher intensity of all ligand-specific F_{CFx}, $N_{CN(coord)}$, C_{CF3} and C_{CF2} signals at 0° and 80° for the **1** solution as compared to the ligand-only solution despite the fact that the amount of ligand atoms in the bulk is the same for both (2.6 vs 1.1 in 0° and 6.8 vs 2.3 in 80° for F_{CFx}; 0.40 vs 0.16 in 0° and 0.32 vs 0.13 in 80° for $N_{CNcoord}/N_{CN}$; and 1.2 vs 0.46 in 80° for C_{CF3}). Accordingly, the solvent-specific C_{alkyl} signal as well as all other signals show a much lower intensity. These findings indicate a much stronger enrichment of the PFC_4 chains bound in the Pt complex as compared to the free ligands.

The degree of surface enrichment of the PFC_4 chains is also reflected in the surface tensions at 298 K presented in Table 2 (the full set of temperature-dependent surface tension graphs is shown in Figure S7). The ligand-only solution shows a lower surface tension than the neat solvent (41.2 vs 43.4 mN/m), which also reflects the surface enrichment of the solute. However, the 5 $\%_{mol}$ solution of the complex **1** shows an even lower surface tension (40.0 mN/m), which is in accordance with the much more pronounced surface enrichment of the fluorinated side chains induced by the Pt(II) center.

A reason for this difference in surface affinity of the PFC_4 chains most likely is due to the design of the metal complex linking two buoy-ligands together via the Pt center: compared to the free ligand with only one buoy-functionality, the complex provides two collaborative anchoring sites at the IL/gas interface shifting the equilibrium for the PFC_4 chains in the bulk or at the surface considerably towards the latter for the complex.

Another factor possibly contributing to the fact that the surface enrichment of the PFC_4 chains is less pronounced for the free ligands than for the complex could be related to attractive interactions of the potentially more bulk-affine nitrile groups with the surrounding, e.g. with the aromatic imidazolium head-group via hydrogen bonding or σ-π interactions,[20] which lower the surface affinity of the free ligands. These interactions would then be reduced (or even suppressed) by coordination to the Pt center. To investigate this effect, we prepared an equivalent solution of the IL $[PFC_4C_1Im][PF_6]$ (that is, the nitrile-functionalized side chain is replaced by a methyl group, see Figure 1) in $[C_4C_1Im][PF_6]$ with equivalent concentration (same PFC_4:IL ratio 2:19). The corresponding ARXPS spectra are shown in Figure 6c (for the full set of XP spectra, see Figure S8). Besides the lack of the N_{CN} signal in the N 1s region and small deviations in the C 1s envelope due to the missing CN-functionalized substituent as expected, the ARXPS spectra are virtually identical with the equivalent solution of $[C_3CNPFC_4Im][PF_6]$. This finding clearly shows that the interfacial behavior of the solute is not affected by the ligand's CN-functionalized chain but predominantly governed by the fluorinated buoy-substituent. Accordingly, the surface tension values of the $[PFC_4C_1Im][PF_6]$ and the $[C_3CNPFC_4Im][PF_6]$ solutions are identical at 298 K within the experimental uncertainty (see Table 2), as are the temperature-dependent

ChemPhysChem
Research Article
doi.org/10.1002/cphc.202300612
Chemistry Europe
European Chemical Societies Publishing

surface tension measurements over the whole temperature range (Figure S7).

Conclusions

We have studied the recently observed buoy effect on Pt complexes in solution of $[C_4C_1Im][PF_6]$ with catalyst concentrations from 1–10 $\%_{mol}$ in more detail combining ARXPS and the PD method under ultraclean vacuum conditions.[14a] Extending the catalyst concentration range of **1** down to 1 $\%_{mol}$ with respect to our previous study revealed excellent agreement with the conclusions drawn previously on the concentration dependence of the surface enrichment effect, namely, that the enrichment is most effective at lowest concentration.[14a] This is a practically very relevant result as concentrations down to 1 $\%_{mol}$ are most relevant for real life multiphase catalysis applications. We furthermore found that the temperature can significantly influence the catalyst concentration at the IL/vacuum interface with the enrichment being more pronounced at lower temperature. This influence was only observed for the 1 $\%_{mol}$ solution, where the surface has shown to be not saturated with the Pt complex. For a 5 $\%_{mol}$ solution and above, the surface was found saturated with the metal complex over the entire temperature range studied and thus did not show a temperature dependent change in the surface composition.

The microscopic picture of the buoy-like behavior was also connected to the macroscopic surface tension probed by the PD measurements under ultraclean conditions in high vacuum. Solutions of complex **1** show a particularly low surface tension, much lower than for a solution of complex **2**, revealing the driving force for the strong enrichment of **1** at the IL/vacuum interface, which is the minimization of the surface free energy by surface accumulation of the fluorinated side chains of the complex ligands. Increasing the nominal concentration of **1** from 0 to 10 $\%_{mol}$ resulted in a decrease of the surface tension. Interestingly, this decrease was even found going from 5 to 10 $\%_{mol}$, even though the composition of the topmost molecular layer of these solutions is the same, that is, saturated with the complex. We also found that **1** shows a much higher surface activity than the free ligands suggesting that a catalyst structure with more than one surface-active ligand attached to the metal is potentially beneficial for a particularly high surface concentration. All in all, our findings are highly relevant for rational catalyst design and underline the potential for application of the enrichment effects in catalyst systems with large contact areas between catalyst phase and reactant/product surrounding, such as SILP catalysis.

Experimental

Materials

Cis-$[PtCl_2(CH_3CN)_2]$ (purity 98 %) was purchased from Sigma-Aldrich and used as delivered. $[C_4C_1Im][PF_6]$ (purity 99 %) was purchased from Iolitec and, unless stated otherwise, used as delivered. Synthesis of $[C_3CNC_1Im][PF_6]$ and of the precursor C_3CNIm required for the synthesis of $[C_3CNPFC_4Im][PF_6]$ was reported before.[14a]

Synthesis $[C_3CNPFC_4Im][PF_6]$

$[C_3CNPFC_4Im][PF_6]$ has been synthesized before in our groups.[14a] Here, we use a slightly adapted route that does not require the use of organic solvents. For the characterization of the product we refer to the synthesis published before.[14a]

C_3CNIm (5.58 g, 41.3 mmol) and 1,1,1,2,2-pentafluoro-4-iodobutane (14.8 g, 54.0 mmol, 1.3 eq.) were combined in an inertized glass pressure vessel sealed with an NBR sealing ring and stirred vigorously for 3 d at 80 °C. After cooling down, excess alkylating agent was decanted off and the reaction vessel coarsely dried under a stream of compressed air. The highly viscous brown oil left behind was dissolved in water (100 ml) and under vigorous stirring, potassium hexafluorophosphate (4.56 g, 24.8 mmol, 0.60 eq.) dissolved in water (100 ml) was slowly added. The mixture was further stirred at room temperature for 30 min and then cooled to 0 °C without stirring. The supernatant was decanted, the residue rinsed with ethanol, dissolved in hot ethanol (50 ml) and cooled to 0 °C. The purification in ethanol was repeated two more times to remove all unreacted precursors. The pure product was dried under vacuum to give a light brown, highly viscous oil that spontaneously solidified forming a waxy beige chunk. Yield: 7.92 g, 18.5 mmol, 44.8 % (based on 4-imidazol-1-ylbutyronitrile).

Sample Preparation

The complexes **1** and **2**, and the investigated solutions in $[C_4C_1Im][PF_6]$ were prepared under vacuum according to reported procedures[14a] with some modifications due to upscaling: since the PD measurements required several g of solution instead of less than 0.5 g for ARXPS, a slightly increased reaction time at T = 100 °C was needed for the larger batches until visual consumption of the Pt precursor was achieved, followed by further stirring at this temperature for about 1 h to ensure full conversion. The 1 $\%_{mol}$ solutions of **1** in $[C_4C_1Im][PF_6]$ were prepared by simple dilution under ambient conditions of freshly prepared ~5-6 $\%_{mol}$ solutions. Note that two different 1 $\%_{mol}$ solutions were used for ARXPS and PD investigations. For the ARXPS investigations of the 1 $\%_{mol}$ solution, the starting materials $[C_3CNPFC_4Im][PF_6]$ and $[C_4C_1Im][PF_6]$ were pre-cleaned with Millipore water (resistivity 18.2 MΩ·cm) to remove any residual halide contaminations: ~15 mL of $[C_4C_1Im][PF_6]$ were overlaid with ~2 mL of Millipore water at room temperature and vigorously stirred to ensure intense contact of the two phases. After phase separation, the water phase was then removed and the procedure repeated again (twelve times). The same procedure was applied for $[C_3CNPFC_4Im][PF_6]$ (melting point:[14a] 62 °C) at T = 80 °C. Thereafter, both ILs were dried for several days under vacuum at T = 80 °C. XPS analyses of these cleaned ILs yielded no significant changes when compared to the non-water treated samples. With these water-cleaned agents, the synthesis of **1** was carried out as stated above. The reason for this purification step was that beam damage effects were observed for non-cleaned 1 $\%_{mol}$ solutions, as detailed in the SI. Note that for all other solutions investigated herein – including the solutions for PD measurements – no such beam damage effects were observed during the ARXPS, and thus, no additional purification was required.

The weighed proportions for preparation of the solutions for ARXPS and PD experiments are given in Table S1. The solutions were introduced into the vacuum systems as reported previously.[14a,b,15]

ChemPhysChem
Research Article
doi.org/10.1002/cphc.202300612
Chemistry Europe
European Chemical Societies Publishing

ARXPS Measurements and Data Evaluation

Details about the experimental setup and XPS analyses were reported previously.[14a,b,21] Our very unique dual-analyzer setup DASSA allows for a simultaneous recording of photoelectrons emitted at an angle of 0°, that is, along the surface normal, with an information depth (ID) in ILs of 6–9 nm and at an angle of 80° (grazing emission) with a much smaller ID of 1.0–1.5 nm.[21] Thus, the 0° spectra are dominated by bulk contributions, while the 80° spectra mainly reflect the surface composition of the sample. All XP spectra were normalized to the overall intensity at 0° (sum over all intensities weighted with atomic sensitivity factors derived from Ref. [22]) of the 5 $\%_{mol}$ solution of **1** in $[C_4C_1Im][PF_6]$. Additional procedures for peak fitting are outlined in the SI.

For the ARXPS temperature series of the 1 $\%_{mol}$ solution of **1** in $[C_4C_1Im][PF_6]$ shown in Figure 4, each set of spectra at a given temperature was measured on a new sample in order to rule out any accumulation of beam damage effects. After measurements of the temperature extremes of the series, the same sample was measured again at room temperature to check for reversibility and to confirm negligible beam damage.

High-Vacuum PD Measurements and Data Evaluation

The setup and procedures for the PD measurements to derive surface tension values of all investigated liquids as a function of temperature under ultraclean vacuum conditions were reported in detail elsewhere.[15] Density values ρ required for evaluation of the PD measurement analysis were experimentally determined for the 5 $\%_{mol}$ solutions of **1** and **2**, as well as for the 9.5 $\%_{mol}$ solution of $[C_3CNPFC_4Im][PF_6]$ and fitted using

$$\rho(T) = \rho_0 + \rho_1 T + \rho_2 T^2 \quad (1)$$

while for the remaining solutions, the densities were calculated assuming ideal behavior using

$$\rho_{mix}(T) = \frac{m_{solute} + m_{IL}}{V_{solute} + V_{IL}} = \frac{m_{solute} + m_{IL}}{\frac{m_{solute}}{\rho_{solute}(T)} + \frac{m_{IL}}{\rho_{IL}(T)}} \quad (2)$$

where $\rho_{mix}(T)$, $\rho_{IL}(T)$ and $\rho_{solute}(T)$ are the temperature-dependent mass densities of a given solution, the neat IL (taken from Ref. [23]) and the pure complex (a solid in the temperature range investigated herein) or the dissolved ligand, respectively, while m_{solute} and m_{IL} are the mass proportions weighed for preparation of the solution (see Table S2 in the SI). Note that for solutions of **1**, $\rho_{solute}(T)$ was first derived from the experimental data from the 5 $\%_{mol}$ solution solving eq. (2), which was then further used to calculate the densities $\rho_{mix}(T)$ of the remaining solutions. For the solution of $[PFC_4C_1Im][PF_6]$, density data of the neat components was taken from Ref. [17] All density values of the pure compounds and of the solutions parameter at 298 K and the corresponding parameter to obtain $\rho(T)$ according to eq. (1) are summarized in Table S3.

Density Measurements

The density measurements were performed using an Anton Paar DSA 5000 M. The degassed samples were injected into the vibrating tube using a 5 mL syringe while visually checking that the filling was bubble-free. As soon as the device indicated temperature stability the measurements were started. For the 5 $\%_{mol}$ solutions of **1** and **2** in $[C_4C_1Im][PF_6]$, the measurements consisted of a temperature rise from 293.15 K to 303.15 K in 2 K increments, while for the 9.5 $\%_{mol}$ solution of $[C_3CNPFC_4Im][PF_6]$ in $[C_4C_1Im][PF_6]$ a temperature rise from 293.15 K to 313.15 K in 5 K increments was applied. The temperature deviation is less than ±0.005 K in each step. The weighed proportions for preparation of the solutions for the density measurements are given in Table S2.

Acknowledgements

The authors acknowledge the DFG for support in the course of the Collaborative Research Council (CRC)/Sonderforschungsbereich (SFB) 1452 (Project-ID 431791331). We furthermore gratefully acknowledge Dr. A. Bösmann for the temperature-dependent density measurements. D. H. thanks the Stiftung Stipendien-Fonds of the German chemical industry association (Verband der Chemischen Industrie, VCI) for a Kekulé fellowship. Open Access funding enabled and organized by Projekt DEAL.

Conflict of Interests

The authors declare no conflict of interest.

Data Availability Statement

The data that support the findings of this study are available from the corresponding author upon reasonable request.

Keywords: ionic liquids · homogeneous catalysis · surface enrichment · surface tension · X-ray photoelectron spectroscopy (XPS)

[1] a) H.-P. Steinrück, P. Wasserscheid, *Catal. Lett.* **2015**, *145*, 380–397; b) T. Welton, *Coord. Chem. Rev.* **2004**, *248*, 2459–2477.
[2] a) D. R. MacFarlane, M. Forsyth, P. C. Howlett, J. M. Pringle, J. Sun, G. Annat, W. Neil, E. I. Izgorodina, *Acc. Chem. Res.* **2007**, *40*, 1165–1173; b) A. Balducci, *Top. Curr. Chem.* **2017**, *375*, 20.
[3] a) S. S. Y. Tan, D. R. MacFarlane, in *Ionic Liquids* (Ed.: B. Kirchner), Springer Berlin Heidelberg, Berlin, Heidelberg, **2010**, pp. 311–339; b) S. Siankevich, Z. Fei, N. Yan, P. J. Dyson, *Chimia* **2015**, *69*, 592.
[4] a) S. P. M. Ventura, F. A. e Silva, M. V. Quental, D. Mondal, M. G. Freire, J. A. P. Coutinho, *Chem. Rev.* **2017**, *117*, 6984–7052; b) Y. Baba, F. Kubota, N. Kamiya, M. Goto, *J. Chem. Eng. Jpn.* **2011**, *44*, 679–685.
[5] a) R. Hayes, G. G. Warr, R. Atkin, *Chem. Rev.* **2015**, *115*, 6357–6426; b) Y.-L. Wang, B. Li, S. Sarman, F. Mocci, Z.-Y. Lu, J. Yuan, A. Laaksonen, M. D. Fayer, *Chem. Rev.* **2020**, *120*, 5798–5877.
[6] a) J. P. Hallett, T. Welton, *Chem. Rev.* **2011**, *111*, 3508–3576; b) R. L. Vekariya, *J. Mol. Liq.* **2017**, *227*, 44–60.
[7] a) X. Marset, D. J. Ramón, G. Guillena, in *Catalyst Immobilization: Methods and Applications* (Eds.: M. Benaglia, A. Puglisi), Wiley-VCH Verlag GmbH & Co. KGaA, Weinheim, **2020**, pp. 187–216; b) P. Wasserscheid, W. Keim, *Angew. Chem. Int. Ed.* **2000**, *39*, 3772–3789; c) C. M. Gordon, *Appl. Catal. A* **2001**, *222*, 101–117.
[8] a) A. Riisager, R. Fehrmann, M. Haumann, P. Wasserscheid, *Eur. J. Inorg. Chem.* **2006**, *2006*, 695–706; b) A. Riisager, B. Jørgensen, P. Wasserscheid, R. Fehrmann, *Chem. Commun.* **2006**, 994–996.
[9] a) C. P. Mehnert, E. J. Mozeleski, R. A. Cook, *Chem. Commun.* **2002**, 3010–3011; b) J. Brünig, Z. Csendes, S. Weber, N. Gorgas, R. W. Bittner, A. Limbeck, K. Bica, H. Hoffmann, K. Kirchner, *ACS Catal.* **2018**, *8*, 1048–1051.
[10] a) R. Kukawka, A. Pawlowska-Zygarowicz, J. Dzialkowska, M. Pietrowski, H. Maciejewski, K. Bica, M. Smiglak, *ACS Sustainable Chem. Eng.* **2019**, *7*,

ChemPhysChem
Research Article
doi.org/10.1002/cphc.202300612
Chemistry Europe
European Chemical Societies Publishing

4699–4706; b) O. Bartlewicz, M. Pietrowski, M. Kaczmarek, H. Maciejewski, *RSC Adv.* **2021**, *11*, 23355–23364.

[11] a) J. M. Marinkovic, A. Riisager, R. Franke, P. Wasserscheid, M. Haumann, *Ind. Eng. Chem. Res.* **2019**, *58*, 2409–2420; b) M. Hatanaka, T. Yasuda, E. Uchiage, M. Nishida, K.-i. Tominaga, *ACS Sustainable Chem. Eng.* **2021**, *9*, 11674–11680.

[12] a) M. Tariq, M. G. Freire, B. Saramago, J. A. P. Coutinho, J. N. C. Lopes, L. P. N. Rebelo, *Chem. Soc. Rev.* **2012**, *41*, 829–868; b) K. Nakajima, M. Lísal, K. Kimura, in *Surface and Interface Science* (Ed.: K. Wandelt), Wiley-VCH Verlag GmbH & Co. KGaA, Weinheim, **2020**, pp. 351–389; c) M. Lexow, F. Maier, H.-P. Steinrück, *Adv. Phys.* **2020**, *5*, 1761266; d) B. S. J. Heller, M. Lexow, F. Greco, S. Shin, G. Partl, F. Maier, H.-P. Steinrück, *Chem. Eur. J.* **2020**, *26*, 1117–1126; e) E. Sloutskin, B. M. Ocko, L. Tamam, I. Kuzmenko, T. Gog, M. Deutsch, *J. Am. Chem. Soc.* **2005**, *127*, 7796–7804; f) C. S. Santos, S. Baldelli, *Chem. Soc. Rev.* **2010**, *39*, 2136–2145; g) S. Baldelli, *J. Phys. Chem. Lett.* **2013**, *4*, 244–252; h) C. Peñalber-Johnstone, G. Adamová, N. V. Plechkova, M. Bahrami, T. Ghaed-Sharaf, M. H. Ghatee, K. R. Seddon, S. Baldelli, *J. Chem. Phys.* **2018**, *148*, 193841; i) S. Krischok, A. Ulbrich, T. Ikari, V. Kempter, M. Marschewski, O. Höfft, *Nucl. Instrum. Methods Phys. Res. B* **2014**, *340*, 51–57; j) L. Winter, R. G. Bhuin, F. Maier, H.-P. Steinrück, *Chem. Eur. J.* **2021**, *27*, 17059–17065; k) Z. Zhai, T. M. Koller, *J. Mol. Liq.* **2023**, *377*, 121491; l) E. F. Smith, I. J. Villar Garcia, D. Briggs, P. Licence, *Chem. Commun.* **2005**, 5633–5635.

[13] E. J. Smoll, X. Chen, L. M. Hall, L. D'Andrea, J. M. Slattery, T. K. Minton, *J. Phys. Chem. C* **2020**, *124*, 382–397.

[14] a) D. Hemmeter, D. Kremitzl, P. S. Schulz, P. Wasserscheid, F. Maier, H.-P. Steinrück, *Chem. Eur. J.* **2023**, *29*, e202203325; b) D. Hemmeter, U. Paap, N. Taccardi, J. Mehler, P. S. Schulz, P. Wasserscheid, F. Maier, H.-P. Steinrück, *ChemPhysChem* **2023**, *24*, e202200391 (DOI: 10.1002/cphc.202200391); c) D. Hemmeter, U. Paap, F. Maier, H.-P. Steinrück, *Catalysts* **2023**, *13*, 871; d) C. Kolbeck, N. Paape, T. Cremer, P. S. Schulz, F. Maier, H.-P. Steinrück, P. Wasserscheid, *Chem. Eur. J.* **2010**, *16*, 12083–12087.

[15] a) U. Paap, V. Seidl, K. Meyer, F. Maier, H.-P. Steinrück, *Molecules* **2022**, *27*, 8561; b) U. Paap, B. Kreß, H.-P. Steinrück, F. Maier, *Int. J. Mol. Sci.* **2022**, *23*, 13158.

[16] A. B. Pereiro, J. L. Legido, A. Rodrı'guez, *J. Chem. Thermodyn.* **2007**, *39*, 1168–1175;'guez, *J. Chem. Thermodyn.* **2007**, *39*, 1168–1175.

[17] T. M. Koller, F. D. Lenahan, P. S. Schmidt, T. Klein, J. Mehler, F. Maier, M. H. Rausch, P. Wasserscheid, H.-P. Steinrück, A. P. Fröba, *Int. J. Thermophys.* **2020**, *41*, 144.

[18] J. M. Gottfried, F. Maier, J. Rossa, D. Gerhard, P. S. Schulz, P. Wasserscheid, H.-P. Steinrück, *Z. Phys. Chem.* **2006**, *220*, 1439–1453.

[19] H. Schott, *J. Pharm. Sci.* **1980**, *69*, 852–854.

[20] a) D. Zhao, Z. Fei, R. Scopelliti, P. J. Dyson, *Inorg. Chem.* **2004**, *43*, 2197–2205; b) Z. Fei, D. Zhao, D. Pieraccini, W. H. Ang, T. J. Geldbach, R. Scopelliti, C. Chiappe, P. J. Dyson, *Organometallics* **2007**, *26*, 1588–1598.

[21] I. Niedermaier, C. Kolbeck, H.-P. Steinrück, F. Maier, *Rev. Sci. Instrum.* **2016**, *87*, 045105.

[22] C. D. Wagner, L. E. Davis, M. V. Zeller, J. A. Taylor, R. H. Raymond, L. H. Gale, *Surf. Interface Anal.* **1981**, *3*, 211–225.

[23] J. Jacquemin, P. Husson, A. A. H. Padua, V. Majer, *Green Chem.* **2006**, *8*, 172–180.

Manuscript received: August 28, 2023
Revised manuscript received: September 22, 2023
Accepted manuscript online: September 22, 2023
Version of record online: November 2, 2023

ChemPhysChem

Supporting Information

Understanding the Buoy Effect of Surface-Enriched Pt Complexes in Ionic Liquids: A Combined ARXPS and Pendant Drop Study

Daniel Hemmeter, Ulrike Paap, Nicolas Wellnhofer, Afra Gezmis, Daniel Kremitzl, Peter Wasserscheid, Hans-Peter Steinrück, and Florian Maier*

Beam damage effects for low Pt concentration

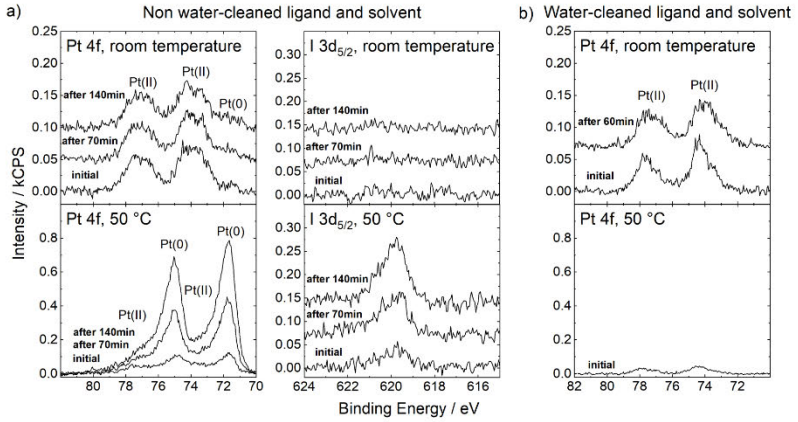

*Figure S1: a) Pt 4f and I $3d_{5/2}$ XP spectra of a $1\%_{mol}$ solution of **1** in $[C_4C_1Im][PF_6]$ prepared according to Ref. [1] (Ref [14a] in main manuscript) after individual time periods of irradiation with the X-ray beam, b) Pt 4f spectra of an equivalent solution prepared with ligand and solvent cleaned using Millipore water before synthesis, recorded at room temperature (top) and 50 °C (bottom). The spectra were recorded in 0° emission.*

Figure S1a shows the Pt 4f and I $3d_{5/2}$ spectra of a $1\%_{mol}$ solution of **1** in $[C_4C_1Im][PF_6]$ which was prepared using $[C_3CNPFC_4Im][PF_6]$ and $[C_4C_1Im][PF_6]$ as described in Ref. [1] (Ref. [14a] in main manuscript). The Pt 4f spectrum showed a signal at lower binding energy (Pt $4f_{5/2}$ ≈ 72 eV) with respect to the expected signal corresponding to the Pt(II) center of **1** at 74.2 eV; this behavior is indicative of beam damage. In the initial spectrum, this feature is slightly visible at room temperature (Figure S1a, top left), but at 50 °C (bottom left), the signal already shows a much higher intensity than the nominally expected Pt signal and increases upon irradiation with the X-ray beam over time for both temperatures. At the same time, an iodine species was detected, which was also found to increase with time of X-ray exposure at 50 °C (bottom right). This feature was not detected at room temperature (top right), since the magnitude of the beam damage is much lower. These effects indicate X-ray-induced formation of metallic Pt(0) in the presence of traces of an iodine species most probably coming from the synthesis of $[C_3CNPFC_4Im][PF_6]$ and/or $[C_4C_1Im][PF_6]$.

Figure S1b shows the corresponding Pt 4f spectra of an equivalent solution prepared after $[C_3CNPFC_4Im][PF_6]$ and $[C_4C_1Im][PF_6]$ were thoroughly cleaned using Millipore water (for details see Experimental Section). The Pt 4f spectra recorded at room temperature (Figure S1b, top) only show a slight broadening upon irradiation with X-rays, which is not significantly affecting the trends described in the main manuscript. Also, the spectrum at 50 °C (Figure S1b, bottom) does not show the effect observed for the uncleaned solution.

Complete set of XP spectra of a 1%$_{mol}$ solution of 1 in [C_4C_1Im][PF_6] at room temperature

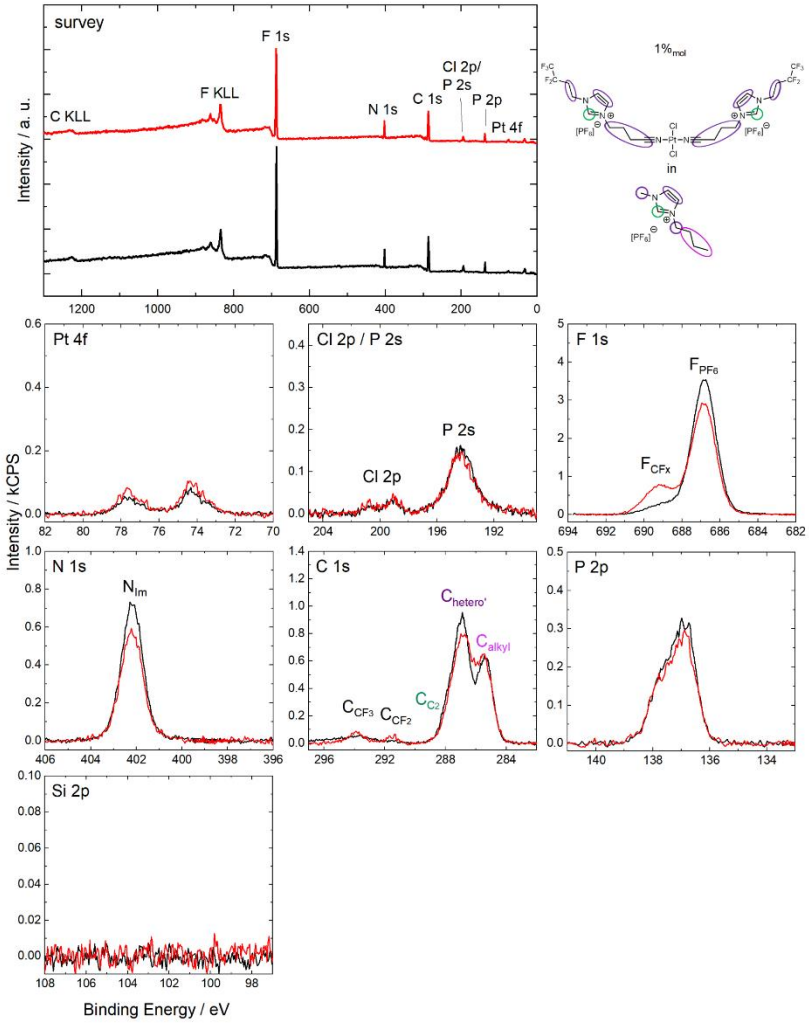

*Figure S2: Survey, Pt 4f, Cl 2p/P 2s, F 1s, N 1s, C 1s, P 2p and Si 2p XP spectra of a 1%$_{mol}$ solution of **1** in [C_4C_1Im][PF_6] in 0° (black) and 80° (red) emission recorded at room temperature with assignment of peaks to the molecular structure. The Si 2p region is shown to exclude surface-active contaminations found previously.[2]*

Peak fitting for solution shown in Figure S2

Peak fitting was achieved using the procedure reported in Ref. [1] (Ref. [14a] in main manuscript). Due to the low concentration of the complex in solution and overlap with the N_{Im} signal, no $N_{CNcoord}$ signal could be accurately deconvolved. Furthermore, due to the low concentration and overlap with the shake-up signal of the imidazolium ring, the C_{CF3} and C_{CF2} signals were only considered in 80° emission. For this, additionally to constraining the area of the C_{CF3} and C_{CF2} signals to equal values[1], the full width at half maximum (FWHM) was set to equal values to prevent unrealistic broadening due to the relatively low intensity. The quantitative analysis of the peak intensities is given in Table 1a. For fitting of the F 1s region at 353 K, due to the rather low intensity of the F_{CFx} signal its position was constraint to 2.0 eV higher binding energy with respect to the F_{PF6} signal. This constraint was chosen according to the binding energy difference found at the other temperatures, where no constraints needed to be used.

Quantitative analysis of the temperature dependence of the XP spectra of all relevant core levels of a 1%$_{mol}$ solution of 1 in [C_4C_1Im][PF_6]

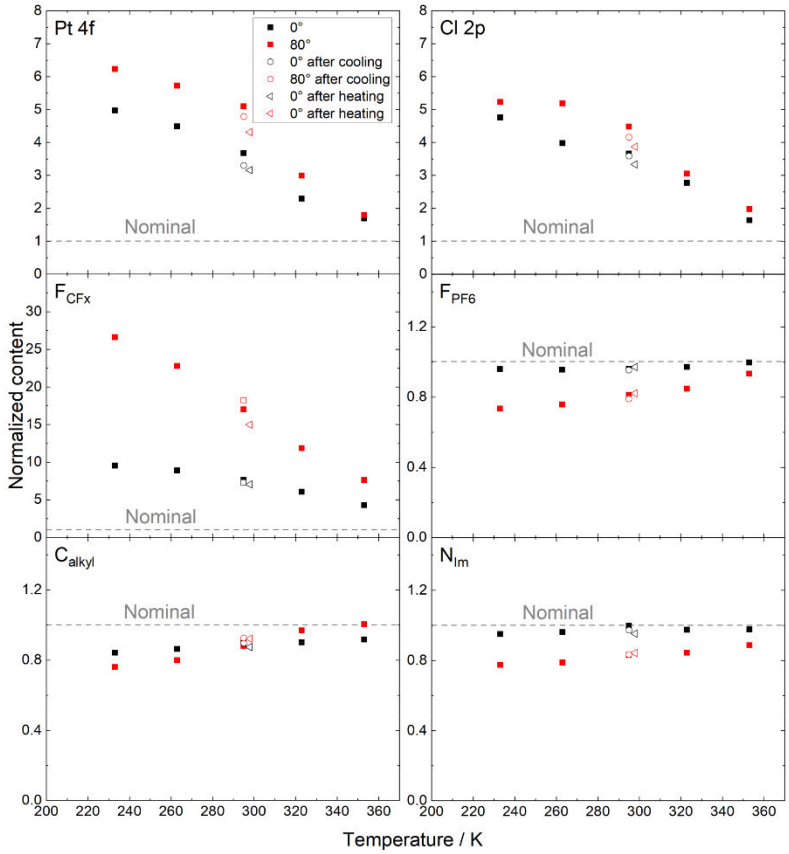

***Figure S3**: Normalized contents derived from Pt 4f, F_{CFx}, C_{alkyl}, Cl 2p, F_{PF6} and N_{Im} signals of a 1%$_{mol}$ solution of **1** in [C_4C_1Im][PF_6] in 0° (black squares) and 80° emission (red squares) upon variation of the sample temperature. After measurements at the temperature extremes at 233 K and 353 K, the sample was allowed to cool/heat to room temperature and measured again (open circles and triangles, respectively).*

Quantitative analysis of the temperature dependence of the XP spectra of all relevant core levels of a 5%$_{mol}$ solution of 1 in [C_4C_1Im][PF_6]

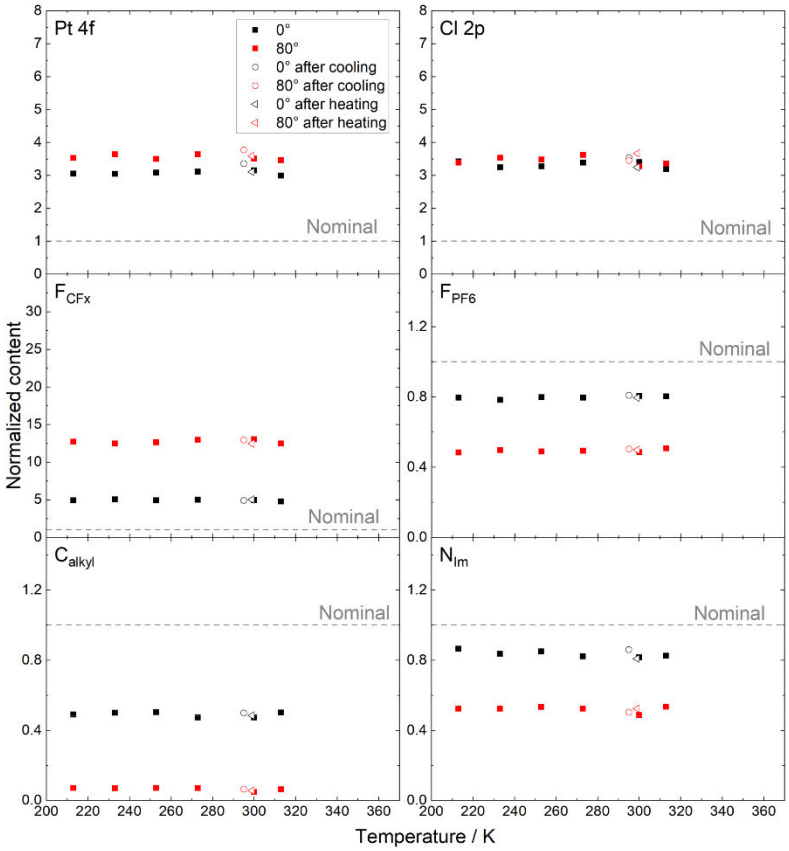

***Figure S4**: Normalized contents derived from Pt 4f, F_{CFx}, C_{alkyl}, Cl 2p, F_{PF6} and N_{im} signals of a 5%$_{mol}$ solution of **1** in [C_4C_1Im][PF_6] in 0° (black squares) and 80° emission (red squares) upon variation of the sample temperature. After measurements at the temperature extremes at 213 K and 313 K, the sample was allowed to cool/heat to room temperature and measured again (open circles and triangles, respectively).*

Temperature dependence of the surface tension for different solution of catalysts 1 and 2 in [C₄C₁Im][PF₆]

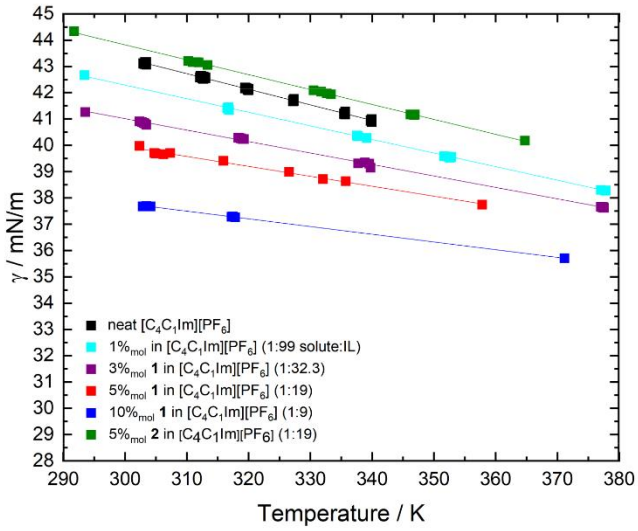

***Figure S5**: Temperature-dependent surface tension γ of neat $[C_4C_1Im][PF_6]$ (black), solutions of **1** in $[C_4C_1Im][PF_6]$ with molar concentrations of 1 (cyan), 3 (violet), 5 (red) and $10\%_{mol}$ (blue), and of a solution of **2** in $[C_4C_1Im][PF_6]$ with molar concentration of $5\%_{mol}$ (green).*

Complete set of XP spectra of a 9.5%$_{mol}$ solution of [C_3CNPFC_4Im][PF_6] in [C_4C_1Im][PF_6]

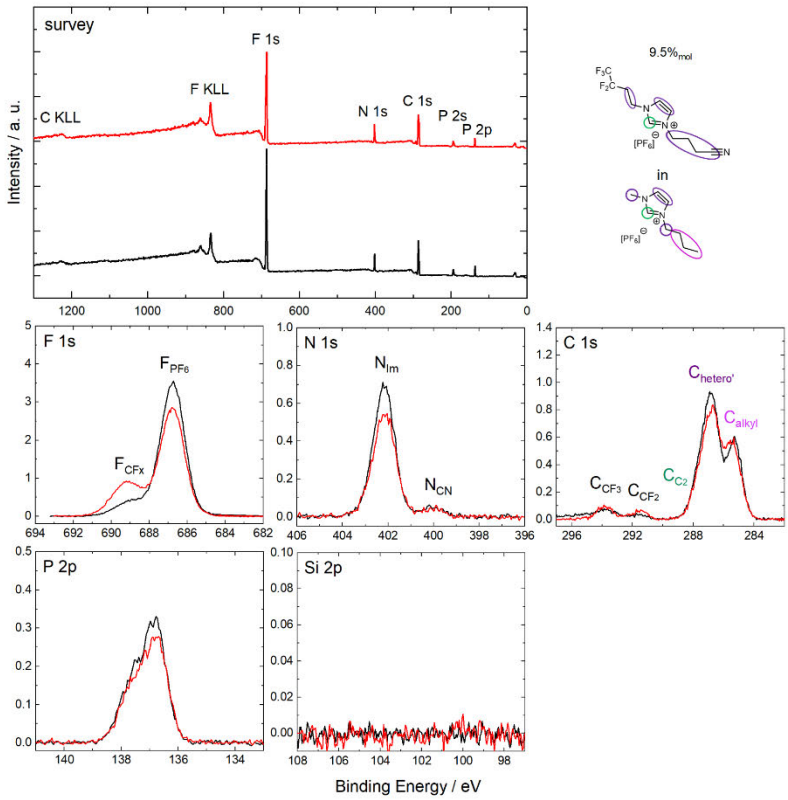

Figure S6: Survey, F 1s, N 1s, C 1s, P 2p and Si 2p XP spectra of a 9.5%$_{mol}$ solution of [C_3CNPFC_4Im][PF_6] in [C_4C_1Im][PF_6] in 0° (black) and 80° (red) emission recorded at room temperature with assignment of peaks to the molecular structure.

Peak fitting for solution shown in Figure S6:

Fitting of the C 1s region was achieved according to the procedure used for the solutions of **1**.[1] Due to the low concentration and overlap with the shake-up signal of the imidazolium ring, the C_{CF3} and C_{CF2} signals were only considered in 80° emission.

Temperature dependence of the surface tension for different solutions in $[C_4C_1Im][PF_6]$

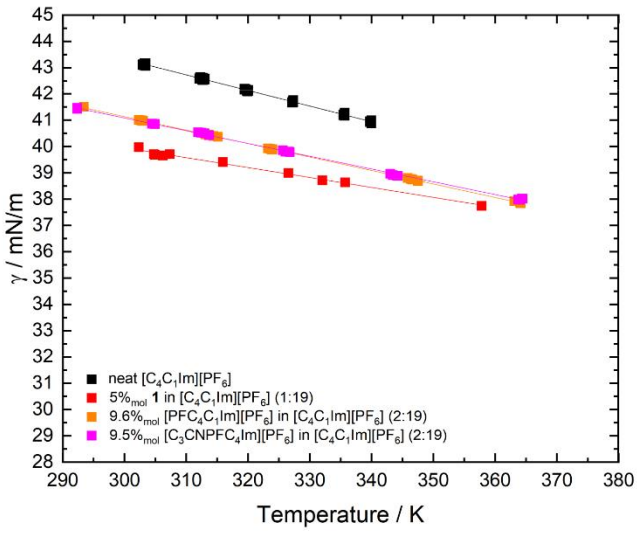

Figure S7: *Temperature-dependent surface tension γ of neat $[C_4C_1Im][PF_6]$ (black), a solution of **1** in $[C_4C_1Im][PF_6]$ with molar concentration of $5\%_{mol}$ (red) and solutions of $[C_3CNPFC_4Im][PF_6]$ (pink) with $9.5\%_{mol}$ and $[PFC_4C_1Im][PF_6]$ (orange) with $9.6\%_{mol}$ in $[C_4C_1Im][PF_6]$. Note that the solutions have the same IL:PFC_4 ratio of 2:19.*

Complete set of XP spectra of a 9.6%$_{mol}$ solution of [PFC$_4$C$_1$Im][PF$_6$] in [C$_4$C$_1$Im][PF$_6$]

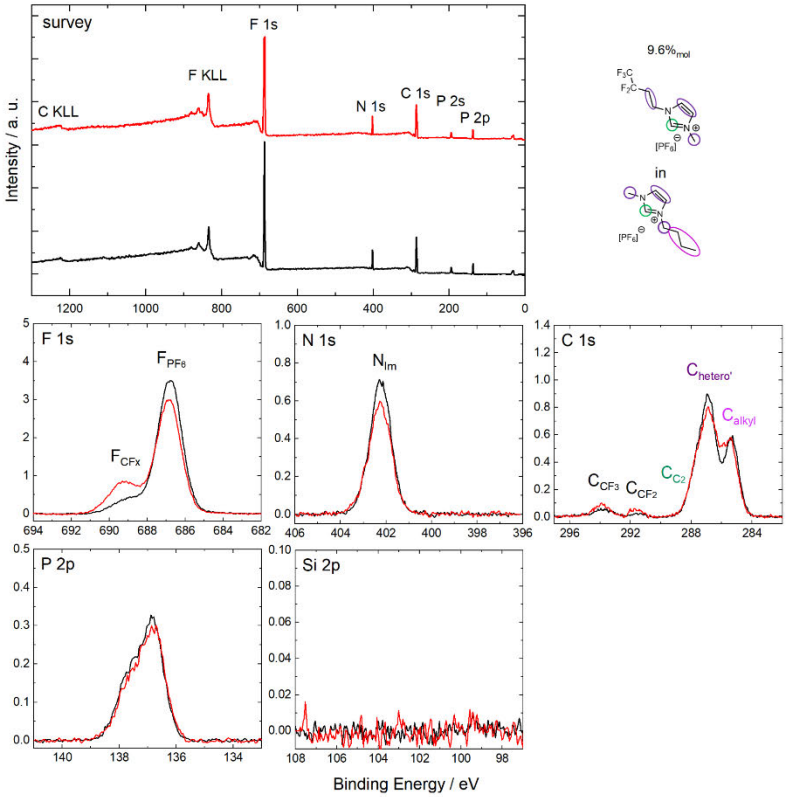

Figure S8: Survey, F 1s, N 1s, C 1s, P 2p and Si 2p XP spectra of a 9.6%$_{mol}$ solution of [PFC$_4$C$_1$Im][PF$_6$] in [C$_4$C$_1$Im][PF$_6$] in 0° (black) and 80° (red) emission recorded at room temperature with assignment of peaks to the molecular structure.

Peak fitting for solution shown in Figure S8:

Fitting of the C 1s region was achieved according to the procedure used for the solutions of **1**.[1] Due to the low concentration and overlap with the shake-up signal of the imidazolium ring, the C_{CF3} and C_{CF2} signals were only considered in 80° emission.

Temperature dependence of the surface tension for all solutions in [C4C1Im][PF6]

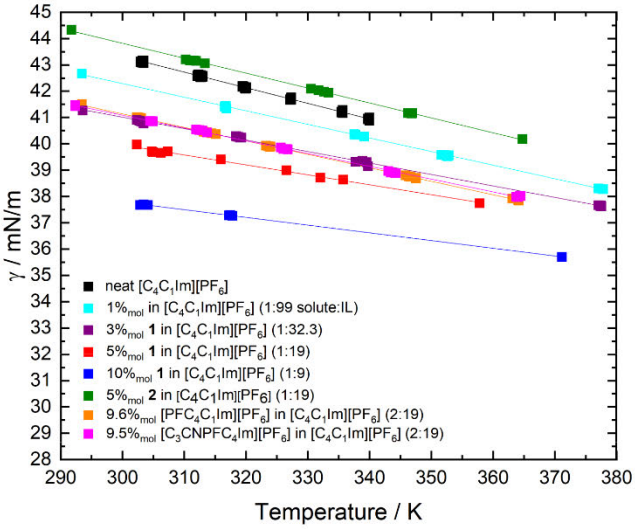

***Figure S9**: Overview on temperature-dependent surface tension γ of all solutions investigated in this work: Neat [C4C1Im][PF6] (black), solutions of **1** in [C4C1Im][PF6] with molar concentrations of 1 (cyan), 3 (violet), 5 (red) and 10%mol (blue) and a solution of **2** in [C4C1Im][PF6] with molar concentration of 5%mol (green), solutions of [C3CNPFC4Im][PF6] (pink) with 9.5%mol and [PFC4C1Im][PF6] (orange) with 9.6%mol in [C4C1Im][PF6].*

Table S1: *Weighed proportions for preparation of solutions investigated by ARXPS and PD.*

	1%$_{mol}$ 1 in $[C_4C_1Im][PF_6]$ for ARXPS	1%$_{mol}$ 1 in $[C_4C_1Im][PF_6]$ for PD	3%$_{mol}$ 1 in $[C_4C_1Im][PF_6]$ for PD	5%$_{mol}$ 1 in $[C_4C_1Im][PF_6]$	5%$_{mol}$ 2 in $[C_4C_1Im][PF_6]$	10%$_{mol}$ 1 in $[C_4C_1Im][PF_6]$	9.5%$_{mol}$ $[C_3CNPFC_4Im][PF_6]$ in $[C_4C_1Im][PF_6]$	9.6%$_{mol}$ $[PFC_4C_1Im][PF_6]$ in $[C_4C_1Im][PF_6]$
Mass *Cis*-$[PtCl_2(CH_3CN)_2]$ / mg	24.0	40.1	81.4	129	182	366		
Amount of substance *Cis*-$[PtCl_2(CH_3CN)_2]$ / mmol	0.068	0.113	0.229	0.362	0.514	1.03		
Mass $[C_3CNPFC_4Im][PF_6]$ / mg	57.9	96.6	196	310		881	328	
Amount of substance $[C_3CNPFC_4Im][PF_6]$ / mmol	0.136	0.226	0.459	0.725		2.06	0.923	
Mass $[C_4C_1Im][PF_6]$ / g	1.921	3.209	2.127	1.975	2.804	2.663	2.096	1.756
Amount of substance $[C_4C_1Im][PF_6]$ / mmol	6.69	11.2	7.41	6.88	9.77	9.28	7.30	6.12
Mass $[PFC_4C_1Im][PF_6]$ / mg								243
Amount of substance $[PFC_4C_1Im][PF_6]$ / mmol								0.650
Mass $[C_3CNC_1Im][PF_6]$ / mg					304			
Amount of substance $[C_3CNC_1Im][PF_6]$ / mmol					1.03			

For information on molar masses and purities of materials used, see next page.

Table S2: *Weighed proportions for preparation of solutions for density measurements.*

	5%$_{mol}$ 1 in $[C_4C_1Im][PF_6]$	5%$_{mol}$ 2 in $[C_4C_1Im][PF_6]$	9.5%$_{mol}$ $[C_3CNPFC_4Im][PF_6]$ in $[C_4C_1Im][PF_6]$
Mass *Cis*-$[PtCl_2(CH_3CN)_2]$ / mg	227	225	
Amount of substance *Cis*-$[PtCl_2(CH_3CN)_2]$ / mmol	0.639	0.633	
Mass $[C_3CNPFC_4Im][PF_6]$ / mg	0.547		690
Amount of substance $[C_3CNPFC_4Im][PF_6]$ / mmol	1.28		1.62
Mass $[C_4C_1Im][PF_6]$ / g	3.485	3.456	4.406
Amount of substance $[C_4C_1Im][PF_6]$ / mmol	12.1	12.0	15.3
Mass $[C_3CNC_1Im][PF_6]$ / mg		374	
Amount of substance $[C_3CNC_1Im][PF_6]$ / mmol		1.27	

$M_{[PtCl_2(CH_3CN)_2]}$ = 348.09 g/mol, $M_{[C_3CNPFC_4Im][PF_6]}$ = 427.20 g/mol, $M_{[C_4C_1Im][PF_6]}$ = 284.18 g/mol, $M_{[C_3CNC_1Im][PF_6]}$ = 295.16 g/mol, $M_{[PFC_4C_1Im][PF_6]}$ = 374.14 g/mol

Purity: $[PtCl_2(CH_3CN)_2]$: 98%, $[C_4C_1Im][PF_6]$: 99%

Table S3: *Density values at 298.15 K and density parameters of solutions investigated in this work obtained from fitting temperature-dependent density values according to eq. (1) (main manuscript). Calculated temperature-dependent density values were derived from eq. (2) (main manuscript).*

	Density ρ at 298.15 K	ρ_0 / g/cm³	ρ_1 / g/cm³·K	ρ_2 / g/cm³·K²	T-dependent density values obtained from
neat $[C_4C_1Im][PF_6]$	1.365	1.665	-0.00115	4.842E-07	experiment[3]
5%$_{mol}$ 1 in $[C_4C_1Im][PF_6]$	1.440	1.680	-0.000753	-1.822E-07	experiment
Neat 1	1.962	1.572	0.00335	-6.852E-06	calculation
1%$_{mol}$ 1 in $[C_4C_1Im][PF_6]$	1.381	1.669	-0.00107	3.480E-07	calculation
3%$_{mol}$ 1 in $[C_4C_1Im][PF_6]$	1.411	1.675	-0.000910	7.980E-08	calculation
10%$_{mol}$ 1 in $[C_4C_1Im][PF_6]$	1.503	1.688	-0.000377	-8.074E-07	calculation
5%$_{mol}$ 2 in $[C_4C_1Im][PF_6]$	1.426	1.665	-0.000746	-1.805E-07	experiment
9.5%$_{mol}$ $[C_3CNPFC_4Im][PF_6]$ in $[C_4C_1Im][PF_6]$	1.392	1.658	-0.000934	1.455E-07	experiment
neat $[PFC_4C_1Im][PF_6]$	1.647	2.262	-0.00287	2.702E-06	experiment[4]
9.6%$_{mol}$ $[PFC_4C_1Im][PF_6]$ in $[C_4C_1Im][PF_6]$	1.394	1.722	-0.00130	6.796E-07	calculation

References

[1] D. Hemmeter, D. Kremitzl, P. S. Schulz, P. Wasserscheid, F. Maier, H.-P. Steinrück, *Chem. Eur. J.* **2023**, *29*, e202203325.
[2] J. M. Gottfried, F. Maier, J. Rossa, D. Gerhard, P. S. Schulz, P. Wasserscheid, H.-P. Steinrück, *Z. Phys. Chem.* **2006**, *220*, 1439-1453.
[3] J. Jacquemin, P. Husson, A. A. H. Padua, V. Majer, *Green Chem.* **2006**, *8*, 172-180.
[4] T. M. Koller, F. D. Lenahan, P. S. Schmidt, T. Klein, J. Mehler, F. Maier, M. H. Rausch, P. Wasserscheid, H.-P. Steinrück, A. P. Fröba, *Int. J. Thermophys.* **2020**, *41*, 144.

8.5 Publication 5, [P5]

[P5] Exploring the Interfacial Behavior of Ruthenium Complexes in Ionic Liquids: Implications for Supported Ionic Liquid Phase Catalysts

D. Hemmeter, L. Sanchez Merlinsky, L. M. Baraldo, F. Maier, F. J. Williams, H.-P. Steinrück, *Phys. Chem. Chem. Phys.* **2024**, *26*, 7602-7610.

DOI: https://doi.org/10.1039/D4CP00247D

The author's contribution is the sample preparation, ARXPS and QMS investigation, data analysis, data interpretation and manuscript preparation.

8.6 Publication 6, [P6]

RESEARCH ARTICLE

ADVANCED MATERIALS INTERFACES Open Access

www.advmatinterfaces.de

Tailoring the Surface Enrichment of a Pt Catalyst in Ionic Liquid Solutions by Choice of the Solvent

*Daniel Hemmeter, Afra Gezmis, Daniel Kremitzl, Peter Wasserscheid, Florian Maier, and Hans-Peter Steinrück**

The so-called buoy-effect, that is, the targeted surface enrichment of a Pt catalyst dissolved in ionic liquids (ILs), is achieved by attaching perfluorinated alkyl chains to the ligand system, which drags the metal complex toward the interface. Using angle-resolved X-ray photoelectron spectroscopy, it is demonstrated how this surface enrichment can be tailored by variation of the solvent IL. In $[C_nC_1Im][PF_6]$ ILs (n = 2, 4, 8), the surface is fully saturated with the complex at $10\%_{mol}$ bulk content, while in $[C_4C_1Im][Tf_2N]$ only at $20\%_{mol}$ saturation is observed. At low catalyst concentrations of $1\%_{mol}$, where saturation is not yet reached, the enrichment increases with decreasing length of the IL alkyl chain. As a general rule, the degree of surface enrichment decreases with the decrease in surface tension of the solvent IL, that is, in the order $[C_2C_1Im][PF_6] > [C_4C_1Im][PF_6] > [C_8C_1Im][PF_6] > [C_4C_1Im][Tf_2N]$. In ILs with very low surface tension, enrichment is even suppressed. These results reveal the surface tension of the solvent IL as rational parameter for tailoring the interfacial structure of IL-based catalyst systems, such as supported ionic liquid phase (SILP) catalysis, where the nature of the IL/gas interface is expected to strongly influence the performance of the process.

1. Introduction

Design, characterization, and optimization of innovative catalytic systems play a central role in modern science and engineering, in order to facilitate both more ecological and economical chemical processes.[1] Commercial-scale catalysis is governed by heterogeneous systems promising, for example, robustness, facile product separation and low catalyst loss. A common challenge with technical heterogeneous catalysts, however, is the oftentimes poor selectivity and low atom utilization,[2] which is undesired in light of the growing demand for more sustainable processes. In addition to interesting advances toward boosting the selectivity of heterogeneous catalysts in the recent past,[2,3] also homogeneous organometallic complexes have become increasingly attractive, as they provide well-defined catalytic centers with uniform reactivity and thus high selectivity. Nonetheless, the attractiveness of these homogeneous catalysts for industry is still widely limited, due to challenging separation protocols and their sensitivity to harsh reaction conditions. Therefore, significant efforts have been dedicated to the design of novel hybrid systems for immobilization of homogeneous catalysts on solid supports, which aim to merge the benefits of homogeneous and heterogeneous catalysis.[4]

Supported Ionic Liquid Phase (SILP) catalysis has emerged as a particularly promising immobilization technique.[5] SILP systems are hybrid materials featuring a thin liquid film of a homogeneous catalyst dissolved in an ionic liquid (IL), which is adsorbed onto a large-surface-area support.[5b,c] The actual catalyst maintains its homogeneous character in the liquid phase, while the macroscopically solid SILP material can be employed just like a heterogeneous catalyst. The choice of ILs as the liquid solvent phase has several benefits: Being liquid salts, ILs show an extremely low vapor pressure and a high thermal stability; thus, they provide durable films suitable for rougher reaction conditions and continuous flow applications.[6] The ionic character of ILs also yields a different spectrum of solvent–solute interactions as compared to conventional molecular solvents, which can indeed be beneficial for the reaction outcome, as has been shown for a variety of catalyzed transformations.[7] Additionally, due to their widely organic composition, the chemical structure of ILs can be tailored toward task-specific properties, for example, regarding solvation and miscibility of/with reactants and products, stabilization of intermediates and transition states, viscosity, and interfacial tension.

D. Hemmeter, A. Gezmis, F. Maier, H.-P. Steinrück
Lehrstuhl für Physikalische Chemie II
Friedrich-Alexander-Universität Erlangen-Nürnberg
Egerlandstr. 3, 91058 Erlangen, Germany
E-mail: hans-peter.steinrueck@fau.de

D. Kremitzl, P. Wasserscheid
Lehrstuhl für Chemische Reaktionstechnik
Friedrich-Alexander-Universität Erlangen-Nürnberg
Egerlandstr. 3, 91058 Erlangen, Germany

P. Wasserscheid
Forschungszentrum Jülich GmbH
Helmholtz-Institute Erlangen-Nürnberg for Renewable Energy (IEK-11)
Cauerstr. 1, 91058 Erlangen, Germany

The ORCID identification number(s) for the author(s) of this article can be found under https://doi.org/10.1002/admi.202301085

DOI: 10.1002/admi.202301085

ADVANCED SCIENCE NEWS
www.advancedsciencenews.com

ADVANCED MATERIALS INTERFACES
www.advmatinterfaces.de

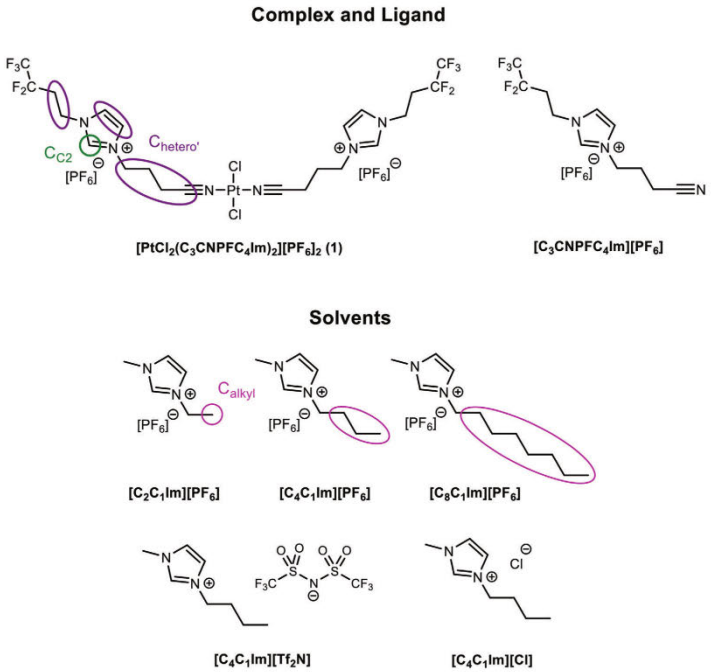

Figure 1. Molecular structures of materials employed in this work: Complex and ligand: $[PtCl_2(C_3CNPFC_4Im)_2][PF_6]_2$ (1) (top left), $[C_3CNPFC_4Im][PF_6]$ (top right), Solvent ILs: $[C_2C_1Im][PF_6]$ (middle left), $[C_4C_1Im][PF_6]$ (center), $[C_8C_1Im][PF_6]$ (middle right), $[C_4C_1Im][Tf_2N]$ (bottom left) and $[C_4C_1Im][Cl]$ (bottom right). Color coding indicates assignment of carbon species detected in XPS.

The large contact area of SILP catalysts with the surrounding reactant/product phase renders a fundamental understanding on the interfacial structures inevitable for most efficient application.[8] In fact, the nature of the IL/gas or vacuum interface of ILs was explored with a wide variety of well-established surface science techniques, targeting surface composition, enrichment effects, and preferential orientation and layering of ions and functional groups at the interface.[9] In particular, X-ray photoelectron spectroscopy (XPS) has been employed intensively in this regard by various groups, including ours.[8,9b,f,10] The power of this technique is that it enables quantitative insights into the elemental composition of the near-surface region along with chemical/electronic information of the atoms probed. The knowledge of these attributes has also shown to be highly beneficial in the study of IL solutions of organometallic catalysts and metal salts.[10h,11] The surface sensitivity of this technique can be tuned by varying the emission angle of the photoelectrons, which is referred to as angle-resolved XPS (ARXPS) and allows for an even more detailed structural picture on the IL/vacuum interface of catalyst systems.[10h,11a–c,k,12]

Using ARXPS, we recently demonstrated the manipulation of the surface concentration of a Pt complex in $[C_4C_1Im][PF_6]$ by attaching perfluorinated alkyl chains to the ligand system.[11a,k] These substituents induce a strong enrichment of the catalyst at the IL/vacuum interface in a buoy-like fashion pulling the molecule toward the surface.[11a] The driving force for the pronounced surface accumulation of the catalyst is the lowering in surface free energy, as was deduced from the surface tension measured using the pendant drop (PD) method.[11k] Our study showed that the magnitude of this so-called buoy effect can be controlled via several parameters: a) Catalyst concentration: The surface enrichment was found most pronounced at lowest concentration promising high atom utilization in catalytic applications;[11a,k] b) temperature: The surface concentration of the catalyst increases with decreasing temperature making this concept particularly interesting for low-temperature catalysis;[11k] c) the number of surface-active ligands attached to the metal center.[11k]

The intention of this study is to evaluate another important parameter for tailoring the surface enrichment and structure of such catalytic systems, that is, the variation of the IL solvent. For this purpose, we investigated solutions of the previously employed Pt catalyst (**1**) in a variety of ILs using ARXPS. The structure of **1** and of the IL solvents are depicted in **Figure 1**. As reported previously, **1** was directly synthesized in $[C_4C_1Im][PF_6]$.[11a,k] Herein, we successfully expanded

ADVANCED SCIENCE NEWS
www.advancedsciencenews.com

ADVANCED MATERIALS INTERFACES
www.advmatinterfaces.de

this preparation procedure to $[C_2C_1Im][PF_6]$, $[C_8C_1Im][PF_6]$, and $[C_4C_1Im][Tf_2N]$; notably, in $[C_4C_1Im][Cl]$, formation of **1** was not successful, which we attribute to coordination of the excess Cl^- anions. The $[PF_6]^-$-based ILs only differ in the chain length of the alkyl substituent on the $[C_nC_1Im]^+$ cation. For a variety of pure imidazolium-based ILs, the alkyl chain length was shown to have decisive influence on the structure of the IL/gas or vacuum interface: longer alkyl chains (number of carbon atoms (n) $\geq$ 4) preferably terminate the surface, while short alkyl chains (n < 4) show no or a much lower surface activity.[9b,d,i,j,l,13] From our ARXP spectra of neat $[C_2C_1Im][PF_6]$ at room temperature, we are able to show that this behavior also holds for the series of $[PF_6]^-$ ILs. By also employing $[C_4C_1Im][Tf_2N]$ as the solvent, we provide additional information on the influence of the IL anion on the surface enrichment of **1**. For all solutions, we found **1** to be strongly surface-enriched, with saturation occurring at sufficiently high catalyst concentrations. At $1\%_{mol}$, where the surface is not saturated yet, the enrichment of **1** follows the trend of the surface tension of the ILs ($[C_2C_1Im][PF_6] > [C_4C_1Im][PF_6] > [C_8C_1Im][PF_6] > [C_4C_1Im][Tf_2N]$). This behavior demonstrates that the surface concentration of the catalyst is strongly influenced by the surface free energy of the solvent. For $[C_4C_1Im][Cl]$, where the preparation of **1** was not successful, we studied solutions of only the ligand $[C_3CNPFC_4Im][PF_6]$ (see Figure 1) in $[C_4C_1Im][Cl]$ and $[C_4C_1Im][PF_6]$, and find the same influence of the solvent's surface tension on the surface enrichment of the ligand. For all neat ILs, the surface tensions were determined in our recently developed chamber ensuring ultraclean vacuum conditions.[14]

2. Results and Discussion

2.1. Expanding the Synthesis of 1 to Several IL Solvents

We recently reported the successful formation of **1** in $[C_4C_1Im][PF_6]$ using XPS on solutions with sufficiently high concentrations to clearly elucidate the stoichiometry of the complex.[11a,k] Herein, we expand this approach to solutions of **1** in $[C_2C_1Im][PF_6]$, $[C_8C_1Im][PF_6]$, and also $[C_4C_1Im][Tf_2N]$. In **Figure 2a–e**, the Pt 4f, F 1s, N 1s, and C 1s spectra of the concentrated solutions of **1** in $[C_2C_1Im][PF_6]$, $[C_4C_1Im][PF_6]$, $[C_8C_1Im][PF_6]$, and $[C_4C_1Im][Tf_2N]$ are plotted on top of each other, in 0° (black, more bulk-sensitive) and 80° emission (red, more surface-sensitive); full sets of spectra are shown in Figures S2–S6 (Supporting Information). The quantitative analyses of binding energies and signal intensities are provided in **Table 1a–e**. For all solutions, the Pt $4f_{7/2}$ signals were detected at 74.2eV ± 0.2 eV, indicating the same ligand environment of the metal center. All other signals also nicely agree with the binding energies expected from previous works on **1**[11a] or similar complexes,[11c] and with those of the $[C_4C_1Im][PF_6]$, $[C_8C_1Im][PF_6]$, and $[C_4C_1Im][Tf_2N]$ from literature.[10a,b,15] Since to the best of our knowledge no detailed ARXPS data of $[C_2C_1Im][PF_6]$ at room temperature was published yet, the corresponding spectra and the quantitative analysis are shown in Figure S1 and Table S1 (Supporting Information). As is evident from Table 1a–e, the detected intensities of the complex-specific signals, that is, Pt 4f, Cl 2p and $N_{CNcoord}$, match the expected stoichiometry (1:2:2 ratio of these signals) of **1**. This agreement confirms the chemical state and stoichiometry of the studied systems since non-volatile degradation products of the synthesis should be visible in the XP spectra. Note that due to the strong surface affinity of the fluorinated side chains in the ligand system, even at 0° (more bulk-sensitive) the F_{CFx} signal in the solutions of the $[PF_6]^-$ ILs always shows a larger intensity than expected, that is, a F_{CFx}:Pt ratio of ≈14:1 instead of the nominal ratio of 10:1.[11a,k] Overall, these results confirm successful formation of **1** also in $[C_2C_1Im][PF_6]$, $[C_8C_1Im][PF_6]$, and $[C_4C_1Im][Tf_2N]$.

To get more detailed insights into the influence of the anion on the enrichment of **1**, we also attempted synthesis of the catalyst in another $[C_4C_1Im]^+$-IL, that is, $[C_4C_1Im][Cl]$. However, this synthesis was not successful, most probably due to the coordinating behavior of the excess Cl^- anions, as is described in detail in the supporting information (see Figure S8 and Table S3 and text, Supporting Information). Since no detailed ARXPS investigation of neat $[C_4C_1Im][Cl]$ at room temperature was published yet, we also show the corresponding spectra (see Figure S7 and Table S2, Supporting Information).

2.2. Surface Composition of Concentrated Solutions of 1

Next, we discuss the surface composition of the concentrated solutions of **1** in $[C_2C_1Im][PF_6]$, $[C_4C_1Im][PF_6]$ and $[C_8C_1Im][PF_6]$, and $[C_4C_1Im][Tf_2N]$ by means of the ARXP spectra shown in Figure 2a–e (the spectra for **1** in $[C_4C_1Im][PF_6]$ have been adapted from Ref. [11a,k]). Overall, the $[PF_6]^-$-based IL solutions in Figure 2a–c shows very similar intensities in 0° and also in 80° emission. This is particularly true for the complex-specific Pt 4f, F_{CFx}, $N_{CNcoord}$, C_{CF3}, and C_{CF2} signals, and for the Cl 2p signal, as is also evident from Table 1a–c and Figures S2–S4 (Supporting Information). Inspection of Table 1a–c reveals that at 80° the complex-specific signals are strongly enhanced as compared to the nominal composition, which indicates that **1** is strongly enriched at the surface. The nearly identical spectra for the three solutions in 80° emission confirm a similar composition at the surface for the three solutions, namely, saturation with **1**, as concluded from previous works on solutions of **1** in $[C_4C_1Im][PF_6]$.[11a,k] Notably, we observe an enhancement also for 0° emission, which is a common observation in case of very strong surface enrichment of a species in IL mixtures and IL solutions.[11a,k] Moreover, if we compare the 80° and 0° spectra, we find more or less no increase for the Pt 4f signals, but a pronounced increase of the F_{CFx} signals. From this observation, we can deduce the orientation of **1** at the surface, with the surface-active fluorinated side chains of the ligand system pointing toward the vacuum and the Pt center toward the bulk. This orientation leads to a relative attenuation of the corresponding Pt signal at 80°, yielding a similar intensity as at 0°.[11a] The small differences in the 0° spectra for the F_{PF6}, N_{Im}, C_2 and $C_{hetero'}$ signals, which stem from both **1** and the ILs, are due the different bulk densities of the solutions (see Table 4). As expected, the IL-specific C_{alkyl} signal at 0° increases with increasing alkyl chain length of the $[C_nC_1Im]^+$ cation. Notably, at 80° for all solutions, the C_{alkyl} signal drastically decreases, so that for the solution of $[C_2C_1Im][PF_6]$ no appropriate fitting could be achieved, while for $[C_4C_1Im][PF_6]$ and $[C_8C_1Im][PF_6]$ low-intensity signals could be

ADVANCED SCIENCE NEWS
www.advancedsciencenews.com

ADVANCED MATERIALS INTERFACES
www.advmatinterfaces.de

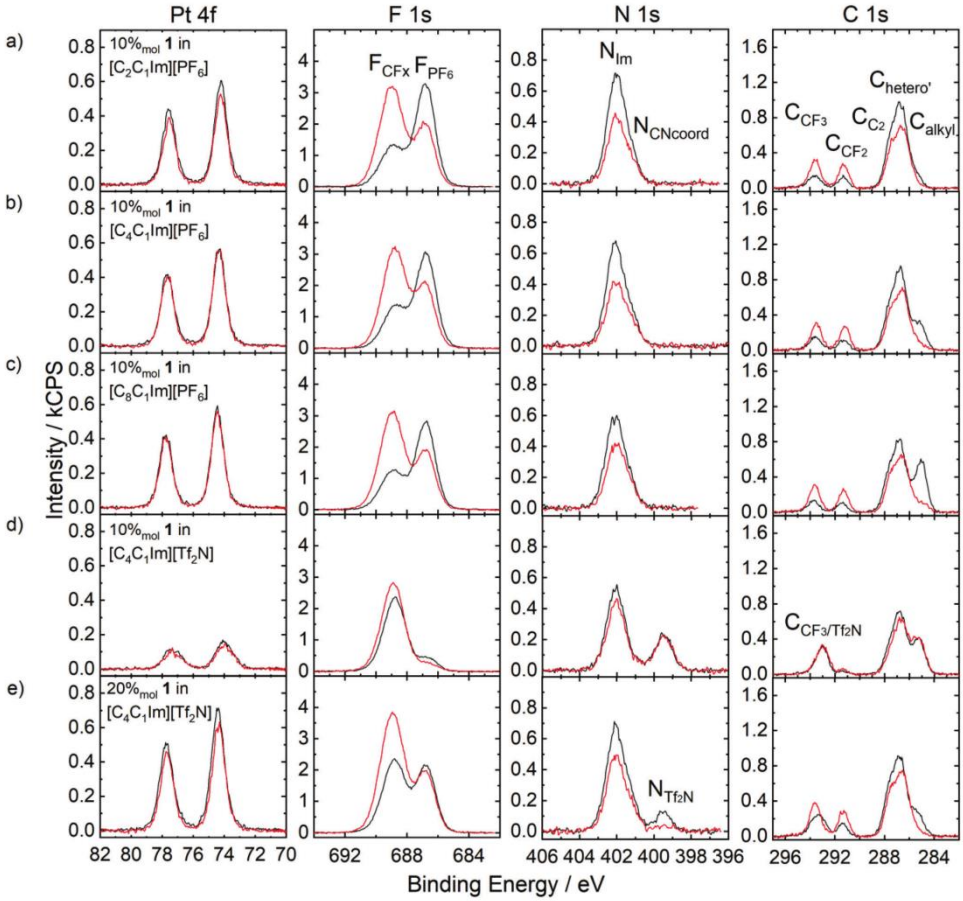

Figure 2. Pt 4f (left), F 1s (middle left), N 1s (middle right) and C 1s (right) XP spectra of 10%$_{mol}$ solutions of **1** in a) $[C_2C_1Im][PF_6]$, b) $[C_4C_1Im][PF_6]$, c) $[C_8C_1Im][PF_6]$ and d) $[C_4C_1Im][Tf_2N]$, as well as e) a 20%$_{mol}$ solution of **1** in $[C_4C_1Im][Tf_2N]$ in 0° (black) and 80° emission (red). For assignment of signals to the molecular structures see Figure 1. All spectra were recorded at room temperature.

deconvolved. This decrease is assigned to the depletion of the solvent IL from the surface layer caused by the enrichment of **1**.

The 10%$_{mol}$ solution of **1** in $[C_4C_1Im][Tf_2N]$ depicted in Figure 2d displays a quite different behavior than the equimolar $[PF_6]^-$ solutions discussed above. The intensity of the complex-specific Pt 4f, $N_{CNcoord}$, and C_{CF2} signals is much lower and, in fact, excellently corresponds to the nominal composition of the solution, as is evident from Table 1d. All other signals also nicely match the nominal values, suggesting a homogeneous distribution of the complex at the IL/vacuum interface and in the bulk at 10%$_{mol}$ catalyst loading. Note that the F_{CFx} and C_{CF3} signals contain contributions from both **1** and the $[Tf_2N]^-$ anion. The relatively broad $C_{CF3/Tf2N}$ signal is attributed to the fact that the carbon atoms of the CF_3 groups in **1** and $[Tf_2N]^-$ are chemically not equal due to different binding partners, that is, carbon (-CF_2) in **1** and sulfur (-SO_2) in $[Tf_2N]^-$. At 80°, the F_{CFx} signal shows an increase of ≈20%, while all other signals remain constant or show a slight decline. This behavior results from the preferential surface orientations of the complex[11a] and the $[Tf_2N]^-$ anion, both of which direct their CF_x groups toward the IL/gas or vacuum interface. Such an orientation is well established, also for other IL anions containing terminal perfluorinated carbon groups.[8,10c,11b,13,15,16]

Increasing the catalyst concentration in $[C_4C_1Im][Tf_2N]$ from 10%$_{mol}$ to 20%$_{mol}$ results in a disproportional increase of the

ADVANCED SCIENCE NEWS
www.advancedsciencenews.com
ADVANCED MATERIALS INTERFACES
www.advmatinterfaces.de

Table 1. Quantitative analysis of XPS core level spectra of 10%$_{mol}$ solutions of $[PtCl_2(C_3CNPFC_4Im)][PF_6]_2$ (**1**) in a) $[C_2C_1Im][PF_6]$, b) $[C_4C_1Im][PF_6]$, c) $[C_8C_1Im][PF_6]$, d) $[C_4C_1Im][Tf_2N]$, and with e) 20%$_{mol}$ catalyst concentration in $[C_4C_1Im][Tf_2N]$. "Nominal" indicates the relative numbers of the atoms derived from the nominal stoichiometry, and "Experimental" the corresponding numbers deduced from the XPS data at 0° and 80°. *For the spin-orbit-split signals, the indicated binding energy values correspond to larger peak, that is, Pt $4f_{7/2}$, Cl $2p_{3/2}$, P $2p_{3/2}$, and S $2p_{3/2}$.

a) 10%$_{mol}$ 1 in $[C_2C_1Im][PF_6]$	Pt 4f*	Cl 2p*	F 1s CFx	F 1s PF_6	N 1s Im	N 1s CNcoord	N 1s Tf_2N	C 1s CF_3	C 1s CF_2	C 1s C_2	C 1s hetero'	C 1s alkyl	P 2p*	O 1s	S 2p*
Binding Energy / eV	74.2	199.0	688.9	686.8	402.1	401.3		293.6	291.3	287.6	286.7	285.3	136.6		
Nominal	0.11	0.22	1.1	7.3	2.4	0.22		0.22	0.22	1.2	5.8	1.0	1.2		
Experimental, 0°	0.22	0.44	3.1	5.7	1.9	0.46		0.61	0.61	0.97	5.6	0.33	1.1		
Experimental, 80°	0.19	0.38	7.3	3.4	1.2	0.37		1.2	1.2	0.58	4.5		0.75		
b) 10%$_{mol}$ 1 in $[C_4C_1Im][PF_6]$ [11a,k]															
Binding Energy / eV	74.3	199.0	688.7	686.8	402.1	401.2		293.6	291.3	287.7	286.8	285.1	136.8		
Nominal	0.11	0.22	1.1	7.3	2.4	0.22		0.22	0.22	1.2	5.8	3.0	1.2		
Experimental, 0°	0.23	0.50	3.3	5.9	2.0	0.53		0.66	0.66	1.0	5.8	1.3	1.1		
Experimental, 80°	0.23	0.44	7.8	3.8	1.3	0.42		1.3	1.3	0.64	4.9	0.13	0.86		
c) 10%$_{mol}$ 1 in $[C_8C_1Im][PF_6]$															
Binding Energy / eV	74.4	199.1	688.9	686.8	402.1	401.4		293.8	291.5	287.7	286.8	285.1	136.9		
Nominal	0.11	0.22	1.1	7.3	2.4	0.22		0.22	0.22	1.2	5.8	7.0	1.2		
Experimental, 0°	0.28	0.55	3.9	6.5	2.2	0.54		0.69	0.69	1.1	6.2	3.2	1.2		
Experimental, 80°	0.26	0.49	9.5	4.2	1.4	0.54		1.5	1.5	0.70	5.7	0.35	0.91		
d) 10%$_{mol}$ 1 in $[C_4C_1Im][Tf_2N]$															
Binding Energy / eV	74.0	198.9	688.8	686.6	402.1	401.2	399.5	293.1	291.3	287.7	286.8	285.2	136.7	532.7	169.1
Nominal	0.11	0.22	7.1	1.3	2.4	0.22	1.0	2.2	0.22	1.2	5.8	3.0	0.22	4.0	2.0
Experimental, 0°	0.12	0.23	7.6	1.0	2.5	0.19	1.0	2.3	0.18	1.2	5.7	2.7	0.22	4.0	2.0
Experimental, 80°	0.11	0.18	9.3	0.6	2.1	0.14	1.0	2.6	0.25	1.0	5.1	2.9	0.17	3.7	2.0
e) 20%$_{mol}$ 1 in $[C_4C_1Im][Tf_2N]$															
Binding Energy / eV	74.4	199.1	688.8	686.8	402.1	401.3	399.5	293.4	291.4	287.7	286.8	285.2	136.8	532.7	169.1
Nominal	0.25	0.50	8.5	3.0	3.0	0.50	1.0	2.5	0.50	1.5	8.0	3.0	0.50	4.0	2.0
Experimental, 0°	0.44	0.88	8.3	5.9	3.1	0.80	0.53	2.4	0.83	1.5	8.7	1.4	0.95	2.0	1.1
Experimental, 80°	0.37	0.75	13.9	5.2	2.2	0.62	0.19	2.8	1.9	1.1	7.9	0	1.1	0.50	0.30

ADVANCED SCIENCE NEWS
www.advancedsciencenews.com

ADVANCED MATERIALS INTERFACES
www.advmatinterfaces.de

complex-specific Pt 4f, F_{CFx}, F_{PF6}, and $N_{CNcoord}$ signals in 0° and 80° (e.g., for Pt by a factor of ≈3.5 in 0°, instead of the expected factor of ≈2), as evident from the comparison of Figure 2d,e. Accordingly, the intensities of all complex-specific signals in Table 1e are much higher than expected from the nominal composition, while signals stemming from **1** and IL (N_{Im}, C_2, and $C_{hetero'}$) agree with the nominal values, and the IL-specific signals (N_{Tf2N}, C_{alkyl}, O 1s, S 2p) are much smaller than the nominal values 0° and 80°. These findings are in line with a strong enrichment of the complex at the IL/vacuum interface, similar to that observed for the surface-saturated $[PF_6]^-$ solutions. The very similar Pt 4f intensity at 80° for the $[Tf_2N]^-$ and the $[PF_6]^-$ solutions (compare Figure 2e vs Figure 2a–c) indicates that at 20%$_{mol}$ the $[Tf_2N]^-$ solution the surface is also saturated with the complex. The surface enrichment of the complex in the 20%$_{mol}$ solution is also evident from the strong increase of the F_{CFx} signal at 80° as compared to 0° (see Figure 2e); notably for the homogeneous 10%$_{mol}$ solution in $[C_4C_1Im][Tf_2N]$ only small increase is observed (see Figure 2d). Overall, these results indicate that inducing surface enrichment of **1** in $[C_4C_1Im][Tf_2N]$ requires a higher concentration of the catalyst than for the $[PF_6]^-$ ILs. This observation is assigned to the particularly low surface tension of $[C_4C_1Im][Tf_2N]$ as will be discussed in more detail later. Due to its lower surface tension, $[C_4C_1Im][Tf_2N]$ exhibits a higher driving force toward the surface than the $[PF_6]^-$ ILs, so that a higher concentration of surface-active catalyst is required to significantly lower the surface free energy by its accumulation at the interface.

For the 20%$_{mol}$ solution of **1** in $[C_4C_1Im][Tf_2N]$, it is also interesting to discuss the surface behavior of the anions in more detail, since for this system solvent and solute have different anions, that is, $[Tf_2N]^-$ and $[PF_6]^-$. Several groups have dedicated significant interest in related IL mixtures with these anions in the recent past.[17] In Figure 2d, the F_{PF6} signal, which is only due to the ionic complex **1**, shows a much higher intensity at both 0° and 80° than expected from the nominal composition. At the same time, the N_{Tf2N} signal, which is only due to the solvent IL, shows a much lower than nominal intensity at 0° and was barely detected at 80°. This behavior reveals that the $[PF_6]^-$ anion is enriched at the IL/vacuum interface, along with its original metal-containing counter ion. This finding is quite surprising since the $[Tf_2N]^-$ anion typically is enriched in binary mixtures of $[Tf_2N]^-$ and $[PF_6]^-$ ILs[17], but also in mixtures with ILs containing other anions.[9g,10f,i] The reason for the enrichment of the $[PF_6]^-$ anion could be a more efficient packing in the closed layer of **1** at the IL/vacuum interface with the smaller $[PF_6]^-$ anion rather than the larger $[Tf_2N]^-$.

2.3. Surface Composition of 1%$_{mol}$ Solutions of 1

After discussing the concentrated solutions, we next address ARXP spectra of more diluted solutions with 1%$_{mol}$ of **1** dissolved in the ILs, that is, a concentration regime, where we do not expect the IL/vacuum interface to be fully saturated with **1**, as was shown for a solution of $[C_4C_1Im][PF_6]$ in a previous study.[11k] **Figure 3** shows the Pt 4f, F 1s, and C 1s spectra of the 1%$_{mol}$ solutions of **1** in $[C_2C_1Im][PF_6]$ (black), $[C_4C_1Im][PF_6]$ (green) and $[C_8C_1Im][PF_6]$ (blue), at 0° (left) and 80° (right). For comparison, also the Pt 4f signals of a 1%$_{mol}$ solution of **1** in $[C_4C_1Im][Tf_2N]$ (orange) are depicted. Full sets of ARXP spectra of these solutions are depicted in Figures S9–S12 (Supporting Information), and the quantitative analysis is provided in **Table 2a–d**.

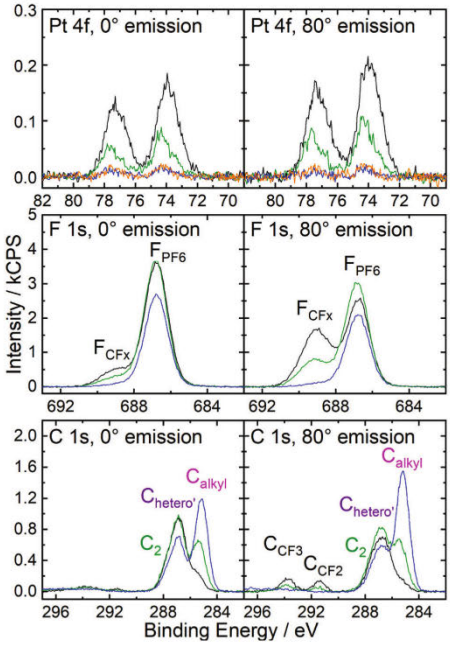

Figure 3. Pt 4f (top), F 1s (middle), and C 1s (bottom) XP spectra of 1%$_{mol}$ solutions of **1** in $[C_2C_1Im][PF_6]$ (black), $[C_4C_1Im][PF_6]$ (green) and $[C_8C_1Im][PF_6]$ (blue) in 0° (left) and 80° emission (right). In addition, Pt 4f spectra of a 1%$_{mol}$ solution of **1** $[C_4C_1Im][Tf_2N]$ (orange) are shown. For assignment of signals to the molecular structures see Figure 1. All spectra were recorded at room temperature.

As evident from Figure 3, the complex-related Pt 4f and F_{CFx} signals at 0° and 80° strongly increase in intensity with decreasing chain length on the $[C_nC_1Im]^+$ cation, that is, they are smallest for the $[C_8C_1Im][PF_6]$ and largest for the $[C_2C_1Im][PF_6]$ solution. This finding reveals that the enrichment of **1** at the IL/vacuum interface is more pronounced for short alkyl substituents on the $[C_nC_1Im]^+$ cation. For the $[C_8C_1Im][PF_6]$ solution, the Pt 4f intensity is actually in line with the nominal composition of the solution indicating homogeneous distribution of **1** at the surface and in the bulk. Hence, the surface activity of **1** can even be suppressed at 1%$_{mol}$ due to competition with the surface-affine octyl chain of the solvent, as will be discussed further below.

The opposite trend is found for the IL-specific C_{alkyl} signals in Figure 3, which show an increase upon increasing the chain length on the imidazolium cation. The magnitude of the increase is stronger than expected from the nominal increase (1, 3, and 7 C_{alkyl} atoms in the different ILs, see Figure 1), which is attributed

ADVANCED SCIENCE NEWS
www.advancedsciencenews.com
ADVANCED MATERIALS INTERFACES
www.advmatinterfaces.de

Table 2. Quantitative analysis of XPS core level spectra of 1%$_{mol}$ solutions of **1** in a) $[C_2C_1Im][PF_6]$, b) $[C_4C_1Im][PF_6]$, c) $[C_8C_1Im][PF_6]$, and d) $[C_4C_1Im][Tf_2N]$. "Nominal" indicates the relative numbers of the atoms derived from the nominal stoichiometry, and "Experimental" the corresponding numbers deduced from the XPS data at 0° and 80°. *For the spin-orbit-split signals, the indicated binding energy values correspond to larger peak, that is, Pt $4f_{7/2}$, Cl $2p_{3/2}$, P $2p_{3/2}$, and S $2p_{3/2}$.

a) 1%$_{mol}$ 1 in $[C_2C_1Im][PF_6]$	Pt 4f*	Cl 2p*	F 1s CFx	F 1s PF_6	N 1s Im	N 1s CNcoord	N 1s Tf_2N	C 1s CF_3	C 1s CF_2	C 1s C_2	C 1s hetero*	C 1s alkyl	P 2p*	O 1s	S 2p*
Binding Energy / eV	73.9	199.1	688.9	686.8	402.1	401.2		293.8 (80°)	291.5 (80°)	287.7	286.8	285.4	136.8		
Nominal	0.010	0.020	0.10	6.1	2.0	0.020		0.020	0.020	1.0	4.2	1.0	1.0		
Experimental, 0°	0.089	0.16	1.1	5.6	1.8	0.11				0.92	4.0	0.73	1.0		
Experimental, 80°	0.11	0.19	3.3	3.9	1.3	0.11		0.60	0.60	0.65	3.7	0.27	0.76		
b) 1%$_{mol}$ 1 in $[C_4C_1Im][PF_6]$[11k]															
Binding Energy / eV	74.2	199.1	688.8	686.8	402.2			293.9 (80°)	291.6 (80°)	287.8	286.9	285.4	136.9		
Nominal	0.010	0.020	0.10	6.1	2.0	0.020		0.020	0.020	1.0	4.2	3.0	1.0		
Experimental, 0°	0.037	0.074	0.77	5.9	2.0					1.0	4.0	2.7	1.1		
Experimental, 80°	0.051	0.090	1.7	5.0	1.7			0.29	0.29	0.85	4.0	2.6	0.98		
c) 1%$_{mol}$ 1 in $[C_8C_1Im][PF_6]$															
Binding Energy / eV	74.2	198.9	688.9	686.8	402.2					287.8	286.9	285.2	136.8		
Nominal	0.010	0.020	0.10	6.1	2.0	0.020		0.020	0.020	1.0	4.2	7.0	1.0		
Experimental, 0°	0.011	0.029	0.27	6.1	2.0					1.0	4.1	6.8	1.1		
Experimental, 80°	0.010		0.36	4.8	1.7					0.85	3.9	8.9	1.1		
d) 1%$_{mol}$ 1 in $[C_4C_1Im][Tf_2N]$															
Binding Energy / eV	74.2		688.8	686.8	402.1		399.5	293.0		287.7	286.8	285.3		532.6	169.1
Nominal	0.010	0.020	6.1	0.12	2.0	0.020	1.0	2.0	0.020	1.0	4.2	3.0	0.020	4.0	2.0
Experimental, 0°	0.011		6.2	0.093	2.0		1.0	2.1		1.0	4.1	2.9		4.0	2.0
Experimental, 80°	0.012		6.9	0.039	1.9		0.97	2.1		0.93	3.8	3.2		3.7	2.0

ADVANCED SCIENCE NEWS
www.advancedsciencenews.com

ADVANCED MATERIALS INTERFACES
www.advmatinterfaces.de

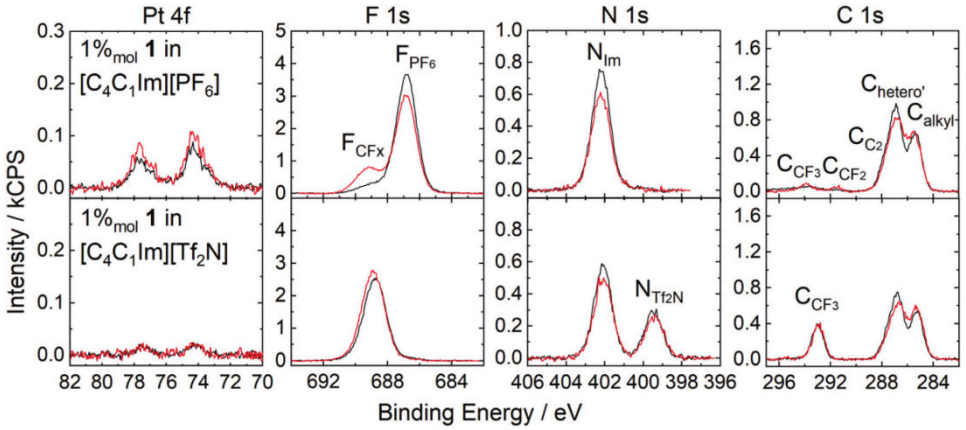

Figure 4. Pt 4f (left), F 1s (middle left), N 1s (middle right) and C 1s (right) XP spectra of 1%$_{mol}$ solutions of **1** in $[C_4C_1Im][PF_6]$ (top) and $[C_4C_1Im][Tf_2N]$ (bottom) in 0° (black) and 80° emission (red). For assignment of signals to the molecular structures see Figure 1. All spectra were recorded at room temperature.

to the different degree of surface enrichment of **1** in the different ILs. For the $[C_2C_1Im][PF_6]$ solution, where the Pt signal shows the strongest enrichment, the C_{alkyl} signal at 0° and even more at 80° is much lower than nominally expected (Table 2a). For the $[C_4C_1Im][PF_6]$ solution, close-to-nominal values are found at both angles (Table 2b), as has been discussed previously.[11k] For $[C_8C_1Im][PF_6]$, where no Pt enrichment is seen in Pt signal, the C_{alkyl} signal at 0° agrees well with the nominal one, and at 80° a significantly enhanced value is observed (Table 2c) which is in line with the absence of surface enrichment. The surface is thus dominated by the IL, with the topmost layer orientated such that the alkyl chain of the $[C_8C_1Im]^+$ cation pointed toward the vacuum, as has been reported for the pure IL.[10b]

Overall, we find that the surface enrichment of the catalyst in the $[PF_6]^-$ ILs shows a strong dependence on the chain length of the alkyl substituent on the $[C_nC_1Im]^+$ cation, which is due to the increasing surface affinity of longer alkyl chains competing with the fluorinated substituents. The latter effect translates into a lower surface tension, which will be correlated to the surface enrichment of **1** below.

Next, we will compare ARXP spectra of 1%$_{mol}$ solutions of **1** in $[C_4C_1Im][PF_6]$ (top) and $[C_4C_1Im][Tf_2N]$ (bottom), that is, changing only the anion of the IL, shown in **Figure 4**. Comparing the Pt 4f signals clearly reveals for the $[C_4C_1Im][PF_6]$ solution (green in Figure 3) a much higher intensity at both angles and with that a much higher surface concentration of **1** as compared to the $[Tf_2N]^-$ solution (orange). As can be seen from the Pt 4f signals in Figure 3, the signal from the $[C_4C_1Im][Tf_2N]$ solution (orange) shows a similar intensity as found for the $[C_8C_1Im][PF_6]$ solution (blue) indicating homogeneous distribution of **1** at the surface also in $[C_4C_1Im][Tf_2N]$. This finding is supported by the quantitative analysis of the peak intensities shown in Table 2d, where the values experimentally derived from the 0° emission spectra agree well with the nominal composition. At 80°, the F_{CFx} signal of $[C_4C_1Im][Tf_2N]$ in Figure 4 shows a slight increase as compared to 0°, which is assigned to the orientation of **1** and the $[Tf_2N]^-$ anion, as discussed above for the 10%$_{mol}$ solution. The C_{alkyl} signal shows a slight increase at 80°, which is due to the orientation of the $[C_4C_1Im]^+$ cation exposing its butyl chain toward the vacuum. This effect was not detected for the $[C_4C_1Im][PF_6]$ solution due to the enrichment of **1** and the concomitant damping of the IL-specific C_{alkyl} signal.[11k] For the $[C_4C_1Im][Tf_2N]$ solution, all other signals show a slight decrease or remain constant at 80° corresponding to the preferred orientations of the ions at the surface, as discussed above. Note that for the very low-intense F_{PF6} signal a large uncertainty must be expected due to close vicinity to the intense F_{CFx} signal. With this, and also due to the absence of a sufficiently intense P 2p signal (due to its low concentration and cross-section), no conclusion about the interfacial behavior of the $[PF_6]^-$ anion could be drawn at this concentration.

2.4. Correlating Surface Enrichment with the Surface Tension of the IL

In the following, we will address the correlation of concentration of **1** at the IL/vacuum interface with the surface tension of the neat IL solvents. The surface tension values γ were obtained by using the PD method under ultraclean vacuum conditions, and the values at 298 K are shown in Table 4 for all ILs investigated. The full sets of temperature-dependent surface tension measurements are depicted in Figure S13 (Supporting Information). The surface tensions of 34.2 mN m^{-1} for $[C_8C_1Im][PF_6]$ and 43.4 mN m^{-1} for $[C_4C_1Im][PF_6]$ were reported before by us, in good agreement with the literature data.[10b,11k,14] For $[C_2C_1Im][PF_6]$, we measured 51.9 mN m^{-1}. For this IL, Ref. [9c] denoted a value ≈50 mN m^{-1} at 298 K, without providing further information like the method used, the experimental

ADVANCED SCIENCE NEWS
www.advancedsciencenews.com

ADVANCED MATERIALS INTERFACES
www.advmatinterfaces.de

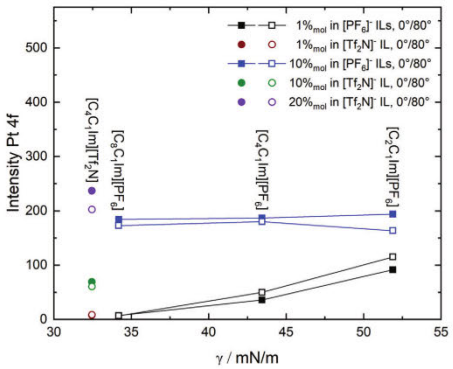

Figure 5. Total Pt 4f peak area detected in XPS of solutions of **1** with concentrations of 1%$_{mol}$ in the $[PF_6]^-$ ILs (black), 1%$_{mol}$ in $[C_4C_1Im][Tf_2N]$ (red brown), 10%$_{mol}$ in the $[PF_6]^-$ ILs (blue), 10%$_{mol}$ in $[C_4C_1Im][Tf_2N]$ (green) and 20%$_{mol}$ in $[C_4C_1Im][Tf_2N]$ (violet) in 0° (full symbols) and 80° emission (open symbols) against the surface tension γ of the neat ILs at 298 K. Note that for 1%$_{mol}$ in $[C_4C_1Im][Tf_2N]$ the signals for 0° (full) and 80° (open) fall on top of each other.

uncertainty, or additional references. Note that $[C_2C_1Im][PF_6]$ is a solid at 298 K (melting point: 331–333 K[18]). Nevertheless, we were able to measure the surface tension of this IL with our vacuum PD setup down to room temperature as a supercooled liquid (see Experimental Section for details). The same was possible also for the ultra-pure and surface-clean $[C_4C_1Im][Cl]$ (melting point: 347 K[19]) sample and we found a surface tension of 49.9 mN m^{-1} at 298 K, which is slightly higher than the value reported in literature of 48.2 mN m^{-1} using the capillary rise method.[20] For $[C_4C_1Im][Tf_2N]$, we obtained 32.5 mN m^{-1}, in excellent agreement with the literature data obtained by the PD method (32.5 mN m^{-1} at 298.15 K[21]). The surface tension values at 298 K decrease in the following order: $[C_2C_1Im][PF_6] > [C_4C_1Im][Cl] > [C_4C_1Im][PF_6] > [C_8C_1Im][PF_6] > [C_4C_1Im][Tf_2N]$ (see Table 4). In other words, the surface tension decreases with increasing chain length of the alkyl substituents for the $[PF_6]^-$ ILs and, in terms of the anion with the same cation, in the order $[Cl]^- > [PF_6]^- > [Tf_2N]^-$.

Figure 5 depicts the obtained absolute Pt 4f intensity of the solutions at 0° and 80° against the surface tension γ of the neat ILs at 298 K. For the three 10%$_{mol}$ $[PF_6]^-$ IL solutions, the Pt intensity is more or less identical at 80° (open blue squares) and also at 0° (full blue squares). For the 10%$_{mol}$ $[C_4C_1Im][Tf_2N]$ solution, the Pt intensity is much smaller (open and full green circles), as discussed above. At this concentration, the relatively high surface tension of the $[PF_6]^-$ ILs facilitates strong enrichment of **1** at the IL/vacuum interface, while for $[C_4C_1Im][Tf_2N]$ it is too low, such that enrichment of **1** does not result in sufficient lowering of the surface free energy. For the latter, only for a higher concentration of 20%$_{mol}$ (open and full violet circles) surface enrichment occurs, as discussed above.

For the 1%$_{mol}$ $[PF_6]^-$ IL solutions (full and open black squares), the Pt 4f intensity increases with increasing surface tension of the solvent, that is, the enrichment of the complex is strongest in the IL with the highest surface tension. For this IL, the strongest lowering in surface free energy is obtained by accumulation of the surface-active complex **1** at the IL/vacuum interface with respect to a reference situation where the complex would be homogeneously distributed in the surface-near region and in the bulk. For the solutions of $[C_8C_1Im][PF_6]$ and also for $[C_4C_1Im][Tf_2N]$ (full and open red brown circles), the surface activity of the solvent, induced by the long alkyl chains or the $[Tf_2N]^-$ anions, respectively, is high enough to compete with the surface-active complex **1**, which results in a homogeneous distribution of solvent and solute in the surface-near region with no surface enrichment, as discussed above. Since the surface tension of $[C_4C_1Im][Tf_2N]$ is lower than that of $[C_8C_1Im][PF_6]$, one could anticipate surface depletion of **1** dissolved in the former, which was, however, not observed. It is possible that surface depletion of the catalyst occurs when being dissolved in an IL with an even lower surface tension.

2.5. Solutions of $[C_3CNPFC_4Im][PF_6]$ in $[C_4C_1Im][PF_6]$ and $[C_4C_1Im][Cl]$

As discussed above, the synthesis of **1** in $[C_4C_1Im][Cl]$ was not successful. To nevertheless obtain some information on enrichment effects, we compare a 9.5%$_{mol}$ solution of $[C_3CNPFC_4Im][PF_6]$, which served as the surface-active ligand in **1**, in $[C_4C_1Im][Cl]$ (top) to a 9.5%$_{mol}$ solution in $[C_4C_1Im][PF_6]$ (bottom). **Figure 6** depicts the corresponding F 1s, N 1s, and C 1s XP spectra; the full sets of spectra are shown in Figures S14 and S15 (Supporting Information), and their quantitative analyses are provided in **Table 3a,b**. The $[PF_6]^-$ solution was studied in detail previously[11k], with the ligand showing a significant, but lower surface enrichment as compared to **1**. Since the spectra of the $[Cl]^-$ and $[PF_6]^-$ solutions show many similarities, we only focus on the most important aspects: For both solutions, the ligand-specific F_{CFx} signals in Figure 6 show a clear enhancement at 80° as compared to 0°, which is due to the surface enrichment of $[C_3CNPFC_4Im][PF_6]$: The increase for the $[C_4C_1Im][Cl]$ solution (factor of 2.4) in Figure 6 is more pronounced than for the $[C_4C_1Im][PF_6]$ solution (factor of 2.0). Moreover, the signals stemming from both ligand and IL, that is, N_{Im}, C_{C2} and $C_{hetero'}$, show a stronger decrease at 80° for the $[C_4C_1Im][Cl]$ than for the $[C_4C_1Im][PF_6]$ solution (see also Table 3a,b). Finally, while the IL-specific C_{alkyl} signals at 0° and 80° have very similar intensities for the $[C_4C_1Im][PF_6]$ solution, a significantly smaller signal is seen at 80° for the $[C_4C_1Im][Cl]$ solution. All these observations indicate that the enrichment of the solute at the IL/vacuum interface is more pronounced in $[C_4C_1Im][Cl]$. This is in line with the conclusion drawn above that employing a solvent with a higher surface tension, that is, 49.9 mN m^{-1} for $[C_4C_1Im][Cl]$ vs 43.4 mN m^{-1} for $[C_4C_1Im][PF_6]$ (see **Table 4**), results in a stronger surface enrichment of the solute.

3. Conclusion

We investigated the surface enrichment of a buoy-type catalyst **1** at the IL/vacuum interface in a variety of IL solvents, that is, $[C_2C_1Im][PF_6]$, $[C_4C_1Im][PF_6]$, $[C_8C_1Im][PF_6]$, and

ADVANCED SCIENCE NEWS
www.advancedsciencenews.com

ADVANCED MATERIALS INTERFACES
www.advmatinterfaces.de

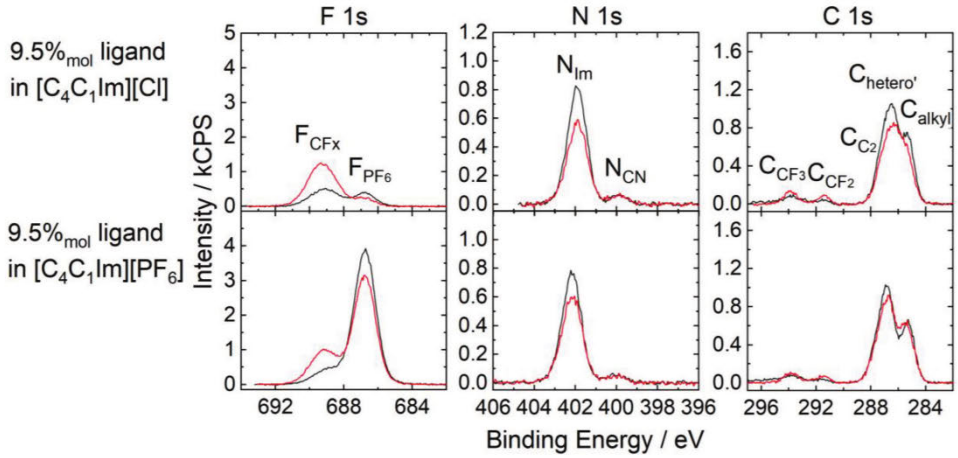

Figure 6. F 1s (left), N 1s (middle), and C 1s (right) XP spectra of 9.5%$_{mol}$ solutions of $[C_3CNPFC_4Im][PF_6]$ in $[C_4C_1Im][Cl]$ (top) and $[C_4C_1Im][PF_6]$ (bottom) in 0° (black) and 80° emission (red). For assignment of signals to the molecular structures see Figure 1. All spectra were recorded at room temperature.

$[C_4C_1Im][Tf_2N]$ using ARXPS. The catalyst was successfully prepared directly in the ILs $[C_2C_1Im][PF_6]$, $[C_8C_1Im][PF_6]$, and $[C_4C_1Im][Tf_2N]$ by employing the same procedure reported previously in $[C_4C_1Im][PF_6]$.[11a,k]

For 10%$_{mol}$ solutions of the catalyst in the $[PF_6]^-$ ILs, we observed strong enrichment of the solute at the surface, which was found fully saturated with the complex. In $[C_4C_1Im][Tf_2N]$, however, a homogeneous distribution of **1** at the surface and in the bulk was found in the 10%$_{mol}$ solution with no surface enrichment, while for a 20%$_{mol}$ solution, the surface was saturated with **1**. For dilute solutions with 1%$_{mol}$ catalyst concentration, we observed for the $[PF_6]^-$ ILs a pronounced increase in surface enrichment of **1** when decreasing the alkyl chain length at the cation. Moreover, we observe as general trend an increase of the surface enrichment with increasing surface tension value of the neat IL, that is, in the following order: $[C_2C_1Im][PF_6]$ > $[C_4C_1Im][PF_6]$ > $[C_8C_1Im][PF_6]$ > $[C_4C_1Im][Tf_2N]$. The surface tension of $[C_8C_1Im][PF_6]$ and $[C_4C_1Im][Tf_2N]$ is even low enough to suppress the surface activity of **1**, resulting in homogeneous distribution of the solute, with no surface enrichment effects.

Since the formation of **1** in $[C_4C_1Im][Cl]$ was not successful, we also investigated 9.5%$_{mol}$ solutions of the neat ligand $[C_3CNPFC_4Im][PF_6]$ in $[C_4C_1Im][Cl]$ and $[C_4C_1Im][PF_6]$. In the latter, the ligand was previously also observed to be surface-active but to a lesser extent than **1**.[11k] The enrichment of the ligand was found to be more pronounced in $[C_4C_1Im][Cl]$, the IL with the higher surface tension, than in $[C_4C_1Im][PF_6]$, which follows the correlation of the enrichment of the solute and the surface tension of the solvent found for the dissolved **1**.

Our results clearly demonstrate that, besides the parameters presented in previous studies,[11a,k] the surface composition of an IL-based catalyst system strongly depends on the surface tension of the solvent, which can be tailored by modification of cation or anion of the solvent IL. These results are highly interesting for the design of catalytic systems, where the interfacial structure can play a significant role for the efficiency of the process, such as in SILP catalysis. With the observed trends, tailoring the concentration of the catalyst at the IL/gas interface for optimum performance in specific transformations becomes realistic by choosing an IL or IL mixture with an appropriate surface tension.

4. Experimental Section

Materials and Sample Preparation: *Cis*-$[PtCl_2(CH_3CN)_2]$ (purity 98%) was purchased from Sigma–Aldrich and used without further treatment. $[C_8C_1Im][PF_6]$, $[C_4C_1Im][Tf_2N]$ (both purity 99%), and $[C_4C_1Im][Cl]$ (purity 99.5%) were purchased from Iolitec and, unless stated otherwise, used as delivered. $[C_2C_1Im][PF_6]$ was purchased from Merck (for synthesis grade). The ARXPS analysis of this IL showed an unexpected O 1s peak at 532.1 eV, which increased at 80°, as well as a more intense C_{alkyl} signal than expected at 80° (not shown). These features were assigned to a significant amount of a surface-active contamination, and the IL was therefore cleaned by extraction using toluene. For this, ≈20mL of $[C_2C_1Im][PF_6]$ were heated to 80 °C (to ensure liquid state) and mixed with ≈1 mL of toluene (purity 99.8%) by vigorous stirring. After the phases separated upon rest, the toluene was removed, and the procedure repeated 10 times before drying the IL at 80 °C for several days. After this procedure, no unexpected signals were observed upon ARXPS analysis.

Complex **1** has shown significant beam damage in a 1%$_{mol}$ solution in $[C_4C_1Im][PF_6]$ in the presence of minor traces of iodine species, as discussed previously.[11k] Therefore, for all 1%$_{mol}$ solutions of **1** shown in this work (for preparation routes see below), water-cleaned ILs were used; the general cleaning procedure is detailed in Ref. [11k]. For $[C_2C_1Im][PF_6]$ and $[C_4C_1Im][Tf_2N]$, also for the more concentrated solutions the water-cleaning procedure was applied to the ILs prior to preparation of the catalyst solution. Note that ARXPS analysis of non-water-treated and water-treated neat ILs did not show significant differences; the ARXP spectra shown in Figure S1 (Supporting Information) were obtained from

ADVANCED SCIENCE NEWS
www.advancedsciencenews.com

ADVANCED MATERIALS INTERFACES
Open Access
www.advmatinterfaces.de

Table 3. Quantitative analysis of XPS core level spectra of 9.5%$_{mol}$ solutions of $[C_3CNPFC_4Im][PF_6]$ in a) $[C_4C_1Im][PF_6]$ and b) in $[C_4C_1Im][Cl]$ and b) in $[C_4C_1Im][PF_6]$. "Nominal" indicates the relative numbers of the atoms derived from the nominal stoichiometry, and "Experimental" the corresponding numbers deduced from the XPS data at 0° and 80°. [a]For the spin-orbit-split signals, the indicated binding energy values correspond to larger peak, that is, Cl $2p_{3/2}$ and P $2p_{3/2}$.

a) 9.5%$_{mol}$ $[C_3CNPFC_4Im][PF_6]$ in $[C_4C_1Im][Cl]$	Cl 2p[a]	F 1s CFx	F 1s PF_6	N 1s Im	N 1s CN	C 1s CF_3	C 1s CF_2	C 1s C_2	C 1s hetero[a]	C 1s alkyl	P 2p[a]
Binding Energy / eV	197.3	689.1	686.8	401.9	399.9	293.9 (80°)	291.5 (80°)	287.4	286.5	285.2	136.7
Nominal	1.0	0.53	0.63	2.2	0.11	0.11	0.11	1.1	4.8	3.0	0.11
Experimental, 0°	0.99	1.1	0.60	2.2	0.15	0	0	1.1	5.1	2.4	0.12
Experimental, 80°	0.75	2.8	0.35	1.6	0.15	0.51	0.51	0.82	4.7	1.5	0.074
b) 9.5%$_{mol}$ $[C_3CNPFC_4Im][PF_6]$ in $[C_4C_1Im][PF_6]$[11k]											
Binding Energy / eV		688.8	686.8	402.2	400.0	293.9 (80°)	291.6 (80°)	287.7	286.8	285.3	136.8
Nominal		0.53	6.6	2.2	0.11	0.11	0.11	1.1	4.8	3.0	1.1
Experimental, 0°		1.1	6.6	2.1	0.16			1.1	4.7	2.7	1.2
Experimental, 80°		2.3	5.5	1.8	0.13	0.46	0.46	0.91	4.4	2.7	1.1

Table 4. Surface tension and density values at 298 K of neat $[C_2C_1Im][PF_6]$, $[C_4C_1Im][PF_6]$, $[C_8C_1Im][PF_6]$, $[C_4C_1Im][Tf_2N]$, and $[C_4C_1Im][Cl]$ obtained from the PD method under vacuum conditions.

	Surface tension γ / mN m^{-1}	Density ρ / g cm^{-3}
$[C_2C_1Im][PF_6]$	51.89	1.47[22]
$[C_4C_1Im][PF_6]$	43.44[11k]	1.36[23]
$[C_8C_1Im][PF_6]$	34.19[10b]	1.24[24]
$[C_4C_1Im][Tf_2N]$	32.46	1.44[25]
$[C_4C_1Im][Cl]$	49.88	1.08[26]

$[C_2C_1Im][PF_6]$ treated with toluene and water. For the more concentrated solutions of the other ILs, no additional water-cleaning step was conducted since no beam damage effects were observed.

$[C_2C_1Im][PF_6]$, and solutions of **1** in $[C_2C_1Im][PF_6]$ and $[C_4C_1Im][Cl]$ were solid at room temperature. For practical reasons, the samples containing these ILs were introduced into the load-lock of the ultra-high vacuum (UHV) chamber as hot liquids (T ≈ 80 °C). The catalyst solutions were introduced freshly after synthesis, while the neat ILs were first molten and stirred for ≈20 h at T = 100– 120 °C before introducing them into the UHV system. The load-lock was immediately pumped down to vacuum conditions after introducing the IL-filled sample holders. With this procedure, the samples remained liquid in a supercooled state, so that acquisition of ARXP spectra in the liquid state was possible even at room temperature. The samples were left for degassing in the load-lock under UHV conditions for several hours. In case of spontaneous solidification upon evacuating the load-lock, the samples were molten again in the UHV chamber; after this, the samples remained liquid. As has been reported previously, owing to the slow diffusion in ILs, 10%$_{mol}$ solutions were heated to T = 60 °C (T = 80 °C in $[C_2C_1Im][PF_6]$) and 1%$_{mol}$ solutions to T = 40 °C (T = 80 °C in $[C_2C_1Im][PF_6]$) for ≈30 min and left for cooling down to room temperature prior to the ARXP analysis to ensure the thermodynamically favored surface structure.[11a,k]

Complex **1** was synthesized in the respective ILs directly in the amount required to give the desired concentration; the procedure was described before for $[C_4C_1Im][PF_6]$ as solvent[11a,k] and was successfully expanded to several ILs in this work (see Results and Discussion). For the solutions of $[C_2C_1Im][PF_6]$ and $[C_4C_1Im][Cl]$, the ILs were added pre-degassed and in liquid state (T ≈ 80 °C) to the precursor mixture. All solutions of **1** were obtained clear and yellow–brown colored. Note that the 1%$_{mol}$ solutions were prepared by simple dilution of freshly-prepared, more concentrated solutions (typically ≈10%$_{mol}$). The weighed amounts of materials for preparation of the solutions are shown in Table S4 (Supporting Information).

The preparation procedure was also attempted for a 20%$_{mol}$ solution of **1** in $[C_4C_1Im][Cl]$. Upon adding the IL and heating to T = 100 °C under vacuum conditions, however, strong bubble formation, quick consumption of the remaining precursor material and coloring of the solution to deep red was observed. The solution was stirred for 3 h under these conditions to yield a clear, deep red-colored solution, which remained liquid even at room temperature. The reaction outcome is discussed in the Supporting Information.

ARXPS Measurements and Data Evaluation: Information on the experimental setup, and on the processing and evaluation of the XPS data is available in previous reports.[11a,c,k] The unique dual analyzer for surface analysis (DASSA) setup is equipped with two analyzers mounted at an angle of 0° with respect to the surface plane (normal emission) and at 80° (grazing emission).[27] The information depth (ID) of measurements in normal emission in IL-based samples is 6–9 nm, whereas at 80° it is only 1–1.5 nm.[27] Therefore, the 80° spectra mainly reflect the composition of the topmost surface layer. In contrast to previous reports on related systems,[11a,k] no normalization to the sum over all atomic sensitivity factor-corrected intensities was performed, which would accout for potential changes of the photon flux between different measurment series. The spectra were fitted according to procedures reported before,[11a,k]

ADVANCED SCIENCE NEWS
www.advancedsciencenews.com

ADVANCED MATERIALS INTERFACES
www.advmatinterfaces.de

with necessary additional information provided in the Supporting Information. For the ARXP spectra of neat $[C_4C_1Im][Cl]$, no referencing of the binding energy of the 0° spectra was applied, since no F_{PF6} signal is present (all other spectra were referenced to the F_{PF6} signal at 686.8 eV in 0°, as done in previous works).[11a,k] With this, the binding energies of the neat IL excellently correspond to the solution, where synthesis of **1** was attempted in this IL shown in Figure S8 (Supporting Information). For the $[C_4C_1Im][Tf_2N]$ solutions, the spectra were referenced to the F_{CFx} at 688.8 eV owing to the low intensity of the F_{PF6} signal.

Pendant Drop Measurements: The surface tension of the neat ILs was determined using our novel high vacuum setup, which was described in detail previously.[14] The uncertainty of the surface tension was obtained from this setup to ± 0.1% (±0.04 mN m^{-1});[14] the uncertainty therefore lies within the size of the data points shown in Figure 5.

The typical procedure for introducing the ILs was outlined before for room temperature ILs.[14] To avoid rapid release of dissolved gases upon melting of $[C_2C_1Im][PF_6]$ and $[C_4C_1Im][Cl]$ (which are solid at room temperature) during the degassing procedure in the high vacuum setup, the ILs were pre-degassed by stirring under reduced pressure for several hours at T ≈ 100–120 °C in a Schlenk-tube. The hot liquids were then introduced into the IL reservoir and the chamber was immediately pumped down to vacuum conditions and heated for further degassing the ILs (final pressure ≈10^{-6} mbar).[14] The measurements were started at high temperature and gradually allowed to cool toward room temperature. $[C_2C_1Im][PF_6]$ and $[C_4C_1Im][Cl]$ remained in a supercooled state over the whole period of the temperature-dependent surface tension measurements so that data points could be taken even at room temperature.

Supporting Information

Supporting Information is available from the Wiley Online Library or from the author.

Acknowledgements

The authors thank the DFG for support through Sonderforschungsbereich (SFB) 1452, Project-ID 431791331. D. H. gratefully acknowledges the Stiftung Stipendien-Fonds of the German chemical industry association (Verband der chemischen Industrie, VCI) for a Kekulé fellowship.

Conflict of Interest

The authors declare no conflict of interest.

Data Availability Statement

The data that support the findings of this study are available from the corresponding author upon reasonable request. Source data are provided at Zenodo: DOI 10.5281/zenodo.10977887.

Keywords

materials properties, Pt catalyst, supported ionic liquid phase catalysis (SILP), surface enrichment, X-ray photoelectron spectrsocopy

Received: December 21, 2023
Revised: March 13, 2024
Published online: April 21, 2024

[1] a) P. Lanzafame, S. Perathoner, G. Centi, S. Gross, E. J. M. Hensen, *Catal. Sci. Technol.* **2017**, *7*, 5182; b) J. García-Serna, R. Piñero-Hernanz, D. Durán-Martín, *Catal. Today* **2022**, *387*, 237.
[2] A. Wang, J. Li, T. Zhang, *Nat. Rev. Chem.* **2018**, *2*, 65.
[3] X. Deng, J. Wang, N. Guan, L. Li, *Cell Rep. Phys. Sci.* **2022**, *3*, 101017.
[4] O. Piermatti, R. Abu-Reziq, L. Vaccaro, in *Catalyst Immobilization* (Eds.: M. Benaglia, A. Puglisi), Wiley-VCH Verlag GmbH & Co. KGaA, Weinheim, Germany **2020**, pp. 1–22.
[5] a) J. M. Marinkovic, A. Riisager, R. Franke, P. Wasserscheid, M. Haumann, *Ind. Eng. Chem. Res.* **2019**, *58*, 2409; b) A. Riisager, R. Fehrmann, M. Haumann, P. Wasserscheid, *Eur. J. Inorg. Chem.* **2006**, *2006*, 695; c) A. Riisager, B. Jørgensen, P. Wasserscheid, R. Fehrmann, *Chem. Commun.* **2006**, 994.
[6] P. Latos, A. Wolny, A. Chrobok, *Materials* **2023**, *16*, 2106.
[7] a) V. I. Pârvulescu, C. Hardacre, *Chem. Rev.* **2007**, *107*, 2615; b) T. Welton, *Coord. Chem. Rev.* **2004**, *248*, 2459; c) J. P. Hallett, T. Welton, *Chem. Rev.* **2011**, *111*, 3508; d) C. Dai, J. Zhang, C. Huang, Z. Lei, *Chem. Rev.* **2017**, *117*, 6929.
[8] H.-P. Steinrück, P. Wasserscheid, *Catal. Lett.* **2015**, *145*, 380.
[9] a) C. S. Santos, S. Baldelli, *Chem. Soc. Rev.* **2010**, *39*, 2136; b) H.-P. Steinrück, *Phys. Chem. Chem. Phys.* **2012**, *14*, 5010; c) M. Tariq, M. G. Freire, B. Saramago, J. A. P. Coutinho, J. N. C. Lopes, L. P. N. Rebelo, *Chem. Soc. Rev.* **2012**, *41*, 829; d) Y.-L. Wang, B. Li, S. Sarman, F. Mocci, Z.-Y. Lu, J. Yuan, A. Laaksonen, M. D. Fayer, *Chem. Rev.* **2020**, *120*, 5798; e) Z. Zhai, U. Paap, A. Gezmis, F. Maier, H.-P. Steinrück, T. M. Koller, *J. Mol. Liq.* **2023**, *386*, 122388; f) K. R. J. Lovelock, I. J. Villar-Garcia, F. Maier, H.-P. Steinrück, P. Licence, *Chem. Rev.* **2010**, *110*, 5158; g) I. J. Villar-Garcia, S. Fearn, N. L. Ismail, A. J. S. McIntosh, K. R. J. Lovelock, *Chem. Commun.* **2015**, *51*, 5367; h) Q. Huang, Y. Huang, Y. Luo, L. Li, G. Zhou, X. Chen, Z. Yang, *Phys. Chem. Chem. Phys.* **2020**, *22*, 13780; i) R. Costa, C. M. Pereira, A. F. Silva, P.-F. Brevet, E. Benichou, *J. Phys. Chem. B* **2020**, *124*, 3954; j) E. J. Smoll Jr., S. M. Purcell, L. D'Andrea, J. M. Slattery, D. W. Bruce, M. L. Costen, K. G. McKendrick, T. K. Minton, *J. Phys. Chem. Lett.* **2019**, *10*, 156; k) E. J. Smoll, M. A. Tesa-Serrate, S. M. Purcell, L. D'Andrea, D. W. Bruce, J. M. Slattery, M. L. Costen, T. K. Minton, K. G. McKendrick, *Faraday Discuss.* **2018**, *206*, 497; l) K. Nakajima, M. Lísal, K. Kimura, in *Surface and Interface Science*, Vol. 7 (Ed.: K. Wandelt), Wiley-VCH Verlag GmbH & Co. KGaA, Weinheim, Germany **2020**, pp. 351–389; m) K. Nakajima, M. Miyashita, M. Suzuki, K. Kimura, *J. Chem. Phys.* **2013**, *139*, 224701.
[10] a) B. S. J. Heller, M. Lexow, F. Greco, S. Shin, G. Partl, F. Maier, H.-P. Steinrück, *Chemistry* **2020**, *26*, 1117; b) U. Paap, V. Seidl, K. Meyer, F. Maier, H.-P. Steinrück, *Molecules* **2022**, *27*, 8561; c) V. Lockett, R. Sedev, S. Harmer, J. Ralston, M. Horne, T. Rodopoulos, *Phys. Chem. Chem. Phys.* **2010**, *12*, 13816; d) E. F. Smith, F. J. M. Rutten, I. J. Villar-Garcia, D. Briggs, P. Licence, *Langmuir* **2006**, *22*, 9386; e) S. Men, B. B. Hurisso, K. R. J. Lovelock, P. Licence, *Phys. Chem. Chem. Phys.* **2012**, *14*, 5229; f) E. Oz, O. Sahin, H. I. Okur, S. Suzer, *ChemPhysChem* **2020**, *21*, 2397; g) N. Calisi, S. Martinuzzi, A. Giaccherini, C. S. Pomelli, L. Guazzelli, S. Caporali, *J. Electron Spectrosc. Relat. Phenom.* **2021**, *247*, 147034; h) S. Caporali, M. Pedio, C. Chiappe, C. S. Pomelli, R. G. Acres, U. Bardi, *Surf. Sci.* **2016**, *648*, 360; i) Y. Zhang, Y. Khalifa, E. J. Maginn, J. T. Newberg, *J. Phys. Chem. C* **2018**, *122*, 27392.
[11] a) D. Hemmeter, D. Kremitzl, P. S. Schulz, P. Wasserscheid, F. Maier, H.-P. Steinrück, *Chem.-Eur. J.* **2023**, *29*, e202203325; b) D. Hemmeter, U. Paap, F. Maier, H.-P. Steinrück, *Catalysts* **2023**, *13*, 871; c) D. Hemmeter, U. Paap, N. Taccardi, J. Mehler, P. S. Schulz, P. Wasserscheid, F. Maier, H.-P. Steinrück, *ChemPhysChem* **2023**, *24*, 202200391; d) E. J. Smoll, X. Chen, L. M. Hall, L. D'Andrea, J. M. Slattery, T. K. Minton, *J. Phys. Chem. C* **2020**, *124*, 382; e) A. Dimitrova, M. Walle, M. Himmerlich, S. Krischok, *J. Mol. Liq.* **2017**, *226*, 78; f) T. Kurisaki, D. Tanaka, Y. Inoue, H. Wakita, B. Minofar, S. Fukuda, S.-i. Ishiguro, Y. Umebayashi, *J. Phys. Chem. B* **2012**, *116*, 10870; g) S. Men, J. Jiang, *Chem. Phys. Lett.* **2016**, *646*, 125; h) S. Men, J. Jiang, *Russ. J. Phys. Chem. A* **2018**, *92*, 1627; i) S. Men, Y. J. Jin, *Russ. J. Phys. Chem. A* **2018**, *92*, 2472; j) S. Men, K. R. J. Lovelock, P. Licence,

RSC Adv. **2015**, *5*, 35958; k) D. Hemmeter, U. Paap, N. Wellnhofer, A. Gezmis, D. Kremitzl, P. Wasserscheid, H.-P. Steinrück, F. Maier, *ChemPhysChem* **2023**, *24*, 202300612.

[12] a) F. Maier, J. M. Gottfried, J. Rossa, D. Gerhard, P. S. Schulz, W. Schwieger, P. Wasserscheid, H.-P. Steinrück, *Angew. Chem., Int. Ed.* **2006**, *45*, 7778; b) C. Kolbeck, N. Paape, T. Cremer, P. S. Schulz, F. Maier, H.-P. Steinrück, P. Wasserscheid, *Chem.-Eur. J.* **2010**, *16*, 12083; c) C. Kolbeck, N. Taccardi, N. Paape, P. S. Schulz, P. Wasserscheid, H.-P. Steinrück, F. Maier, *J. Mol. Liq.* **2014**, *192*, 103.

[13] F. Maier, T. Cremer, C. Kolbeck, K. R. J. Lovelock, N. Paape, P. S. Schulz, P. Wasserscheid, H. P. Steinrück, *Phys. Chem. Chem. Phys.* **2010**, *12*, 1905.

[14] U. Paap, B. Kreß, H.-P. Steinrück, F. Maier, *Int. J. Mol. Sci.* **2022**, *23*, 13158.

[15] K. R. J. Lovelock, C. Kolbeck, T. Cremer, N. Paape, P. S. Schulz, P. Wasserscheid, F. Maier, H. P. Steinrück, *J. Phys. Chem. B* **2009**, *113*, 2854.

[16] a) K. Nakajima, A. Ohno, M. Suzuki, K. Kimura, *Langmuir* **2008**, *24*, 4482; b) A. Sanmartín Pensado, P. Malfreyt, A. A. H. Pádua, *J. Phys. Chem. B* **2009**, *113*, 14708; c) T. Iwahashi, T. Miyamae, K. Kanai, K. Seki, D. Kim, Y. Ouchi, *J. Phys. Chem. B* **2008**, *112*, 11936.

[17] a) R. Souda, *Surf. Sci.* **2010**, *604*, 1694; b) K. Nakajima, S. Nakanishi, M. Lísal, K. Kimura, *J. Mol. Liq.* **2017**, *230*, 542; c) K. Nakajima, S. Oshima, M. Suzuki, K. Kimura, *Surf. Sci.* **2012**, *606*, 1693; d) B. S. J. Heller, C. Kolbeck, I. Niedermaier, S. Dommer, J. Schatz, P. Hunt, F. Maier, H.-P. Steinrück, *ChemPhysChem* **2018**, *19*, 1733.

[18] J. Fuller, R. T. Carlin, H. C. De Long, D. Haworth, *J. Chem. Soc., Chem. Commun.* **1994**, 299.

[19] A. Efimova, G. Hubrig, P. Schmidt, *Thermochim. Acta* **2013**, *573*, 162.

[20] M. H. Ghatee, A. R. Zolghadr, *Fluid Phase Equilib.* **2008**, *263*, 168.

[21] M. Geppert-Rybczyńska, J. K. Lehmann, J. Safarov, A. Heintz, *J. Chem. Thermodyn.* **2013**, *62*, 104.

[22] C. M. S. S. Neves, K. A. Kurnia, K. Shimizu, I. M. Marrucho, L. P. N. Rebelo, J. A. P. Coutinho, M. G. Freire, J. N. Canongia Lopes, *Phys. Chem. Chem. Phys.* **2014**, *16*, 21340.

[23] J. Jacquemin, P. Husson, A. A. H. Padua, V. Majer, *Green Chem.* **2006**, *8*, 172.

[24] R. L. Gardas, M. G. Freire, P. J. Carvalho, I. M. Marrucho, I. M. A. Fonseca, A. G. M. Ferreira, J. A. P. Coutinho, *J. Chem. Eng. Data* **2007**, *52*, 80.

[25] C. A. Nieto de Castro, E. Langa, A. L. Morais, M. L. M. Lopes, M. J. V. Lourenço, F. J. V. Santos, M. S. C. S. Santos, J. N. C. Lopes, H. I. M. Veiga, M. Macatrão, J. M. S. S. Esperança, C. S. Marques, L. P. N. Rebelo, C. A. M. Afonso, *Fluid Phase Equilib.* **2010**, *294*, 157.

[26] J. Li, H. Zhu, C. Peng, H. Liu, *Chin. J. Chem. Eng.* **2019**, *27*, 2994.

[27] I. Niedermaier, C. Kolbeck, H.-P. Steinrück, F. Maier, *Rev. Sci. Instrum.* **2016**, *87*, 045105.

ADVANCED MATERIALS INTERFACES
Open Access

Supporting Information

for *Adv. Mater. Interfaces*, DOI 10.1002/admi.202301085

Tailoring the Surface Enrichment of a Pt Catalyst in Ionic Liquid Solutions by Choice of the Solvent

*Daniel Hemmeter, Afra Gezmis, Daniel Kremitzl, Peter Wasserscheid, Florian Maier and Hans-Peter Steinrück**

Supporting information:

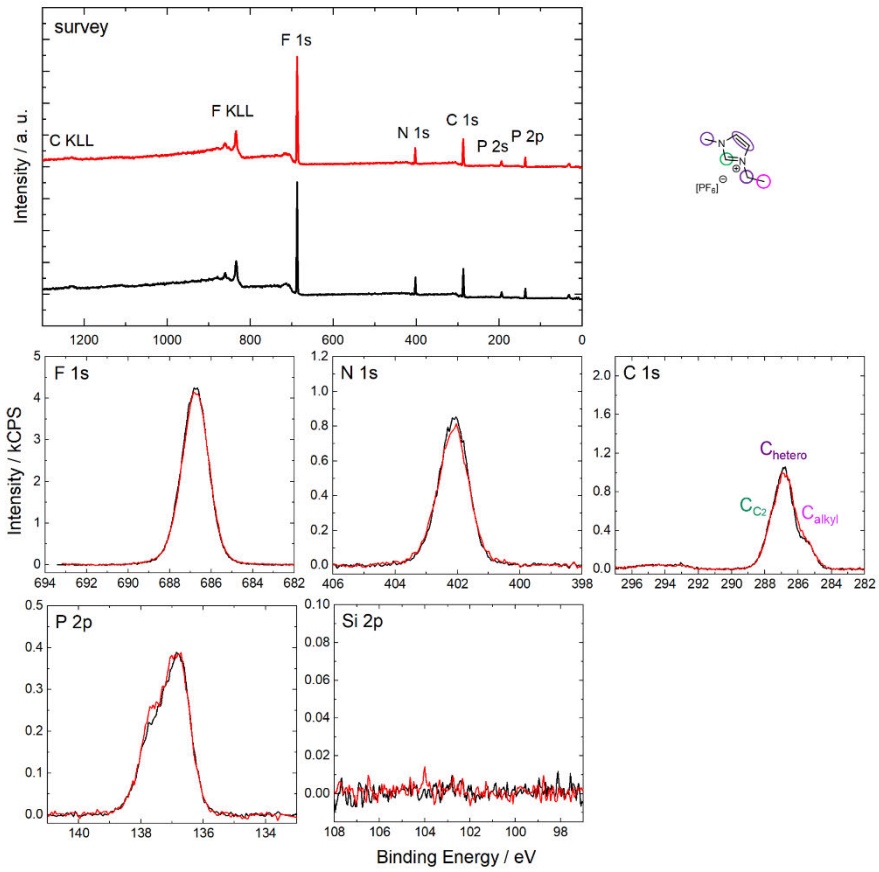

***Figure S1**: Survey, F 1s, N 1s, C 1s, P 2p and Si 2p XP spectra of neat [C_2C_1Im][PF_6] in 0° (black) and 80° (red) emission recorded at room temperature with assignment of peaks to the molecular structure. The Si 2p region is shown to exclude common surface-active contaminations.*[1]

Peak fitting for spectra shown in Figure S1:

Peak fitting was achieved using the procedure well-established for 1,3-dialkylimiadzolium ILs.[2]

***Table S1:** Quantitative analysis of XPS core level spectra of neat [C_2C_1Im][PF_6] shown in Figure S1. Note that for the spin-orbit-split P 2p signal, the indicated binding energy value corresponds to the more intense P $2p_{3/2}$ peak.*

neat [C_2C_1Im][PF_6]	F 1s PF_6	N 1s Im	C 1s C_2	C 1s hetero	C 1s alkyl	P 2p*
Binding Energy / eV	686.8	402.1	287.7	286.8	285.5	136.8
Nominal	6	2	1	4	1	1
Experimental, 0°	6.2	2.0	1.0	3.9	0.9	1.1
Experimental, 80°	6.1	1.9	1.0	4.0	0.9	1.1

Discussion of ARXP spectra of neat $[C_2C_1Im][PF_6]$:

The recorded intensities shown in Figure S1 and listed in Table S1 excellently match the nominal values at 0° (black, more bulk-sensitive) and 80° (red, more surface-sensitive). These observations indicate that there is no preferential surface orientation of the $[C_2C_1Im]^+$ cation, which is well-known for longer-chained derivatives, where the surface is typically terminated with the alkyl substituents.[3] Overall, this behavior is in line with previous results found for the influence of the chain length on the preferred surface orientation in $[Tf_2N]^-$-based ILs.[4]

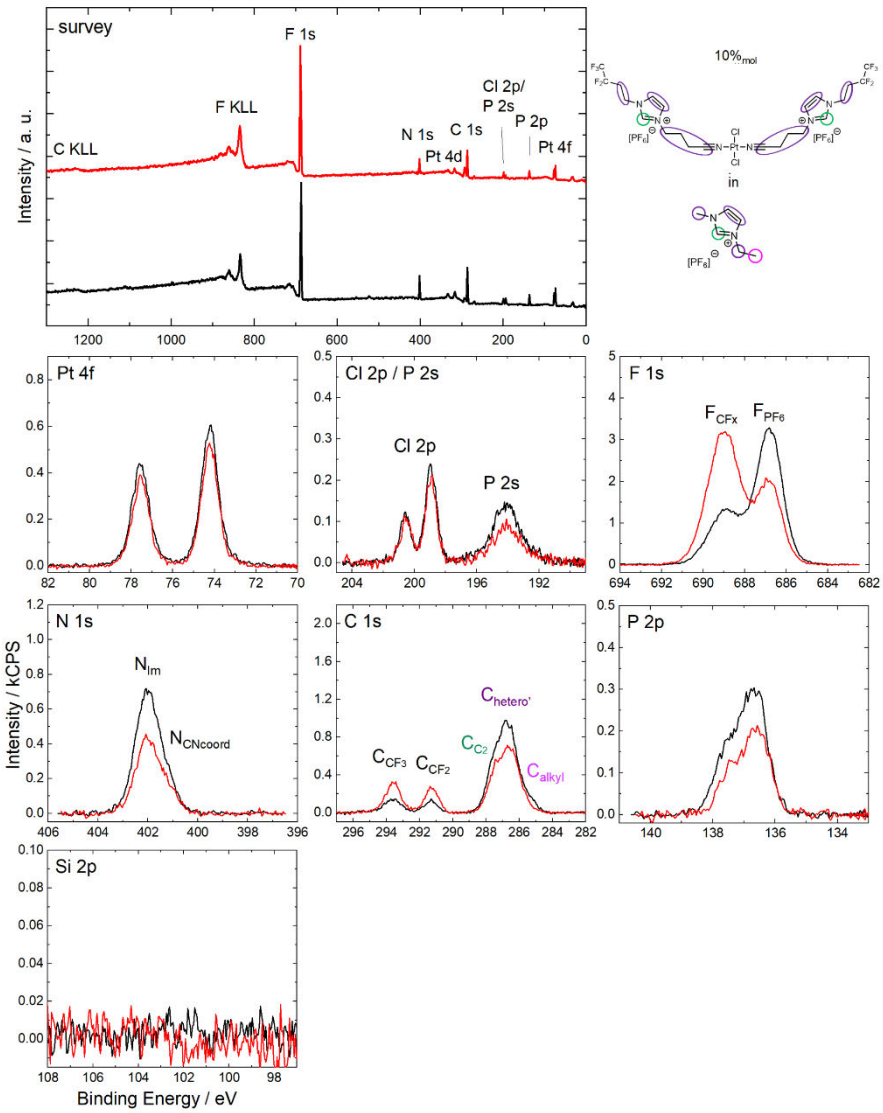

Figure S2: *Survey, Pt 4f, Cl 2p/P 2s, F 1s, N 1s, C 1s, P 2p and Si 2p XP spectra of a 10%$_{mol}$ solution of **1** in [C_2C_1Im][PF_6] in 0° (black) and 80° (red) emission recorded at room temperature with assignment of peaks to the molecular structure.*

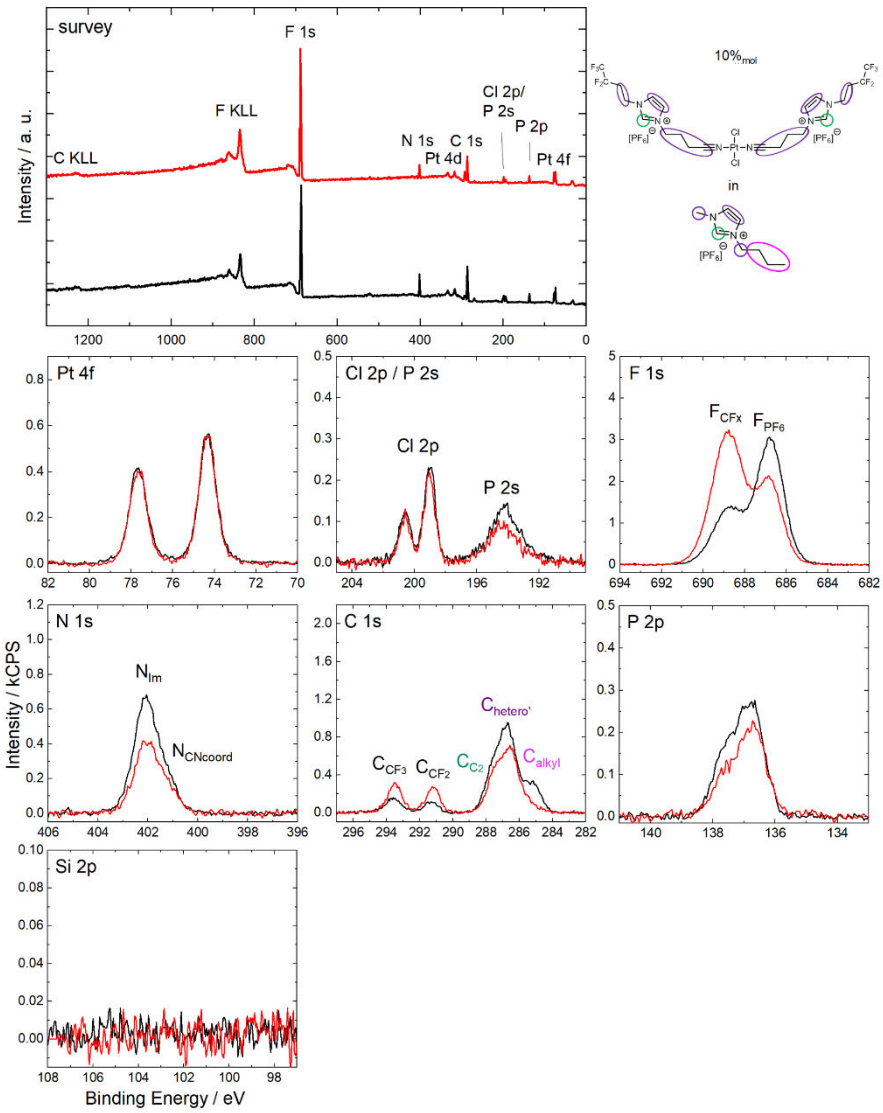

***Figure S3**: Survey, Pt 4f, Cl 2p/P 2s, F 1s, N 1s, C 1s, P 2p and Si 2p XP spectra of a 10%$_{mol}$ solution of **1** in [C_4C_1Im][PF_6] in 0° (black) and 80° (red) emission recorded at room temperature with assignment of peaks to the molecular structure. Adapted from Ref. [5].*

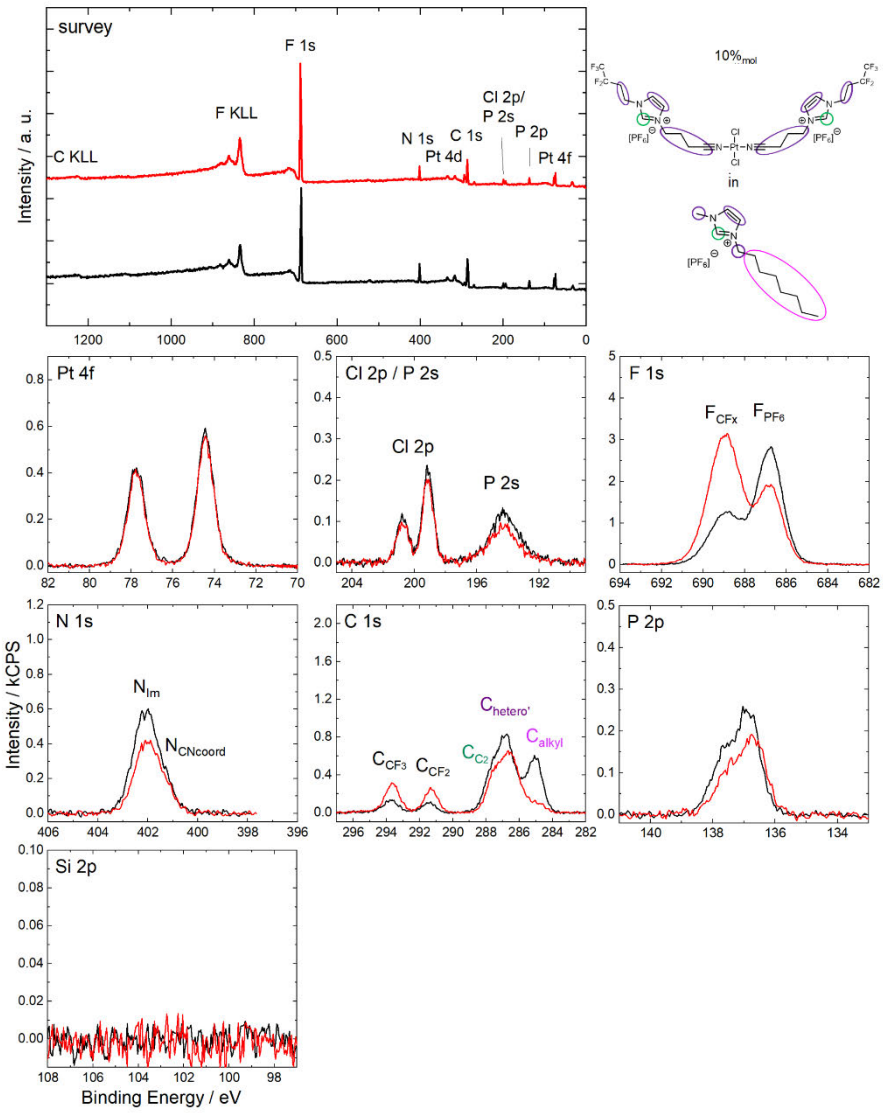

*Figure S4: Survey, Pt 4f, Cl 2p/P 2s, F 1s, N 1s, C 1s, P 2p and Si 2p XP spectra of a 10%$_{mol}$ solution of **1** in [C_8C_1Im][PF_6] in 0° (black) and 80° (red) emission recorded at room temperature with assignment of peaks to the molecular structure.*

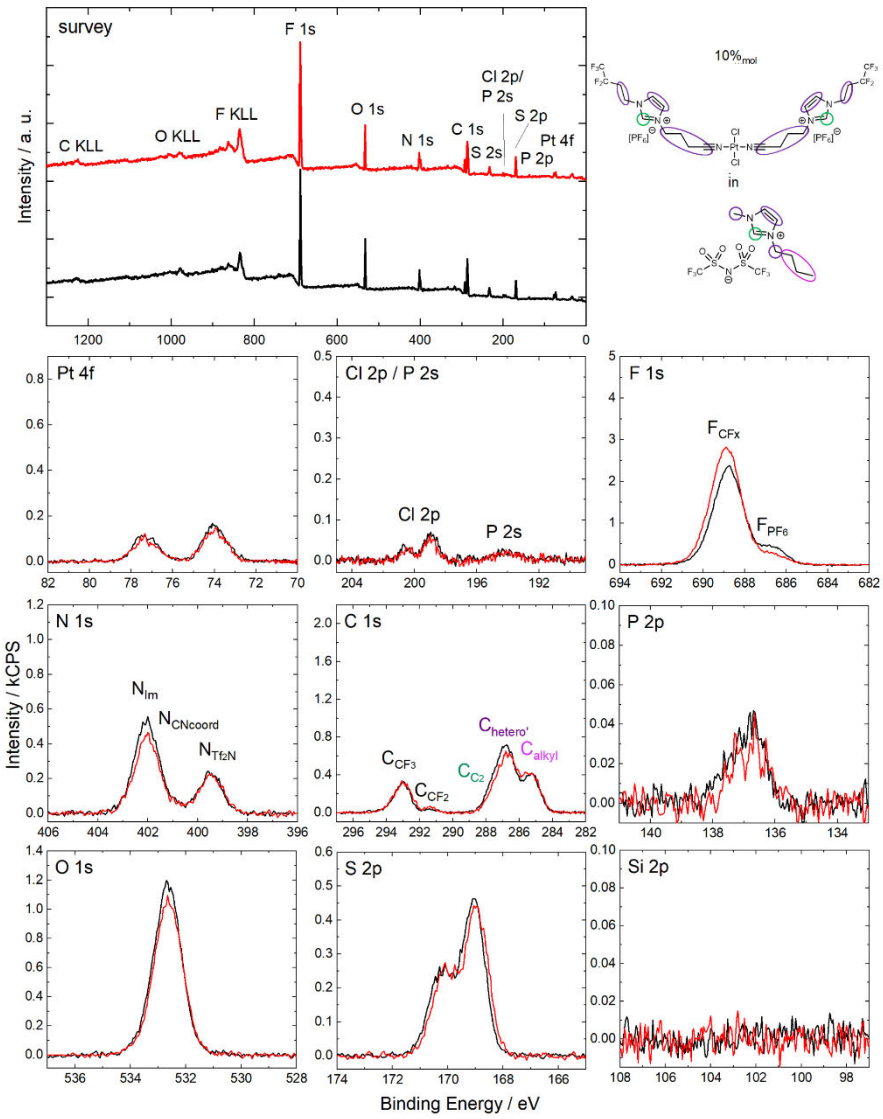

*Figure S5: Survey, Pt 4f, Cl 2p/P 2s, F 1s, N 1s, C 1s, P 2p and Si 2p XP spectra of a 10%$_{mol}$ solution of **1** in [C_4C_1Im][Tf_2N] in 0° (black) and 80° (red) emission recorded at room temperature with assignment of peaks to the molecular structure.*

Additional information on the peak fitting for solution shown in Figure S5:

The position of the $N_{CNcoord}$ signal was set to a binding energy of -0.9 eV with respect to the N_{Im} signal, which was concluded from the $[PF_6]^-$ solutions and the 20%$_{mol}$ solution of **1** in [C_4C_1Im][Tf_2N].

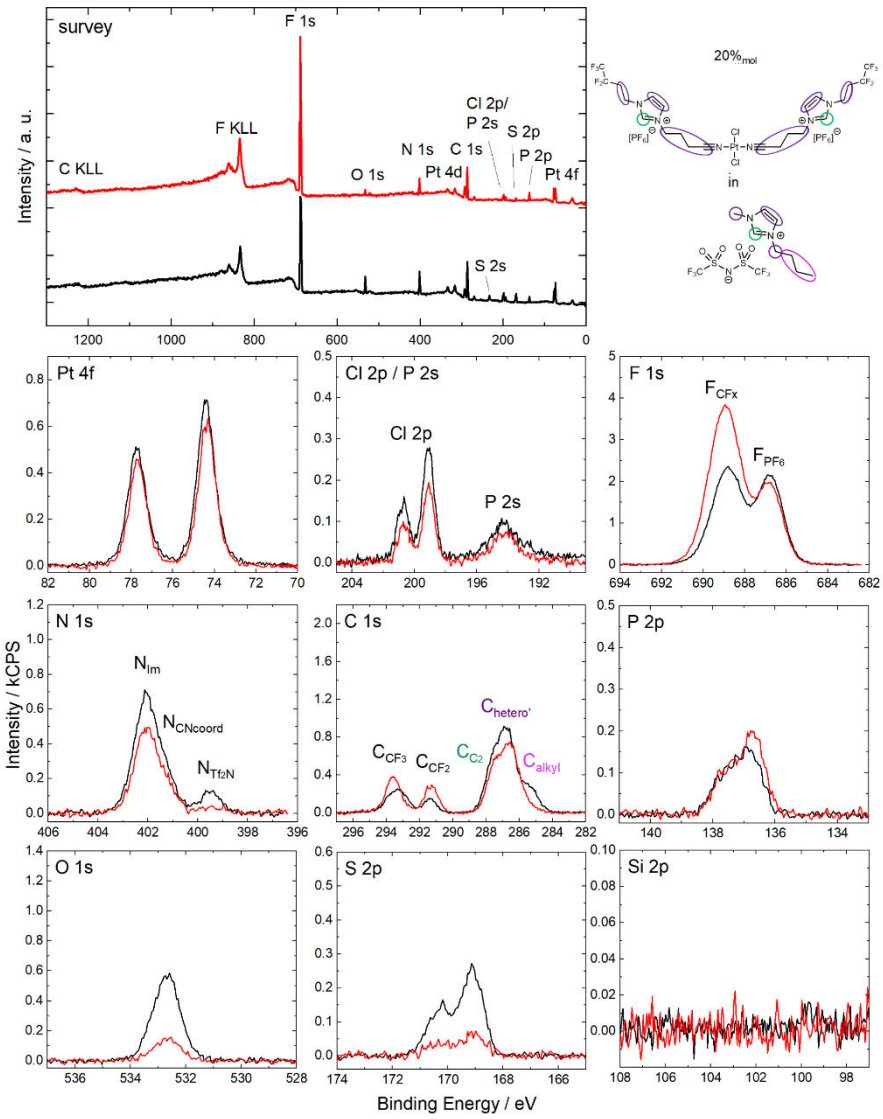

***Figure S6**: Survey, Pt 4f, Cl 2p/P 2s, F 1s, N 1s, C 1s, P 2p and Si 2p XP spectra of a 20%$_{mol}$ solution of **1** in [C_4C_1Im][Tf_2N] in 0° (black) and 80° (red) emission recorded at room temperature with assignment of peaks to the molecular structure.*

Additional information on the peak fitting for solution shown in Figure S6:

Note that in contrast to the 10%$_{mol}$ solution shown in Figure S5, no position constraint was used for the $N_{CNcoord}$ signal.

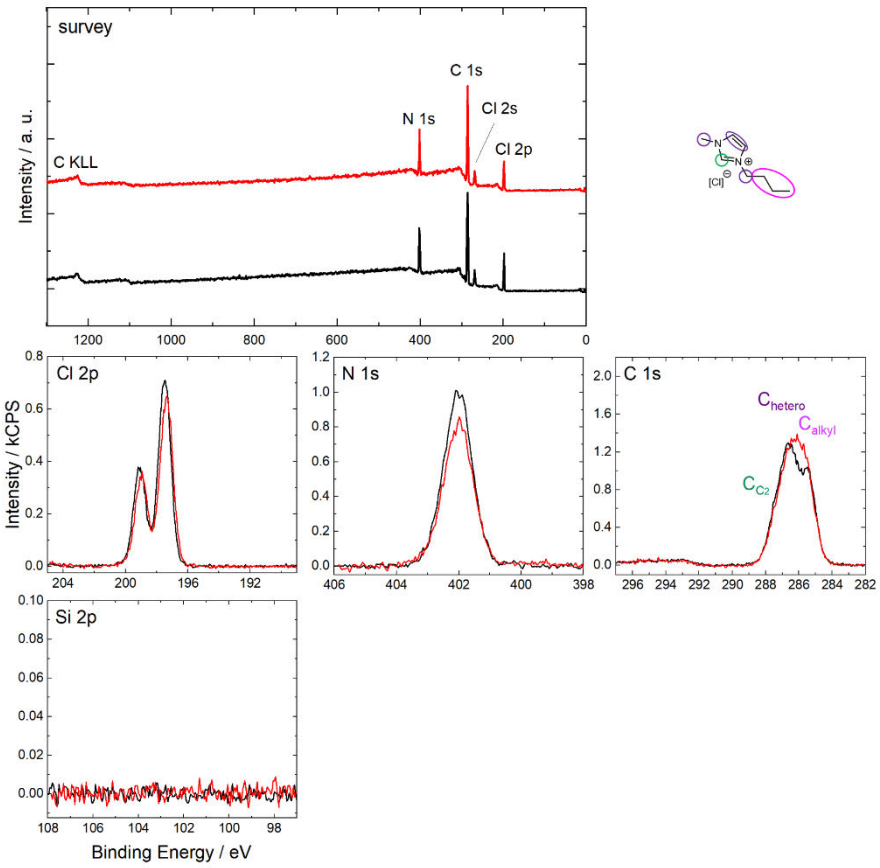

***Figure S7**: Survey, Cl 2p, N 1s, C 1s and Si 2p XP spectra of neat [C_4C_1Im][Cl] in 0° (black) and 80° (red) emission recorded at room temperature with assignment of peaks to the molecular structure.*

<u>Peak fitting for spectra shown in Figure S7:</u>

Peak fitting was achieved using the procedure well-established for 1,3-dialkylimiadzolium ILs.[2]

***Table S2:** Quantitative analysis of XPS core level spectra of neat [C_4C_1Im][Cl] shown in Figure S7. Note that for the spin-orbit-split Cl 2p signal, the indicated binding energy value corresponds to the more intense Cl $2p_{3/2}$ peak.*

neat [C_4C_1Im][Cl]	Cl 2p*	N 1s Im	C 1s C_2	C 1s hetero'	C 1s alkyl
Binding Energy / eV	197.5	402.0	287.5	286.6	285.4
Nominal	1	2	1	4	3
Experimental, 0°	1.0	2.0	1.0	4.1	2.8
Experimental, 80°	1.0	1.7	1.0	4.1	3.2

Discussion of the ARXP spectra of neat [C_4C_1Im][Cl]:

The 0° spectra (black) depicted in Figure S7 show excellent agreement with the nominal composition of the IL, as is evident from the quantitative analysis of the peak intensities shown in Table S2. At 80° (red), the C_{alkyl} signal shows an increase, while all other signals remain constant or slightly decrease as compared to 80°, which is assigned to a preferential surface orientation of the $[C_4C_1Im]^+$ cation with the C_4 chain pointing towards the vacuum. This effect is well-known for $[C_nC_1Im]^+$ cations with linear, non-functionalized alkyl substituents with a number of carbon atoms $n \geq 4$.[3c, 6] It is worth noting that no O 1s species was observed, which would correspond to minor amounts of water due to the strong hygroscopicity of the IL, as has been reported before by our group.[7] The water-free IL was obtained due to the applied procedure involving pre-degassing and introduction into the chamber as a hot liquid, as outlined in the experimental section. In a previous study using non-monochromatized Al-Kα radiation, the IL also showed an additional peak in the N 1s region at 400 eV, which was assigned to beam damage[7]. This additional peak was also observed in the current work using monochromatized Al-Kα radiation after roughly 90 mins of irradiating the sample. For the set of spectra shown in Figure S7, the effect could be suppressed by recording the N 1s region as first spectrum.

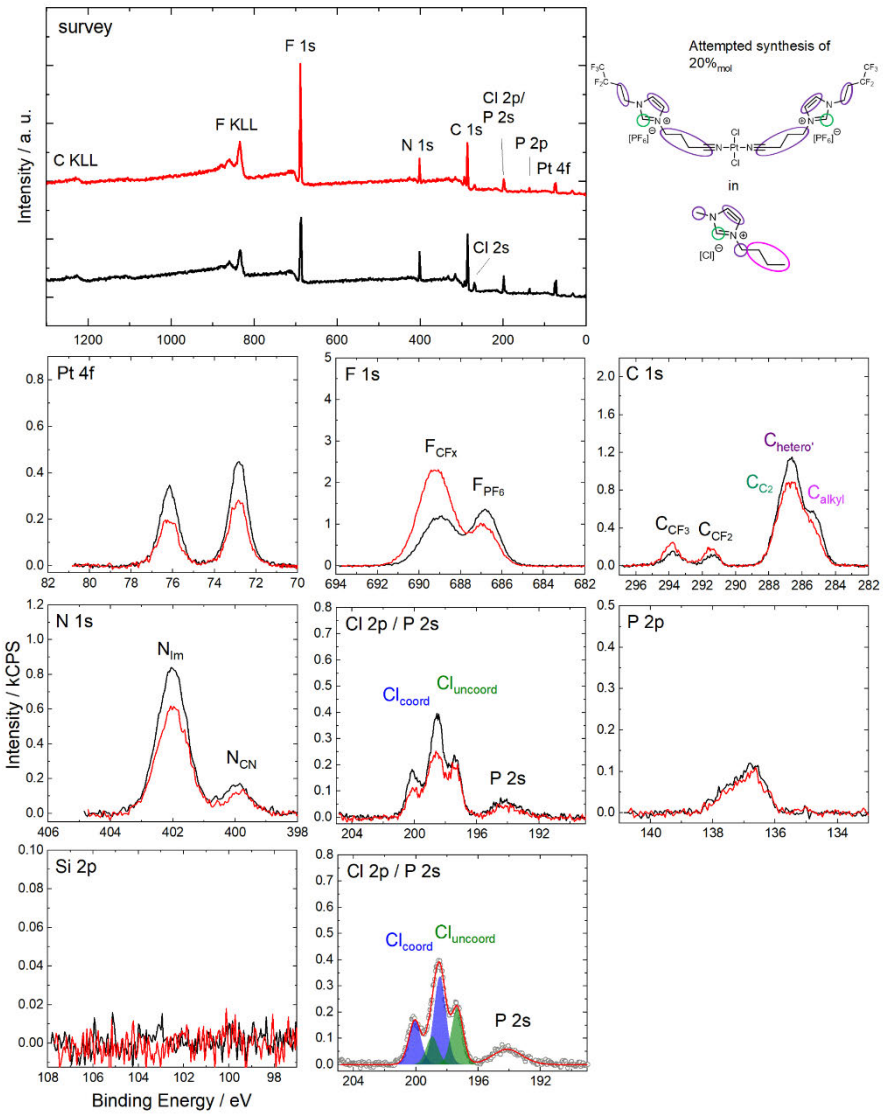

***Figure S8**: Survey, Pt 4f, Cl 2p/P 2s, F 1s, N 1s, C 1s, P 2p and Si 2p XP spectra of a solution with a targeted content of 20%$_{mol}$ of **1** in [C_4C_1Im][Cl] in 0° (black) and 80° (red) emission recorded at room temperature with assignment of peaks to the molecular structure.*

Table S3: Quantitative analysis of XPS core level spectra of a solution with a targeted content of 20%$_{mol}$ of **1** in [C_4C_1Im][Cl]. Note that for the spin-orbit-split Pt 4f, Cl 2p and P 2p signals, the indicated binding energy value corresponds to the more intense Pt 4f$_{7/2}$, Cl 2p$_{3/2}$ and P 2p$_{3/2}$ peaks.

Attempt 20%$_{mol}$ 1 in [C_4C_1Im][Cl]	Pt 4f*	Cl 2p* coord	Cl 2p* uncoord	F 1s CFx	F 1s PF_6	N 1s Im	N 1s CNcoord	N 1s CN	C 1s CF_3	C 1s CF_2	C 1s C_2	C 1s hetero′	C 1s alkyl	P 2p*
Binding Energy / eV	72.8	198.5	197.4	689.0	686.8	402.0		400.0	293.8	291.4	287.5	286.6	285.2	136.7
Nominal	0.25	0.50	1.0	2.5	3.0	3.0	0.50	0	0.50	0.50	1.5	8.0	3.0	0.50
Experimental, 0°	0.21	0.83	0.50	3.5	2.8	3.0		0.56	0.72	0.72	1.5	7.2	2.6	0.49
Experimental, 80°	0.14	0.56	0.44	6.7	2.1	2.4		0.42	1.2	1.2	1.2	6.4	1.8	0.42

Discussion of the ARXP spectra of the solution shown in Figure S8:

The full set of spectra of a solution, where 20%$_{mol}$ content of **1** was targeted (but not achieved) are shown in Figure S8, with their quantitative analysis provided in Table S3. The Pt 4f$_{7/2}$ signal at 72.8 eV is shifted to lower binding energy about 0.2-0.6 eV with respect to the 10%$_{mol}$ or 20%$_{mol}$ solutions of [C_2C_1Im][PF_6], [C_4C_1Im][PF_6], [C_8C_1Im][PF_6] and [C_4C_1Im][Tf_2N], which indicates a different ligand environment of the Pt center. This finding is supported by the observation of a N 1s signal at 400.0 eV, corresponding to uncoordinated N atoms from the CN groups N_{CN} of [C_3CNPFC_4Im][PF_6].[5] $N_{CNcoord}$ atoms coordinated to Pt would be expected at 401.4 – 401.2 eV (see Table 1a), but were not detected. The N_{CN} signal is slightly higher than nominally expected for $N_{CNcoord}$ (0.56 vs 0.50), indicating that all [C_3CNPFC_4Im][PF_6] remained uncoordinated in this solution. The two Cl 2p doublets correspond to coordinated Cl species Cl_{coord} (blue) and uncoordinated Cl species $Cl_{uncoord}$ (green); their deconvolution (Figure S8) reveals a Pt:Cl_{coord} ratio of 1:3.9, indicating the formation of $[PtCl_4]^{2-}$ upon excess of Cl^- anions in the IL solution; this finding is supported by a deep red coloring of the solution immediately after adding the IL to the precursor mixture (see experimental section), which is typical for $[PtCl_4]^{2-}$ salts. The interfacial behavior of the formed Pt species differs from the targeted surface-active complex **1**: The Pt signal in 0° is slightly lower than nominally expected and decreases by a factor of 1.5 at 80° (0.21 vs 0.14). A similar decrease was also observed for the Cl_{coord} species (0.83 vs 0.56), while the $Cl_{uncoord}$ signal only slightly decreases (0.50 vs 0.44). The signals specific for the surface-active ligand [C_3CNPFC_4Im][PF_6] F_{CFx}, C_{CF3}, C_{CF2} show a higher intensity at 0° (3.5 vs 2.5 nominal for F_{CFx}) and increase at 80° (6.7 vs. 3.5) indicating surface enrichment of this compound. As discussed above, the N_{CN} signal shows a slightly higher intensity at 0° but decreases at 80°, which is indicative for the preferred surface orientation of [C_3CNPFC_4Im][PF_6], with the CFx groups terminating the surface, while the CN groups are directed towards the bulk.[5] Due to the enrichment of [C_3CNPFC_4Im][PF_6], all other signals show a slight decrease. Overall, the surface is preferably populated by the non-coordinated ligand, while the formed Pt species does not exhibit affinity to the IL/gas interface.

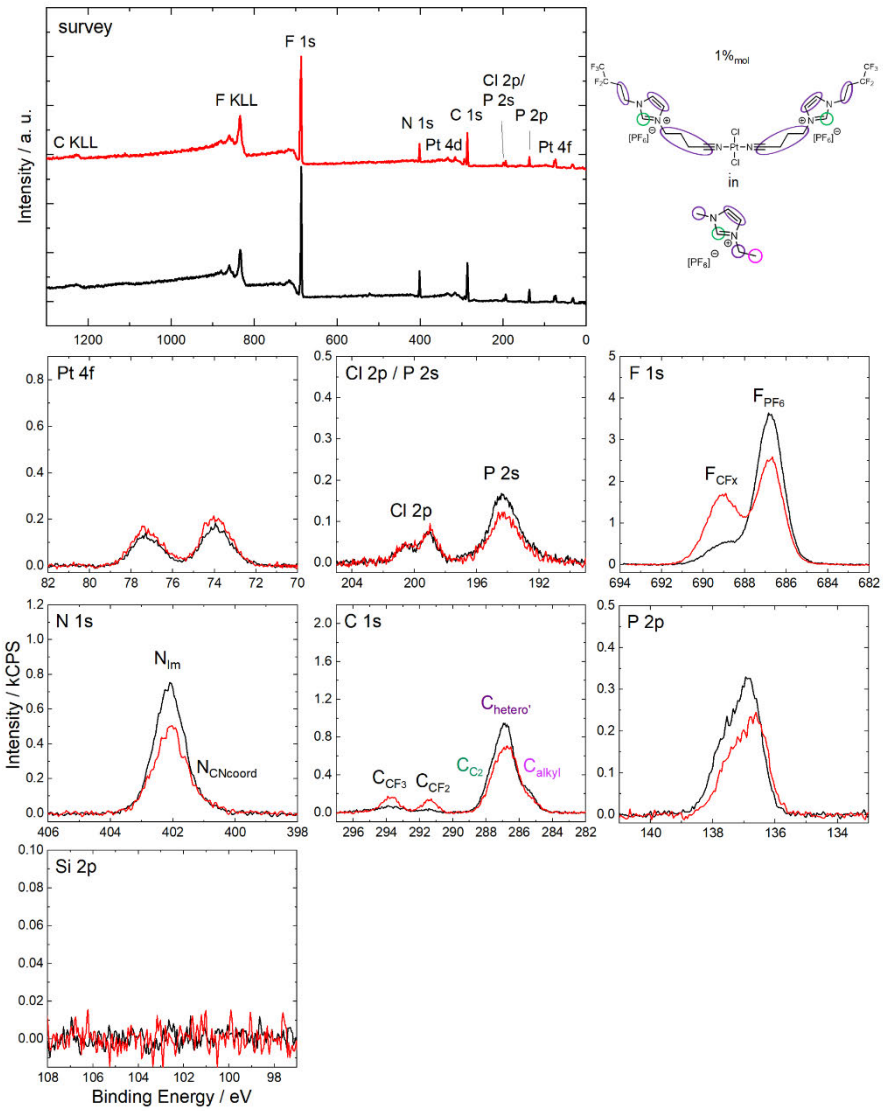

***Figure S9**: Survey, Pt 4f, Cl 2p/P 2s, F 1s, N 1s, C 1s, P 2p and Si 2p XP spectra of a 1%$_{mol}$ solution of **1** in [C_2C_1Im][PF_6] in 0° (black) and 80° (red) emission recorded at room temperature with assignment of peaks to the molecular structure.*

<u>Additional information on the peak fitting for solution shown in Figure S9:</u>

Owing to the particularly strong enrichment of **1** in the IL, a higher intensity of the complex-related signals was detected and therefore, we included the $N_{CNcoord}$ signal into the fitting, which is in contrast to the 1%$_{mol}$ solutions in the other ILs.

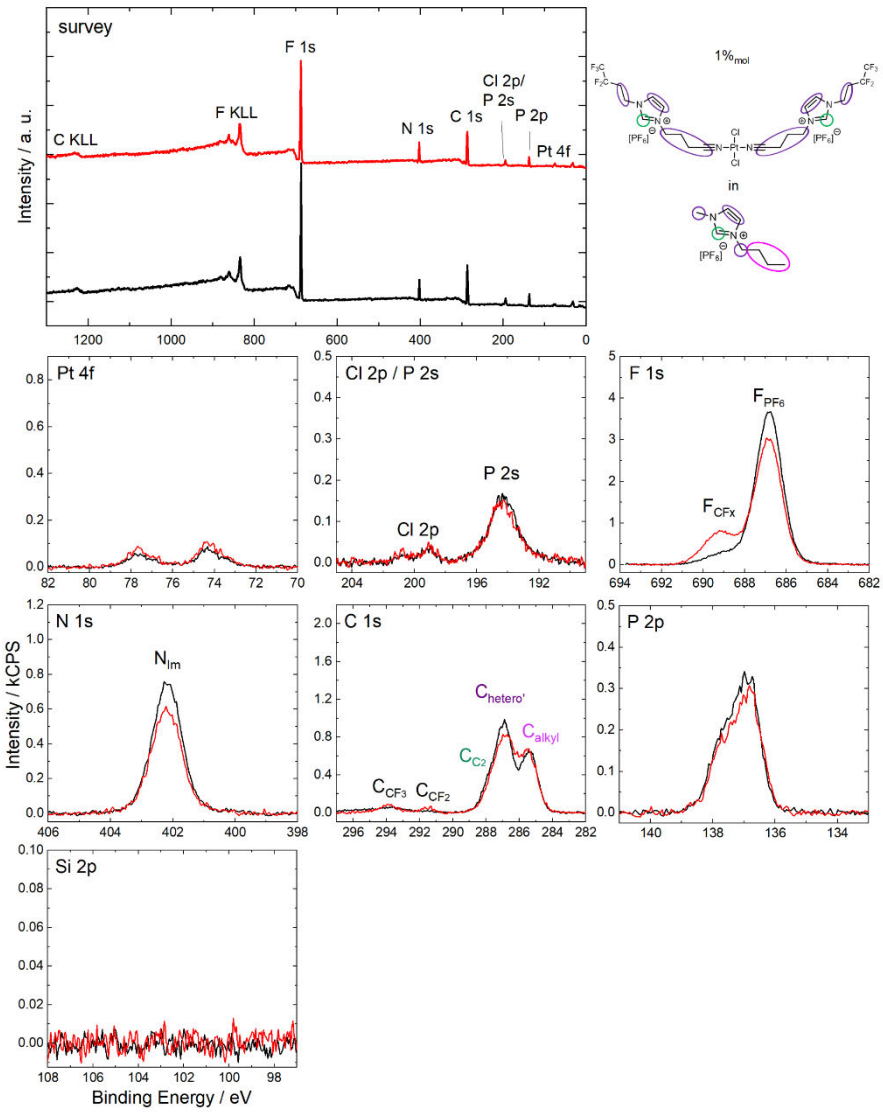

***Figure S10**: Survey, Pt 4f, Cl 2p/P 2s, F 1s, N 1s, C 1s, P 2p and Si 2p XP spectra of a 1%$_{mol}$ solution of **1** in [C_4C_1Im][PF_6] in 0° (black) and 80° (red) emission recorded at room temperature with assignment of peaks to the molecular structure. Adapted from Ref. [8].*

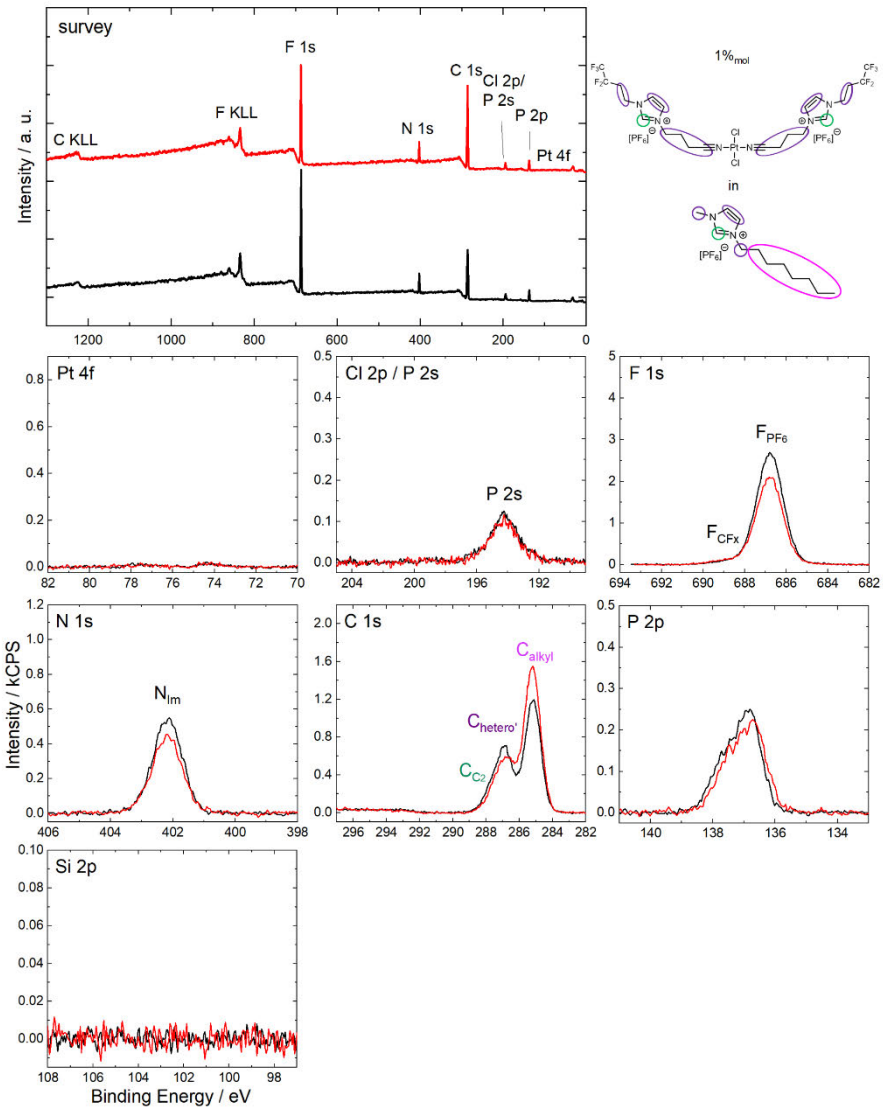

***Figure S11**: Survey, Pt 4f, Cl 2p/P 2s, F 1s, N 1s, C 1s, P 2p and Si 2p XP spectra of a 1%$_{mol}$ solution of **1** in [C_8C_1Im][PF_6] in 0° (black) and 80° (red) emission recorded at room temperature with assignment of peaks to the molecular structure.*

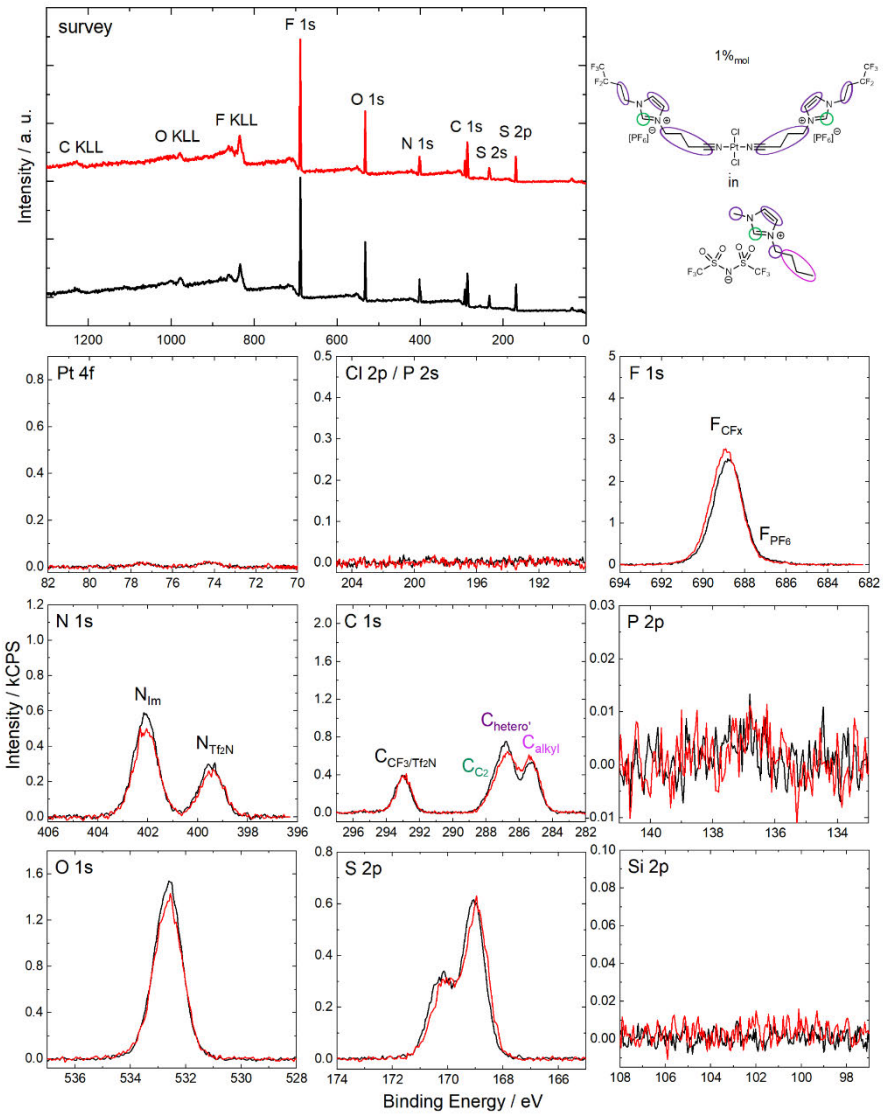

***Figure S12**: Survey, Pt 4f, Cl 2p/P 2s, F 1s, N 1s, C 1s, P 2p and Si 2p XP spectra of a 1%$_{mol}$ solution of **1** in [C_4C_1Im][Tf_2N] in 0° (black) and 80° (red) emission recorded at room temperature with assignment of peaks to the molecular structure.*

<u>Additional information on the peak fitting for solution shown in Figure S12:</u>

Owing to the low intensity of the P 2p signal, no fitting was conducted.

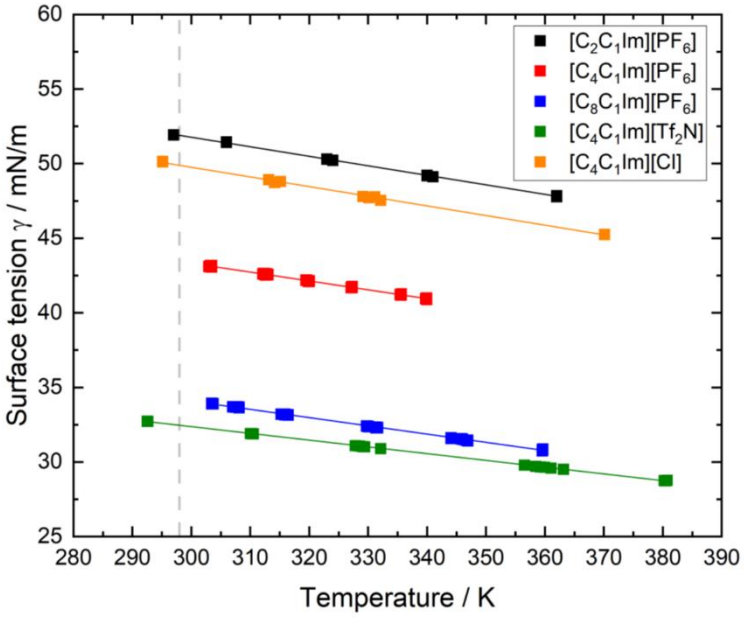

***Figure S13**: Temperature-dependent surface tension γ of neat ILs employed in this work [C_2C_1Im][PF_6] (black), [C_4C_1Im][PF_6] (red), [C_8C_1Im][PF_6] (blue), [C_4C_1Im][Tf_2N] (green) and [C_4C_1Im][Cl] (orange). The grey dashed line indicates the temperature for the surface tension values given in Table 4 in the main manuscript.*

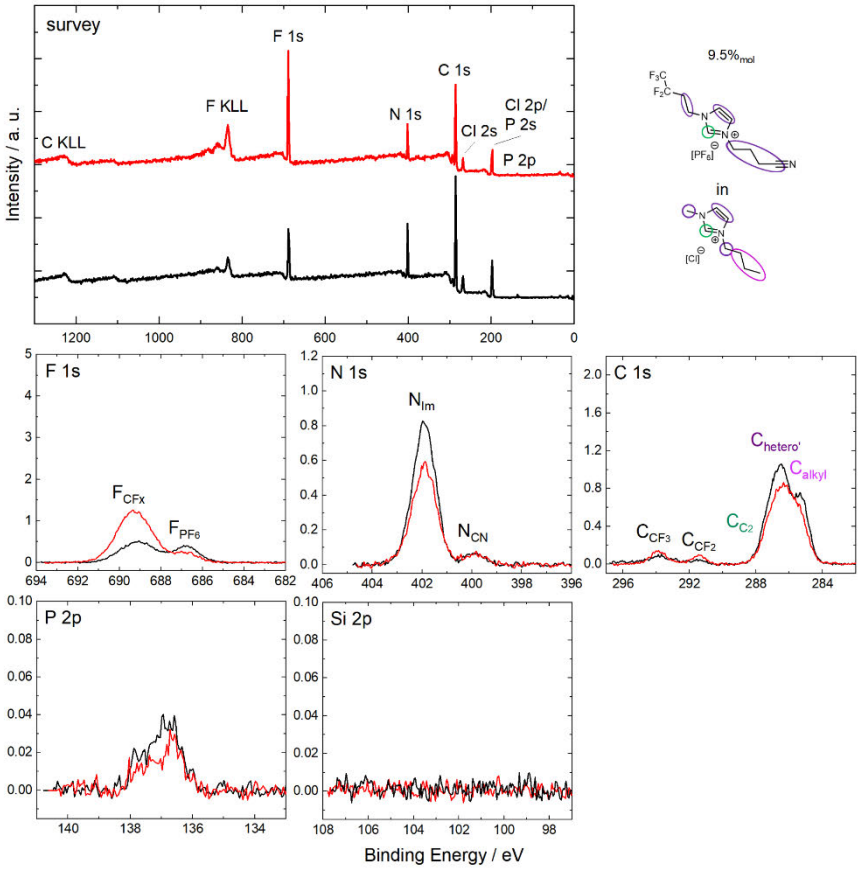

***Figure S14**: Survey, F 1s, N 1s, C 1s, P 2p and Si 2p XP spectra of a 9.5%$_{mol}$ solution of [C_3CNPFC_4Im][PF_6] in [C_4C_1Im][Cl] in 0° (black) and 80° (red) emission recorded at room temperature with assignment of peaks to the molecular structure.*

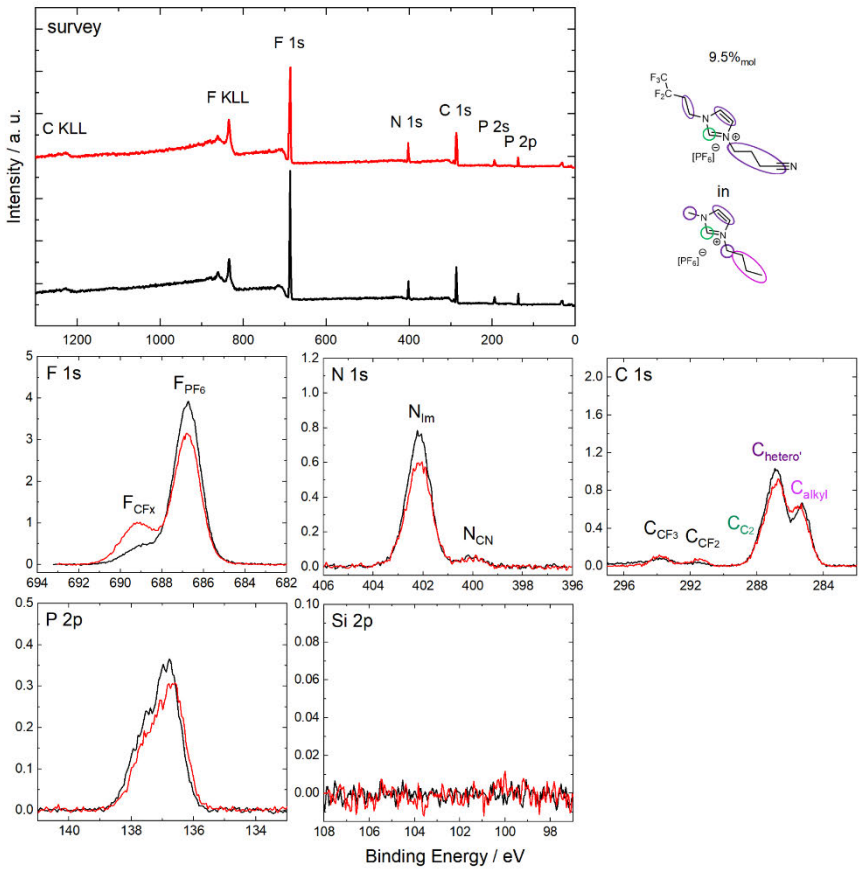

***Figure S15**: Survey, F 1s, N 1s, C 1s, P 2p and Si 2p XP spectra of a 9.5%$_{mol}$ solution of [C_3CNPFC_4Im][PF_6] in [C_4C_1Im][PF_6] in 0° (black) and 80° (red) emission recorded at room temperature with assignment of peaks to the molecular structure. Adapted from Ref. [8].*

Table S4: *Weighed proportions for preparation of solutions investigated by ARXPS.*

	10%$_{mol}$ 1 in [C_2C_1Im][PF_6]	10%$_{mol}$ 1 in [C_8C_1Im][PF_6]	10%$_{mol}$ 1 in [C_4C_1Im][Tf_2N]	20%$_{mol}$ 1 in [C_4C_1Im][Tf_2N]	1%$_{mol}$ 1 in [C_2C_1Im][PF_6]	1%$_{mol}$ 1 in [C_8C_1Im][PF_6]	1%$_{mol}$ 1 in [C_4C_1Im][Tf_2N]	9.5%$_{mol}$ ligand in [C_4C_1Im][Cl]
Mass *Cis*-[$PtCl_2(CH_3CN)_2$] / mg	20.4	30.3	30.8	29.5	20.9	13.4	16.9	
Amount of substance *Cis*-[$PtCl_2(CH_3CN)_2$] / mmol	0.057	0.085	0.087	0.083	0.059	0.038	0.048	
Mass [C_3CNPFC_4Im][PF_6] / mg	49.1	73.0	74.1	71.1	50.3	32.2	40.8	55.0
Amount of substance [C_3CNPFC_4Im][PF_6] / mmol	0.115	0.171	0.173	0.166	0.118	0.075	0.096	0.129
Mass IL / mg	132.4	263.9	330.5	140.5	1492	1284	1996	214.7
Amount of substance IL / mmol	0.517	0.768	0.780	0.332	5.83	3.74	4.71	1.22

$M_{[PtCl_2(CH_3CN)_2]}$ = 348.09 g/mol, $M_{[C_3CNPFC_4Im][PF_6]}$ = 427.20 g/mol, $M_{[C_2C_1Im][PF_6]}$ = 256.13 g/mol, $M_{[C_4C_1Im][PF_6]}$ = 284.18 g/mol, $M_{[C_8C_1Im][PF_6]}$ = 340.29 g/mol, $M_{[C_4C_1Im][Tf2N]}$ = 419.37 g/mol, $M_{[C_4C_1Im][Cl]}$ = 174.68 g/mol

Purity: [$PtCl_2(CH_3CN)_2$]: 98%, [C_4C_1Im][PF_6], [C_8C_1Im][PF_6], [C_4C_1Im][Tf_2N]: 99%, [C_4C_1Im][Cl]: 99.5%, The final purity grade of [C_2C_1Im][PF_6] is unknown (see experimental section in main manuscript); due to the thorough cleaning procedures, however, the grade of contamination is negligible.

References

[1] J. M. Gottfried, F. Maier, J. Rossa, D. Gerhard, P. S. Schulz, P. Wasserscheid, H.-P. Steinrück, *Z. Phys. Chem.* **2006**, *220*, 1439-1453.

[2] I. Niedermaier, C. Kolbeck, H.-P. Steinrück, F. Maier, *Rev. Sci. Instrum.* **2016**, *87*, 045105.

[3] a) H.-P. Steinrück, P. Wasserscheid, *Catal. Lett.* **2015**, *145*, 380-397; b) U. Paap, V. Seidl, K. Meyer, F. Maier, H.-P. Steinrück, *Molecules* **2022**, *27*, 8561; c) B. S. J. Heller, M. Lexow, F. Greco, S. Shin, G. Partl, F. Maier, H.-P. Steinrück, *Chem. Eur. J.* **2020**, *26*, 1117-1126; d) M. A. Tesa-Serrate, B. C. Marshall, E. J. Smoll, Jr., S. M. Purcell, M. L. Costen, J. M. Slattery, T. K. Minton, K. G. McKendrick, *The Journal of Physical Chemistry C* **2015**, *119*, 5491-5505; e) K. R. J. Lovelock, *Phys. Chem. Chem. Phys.* **2012**, *14*, 5071-5089.

[4] F. Maier, T. Cremer, C. Kolbeck, K. R. J. Lovelock, N. Paape, P. S. Schulz, P. Wasserscheid, H. P. Steinrück, *Phys. Chem. Chem. Phys.* **2010**, *12*, 1905-1915.

[5] D. Hemmeter, D. Kremitzl, P. S. Schulz, P. Wasserscheid, F. Maier, H.-P. Steinrück, *Chem. Eur. J.* **2023**, *29*, e202203325.

[6] a) C. Kolbeck, I. Niedermaier, A. Deyko, K. R. J. Lovelock, N. Taccardi, W. Wei, P. Wasserscheid, F. Maier, H.-P. Steinrück, *Chem. Eur. J.* **2014**, *20*, 3954-3965; b) K. R. J. Lovelock, C. Kolbeck, T. Cremer, N. Paape, P. S. Schulz, P. Wasserscheid, F. Maier, H. P. Steinrück, *The Journal of Physical Chemistry B* **2009**, *113*, 2854-2864.

[7] L. Winter, R. G. Bhuin, F. Maier, H.-P. Steinrück, *Chem. Eur. J.* **2021**, *27*, 17059-17065.

[8] D. Hemmeter, U. Paap, N. Wellnhofer, A. Gezmis, D. Kremitzl, P. Wasserscheid, H.-P. Steinrück, F. Maier, *ChemPhysChem*, *n/a*, e202300612.

8.7 Publication 7, [P7]

Check for updates

ChemistryOpen

Research Article
doi.org/10.1002/open.202400092

Chemistry Europe
European Chemical Societies Publishing

www.chemistryopen.org

Unlocking the Fluorine-Free Buoy Effect: Surface-Enriched Ruthenium Polypyridine Complexes in Ionic Liquids

Luciano Sanchez Merlinsky+,[a, b] Daniel Hemmeter+,[c] Luis M. Baraldo,[a, b] Florian Maier,[c] Hans-Peter Steinrück,*[c] and Federico J. Williams*[a, b]

Controlling the local concentration of metal complexes at the surface of ionic liquids (ILs) is a highly sought-after objective due to its pivotal implications in supported ionic liquid phase (SILP) catalysis. Equally important is to avoid per- and polyfluorinated substances due to environmental concerns. Herein, we investigate the surface enrichment of Ru polypyridyl complexes with fluorine-free alkylic side groups of varying lengths and shapes, using the hydrophilic IL $[C_2C_1Im][OAc]$ as solvent. Additional charged carboxylate groups are included into the polypyridyl ligands to increase the solubility of the complex in the IL. When the ligand system is functionalized with long and hydrophobic alkyl side chains, the complex predominantly localizes at the IL/vacuum interface, as deduced from angle-resolved X-ray photoelectron spectroscopy. Conversely, in the presence of short or more bulky substituents, no surface enrichment is observed. This buoy-like behaviour with fluorine-free side groups is explored for 0.05 $\%_{mol}$ to 1 $\%_{mol}$ solutions. Intriguingly, surface saturation occurs at approximately 0.5 $\%_{mol}$, which is beneficial to the efficient operation of catalytic systems featuring high surface areas, such as SILP catalysts.

Introduction

Ionic liquids (ILs) have recently found applications as alternative solvents in numerous transition-metal-catalysed reactions due to their extremely low volatility, non-flammability, thermal stability, and wide-ranging tailorable properties.[1] A particularly crucial application is in supported ionic liquid phase (SILP) catalysis, where IL thin films containing dissolved metal catalysts impregnate high-surface area supports.[2] These macroscopically solid systems combine the advantages of heterogeneous catalysis, enabling efficient separation of products and catalysts, with the benefits of homogeneous catalysis, conferring high selectivity. SILP catalysts exhibit promising performance in many gas-phase reactions of industrial relevance.[3] In many cases, they operate under milder conditions and show higher selectivity than their heterogeneous counterparts.[4] SILP systems containing Ru complexes can catalyse important reactions such as methanol reforming,[5] the water-gas shift reaction,[6] CO_2 hydrogenation,[7] and the alkoxy carbonylation of olefins with CO_2.[8] Furthermore, Ru polypyridyl complexes dissolved in ILs are promising candidates to reduce carbon dioxide,[9] or in the construction of stable and efficient dye-sensitized solar cells.[10]

Catalytic reactions in SILP systems require that the reactants enter the IL film from the gas phase, diffuse towards the catalytically active species, react to form products, which diffuse out of the IL phase.[11] The processes of dissolution and diffusion in the IL phase can pose significant limitations to the performance of SILP catalysts. Therefore, a preferential placement of the catalytically active complex right at the IL/gas interface could minimize transport barriers enhancing the overall catalytic efficiency. Thus, an ideal SILP catalyst should promote surface enrichment of the dissolved metallic complex at the IL/gas interface.

Over the past decades, much research has been carried out to understand surfaces of neat ILs or mixture of ILs.[12] However, the number of surface investigations on IL films containing dissolved metal complexes is much lower. Different studies indicate that the chemical nature of the ligands influences the local concentration of the metal complex at the IL/vacuum interface.[13] For example, functionalization of $[Rh(acac)(CO)_2]$ with the trisodium 3,3′,3″-phosphanetriyltri(benzene-1-sulfonate) (TPPTS) ligand resulted in surface enrichment,[13a] whereas Pt(II) and Pd(II) complexes with ligand systems derived from nitrile-functionalized ionic liquids showed homogeneous distribution of the complexes in the IL with no enrichment in the outermost surface layers.[13c] Notably, adding perfluorinated substituents to Pt(II) complexes resulted in surface enrichment, while without these substituents no such effect could be observed.[13d,e] However, the former suffer from the environmental problems associated with per- and polyfluorinated

[a] L. Sanchez Merlinsky,+ Prof. Dr. L. M. Baraldo, Prof. Dr. F. J. Williams
Departamento de Química Inorgánica, Analítica y Química Física, Facultad de Ciencias Exactas y Naturales, Universidad de Buenos Aires, Buenos Aires, Argentina
E-mail: fwilliams@qi.fcen.uba.ar

[b] L. Sanchez Merlinsky,+ Prof. Dr. L. M. Baraldo, Prof. Dr. F. J. Williams
Instituto de Química Física de los Materiales, Medio Ambiente y Energía, CONICET-Universidad de Buenos Aires, Buenos Aires, Argentina

[c] D. Hemmeter,+ Dr. F. Maier, Prof. Dr. H.-P. Steinrück
Lehrstuhl für Physikalische Chemie II, Friedrich-Alexander-Universität Erlangen-Nürnberg, Egerlandstraße 3, Erlangen, Germany
E-mail: hans-peter.steinrueck@fau.de

[+] L. Sanchez Merlinsky and D. Hemmeter contributed equally to the manuscript.

Supporting information for this article is available on the WWW under https://doi.org/10.1002/open.202400092

ChemistryOpen
Research Article
doi.org/10.1002/open.202400092
Chemistry Europe
European Chemical Societies Publishing

substances (PFAS).[14] Therefore, it is important to continue exploring and tailoring ligands for transition metals that promote surface enrichment and are free of polyfluorinated alkyl groups.

Previous studies have shown that adding surfactants or surface-active contaminations (e.g. polysiloxanes) with long hydrophobic tails in ILs can lead to the formation of a surfactant layer at the liquid/gas interface with their non-polar tails directed towards the gas phase forming the typical monolayer that is usually seen in analogous aqueous systems, accompanied by a decrease in surface tension.[15] Moreover, a series of metallosurfactants has been investigated in aqueous media under ambient conditions.[16] For example, $[Ru(bipyridine)_3]^{2+}$ complexes with alkyl side chains between 12 and 19 carbon atoms attached to one of the bidentate ligands have shown to be surface-active, with different micelle shapes, adsorption rates and structures at the water/air interface depending on the length, position and number of side chains in the molecule.[16b–e]

Recently for ILs, a first example of surface enrichment was reported for a metallosurfactant-type Ru complex with a trioctyl phosphine ligand when dissolved in $[C_2C_1Im][Tf_2N]$ as based on non-reactive atom scattering with an hyperthermal F-Atoms probe, X-ray photoelectron spectroscopy and time-of-flight secondary ion mass spectrometry.[13b] This study was, however, performed for only one type of complex and only for one single complex concentration, and with a limited XPS surface sensitivity of ~7 nm; moreover, the solution was also contaminated with a highly surface-active polysiloxane, which might had an influence on the surface enrichment of the complex.[13b]

In order to obtain a more detailed understanding, we herein focus on evaluating routes to tailor the surface enrichment of PFA-free Ru complexes in ionic liquids. For this purpose, we have designed Ru polypyridyl complexes with alkyl chains of varying lengths and shapes to investigate surface enrichment at the IL/vacuum interface using angle-resolved X-ray Photoelectron Spectroscopy (ARXPS) under ultraclean vacuum conditions. We performed our measurements at 0° (bulk-sensitive) and 80° (sensitive to the topmost layer) emission angle (see below). Specifically, we examined the behaviour of Ru complexes with bipyridine ligands functionalized with four carboxylate side groups, creating a highly polar headgroup to enhance their solubilities. We introduced two methyl (Ru-C_1), ethoxy (Ru-C_2), tert-butyl (Ru-tC_4) or n-nonyl (Ru-C_9) side chains to control the surface composition in 1-ethyl-3-methylimidazolium acetate $[C_2C_1Im][OAc]$ (Figure 1), which is highly hydrophilic and has a high surface tension.[17] Our findings demonstrate that the non-fluorinated, hydrophobic nonyl chains induce a strong enrichment of the complex at the surface of the solution, similar to a comparable metallosurfactant Ru polypyridyl complex in aqueous solution.[16b–e] Conversely, we find no such enrichment for a complex with shorter alkyl chains or with bulky hydrophobic tert-butyl groups.

Experimental Methods

Experimental details, such as syntheses, sample preparation and information on ARXPS analyses can be found in the supporting information (SI).

Results and Discussion

ARXPS is a powerful technique for characterizing the near-surface region of ILs in detail, providing information on

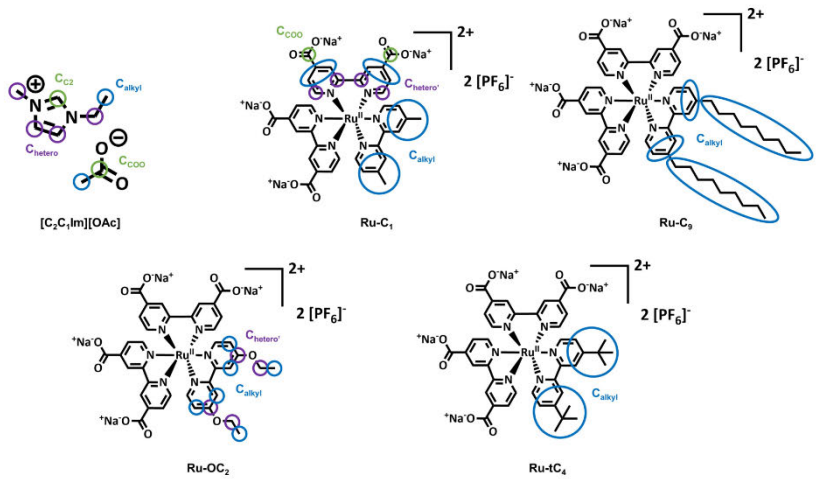

Figure 1. Molecular structures of the complexes and the IL employed in this work with the corresponding assignment of carbon species to the deconvolved XPS signals. The complexes were synthesized as Na^+ and $[PF_6]^-$ salts in all cases.

ChemistryOpen
Research Article
doi.org/10.1002/open.202400092
Chemistry Europe
European Chemical Societies Publishing

chemical state and compositional depth-distributions.[18] When using Al Kα radiation, electron emission normal to the surface (at 0°) yields information on the top 6–9 nm of organic films, which typically reflects the bulk composition. On the other hand, grazing electron emission (at 80°) offers insights into the top 1–1.5 nm, mainly capturing details of the topmost molecular layer.[19]

Figure 2a shows the C 1s/Ru 3d, N 1s and O 1s regions measured for a 1 $\%_{mol}$ Ru-C_9 solution in $[C_2C_1Im][OAc]$ at 0° (black) and 80° (red) emission. Note that the full set of spectra is displayed in Figure S1 in the SI, and the quantitative analysis of the binding energies and peak intensities is provided in Table S1a. In the C 1s/Ru 3d region, a broad signal envelope centred at 286 eV is observed, which corresponds to the C atoms of the complex and the IL; it is typically deconvolved using three contributions:[19,20] the carboxylate groups and the C_2 imidazolium carbon were fitted as one signal $C_{C2/COO}$ at 287.4 eV, the carbon atoms bound to one heteroatom as $C_{hetero'}$ at 286.3 eV, and the alkylic carbon atoms as C_{alkyl} at 285.0 eV. Figure 2b illustrates the fitting employed at 0° emission; for assignment of the peaks to the molecular structures, see Figure 1. The Ru $3d_{5/2}$ signal at 280.9 eV is consistent with an oxidation state of +2.[20] Note that the Ru $3d_{3/2}$ peak at 285.1 eV is hidden under the prominent C_{alkyl} signal (Figure 2b). In the N 1s region, the peak at 401.7 eV is assigned to the imidazolium nitrogen atoms from the IL and the signal at 400.0 eV to the bipyridine ligands from the complex.[20] The single O 1s signal at 530.4 eV stems from the $[OAc]^-$ anion of the IL and the COO^- groups of the complex. The Na 1s signal at 1070.8 eV originates from the dissolved Na^+ counterions of the carboxylate groups (see Figure S1). Interestingly, no F 1s and P 2p signals from the $[PF_6]^-$ counterions of the complex are detected, which indicates a strong surface depletion of these anions in solution. Notably, XPS of solid Ru-C_9 confirmed the presence of $[PF_6]^-$ in the compound (see Figure S2). Concerning the absence of the $[PF_6]^-$ signal in the Ru-C_9 solution, we rule out the possibility of $Na[PF_6]$ precipitation from the solution, as both Na^+ and $[PF_6]^-$ ions are observed in the Ru-C_1 solution, where the complex is not surface-enriched – see below. Since the overall charge of the dissolved complex without counterions is −2 (considering Ru^{II} and the four negatively charged carboxylate groups), we anticipate electrostatic repulsion of negatively charged ions, including $[PF_6]^-$, from the topmost layer. We expect the anions in the underlying layers to be dominated by $[OAc]^-$ due to its much larger concentration than $[PF_6]^-$. Moreover, considering the orientation of the C_9 alkyl chains towards the vacuum, the XPS signals from the underlying layers will be strongly attenuated, and thus, any $[PF_6]^-$ present in the layers below the topmost layer would be hardly detected due to its very low overall concentration.

The Ru : N ratio calculated from the 0° spectra is 1 : 5.1 (see Table S1a), in good agreement with the expected 1 : 6 ratio, indicating that the bpy ligands are coordinated to the Ru center in solution.

Most notably, the complex-specific Ru $3d_{5/2}$ and N_{bpy} signals show a much larger intensity than nominally expected even in the bulk-sensitive 0° spectra, and with a slight increase at 80° (see Table S1). The same is true for the C_{alkyl} signal, which has a large contribution from the complex, with a much stronger increase at 80°. These observations indicate a pronounced enrichment of the complex at the IL/vacuum interface. The larger increase of the C_{alkyl} signal compared to the Ru $3d_{5/2}$ (see inset in Figure 2a) and N_{bpy} signals at 80° suggests that the surface is terminated with the C_9 chains of the complex pointing towards the IL/vacuum interface, while the metal center is located below. Thus, we identify the C_9 chains as the surface-active moiety, which act like buoys pulling the complex to this interface. In line with the enrichment of the complex, the C_{C2}, $C_{hetero'}$ and $O_{OAc/COO}$ signals with major contributions from the IL are smaller than nominally expected, indicative of the depletion of $[C_2C_1Im][OAc]$ from the IL/vacuum interface. This depletion of the IL is most evident from the IL-specific N_{Im}

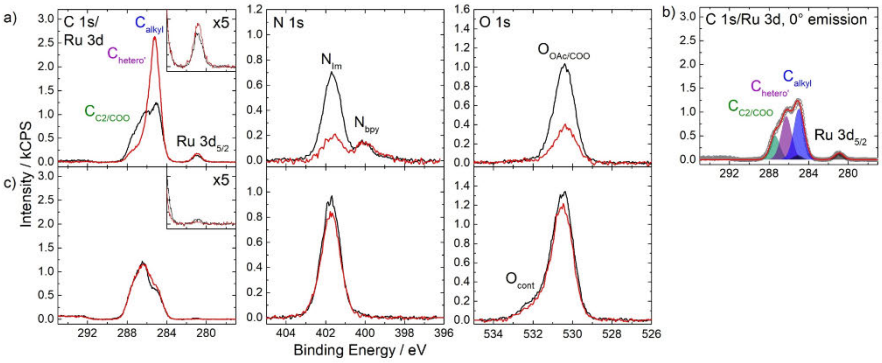

Figure 2. C 1s/Ru 3d, N 1s and O 1s XPS spectra regions of 1 $\%_{mol}$ solutions of a) Ru-C_9 (top row) and c) Ru-C_1 (bottom row) in $[C_2C_1Im][OAc]$ at 0° (black) and 80° (red) emission. Upscaled Ru $3d_{5/2}$ signals (x5) are depicted in the insets. b) Fitting of the C 1s/Ru 3d XPS spectra region of the Ru-C_9 solution at 0° emission and assignment of peaks to the molecular structure (cf. Figure 1). In the O 1s region of the solution of Ru-C_1 a small amount of a non-surface-active contamination O_{cont} from the synthesis procedure was also identified which is not expected to affect the surface structure.

ChemistryOpen
Research Article
doi.org/10.1002/open.202400092
Chemistry Europe
European Chemical Societies Publishing

signal, which shows a low intensity at 0° and strongly decreases at 80°.

The buoy effect is not observed for the complex with C_1 chains instead of C_9 chains, as evident from Figure 2c (full set of XP spectra shown in Figure S3): The Ru $3d_{5/2}$, N_{bpy} and C_{alkyl} signals of a 1 $\%_{mol}$ Ru-C_1 solution clearly show a much lower intensity than those of the 1 $\%_{mol}$ Ru-C_9 solution. The Ru 3d and N_{bpy} signals 0° are even lower than nominally expected (Table S1b), and decrease at 80°, indicating depletion of the complex from the IL/vacuum interface. The slight increase of the C_{alkyl} and the slight decrease of the N_{Im} and $O_{OAc/COO}$ signals at 80° stem from the preferential surface orientation of the $[C_2C_1Im]^+$ and $[OAc]^-$ ions, with the ethyl and methyl moieties pointing towards the vacuum.[20] These observations reveal that the Ru-C_1 complex has no surface affinity and is depleted from the interface, in contrast with the buoy-like behaviour found for the Ru-C_9 complex.

To investigate the concentration dependence, we studied Ru-C_9 solutions from 1 $\%_{mol}$ to 0.05 $\%_{mol}$; see Figure 3, Figures S1 and S5-S7 and the quantitative analysis in Table S2 in the SI. While the C 1s/Ru 3d XP spectra at 0° (top) and 80° (bottom) show no significant differences at 1 $\%_{mol}$ (red) and 0.5 $\%_{mol}$ (blue), the spectra for 0.1 $\%_{mol}$ (green) and 0.05 $\%_{mol}$ (violet) gradually decrease (for comparison, also the spectra of the neat IL are shown in black). This behaviour is also evident from Figure 3b, depicting the absolute intensity of the Ru 3d signal at different concentrations. The decrease is accompanied by an increase of the $C_{C2/COO}$ and $C_{hetero'}$ signals at 80°. These observations imply that at concentrations of 0.5 $\%_{mol}$ and above, the IL/vacuum interface is saturated with Ru-C_9, while at lower concentrations no saturation is achieved. It should be noted that at saturation of the interface with the complex, the outermost surface layer must also include IL $[C_2C_1Im]^+$ cations and potentially $[OAc]^-$ anions to maintain charge neutrality, compensating for the depletion of Na^+ and $[PF_6]^-$ ions. Additionally, the XP signal at 80° predominantly originates from the topmost layer, constituting approximately 80% of the total signal (assuming a layer thickness of 0.7–0.8 nm) with the remaining 20% originating from underlying layers. Consequently, IL ions from the layers underneath inevitably contribute to the signal.[19] Remarkably, the concentration required to facilitate surface saturation is much lower as observed for the PFAS-based catalyst in $[C_4C_1Im][PF_6]$.[13d,e] We attribute this behaviour predominantly to the higher surface tension of our hydrophilic solvent IL $[C_2C_1Im][OAc]$ of 47.1 mN/m at 298 K,[17] as compared to the more hydrophobic $[C_4C_1Im][PF_6]$ with its lower surface tension of 43.4 mN/m at 298 K,[13e] which favours a stronger enrichment of the surface-active complex at the IL/vacuum interface in $[C_2C_1Im][OAc]$.

To quantify the surface enrichment, we plotted the normalized Ru 3d content, representing the ratio of the experimental and nominal Ru contents at 0° (black) and 80° (red) vs concentration, in Figure 3c; thereby, a value of 1 (grey dashed line) corresponds to a homogeneously distributed and

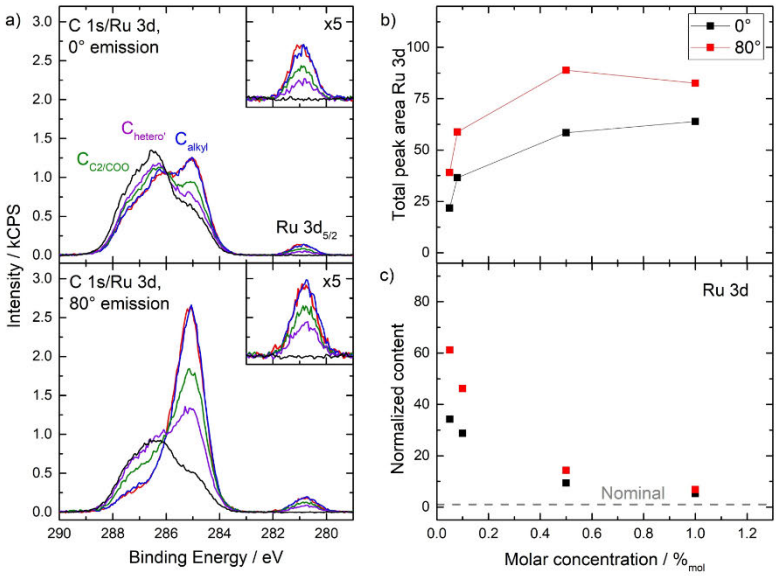

Figure 3. a) C 1s/Ru 3d XP spectra of solutions of Ru-C_9 in $[C_2C_1Im][OAc]$ at 0° (top) and 80° emission (bottom) with concentrations of 1 $\%_{mol}$ (red), 0.5 $\%_{mol}$ (blue), 0.1 $\%_{mol}$ (green) and 0.05 $\%_{mol}$ (violet); upscaled Ru $3d_{5/2}$ signals (x5) are depicted in the insets. For comparison, we also show the spectra of neat $[C_2C_1Im][OAc]$ (black). b) Absolute Intensities of Ru 3d signal and c) normalized content derived from Ru 3d signal at 0° (black) and 80° (red) over a concentration range from 1 $\%_{mol}$ to 0.05 $\%_{mol}$.

ChemistryOpen
Research Article
doi.org/10.1002/open.202400092
Chemistry Europe
European Chemical Societies Publishing

randomly orientated complex. The strong increase in normalized Ru content at both emission angles at low concentrations of Ru-C_9, reflects the enhanced surface enrichment relative to the bulk content. The enhancement factor in the top-most layer is ~61 at 0.05 $\%_{mol}$ as compared to ~7 at 1 $\%_{mol}$. This finding is particularly promising for catalytic applications, as it opens the door towards a most efficient atom utilization. As pointed out above, a similar surface enhancement was derived from reactive ion scattering for a Ru complex with a tri-octylphosphine ligand dissolved in the IL $[C_2C_1Im][Tf_2N]$ (2–3 $\%_{mol}$ at the surface vs. 0.04 $\%_{mol}$ in the bulk).[13b]

As a final step, we modified the length and shape of the side chains by replacing the nonyl groups with ethoxy and tert-butyl groups (see Figure 1 for structures, and Figure S8 and S9 for full sets of XP spectra). Figures 4a and 4b show the C 1s/Ru 3d, N 1s, and O 1s spectra for 1 $\%_{mol}$ Ru-OC_2 and Ru-tC_4 solutions in $[C_2C_1Im][OAc]$, with the quantitative analyses provided in Table S1c–d. Overall, the measured spectra resemble those obtained for the neat $[C_2C_1Im][OAc]$, as discussed above, with the very small Ru $3d_{5/2}$ and N_{bpy} signals indicating a very low concentration of the Ru complex at the IL/vacuum interface. These findings imply the absence of surface enrichment of these complexes.

Conclusions

Our goal was to evaluate different routes to tailor and quantify the surface enrichment of fluorine-free metal complexes in SILP systems. We have successfully demonstrated that the introduction of non-fluorinated long hydrophobic alkyl chains into the ligand system of Ru polypyridyl complexes leads to a strong surface enrichment at the IL/vacuum interface when dissolved in the hydrophilic IL $[C_2C_1Im][OAc]$. The long alkyl chains act in a buoy-like fashion localizing the complex at the outer surface. The fluorine-free buoy effect provides an environmentally more benign route for surface-enriching organometallic catalysts. Ligands with shorter or bulkier groups fail to promote the accumulation of the complex at the IL surface, which underscores the buoy-like behaviour of the long alkyl substituents. Also, the IL/vacuum interface is found to be saturated at bulk concentrations of the complex as low as of 0.5 $\%_{mol}$, which holds particular significance for catalytic applications such as in SILP, where the preferential localization of catalytically active sites at the IL/gas interface is essential for optimum atom utilization. Although the suitability of these specific complexes for the SILP concept was not shown so far, the fact that the surface enrichment is induced by the alkyl chains makes them excellent model catalysts for demonstrating this effect.

Acknowledgements

Luciano Sanchez Merlinsky acknowledges a PhD scholarship from CONICET. Financial support from Agencia I+D+i (PICT 2018-03276), Universidad de Buenos Aires (UBACyT 2020) and CONICET (PIP 2021) is gratefully acknowledged. Daniel Hemmeter, Florian Maier and Hans-Peter Steinrück acknowledge the Deutsche Forschungsgemeinschaft (DFG, German Research Foundation) for financial support (Project-ID 431791331 – SFB 1452). Daniel Hemmeter furthermore thanks the Stiftung Stipendien-Fonds of the German chemical industry association (Verband der Chemischen Industrie, VCI) for a Kekulé fellowship. Open Access funding enabled and organized by Projekt DEAL.

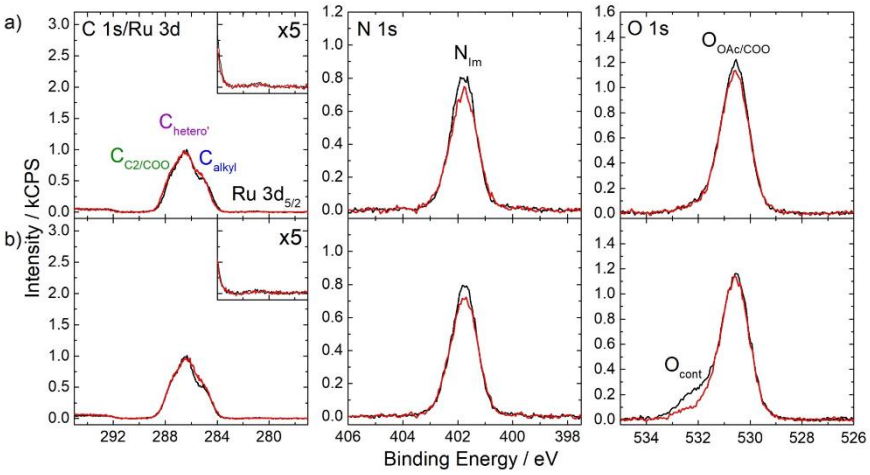

Figure 4. C 1s/Ru 3d, N 1s and O 1s XPS spectra regions of 1 $\%_{mol}$ solutions of a) Ru-OC_2 and b) Ru-tC_4 in $[C_2C_1Im][OAc]$ at 0° (black) and 80° (red) emission. Upscaled Ru $3d_{5/2}$ signals (x5) are depicted in the insets. In the O 1s region of the solution of Ru-tC_4 a small amount of a non-surface-active contamination O_{cont} from the synthesis procedure was also identified which is not expected to affect the surface structure.

ChemistryOpen
Research Article
doi.org/10.1002/open.202400092
Chemistry Europe
European Chemical Societies Publishing

Conflict of Interests

The authors declare no conflict of interest.

Data Availability Statement

The data that support the findings of this study are available from the corresponding author upon reasonable request. Source data are provided at Zenodo: DOI: 10.5281/zenodo.11032159

[1] a) P. Wasserscheid, W. Keim, *Angew. Chem.* **2000**, *39*, 3772–3789; b) J. P. Hallett, T. Welton, *Chem. Rev.* **2011**, *111*, 3508–3576.
[2] a) A. Riisager, R. Fehrmann, M. Haumann, P. Wasserscheid, *Eur. J. Inorg. Chem.* **2006**, *2006*, 695–706; b) C. P. Mehnert, *Chemistry A European J* **2005**, *11*, 50–56.
[3] a) J. M. Marinkovic, A. Riisager, R. Franke, P. Wasserscheid, M. Haumann, *Ind. Eng. Chem. Res.* **2019**, *58*, 2409–2420; b) J. Scholz, S. Loekman, N. Szesni, W. Hieringer, A. Görling, M. Haumann, P. Wasserscheid, *Adv. Synth. Catal.* **2011**, *353*, 2701–2707; c) S. Werner, N. Szesni, M. Kaiser, R. W. Fischer, M. Haumann, P. Wasserscheid, *ChemCatChem* **2010**, *2*, 1399–1402; d) P. Virtanen, T. Salmi, J.-P. Mikkola, *Ind. Eng. Chem. Res.* **2009**, *48*, 10335–10342; e) P. Latos, A. Wolny, A. Chrobok, *Materials* **2023**, *16*, 2106.
[4] a) M. Haumann, M. Jakuttis, R. Franke, A. Schönweiz, P. Wasserscheid, *ChemCatChem* **2011**, *3*, 1822–1827; b) S. Werner, N. Szesni, R. W. Fischer, M. Haumann, P. Wasserscheid, *Phys. Chem. Chem. Phys.* **2009**, *11*, 10817; c) U. Hintermair, G. Franciò, W. Leitner, *Chem. Eur. J.* **2013**, *19*, 4538–4547.
[5] C. H. Schwarz, A. Agapova, H. Junge, M. Haumann, *Catal. Today* **2020**, *342*, 178–186.
[6] P. Wolf, C. R. Wick, J. Mehler, D. Blaumeiser, S. Schötz, T. Bauer, J. Libuda, D. Smith, A.-S. Smith, M. Haumann, *ACS Catal.* **2022**, *12*, 5661–5672.
[7] L. Piccirilli, B. Rabell, R. Padilla, A. Riisager, S. Das, M. Nielsen, *J. Am. Chem. Soc.* **2023**, *145*, 5655–5663.
[8] S.-P. Xia, G.-R. Ding, R. Zhang, L.-J. Han, B.-H. Xu, S.-J. Zhang, *Green Chem.* **2021**, *23*, 3073–3080.
[9] S. Kern, R. Van Eldik, *Inorg. Chem.* **2012**, *51*, 7340–7345.
[10] D. Shi, N. Pootrakulchote, R. Li, J. Guo, Y. Wang, S. M. Zakeeruddin, M. Grätzel, P. Wang, *J. Phys. Chem. C* **2008**, *112*, 17046–17050.
[11] S. Werner, M. Haumann, P. Wasserscheid, *Annu. Rev. Chem. Biomol. Eng.* **2010**, *1*, 203–230.
[12] a) H.-P. Steinrück, J. Libuda, P. Wasserscheid, T. Cremer, C. Kolbeck, M. Laurin, F. Maier, M. Sobota, P. S. Schulz, M. Stark, *Adv. Mater.* **2011**, *23*, 2571–2587; b) H.-P. Steinrück, P. Wasserscheid, *Catal. Lett.* **2015**, *145*, 380–397; c) K. R. J. Lovelock, *Phys. Chem. Chem. Phys.* **2012**, *14*, 5071; d) C. S. Santos, S. Baldelli, *Chem. Soc. Rev.* **2010**, *39*, 2136; e) M. Tariq, M. G. Freire, B. Saramago, J. A. P. Coutinho, J. N. C. Lopes, L. P. N. Rebelo, *Chem. Soc. Rev.* **2012**, *41*, 829–868; f) K. Nakajima, M. Lísal, K. Kimura, in *Surface and Interface Science* (Ed.: K. Wandelt), Wiley, **2020**, pp. 351–389; g) E. Oz, O. Sahin, H. I. Okur, S. Suzer, *ChemPhysChem* **2020**, *21*, 2397–2401; h) Y. Zhang, Y. Khalifa, E. J. Maginn, J. T. Newberg, *J. Phys. Chem. C* **2018**, *122*, 27392–27401.
[13] a) C. Kolbeck, N. Paape, T. Cremer, P. S. Schulz, F. Maier, H. Steinrück, P. Wasserscheid, *Chem. Eur. J.* **2010**, *16*, 12083–12087; b) E. J. Smoll, X. Chen, L. M. Hall, L. D'Andrea, J. M. Slattery, T. K. Minton, *J. Phys. Chem. C* **2020**, *124*, 382–397; c) D. Hemmeter, U. Paap, N. Taccardi, J. Mehler, P. S. Schulz, P. Wasserscheid, F. Maier, H. Steinrück, *ChemPhysChem* **2023**, *24*, e202200391; d) D. Hemmeter, D. Kremitzl, P. S. Schulz, P. Wasserscheid, F. Maier, H. Steinrück, *Chem. Eur. J.* **2023**, *29*, e202203325; e) D. Hemmeter, U. Paap, N. Wellnhofer, A. Gezmis, D. Kremitzl, P. Wasserscheid, H. Steinrück, F. Maier, *ChemPhysChem* **2023**, *24*, e202300612.
[14] S. Brendel, É. Fetter, C. Staude, L. Vierke, A. Biegel-Engler, *Environ. Sci. Eng.* **2018**, *30*, 9.
[15] a) J. L. Anderson, V. Pino, E. C. Hagberg, V. V. Sheares, D. W. Armstrong, *Chem. Commun.* **2003**, 2444; b) W. Zhuang, C. Zhao, Y. Pan, Q. Li, *Soft Matter* **2021**, *17*, 3494–3502; c) T. L. Greaves, C. J. Drummond, *Chem. Soc. Rev.* **2013**, *42*, 1096–1120; d) J. M. Gottfried, F. Maier, J. Rossa, D. Gerhard, P. S. Schulz, P. Wasserscheid, H.-P. Steinrück, *Zeitschrift für Phys. Chemie* **2006**, *220*, 1439–1453.
[16] a) P. C. Griffiths, I. A. Fallis, T. Chuenpratoom, R. Watanesk, *Advances in Colloid and Interface Science* **2006**, *122*, 107–117; b) J. Bowers, M. J. Danks, D. W. Bruce, R. K. Heenan, *Langmuir* **2003**, *19*, 292–298; c) J. Bowers, M. J. Danks, D. W. Bruce, J. R. P. Webster, *Langmuir* **2003**, *19*, 299–305; d) J. Bowers, K. E. Amos, D. W. Bruce, J. R. P. Webster, *Langmuir* **2005**, *21*, 1346–1353; e) J. Bowers, K. E. Amos, D. W. Bruce, R. K. Heenan, *Langmuir* **2005**, *21*, 5696–5706.
[17] H. F. D. Almeida, A. R. R. Teles, J. A. Lopes-da-Silva, M. G. Freire, J. A. P. Coutinho, *J. Chem. Thermodyn.* **2012**, *54*, 49–54.
[18] K. R. J. Lovelock, I. J. Villar-Garcia, F. Maier, H.-P. Steinrück, P. Licence, *Chem. Rev.* **2010**, *110*, 5158–5190.
[19] I. Niedermaier, C. Kolbeck, H.-P. Steinrück, F. Maier, *Rev. Sci. Instrum.* **2016**, *87*, 045105.
[20] D. Hemmeter, L. Sanchez Merlinsky, L. M. Baraldo, F. Maier, F. J. Williams, H. Steinrück, *Phys Chem Chem Phys* **2024**, *26*, 7602–7610, DOI: 10.1039/D4CP00247D.

Manuscript received: March 22, 2024
Version of record online: April 30, 2024

ChemistryOpen

Supporting Information

Unlocking the Fluorine-Free Buoy Effect: Surface-Enriched Ruthenium Polypyridine Complexes in Ionic Liquids

Luciano Sanchez Merlinsky, Daniel Hemmeter, Luis M. Baraldo, Florian Maier, Hans-Peter Steinrück,* and Federico J. Williams*

Supporting Information

Unlocking the Fluorine-Free Buoy Effect: Surface-Enriched Ruthenium Polypyridine Complexes in Ionic Liquids

Luciano Sanchez Merlinsky[a,b,#], Daniel Hemmeter[c,#], Luis M. Baraldo[a,b], Florian Maier[c], Hans-Peter Steinrück[c*] and Federico J. Williams[a,b*]

[a]Departamento de Química Inorgánica, Analítica y Química Física, Facultad de Ciencias Exactas y Naturales, Universidad de Buenos Aires, Buenos Aires, Argentina

[b]Instituto de Química Física de los Materiales, Medio Ambiente y Energía, CONICET-Universidad de Buenos Aires, Buenos Aires, Argentina

[c]Lehrstuhl für Physikalische Chemie II, Friedrich-Alexander-Universität Erlangen-Nürnberg, Egerlandstraße 3, Erlangen, Germany

[*] Corresponding author email: hans-peter.steinrueck@fau.de and fwilliams@qi.fcen.uba.ar

[#] L. Sanchez Merlinsky and D. Hemmeter contributed equally to the manuscript.

Experimental section

$Ru(dcb)_2Cl_2$ (dcb = 4,4'-dicarboxy-2,2'-bipyridine) and 4,4'-diethoxy-2,2'-bipyridine were prepared according to previous reports.[1] 1-ethyl-3-methylimidazolium acetate ($[C_2C_1Im][OAc]$) and all other materials used in this work were obtained commercially and used without further purification.

Ru-C_1, Ru-OC_2 and Ru-tC_4: 50 mg of $Ru(dcb)_2Cl_2$ (0.076 mmol, 1.0 eq), 43 mg of silver triflate (0.17 mmol, 2.2 eq) and the corresponding ligand (4,4'-dimethyl-2,2'-bipyridine, 4,4'-diethoxy-2,2'-bipyridine and 4,4'-ditertbutyl-2,2'-bipyridine, respectively; 0.11 mmol, 1.5 eq) were heated at reflux covered from light for 3 h in 20 mL of ethanol. The mixture was filtered hot and its contents reduced to 5 mL. 30 mL of water was then added to precipitate the excess of ligand. After filtering the solid, the volume was reduced to 10 mL and 1 mL of HPF_6 (55 % wt. solution) was added, affording a dark red suspension of the protonated complex as the hexafluorophosphate salt. The complex was filtered, washed with water and dried in a vacuum desiccator overnight. Finally, the product was dissolved in 5 mL of water with 4 eq of NaOH and taken to dryness. Yield: Ru-C_1, 52 %; Ru-OC_2, 15 %; Ru-tC_4, 13 %. ^{1}H-NMR (500 MHz, D_2O-K_2CO_3): Ru-C_1, δ

ppm 8.86 (d, 4H); 8.35 (d, 2H); 7.89 (dd, 4H); 7.66 (t, 4H); 7.54 (d, 2H); 7.20 (d, 2H); 2.51 (t, 6H). Ru-OC_2, δ ppm 8.86 (d, 4H); 7.98 (d, 2H); 7.88 (dd, 4H); 7.72 (dd, 2H); 7.64 (dd, 2H); 7.48 (d, 2H); 6.91 (dd, 2H); 4.23 (m, 4H); 1.39 (t, 6H). Ru-tC_4, δ ppm 8.82 (d, 4H); 8.39 (d, 2H); 7.85 (dd, 4H); 7.61 (m, 6H); 7.35 (dd, 2H); 1.31 (s, 18H).

Ru-C_9: 50 mg of $Ru(dcb)_2Cl_2$ (0.076 mmol, 1.0 eq), 43 mg of silver triflate (0.17 mmol, 2.2 eq) and 46 mg of 4,4'-dinonyl-2,2'-bipyridine (0.11 mmol, 1.5 eq) were heated at reflux covered from light for 3 h in 20 mL of ethanol. The mixture was filtered hot and its contents reduced to 5 mL. 3 mL of saturated KPF_6 water solution were added and then another 10 mL of water to precipitate the product as the hexafluorophosphate salt together with the excess of ligand. After filtering the solid and washing it with water, it was dissolved in 5 mL of NaOH 0.1 M, filtered and neutralized with 2 mL of HCl 0.5 M, affording a dark red suspension. The complex was filtered, washed with water and dried in a vacuum desiccator overnight. Finally, the product was dissolved in 5 mL of water with 4 eq of NaOH and taken to dryness. Yield: 63 %. ^{1}H-NMR (500 MHz, D_2O-K_2CO_3): δ ppm 8.91 (dd, 2H); 8.85 (d, 2H); 8.28 (d, 2H); 7.80 (d, 2H); 7.68 (m, 8H); 7.25 (d, 2H); 2.60 (t, 4H); 1.41 (m, 4H); 0.91 (m, 24H); 0.57 (t, 6H).

Solutions of the complexes were prepared by stirring the compounds for at least 2 h under ambient conditions in the IL before introducing them into the load lock of the ultra-high vacuum (UHV) system, where the samples were left for degassing for several hours. The weighed proportions for preparation of the solutions are shown in Table S3.

ARXPS analyses were conducted using the unique Dual Analyzer System for Surface Analysis (DASSA), which is described elsewhere.[2] In brief, the setup comprises two analyzers at 0° (normal emission) and 80° (grazing) emission angle allowing for simultaneous recording of XP spectra in these geometries. Using Al Kα radiation, at 0° the information depth (ID) in organic matter is 6-9 nm and the spectra are dominated by bulk contributions; at 80°, the ID is only 1-1.5 nm and the spectra are dominated by to the first molecular layer of the sample. The intensity detected in the XP spectra was normalized to the overall intensity (sum over all intensities corrected by the atomic sensitivity factors (ASF)[3] of the 0.1%$_{mol}$ solution of Ru-C_9 at 0°. Further information on treatment and fitting of the ARXP spectra can be found elsewhere.[4]

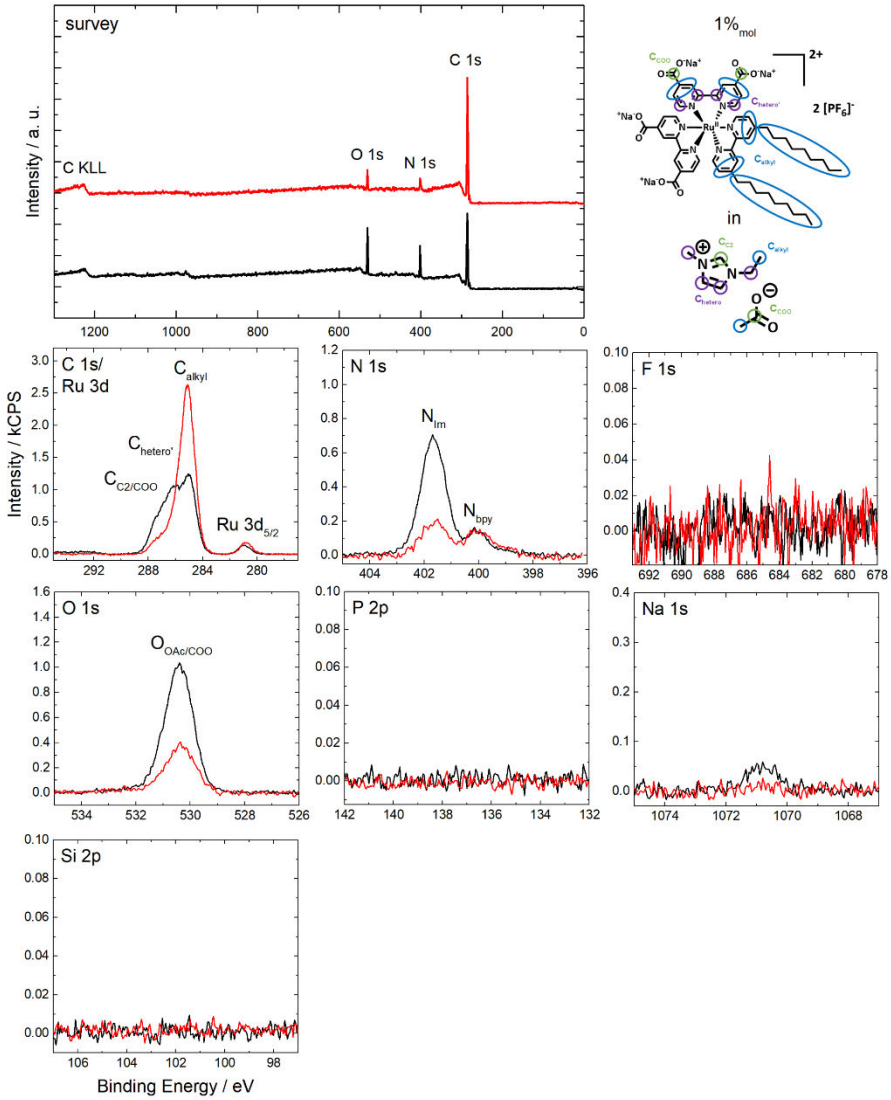

Figure S1: Survey, C 1s/Ru 3d, N 1s, F 1s, O 1s, P 2p, Na 1s and Si 2p XP spectra of 1%$_{mol}$ Ru-C$_9$ in [C$_2$C$_1$Im][OAc] in 0° (black) and 80° (red) emission recorded at room temperature. The Si 2p spectra are shown to confirm absence of common surface-active contaminations.[5]

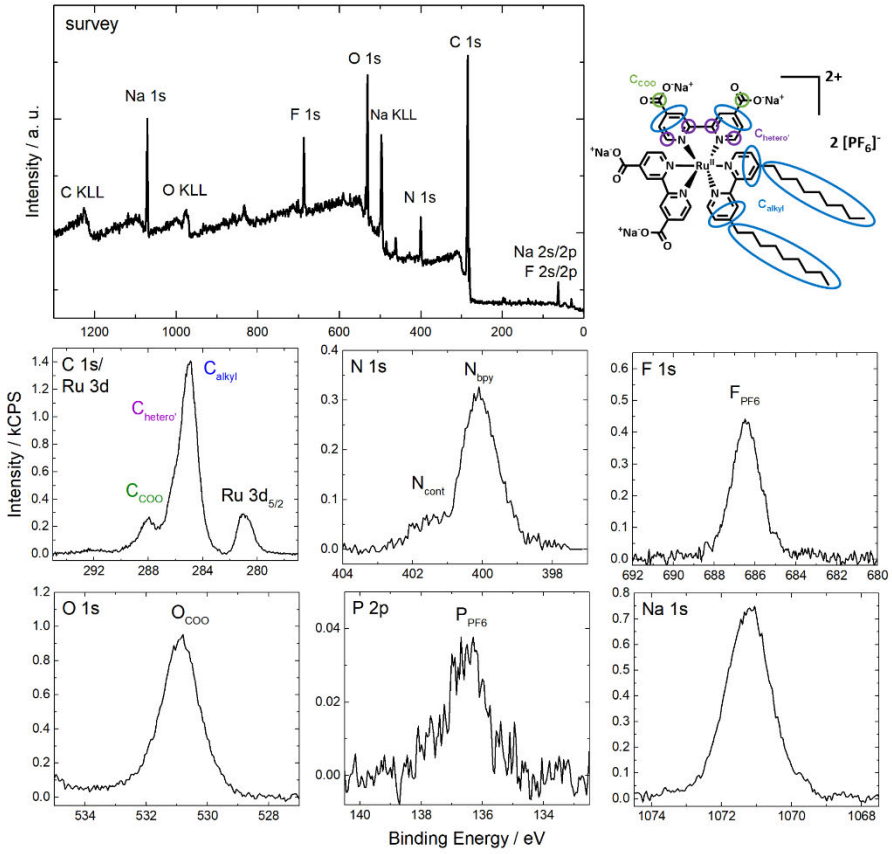

Figure S2: Survey, C 1s/Ru 3d, N 1s, F 1s, O 1s, P 2p and Na 1s XP spectra of solid Ru-C_9 in 0° emission recorded at room temperature. Nominal Ru:N:Na ratio for Ru-C_9: 1:6:4. Found: 1:5.3:3.5. A small amount of contaminations from the synthesis procedure is also identified at the N 1s region. Due to sample charging, all spectra are referenced to the C_{alkyl} signal, which was set to 285 eV as in solution.

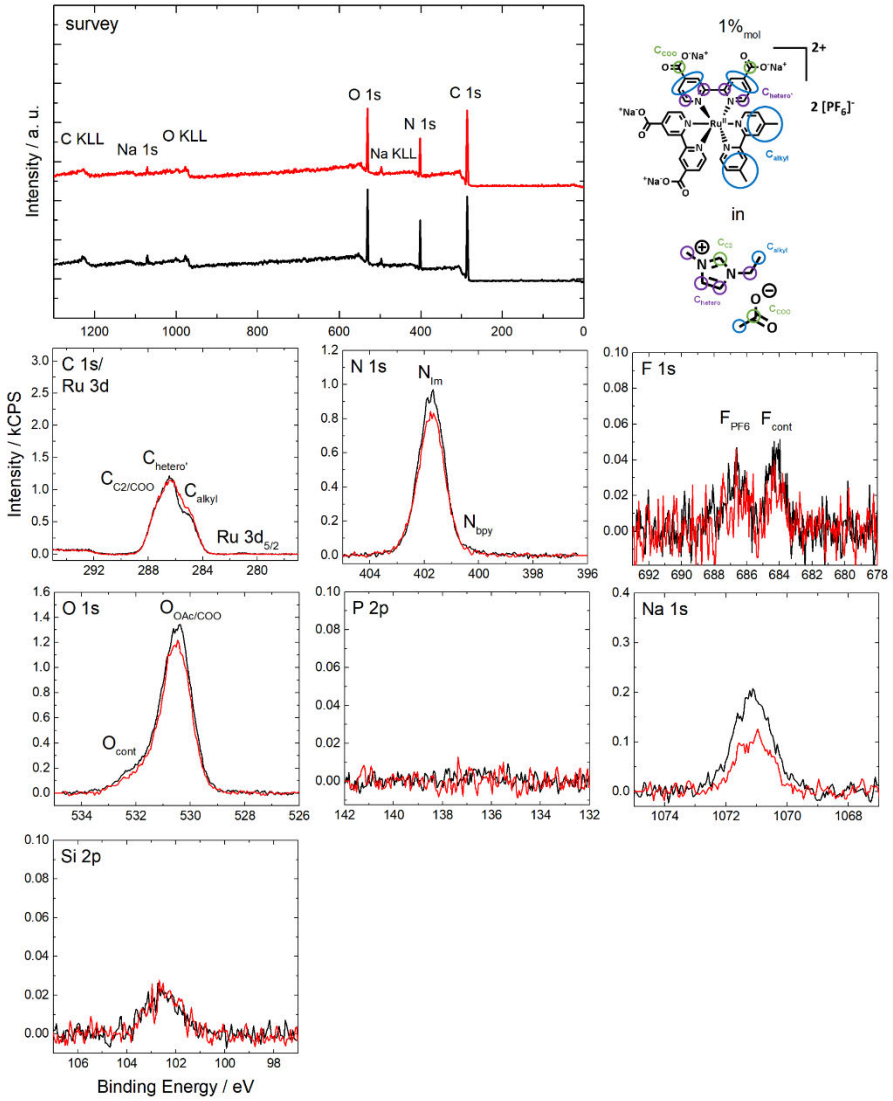

Figure S3: Survey, C 1s/Ru 3d, N 1s, F 1s, O 1s, P 2p, Na 1s and Si 2p XP spectra of 1%$_{mol}$ Ru-C$_1$ in [C$_2$C$_1$Im][OAc] in 0° (black) and 80° (red) emission recorded at room temperature. A small amount of non-surface-active contaminations from the synthesis procedure is also identified at the F 1s, O 1s and Si 2p regions.

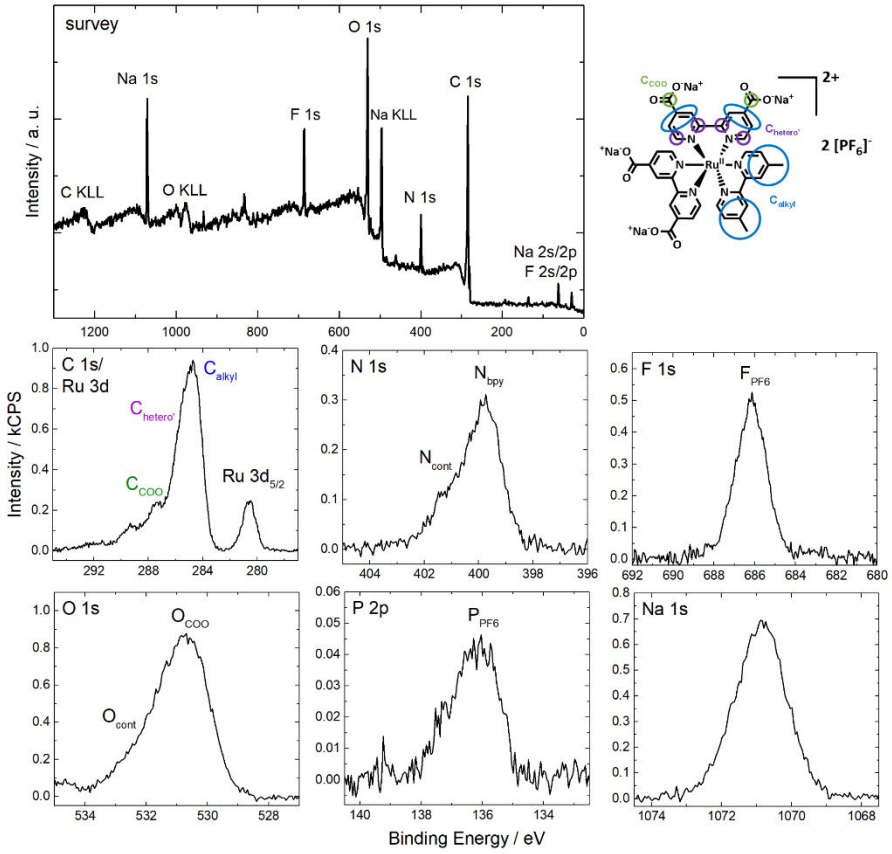

Figure S4: Survey, C 1s/Ru 3d, N 1s, F 1s, O 1s, P 2p and Na 1s XP spectra of solid Ru-C_1 in 0° emission recorded at room temperature. Nominal Ru:N:Na ratio for Ru-C_1: 1:6:4. Found: 1:5.7:3.7. A small amount of contaminations from the synthesis procedure is also identified at the N 1s and O 1s regions. Due to sample charging, all spectra are referenced to the C_{alkyl} signal, which was set to 285 eV as in solution.

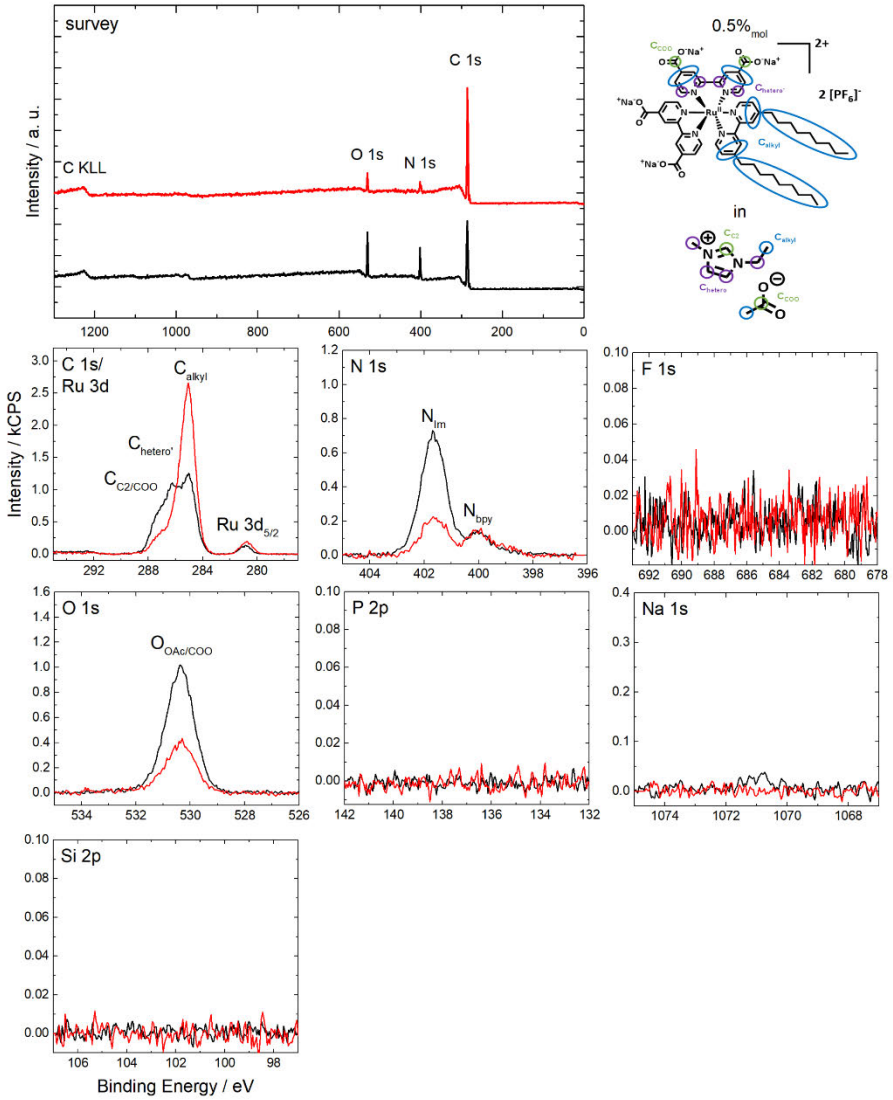

Figure S5: Survey, C 1s/Ru 3d, N 1s, F 1s, O 1s, P 2p, Na 1s and Si 2p XP spectra of 0.5%$_{mol}$ Ru-C$_9$ in [C$_2$C$_1$Im][OAc] in 0° (black) and 80° (red) emission recorded at room temperature.

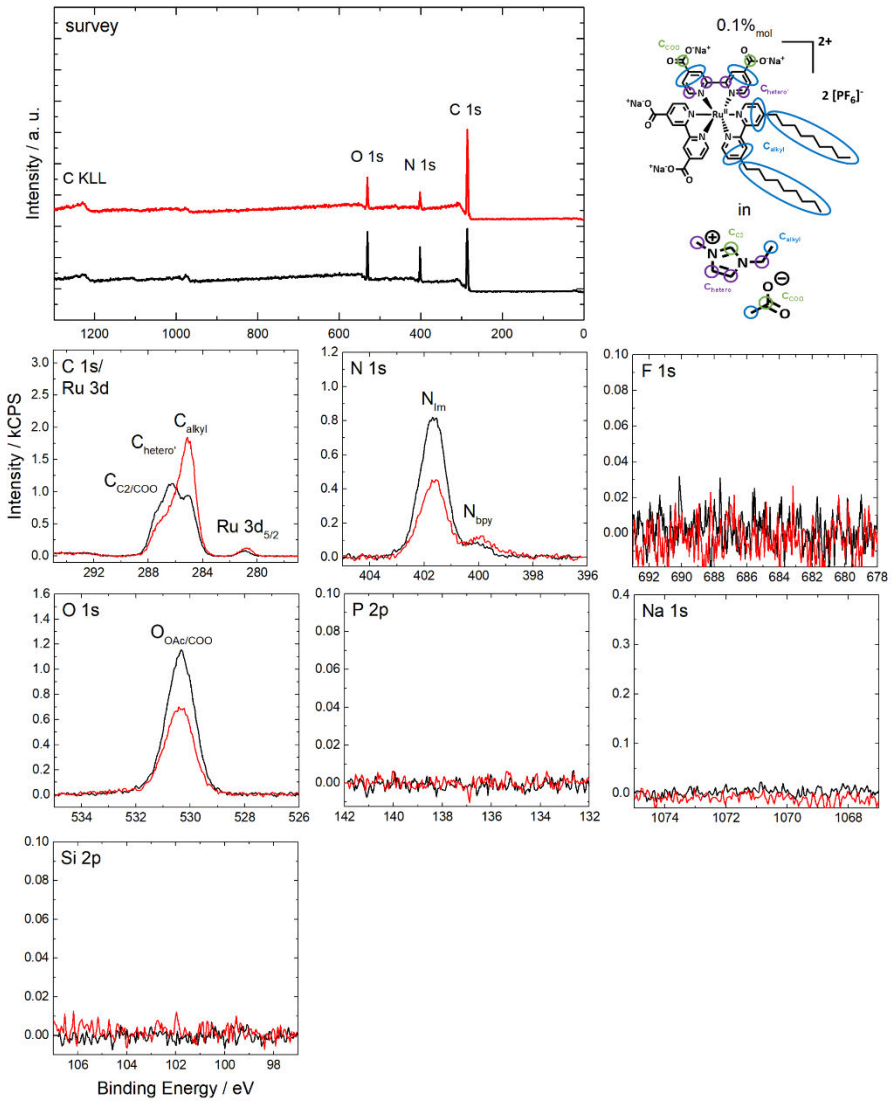

Figure S6: Survey, C 1s/Ru 3d, N 1s, F 1s, O 1s, P 2p, Na 1s and Si 2p XP spectra of 0.1%$_{mol}$ Ru-C$_9$ in [C$_2$C$_1$Im][OAc] in 0° (black) and 80° (red) emission recorded at room temperature.

8

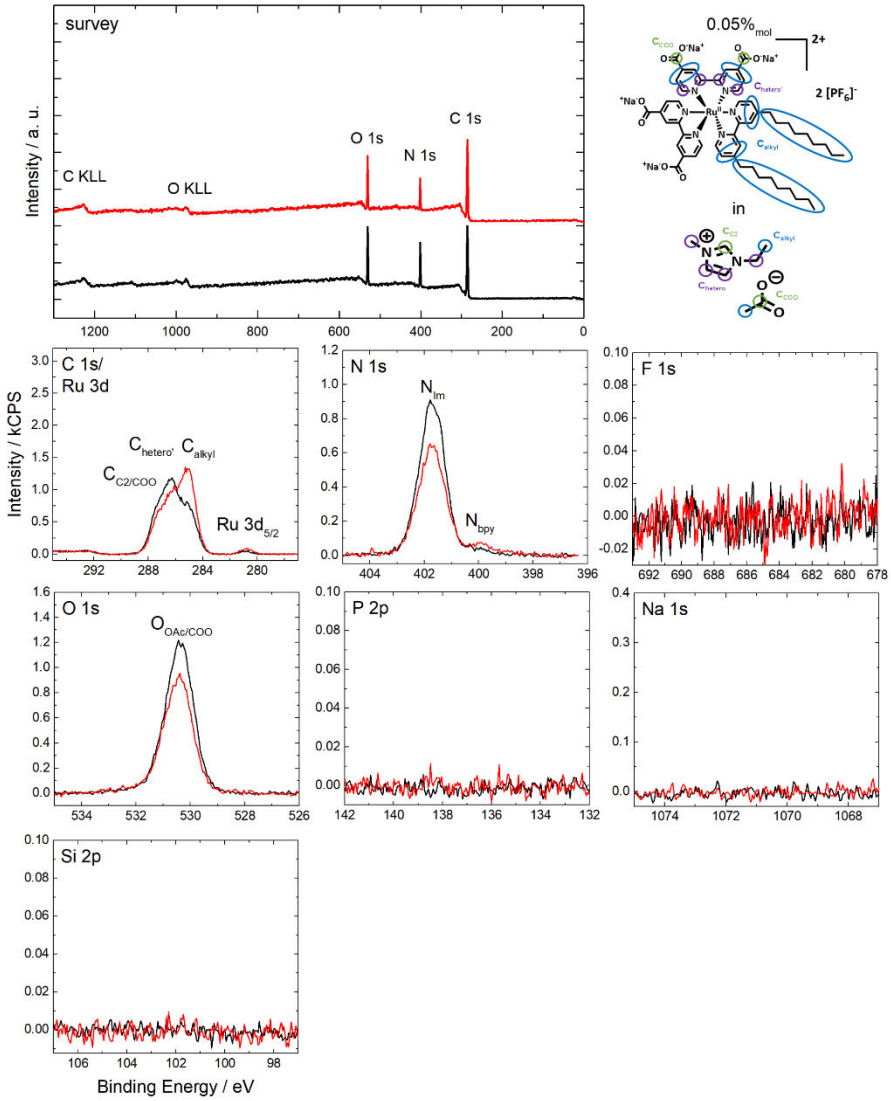

Figure S7: Survey, C 1s/Ru 3d, N 1s, F 1s, O 1s, P 2p, Na 1s and Si 2p XP spectra of 0.05%$_{mol}$ Ru-C$_9$ in [C$_2$C$_1$Im][OAc] in 0° (black) and 80° (red) emission recorded at room temperature.

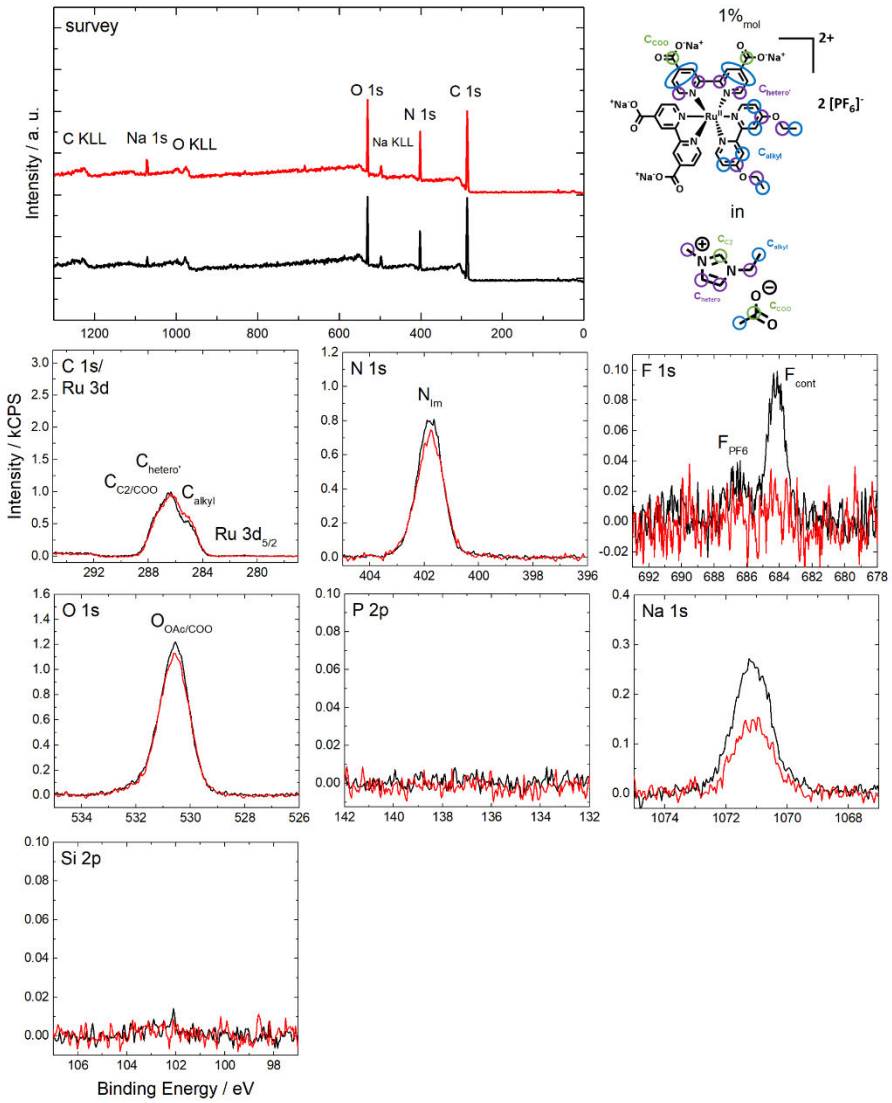

***Figure S8**: Survey, C 1s/Ru 3d, N 1s, F 1s, O 1s, P 2p, Na 1s and Si 2p XP spectra of 1%$_{mol}$ Ru-OC$_2$ in [C$_2$C$_1$Im][OAc] in 0° (black) and 80° (red) emission recorded at room temperature. A small amount of non-surface-active contaminations from the synthesis procedure is also identified at the F 1s region which is not expected to affect the surface structure.*

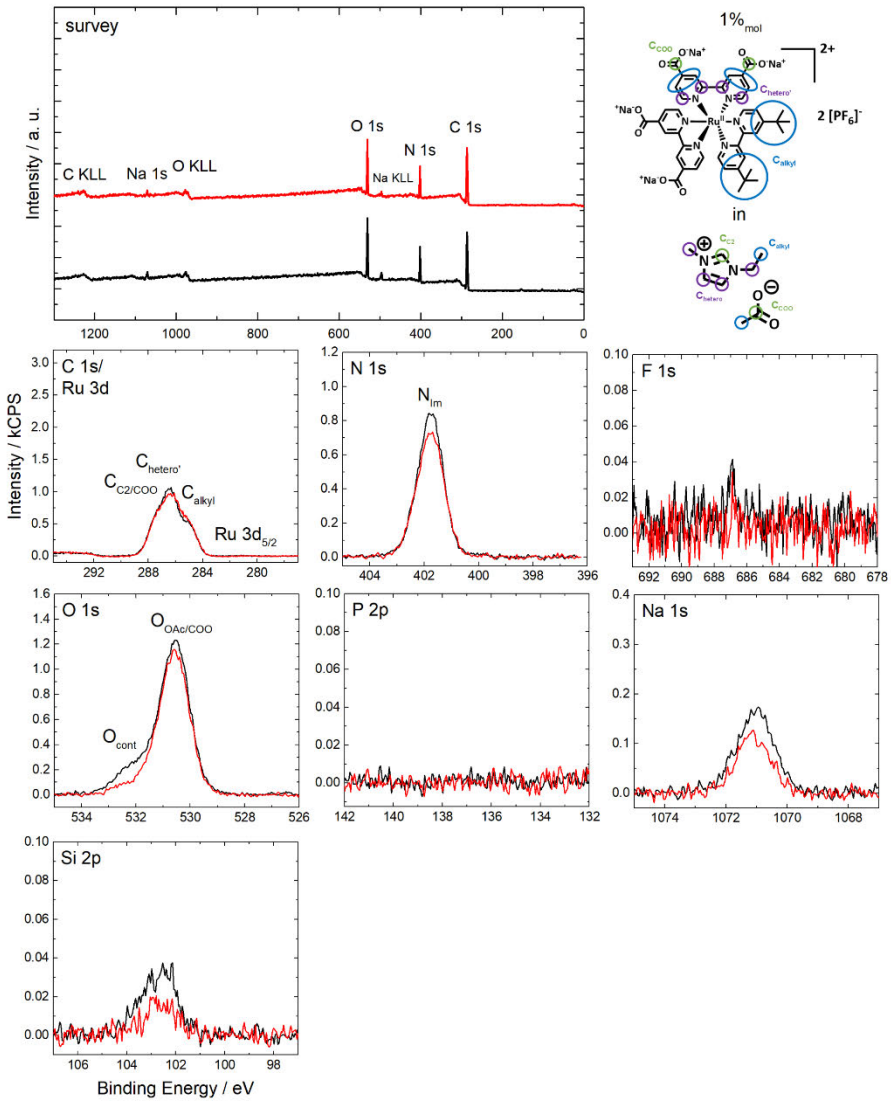

Figure S9: Survey, C 1s/Ru 3d, N 1s, F 1s, O 1s, P 2p, Na 1s and Si 2p XP spectra of 1%$_{mol}$ Ru-tC_4 in [C_2C_1Im][OAc] in 0° (black) and 80° (red) emission recorded at room temperature. A small amount of non-surface-active contaminations from the synthesis procedure is also identified at the O 1s and Si 2p regions which is not expected to affect the surface structure.

***Table S1**. Quantitative analysis of XPS core level spectra of 1%$_{mol}$ solutions employed in this work: a) Ru-C$_9$, b) Ru-C$_1$, c) Ru-OC$_2$, d) Ru-tC$_4$ in [C$_2$C$_1$Im]OAc]. Note that the binding energies of spin-orbit-resolved signals correspond to the more intense signal at lower binding energy, that is, Ru 3d$_{5/2}$ and P 2p$_{3/2}$.*

a) 1%$_{mol}$ Ru-C$_9$ in [C$_2$C$_1$Im][OAc]	**Ru 3d**	**C 1s C$_2$/COO**	**C 1s hetero**	**C 1s alkyl**	**N 1s Im**	**N 1s ligand**	**O 1s OC$_2$**	**O 1s OAc**	**F 1s**	**P 2p**	**Na 1s**
Binding Energy / eV	280.9	287.4	286.3	285.0	401.7	400.0		530.4			1070.8
Nominal	0.010	2.0	4.1	2.4	2.0	0.061		2.1	0.12	0.020	0.040
Experimental, 0°	0.054	1.8	3.5	4.1	1.5	0.27		1.7			0.027
Experimental, 80°	0.069	0.82	1.6	8.8	0.42	0.41		0.67			
b) 1%$_{mol}$ Ru-C$_1$ in [C$_2$C$_1$Im][OAc]											
Binding Energy / eV	281.1	287.5	286.4	285.0	401.7	400.1		530.5	686.7		1071.1
Nominal	0.010	2.0	4.1	2.2	2.0	0.061		2.1	0.12	0.020	0.040
Experimental, 0°	0.006	2.2	4.3	2.1	2.0	0.036		1.9	0.046		0.12
Experimental, 80°	0.004	2.2	4.3	2.5	1.9			1.8	0.029		0.065
c) 1%$_{mol}$ Ru-OC$_2$ [C$_2$C$_1$Im][OAc]											
Binding Energy / eV	281.0	287.5	286.4	285.0	401.8		531.8	530.6	686.6		1071.1
Nominal	0.010	2.0	4.2	2.2	2.0	0.061	0.020	2.1	0.12	0.020	0.040
Experimental, 0°	0.005	2.0	4.1	2.0	2.0		0.19	2.2	0.043		0.189
Experimental, 80°		2.0	4.1	2.4	1.8		0.11	2.2			0.11
d) 1%$_{mol}$ Ru-tBu [C$_2$C$_1$Im][OAc]											
Binding Energy / eV	281.3	287.5	286.4	285.0	401.8			530.5			1071.0
Nominal	0.010	2.0	4.1	2.3	2.0	0.060		2.1	0.12	0.020	0.040
Experimental, 0°	0.006	2.2	4.3	2.0	2.0			2.2			0.12
Experimental, 80°		2.1	4.2	2.3	1.9			2.2			0.077

Table S2: *Quantitative analysis of XPS core level spectra of solutions of Ru-C_9 in [C_2C_1Im][OAc] with catalyst concentrations of a) $1\%_{mol}$, b) $0.5\%_{mol}$, c) $0.1\%_{mol}$ and d) $0.05\%_{mol}$.*

a) $1\%_{mol}$ Ru-C_9 in [C_2C_1Im][OAc]	**Ru 3d**	**C 1s C_2/COO**	**C 1s hetero**	**C 1s alkyl**	**N 1s Im**	**N 1s ligand**	**O 1s OAc**	**F 1s**	**P 2p**	**Na 1s**
Binding Energy / eV	280.9	287.4	286.3	285.0	401.7	400.0	530.4			1070.8
Nominal	0.010	2.0	4.1	2.4	2.0	0.061	2.1	0.12	0.020	0.040
Experimental, 0°	0.054	1.8	3.5	4.1	1.5	0.27	1.7			0.027
Experimental, 80°	0.069	0.82	1.6	8.8	0.42	0.41	0.67			
b) $0.5\%_{mol}$ Ru-C_9 in [C_2C_1Im][OAc]										
Binding Energy / eV	280.9	287.4	286.3	285.0	401.7	400.0	530.4			1070.9
Nominal	0.005	2.0	4.1	2.2	2.0	0.030	2.0	0.060	0.010	0.020
Experimental, 0°	0.047	1.7	3.5	3.8	1.4	0.28	1.6			0.016
Experimental, 80°	0.072	0.88	1.8	8.2	0.43	0.36	0.68			
c) $0.1\%_{mol}$ Ru-C_9 in [C_2C_1Im][OAc]										
Binding Energy / eV	280.9	287.4	286.3	285.0	401.7	400.0	530.4			
Nominal	0.001	2.0	4.0	2.0	2.0	0.006	2.0	0.012	0.002	0.004
Experimental, 0°	0.029	1.9	3.7	2.9	1.7	0.12	1.7			
Experimental, 80°	0.046	1.2	2.5	6.0	0.94	0.25	1.1			
d) $0.05\%_{mol}$ Ru-C_9 in [C_2C_1Im][OAc]										
Binding Energy / eV	280.9	287.4	286.3	285.0	401.7	400.0	530.4			
Nominal	0.0005	2.0	4.0	2.0	2.0	0.003	2.0	0.006	0.001	0.002
Experimental, 0°	0.017	2.0	3.9	2.4	1.8	0.060	1.8			
Experimental, 80°	0.031	1.5	3.1	4.5	1.4	0.14	1.5			

Table S3: Weighed proportions for preparation of the [C_2C_1Im][OAc] solutions investigated in this work.

	1%$_{mol}$ Ru-C_9	1%$_{mol}$ Ru-C_1	0.5%$_{mol}$ Ru-C_9	0.1%$_{mol}$ Ru-C_9	0.05%$_{mol}$ Ru-C_9	1%$_{mol}$ Ru-OC_2	1%$_{mol}$ Ru-tC_4
Mass complex / mg	34.8	10.4	8.4		10.0	7.9	7.2
Amount of substance complex / mmol	0.025	0.009	0.006	0.003	0.007	0.007	0.006
Mass [C_2C_1Im][OAc] / mg	434.7	155.0	211.6	538.1	2523	111.8	100.9
Amount of substance [C_2C_1Im][OAc] / mmol	2.50	0.892	1.22	3.10	14.5	0.644	0.581
Mass 0.5%$_{mol}$ solution Ru-C_9 in [C_2C_1Im][OAc] / mg				111.4			
Exact molar concentration of complex in IL / %$_{mol}$	1.00	1.00	0.50	0.10	0.050	1.00	1.03
Exact ratio IL:complex$_i$	99.0:1	99.0:1	199.0:1	999.0:1	1999:0	99.0:1	99.7:1

$M_{[Ru\text{-}C_9]}$ = 1376.01 g/mol, $M_{[Ru\text{-}C_1]}$ = 1151.58 g/mol, $M_{[Ru\text{-}OC_2]}$ = 1211.63 g/mol,

$M_{[Ru\text{-}tC_4]}$ = 1235.74 g/mol, $M_{[C_2C_1Im][OAc]}$ = 170.21 g/mol

Purity [C_2C_1Im][OAc]: 98%

References

[1] a) G. Maerker, F. H. Case, *J. Am. Chem. Soc.* **1958**, *80*, 2745-2748; b) M. Zhou, G. P. Robertson, J. Roovers, *Inorg. Chem.* **2005**, *44*, 8317-8325.

[2] I. Niedermaier, C. Kolbeck, H.-P. Steinrück, F. Maier, *Rev. Sci. Instrum.* **2016**, *87*, 045105.

[3] C. D. Wagner, L. E. Davis, M. V. Zeller, J. A. Taylor, R. H. Raymond, L. H. Gale, *Surf. Interface Anal.* **1981**, *3*, 211-225.

[4] D. Hemmeter, L. Sanchez Merlinsky, L. M. Baraldo, F. Maier, F. J. Williams, H.-P. Steinrück, *Phys. Chem. Chem. Phys.* **2023**, submitted.

[5] J. M. Gottfried, F. Maier, J. Rossa, D. Gerhard, P. S. Schulz, P. Wasserscheid, H.-P. Steinrück, *Z. Phys. Chem.* **2006**, *220*, 1439-1453.

8.8 Publication 8, [P8]

Check for updates

ChemCatChem

Research Article
doi.org/10.1002/cctc.202400574

Chemistry Europe
European Chemical Societies Publishing

www.chemcatchem.org

Hydrogenation with Dissolved Pt-Complexes Homogenously Distributed in the Ionic Liquid or Enriched at the Gas/Ionic Liquid Interface

Sharmin Khan Antara,[a] Daniel Hemmeter,[b] Ziwen Zhai,[c] Daniel Kremitzl,[a] Florian Maier,[b] Thomas M. Koller,[c] Hans-Peter Steinrück,[b] and Marco Haumann*[a, d]

The use of homogeneous catalysts dissolved in ionic liquids (ILs) is an established field of research. Thin IL films containing dissolved catalyst complexes can be immobilized on solid porous supports, thereby creating a heterogenized catalyst material. Aiming at the deliberate positioning of such supported ionic liquid phase (SILP) catalyst, we carried out investigations of two very similar Pt-complexes: depending on the ligand periphery, the first one is homogeneously dissolved in the IL while the second one strongly enriches at the gas/IL interface. To study these different locations within thick IL films of approximately 1 mm thickness, we investigated the hydrogenation of ethene in a continuous pool-reactor setup. The two complexes dissolved in the IL $[C_4C_1Im][PF_6]$ showed different activity which can be attributed to their different locations. At 313 K and 0.62 MPa total pressure, the surface-enriched complex was approximately two times more active. However, under these conditions the formation of Pt particles could be observed, with the surface-enriched complex exhibiting a stronger tendency for particle formation compared to the one homogeneously distributed in the IL, as derived from XPS and light-scattering measurements.

Introduction

Today, most of the chemical transformations in industry are catalyzed by heterogeneous catalysts.[1] The main reason for their dominance compared to homogeneous catalysts is attributed to the ease of product separation and catalyst recycling, two important requirements for efficient chemical processes. Since homogeneous catalysts, including biocatalysts, offer significant advantages for more benign chemical processes like high selectivity, milder reaction conditions and higher specific activity, concepts to bridge the gap between the two fields of catalysis are manifold.[1–5] In recent years, the use of non-volatile ionic liquids on porous supports has shown to be promising to bridge this gap. In supported ionic liquid phase (SILP) materials, the IL is dispersed over the large inner surface of a porous support material.[6–12] These thin films usually have a nominal thickness of < 10 nm and contain the catalytic functionality either dissolved in the form of transition metal complexes or the IL itself is catalytically active. For catalysis, the amount of IL is adjusted in such a way that only a small fraction of the support's pore volume is filled with IL, thereby leaving enough pore space open for efficient mass transport. Most supports used in SILP catalysis up to date are commercially available porous silica and alumina with a moderate to high surface area of 300–500 $m^2\,g^{-1}$.[11,13] A major advantage of the SILP concept is the fact that ILs exhibit extremely low vapor pressure under typical reaction conditions for homogeneous catalysts. Therefore, efficient and long-term catalyst performance can be achieved in continuous gas-phase reactions like hydroformylation of short alkenes, the water-gas shift reaction, methanol carbonylation, methoxycarbonylation of ethene, hydroamination of styrene, hydroaminomethylation of ethene, metathesis of propene, hydrochlorination of acetylene, and several asymmetric hydrogenation reactions.[14–31]

However, in none of these applications, the position of the active catalyst complex under reaction conditions was investigated in detail or its actual position inside the IL film was deliberately adjusted. A detailed NMR study of propene hydrogenation using Rh-SILP catalysts was reported by the Klankermeyer group in 2011 using the para-hydrogen induced polarization (PHIP) technique.[32] Based on the PHIP signal enhancement, it was possible to assign an enrichment of the rhodium species at the gas/IL interface in the early stage of the reaction. Such enrichment was also reported for ligand

[a] S. K. Antara, D. Kremitzl, M. Haumann
Friedrich-Alexander-Universität Erlangen-Nürnberg (FAU), Lehrstuhl für Chemische Reaktionstechnik (CRT), Egerlandstr. 3, 91058 Erlangen, Germany
E-mail: marco.haumann@fau.de

[b] D. Hemmeter, F. Maier, H.-P. Steinrück
Friedrich-Alexander-Universität Erlangen-Nürnberg (FAU), Lehrstuhl für Physikalische Chemie 2, Egerlandstr. 3, 91058 Erlangen, Germany

[c] Z. Zhai, T. M. Koller
Friedrich-Alexander-Universität Erlangen-Nürnberg (FAU), Institute of Advanced Optical Technologies – Thermophysical Properties (AOT-TP), Paul-Gordan-Straße 8, 91052 Erlangen, Germany

[d] M. Haumann
Research Centre for Synthesis and Catalysis, Department of Chemistry, University of Johannesburg, P.O. Box 524, Auckland Park 2006, Johannesburg, South Africa

Supporting information for this article is available on the WWW under https://doi.org/10.1002/cctc.202400574

ChemCatChem
Research Article
doi.org/10.1002/cctc.202400574
Chemistry Europe
European Chemical Societies Publishing

modified rhodium species by using angle-resolved X-ray photoelectron spectroscopic (ARXPS).[33] Here, the well-known tppts ligand (tppts = triphenylphosphine-3,3′,3″-trisulfonic acid trisodium salt) of the Ruhrchemie/Rhône-Poulenc hydroformylation process led to surface enrichment compared to unmodified Rh species. Other complexes showed little to no enrichment at the gas/IL interface.[34] From their PHIP data, the group of Klankermeyer concluded that at longer reaction times a relocation of the rhodium complex occurred from the near IL/gas interface region towards the near IL/support interface region in the SILP catalyst. The origin of this migration was not elucidated any further. On the catalyst pellet level, it was reported that Pd nanoparticles penetrated IL-functionalized silica as a function of support texture and ionic liquid hydrophobicity, leading to eggshell Pd-SILP materials with higher catalytic activity in the hydrogenation of 1,3-cyclohexadiene.[35] Until today, no attempts have been reported in the open literature to deliberately control the location of the active molecular catalyst species within the IL film and to connect this behavior with the catalytic performance.

From an application point of view, the option to deliberately control the concentration of the catalyst at either the gas/IL or the IL/support interface would be of high interest. In such interface-enhanced SILP systems (see Figure 1), this would allow to control the activity and selectivity of the reaction. A catalyst enriched at the gas/IL interface (scenario 2 in Figure 1) shows a higher local concentration at the interface compared to the bulk or the support region. In this case, the reactants coming from the gas phase have a direct and easy access to the catalyst at the interface. Hence, the rate limiting step will be the chemical kinetics, while the diffusion limitations related to the IL film will not play a major role here. At the same time, complexes placed in the bulk or at the IL/support interface of thick (>10 nm) IL films will be harder to reach and diffusion inside the viscous IL might become the rate-determining step. On the other hand, such complexes (scenario 1 in Figure 1) could exhibit higher selectivity towards the reactant connected with the highest diffusion coefficient and hence may allow selective conversion of mixed feedstock.

For our studies, we will start with IL-catalyst solutions placed in a pool-reactor, over which the reactants mixture is passed. The pool-reactor (see Figure 2 for details) allows us to study a stagnant IL film and, even more interesting, creates a nominal IL film thickness of approximately 1 mm. This is many orders of magnitude larger than film thicknesses inside typical SILP materials used so far, where due to the very small pore diameters, nominal thicknesses of less than 10 nm are present.[36] At such extremely small thickness levels, no clear distinction between the role of the gas/IL and the IL/support interface on the catalytic activity can be made since diffusion times inside such small films are relatively fast. In contrast at 1 mm film thickness in the pool reactor, we anticipate different activities to be seen in case of different locations of catalysts.

To investigate the interface-enhanced SILP concept with respect to the catalytic performance, we decided to study the hydrogenation of ethene in the presence of the Pt complexes **1** and **2** (see Scheme 1). Some of us recently reported that the non-fluorinated Pt complex **1** is homogeneously distributed within the IL 1-butyl-3-methylimidazolium hexafluorophosphate ($[C_4C_1Im][PF_6]$), while the fluorinated complex **2** shows significant surface enrichment at the vacuum/IL interface, as confirmed by angle-resolved XPS studies.[37,38]

Results and Discussion

In a first set of experiments, we tested a 1 mol% solution of the non-fluorinated catalyst complex **1** in $[C_4C_1Im][PF_6]$ in the pool-reactor. The concentration of 1 mol% was chosen to match the concentrations of our previous XPS studies.[38] It should be noted here that the blind activity of the empty pool reactor was close to 0%. The conversion over time on stream (TOS) for complex **1** is shown for two independent experiments (Figure 2a, runs 1 and 2) to check reproducibility. In the beginning,

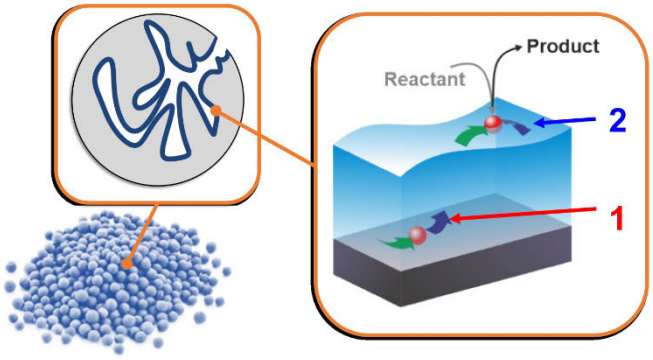

Figure 1. Schematic representation of the interface-enhanced SILP concept, where enrichment of the catalyst concentration over the bulk concentration can be adjusted at the IL/support (1) or the gas/IL (2) interface.

ChemCatChem
Research Article
doi.org/10.1002/cctc.202400574
Chemistry Europe
European Chemical Societies Publishing

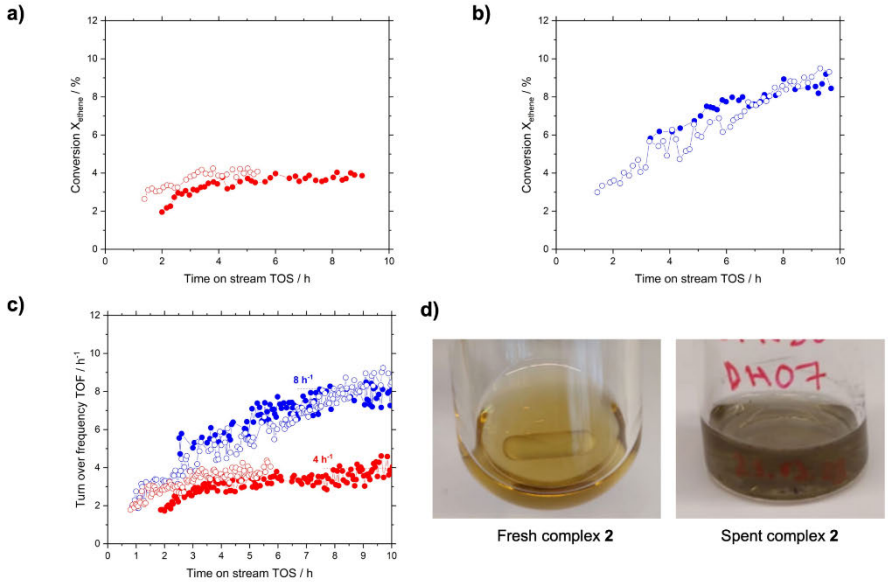

Figure 2. Hydrogenation of ethene in the pool reactor using the two different Pt complexes **1** (red) and **2** (blue) in $[C_4C_1Im][PF_6]$. Conversion for two runs (open and closed symbols) using the not interface-enriched complex **1** is in a) and the interface-enriched complex **2** in b). The calculated turnover frequency (TOF) values are plotted for both complexes in c). Photographs of fresh and spent complex **2** in $[C_4C_1Im][PF_6]$ after 10 h (at T = 313 K) are shown in d). Reaction conditions: 1.6 ml catalyst, 1.0 mol% Pt, T = 313 K, pressure 0.62 MPa, composition of feed stream: 68 vol.% Ar, 16 vol.% H_2, 16 vol.% C_2H_4: residence time 42 s.

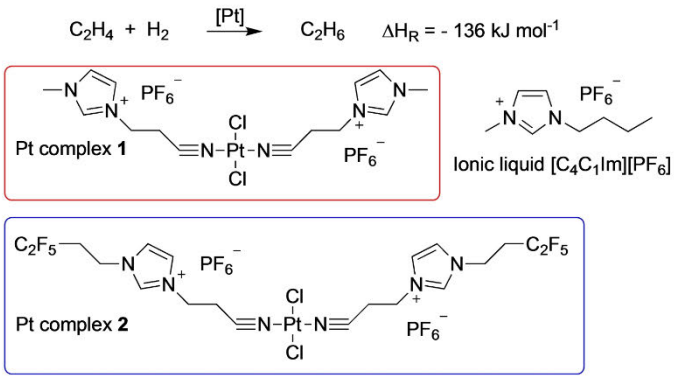

Scheme 1. The exothermic hydrogenation of ethene is used as test reaction for the two Pt complexes **1** and **2** dissolved in the IL $[C_4C_1Im][PF_6]$. The non-fluorinated complex **1** is homogeneously distributed in the IL, while the fluorinated complex **2** is known to be located preferentially at the gas/IL interface (see Figure 1).

an induction period was observed, after which all flows had stabilized. The two runs required an activation phase of 4 h at 313 K, before a stable conversion level around 3.8% was obtained. In contrast, the two runs using the fluorinated complex **2** did not reach such a steady state even after 9 h time on stream (Figure 2b). Here, both runs experienced a continuous rise in activity and at the end of the run ca. 9% conversion was achieved. This value is more than double compared to complex **1**. Given the same catalyst concentration in the IL, the turnover frequency of complex **2** was therefore higher by a

ChemCatChem
Research Article
doi.org/10.1002/cctc.202400574
Chemistry Europe
European Chemical Societies Publishing

factor of approximately two (see Figure 2c). We attribute this behavior to the higher local concentration of catalyst **2** at the gas/IL interface compared to catalyst **1** that is not surface-enriched. The fluorinated groups are located spatially separated from the metal center, and we therefore expect these C_2F_5 groups to cause little electronic modification on the Pt center.

When opening the reactor after each of the four runs, particle formation was visible with the naked eye. All initially yellow solutions showed black coloration and particles at the bottom of the pool were visible with the naked eye (see Figure 2d). Such particle formation is, however, very common for transition metal complexes in ionic liquids under reducing atmosphere.[39] The group of Leitner deliberately generates nano-particles within supported ionic liquid films.[40] For our interface-enhanced SILP concept, this particle formation is an unwanted effect, since the ligands get detached from the Pt centers, thereby losing the ability to control the catalyst complex location.

To minimize particle formation, we carried out the same reaction using the two complexes under similar reaction conditions, but significantly lowered the Pt concentration to 0.05 mol% (~290 ppm). Not surprisingly, the observed conversion levels now were lower compared to the 1 mol% runs, as summarized in Figures 3a) and b). For the non-fluorinated complex **1**, which is homogeneously distributed in the IL, the two reproducibility runs showed similar conversion levels around 0.8% at 313 K that stabilized after the induction period (Figure 3a). Increasing the temperature to 323 K initially led to increased conversion of 1%. For complex **2** (see Figure 3b), at 313 K the conversion kept increasing slightly from 0.7 to 0.8%, after which it stabilized. Once stabilized, the complex **2** responded quickly toward a change in temperature from 313 to 323 K after 10 h TOS. The conversion level was 1.0% and it remained nearly constant for the next 4 h. Here, the repetition runs 2 and 3 did not stabilize but showed a slow or rapid increase in conversion soon after the higher temperature was reached. At this point, we decided to stop the runs, since this type of activity boost is a clear indication of particle formation.

Indeed, when opening the pool reactor, the solution was colorless and small particles were found at the bottom of the pool (see Figure 3d). When maintaining 313 K for more than 40 h, no particles could be observed with the naked eye. Since the exact concentrations of both complexes differed, we calculated TOFs as summarized in Figure 3c. Here, a clear difference can be observed, with higher activity for the surface-enriched complex **2** compared to the not surface-enriched complex **1**. At 313 K, complex **1** resulted in an average TOF_{av}, calculated from both runs after the induction period and during the first nine hours TOS, of 48 h^{-1}, while the TOF_{av} for complex **2** was 92 h^{-1}. This constitutes an activity increase by around 90%. A similar trend was observed at 323 K (see Figure S4 in ESI for details), where complex **1** yielded a TOF of 67 h^{-1} and

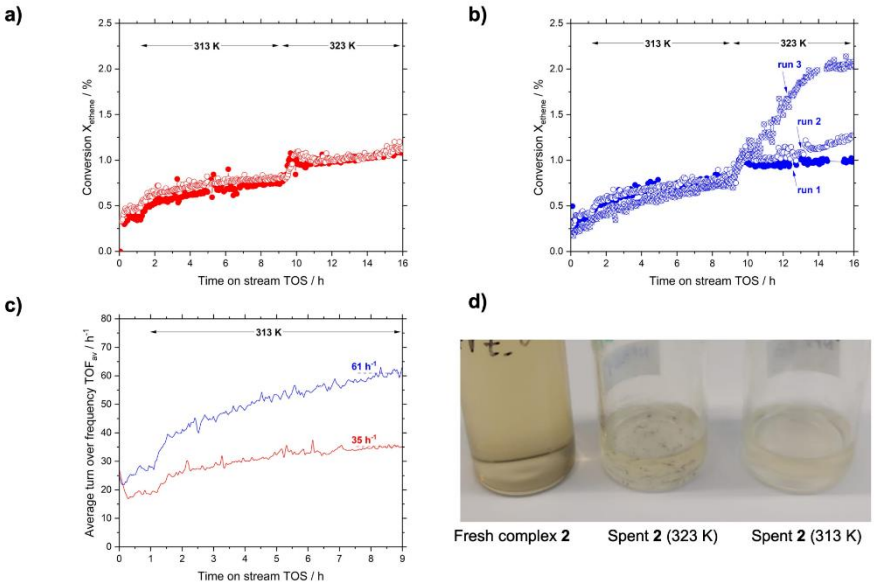

Figure 3. Hydrogenation of ethene in the pool reactor using the two different Pt complexes **1** (red) and **2** (blue) in $[C_4C_1Im][PF_6]$. Conversion for two runs using bulk-phase complex **1** is shown in a), while the gas/IL interface-enriched complex **2** is shown in b). The averaged turn over frequency (TOF_{av}) values for the first nine hours at 313 K are plotted for both complexes in c). Photographs of fresh complex **2** in [C4 C1Im][PF6], spent complex **2** after 24 h (at T = 333 K), and spent complex **2** after 45 h (at T = 313 K) are shown in d). Reaction conditions: 1.6 ml catalyst, 0.05 mol% Pt, Temp: 313 and 323 K, 0.62 MPa, 20 vol.% Ar, 40 vol.% H_2, 40 vol.% C_2H_4, residence time 42 s.

ChemCatChem
Research Article
doi.org/10.1002/cctc.202400574
Chemistry Europe
European Chemical Societies Publishing

complex **2** yielded a 74% higher value of 117 h^{-1}. We assume that this more intense formation of (nano) particles and hence higher activity stems from the fact that complex **2** is located at the interface, being more easily accessible, for the reducing agent H_2.

To shed more light on the formation of nanoparticles during hydrogenation, we carried out light-scattering and PD measurements at 343.15 K based on the IL systems with 0.05 mol% (290 ppm) Pt complexes. Three independent measurement series were performed, one for the system with complex **1** and two (initial and repetition run) for the system with complex **2**. The surface tension results for complex **1** (σ = 41.06 mN·m^{-1}) and complex **2** (σ=40.49 mN·m^{-1}; repetition run) at 0.1 MPa Ar and for complex **2** (σ=40.38 mN·m^{-1}; repetition run) at 0.25 MPa H_2 at the end of the long-time experiment agree within 1.4%. Nevertheless, the data measured in the presence of Ar show about 1% lower surface tension for IL-complex **2** than for IL-complex **1**, which is in accordance with the larger surface activity of complex **2** shown by ARXPS.[37] Furthermore, a negligible change in σ caused by the addition of H_2 and the induced nanoparticle formation can be observed. A summary of the experimental surface tensions for the IL-complex mixtures and for the neat IL can be found in Table S1 of the Supporting Information.

In the *in-situ* light-scattering experiments, the laser power impinging the samples was intentionally kept very low at about 8 mW to avoid a local sample heating. Furthermore, a volume swelling of the liquid phase during the dynamic measurement series can be safely neglected. Figure 4 shows the scattered light intensity recorded by the detector as a function of time before and after adding H_2 for the three different measurement series. Here, the time t=0 corresponds to the time where H_2 was injected into the cell. For visibility purposes, the time axis is limited to 5 h, while the measurements were conducted up to 12.5 h. In Figure 4, also two representative photographs of the gas-liquid sample recorded via the front window of the sample cell are included for each system at defined times. For the repetition measurement on IL/complex **2**, a dense sequence of high-resolution photographs visualizing sample discoloration,

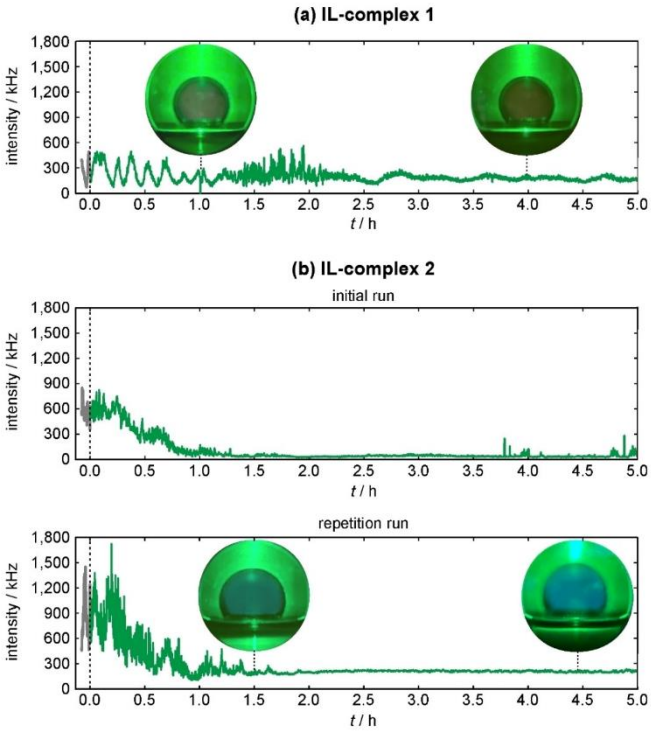

Figure 4. Light-scattering intensity recorded for the two $[C_4C_1Im][PF_6]$-based systems containing the two Pt complexes **1** and **2** at a concentration of 500 ppm as a function of time before (t <0) and after (t >0) addition of H_2 with a partial pressure of 0.25 MPa at 343.15 K. The upper row a) shows the results for the system with complex **1**, while b) shows the two independent runs (second row: initial run; third row: repetition run) carried out for the system with complex **2**. Additional representative photographs of the samples during the measurement are also included.

ChemCatChem
Research Article
doi.org/10.1002/cctc.202400574
Chemistry Europe
European Chemical Societies Publishing

along with particle formation and sedimentation, is available in Figure S5 of the Supporting Information.

For the sample with the non-fluorinated complex **1**, a gradual color change of the originally transparent sample became observable after around 1 h, which was visible by a black coloration. We believe that the observed color change is due to particle formation induced by the reduction of the Pt complexes to Pt atoms via H_2. This is evidenced by the appearance of black particles at the bottom window of the cell after extended periods. As can be seen in Figure 4a (first row), the light-scattering intensity was strongly fluctuating after adding H_2 up to about 1.2 h. This oscillation was found to have a mean frequency of about 0.002 Hz, although its origin is speculative at the current stage. After the predominant oscillation disappeared after about 2 h, the scattered light intensity stabilized on a similar level with an average intensity of about 200 kHz.

The results for the IL system with the fluorinated complex **2** show clear differences to those with complex **1** and agree qualitatively well between the initial and repetition runs. As depicted in Figure 4b (second row), the initial run using IL-complex **2** discussed here first reveals a distinct decrease in the light-scattering intensity starting from around 600 Hz down to about 20 Hz, accompanied by a sample discoloration. The originally transparent sample showed a relatively fast dark coloration about 0.5 h after H_2 dosing. Over time, the degree of the discoloration progressively increased, which was much more intense than for complex **1**. Within the first hour, a periodic oscillation at a mean frequency of about 0.001 Hz was found. Thereafter ($t > 1.5$ h), the intensity was at a quite low level (20 kHz) for several h, while the particle formation seemed to be further ongoing. After about 3.5 h, larger intensities in the form of spikes appeared, which is an indication of larger Pt particle aggregates diffusing in the liquid phase through the scattering volume. Especially after 6.5 h, the peaks showed up more frequently and became larger, suggesting that the size of the particles further increased. Two days after the measurement run, we observed few very large particles in the mm-scale deposited on the bottom of the measurement cell.

During the repetition run on the sample with complex **2** (Figure 4b, third row), we put additional focus on recording photographs in a dense temporal evolution. After the injection of H_2, the sample exhibited discoloration, a weak oscillation in the light-scattering intensity, and a gradual decrease of the latter from about 1,000 kHz down to a lower level of about 200 kHz after about 1.5 h. These observations closely resemble those observed in the initial run. The time-dependent pictures in Figure S5 illustrate that the black coloration zone related to the Pt nanoparticle formation initiates at the interface, where H_2 is absorbed from the gas phase first, and propagates deeper into the liquid phase with increasing time. This propagation is connected to the mass diffusion of H_2 that induces the subsequent reduction process. At the same time, the sedimentation of the Pt nanoparticles, which show a clearly larger density than the surrounding IL phase, takes place and is superimposed to the H_2 diffusion. After about 5 h, Figure S5 shows a clearance of the supernatant liquid above the settled dark part at the bottom at the end. The only difference between the two runs for complex **2** is the absence of spikes in the scattered light intensity throughout the entire duration of the repetition run, which extended up to 7 h. It seems that most of the particles were rather evenly distributed and had the tendency to sediment towards the bottom of the cell. Here, a layer of particle aggregates was evident at the end of the run. One should keep in mind that the particle formation and aggregation process is highly statistical and can never be fully reproduced in a quantitative way.

The photographs help to interpret the time-dependent behavior of the light scattering intensity. Although the scattering volume includes both the interface and the bulk liquid phase (see Figure 7 for details), the light scattering intensity is mainly governed by the region at the interface due to the large refractive index difference between the liquid and the gas phases. With the onset of nanoparticle formation, part of the incident laser light was absorbed by the liquid sample, which can be seen by comparison of the pictures at 0 h and 1.5 h in Figure S5. The more nanoparticles are formed, the more light is absorbed and the lower is the scattered light intensity. Since complex **2** is more surface-enriched than complex **1**, it is possible that more particles are formed per time in interface-near regions. All this may explain the much more pronounced decrease in the intensity for the system with complex **2** compared to complex **1** (see Figure 4). Although the coloration zone moves towards the bottom of the cell with time, the optical properties of the liquid sample including interface remain different due to the presence of nanoparticles. This can be seen from the still low laser intensity visible in the liquid phase up to 7.5 h in Figure S5 and is reflected in the stabilization of the light scattering intensity in the longer time range.

Overall, the *in-situ* light-scattering data as a function of time, together with the pictures from the samples, clearly indicate that nanoparticle formation sets in almost immediately after adding H_2 with a partial pressure of 0.25 MPa at 343.15 K. Notably, this formation is more pronounced for the solution with complex **2**, i.e. the one with the fluorinated chains. While the partial pressure matched the one in the pool-reactor studies, the temperature was intentionally set higher to shorten the measurements times. However, the almost spontaneous formation of nanoparticles is in good agreement with the drastic increase of activity around 323 K in the pool reactor. When a sample of the 0.05 mol% catalyst solution was removed from the pool reactor after exposure to 313 K only, it was still colored and free of particles, while all end-of-run samples that were exposed to temperature above 323 K contained clearly visible particles in the sub-mm range (see Figure 3d).

Additional insights into the observed particle formation upon catalytic conversion was obtained from ARXPS. Since this technique requires higher catalyst concentrations than employed above, we analyzed 1 mol% solutions of complexes **1** and **2** in $[C_4C_1Im][PF_6]$, which yielded adequate signal intensities of the complex-related signals. The hydrogenation experiment for the 1 mol% solutions of **2** and **1** in $[C_4C_1Im][PF_6]$ was run at 313 K for 18 h with a gas feed of 17 mL_N min^{-1}, Ar, 4 mL min^{-1}

ChemCatChem
Research Article
doi.org/10.1002/cctc.202400574
Chemistry Europe
European Chemical Societies Publishing

H_2 and 4 mL min^{-1} C_2H_4 at a partial pressure of 0.1 MPa H_2. After the hydrogenation experiment, the sample was removed from the reactor using a pipette and transferred onto a setup-compatible sample holder for ARXPS analysis.

Notably, the interfacial behavior of solutions of catalysts **1** and **2** in $[C_4C_1Im][PF_6]$ was studied previously.[37,38] These studies showed pronounced enrichment of **2** at the IL/vacuum interface, which was referred to as the buoy effect; on the other hand, for **1** no enrichment was observed. Herein, we concentrate on the changes of the behavior of the complexes upon exposing the catalyst solution to reaction conditions. The corresponding Pt 4f and F 1s spectra are shown in Figure 5. Notably, the complete set of XP spectra and their detailed quantitative analysis are provided in Figures S6 – S9, and Table S2 in the Supporting information.

The spectra of the as-prepared solutions **1** and **2** in Figure 5 (black), that is, before the hydrogenation experiment, are in excellent agreement with the previously published results.[38] For the nonfluorinated complex **1** (bottom), weak Pt signals are observed at 0°, which decrease at 80°, that is, in the more surface-sensitive geometry (see experimental section). At the same time, the solvent-specific C_{alkyl} signal increased at 80° (see Figure S8). These observations are in line with the catalyst homogenously distributed in the IL beneath a domain of the IL butyl chains terminating the surface. On the other hand, for the fluorinated complex **2** (top), the significantly enhanced Pt and CF_x signals at 0°, which are both larger at 80° compared to 0°, demonstrate the pronounced surface enrichment, in line with previous studies.[38]

After the hydrogenation experiment, we observe pronounced changes for the solution with the fluorinated complex **2** in Figure 5 (top): The complex-specific Pt 4f and F_{CFx} signals (blue) show a pronounced decrease to ~60% of their intensity prior to the experiment (black), in both 0° and 80° emission; at the same time the F_{PF6} signals from the complex and the IL remain nearly constant at 0° and show a minor increase at 80°. Similar observations can also be extracted from all other core levels, as is evident from comparison of Figures S6 and S7 and Tables S2a and S2b. Only, the solvent-specific C_{alkyl} signals show a slight increase in 0°, which is more pronounced at 80°, when comparing spectra before and after catalysis. Overall, these findings are in accordance with a lower amount of dissolved complex in solution due to precipitation of metallic Pt particles, as discussed above. It is important to note that during sample transfer from the catalytic reactor to the UHV chamber for XPS analysis, the formed particles settled to the ground of the vessel and thus, no Pt signals characteristic for metallic particles species (Pt $4f_{7/2}$ expected at ~71.7 eV, see[38]) could be observed in the XPS spectra.

Interestingly, for the solution of the non-fluorinated complex **1** in Figure 5 (bottom), the intensities of the Pt 4f and F_{PF6} signals remain constant during the hydrogenation experiment. Within the experimental uncertainty, this is also true for all other recorded core levels as can be extracted by comparing Figures S8 and S9, as well as Tables S2c and S2d. These observations confirm the much lower degree of Pt particle formation for complex **1**, which is in line with a lower catalytic activity. As discussed above, we assign this to the much higher local concentration of complex **2** at the IL/gas interface, where also the concentration of the reducing agent H_2 is highest and hence formation of Pt particles by the H_2 happens more readily.

Taking all observations into account, we propose the following reaction scheme for the hydrogenation in the stagnant film of the ionic liquid inside the pool-reactor (see Scheme 2).

In the initial stage of the reaction at 313 K, both complexes remain at their dedicated location, with complex **1** being homogenously distributed in the IL, while complex **2** is enriched at the gas/IL interface. As a result, a higher activity is observed under otherwise identical conditions, as indeed observed in the pool-reactor. Due to the exothermic nature of the hydrogenation reaction and higher availability of reducing H_2 at the

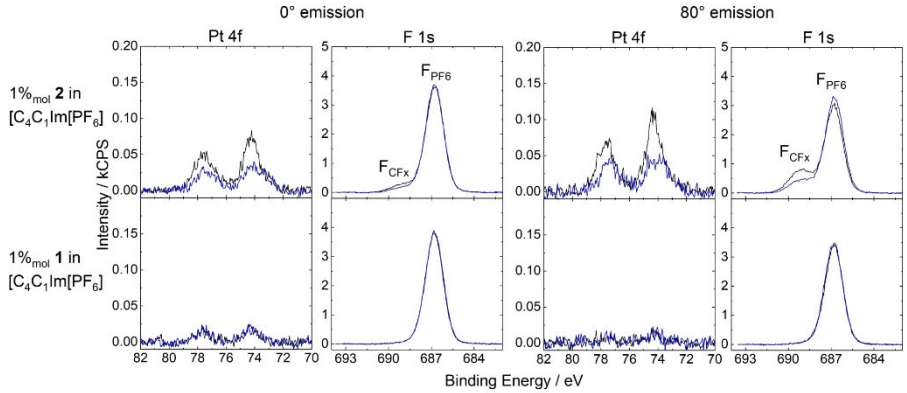

Figure 5. Pt 4f and F 1s XP spectra of 1%$_{mol}$ solutions of **2** (top) and **1** (bottom) in $[C_4C_1Im][PF_6]$ in 0° (left) and 80° (right) emission recorded at room temperature before (black) and after (blue) the catalytic hydrogenation experiments were conducted.

ChemCatChem
Research Article
doi.org/10.1002/cctc.202400574
Chemistry Europe
European Chemical Societies Publishing

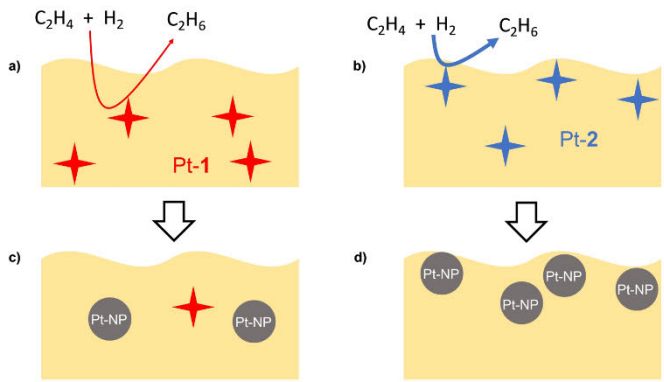

Scheme 2. Proposed reaction scheme for hydrogenation of ethene using < 500 ppm Pt complexes **1** and **2** in the IL $[C_4C_1Im][PF_6]$. a) and b) Initial stage of the reaction (at T = 313 K), both complexes are present in the IL (yellow). c) Nanoparticles are slowly formed from complex **1** homogeneously distributed inside the bulk. d) Pt-nanoparticle formation starting from the interface-enriched complex **2** after short reaction time or at T > 313 K preferentially at the gas/IL interface. The thickness of the reaction arrow indicates the magnitude reaction rate.

interface, the formation of nanoparticles sets in earlier for complex **2** than for complex **1**. Since Pt-NPs are known to exhibit high hydrogenation activity, the reaction gets accelerated and conversion levels seem to "ignite" (see Figure 3). At higher pool-reactor temperatures or over prolonged reaction times, also complex **1** forms nano-particles. As a result, after high reaction temperatures or very long TOS, most of the homogeneously dissolved complexes transform into nanoparticles (see XPS studies in Figure 5).

Conclusions

In this study, we have investigated two Pt-complexes which are known to show different surface concentration behavior in mixtures with the IL $[C_4C_1Im][PF_6]$. The non-fluorinated complex **1** was previously reported to be homogeneously distributed in the IL, with no interface enrichment or depletion, while fluorination of the attached ligand allowed enrichment of the complex **2** at the gas/IL interface. In a pool-reactor, which allowed the use of very thick ionic liquid films (1 mm), we tested the performance of the two complexes in hydrogenation of ethene at 313 K and 0.62 MPa. A difference in activity was observed, with the fluorinated and interface-enriched complex **2** being approximately two times more active compared to complex **1**. This behavior was observed for high (1 mol%) and low (0.05 mol%) concentrations of Pt. However, the higher concentration led to more pronounced particle formation for both complexes. In *in situ* light scattering measurements during H_2 dosing, particle formation was observed, which was more pronounced for complex **2**. The higher tendency for the formation of Pt particles, which will sink to the bottom of the vessel with time, was also found in ARXPS studies, where a clear decline of the complex-specific signals was observed for complex **2** after the reaction, while complex **1** showed no significant differences in ARXPS before and after the catalytic experiment. While we could not maintain the two complexes intact during hydrogenation, we could clearly pinpoint the different catalytic activities to the different concentrations of complex **1** (low) and **2** (high) at the gas/IL interface. This demonstrates the possibility to deliberately tune the location of the chemical reaction inside thick films of ILs. As such, we consider these results as highly promising for future interface-enhanced SILP systems, in which the different locations could not only have an influence on the activity, but also on the selectivity. On the path, the search for more stable catalyst complexes in hydrogenation is currently ongoing.

Experimental Section

All chemicals have been purchased from commercial suppliers and were used as received without further purification steps. Details can be found in Table 1.

Table 1. Chemicals and gases used in the hydrogenation study with Pt complexes **1** and **2**.

Material	CAS-Number	Supplier	Purity
$[C_4C_1Im][PF_6]$	174501-64-5	Iolitec	99 wt%
$(CH_3CN)_2PtCl_2$	13869-38-0	Sigma-Aldrich	98 wt%
Ligands for **1** and **2**	–	Synthesis, see [37,38]	–
C_2H_4	74-85-1	Air Liquide	99.9 vol%
H_2	1333-74-0	Air Liquide	99.999 vol%
Ar	7440-37-1	Air Liquide	99.998 vol%

ChemCatChem
Research Article
doi.org/10.1002/cctc.202400574
Chemistry Europe
European Chemical Societies Publishing

Catalyst Synthesis and Preparation of Solution

Details on materials, syntheses and sample preparation were reported previously.[38] Generally, the solutions were prepared by directly synthesizing the complexes in the IL under vacuum conditions. Diluted solutions (molar concentration < 5 mol%) were prepared from fresh, more concentrated solutions (typically in a concentration regime between 5 to 10 mol%), as reported before.[38]

Catalytic Studies

Catalytic studies were conducted using a pool reactor setup (see Figure 6 and Figures S1 and S2 for details). For the ethene hydrogenation experiments, 1.6 ml of pale-yellow catalyst solution, containing either complex **1** or **2**, was transferred into the pool (length 71 mm, width 22.5 mm, height 3.9 mm; IL film thickness 1.0 mm) using an Eppendorf pipette. The pool was initially weighed when empty and then again after adding the catalyst solution. Subsequently, the pool was placed inside the round reactor housing and then the reactor was sealed. The top cover contained a thermocouple to monitor the temperature of the internal gas flow and control the heating process.

The reactor setup was pressurized with the reaction mixture at ambient temperature, and on attaining steady pressure, the reaction was initiated by increasing the temperature to 313 K. The outlet from the reactor was continuously analyzed using either a micro gas chromatograph (I-GRAPHX PR; Industrial Graph Xolutions, Germany) or a gas chromatograph (Varian Gas chromatograph 3900-GC).

The turnover frequency (in h^{-1}) of ethene hydrogenation was calculated according to Equation (1) based on the conversion X_{ethene}, the known molar flow rate of ethene ($\dot{F}_{n,ethene}$) and moles of Pt in the pool (n_{Pt}).

$$TOF_{ethene} = \frac{\dot{F}_{n,ethene}\, X_{ethene}}{n_{Rh}} \quad (1)$$

Details on the calculation of conversion from GC data can be found in Figure S3 in the ESI.

Light-Scattering and Pendant-Drop Experiments

To investigate the IL-complex systems during H_2 exposure an experimental setup was used which combines surface light scattering (SLS) and the pendant-drop (PD) method. A description of this setup is available in previous studies.[41,42] At first, about 20 and 3 mL of the IL-complex system were placed inside the measurement cell and a connected sample vessel, respectively; the latter is used to supply liquid for PD experiments. The entire system was degassed for five min and then filled with the inert gas argon (Ar) at a pressure of about 0.1 MPa. Thereafter, the cell and the sample vessel were heated to a temperature of 343.15 K. In the next step, H_2 with a partial pressure of 0.25 MPa was dosed to the measurement cell and sample vessel, which defines the start of a time-dependent observation. In the PD method used to measure the gas-liquid surface tension σ, the experimentally recorded contour of a PD suspended on a capillary tip is compared with the Young-Laplace (YL) equation.[43] Details on the measurement and evaluation procedure of PD experiments is described in literature.[41] The required liquid density of the IL-complex systems was approximated by that of pure $[C_4C_1Im][PF_6]$ at 343.15 K.[44] The PD method was applied in the presence of Ar atmosphere at 0.1 MPa as well as at the end of the experiment in the presence of H_2 with a partial pressure of about 0.25 MPa. During this entire period, the liquid sample on the bottom of the measurement cell, showing a filling level of about 5 mm, was used to conduct light-scattering measurements. By irradiating the gas-liquid interface with laser light (wavelength 532 nm) under an incident angle of 2.5° relative to the interface normal, the scattered light intensity was detected in reflection direction perpendicularly to the interface. Figure 7 shows a schematic representation of the probed scattering volume which is given by the waist of the incident laser light and the detection direction defined by an aperture. This volume includes the gas-liquid interface along with portions of both the liquid and gas phases.

Angle-Resolved XPS Measurements and Data Evaluation

Detailed information on the experimental setup, and the processing, evaluation and analyses of the acquired data was reported previously.[37] Using our unique dual-analyzer system for surface analysis (DASSA), we simultaneously acquire XP spectra at an electron emission angle of 0° with respect to the surface normal (normal emission) and at 80° (grazing emission). In ILs, when using Al K radiation, 0° spectra have an information depth (ID) of 6–9 nm and thus are dominated by bulk contributions; at 80° the ID is 1.0-1.5 nm and therefore the spectra are dominated by the topmost

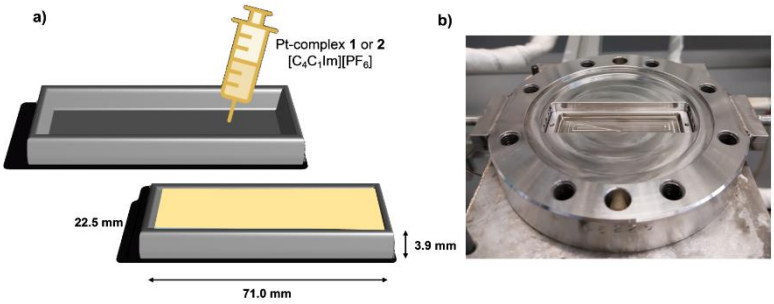

Figure 6. Schematic representation of the filling procedure of the pool insert made of stainless steel shown in a), with the bottom part of the pressure housing and the insert containing the pale-yellow Pt solution of complex **1** dissolved in IL $[C_4C_1Im][PF_6]$ shown in b).

ChemCatChem
Research Article
doi.org/10.1002/cctc.202400574
Chemistry Europe
European Chemical Societies Publishing

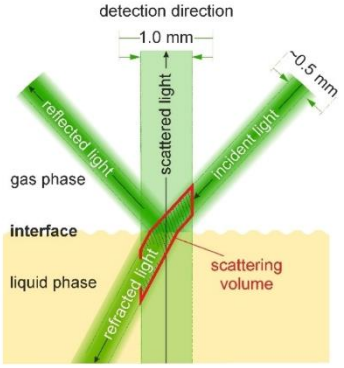

Figure 7. Schematics of the scattering volume probed in the light-scattering measurements on the IL-complex systems in the presence of H_2.

molecular layer of the sample. The XP spectra were normalized to the sum of intensities of the 0° spectra (corrected by the atomic sensitivity factors derived from Ref.[45]) of the as-prepared 1 mol% solution of **2** in $[C_4C_1Im][PF_6]$. Fitting procedures differing from the reported practices are detailed in the ESI.[46]

All samples shown herein were carefully checked by ARXPS to confirm the absence of surface-active contaminants, which can pose a challenge in the study of IL surfaces.

Role of Authors

Sharmin Khan, Ziwen Zhai, Daniel Hemmeter – Investigation, Formal Analysis, and Visualization; Florian Maier, Thomas Koller, Hans-Peter Steinrück – Project Administration, Writing and Proof Reading; Marco Haumann – Project Administration, Conceptualization, and Writing

Acknowledgements

Financial support by the Deutsche Forschungsgemeinschaft (DFG, German Research Foundation) in the frame of the SFB 1452 (Project-ID 431791331) is gratefully acknowledged. Daniel Hemmeter acknowledges the support by the German Chemical Industry Association (Verband der Chemischen Industrie, VCI) within a Kekulé fellowship. Open Access funding enabled and organized by Projekt DEAL.

Conflict of Interests

There are no conflicts of interest to report.

Data Availability Statement

The data that support the findings of this study are available from the corresponding author upon reasonable request.

Keywords: Hydrogenation · ethene · ionic liquid · interface enrichment · light-scattering · platinum · XPS

[1] F. Poovan, V. G. Chandrashekhar, K. Natte, R. V. Jagadeesh, . *Sci. Techno.* **2022**, *12* (22), 6623–6649.
[2] W. Keim, *Green Chem.* **2003**, *5* (2), 105–111.
[3] C. Li, Y. Liu, *Bridging Heterogeneous and Homogeneous Catalysis: Concepts, Strategies, and Applications*, Wiley, **2014**.
[4] Boy Cornils, W. A. H., Horst-Werner Zanthoff, Jian-He Xu, Chi-Huey Wong, *Catalysis from A to Z: A Concise Encyclopedia (5th Edition)*, Wiley-VCH **2019**.
[5] J. G. S. Marcano, T. T. Tsotsis, *Catalytic Membranes and Membrane Reactors*, Wiley-VCH, **2002**.
[6] R. Fehrmann, A. Riisager, M. Haumann, *Supported Ionic Liquids: Fundamentals and Applications*, **2014**, p 1–474.
[7] A. Riisager, R. Fehrmann, M. Haumann, P. Wasserscheid, *Eur. J. Inorg. Chem.* **2006**, *2006* (4), 695–706.
[8] A. Riisager, R. Fehrmann, M. Haumannb, P. Wasserscheid, *Top. Catal.* **2006**, *40*, 91–102.
[9] Y. Gu, G. Li, *Adv. Synth. Catal.* **2009**, *351* (6), 817–847.
[10] C. Van Doorslaer, J. Wahlen, P. Mertens, K. Binnemans, D. De Vos, *Dalton Trans.* **2010**, *39* (36), 8377–8390.
[11] T. Selvam, A. Machoke, W. Schwieger, *Appl. Catal. A* **2012**, *445–446*, 92–101.
[12] A. Bohre, A. Modak, V. Chourasia, P. Ram Jadhao, K. Sharma, K. Kishore Pant, *J. Chem. Eng.* **2022**, *450*.
[13] J. Lemus, J. Palomar, M. A. Gilarranz, J. J. Rodriguez, *Adsorption* **2011**, *17* (3), 561–571.
[14] J. M. Marinkovic, A. Riisager, R. Franke, P. Wasserscheid, M. Haumann, *Ind. Eng. Chem. Res.* **2019**, *58* (7), 2409–2420.
[15] S. Werner, N. Szesni, R. W. Fischer, M. Haumann, P. Wasserscheid, *Phys. Chem. Chem. Phys.* **2009**, *11* (46), 10817–10819.
[16] S. Werner, N. Szesni, M. Kaiser, R. W. Fischer, M. Haumann, P. Wasserscheid, *ChemCatChem* **2010**, *2* (11), 1399–1402.
[17] R. Stepić, C. R. Wick, V. Strobel, D. Berger, N. Vučemilović-Alagić, M. Haumann, P. Wasserscheid, A.-S. Smith, D. M. Smith, *Angew. Chem. Int. Ed. Engl.* **2019**, *58* (3), 741–745.
[18] A. Riisager, B. Jørgensen, P. Wasserscheid, R. Fehrmann, *Chem. Commun.* **2006**, *9*, 994–996.
[19] E. J. García-Suárez, S. G. Khokarale, O. N. van Buu, R. Fehrmann, A. Riisager, *Green Chem.* **2014**, *16* (1), 161–166.
[20] S. G. Khokarale, E. J. García-Suárez, R. Fehrmann, A. Riisager, *ChemCatChem* **2017**, *9* (10), 1824–1829.
[21] O. Jimenez, T. E. Müller, C. Sievers, A. Spirkl, J. A. Lercher, *Chem. Commun.* **2006**, *28*, 2974–2976.
[22] M. J. Schneider, M. Lijewski, R. Woelfel, M. Haumann, P. Wasserscheid, *Angew. Chem. Int. Ed. Engl.* **2013**, *52* (27), 6996–6999.
[23] J. Scholz, S. Loekman, N. Szesni, W. Hieringer, A. Görling, M. Haumann, *Adv. Synth. Catal.* **2011**, *353* (14-15), 2701–2707.
[24] J. Zhao, S. Gu, X. Xu, T. Zhang, Y. Yu, X. Di, J. Ni, Z. Pan, X. Li, *Catal. Sci. Technol.* **2016**, *6* (9), 3263–3270.
[25] J. Zhao, Y. Yu, X. Xu, S. Di, B. Wang, H. Xu, J. Ni, L. Guo, Z. Pan, X. Li, *Appl. Catal. B* **2017**, *206*, 175–183.
[26] J. Zhao, S. Wang, B. Wang, Y. Yue, C. Jin, J. Lu, Z. Fang, X. Pang, F. Feng, L. Guo, Z. Pan, X. Li, *Chin. J. Catal.* **2021**, *42* (2), 334–346.
[27] U. Hintermair, T. Höfener, T. Pullmann, G. Franciò, W. Leitner, *ChemCatChem* **2010**, *2* (2), 150–154.
[28] U. Hintermair, G. Franciò, W. Leitner, *Chem. Eur. J.* **2013**, *19* (14), 4538–4547.
[29] U. Hintermair, C. Roosen, M. Kaever, H. Kronenberg, R. Thelen, S. Aey, W. Leitner, L. Greiner, *Org. Process Res. Dev.* **2011**, *15* (6), 1275–1280.
[30] E. Öchsner, M. J. Schneider, C. Meyer, M. Haumann, P. Wasserscheid, *Appl. Catal. A* **2011**, *399* (1), 35–41.
[31] M. J. Schneider, M. Haumann, P. Wasserscheid, *Mol. Catal. A: Chem.* **2013**, *376*, 103–110.
[32] Q. Gong, J. Klankermayer, B. Blümich, *Chem. Eur. J.* **2011**, *17* (49), 13795–13799.

ChemCatChem
Research Article
doi.org/10.1002/cctc.202400574
Chemistry Europe
European Chemical Societies Publishing

[33] C. Kolbeck, N. Paape, T. Cremer, P. Schulz, F. Maier, H.-P. Steinrück, P. Wasserscheid, *Chem. (Weinheim Bergstr Ger).* **2010**, *16*, 12083–7.
[34] D. Hemmeter, L. S. Merlinsky, L. M. Baraldo, F. Maier, F. J. Williams, H.-P. Steinrück, *Phys. Chem. Chem. Phys.* **2024**, *26* (9), 7602–7610.
[35] L. Luza, A. Gual, C. P. Rambor, D. Eberhardt, S. R. Teixeira, F. Bernardi, D. L. Baptista, J. Dupont, *Phys. Chem. Chem. Phys.* **2014**, *16* (34), 18088–18091.
[36] U. Kernchen, B. Etzold, W. Korth, A. Jess, *Chem. Eng. Technol.* **2007**, *30* (8), 985–994.
[37] D. Hemmeter, D. Kremitzl, P. S. Schulz, P. Wasserscheid, F. Maier, H.-P. Steinrück, *Chem. Eur. J.* **2023**, *29* (3), e202203325.
[38] D. Hemmeter, U. Paap, N. Wellnhofer, A. Gezmis, D. Kremitzl, P. Wasserscheid, H.-P. Steinrück, F. Maier, *ChemPhysChem.* **2023**, *24* (24), e202300612.
[39] J. D. Scholten, B. C. Leal, J. Dupont, *ACS Catal.* **2012**, *2* (1), 184–200.
[40] K. L. Luska, P. Migowski, W. Leitner, *Green Chem.* **2015**, *17* (6), 3195–3206.
[41] Z. Zhai, J. H. Jander, A. Bergen, J. Cui, K. Meyer, T. M. Koller, *Int. J. Thermophys.* **2022**, *43* (12), 178.
[42] Z. Zhai, T. M. Koller, *J. Mol. Liq.* **2023**, *377*, 121491.
[43] J. D. Berry, M. J. Neeson, R. R. Dagastine, D. Y. C. Chan, R. F. Tabor, *J. Colloid Interface Sci.* **2015**, *454*, 226–237.
[44] T. M. Koller, F. D. Lenahan, P. S. Schmidt, T. Klein, J. Mehler, F. Maier, M. H. Rausch, P. Wasserscheid, H.-P. Steinrück, A. P. Fröba, *Int. J. Thermophys.* **2020**, *41* (10), 144.
[45] C. D. Wagner, L. E. Davis, M. V. Zeller, J. A. Taylor, R. H. Raymond, L. H. Gale, *Surf. Interface Anal.* **1981**, *3* (5), 211–225.
[46] D. Hemmeter, U. Paap, N. Taccardi, J. Mehler, P. S. Schulz, P. Wasserscheid, F. Maier, H.-P. Steinrück, *ChemPhysChem.* **2023**, *24* (2), e202200391.

Manuscript received: March 26, 2024
Revised manuscript received: May 28, 2024
Accepted manuscript online: June 2, 2024
Version of record online: July 24, 2024

ChemCatChem

Supporting Information

Hydrogenation with Dissolved Pt-Complexes Homogenously Distributed in the Ionic Liquid or Enriched at the Gas/Ionic Liquid Interface

Sharmin Khan Antara, Daniel Hemmeter, Ziwen Zhai, Daniel Kremitzl, Florian Maier, Thomas M. Koller, Hans-Peter Steinrück, and Marco Haumann*

Supporting Information

Hydrogenation with Dissolved Pt-complexes Homogenously Distributed in the Ionic Liquid or Enriched at the Gas/Ionic Liquid Interface

Sharmin Khan Antara [1], Daniel Hemmeter [2], Ziwen Zhai [3], Daniel Kremitzl [1], Florian Maier [2], Thomas M. Koller [3], Hans-Peter Steinrück [2], Marco Haumann [1,4]*

1 Friedrich-Alexander-Universität Erlangen-Nürnberg (FAU), Lehrstuhl für Chemische Reaktionstechnik (CRT), Egerlandstr. 3, 91058 Erlangen, Germany

2 Friedrich-Alexander-Universität Erlangen-Nürnberg (FAU), Lehrstuhl für Physikalische Chemie 2, Egerlandstr. 3, 91058 Erlangen, Germany

3 Friedrich-Alexander-Universität Erlangen-Nürnberg (FAU), Institute of Advanced Optical Technologies – Thermophysical Properties (AOT-TP), Paul-Gordan-Straße 8, 91052 Erlangen, Germany

4 Research Centre for Synthesis and Catalysis, Department of Chemistry, University of Johannesburg, P.O. Box 524, Auckland Park 2006, South Africa

Continuous gas-phase pool reactor setup

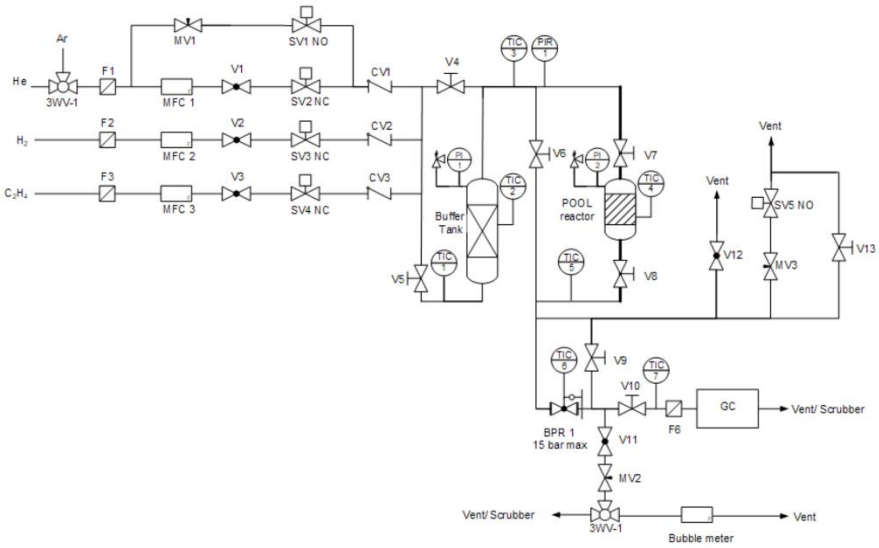

Figure S1. Flow scheme of the pool reactor.

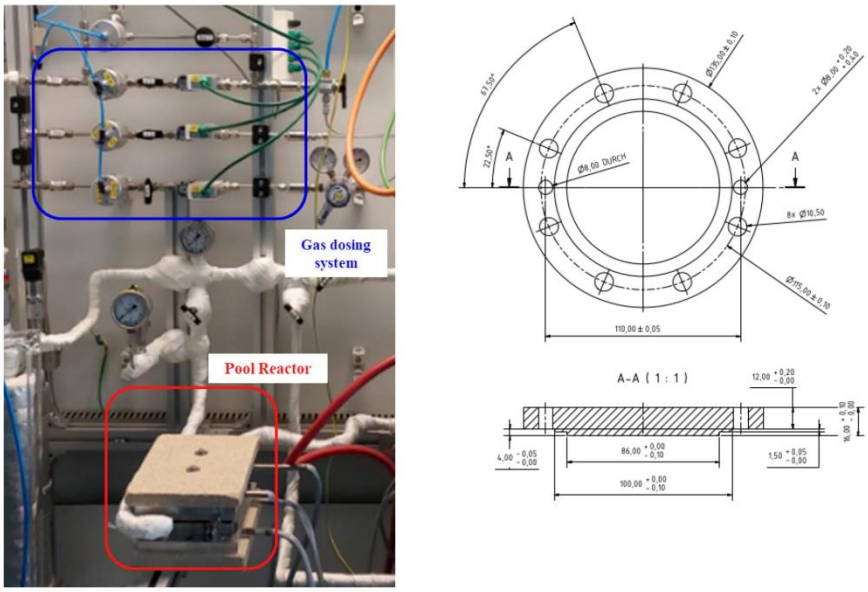

Figure S2. Photograph of the pool reactor housing shown in a), while the technical drawing of the pool housing is shown in b).

Analytics and calculations

For I-GRAPHX PR, which utilizes a thermal conductivity detector, a response factor of 1.01 was used for ethene and 1.12 for ethane.

$$TOF_{ethene} = \frac{F_{n,ethene}\, X_{ethene}}{n_{Pt}}$$

$$X_{ethene} = \frac{n_{ethane}}{n_{ethene} + n_{ethane}}$$

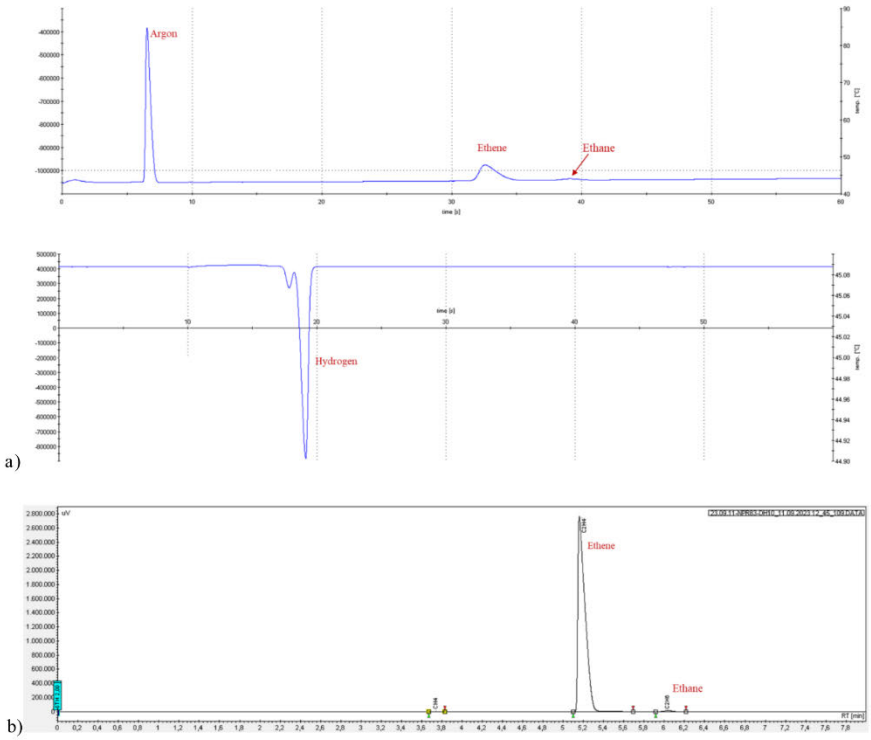

Figure S3. Typical gas chromatogram from the micro-GC in a), and GC in b). Peaks are labelled based on calibration.

Catalytic ethene hydrogenation in the pool reactor

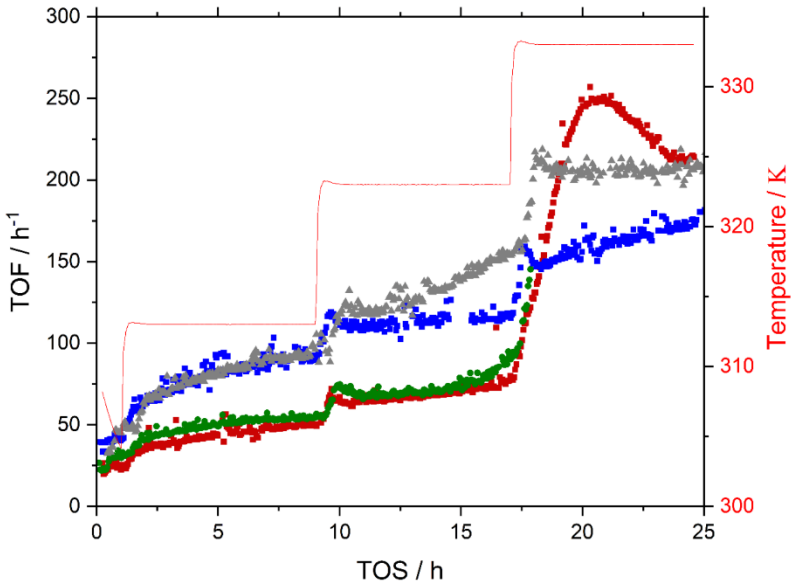

Figure S4. Hydrogenation of ethene in the pool reactor using the two different Pt complexes **1** (red and green) and **2** (blue and grey) in $[C_4C_1Im][PF_6]$. Reaction conditions: 1.6 ml catalyst, 0.05 mol% Pt, Temp: 313 - 333 K, 0.62 MPa, 20 vol.% Ar, 40 vol.% H_2, 40 vol.% C_2H_4, residence time 42s.

Light scattering and pendant drop studies

Figure S5 shows a sequence of high-resolution photographs during the light scattering experiments on IL/complex **2** (repetition run). A detailed discussion on these photographs is given in the main manuscript.

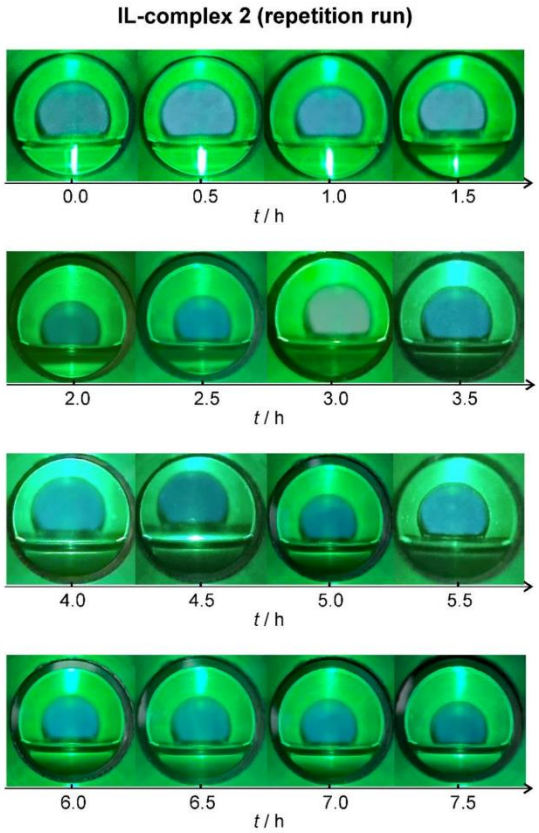

Figure S5. Photographs recorded during the light scattering experiments on $[C_4C_1Im][PF_6]$ containing complex 2 after addition of H_2 with a partial pressure of 2.5 bar at 343.15 K.

Table S1. Surface tension σ for binary mixtures of $[C_4C_1Im][PF_6]$ with complex **1** or **2** measured by the PD method including liquid density ρ used for data evaluation. Comparison of results for IL+ 500 ppm complex with data from Hemmeter et al [1] for neat IL and mixture with 1.5×10^4 ppm complex.

	T / K	p / MPa	σ / (mN·m^{-1})	ρ / (kg·m^{-3})
IL + 500 ppm complex **1**[a]	343.12	0.11	41.06	1330.19[c]
IL + 500 ppm complex **2**[a]	343.19	0.10	40.49	1330.13[c]
IL + 500 ppm complex **2**[b] after 9 h	343.29	0.36	40.32	1330.06[c]
IL + 500 ppm complex **2**[b] after 24 h	343.29	0.36	40.38	1330.06[c]
neat IL	343.29	10^{-10}	40.74[d]	1328.79[e]
IL + 1.5×10^4 ppm complex **2**	343.29	10^{-10}	40.04[d]	1301.68[d]

[a] gas phase contains 0.11 MPa Ar

[b] gas phase contains 0.11 MPa Ar and 0.26 MPa H_2

[c] density value is obtained from temperature-dependent density fit according to Ref. [1]

[d] density value is calculated based on the temperature-dependent fit from Ref. [2]

[e] density value is obtained from temperature-dependent density fit according to Ref. [3]

XPS studies on spent Pt complexes

The complete set of XP spectra of a 1 mol% solution of complex **2** in $[C_4C_1Im][PF_6]$ at room temperature **before** conducting the hydrogenation experiment is shown in Figure S6.

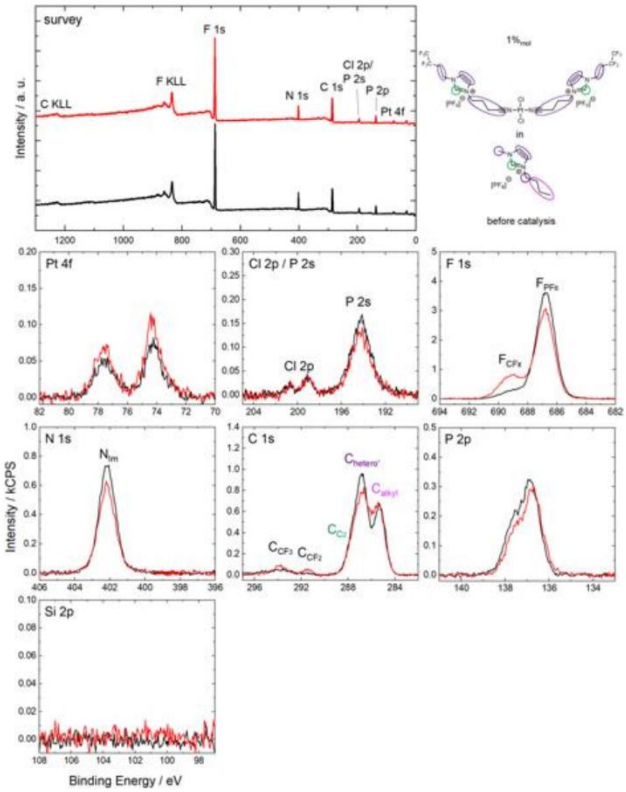

Figure S6. Survey, Pt 4f, Cl 2p/P 2s, F 1s, N 1s, C 1s, P 2p and Si 2p XP spectra of a 1 mol% solution of **2** in $[C_4C_1Im][PF_6]$ in 0° (black) and 80° (red) emission recorded at room temperature before the catalytic hydrogenation experiment was conducted. The color coding indicates assignment of carbon peaks to the molecular structure. The Si 2p region is shown to exclude surface-active contaminations found previously.[5]

The complete set of XP spectra of a 1 mol% solution of complex **2** in $[C_4C_1Im][PF_6]$ at room temperature **after** conducting the hydrogenation experiment is shown in Figure S7.

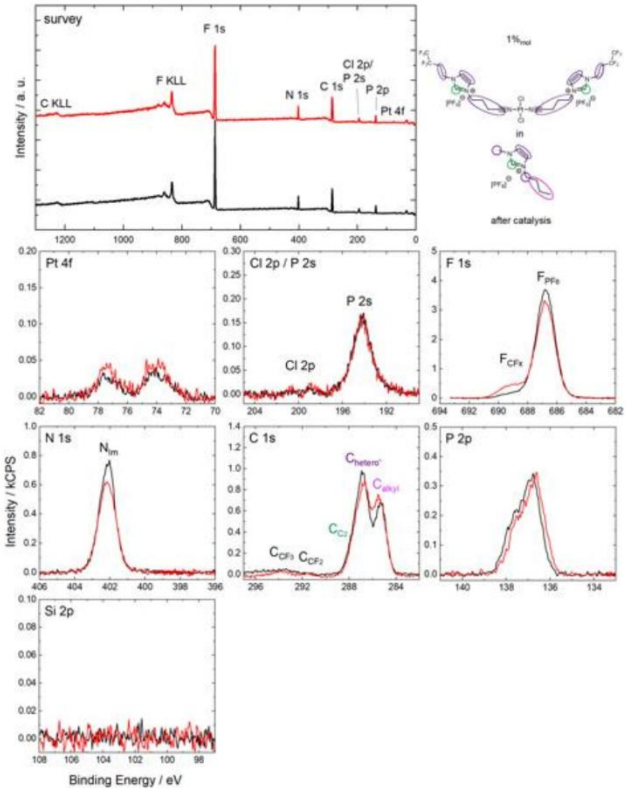

Figure S7. Survey, Pt 4f, Cl 2p/P 2s, F 1s, N 1s, C 1s, P 2p and Si 2p XP spectra of a $1\%_{mol}$ solution of **2** in $[C_4C_1Im][PF_6]$ in 0° (black) and 80° (red) emission recorded at room temperature after the catalytic hydrogenation experiment was conducted.

Due to the low intensity of the C_{CF3} and C_{CF2} signals even in 80°, these signals were not fitted, which contrasts with the spectra recorded before the catalysis experiment (see Figure S6).

Furthermore, background subtraction of the Cl 2p region was achieved using a three-point linear background instead of the usual two-point background procedure due to unrealistic broadening of the Cl 2p signals.

The complete set of XP spectra of a 1 mol% solution of **1** in $[C_4C_1Im][PF_6]$ at room temperature **before** conducting the hydrogenation experiment is shown in Figure S8.

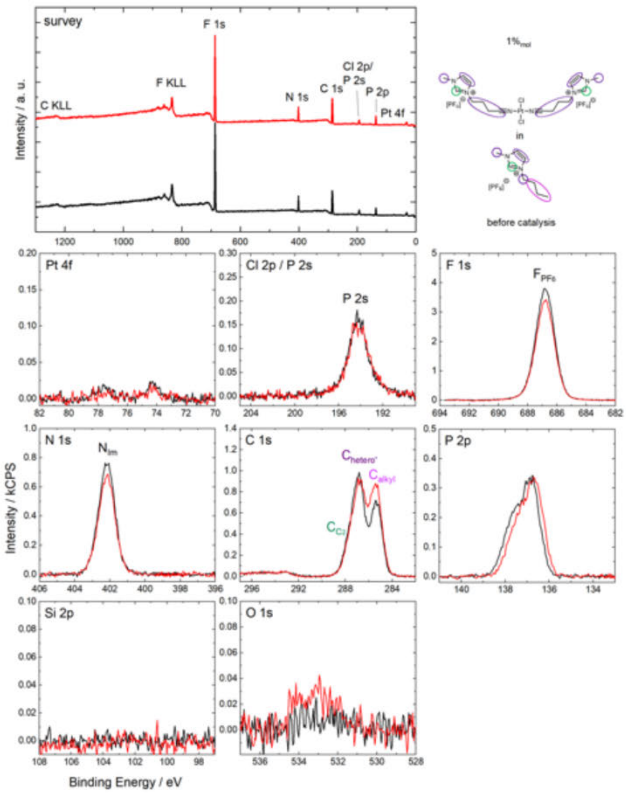

Figure S8. Survey, Pt 4f, Cl 2p/P 2s, F 1s, N 1s, C 1s, P 2p, Si 2p and O 1s XP spectra of a $1\%_{mol}$ solution of **1** in $[C_4C_1Im][PF_6]$ in 0° (black) and 80° (red) emission recorded at room temperature before the catalytic hydrogenation experiment was conducted.

Finally, the complete set of XP spectra of a 1 mol% solution of **1** in $[C_4C_1Im][PF_6]$ at room temperature after conducting the hydrogenation experiment is shown in Figure S9.

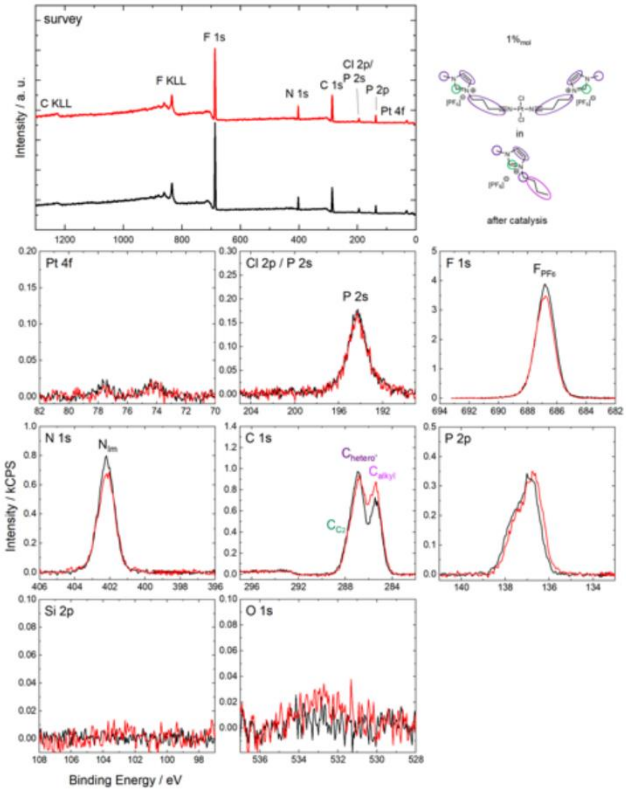

Figure S9. Survey, Pt 4f, Cl 2p/P 2s, F 1s, N 1s, C 1s, P 2p, Si 2p and O 1s XP spectra of a $1\%_{mol}$ solution of **1** in $[C_4C_1Im][PF_6]$ in 0° (black) and 80° (red) emission recorded at room temperature after the catalytic hydrogenation experiment was conducted.

Table S2. Quantitative analysis of XPS core level spectra of 1%mol solutions of 1 and 2 in [C4C1Im][PF6] before and after conducting catalytic hydrogenation of ethene. *For the spin-orbit-split signals, the indicated binding energy values correspond to larger peak, that is, Pt 4f7/2, Cl 2p3/2 and P 2p3/2.

a) $1\%_{mol}$ 2 in $[C_4C_1Im][PF_6]$ before catalysis	Pt 4f*	Cl 2p*	F 1s CFx	F 1s PF_6	N 1s Im	N 1s CNcoord	C 1s CF_3	C 1s CF_2	C 1s C_2	C 1s hetero′	C 1s alkyl	P 2p*
Binding Energy / eV	74.2	199.1	688.8	686.8	402.2		293.9 (80°)	291.6 (80°)	287.7	286.8	285.3	136.8
Nominal	0.010	0.020	0.10	6.1	2.0	0.020	0.020	0.020	1.0	4.2	3.0	1.0
Experimental, 0°	0.037	0.077	0.77	5.9	2.0				1.0	4.1	2.6	1.1
Experimental, 80°	0.050	0.084	1.8	4.9	1.7		0.33	0.33	0.84	3.9	2.7	0.95
b) $1\%_{mol}$ 2 in $[C_4C_1Im][PF_6]$ after catalysis												
Binding Energy / eV	74.0	199.0	688.7	686.8	402.1				287.7	286.8	285.3	136.8
Nominal	0.010	0.020	0.10	6.1	2.0	0.020	0.020	0.020	1.0	4.2	3.0	1.0
Experimental, 0°	0.21	0.026	0.47	6.1	2.0				0.98	4.1	2.8	1.1
Experimental, 80°	0.30	0.046	1.1	5.4	1.8				0.90	4.1	3.1	1.1
c) $1\%_{mol}$ 1 in $[C_4C_1Im][PF_6]$ before catalysis												
Binding Energy / eV	74.3			686.8	402.2				287.8	286.8	285.3	136.8
Nominal	0.010	0.020		6.1	2.0	0.020			1.0	4.1	3.0	1.0
Experimental, 0°	0.008			6.3	2.0				1.0	4.0	2.9	1.1
Experimental, 80°	0.007			5.7	1.8				0.92	4.1	3.7	1.1
d) $1\%_{mol}$ 1 in $[C_4C_1Im][PF_6]$ after catalysis												
Binding Energy / eV	74.3			686.8	402.2				287.8	286.9	285.4	136.8
Nominal	0.010	0.020		6.1	2.0	0.020			1.0	4.1	3.0	1.0
Experimental, 0°	0.009			6.4	2.0				1.0	4.0	2.8	1.1
Experimental, 80°	0.005			5.9	1.9				0.96	4.0	3.5	1.1

References

[1] Koller, T.M., Lenahan, F.D., Schmidt, P.S. et al. *Int J Thermophys* 41, 144 (2020). https://doi.org/10.1007/s10765-020-02720-w

[2] Hemmeter, D., Paap, U., Wellnhofer, N., Gezmis, A., Kremitzl, D., Wasserscheid ,P., Maier, F., Steinrück, H.-P.,ChemPhysChem, 1439-4235, https://doi.org/10.1002/cphc.202300612

[3] Jacquemin, J., Husson, P., Padua, A. A. H., Majer, V., Green Chem. 2006, 8, 172–180, https://doi.org/10.1039/B513231B

9 Unpublished Results

9.1 Surface Enrichment of a Pt bis(NHC) Complex in IL Solution

A series of measurements on the neutral complex *trans*-[$PtCl_2(C_8PEG_3Im_{NHC})_2$] (**14**) in solution of the polyethylene glycol (PEG)-functionalized ILs [$(PEG_2)_2Im$][I] and [$(PEG_2)_2Im$][PF_6] conducted within the framework of this thesis was not published yet and will be presented in the following. The molecular structures with assignment of carbon species to XPS signals and molecular weights of **14** and the ILs are shown in *Figure 20*.

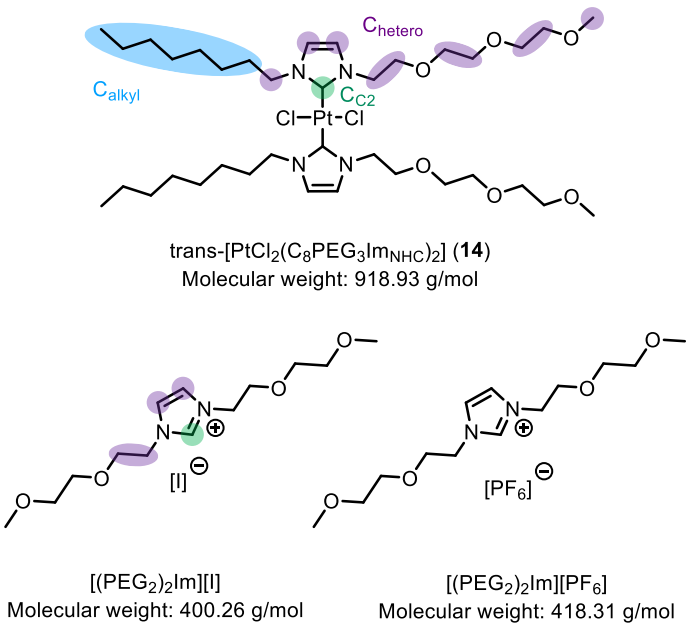

Figure 20: Molecular structures and molecular weights of *trans*-[$PtCl_2(C_8PEG_3Im_{NHC})_2$] (**14**) (top), [$(PEG_2)_2Im$][I] (bottom left) and [$(PEG_2)_2Im$][$PF_6$] (bottom right).

14 comprises two NHC ligands carrying a C_8 chain with the intention to induce surface enrichment, similar to the C_9 chains in **8** presented in *Chapter 4.1.2*, as well as a PEG_3 chain to ensure satisfying solubilities in PEG-functionalized ILs. PEG-ILs have attracted significant attention as solvents and electrolytes in the recent past[90, 149-151]. It has been shown that incorporating ester and ther functionalities into the molecular structure of ILs can result in an enhanced biodegradability and lower toxicity[152, 153], as well as interesting physiochemical properties, such as relatively low viscosities[153, 154]. PEG-ILs, including [$(PEG_2)_2Im$][I], which will be used as a solvent herein, have been object of recent ARXPS and PD investigations in our group.[90, 98] These studies revealed a preferential termination

of the IL/vacuum interface with the PEG-functionalized chains in the neat ILs.[90, 98] In a mixture with [C_8C_1Im][PF_6], [(PEG_2)$_2$Im][I] was strongly depleted from the IL/vacuum interface owing to the much higher surface tension of 46.7 mN/m at room temperature compared to 34.2 mN/m for [C_8C_1Im][PF_6].[98] Also, other ether-functionalized ILs were successfully characterized using XPS.[97, 155]

14 was synthesized by Alexander Bergen (Chair of Inorganic and General Chemistry, FAU Erlangen-Nürnberg) and [(PEG_2)$_2$Im][I] and [(PEG_2)$_2$Im][PF_6] were synthesized by Vera Seidl and Junyu Chu (both Chair of Inorganic and General Chemistry, FAU Erlangen-Nürnberg), respectively. Since the ILs showed significant amounts of a surface-active hydrocarbon-containing contamination, evident from an unexpected C_{alkyl} signal found in ARXPS analyses of the neat ILs, which increased at 80° (not shown), the ILs were cleaned by extraction using a 1:1 mixture of pentane/toluene (for [(PEG_2)$_2$Im][PF_6], conducted by Dr. Jade Barreto, Chair of Physical Chemistry II, FAU Erlangen-Nürnberg), similar to the procedure applied for [C_2C_1Im][PF_6] (see *Chapter 3*) reported in [P6]. By means of this procedure, the presence of the surface-active contamination was reduced to an extent, where for [(PEG_2)$_2$Im][I] no significant C_{alkyl} signal was found and for [(PEG_2)$_2$Im][PF_6] only a minor C_{alkyl} signal was detected (not shown), which is not expected to qualitatively affect the findings observed and discussed in the following.

Owing to slight overall differences in binding energy between the XP spectra of the different solutions and ILs shown in the following, the spectra were referenced to the O 1s signal of the PEG chains at 538.2 eV, which agrees with the reported literature value.[90, 98] The 80° spectra were referenced to the N_{Im} signal at 0°; 80° and 0° spectra of Pt 4f and Cl 2p signals were aligned (see *Chapter 3*). For fitting of the C 1s region, the peak area of C_{hetero} was constraint according to the nominal C_{C2}:C_{hetero} ratio, that is, 1:12, the FWHM of C_{hetero} and C_{alkyl} was constraint using a factor of 1.1 and 1.0 to the value of C_{C2} and the position of C_{hetero} was set to a value 0.9 eV lower than C_{C2}, which is the typical procedure applied in this thesis. Furthermore, the FWHM values of N_{Im} and N_{NHC} were set to equal values.

Pt 4f, N 1s, C 1s and I $3d_{5/2}$ XP spectra of a 1%$_{mol}$ solution of **14** in [(PEG_2)$_2$Im][I] (exact concentration: 1.00%$_{mol}$) are depicted in *Figure 21a*, and the quantitative analysis of the spectra is shown in *Table 4a*. For comparison and better identification of the complex-

related signals, also the respective XP spectra of neat [(PEG$_2$)$_2$Im][I] are depicted in *Figure 21b*. The spin-orbit-resolved Pt 4f peaks were detected at 76.1 and 72.7 eV. In the N 1s region, the major N_{Im} signal was detected at 401.7 eV accompanied with a clearly discernible low-binding energy shoulder at 400.6 eV corresponding to the N atoms of the NHC ligands, N_{NHC}. The Pt:N_{NHC} ratio of 1.0:4.3 at 0° was in good agreement with the nominal composition of **14**, confirming the coordination of the two NHC ligands to the metal center in solution of the IL. The C 1s region was again deconvoluted with the three peaks, as discussed in *Chapter 2.2*: C_{C2} atoms of the IL and the coordinated C_{C2} atoms of the NHC ligands were treated as a joint signal, $C_{C2/NHC}$, at 287.3 eV, the C_{hetero} atoms from **14** and the IL yielded a peak at 286.4 eV and the C_{alkyl} signal only corresponding to the alkyl chains in **14** was detected at 285.0 eV.

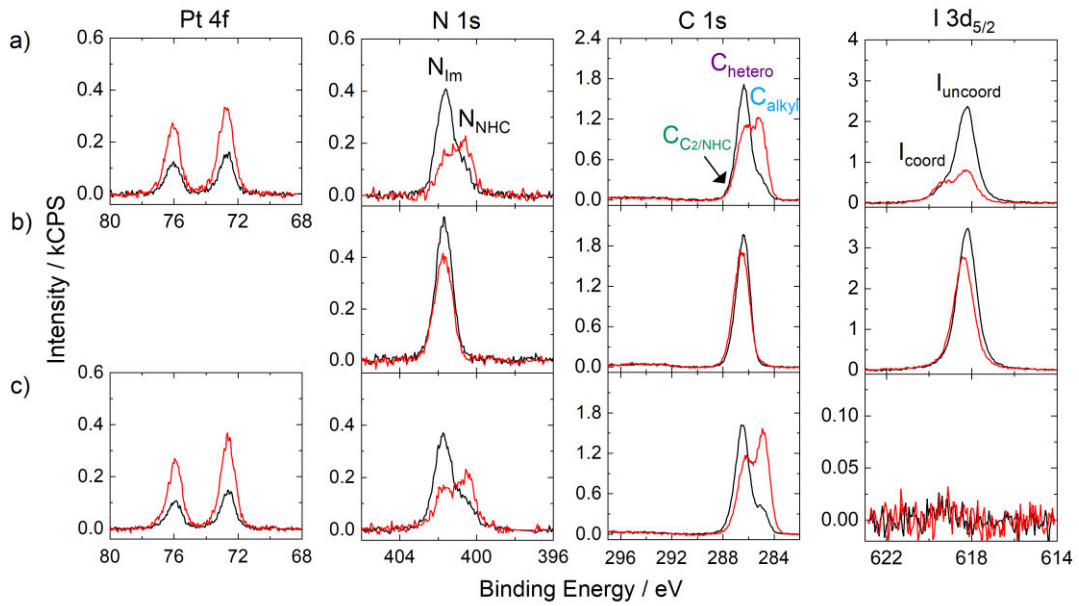

Figure 21: Pt 4f, N 1s, C 1s and I 3d$_{5/2}$ XP spectra of 1%$_{mol}$ solutions of **14** in a) [(PEG$_2$)$_2$Im][I] and c) in [(PEG$_2$)$_2$Im][PF$_6$], b) N 1s, C 1s, I 3d$_{5/2}$ XP spectra of neat [(PEG$_2$)$_2$Im][I] in 0° (black) and 80° emission (red).

Unexpectedly, the I 3d$_{5/2}$ region showed two species, that is, a high-binding energy shoulder at 619.4 eV, I_{coord}, besides the major peak at 618.2 eV, $I_{uncoord}$. The latter signal corresponded to the free I^- anions of the IL, as is evident from the spectrum of neat [(PEG$_2$)$_2$Im][I] provided in *Figure 21b*, which only showed the signal at 618.2 eV. The presence of the I_{coord} signal found for the solution of **14** indicated coordination of at least a fraction of the I^- anions to the Pt center, possibly substituting a Cl ligand. In fact, from the XP spectra a Pt:Cl ratio of only 1.0:1.3 was derived at 0°, indicating a deficiency of Cl

ligands in the near-surface region. It is essential to note, however, that NMR studies (conducted by Alexander Bergen, Chair of Inorganic and General Chemistry, FAU Erlangen-Nürnberg) have revealed a second Pt-containing species differing from the stoichiometry of **14**, which was not identified using ARXPS but might influence the Pt:Cl ratio. Synthesis of a batch without this second Pt species resulted in a Pt:Cl ratio only slightly below the nominal 1:2 ratio (not shown); this batch, however, contained a surface-active Si contamination limiting the expressiveness of the spectra for discussion of the surface composition. As is shown in *Figure 21c*, no I $3d_{5/2}$ was detected from an equimolar solution of **14** in $[(PEG_2)_2Im][PF_6]$ (exact concentration: 0.97%$_{mol}$, solution prepared and XP spectra acquired by Dr. Jade Barreto, Chair of Physical Chemistry II, FAU Erlangen-Nürnberg), which excluded that the I_{coord} peak was due to a contamination from synthesis.

As is evident from the quantitative analysis of the 0° spectra of **14** in $[(PEG_2)_2Im][I]$ presented in *Table 4a*, the complex-specific Pt 4f, Cl 2p, N_{NHC} and C_{alkyl} signals showed much higher intensities than expected from the nominal composition of the solution (0.088 vs 0.010 for Pt and 1.7 vs 0.14 for C_{alkyl}). On the contrary, the C_{C2}, C_{hetero} and O 1s signals, which originate from both **14** and the IL showed values close to the nominal ones or slightly lower, and the solvent-specific N_{Im} signal was detected with much lower intensity compared to the nominal value (1.5 vs 2.0). These observations were assigned to strong accumulation of **14** at the IL/vacuum interface. At 80°, the complex-specific Pt 4f, Cl 2p and N_{NHC} signals showed a strong rise by more than a factor of 2, while the C_{alkyl} signal exhibited an even much more pronounced increase of more than a factor of 4. Consequently, the IL/vacuum interface is preferentially populated with the C_8 chains, while the Pt-bis(NHC) moiety and the PEG_3 chains are located more distant from the surface. In compliance with the strong surface enrichment of **14**, all other signals, in particular, the IL-specific N_{Im} peak showed a strong decline at 80°, which largely exceeded the decline observed in the neat IL spectra depicted in *Figure 21b*. The solution of **14** in $[(PEG_2)_2Im][PF_6]$ yielded almost identical XP spectra as found for the solution of $[(PEG_2)_2Im][I]$, as is evident from comparing Figures *21a* and *21c*, confirming a similar degree of surface enrichment (see also *Table 4c*). Overall, the results obtained for the solutions of **14** in the PEG-functionalized ILs nicely agreed with the interfacial behavior of **8** in $[C_2C_1Im][OAc]$, revealing the applicability of the buoy effect of long alkyl chains also for the neutral complex **14**.

Table 4: Quantitative analysis of XPS core level spectra of a) 1%$_{mol}$ **14** in [(PEG$_2$)$_2$Im][I], b) neat [(PEG$_2$)$_2$Im][I] and c) 1%$_{mol}$ **14** in [(PEG$_2$)$_2$Im][PF$_6$]. For spin-orbit-split signals, the indicated binding energy values correspond to larger peak, that is, Pt 4f$_{7/2}$, Cl 2p$_{3/2}$, I 3d$_{5/2}$ and P 2p$_{3/2}$.

a) 1%$_{mol}$ 14 in [(PEG$_2$)$_2$Im][I] (exact conc.: 1.00%$_{mol}$)	**Pt 4f**	**Cl 2p**	**N$_{Im}$**	**N$_{NHC}$**	**C$_{C2/NHC}$**	**C$_{hetero}$**	**C$_{alkyl}$**	**O 1s**	**I 3d$_{5/2}$ coord**	**I 3d$_{5/2}$ uncoord**
Binding Energy / eV	72.7	198.4	401.7	400.6	287.3	286.4	285.0	532.8	619.4	618.2
Nominal	0.010	0.020	2.0	0.040	1.0	12.2	0.14	4.1	0	1.0
Experimental, 0°	0.088	0.11	1.5	0.37	0.92	11.1	1.7	3.9	0.12	0.67
Experimental, 80°	0.20	0.24	0.55	0.75	0.63	7.6	7.6	2.6	0.16	0.22
b) neat [(PEG$_2$)$_2$Im][I]										
Binding Energy / eV			401.7		287.3	286.4		532.8		618.2
Nominal			2.0		1.0	12		4.0		1.0
Experimental, 0°			1.9		1.0	11.9		4.2		1.0
Experimental, 80°			1.5		1.0	12.1		4.6		0.79
c) 1%$_{mol}$ 14 in [(PEG$_2$)$_2$Im][PF$_6$] (exact conc.: 0.97%$_{mol}$)	**Pt 4f**	**Cl 2p**	**N$_{Im}$**	**N$_{NHC}$**	**C$_{C2}$**	**C$_{hetero}$**	**C$_{alkyl}$**	**O 1s**	**F 1s**	**P 2p**
Binding Energy / eV	72.6	198.2	401.8	400.5	287.4	286.5	284.9	532.8	686.5	136.3
Nominal	0.010	0.020	2.0	0.039	1.0	12.2	0.14	4.1	6.0	1.0
Experimental, 0°	0.080	0.14	1.5	0.42	0.92	11.0	2.4	5.3	4.0	0.79
Experimental, 80°	0.20	0.35	0.63	0.85	0.68	8.2	10.0	3.6	1.6	0.41